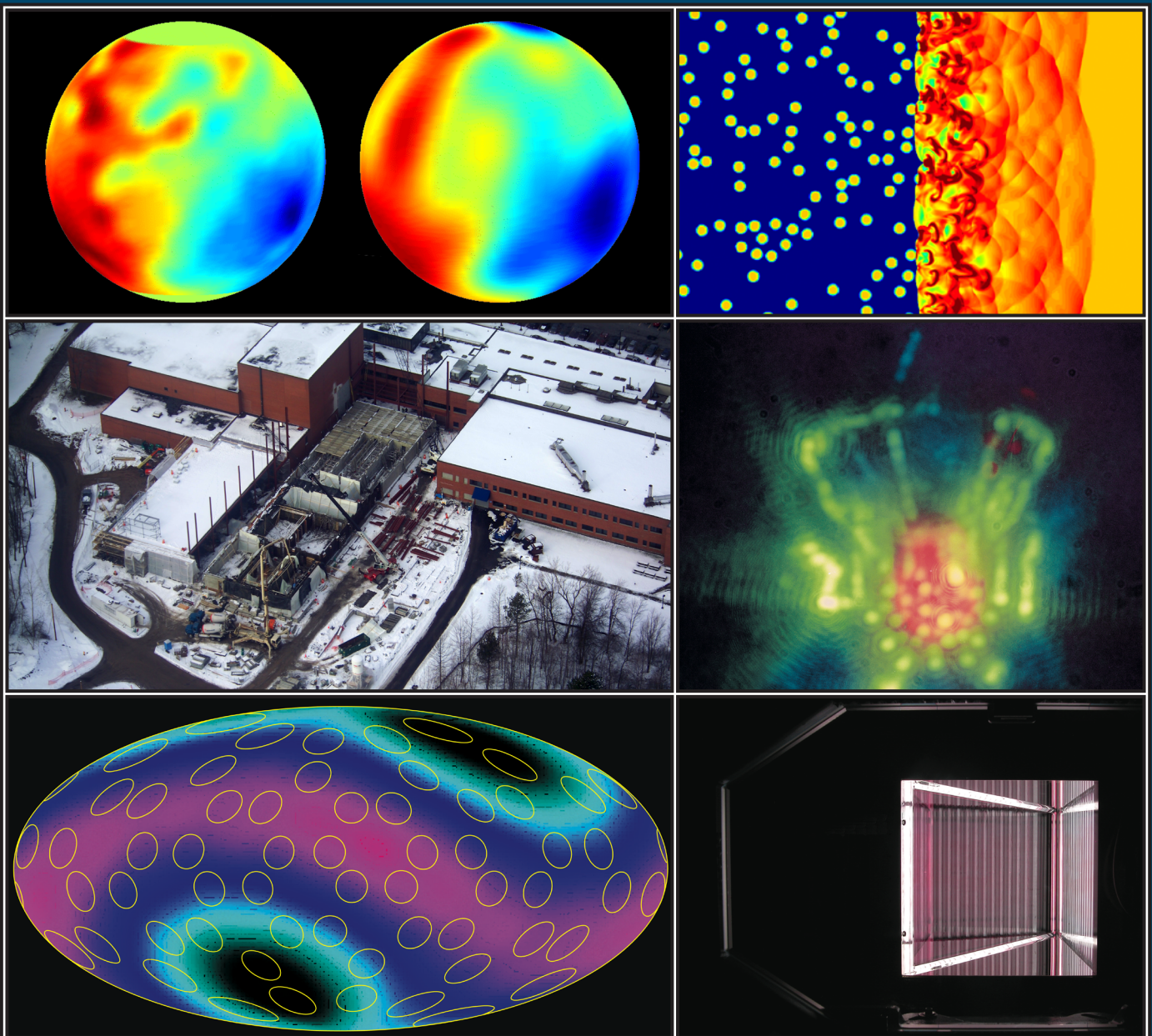


LLE 2003 Annual Report

October 2002 – September 2003



Cover Photos

Upper Left: *Cryogenic Target Characterization*. Thirty-one cryogenic targets were produced, characterized, and shot on OMEGA in 2003. The characterization is based on shadowgraphy. Software tools were created at LLE to analyze the data and determine the capsule surface and ice-thickness variations. The two color-coded images shown in this figure are three-dimensional views of the ice-layer variations of a cryogenic capsule. These images were obtained by analyzing as many as 30 shadowgrams taken from different directions.

Middle Left: *OMEGA EP Construction*. An aerial view of the construction of the addition to the LLE building. The OMEGA EP (Extended Performance) project began in 2003.

Lower Left: *Direct-Drive Symmetry Control*. The OMEGA laser is designed to achieve a high degree of uniformity and flexibility in target irradiation. The ability to impose a controlled (nonsymmetric) on-target irradiation pattern is useful for benchmarking multidimensional hydrodynamic simulations and simulating direct-drive irradiation patterns that may be attained on the NIF. The image depicts an Aitoff projection showing the measured intensity pattern on a spherical target in an experiment in which the polar intensity on target was intentionally reduced from the average intensity by 15% to 30%.

Upper Right: *Wetted-Foam Targets*. Direct-drive capsule designs with “wetted-foam” ablaters offer the potential of a substantial target gain on the NIF. The image shows the density profile of a shock moving through a DT-wetted foam layer as calculated using adaptive-mesh-refinement simulations carried out by scientists from LLE and the University of Rochester’s Department of Physics.

Middle Right: *Fast Ignition Research*. Time-integrated photograph of an imploding direct-drive cone target used to test elements of the “fast-ignition” approach to ICF on OMEGA.

Lower Right: *OMEGA EP Amplifier*. Photograph of the prototype OMEGA EP amplifier module undergoing a pulsed-ionization lamp check. The amplifier is shown through the end of a single-disk module.

Prepared for
U.S. Department of Energy
San Francisco Operations Office
DOE/SF/19460-510

Distribution Category UC712
October 2002–September 2003

Printed in the United States of America
Available from

National Technical Information Services
U.S. Department of Commerce
5285 Port Royal Road
Springfield, VA 22161

Price codes: Printed Copy A13
Microfiche A01

This report was prepared as an account of work conducted by the Laboratory for Laser Energetics and sponsored by New York State Energy Research and Development Authority, the University of Rochester, the U.S. Department of Energy, and other agencies. Neither the above named sponsors, nor any of their employees, makes any warranty, expressed or implied, or assumes any legal liability or responsibility for the accuracy, completeness, or usefulness of any information, apparatus, product, or process disclosed, or represents that its use would not infringe privately owned rights. Reference herein to any specific commercial product, process, or service by trade name, mark, manufacturer, or otherwise, does not necessarily constitute or imply its endorsement, recommendation, or favoring by the United States Government or any agency thereof or any other sponsor. Results reported in the LLE Review should not be taken as necessarily final results as they represent active research. The views and opinions of authors expressed herein do not necessarily state or reflect those of any of the above sponsoring entities.

The work described in this volume includes current research at the Laboratory for Laser Energetics, which is supported by New York State Energy Research and Development Authority, the University of Rochester, the U.S. Department of Energy Office of Inertial Confinement Fusion under Cooperative Agreement No. DE-FC03-92SF19460, and other agencies.

For questions or comments, contact Laboratory for Laser Energetics, 250 East River Road, Rochester, NY 14623-1299, (585) 275-5286.
Worldwide-Web Home Page: <http://www.lle.rochester.edu/>

University of Rochester
Laboratory for Laser Energetics

DOE/SF/19460-510
January 2004

LLE 2003 Annual Report

October 2002 – September 2003



**Inertial Fusion Program and
National Laser Users' Facility Program**

Contents

| | |
|--|-----|
| Executive Summary | v |
| Direct-Drive Cryogenic Target Implosion Performance on OMEGA | 1 |
| Hydrodynamic Growth of Shell Modulations in the Deceleration Phase of Spherical Direct-Drive Implosions | 11 |
| Improved Performance of Direct-Drive ICF Target Designs with Adiabatic Shaping Using an Intensity Picket | 18 |
| High-Conversion-Efficiency Optical Parametric Chirped-Pulse Amplification System Using Spatiotemporally Shaped Pump Pulses | 33 |
| Ultrafast Superconducting Single-Photon Optical Detectors and Their Applications | 38 |
| Very Fast Metal–Semiconductor–Metal Ultraviolet Photodiodes on GaN with Submicron Finger Width | 46 |
| Glassy Liquid Crystals for Tunable Reflective Coloration | 50 |
| High-Resolution Near-Field Raman Microscopy of Single-Walled Carbon Nanotubes | 61 |
| Optimization of Deposition Uniformity for Large-Aperture NIF Substrates in a Planetary Rotation System | 67 |
| Multibeam Effects on Fast-Electron Generation from Two-Plasmon-Decay Instability | 76 |
| On the Bell–Plesset Effects: The Effects of Uniform Compression and Geometrical Convergence on the Classical Rayleigh–Taylor Instability | 81 |
| Laser-Induced Adiabatic Shaping by Relaxation in Inertial Confinement Fusion Implosions | 91 |
| Demonstration of a Room-Temperature Single-Photon Source for Quantum Information: Single-Dye-Molecule Fluorescence in a Cholesteric Liquid Crystal Host | 97 |
| EXAFS Measurements of Laser-Generated Shocks with an Imploded Target as a Radiation Source | 107 |
| Modeling Temperature and Pressure Gradients During Cooling of Thin-Walled Cryogenic Targets | 118 |
| Development of an Elementary Climate Model: Two-Layer Cellular Case | 128 |

| | |
|--|-----|
| Reduction of the Ablative Rayleigh–Taylor Growth Rate with Gaussian Picket Pulses | 139 |
| Theory of Laser-Induced Adiabatic Shaping in Inertial Fusion Implosions: The Decaying Shock | 147 |
| Design of a Highly Stable, High-Conversion-Efficiency, Optical Parametric Chirped-Pulse Amplification System with Good Beam Quality | 167 |
| Nonlinear Propagation of Laser Beams near the Critical-Density Surface in the Plasmas of Direct-Drive Targets | 179 |
| Time-Resolved Photoresponse in the Resistive Flux-Flow State in Y-Ba-Cu-O Superconducting Microbridges | 186 |
| Ultrafast and Highly Sensitive Photodetectors Fabricated on High-Energy- Nitrogen–Implanted GaAs | 192 |
| Tritiated Amorphous Silicon Betavoltaic Devices | 196 |
| The Coherent Addition of Gratings for Pulse Compression in High-Energy Laser Systems | 207 |
| Polar Direct Drive on the National Ignition Facility | 212 |
| Properties of Fluid Deuterium Under Double-Shock Compression to Several Megabars | 220 |
| Independent Phase and Amplitude Control of a Laser Beam Using a Single-Phase-Only Spatial Light Modulator | 225 |
| Proton Temporal Diagnostic for ICF Experiments on OMEGA | 230 |
| Polishing PMMA and Other Optical Polymers with Magnetorheological Finishing | 239 |
| LLE’s Summer High School Research Program | 250 |
| FY03 Laser Facility Report | 252 |
| National Laser Users’ Facility and External Users’ Programs | 254 |
| Publications and Conference Presentations | 287 |

Executive Summary

The fiscal year ending September 2003 concluded the first year of the second five-year renewal of cooperative agreement DE-FC03-92SF19460 with the U.S. Department of Energy (DOE). This report summarizes research at the Laboratory for Laser Energetics (LLE) conducted during the year, the operation of the National Laser Users' Facility (NLUF), the status of the new OMEGA Extended Performance (EP) laser project, and programs concerning the education of high school, undergraduate, and graduate students during the year.

Progress in Laser Fusion Research

“Direct-Drive Cryogenic Target Implosion Performance on OMEGA” (p. 1) describes progress toward validating the predicted performance of direct-drive capsules that are hydrodynamically equivalent to the baseline direct-drive ignition design for the National Ignition Facility (NIF). These experiments measure the sensitivity of direct-drive implosion performance to parameters such as inner-ice-surface roughness, the adiabat of the cryogenic fuel during the implosion, laser power balance, and single-beam nonuniformity. These capsules have been imploded using ~17 to 23 kJ of 351-nm laser light with a beam-to-beam rms energy imbalance of less than 5% and full beam smoothing (1-THz bandwidth, 2-D smoothing by spectral dispersion, and polarization smoothing). Near 1-D hydrocode performance has been measured with a high-adiabat drive pulse on a capsule containing a 100- μm -thick layer of D_2 ice, and near 2-D hydrocode performance has been measured on a similar capsule with a low-adiabat drive.

The article beginning on p. 11 describes the growth of inner-surface modulations near peak compression in deuterium-helium 3 (D^3He)-filled spherical targets imploded on OMEGA by using differential imaging of titanium-doped layers placed at various distances from the inner surface of the shell. Time histories of shell temperature and density were measured with titanium *K*-shell absorption spectroscopy, and the shell areal density was estimated using 14.7-MeV D^3He proton spectra. These experiments provide a better quantitative understanding of the evolution of inner-shell modulations

that grow due to the Rayleigh–Taylor instability and Bell–Plesset convergence effects in the deceleration phase of a spherical direct-drive implosion.

Improved target performance in direct-drive implosions using adiabat shaping with a high-intensity picket in front of the main-drive pulse is described analytically beginning on p. 18. The picket is used to increase the entropy of only the outer portion of the shell, reducing the growth of hydrodynamic instabilities, while the inner portion of the shell maintains lower entropy to maximize shell compressibility. Experiments have demonstrated an improvement in target yields by a factor of up to 3 for the pulses with the picket compared to the pulses without the picket. Results of the theory and experiments with adiabat shaping are also extended to future OMEGA and NIF cryogenic target designs.

LLE and Lawrence Livermore National Laboratory (LLNL) scientists used multiple OMEGA laser beams to study two-plasmon-decay instability, which is the predominant source of suprathermal electrons in direct-drive inertial confinement fusion experiments (p. 76). The authors show for the first time that the total overlapped intensity governs the scaling of the suprathermal-electron generation regardless of the number of overlapped beams, in contrast to conventional theories that are based on the single-beam approximation.

The classical Rayleigh–Taylor instability of the interface separating two homogeneous inviscid fluid layers undergoing uniform acceleration was examined (p. 81), giving particular attention to the effects of uniform isentropic compression of the fluids and geometrical convergence of the interface and to the role of these effects in the implosion of inertial confinement fusion (ICF) capsules. The formulation presented makes a formal distinction between perturbation behavior under acceleration and perturbation behavior as modified by compression and by convergence of a cylindrical or spherical interface.

The theoretical basis for laser-induced adiabat shaping in ICF spherical targets by a technique referred to as “relaxation” is presented beginning on p. 91. In this approach, the density profile of the capsule’s shell is shaped using a weak prepulse followed by a main pulse with a high-intensity foot. The required laser pulse shape is easier to implement on current laser systems than the alternate technique described in the article. Rayleigh–Taylor growth rates are reduced without significantly degrading 1-D capsule performance.

The properties of compressed titanium are studied (p. 107) using laser-launched shocks and extended x-ray absorption fine structure (EXAFS). The EXAFS absorption spectrum is produced when backlighting a CH-coated Ti foil by the spectrally smooth radiation from a CH shell imploded on the 60-beam OMEGA laser system. Fitting an EXAFS model to the data indicates compression by a factor of 1.3, in agreement with shock-speed measurements and with hydrodynamic simulations. The rate of decay of the modulation with wave number is shown to include a significant contribution from static disorder, in addition to thermal vibration, due possibly to an α -Ti to ω -Ti crystal phase transition.

Filling and cooling thin-walled ($<3\text{-}\mu\text{m}$) cryogenic capsules with deuterium–tritium fuel is a critical phase of operation for providing direct-drive targets. Permeation filling at room temperature to high pressures subjects the capsules to a buckling force. In addition, during cooling to 20 K, buckling and burst forces develop due to transient thermal gradients, thermal expansion differences, and changing permeability of the capsule wall. The article beginning on p. 118, quantifies the forces on the capsule by modeling the thermal conditions inside the permeation cell. Results of cooldown cycles of OMEGA cryogenic targets agreed well with the simulation, and a cooling program was devised whereby the time for a capsule to reach the frozen state was reduced by 30%.

A report on the seminal work to experimentally validate the reduction in the Rayleigh–Taylor (RT) growth rate using a prepulse, or picket, preceding the main laser-drive pulse in planar-target experiments begins on p. 139. The experimental results showed that a high-intensity picket ($\sim 50\%$ of the drive-pulse intensity) significantly reduced the RT growth rate for a $20\text{-}\mu\text{m}$ -wavelength surface perturbation but had no effect on the growth rates of longer-wavelength perturbations (30 and $60\ \mu\text{m}$). Both the 20- and $30\text{-}\mu\text{m}$ -wavelength perturbations showed no appreciable growth rate, however, with a prepulse intensity equal to the drive-pulse intensity. These

results suggest that the acceleration-phase RT growth rates for short-wavelength, laser-induced imprint perturbations may be virtually eliminated in spherical implosions by modifying the drive pulse to include a high-intensity picket on the leading edge. This work will be applied to spherical implosions in the near future.

An in-depth, analytic analysis of laser-induced adiabat shaping in inertial fusion implosions shows that the adiabat profile between the ablation surface and the fuel–shell interface induced by a decaying shock follows a simple power law of the shell areal density (p. 147). Significantly, the calculated profiles are nearly identical to those observed in 1-D hydrodynamic simulations. This similarity suggests that the calculated profiles can be used to quickly and easily design an optimal laser prepulse to maximize the adiabat ratio between the inner- and outer-shell surfaces, leading to improved hydrodynamic stability.

“Polar direct drive (PDD)” — a new topic of research this year — examines (p. 212) the feasibility of using the x-ray-drive beam configuration at the National Ignition Facility (NIF) to achieve direct-drive ignition. The baseline x-ray-drive beam configuration was designed to illuminate a vertically oriented hohlraum with beams arrayed symmetrically around the polar regions of the target chamber. The authors realized that nearly symmetric direct-drive illumination could be achieved by repointing some of the polar beams toward the equator of the capsule and adjusting the beam-spot sizes and energies. The article describes the current status of work focusing, in particular, on beam-pointing strategy. The long-term impact of this work within the national ICF program is potentially of great importance if ignition conditions can be achieved on the NIF using the PDD concept.

In stockpile stewardship–related work, the article beginning on p. 220 provides the latest experimental results on the equation of state (EOS) of hydrogen at pressures of a few megabars, temperatures of a few electron volts, and compressions of up to several times liquid density. A better understanding of the hydrogen EOS is important for the accurate simulation of direct and indirect ignition target designs on the NIF. At present, there are several different models for the hydrogen EOS, and it is exceptionally difficult to measure experimental observables with sufficient accuracy to discriminate among the models. The experimental results reported here are based on a new re-shock technique that is more sensitive to differences between the EOS models.

An important new diagnostic system (described beginning on p. 230) for direct-drive-implosion studies on OMEGA is the proton temporal diagnostic (PTD), which was designed to measure the fusion reaction history in capsule implosions containing D^3He fuel. By measuring the temporal emission history and final energy spectrum of this high-energy proton, it is possible to study the areal-density evolution of the shell during the shock and compressive burn phases of an implosion. Existing range-filter spectrometers routinely measure the high-energy proton spectra from both D_2 and D^3He implosions. This data can now be combined with the temporal emission history of the new PTD to provide new constraints on the multidimensional hydrocodes used to understand implosion performance on OMEGA.

Laser and Optical Materials Research

A high-conversion-efficiency optical parametric chirped-pulse amplification (OPCPA) system using a spatiotemporally shaped pump pulse to maximize the conversion efficiency of the OPCPA process has been demonstrated (p. 33). Highly stable, 5-mJ pulses have been produced at a 5-Hz repetition rate with 29% overall pump-to-signal conversion efficiency. This system is a test bed for a similar OPCPA design that will be used for pulse injection in a short-pulse, petawatt-class laser.

Novel glassy liquid crystals with tunable spectral characteristics have been developed for photonic applications (p. 50). The authors also describe the molecular design of photo-responsive systems that combine reversible spectral tunability with superior fatigue resistance and thermal stability.

The article beginning on p. 67 describes the design and performance of a thin-film-deposition system used to produce multilayer dielectric thin-film coatings with highly uniform thickness over a full NIF aperture. This system meets the NIF specifications.

A number of professors from The Institute of Optics and a scientist from LLE have demonstrated the operation of a single-photon source (p. 97)—a key hardware element of quantum information technologies—via photon antibunching in the fluorescence of single terrylene molecules embedded in a cholesteric liquid crystal host. Planar-aligned cholesteric layers provide a one-dimensional photonic band gap, allowing an enhancement of the source efficiency.

The development and application of a numerical model that systematically investigates the performance of an optical parametric chirped-pulse amplification (OPCPA) system are described beginning on p. 167. The model uses both Gaussian and super-Gaussian spatial and temporal pump laser pulse shapes and includes the effects of pump-signal spatial walk-off and spatiotemporal noise. The results of this numerical investigation show that good energy stability, good beam quality, and high overall conversion efficiency can be obtained by carefully designing the OPCPA configuration and optimizing the spatiotemporal profile of the pump laser.

The nonlinear propagation of light through a plasma (p. 179) near the critical density is examined using a model that includes filamentation, forward stimulated Brillouin scattering (SBS), backward SBS, the reflection of light from the critical-density surface, and the absorption of light. Because the model incorporates nonparaxial propagation of light, it can describe the reflection of light from the critical-density surface and the propagation of crossing laser beams. The model successfully describes experimentally observed features of scattered light and is well suited to describe the oblique incidence of laser beams on a critical-density surface.

Conventional magnetorheological finishing (MRF) techniques have been used (p. 239) to improve the surface finish and figure of several standard polymer optics. Since these optics are generally soft with high linear expansion coefficients and poor thermal conductivities, they are typically used as manufactured even though, in some instances, it would be desirable to have much better surface finishes. In this article, the authors show that the rms surface roughness of four different optical polymers can be reduced significantly using MRF.

The conceptual development and experimental demonstration of the coherent summation of multiple gratings to form a larger grating are described beginning on p. 207. The most-promising reflection-grating technology for short-pulse, high-energy petawatt-class laser systems utilizing chirped-pulse amplification (CPA) is a holographically formed grating combined with a multilayer dielectric (MLD) coating. The aperture size and damage threshold of such gratings determine the ultimate short-pulse energy capability of these laser systems. Current state-of-the-art gratings would limit a laser such as OMEGA EP to an energy of less than 1 kJ per beam. While it may be possible in the future to manufacture very large gratings, tiling the MLD gratings available today represents

an extremely attractive alternative for the OMEGA EP. The key result presented in this article is the conclusive demonstration of subpicosecond pulse compression using tiled gratings. This is truly an enabling technology for the high-energy, short-pulse lasers planned for the coming decade.

A method has been developed that will modulate both the phase and amplitude of a laser beam with a single-phase-only spatial light modulator (SLM) using a carrier spatial frequency and a spatial filter (p. 225). With this technique, the authors show that dynamic corrections to a laser-beam profile are possible.

Advanced Technology

A new class of ultrafast, superconducting single-photon detectors for counting both visible and infrared photons is examined beginning on p. 38. The detection mechanism is based on photon-induced hotspot formation, which forces supercurrent redistribution and leads to the appearance of a transient resistive barrier across an ultrathin, submicrometer-width, superconducting stripe. Applications for these devices range from noncontact testing of semiconductor CMOS VLSI circuits to free-space quantum cryptography and communications.

New detectors have been used to measure the temporal response characteristics of fast metal–semiconductor–metal ultraviolet photodiodes fabricated on GaN with finger width and pitch ranging from 0.3 μm to 5 μm (p. 46). These detectors are attractive because they are relatively easy to fabricate and have no response in the visible region of the spectrum. A temporal response of less than 26 ps at low illumination is observed.

Near-field Raman spectroscopy and imaging of single-walled carbon nanotubes (SWNT) with unprecedented spatial resolution of less than 30 nm are presented beginning on p. 61. This high-resolution capability is applied to resolve local variations in the Raman spectrum along a single SWNT that would be hidden in far-field measurements.

The ultrafast voltage transients in optically thick YBCO superconducting microbridges driven into the resistive flux state by nanosecond-wide supercritical current pulses and synchronously excited by femtosecond optical pulses have been investigated (p. 186). Using a flexible experimental setup, the authors are able to describe the dynamics of the YBCO photoresponse and demonstrate that a YBCO super-

conductor in the flux-flow state can operate as a GHz-rate, high-power, optically triggered switch for microwave-based telecommunication applications.

Ultrafast photodetectors fabricated on high-energy-nitrogen–implanted gallium-arsenide (GaAs) have been tested (p. 192). By direct comparison these novel photodetectors have been shown to be significantly more sensitive than commercially available low-temperature GaAs photodevices used extensively for high-speed applications.

Tritiated amorphous silicon (a-Si:T) devices have been developed (p. 196). By incorporating tritium—the radioactive isotope of hydrogen—into standard hydrogenated amorphous silicon (a-Si:H) devices, it may be possible to establish a new family of devices in which the energy output of the tritium decay is integrated with the optoelectronic properties of a-Si:H (e.g., photovoltaics and active matrix displays). This article describes the fabrication process and shows unequivocally that tritium bonds stably in amorphous silicon.

A qualitative understanding of the greenhouse effect has long been available through models based on globally and time-averaged quantities. University of Rochester Physics Department faculty and LLE scientists have examined a simple 864-cell climatological model that reproduces yearly average temperatures obtained earlier from one of these global models and predicts a locally distributed nonradiative flux when observed temperatures are employed as input data (p. 128). The model emphasizes vertical radiative energy transport within each cell and is a useful stepping stone for learning about radiative energy transfer into and out of Earth's atmosphere.

Status and Progress on the OMEGA EP Project

The OMEGA EP (Extended Performance) Project began on 1 April 2003 with \$13 million FY03 funding. The National Nuclear Security Administration's (NNSA's) approval of Mission Need followed in May 2003. The University of Rochester authorized funding for an 82,000-sq-ft addition to LLE adjacent to the OMEGA laser to house the new laser beams. The building construction began in August 2003 and will be completed in January 2005. In September 2003, NNSA elected to proceed with the design and construction of the first two beams of the EP system. NNSA also authorized starting a selection of long-lead material procurements, which has led to the completion of the designs and solicitation packages for several key elements. As an example, the large vacuum vessel

that will hold the diffraction-grating compression system will be procured in advance of the building's completion. This 70-ft-long vessel will be installed during the building construction to sequence it correctly prior to the activation of the facility's clean room systems.

OMEGA EP will couple short-pulse laser technology with the 60-beam compression facility by the end of FY07. Since the early 1990s when OMEGA was constructed, progress in laser technology has included the development of high-power, high-energy laser systems using chirped-pulse amplification (CPA) and the NIF multipass architecture. Incorporating these new technologies will modernize OMEGA and significantly expand the range of high-energy-density (HED) physics experiments carried out during the second half of this decade and beyond. The primary system requirement to meet mission need is the addition of two short-pulse (1- to 100-ps), high-power, high-energy beams to OMEGA with greater than 2 kJ per beam, motivated by two specific needs:

- To provide OMEGA with a short-pulse, high-energy back-lighting capability for new HED physics experiments under conditions that also allow the development of backlighting techniques for the NIF; and
- To carry out integrated fast-ignition experiments on OMEGA using its unique cryogenic target implosion capability.

The system that is currently being designed meets the Mission Need Requirements and in a later phase of the project can, for a modest incremental cost, significantly extend the HED physics possibilities. The primary design consists of two NIF-like laser beamlines, with a pulse compression chamber, and relies heavily on proven CPA and NIF technology and LLE's engineering design capability. An auxiliary target chamber, funded through a grant from New York State, will be incorporated, and, later in the program, two additional long-pulse beamlines will be added, subject to available funding. The first two beams will use CPA to provide high-energy short pulses that can be routed into either the OMEGA or the auxiliary OMEGA EP target chamber. Later, all four beams can be operated in long-pulse mode (1 to 10 ns) with 20 kJ (minimum) of UV energy into the OMEGA EP target chamber. This flexibility significantly extends the HED physics capabilities of OMEGA, maintaining LLE's ability to perform forefront HED science.

National Laser Users' Facility and External Users' Programs

During FY03, the number of target shots dedicated to external users of OMEGA continued to increase as 733 target shots were provided. This represents 53% of the total target shots produced by the laser in the last year. External users' experiments were carried out by collaborative teams under the National Laser Users' Facility (NLUF) Program as well as by teams led by scientists from Lawrence Livermore National Laboratory (LLNL), Los Alamos National Laboratory (LANL), Sandia National Laboratory (SNL), and the Commissariat à l'Énergie Atomique (CEA) of France. Some of these collaborations included participants from AWE in the United Kingdom and other universities in the U.S. and U.K.

Seven of the nine NLUF programs approved in the last NLUF Review carried out a total of 123 target shots on OMEGA in FY03, and included experiments in the following areas: collapsing radiative shocks and compressible nonlinear hydrodynamics of importance to the study of various astrophysical phenomena; optical mixing controlled stimulated scattering instabilities; time evolution of capsule ρR and proton emission imaging of compressed cores; laboratory simulations of the interaction of supernova blast waves with interstellar clouds; dynamic properties of shock-compressed single crystals; laboratory simulations of planetary core conditions; and spatially and temporally resolved temperature and density measurements of the compressed cores of indirectly driven capsules.

Collaborative teams led by LLNL scientists carried out 390 target shots on OMEGA for ICF and high-energy-density sciences (HEDS) experiments, including diagnostic development for the NIF; x-ray scattering measurements on near-solid-density plasmas; x-ray conversion efficiency optimization using "cocktail" hohlraums; planar and spherically converging Rayleigh–Taylor instability measurements; laser–plasma interaction; development of techniques for measuring material properties at substantial pressures; preparation of NIF early-light (NEL) experiments; equation of state (EOS) of various materials; development of high-temperature hohlraums; double-shell capsules; propagation of radiation through low-density materials; and development of direct-drive configurations to create a dynamic hohlraum.

LANL scientists led collaborative teams in carrying out 158 target shots on OMEGA in the following areas:

Richtmyer–Meshkov instability (RMI) in convergent compressible, miscible plasma systems; asymmetric direct-drive implosions; neutron diagnostic development; double-shell-target implosions; supersonic jet experiments; x-ray backlighting development; studies of time-dependent mix in direct-drive targets; x-ray radiography development for ICF, HEDP and AGEX experiments; and shock propagation properties of beryllium ablaters.

SNL scientists carried out 30 OMEGA target experiments to investigate ICF ablator x-ray burnthrough, shock propagation, and preheat issues associated with indirect-drive ablaters.

A total of 32 OMEGA target shots were taken by CEA scientists for experiments in neutron diagnostic development and laser–matter interaction physics.

The impact of experiments conducted on OMEGA by the ICF and high-energy-density physics community has steadily increased over the years. For example, approximately 27% of the total ICF/HED papers presented at the recent 45th Annual Meeting of the American Physical Society (APS) Division of Plasma Physics were based on work carried out on OMEGA by national laboratories, NLUF, and LLE scientists.

Significantly, OMEGA-related work dominated the ICF/HED invited papers given at the conference by accounting for 53% of these papers. These invited papers reported on some of the most important new work in the field, including implosions of cryogenic direct-drive capsules; measurements and simulations of mix in convergent geometries; high-gain, direct-drive targets; NIF direct-drive targets; ICF diagnostics; shock timing; laser–plasma interactions; shock compression; and other key aspects of ICF and HED.

The OMEGA-related invited papers presented at the APS meeting are listed below.

| Presenter | Affiliation | Title |
|-------------------|------------------------|--|
| R. P. Drake | University of Michigan | Progress in Experimental Astrophysics at High-Energy Density |
| J. A. Frenje | MIT-PSFC | Measuring Shock-Coalescence Timing and ρR Evolution in D^3He Implosions on OMEGA |
| D. Cohen | Swarthmore College | Tracer Spectroscopy Diagnostics of Inertial Confinement Fusion Experiments on OMEGA |
| P. W. McKenty | UR/LLE | Direct-Drive Cryogenic Target Implosion Performance on OMEGA |
| S. Skupsky | UR/LLE | Polar Direct Drive |
| G. Gregori | LLNL | Electronic Properties Measurements in Solid Density Plasmas by Spectrally Resolved X-Ray Scattering |
| B. Yaakobi | UR/LLE | EXAFS Studies of Shock Compression and Heating in Ti and V |
| M. Stevenson | AWE, UK | Effects of Plasma Composition on Backscatter and Hot-Electron Production in Underdense Plasmas |
| R. Olson | SNL | Shock Propagation, Preheat, and X-Ray Burnthrough Measurements in NIF Ignition Capsule Ablator Materials |
| M. C. Herrmann | LLNL | An Investigation of Directly Driven Xenon-Filled Capsules |
| D. Wilson | LANL | Multi-Fluid Interpenetration Mixing in X-Ray and Directly Laser Driven ICF Capsule Implosions |
| C. R. Christensen | LANL | The Influence of Asymmetry on Mix in Direct-Drive ICF Experiments |
| K. Parker | AWE, UK | Observation and Simulation of Plasma Mix After Reshock in a Convergent Geometry |

FY03 Laser Facility Report

User demand was met in FY03 by continuing to operate extended shifts during select weeks. Over 95% of planned target shots were executed for a total of 1381 shots (see Table 96.VI on p. 253). Shaped-pulse cryogenic implosions highlighted the ongoing development of direct-drive cryogenic capability. A total of 20 spherical and 51 planar cryogenic D₂ shots were performed. Highlights of other achievements and active projects as of the end of FY03 include the following:

- Installation of LLE-built, diode-pumped regenerative amplifiers on all three laser drivers improved pulse shape and energy stability. Production model regens were installed on both the main and backlighter drivers, replacing flashlamp-pumped units. Additionally, the prototype diode-pumped regen on the SSD driver was replaced with a production model. A concomitant increase in pulse-shape effectiveness from 93% in FY02 to 98% in FY03 resulted.
- Adiabatic shaping using picket pulses improves the performance of direct-drive ICF targets. Picket-pulse development continued with the application of new techniques for improving picket pulse quality and stability. Improved picket-pulse prediction routines and IR streak cameras resulted in improved picket-pulse performance.
- Modifications to the laser-driver timing system provided the capability to more precisely delay individual drivers with increased range. All drivers are now capable of being delayed or advanced hundreds of nanoseconds with ~100-ps precision. This new capability has been utilized extensively to improve the effectiveness of experimental campaigns.
- The implementation of a new set of distributed phase plates (DPP's) provided improved irradiation uniformity for direct-drive spherical capsules. The new DPP's—designated SG4—produce a flatter intensity distribution on target than the previous set (SG3). In addition to producing a larger effective beam area on target, the SG4 DPP's have a smaller beam-to-beam shape variation than their predecessors.
- Distributed polarization rotators (DPR's) continued heavy use in FY03. All DPR's were modified for remote retraction and reinstallation, improving flexibility for reconfiguring to indirect-drive setups. Nonlinear losses in the UV were observed due to DPR reconversion. This phenomenon was investigated and corrective action initiated.
- The overall OMEGA irradiation uniformity on target was improved by using active repointing. Active repointing consists of evaluating the actual beam positions on target using x-ray images of the beam spots on a 4-mm, Au-coated pointing target and then repointing individual beams. Subsequent pointing shot offsets have been reduced from ~23 μm rms to 11 μm rms.
- To allow lower beam energy while preserving pulse shape, the use of frequency-conversion crystal doubler detuning has been implemented. Frequency-conversion crystal doubler detuning was used extensively in FY03 on limited beam sets.
- Scientists and engineers from Lawrence Livermore National Laboratory along with LLE collaborators successfully implemented a 4ω (fourth harmonic, 263 nm) target irradiation capability on one of the 60 OMEGA beams. Experiments utilizing the 4ω capability were conducted in FY03, and more extensive use is planned for FY04.
- Shot operations continued in parallel with construction of the new OMEGA EP building, which commenced in July 2003. Building construction activities were carefully monitored to ensure the stability of target positioning and beam pointing at shot time. An EP beam transport opening was also created in the east target bay wall for propagating future EP beamlines into the OMEGA target chamber.

Education at LLE

As the only major university participant in the National ICF Program, education continues to be an important mission for the Laboratory. Graduate students are using the world's most powerful ultraviolet laser for fusion research on OMEGA, making significant contributions to LLE's research activities. Twenty UR faculty from five departments collaborate with LLE's scientists and engineers. Presently 63 graduate students are pursuing graduate degrees at the Laboratory, and LLE is directly funding 45 University of Rochester Ph.D. students through the Horton Fellowship Program. The research includes theoretical and experimental plasma physics, high-energy-density physics, x-ray and atomic physics, nuclear fusion, ultrafast optoelectronics, high-power-laser development and applications, nonlinear optics, optical materials and optical fabrications technology, and target fabrication. Technological developments from ongoing Ph.D. research will continue to play an important role on OMEGA.

One hundred and sixty-one students have earned Ph.D. degrees at LLE since its founding. An additional 81 graduate students and 23 postdoctoral positions from other universities were funded by NLUF grants. The most-recent University of Rochester Ph.D. graduates and their thesis titles are

Philip Chen Huang-Ming *Synthesis and Characterization of Novel Glassy Liquid Crystals*

Tanya Kosc *Motion of Polymer Cholesteric Liquid Crystal Flakes in an Electric Field*

Raphael Panfili *Double Ionization of Multi-Electron Atoms Exposed to Intense Femtosecond Laser Pulses*

Approximately 64 University of Rochester undergraduate students participated in work or research projects at LLE this past year. Student projects include operational maintenance of the OMEGA laser system; work in laser development, materials, and optical thin film coating laboratories; and programming, image processing, and diagnostic development. This is a unique opportunity for students, many of whom will go on to pursue a higher degree in the area in which they gained experience at the Laboratory.

In addition, LLE directly funds research programs within the MIT Plasma Science and Fusion Center, the State University of New York (SUNY) at Geneseo, and the University of Wisconsin. These programs involve a total of approximately 18 graduate and 23 undergraduate students from other universities.

For the past 15 years LLE has run a Summer High School Student Research Program (p. 250) in which this year 15 high school juniors spent eight weeks performing individual research projects. Each student is individually supervised by a staff scientist or an engineer. At the conclusion of the program, the students make final oral and written presentations on their work. The reports are published as an LLE report.

In 2003, LLE presented its seventh William D. Ryan Inspirational Teacher Award to Mr. Michael Carges, a former Physics Teacher at Pittsford-Mendon High School and currently at Greece Athena High School. Alumni of our Summer High School Student Research Program were asked to nominate teachers who had a major role in sparking their interest in science, mathematics, and/or technology. This award, which includes a \$1000 cash prize, was presented at the High School Student Summer Research Symposium. Mr. Carges was nominated Joy Yuan and Siddhartha Ghosh, participants in the 2002 Summer Program.

Robert L. McCrory
Director

Direct-Drive Cryogenic Target Implosion Performance on OMEGA

Introduction

In the direct-drive inertial confinement fusion (ICF)¹ concept, a spherical capsule containing thermonuclear fuel is imploded by the direct illumination of laser beams focused on the surface of the capsule in a near-uniform pattern. The capsule can also be mounted in a high-Z cavity, generally referred to as a hohlraum, which is then heated by the laser beams, producing a uniform radiation field of x rays. In this indirect-drive ICF concept,² the x rays, rather than the laser beams, ablate the outside of the capsule and drive the implosion. While the drive uniformity with x-ray (or indirect) drive may be currently superior to that of direct drive, it is possible to couple a significantly larger fraction of the laser energy into the hydrodynamic motion of the imploding fuel with direct drive. It is possible, therefore, with direct drive to achieve temperatures and densities that are comparable to indirect drive but with considerably less laser energy.

Within a decade or so, implosions of capsules containing cryogenic-DT-fuel layers are expected to ignite and burn at the National Ignition Facility (NIF)³ currently under construction at the Lawrence Livermore National Laboratory. Independent of the drive scheme, the basic capsule concept for ignition on the NIF is a relatively thick, cryogenic-DT-fuel layer inside a thin, spherical ablator² or foam shell.⁴ At peak compression, the high areal density (ρR) of the compressed cryogenic DT fuel can support a propagating thermonuclear burn wave due to the local bootstrap heating of the DT alpha-particle energy deposited in the fuel. Although this target concept has been under development for many years, only recently have implosions of appropriately scaled, layered, cryogenic D₂ capsules on the 60-beam, 30-kJ UV OMEGA laser system⁵ at the Laboratory for Laser Energetics begun to provide important data for the validation of both direct- and indirect-drive ignition target designs for the NIF.

The OMEGA cryogenic capsules and laser-drive pulses are energy scaled from the direct-drive NIF ignition designs^{4,6,7} to provide hydrodynamically equivalent implosions (e.g., matching implosion velocities, hot-spot convergence, and

in-flight aspect ratios). The ignition design for the NIF is driven by a 1.5-MJ, high-contrast pulse shape that puts the fuel layer on an adiabat α , of approximately 3 ($\alpha \sim 3$), where α is defined as the ratio of the electron pressure in the shell to the Fermi-degenerate pressure. To achieve hydrodynamic equivalence on OMEGA, the energy absorbed by the capsule per unit mass must be approximately the same as the NIF design. Therefore, the energy scales as the volume of the capsule or (radius³), the power scales as the surface area of the capsule or (radius²), and the duration of the drive pulse scales as the capsule radius (the distance to be traveled by the shell). On the 30-kJ OMEGA laser, this leads to a cryogenic capsule radius of approximately 920 μm containing an ice layer that is approximately 100 μm thick.⁶

An analysis⁷ of the relative performance of the NIF baseline direct-drive ignition target and the scaled OMEGA cryogenic capsule design using the 2-D hydrocode *ORCHID*⁸ has shown that the performance of the two designs can be related using the stability parameter $\bar{\sigma}$, defined as

$$\bar{\sigma}^2 = 0.06 \times \sigma_\ell^2 (\ell < 10) + \sigma_\ell^2 (\ell \geq 10), \quad (1)$$

where the σ_ℓ 's are the modal rms amplitudes of the perturbations on the inner surface of the ice layer at the end of the acceleration phase. The normalized performance curves plotted as a function of the $\bar{\sigma}$ parameter for the scaled OMEGA (green circles) and the NIF (blue squares) ignition designs are shown in Fig. 93.1 for equivalent $\alpha \sim 3$ implosions. The performance curve for a similarly scaled OMEGA $\alpha \sim 4$ design is also shown (red triangles). Although the smaller OMEGA capsule is more severely disrupted due to the perturbations associated with a given value of $\bar{\sigma}$, the $\alpha \sim 3$ and $\alpha \sim 4$ curves can be used to establish performance requirements for cryogenic implosions on OMEGA that would (computationally) ensure direct-drive ignition on the NIF under equivalent uniformity conditions.

For example, the two dashed lines associated with the NIF $\alpha \sim 3$ and OMEGA $\alpha \sim 4$ curves represent equivalent implo-

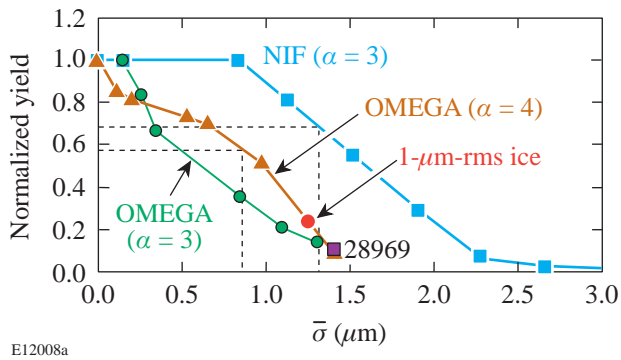


Figure 93.1

Normalized performance curves using the 2-D hydrocode *ORCHID* are shown as a function of the $\bar{\sigma}$ parameter for the scaled OMEGA (green circles) and the NIF (blue squares) ignition designs for equivalent $\alpha \sim 3$ implosions. The performance curve for a scaled OMEGA $\alpha \sim 4$ design is also shown (red triangles). The dashed lines on the $\bar{\sigma}$ axis represent implosions with equivalent uniformity on the NIF and on OMEGA. The point labeled as 28969 is the result of an $\alpha \sim 4$ cryogenic implosion and is discussed in the text. The value of $\bar{\sigma}$ for this implosion is based on a 2-D hydrocode calculation using the known laser and ice-surface nonuniformities, and the measured yield is used to determine the normalized yield. The point labeled as 1- μm -rms ice is based on the calculation for shot 28969 but assumes the NIF ignition specification for the inner-ice-layer-surface roughness.

sion conditions: the uniformity of the laser illumination and the outer and inner surfaces of the capsule are identical. Nonuniformities in the laser illumination and the outer surface of the capsule generate perturbation seeds that grow during the acceleration phase due to the Rayleigh–Taylor (RT) instability.^{9,10} These perturbations feed through to the inner ice surface, combine with the original ice perturbations, and continue to grow during the deceleration phase. This phase of the perturbation growth leads to mixing of cryogenic fuel into the hot spot and a subsequent reduction in the performance of the implosion. Therefore, under equivalent uniformity conditions, a normalized yield of 55%–60% on OMEGA ($\alpha \sim 4$) would correspond to achieving a normalized yield of approximately 70% on the NIF ($\alpha \sim 3$). Much of the work on cryogenic implosions on OMEGA is focused on achieving uniformity conditions in both the laser and the surface of the cryogenic fuel that will correspond to ignition conditions expected on the NIF.

To help achieve these conditions, a standard capsule design has been adopted to minimize variations in the fabrication process (filling, layering, and characterization). A standard low-adiabat pulse shape was also adopted for ease of data comparison among implosions with differing levels of inner ice smoothness. The pulse shape was designed to put the

cryogenic-fuel shell on an adiabat of approximately 4 (this capsule and drive pulse were used to generate the OMEGA $\alpha \sim 4$ curve shown in Fig. 93.1).

Details of the capsule design and pulse shape are discussed in the next section. The remaining three sections in this article (1) discuss experimental results from two different adiabat implosions and compare them with 1-D and 2-D hydrocode predictions; (2) discuss laser system and Cryogenic Target Handling System (CTHS) improvements that are expected to lead to ignition-equivalent implosions with cryogenic DT capsules in the near future; and (3) present conclusions.

Experimental

1. Cryogenic Target Design

The “standard” cryogenic capsule design and the low-adiabat pulse shape for the experiments reported in this article are shown in Fig. 93.2 along with the NIF direct-drive ignition point design. The shell material is either strong GDP (a high-strength plastic) or CD¹¹ and is typically $5.0 \pm 0.1 \mu\text{m}$ thick. When permeation filled with approximately 1200 atm of D₂ and then cooled to the triple point (18.73 K), the resulting ice-layer thickness is $100 \mu\text{m}$. This shell is somewhat thicker than the capsule designs scaled from the baseline 1.5-MJ ignition design for the NIF and described in Ref. 12. The thicker shell was chosen to increase the laser absorption with the low-adiabat drive pulses (the average atomic number is higher for CH than for the D₂ ice and the thicker CH shell is ablated away later in the drive pulse) and to reduce the length of time required to fill and cool the capsules with D₂ fuel (a thicker shell is more robust). A corresponding thick-plastic-shell (17- μm) ignition design for the NIF has also been developed¹³ to take advantage of the higher absorption. By tailoring the adiabat in the shell and fuel, the expected increase in imprint perturbation growth for such a thick shell is substantially reduced. Therefore, the higher absorption and hydrodynamic efficiency lead to improved ignition performance with the additional advantage of the superior mechanical properties of a much thicker shell.

While the relatively low stability of the OMEGA $\alpha \sim 3$ design in Fig. 93.1 would provide enhanced performance sensitivity to nonuniformities for parametric studies and comparison to implosion models, the current levels of laser system nonuniformity would dominate the performance of this capsule design. To enhance the performance margin of cryogenic implosions on OMEGA, a pulse shape was developed that puts the fuel layer of the standard capsule described above at $\alpha \geq 4$. An analysis of the performance of this capsule and pulse

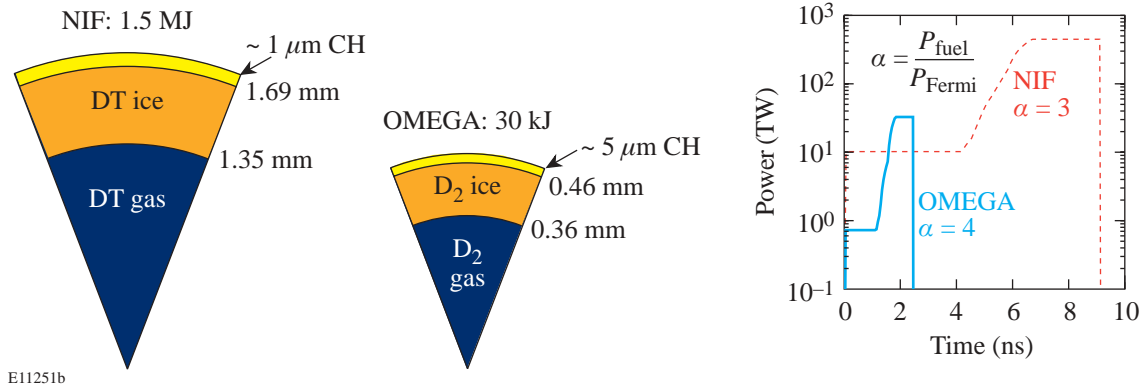


Figure 93.2

The baseline direct-drive ignition design for the NIF is shown along with the energy-scaled, hydrodynamically equivalent cryogenic design imploded on OMEGA and reported in this article. The right-hand panel shows the $\alpha \sim 3$ and $\alpha \sim 4$ pulse shapes for the NIF ignition design and the OMEGA cryogenic implosions, respectively.

shape with a stability postprocessor¹⁴ indicates that the mix width at the end of the acceleration phase is approximately 40%, considerably smaller than the 60% estimated for the scaled $\alpha \sim 3$ OMEGA design. Here the mix width is simply the peak-to-valley of the RT-growth amplitudes, and the ratio of the mix width to the shell thickness is a measure of the shell stability. For equivalent uniformity, the $\alpha \sim 4$ design should perform significantly better than the $\alpha \sim 3$ design. This is demonstrated in Fig. 93.1: the equivalent scaling to ignition performance requires a normalized yield of 55%–60% for this design compared with only 30% for the scaled $\alpha \sim 3$ design. Since an $\alpha \sim 4$ pulse shape applied to the 1.5-MJ NIF baseline direct-drive design still leads to ignition,⁴ the OMEGA $\alpha \sim 4$ design described above should be adequate to validate ignition-equivalent performance on OMEGA.

A thorough description of the layering and shadowgraphic characterization of cryogenic capsules is given in Ref. 12. Up to four thin-shell capsules are filled and cooled in the Fill/Transfer Station (FTS) and then individually loaded into moving cryostat transfer carts (MCTC's). These carts contain all of the necessary systems to create, manipulate, and maintain an ice layer inside the plastic capsule. The capsule is located inside a small layering sphere that has four viewing ports and an opening for a laser fiber to deliver up to 150 mW of 3.16- μm IR laser power to the inside surface of the layering sphere. This IR energy is preferentially absorbed in the D_2 -ice layer, and low-pressure (~ 100 -mTorr) helium exchange gas conducts heat from the capsule to the layering sphere, which is maintained at approximately 15 K. The settings for the exchange gas pressure, the layering sphere temperature, and

the IR laser power control the layering rate of the ice. Thin sapphire windows on the viewing ports provide two orthogonal views of the capsule for shadowgraphic analysis of the layer quality and later alignment at target chamber center for implosion experiments. At shot time, the cryogenic assembly containing the layering sphere (the shroud) is rapidly removed, exposing the capsule, still mounted to the MCTC, to the laser beams. The delay between the shroud removal and laser interaction is approximately 50 ms.

While early 60-beam cryogenic capsule implosions (reported in Ref. 8) were characterized by a single shadowgraphic view,¹² recent improvements to the characterization station permit the capsule to be rotated $\pm 180^\circ$ to obtain multiple views of the inner-ice-surface quality. Although multiple views do not provide a true three-dimensional picture of the inner ice surface, an average over multiple views does provide a more accurate representation of the modal structure of the ice for 2-D simulations. For most targets, a layer is characterized by at least four views. Techniques are being developed to construct a 3-D representation of the ice layer from multiple (up to 12) 2-D shadowgraphic measurements.

A well-layered capsule is produced in approximately 24 h. Much of this time is spent searching for the triple-point isotherm in the capsule by slowly varying the IR power delivered to the layering sphere while the temperature of the layering sphere and pressure of the exchange gas are held constant. Once the settings for the triple point have been identified, a sub-10- μm -rms layer can usually be formed quickly and the modal structure will slowly anneal with time

(hours). Occasionally, a near-single-crystal layer can be grown, and these capsules generally have very smooth layers (the total rms of modes greater than 3 is about $1\ \mu\text{m}$). Figure 93.3 shows an example of two near-single-crystal-layer capsules and their multiview-averaged power spectra. Both of these capsules were imploded on the OMEGA laser system.

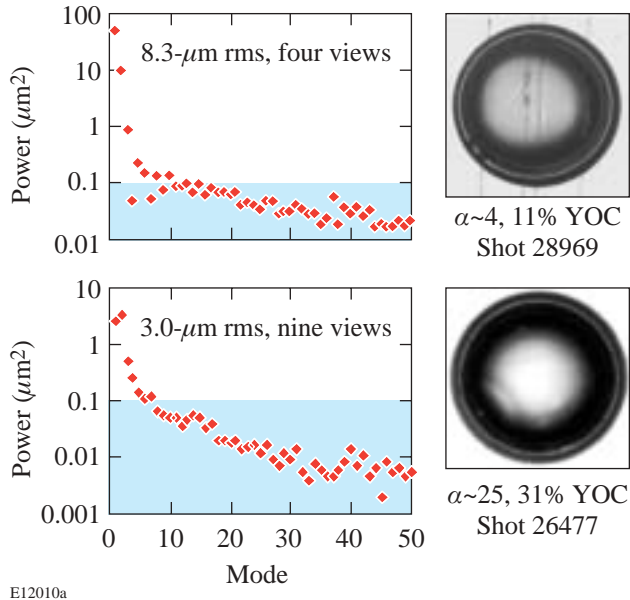


Figure 93.3
Shadowgraphs of two layered and fully characterized cryogenic D_2 capsules prior to being imploded on OMEGA. The average power spectra for the modal structure of the inner ice surface just prior to the implosions are also shown.

2. Laser-Drive Pulses

Cryogenic capsules have been imploded using two pulse shapes: a high-adiabat ($\alpha \sim 25$), 23-kJ, 1-ns square pulse (~ 0.5 -TW peak intensity) and a low-adiabat ($\alpha \sim 4$), 17-kJ, 2.5-ns shaped pulse. The $\alpha \sim 4$ pulse shape is shown in Fig. 93.2. Full single-beam smoothing was applied during all pulses by using distributed phase plates (DPP's),¹⁵ polarization smoothing (PS) with birefringent wedges,¹⁶ and 2-D, single-color-cycle, 1-THz smoothing by spectral dispersion (SSD).¹⁷ Perturbations seeded by single-beam nonuniformities experience RT growth during the acceleration phase, initiated by the arrival of the rarefaction wave (traveling outward from the inner ice surface) at the ablation surface. Since the rarefaction wave does not reach the ablation surface before the end of the high-adiabat pulse (1-ns square), the implosion performance is not particularly sensitive to the acceleration-phase perturbations introduced by laser system imprint (i.e., the acceleration phase is short). The resulting

higher performance generally leads to improved diagnostic measurements for comparison to 1-D and 2-D hydrocodes. Implosion performance with the low-adiabat, $\alpha \sim 4$ pulse is considerably more sensitive to imprint. There is less stabilization during the foot of the pulse (see Fig. 93.2) due to the lower ablation velocity. This leads to greater perturbation amplitudes at the end of the acceleration phase that feed through to the inner ice surface and continue to grow during the deceleration phase.

3. Target Alignment

The cryogenic capsules are suspended on a web of spider silks across a "C"-style mount.¹⁸ The C is designed to avoid intercepting the beams, and the use of spider silk minimizes both mass perturbations on the capsule surface that might affect implosion performance and thermal perturbations that might affect the D_2 -ice-layering process. Cryogenic capsule alignment inside the OMEGA target chamber utilizes the Target Viewing System (TVS). Each of the two orthogonal TVS lines of sight views the capsule through six independently mounted sapphire windows. These windows provide the only optical access to the layering sphere through the various thermal barriers. The alignment accuracy of the TVS to target chamber center (TCC) is better than $5\ \mu\text{m}$ for noncryogenic, stalk-mounted targets. The alignment accuracy for cryogenic capsules, however, is limited due to focal blurring through the sapphire windows; for cryogenic capsules, the alignment accuracy is estimated to be approximately $10\ \mu\text{m}$.

In addition to blurring the capsule images in the TVS, it was found that the target optical offset (the difference between the capsule location viewed through the sapphire windows and the actual location of the capsule) established at room temperature, $< 5\ \mu\text{m}$, during the assembly of the MCTC was significantly different once the cryogenic systems were cooled. An analysis of chamber-mounted x-ray pinhole camera (XPHC) images taken during the implosions showed that virtually every cryogenic implosion prior to the identification of a target alignment problem had been offset from TCC by 60 to $120\ \mu\text{m}$. Using up to five fixed XPHC images on each shot, the magnitude and direction of the capsule offsets were determined with high accuracy. The influence of this offset on the cryogenic implosion performance is presented in the **Discussion** section.

To accurately align cryogenic capsules to TCC, a calibration procedure was developed to generate offset alignment reticles for the TVS. A stalk-mounted surrogate capsule is loaded into the MCTC, the system is cooled to the nominal operating temperature, and the surrogate capsule is inserted

into the target chamber. The capsule is aligned to the TCC using the TVS and then the shroud is removed, exposing the capsule. TVS images of the “bare” capsule are then acquired, and the optical offset caused by the sapphire windows in the shroud is calculated. This offset is then used to generate a unique alignment reticle for each MCTC.

4. Experimental Setup and Diagnostics

The primary diagnostics for cryogenic implosions include the fixed XPHC's mentioned above,¹⁹ x-ray framing cameras,²⁰ high-resolution Kirkpatrick–Baez (KB) microscopes,²¹ primary and secondary neutron yield,²² secondary proton yield,²³ the ion temperature,²⁴ and the neutron reaction history.²⁵ The energy loss of the secondary protons is used to infer the total areal density.²⁶ The XPHC's provide a low-resolution, time-integrated x-ray image of the capsule shell and core. The framing cameras provide sequential, time-gated core images from just before fusion burn until well after stagnation. These images can be used to assess time-dependent, low-mode asymmetries during the assembly of the core. The high-resolution ($\sim 5\text{-}\mu\text{m}$), time-integrated KB microscopes offer the best images of the core at peak x-ray emission. Asymmetries in the core are related to both laser system nonuniformities and low-mode inner-ice-surface structure. The primary and secondary fusion yields are the most direct measure of the capsule performance and are most sensitive to mix and ion temperature. The reaction history provides crucial validation for hydrocode performance and laser absorption, while the total areal density is perhaps the most important measure of the hydrodynamic performance of the implosion: an areal density of at least 300 mg/cm^2 is required to absorb the full energy of the DT alpha in an ignition target.

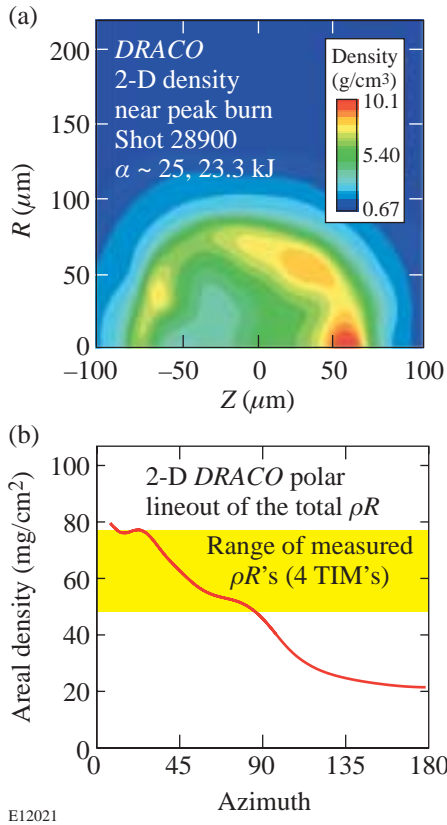
Results

As described above, most of the recent cryogenic targets have been significantly offset from TCC at the beginning of the laser pulse. Distributed phase plates (DPP's) on each of the 60 OMEGA beams are used to define the focal-spot distribution of the beams on the target. The minimum spot size of each individual beam is nominally $920\text{ }\mu\text{m}$, and the intensity distribution is a super-Gaussian of the order of 2.2. Although the effective f number of each beam with the DPP is large, the near-Gaussian intensity distribution imposes a large intensity perturbation on the surface of the capsule when the capsule is offset from the nominal best focus of all 60 beams (each of the beams is independently pointed to an alignment surrogate at TCC with an rms deviation of less than $20\text{ }\mu\text{m}$). This laser-intensity perturbation causes the fuel shell to converge asymmetrically, significantly degrading the performance of the

implosion. For example, the peak-to-valley intensity variation on the surface of a $920\text{-}\mu\text{m}$ -diam capsule offset by $50\text{ }\mu\text{m}$ from TCC is approximately $\pm 40\%$ and climbs to nearly $\pm 70\%$ for a $100\text{-}\mu\text{m}$ offset with the standard OMEGA power balance. The effect of this offset on implosion performance is similar to a large $\ell = 1$ mode in the ice (i.e., the ice is thicker on one side of the capsule than on the other; see the capsule shadowgraph of shot 28969 in Fig. 93.3). Not only is the capsule imploded asymmetrically, but the capsule center shifts during the implosion under the influence of the greater pressure generated by the higher laser intensity on the side of the capsule closest to TCC. A higher-order, super-Gaussian, single-beam intensity profile would reduce the effect of an alignment offset and is being pursued in parallel with improvements in the target alignment procedures. Similarly, a larger focal-spot size relative to the target diameter would somewhat mitigate the alignment sensitivity but at the expense of energy loss around the target.

After developing the target alignment procedure described above, several implosions were performed with the capsule less than $25\text{ }\mu\text{m}$ from TCC at the start of the laser pulse. The performance of these implosions can be simulated using the 2-D hydrocode *DRACO*.²⁷ A comparison will be made between the performance of two cryogenic target implosions (shots 28900 and 28969) and *DRACO* simulations. Shot 28900 imploded a $100\text{-}\mu\text{m}$ -thick D_2 -ice layer with a $6.5\text{-}\mu\text{m}$ -rms inner ice layer (pre-shot characterization) using a high-adiabat ($\alpha \sim 25$), 1-ns square pulse with a UV energy on target of 23.3 kJ and an rms energy variation among the 60 OMEGA beams of 2.9%. Shot 28969 imploded a $100\text{-}\mu\text{m}$ -thick D_2 -ice layer with an $8.3\text{-}\mu\text{m}$ -rms inner ice layer dominated by the $\ell = 1$ component (see Fig. 93.3 and the modal spectrum for this capsule); the measured rms energy variation of the beams was 3.4% and the low-adiabat $\alpha \sim 4$ pulse shape delivered 16.6 kJ to the target. Analysis of the PHC data showed that both capsules were offset from TCC by less than $20\text{ }\mu\text{m}$ at the beginning of the laser pulse. Although the effect of this small offset on the implosion performance is not negligible (especially for the low-adiabat drive pulse), it does not dominate the performance. The 2-D *DRACO* simulations neglect the offset, and the predicted performance is based entirely on the laser system power balance and the quality of the inner surface of the ice layer.

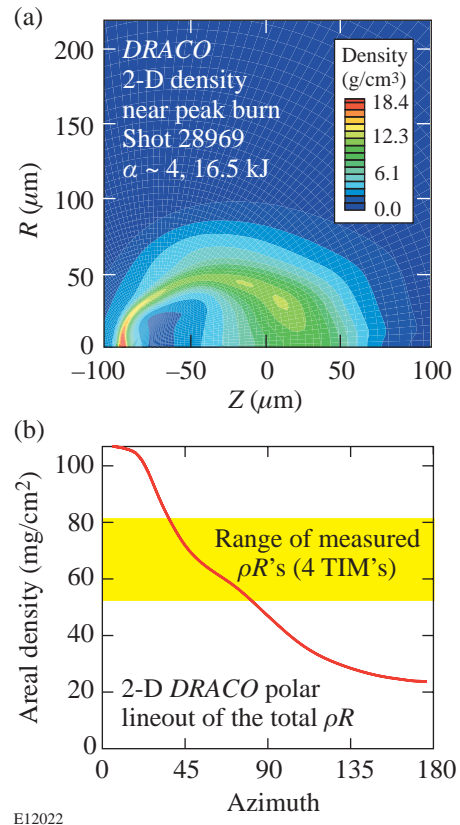
Figures 93.4 and 93.5 show the 2-D *DRACO* predictions for the fuel-density contours [panel (a)] and a polar lineout of the total areal density [panel (b)] for the two implosions. It is immediately apparent that both cores have been offset by the



E12021

Figure 93.4

(a) A plot of the fuel-density contours at peak burn for shot 28900 ($\alpha \sim 25$, 23.3 kJ) from the 2-D hydrocode *DRACO*. (b) Polar lineout of the total areal density from the center of the core derived from the density contours shown in (a). The yellow region shows the range of the individual areal-density measurements inferred from the average energy loss of secondary protons.



E12022

Figure 93.5

(a) A plot of the fuel-density contours at peak burn for shot 28969 ($\alpha \sim 4$, 16.5 kJ) from the 2-D hydrocode *DRACO*. (b) Polar lineout of the total areal density from the center of the core derived from the density contours shown in (a). The yellow region shows the range of the individual areal-density measurements inferred from the average energy loss of the secondary protons.

influence of the low-mode nonuniformity of the ice layers. The effect of the large $\ell = 1$ mode on the inner ice surface in shot 28969 is especially apparent in Fig. 93.5(a). The core offsets lead to a significant asymmetry in the predicted areal density. The areal densities predicted by the 2-D simulations agree well with the measured values, which fall within the yellow regions in Figs. 93.4(b) and 93.5(b). It is not currently possible to correlate the polar angles of the areal-density lineouts from either shot with the orientation of the experimental measurements. However, the roughly factor-of-5 variation in the 2-D areal density for shot 28969 (and the factor-of-4 variation for shot 28900) is consistent with some of the experimental variations measured on other implosions in which the capsule was significantly offset from TCC. The extreme values of areal density are not likely to be observed on most shots with only a limited number of individual measurements (typically four per shot) available.

Table 93.I gives a comparison between experimentally measured or inferred quantities and the 1-D *LILAC*²⁸ and 2-D *DRACO* predictions. The 1-D yield from shot 28900 ($\alpha \sim 25$) is considerably higher than the 2-D *DRACO* yield (57% of the 1-D value) and virtually identical to the measured yield. This suggests that the at-shot state of the capsule may have been different from the pre-shot characterization used in the 1-D and 2-D hydrocodes. Assuming that the temperature of the capsule might have changed prior to the shot (evidence for this is discussed in the following section), a series of 1-D *LILAC* calculations were performed in which the temperature of the capsule was varied above and below the nominal value from the pre-shot characterization (typically 100 mK below the triple point). These simulations did not provide a satisfactory explanation for the high performance of the capsule relative to the 2-D predictions (the yield was nearly a factor of 4 higher than any previous $\alpha \sim 25$ implosion with $\sim 100 \mu\text{m}$ of ice; the

Table 93.I: A comparison of the experimental measurements with the 1-D and 2-D hydrocode predictions. The hydrocode predictions are given as the ratio of the experimental measurement to the predicted value (in percent).

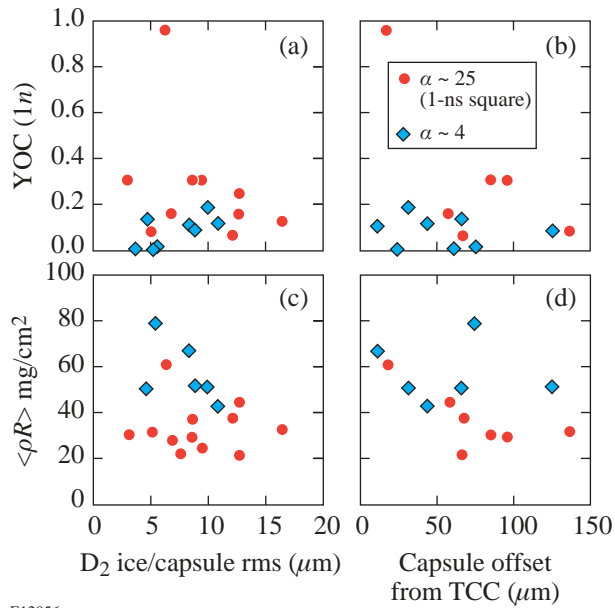
| Measurement | Shot 28900 | Experimental/ 1-D <i>LILAC</i> (%) | Experimental/ 2-D <i>DRACO</i> (%) | Shot 28969 | Experimental/ 1-D <i>LILAC</i> (%) | Experimental/ 2-D <i>DRACO</i> (%) |
|---|-----------------------|---------------------------------------|---------------------------------------|--------------------|---------------------------------------|---------------------------------------|
| Primary neutron yield | 1.27×10^{11} | 96 | 171 | 5.95×10^9 | 11 | 112 |
| Secondary neutron yield | 1.17×10^9 | 84 | 132 | 6.75×10^7 | 9.7 | 107 |
| Secondary proton yield | 2.03×10^8 | 112 | | 7.14×10^6 | 11 | |
| $\langle \rho R \rangle$ mg/cm ² | 61 | 133 | 120 | 67.00 | 84 | 115 |
| T_{ion} (keV) | 3.6 | 157 | 139 | 2.5 | 145 | 125 |
| Y_{2n}/Y_{1n} | 0.0092 | 85 | 77 | 0.0113 | 91 | 95 |
| Y_{2p}/Y_{1p} | 0.0016 | 114 | | 0.0012 | 104 | |
| Offset (μm) | 14 | | | 11 | | |

primary difference from previous shots is the small TCC offset). A further series of calculations were performed in which the flux limiter²⁹ was increased from 0.060 to 0.068. This increased the 1-D yield by a factor of 2, lowering the yield-over-clean (YOC) to approximately 50% and bringing the predicted neutron bang time into agreement with the measured value. A similar treatment within *DRACO* would have a comparable result and bring the 2-D yield prediction into agreement with the experimental measurement. While a higher value of the flux limiter for this shot is suggested by the bang-time measurement, a change in the flux limiter is not supported by recent absorption measurements on CH at OMEGA. In contrast to shot 28900, the 2-D yield for shot 28969 ($\alpha \sim 4$) is in very good agreement with the experimental measurement. Both are approximately 10% of the 1-D yield. Indeed, all of the 2-D predictions are reasonably close to the experimental measurements for this shot. This is a very encouraging result given the large amplitude of the low-mode nonuniformity on the inner ice surface layer.

Figure 93.6 shows the primary neutron YOC and the average total areal density as a function of the measured capsule offset and the pre-shot characterization of the D₂ inner-ice-surface rms for all of the cryogenic implosions to date in which the ice layer appears to have been intact at shot time. Based on the analysis shown in Fig. 93.1, the primary yield is expected to increase with increasing smoothness of the inner ice layer [Fig. 93.6(a)]. For most of the shots, the influence of the ice-surface perturbations on the implosion performance

is obscured by the gross low-mode nonuniformity caused by the capsule offset [Fig. 93.6(b)]. With no capsule characterization in the target chamber prior to the shot, there is also uncertainty in the inner-ice-surface roughness at shot time. In Fig. 93.6(b), there is evidence with the high-adiabat implosions that the capsule performance is significantly degraded due to the capsule offset. As expected, the average total areal density for the high-adiabat implosions does not appear to depend on the ice-layer quality [Fig. 93.6(c)]; however, there appears to be a correlation for increasing total areal density with decreasing ice roughness for the low-adiabat ($\alpha \sim 4$) implosions, where the convergence ratio at stagnation is expected to be somewhat larger. As a function of decreasing capsule offset from TCC, there is a general trend of increasing areal density for both the low- and high-adiabat implosions [Fig. 93.6(d)]. This also correlates with the observation that the asymmetry in the individual areal-density measurements (the spread divided by the mean) decreases with decreasing target offset.

The measured ion temperatures in all of the cryogenic implosions exceed the 1-D hydrocode predictions. In the absence of a significant shock yield (there is no evidence for a shock yield from the neutron temporal diagnostic), this is usually understood as a phenomenon associated with the mixing of cold fuel into the hot spot. The measured yield preferentially samples the small hot-spot volume, which is surrounded by a steep, mix-induced temperature gradient. The yield from this mix region is considerably less than the ratio of the fuel



E12056

Figure 93.6

(a) The ratio of the primary neutron yield to the predicted yield from the 1-D hydrocode *LILAC* [the yield-over-clean (YOC)] as a function of the pre-shot D_2 -ice roughness. (b) The same YOC values plotted as a function of the capsule offset from TCC [for some of the points shown in panel (a), the offset was not measured] at the start of the laser pulse. (c) The average areal density as a function of the pre-shot D_2 -ice roughness. Increasing areal density appears to be correlated with a reduction in the inner-ice-surface roughness for the low-adiabat implosions. Such a correlation does not exist for the high-adiabat implosions that are expected to be much less sensitive to laser imprint and acceleration-phase perturbation growth. (d) The average areal density as a function of the capsule offset from TCC. For both low- and high-adiabat implosions, the areal density increases with decreasing capsule offset.

volumes (hot spot and mix regions). However, the large offsets and uncertainties in the layer quality at shot time make it difficult to interpret the ion temperature data. For example, the average ion temperature measured for implosions where other experimental evidence (e.g., reaction histories and core images) suggests that the ice layer was compromised prior to the shot is 4.4 keV and only 2.7 keV for implosions in which the experimental evidence suggests an intact layer. In Table 93.I, the measured ion temperatures for the two implosions suggest some degree of mix when compared with the hydrocode predictions.

Finally, secondary proton production in shots 28900 and 28969 indicate a hot-spot areal density between 10 and 12 mg/cm^2 according to the uniform density model of Azechi and Cable.³⁰ The hot-spot areal density inferred from shot 28900 ($\alpha \sim 25$) is somewhat larger than that inferred for the lower-

adiabat implosion. These hot-spot areal densities are about a factor of 2 larger than those reported in Ref. 12 and are at or near the saturation limit of the model for the measured ion temperatures.

Discussion

The rms amplitudes of the inner-ice-surface roughness at the end of the acceleration phase in the 2-D *DRACO* simulation of shot 28969 ($\alpha \sim 4$) can be used to calculate the value of the $\bar{\sigma}$ parameter used by McKenty⁷ to define the scaling performance of cryogenic implosions on OMEGA and the NIF. This point falls very close to the OMEGA $\alpha \sim 4$ curve in Fig. 93.1 and should be compared with the point labeled as 1- μm -rms ice. The 1- μm -rms ice point represents an identical 2-D simulation (i.e., current laser system nonuniformity on OMEGA) assuming the NIF specification for ice smoothness (total rms of 1 μm). This comparison clearly shows that scaled ignition performance on OMEGA will require improvements in the OMEGA laser system uniformity as well as improvements to the inner-ice-layer smoothness. Achieving ignition-equivalent performance on OMEGA (e.g., a normalized 2-D yield of approximately 60%) will require a laser system nonuniformity of 1% or less and an rms inner-ice-surface roughness of approximately 1 μm .

Although outstanding inner-ice-layer smoothness has been achieved (approximately 3- μm rms including contributions from the thin plastic shell; see also Fig. 93.2), the stability of the IR laser used to layer the D_2 ice and the fiber-optic transport used to deliver IR power to the layering sphere does not appear to be adequate to produce and maintain high-surface-quality layers (sub-3- μm rms). An IR power feedback control system based on the measured power into the layering sphere is currently being implemented to establish the triple point to the required accuracy (a high-quality layer requires single-crystal growth within approximately 1 mK of the triple point). The goal of the feedback system is to regulate the power in the layering sphere to 0.1%.

As described in the previous section, improvements to the laser system uniformity include the development of new distributed phase plates (DPP's) with tight tolerances on spot size, ellipticity, and order; new techniques for enhanced power balance³¹ and target alignment; and new specifications for beam pointing. Based on measurements of the prototype DPP, an analysis of the potential improvements to the overall laser system nonuniformity suggests that the requirement for <1% rms will be achieved in the near future. Low-adiabat drive pulses that include a picket to tailor the adiabat across the

cryogenic fuel shell are expected to significantly reduce the imprint and subsequent growth rates from single-beam nonuniformities.¹³ By tailoring the adiabat with a picket pulse, the ablation velocity can be increased without significantly raising the internal pressure of the capsule. This helps to minimize the growth of imprint perturbations during the acceleration phase. A future study of cryogenic capsule performance with and without these pickets is one of the highest priorities within the direct-drive program at LLE.

Conclusions

The performance of hydrodynamically scaled cryogenic ignition capsules with both low- and high-adiabat pulse shapes has been reported. The primary goal of these experiments is to demonstrate equivalent direct-drive ignition performance using pulse shapes and capsule designs scaled from the baseline ignition design for the NIF. Near 1-D hydrocode performance has been measured with a high-adiabat ($\alpha \sim 25$) drive pulse on a capsule containing a 100- μm -thick layer of cryogenic D_2 , and near 2-D hydrocode performance has been measured on a similar capsule with a low-adiabat ($\alpha \sim 4$) drive. The fabrication and the characterization of layered cryogenic capsules with inner-ice-surface roughness of between 3- and 12- μm rms are now routine (see Fig. 93.3). A new cryogenic target characterization diagnostic is under development to provide a single view of the inner ice surface within 50 ms of the shot. A feedback system is being developed to stabilize the IR laser power in the layering sphere. These upgrades will significantly improve implosion performance in future cryogenic experiments. Additionally, improvements to the overall laser system uniformity are being pursued. These include the development of a new distributed phase plate with a high-order super-Gaussian intensity profile and much tighter tolerances on plate-to-plate spot size and ellipticity. These new DPP's will immediately reduce the overall laser system power imbalance. Coupled with more-accurate UV energy transport measurements and tighter tolerances on beam pointing, the overall laser system nonuniformity should approach 1% rms. With this level of laser system uniformity and continued improvements in the inner-ice-surface smoothness, it will be possible to validate the performance of direct-drive ignition capsule designs on OMEGA.

ACKNOWLEDGMENT

The authors are grateful to the staff of the Laboratory for Laser Energetics for their tireless dedication to the cryogenic implosion program and the operation of the OMEGA laser system. In particular, the authors would like to acknowledge the efforts of the Cryogenic Target Fabrication Group for the production of layered and characterized capsules on a regular schedule. This work was supported by the U. S. Department of Energy Office of Inertial

Confinement Fusion under Cooperative Agreement No. DE-FC03-92SF19460, the University of Rochester, and the New York State Energy Research and Development Authority. The support of DOE does not constitute an endorsement by DOE of the views expressed in this article.

REFERENCES

1. J. Nuckolls *et al.*, *Nature* **239**, 139 (1972).
2. J. D. Lindl, *Inertial Confinement Fusion: The Quest for Ignition and Energy Gain Using Indirect Drive* (Springer-Verlag, New York, 1998).
3. W. J. Hogan, E. I. Moses, B. E. Warner, M. S. Sorem, and J. M. Soures, *Nucl. Fusion* **41**, 567 (2001).
4. S. E. Bodner, D. G. Colombant, J. H. Gardner, R. H. Lehmborg, S. P. Obenschain, L. Phillips, A. J. Schmitt, J. D. Sethian, R. L. McCrory, W. Seka, C. P. Verdon, J. P. Knauer, B. B. Afeyan, and H. T. Powell, *Phys. Plasmas* **5**, 1901 (1998).
5. T. R. Boehly, D. L. Brown, R. S. Craxton, R. L. Keck, J. P. Knauer, J. H. Kelly, T. J. Kessler, S. A. Kumpan, S. J. Loucks, S. A. Letzring, F. J. Marshall, R. L. McCrory, S. F. B. Morse, W. Seka, J. M. Soures, and C. P. Verdon, *Opt. Commun.* **133**, 495 (1997).
6. Laboratory for Laser Energetics LLE Review **79**, 121, NTIS document No. DOE/SF/19460-317 (1999). Copies may be obtained from the National Technical Information Service, Springfield, VA 22161.
7. P. W. McKenty, V. N. Goncharov, R. P. J. Town, S. Skupsky, R. Betti, and R. L. McCrory, *Phys. Plasmas* **8**, 2315 (2001).
8. R. L. McCrory and C. P. Verdon, in *Inertial Confinement Fusion*, edited by A. Caruso and E. Sindoni (Editrice Compositori, Bologna, Italy, 1989), pp. 83–124.
9. Lord Rayleigh, *Proc. London Math Soc.* **XIV**, 170 (1883).
10. G. Taylor, *Proc. R. Soc. London Ser. A* **201**, 192 (1950).
11. A. Nikroo *et al.*, *Fusion Sci. Technol.* **41**, 214 (2002).
12. C. Stoeckl, C. Chiritescu, J. A. Delettrez, R. Epstein, V. Yu. Glebov, D. R. Harding, R. L. Keck, S. J. Loucks, L. D. Lund, R. L. McCrory, P. W. McKenty, F. J. Marshall, D. D. Meyerhofer, S. F. B. Morse, S. P. Regan, P. B. Radha, S. Roberts, T. C. Sangster, W. Seka, S. Skupsky, V. A. Smalyuk, C. Sorce, J. M. Soures, R. P. J. Town, J. A. Frenje, C. K. Li, R. D. Petrasso, F. H. Séguin, K. Fletcher, S. Padalino, C. Freeman, N. Izumi, R. Lerche, and T. W. Phillips, *Phys. Plasmas* **9**, 2195 (2002).
13. V. N. Goncharov, "Improved Performance of Direct-Drive ICF Target Designs with Adiabat Shaping Using an Intensity Picket," to be published in *Physics of Plasmas*; see also this issue of the LLE Review, p. 18.
14. V. N. Goncharov, P. McKenty, S. Skupsky, R. Betti, R. L. McCrory, and C. Cherfils-Clérouin, *Phys. Plasmas* **7**, 5118 (2000).
15. T. J. Kessler, Y. Lin, J. J. Armstrong, and B. Velazquez, in *Laser Coherence Control: Technology and Applications*, edited by H. T. Powell and T. J. Kessler (SPIE, Bellingham, WA, 1993), Vol. 1870, pp. 95–104.

16. T. R. Boehly, V. A. Smalyuk, D. D. Meyerhofer, J. P. Knauer, D. K. Bradley, R. S. Craxton, M. J. Guardalben, S. Skupsky, and T. J. Kessler, *J. Appl. Phys.* **85**, 3444 (1999).
17. S. Skupsky, R. W. Short, T. Kessler, R. S. Craxton, S. Letzring, and J. M. Soures, *J. Appl. Phys.* **66**, 3456 (1989).
18. Laboratory for Laser Energetics LLE Review **81**, 21, NTIS document No. DOE/SF/19460-335 (1999). Copies may be obtained from the National Technical Information Service, Springfield, VA 22161.
19. F. J. Marshall, T. Ohki, D. McInnis, Z. Ninkov, and J. Carbone, *Rev. Sci. Instrum.* **72**, 713 (2001).
20. D. K. Bradley *et al.*, *Rev. Sci. Instrum.* **66**, 716 (1995).
21. F. J. Marshall and J. A. Oertel, *Rev. Sci. Instrum.* **68**, 735 (1997); F. J. Marshall, M. M. Allen, J. P. Knauer, J. A. Oertel, and T. Archuleta, *Phys. Plasmas* **5**, 1118 (1998).
22. V. Yu. Glebov, D. D. Meyerhofer, C. Stoeckl, and J. D. Zuegel, *Rev. Sci. Instrum.* **72**, 824 (2001); M. D. Cable and M. B. Nelson, *Rev. Sci. Instrum.* **59**, 1738 (1988).
23. F. H. Séguin, C. K. Li, D. G. Hicks, J. A. Frenje, K. M. Green, R. D. Petrasso, J. M. Soures, D. D. Meyerhofer, V. Yu. Glebov, C. Stoeckl, P. B. Radha, S. Roberts, C. Sorce, T. C. Sangster, M. D. Cable, S. Padalino, and K. Fletcher, *Phys. Plasmas* **9**, 2725 (2002).
24. T. J. Murphy, R. E. Chrien, and K. A. Klare, *Rev. Sci. Instrum.* **68**, 610 (1997); R. A. Lerche *et al.*, *Appl. Phys. Lett.* **31**, 645 (1977).
25. C. Stoeckl, V. Yu. Glebov, S. Roberts, T. C. Sangster, R. A. Lerche, R. L. Griffith, and C. Sorce, to be published in the Review of Scientific Instruments; see also Laboratory for Laser Energetics LLE Review **92**, 156, NTIS document No. DOE/SF/19460-465 (2002). Copies may be obtained from the National Technical Information Service, Springfield, VA 22161.
26. F. H. Séguin, C. K. Li, J. A. Frenje, S. Kurebayashi, R. D. Petrasso, F. J. Marshall, D. D. Meyerhofer, J. M. Soures, T. C. Sangster, C. Stoeckl, J. A. Delettrez, P. B. Radha, V. A. Smalyuk, and S. Roberts, *Phys. Plasmas* **9**, 3558 (2002).
27. P. B. Radha, V. N. Goncharov, T. J. B. Collins, J. A. Delettrez, and P. W. McKenty, "Multidimensional Effects in Plastic Shell Implosions on the OMEGA Laser," to be submitted to *Physics of Plasmas*.
28. M. C. Richardson, P. W. McKenty, F. J. Marshall, C. P. Verdon, J. M. Soures, R. L. McCrory, O. Barnouin, R. S. Craxton, J. Delettrez, R. L. Hutchison, P. A. Jaanimagi, R. Keck, T. Kessler, H. Kim, S. A. Letzring, D. M. Roback, W. Seka, S. Skupsky, B. Yaakobi, S. M. Lane, and S. Prussin, in *Laser Interaction and Related Plasma Phenomena*, edited by H. Hora and G. H. Miley (Plenum Publishing, New York, 1986), Vol. 7, pp. 421–448.
29. R. C. Malone, R. L. McCrory, and R. L. Morse, *Phys. Rev. Lett.* **34**, 721 (1975).
30. H. Azechi, M. D. Cable, and R. O. Stapf, *Laser Part. Beams* **9**, 119 (1991); M. D. Cable and S. P. Hatchett, *J. Appl. Phys.* **62**, 2233 (1987).
31. Laboratory for Laser Energetics LLE Review **91**, 116, NTIS document No. DOE/SF/19460-458 (2002). Copies may be obtained from the National Technical Information Service, Springfield, VA 22161.

Hydrodynamic Growth of Shell Modulations in the Deceleration Phase of Spherical Direct-Drive Implosions

Introduction

The goal of inertial confinement fusion (ICF)^{1,2} is to implode a spherical target to achieve fuel densities and temperatures adequate to sustain thermonuclear burn. In a spherical implosion the target is driven either by direct illumination with laser beams (direct drive)¹ or by x rays produced in a high-Z enclosure (hohlraum) containing the target (x-ray drive).² The unstable growth of target nonuniformities is the most significant factor disrupting the symmetry of implosions, reducing the target compression and fusion yield.² A direct-drive implosion begins with an acceleration phase when the laser beams ablate the shell surface directly and the capsule starts to converge. At this stage, outer-shell nonuniformities, both existing imperfections in the shell surface and imprinted due to nonuniformities in the laser drive, grow due to the acceleration-phase Rayleigh–Taylor (RT) instability.^{3–16} As the shell accelerates, these front-surface perturbations feed through the shell, seeding perturbations on the inner surface. After the laser is turned off, the ablation front becomes stable and the shell starts to decelerate while continuing to converge. At stagnation, the shell stops (peak compression) and then rebounds. During the deceleration phase, the inner surface of the shell is subject to RT instability.^{17–22} In addition, the modulations grow due to Bell–Plesset (BP) convergent effects²³ throughout the compression.

Experimentally, the hydrodynamic growth of target perturbations has been extensively studied using both x-ray^{2–7} and direct^{8–16} drive mostly in planar geometry. Both classical^{3–5} and ablative^{3–5,8–10} RT-instability linear growth rates have been measured using single-mode perturbations. Multimode^{6,7} and broadband¹⁶ perturbations were used to measure nonlinear saturation^{24–26} and mode-coupling effects. The highly nonlinear, turbulent mixing regime of the RT-instability relevant to ICF conditions has been studied using planar geometry.^{27–31} Experiments in both cylindrical^{32,33} and spherical geometries^{34,35} were used to measure acceleration-phase hydrodynamic growth including BP convergent effects. Small-scale mix of the highly nonlinear classical RT instability has been inferred in both x-ray^{36,37} and direct-drive^{38–40} spherical

implosions. The deceleration-phase RT growth has been measured in spherical implosions using shell radiography by the x rays coming from the hot core emitted near peak compression.^{41–43} This article presents the status of deceleration-phase hydrodynamic growth measurements and discusses future experiments.

Experimental Conditions

The modulation evolution measurements are based on differential imaging^{41–43} of shells with diagnostic titanium-doped layers. Near peak compression of a spherical target implosion, when the maximum density and temperature occur, the hot, compressed core and inner surface of the shell produce strong x-ray emission. This emission can be used as a backlighter to probe the outer, colder shell. The experiments use shells with titanium-doped layers and imaging at photon energies above and below the titanium *K* edge. Core images at photon energies below the *K* edge (not absorbed by the shell) provide the spatial shape of the backlighter, while core images at photon energies above the *K* edge (highly absorbed by the shell's titanium) contain information about the structure of shell-areal-density modulations in the titanium-doped layer. The modulations in the cold, or absorbing, part of the shell areal density $\delta[\rho d](\mathbf{r}, t)$ at time t (\mathbf{r} is the spatial coordinate) are proportional to the modulation in the logarithm of the ratio of intensities of the two images at photon energies above (highly absorbing by the shell) and below (weakly absorbing by the shell) the titanium *K* edge.^{41–43}

Figure 93.7(a) shows a schematic of a spherical target and the position of the diagnostic titanium layer used in these experiments. The targets with $\sim 450\text{-}\mu\text{m}$ initial radii and $20\text{-}\mu\text{m}$ -thick shells, filled with 4 or 18 atm of D^3He gas, were imploded by 351-nm laser light using the 60-beam OMEGA laser system⁴⁴ with a 1-ns square pulse shape at a total energy of ~ 23 kJ. All shots were taken with laser beams smoothed by distributed phase plates (DPP's);⁴⁵ 1-THz, two-dimensional smoothing by spectral dispersion (2-D SSD);⁴⁶ and polarization smoothing (PS)⁴⁷ using birefringent wedges. The average beam-to-beam energy imbalance was $\sim 3\%$ in all

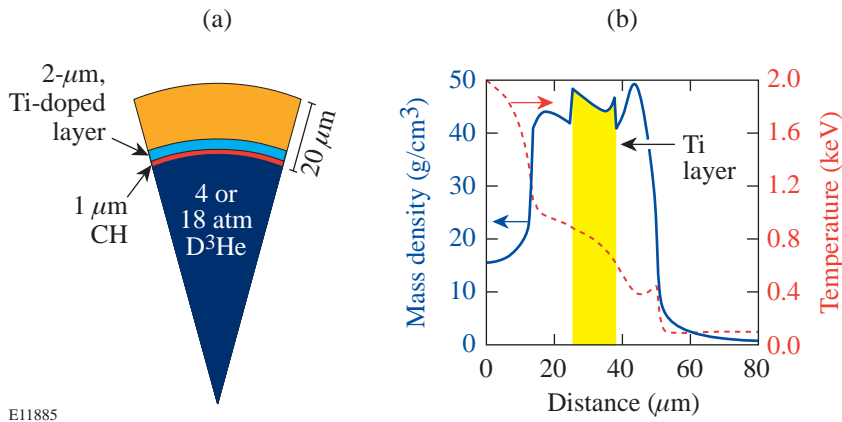


Figure 93.7

Schematic of spherical targets: (a) a 20- μm -thick shell filled with 4 or 18 atm of D^3He gas. (b) Simulated profiles of target density (solid line) and temperature (dashed line) at peak compression for the 18-atm target. The position of a diagnostic titanium-doped layer is shown by the yellow region.

E11885

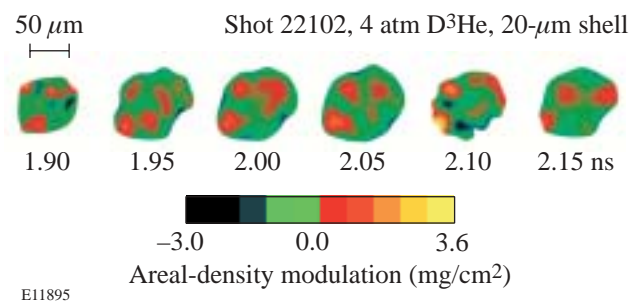
implosions. Targets with 20- μm -thick shells filled with 4 or 18 atm of D^3He gas exhibit similar behavior during their laser-driven acceleration phases and therefore have similar perturbations at the beginning of the deceleration phase. Because of their differing gas-fill pressures (4 or 18 atm), these targets experience different deceleration-phase growth near peak compression.

The $\sim 2\text{-}\mu\text{m}$ -thick, titanium-doped ($\sim 6\%$ by atom) CH layers were offset from the inner surface by $\sim 1\ \mu\text{m}$ of pure CH. These layers were expected to be located at the unstable RT interface near peak compression. Figure 93.7(b) shows the temperature and density profiles of one of the targets [shown in Fig. 93.7(a)] with a 20- μm -thick shell filled with 18 atm of gas, calculated at peak compression by the 1-D code *LILAC*.⁴⁸ The diagnostic titanium layer (shown by the yellow region) is located on the slope of the density profile of the inner shell, where the unstable surface is located. The measured evolution of titanium-doped layer uniformity around peak compression is used to quantify the deceleration RT growth in these implosions.

The areal-density modulations in the titanium layer have been measured with differential imaging^{41–43,49,50} using a framing camera. Simultaneously, the spectral evolution of core emission was captured on an x-ray streak camera. The relative areal-density modulations $\delta[\rho d]/\rho d$ in the titanium-doped layers—a measure of the shell integrity—have been obtained by normalizing the framing camera images of areal-density modulations $\delta[\rho d](\mathbf{r}, t)$ to the average areal density $[\rho d](t)$ measured with the streak camera. Figure 93.8 presents images of measured areal-density modulations $\delta[\rho d](\mathbf{r}, t)$ for a shot with a 20- μm -thick shell and 4 atm of D^3He fill around peak compression. The average titanium areal density $[\rho d](t)$ is not an accurate measure of compression in the layer because the amount of titanium atoms and ions available for absorption

can be modified by the rapidly changing core radiation and the increasing temperature in the shell around peak compression. The shell integrity $\delta[\rho d]/\rho d$ is not affected by these effects; however, an understanding of the implosion hydrodynamics requires measurements of shell-areal-density evolution along with that of the modulations.

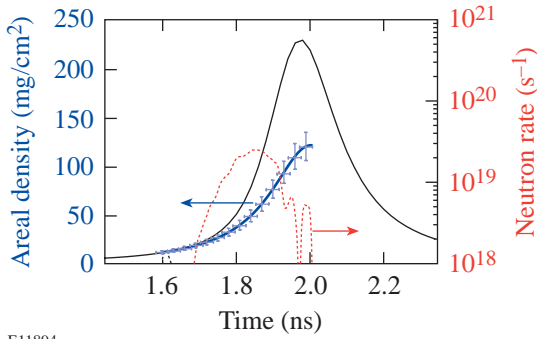
The temporal history of the shell areal density has been inferred⁵¹ from the spectra of primary protons from the D^3He fusion reaction and the evolution of the primary neutrons from the simultaneous DD reaction. The emitted primary 14.7-MeV, D^3He protons are slowed down by the relatively low-density fuel and the high-density shell while exiting the target. The time-integrated proton energy spectrum contains information about the target-areal-density evolution. When the measured proton energy spectrum is coupled with the neutron production history, the areal-density evolution can be inferred during the time of particle production.⁵¹ Figure 93.9 shows the inferred temporal history of total target areal density (thick blue line) compared to a 1-D *LILAC* prediction (thin black line) in the shot with a 20- μm -thick shell and 4 atm of D^3He fill. The



E11895

Figure 93.8

Images of areal-density modulations for a target with a 20- μm -thick shell filled with 4 atm of D^3He gas taken at times 1.90, 1.95, 2.00, 2.05, 2.10, and 2.15 ns.



E11894

Figure 93.9 Inferred (thick blue line) and simulated (thin black line) target-areal-density evolutions for a 4-atm implosion. The measured (dotted line) neutron production history for the 4-atm implosion is from Ref. 51.

neutron-production history is shown by the dotted line for comparison. The total target areal density shown in Fig. 93.9 consists of the shell areal density (about 90% to 95%) and the gas fuel areal density (about 5% to 10%). The target (and shell) areal density grows by a factor of ~ 1.5 from the time of peak neutron production at ~ 1.9 ns to the time of peak compression at ~ 2.0 ns. This growth will be used below to estimate the BP contribution in the total modulation growth.

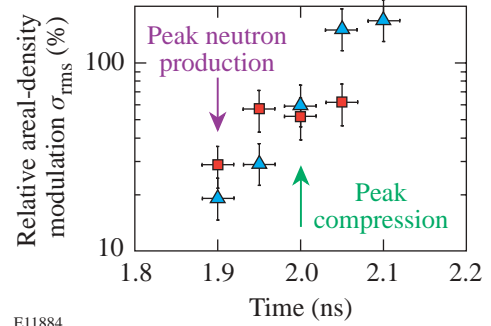
Experimental Results

Figure 93.10 shows the modulation growth inferred for two shots with 20- μm -thick shells and 4 atm of D^3He fill around peak compression. The σ_{rms} of the relative areal-density modulations $\delta[\rho d]/\rho d$ grows by a factor of ~ 10 during the ~ 200 ps around peak compression. The modulation levels are $\sim 20\%$ at peak neutron production (~ 1.9 ns) and $\sim 50\%$ at peak compression (~ 2.0 ns). Figure 93.11 shows a comparison of the non-uniformity spectra taken at peak compression for targets with 20- μm -thick shells filled with 18 atm and 4 atm of D^3He , respectively. These targets exhibit similar behavior during their laser-driven acceleration phases and therefore have similar perturbations at the beginning of the deceleration phase. Because of the different gas-fill pressures (4 or 18 atm), however, these targets experience different deceleration growths near peak compression. The power per mode of relative modulation levels $\delta[\rho d]/\rho d$ as a function of spatial frequency is shown in Fig. 93.11(a) for the more-stable 18-atm and in Fig. 93.11(b) for the more-unstable 4-atm- D^3He fills. The measured areal-density modulation levels are $23\pm 5\%$ and $53\pm 11\%$ for shots with 18-atm- and 4-atm- D^3He fills, respectively. In both spectra, measured perturbations have the highest amplitudes at spatial frequencies of about 20 to 25 mm^{-1} corresponding to spatial wavelengths of 40 to 50 μm (or a

mode number of $\ell \sim 6$), with the smallest detectable features having wavelengths of about 15 to 20 μm .

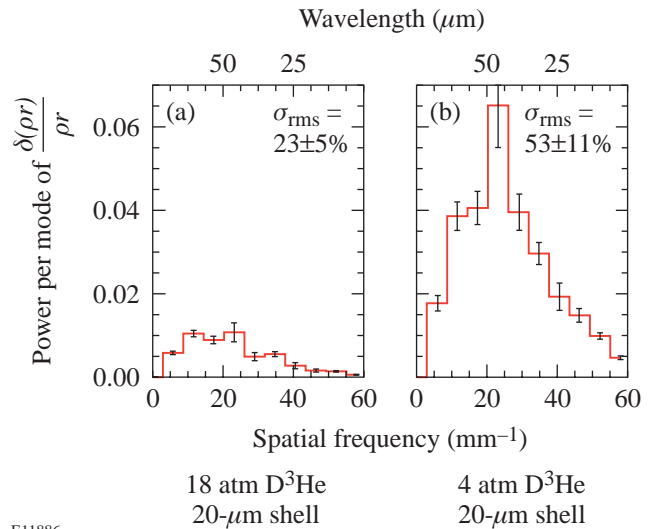
Discussion

The shell’s inner-surface modulations grow due to the RT instability during the deceleration phase since the higher-density shell is slowed down by the lower-density gas of the



E11884

Figure 93.10 The evolution of inner-shell relative areal-density modulation σ_{rms} as a function of time for two shots [shown by triangles (shot 22102) and squares (shot 22103)] with 20- μm -thick shells filled with 4 atm of D^3He gas.



E11886

Figure 93.11 Power-per-mode spectra of relative areal-density modulations as a function of spatial frequency for 20- μm -thick shells filled with (a) 18 atm and (b) 4 atm of D^3He gas taken at peak compression and averaged over two or three shots per condition.

target core.^{25–30} Unlike the acceleration-phase RT instability, where the outer-surface modulation growth is stabilized by mass ablation, the deceleration-phase RT instability is classical, with no ablative stabilization for these targets. In the linear regime of the classical RT instability, the modulation amplitude δr_1 for mode number ℓ [$\ell = kR$, where k is a modulation wave number and $R(t)$ is the radius, or position of the unstable surface] grows exponentially in time:²

$$\delta r_1 = \delta r_0 \exp\left[\sqrt{A_T(\ell/R)gt^2}\right], \quad (1)$$

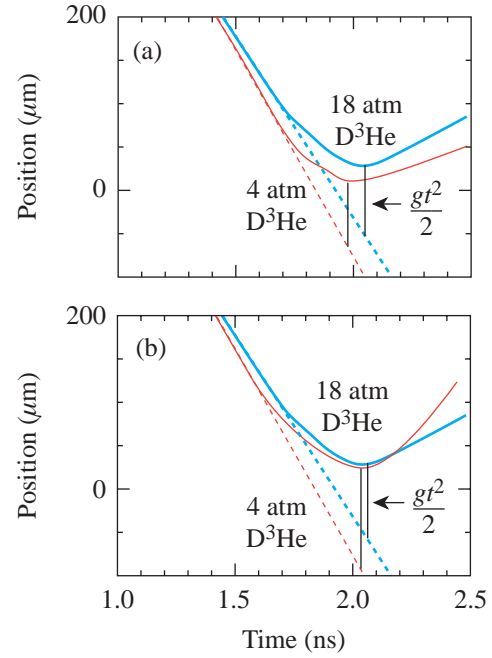
where A_T is the Atwood number, δr_0 is the initial perturbation amplitude, g is the deceleration, and t is time. The characteristic of the classical RT instability is the rapid growth of short-scale perturbation that quickly enters the highly nonlinear regime causing shell-density perturbations $\delta\rho$ in addition to shell-amplitude perturbations δr and shell–fuel mix. The growth of longer-wavelength perturbations can be modified by the presence of mix because the mix increases the core pressure by supplying additional material into the core. As a result, the deceleration g increases and the Atwood number A_T decreases, modifying the shell trajectory and the modulation growth.

The other factor contributing to perturbation growth is Bell–Plesset (BP) convergent effects. As the shell converges from radius R_0 (with thickness d_0 and density ρ_0) to radius R_1 (with thickness d_1 and density ρ_1), the shell modulation δr_1 grows due to BP effects²³ as

$$\delta r_1 = \delta r_0 (\rho_0 R_0^2) / (\rho_1 R_1^2) = \delta r_0 d_1 / d_0.$$

The shell modulation due to BP growth is proportional to shell thickness: $\delta r \sim d$. Note that the modulation growth of shell integrity, $\delta[\rho d]/\rho d$ does not explicitly include BP effects { $\delta[\rho d]/\rho d$ due to BP effects is constant because $\delta(\rho d) \sim (\rho d)$ }; however, the convergent effects constantly modify the RT instability, which is responsible for the modulation growth.

Figure 93.12 presents schematically a physical picture of the implosions to explain the experimental data. One-dimensional *LILAC* predictions of the implosion trajectories with 4 (thin) and 18 atm (thick) of D^3He are shown in Fig. 93.12(a). The solid lines show the trajectories of the shell–fuel interfaces, $R(t) = R_0 - vt + gt^2/2$, for both implosions, and the dashed lines show the free-fall trajectories of these interfaces,



E11881

Figure 93.12

(a) *LILAC*-simulated inner-surface trajectories (solid lines) and free-fall trajectories (dashed lines) as a function of time for 20- μm -thick shells filled with 18 atm (thick) and 4 atm (thin) of D^3He gas. (b) The same trajectories as inferred from the experimental data.

$R_{ff}(t) = R_0 - vt$, where R_0 is the radius and v is the velocity of the inner-shell surface at the beginning of the deceleration phase. The shell velocity v is higher in the 4-atm implosion compared to the 18-atm implosion because the pressure difference between the shell and the gas is higher in the 4-atm case. The RT-growth rate of the unstable modulations in the deceleration phase of the implosion are related to the difference between inner surface and free-fall trajectories, $R(t) - R_{ff}(t) = gt^2/2$. For any mode number ℓ , the growth factor is higher in an implosion with a 4-atm fill compared to an 18-atm fill of D^3He because the $R(t)$ is smaller in the 4-atm implosion, and factors $gt^2/2$ are similar for both implosions at peak compression. In the experiment the expected trajectory for an 18-atm implosion is close to the 1-D *LILAC* prediction because the measured evolution of target areal density is close to 1-D. In the 4-atm implosion, however, the measured target areal density evolution is much lower than the 1-D prediction (as shown in Fig. 93.9) and only about 10% higher than for the 18-atm implosion.⁵¹ The trajectories inferred from the experimental observations are shown schematically in Fig. 93.12(b) for both implosions. At peak compression the trajectories $R(t)$ are similar but the factor $gt^2/2$ is higher in the implosion with a 4-atm fill than in the 18-atm case. The

higher fuel–shell mix is responsible for the higher deceleration in the 4-atm implosion because the core pressure is increased by the addition of shell material from the mix.^{38–40,52}

In the experiments, the relative areal-density modulations with spatial wavelengths ranging from about 15 to 60 μm , $\delta[\rho d]/\rho d$, grow by a factor of ~ 2.5 during the ~ 100 ps from peak neutron production (~ 1.9 ns) to peak compression (~ 2.0 ns) in the 4-atm implosion (see Fig. 93.10). The shell areal density $[\rho d]$ grows by a factor of 1.5 for the same period (see Fig. 93.9) due to the growth of both the density ρ and the thickness d ; therefore, the shell modulations ($\delta r \sim d$) should grow by up to a factor of 1.5 due to BP convergent effects. The BP effects do not contribute directly to the growth of shell integrity, $\delta[\rho d]/\rho d$ therefore, the measured growth of relative areal-density modulation should be entirely due to the RT instability. In addition, the modulation growth modifies the shell trajectories leading to lower compression than predicted by 1-D in the more-unstable 4-atm implosion. At peak compression, the measured areal-density modulation levels are $23 \pm 5\%$ and $53 \pm 11\%$ for shots with 18-atm- and 4-atm- D^3He fills, respectively.

Future Experiments

The RT instability and BP growth are defined by the growth of amplitude modulations δr . In future experiments it will be necessary to measure the evolution of density along with average areal density and areal-density modulations in the

titanium-doped layers to infer the evolution of amplitude modulations δr from the relative areal-density modulations $\delta[\rho d]/\rho d$. The x-ray spectrum in the titanium $1s\text{--}2p$ absorption region is sensitive to the density, areal density, and temperature of the layer. The time-resolved titanium absorption spectroscopy will provide the required information to better understand the unstable growth. In addition, the absorption in the titanium $1s\text{--}2p$ spectral region is higher by a factor of ~ 10 than in the region above the titanium K edge; therefore, differential imaging of shell modulations using $1s\text{--}2p$ absorption will be more sensitive than the results presented here.

As an example, preliminary, time-integrated shell-integrity experiments⁵³ based on titanium $1s\text{--}2p$ absorption were conducted with 20- μm -thick plastic CH shells filled with 18 atm of D^3He gas. The diagnostic was a 1- μm -thick, titanium-doped ($\sim 2\%$ by atom) CH layer offset from the inner surface by $\sim 1, 5, 7,$ or $9 \mu\text{m}$ of pure CH. These layers infer the shell-areal-density modulations at the inner, central, and outer parts of the shell at peak compression. Figure 93.13(a) shows the temperature and density profiles at peak compression of a representative target calculated by the 1-D code *LILAC*. At peak compression, the diagnostic titanium layer offset by $1 \mu\text{m}$ is located on the slope of the density profile at the inner shell, where the unstable surface is located. Titanium layers offset by $5 \mu\text{m}$ and $7 \mu\text{m}$ sample the central part of the shell, and the layer offset by $9 \mu\text{m}$ represents the outer part of the shell at peak compression.

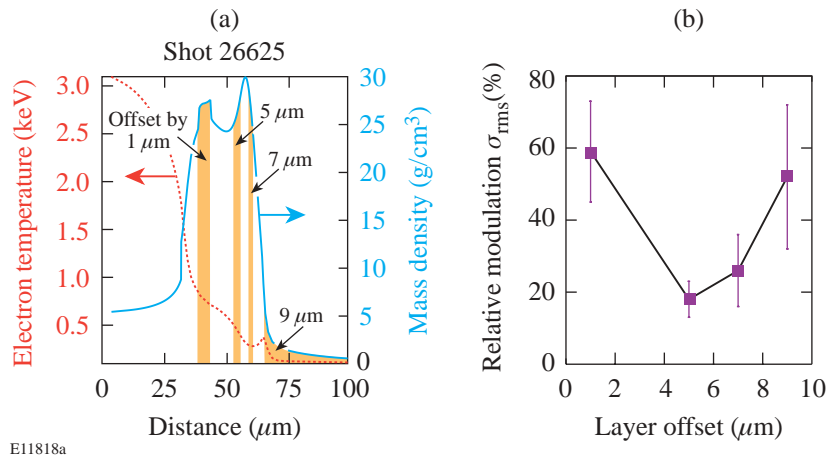


Figure 93.13

(a) *LILAC*-simulated profiles of target density and temperature at peak compression for the implosion of a 20- μm -thick shell filled with 18 atm of D^3He gas. The locations of titanium-doped (2% by atom) layers offset by 1, 5, 7, and 9 μm of pure CH from the inner surface are shown by the gold areas. (b) Peak-compression, relative areal-density modulation σ_{rms} as a function of the layer offset.

At peak compression, time-integrated areal-density modulations were measured using the ratios of monochromatic core images taken inside and outside of the titanium $1s-2p$ absorption spectral region. The relative areal-density modulation σ_{rms} was $59\pm 14\%$, $18\pm 5\%$, $26\pm 10\%$, and $52\pm 20\%$ in the layers offset by 1, 5, 7, and 9 μm , respectively, as shown in Fig. 93.13(b). The modulations are highest at the inner surface (in the 1- μm -offset layer), which is unstable during the deceleration phase of the implosion near peak compression. As expected, the modulations decrease in the bulk of the shell (in the 5- and 7- μm -offset layers) but then increase at the outer surface (in the 9- μm -offset layer), which is unstable during the acceleration phase of the implosion. Time-resolved experiments based on differential imaging using the titanium $1s-2p$ absorption region will be conducted to study the evolution of shell nonuniformities in different parts of the shell.

As discussed in the previous section, the modulation growth of longer spatial wavelengths is modified by the presence of fuel-shell mix, which comes from the growth of shorter spatial wavelengths in the highly nonlinear phase of the classical deceleration-phase RT instability. Direct measurements of mix evolution are essential not only to quantify the short-wavelength RT growth but also to explain the observed reduction of shell compression and the modification of the longer-wavelength RT growth.

Conclusions

Shell modulation growth has been measured on targets with titanium-doped layers using differential imaging near peak compression of spherical implosions with 20- μm -thick plastic CH shells filled with 4 atm of D^3He gas. The measured perturbations have the highest amplitudes at spatial wavelengths of about 40 to 50 μm (corresponding to a mode number $\ell \sim 6$), with the shortest detectable features corresponding to wavelengths of about 15 to 20 μm . At peak neutron production, the relative areal-density modulation level $\delta[\rho d]/\rho d$ is $\sim 20\%$ and grows to $\sim 50\%$ at peak compression 100 ps later due to RT instability. For the same time period, the shell modulations grow up to about 1.5 times due to BP convergent effects. At peak compression the inner part of the shell has a higher modulation level than the bulk of the shell.

ACKNOWLEDGMENT

This work was supported by the U.S. Department of Energy Office of Inertial Confinement Fusion under Cooperative Agreement No. DE-FC03-92SF19460, the University of Rochester, and the New York State Energy Research and Development Authority. The support of DOE does not constitute an endorsement by DOE of the views expressed in this article.

REFERENCES

1. J. Nuckolls *et al.*, *Nature* **239**, 139 (1972).
2. J. D. Lindl, *Inertial Confinement Fusion: The Quest for Ignition and Energy Gain Using Indirect Drive* (Springer-Verlag, New York, 1998), Chap. 6, pp. 61–82.
3. S. G. Glendinning, S. N. Dixit, B. A. Hammel, D. H. Kalantar, M. H. Key, J. D. Kilkenny, J. P. Knauer, D. M. Pennington, B. A. Remington, R. J. Wallace, and S. V. Weber, *Phys. Rev. Lett.* **78**, 3318 (1997).
4. K. S. Budil *et al.* *Phys. Rev. Lett.* **76**, 4536 (1996).
5. K. S. Budil *et al.*, *Phys. Plasmas* **8**, 2344 (2001).
6. B. A. Remington *et al.*, *Phys. Rev. Lett.* **73**, 545 (1994).
7. M. M. Marinak *et al.*, *Phys. Rev. Lett.* **80**, 4426 (1998).
8. J. Grun *et al.*, *Phys. Rev. Lett.* **58**, 2672 (1987).
9. K. Shigemori *et al.*, *Phys. Rev. Lett.* **78**, 250 (1997).
10. J. P. Knauer, R. Betti, D. K. Bradley, T. R. Boehly, T. J. B. Collins, V. N. Goncharov, P. W. McKenty, D. D. Meyerhofer, V. A. Smalyuk, C. P. Verdon, S. G. Glendinning, D. H. Kalantar, and R. G. Watt, *Phys. Plasmas* **7**, 338 (2000).
11. R. J. Taylor *et al.*, *Phys. Rev. Lett.* **76**, 1643 (1996).
12. D. H. Kalantar, M. H. Key, L. B. Da Silva, S. G. Glendinning, B. A. Remington, J. E. Rothenberg, F. Weber, S. V. Weber, E. Wolfgram, N. S. Kim, D. Neely, J. Zhang, J. S. Wark, A. Demir, J. Lin, R. Smith, G. J. Tallents, C. L. S. Lewis, A. MacPhee, J. Warwick, and J. P. Knauer, *Phys. Plasmas* **4**, 1985 (1997).
13. H. Azechi *et al.*, *Phys. Plasmas* **4**, 4079 (1997).
14. C. J. Pawley *et al.*, *Phys. Plasmas* **6**, 565 (1999).
15. T. R. Boehly, V. N. Goncharov, O. Gotchev, J. P. Knauer, D. D. Meyerhofer, D. Oron, S. P. Regan, Y. Srebro, W. Seka, D. Shvarts, S. Skupsky, and V. A. Smalyuk, *Phys. Plasmas* **8**, 2331 (2001).
16. V. A. Smalyuk, T. R. Boehly, D. K. Bradley, V. N. Goncharov, J. A. Delettrez, J. P. Knauer, D. D. Meyerhofer, D. Oron, and D. Shvarts, *Phys. Rev. Lett.* **81**, 5342 (1998).
17. H. Sakagami and K. Nishihara, *Phys. Rev. Lett.* **65**, 432 (1990).
18. R. P. J. Town and A. R. Bell, *Phys. Rev. Lett.* **67**, 1863 (1991).
19. M. M. Marinak *et al.*, *Phys. Plasmas* **3**, 2070 (1996).
20. V. Lobatchev and R. Betti, *Phys. Rev. Lett.* **85**, 4522 (2000).
21. M. C. Herrmann, M. Tabak, and J. D. Lindl, *Phys. Plasmas* **8**, 2296 (2001).
22. R. Betti, K. Anderson, V. N. Goncharov, R. L. McCrory, D. D. Meyerhofer, S. Skupsky, and R. P. J. Town, *Phys. Plasmas* **9**, 2277 (2002).

23. M. S. Plesset and T. P. Mitchell, *Q. Appl. Math.* **13**, 419 (1956).
24. S. W. Haan, *Phys. Rev. A* **39**, 5812 (1989).
25. S. W. Haan, *Phys. Fluids B* **3**, 2349 (1991).
26. M. J. Dunning and S. W. Haan, *Phys. Plasmas* **2**, 1669 (1995).
27. D. L. Youngs, *Physica D* **37**, 270 (1989).
28. K. I. Read, *Physica* **12D**, 45 (1984).
29. G. Dimonte and M. Schneider, *Phys. Rev. E* **54**, 3740 (1996).
30. G. Dimonte, *Phys. Plasmas* **6**, 2009 (1999).
31. M. B. Schneider, G. Dimonte, and B. Remington, *Phys. Rev. Lett.* **80**, 3507 (1998).
32. W. W. Hsing *et al.*, *Phys. Plasmas* **4**, 1832 (1997).
33. D. L. Tubbs, C. W. Barnes, J. B. Beck, N. M. Hoffman, J. A. Oertel, R. G. Watt, T. Boehly, D. Bradley, P. Jaanimagi, and J. Knauer, *Phys. Plasmas* **6**, 2095 (1999).
34. C. Cherfils *et al.*, *Phys. Rev. Lett.* **83**, 5507 (1999).
35. S. G. Glendinning *et al.*, *Phys. Plasmas* **7**, 2033 (2000).
36. T. R. Dittrich *et al.*, *Phys. Rev. Lett.* **73**, 2324 (1994).
37. M. D. Cable *et al.*, *Phys. Rev. Lett.* **73**, 2316 (1994).
38. D. D. Meyerhofer, J. A. Delettrez, R. Epstein, V. Yu. Glebov, V. N. Goncharov, R. L. Keck, R. L. McCrory, P. W. McKenty, F. J. Marshall, P. B. Radha, S. P. Regan, S. Roberts, W. Seka, S. Skupsky, V. A. Smalyuk, C. Sorce, C. Stoeckl, J. M. Soures, R. P. J. Town, B. Yaakobi, J. D. Zuegel, J. Frenje, C. K. Li, R. D. Petrasso, D. G. Hicks, F. H. Séguin, K. Fletcher, S. Padalino, M. R. Freeman, N. Izumi, R. Lerche, T. W. Phillips, and T. C. Sangster, *Phys. Plasmas* **8**, 2251 (2001).
39. P. B. Radha, J. Delettrez, R. Epstein, V. Yu. Glebov, R. Keck, R. L. McCrory, P. McKenty, D. D. Meyerhofer, F. Marshall, S. P. Regan, S. Roberts, T. C. Sangster, W. Seka, S. Skupsky, V. Smalyuk, C. Sorce, C. Stoeckl, J. Soures, R. P. J. Town, B. Yaakobi, J. Frenje, C. K. Li, R. Petrasso, F. Séguin, K. Fletcher, S. Padalino, C. Freeman, N. Izumi, R. Lerche, and T. W. Phillips, *Phys. Plasmas* **9**, 2208 (2002).
40. S. P. Regan, J. A. Delettrez, F. J. Marshall, J. M. Soures, V. A. Smalyuk, B. Yaakobi, V. Yu. Glebov, P. A. Jaanimagi, D. D. Meyerhofer, P. B. Radha, W. Seka, S. Skupsky, C. Stoeckl, R. P. J. Town, D. A. Haynes, Jr., I. E. Golovkin, C. F. Hooper, Jr., J. A. Frenje, C. K. Li, R. D. Petrasso, and F. H. Séguin, *Phys. Rev. Lett.* **89**, 085003 (2002).
41. B. Yaakobi, V. A. Smalyuk, J. A. Delettrez, F. J. Marshall, D. D. Meyerhofer, and W. Seka, *Phys. Plasmas* **7**, 3727 (2000).
42. V. A. Smalyuk, V. N. Goncharov, J. A. Delettrez, F. J. Marshall, D. D. Meyerhofer, S. P. Regan, and B. Yaakobi, *Phys. Rev. Lett.* **87**, 155002 (2001).
43. V. A. Smalyuk, J. A. Delettrez, V. N. Goncharov, F. J. Marshall, D. D. Meyerhofer, S. P. Regan, T. C. Sangster, R. P. J. Town, and B. Yaakobi, *Phys. Plasmas* **9**, 2738 (2002).
44. T. R. Boehly, D. L. Brown, R. S. Craxton, R. L. Keck, J. P. Knauer, J. H. Kelly, T. J. Kessler, S. A. Kumpan, S. J. Loucks, S. A. Letzring, F. J. Marshall, R. L. McCrory, S. F. B. Morse, W. Seka, J. M. Soures, and C. P. Verdon, *Opt. Commun.* **133**, 495 (1997).
45. Y. Lin, T. J. Kessler, and G. N. Lawrence, *Opt. Lett.* **20**, 764 (1995).
46. S. P. Regan, J. A. Marozas, J. H. Kelly, T. R. Boehly, W. R. Donaldson, P. A. Jaanimagi, R. L. Keck, T. J. Kessler, D. D. Meyerhofer, W. Seka, S. Skupsky, and V. A. Smalyuk, *J. Opt. Soc. Am. B* **17**, 1483 (2000).
47. T. R. Boehly, V. A. Smalyuk, D. D. Meyerhofer, J. P. Knauer, D. K. Bradley, R. S. Craxton, M. J. Guardalben, S. Skupsky, and T. J. Kessler, *J. Appl. Phys.* **85**, 3444 (1999).
48. J. Delettrez, R. Epstein, M. C. Richardson, P. A. Jaanimagi, and B. L. Henke, *Phys. Rev. A* **36**, 3926 (1987).
49. V. A. Smalyuk, T. R. Boehly, L. S. Iwan, T. J. Kessler, J. P. Knauer, F. J. Marshall, D. D. Meyerhofer, C. Stoeckl, B. Yaakobi, and D. K. Bradley, *Rev. Sci. Instrum.* **72**, 635 (2001).
50. V. A. Smalyuk, B. Yaakobi, J. A. Delettrez, F. J. Marshall, and D. D. Meyerhofer, *Phys. Plasmas* **8**, 2872 (2001).
51. V. A. Smalyuk, P. B. Radha, J. A. Delettrez, V. Yu. Glebov, V. N. Goncharov, D. D. Meyerhofer, S. P. Regan, S. Roberts, T. C. Sangster, J. M. Soures, C. Stoeckl, J. A. Frenje, C. K. Li, R. D. Petrasso, and F. H. Séguin, "Time-Resolved Areal-Density Measurements with Proton Spectroscopy in Spherical Implosions," to be published in *Physical Review Letters*.
52. C. K. Li, F. H. Séguin, J. A. Frenje, S. Kurebayashi, R. D. Petrasso, D. D. Meyerhofer, J. M. Soures, J. A. Delettrez, V. Yu. Glebov, P. B. Radha, F. J. Marshall, S. P. Regan, S. Roberts, T. C. Sangster, and C. Stoeckl, *Phys. Rev. Lett.* **89**, 165002 (2002).
53. V. A. Smalyuk, S. B. Dumanis, F. J. Marshall, J. A. Delettrez, D. D. Meyerhofer, S. P. Regan, T. C. Sangster, B. Yaakobi, and J. A. Koch, to be published in *Physics of Plasmas*.

Improved Performance of Direct-Drive ICF Target Designs with Adiabatic Shaping Using an Intensity Picket

Introduction

Hydrodynamic instabilities put severe constraints on target designs for inertial confinement fusion (ICF) experiments.^{1,2} A large number of papers published over the last 30 years have been dedicated to the study of the seeding and subsequent growth of the hydrodynamic instabilities that develop during the shell implosion.³ A particularly large effort (both theoretical and experimental) has been directed to understanding the growth rate of the dominant hydrodynamic instability—the Rayleigh–Taylor (RT) instability.⁴ The RT instability inevitably occurs in systems where the heavier fluid is accelerated by the lighter fluid. Such conditions arise during the shell compression in ICF implosions, where the heavier shell material is accelerated by the lighter blowoff plasma.¹ The RT-instability growth amplifies the shell distortions seeded by initial surface roughness and laser nonuniformities (laser “imprint”). Grown to substantial amplitudes, the shell nonuniformities reduce the shell ρR and the neutron yield. Fortunately for ICF implosions, the thermal conduction that drives the ablation process creates several stabilizing effects that reduce both the nonuniformity seeding and the RT-growth rates.³ Indeed, seeding due to the laser nonuniformity is determined by how quickly the plasma atmosphere is created around the imploding shell. The laser radiation is absorbed at some distance from the cold shell. The larger this distance (the conduction zone), the larger the smoothing effect⁵ of the thermal conductivity within the conduction zone and the smaller the laser imprint. The stabilization of the RT modes is also due to the thermal conductivity that drives the mass ablation of the shell material. The ablation process is characterized by the ablation velocity V_a , which is defined as the ratio of the mass ablation rate to the shell density, $V_a = \dot{m}/\rho_{sh}$. The larger the value of the ablation velocity, the larger the ablative stabilization.³ Taking thermal smoothing and ablative stabilization into account, one can make a general statement that the higher the initial intensity of the drive laser pulse, the smaller the nonuniformities and the more stable the implosion. Indeed, the higher intensity tends to create the conduction zone in shorter time, reducing the laser imprint. In addition, the initial shock launched by the higher-intensity pulse is stronger, resulting in larger shock preheat. This re-

duces the shell density, increasing the ablation velocity. Furthermore, a lower density leads to an increase in the shell thickness and a reduction in the perturbation feedthrough from the ablation front to the shell’s rear surface (which becomes unstable during the deceleration phase of the implosion). There is a price to pay, however, for the greater stability. As the stronger shock propagates through the shell, it increases the shell entropy. A parameter (commonly used in the ICF community^{1,2}) that characterizes the shell entropy during the implosion is the shell adiabat α . The adiabat is defined as the ratio of the shell pressure to the Fermi-degenerate pressure calculated at the shell density. Since the shell compressibility is reduced by an increase in the adiabat, the final compression ratio and the target neutron yield are also reduced. A common practice in designing direct-drive targets is to find the delicate balance between reduction in the target performance due to an increase in the adiabat and the increase in shell stability.

In optimizing the target design, one can take into consideration that the RT modes are surface modes peaked at the ablation surface of the shell. Therefore, to reduce the instability growth, it is sufficient to raise the adiabat only at the outer region of the shell, which ablates during the implosion. If the inner portion of the shell is kept on a lower adiabat, the shell and vapor compressibility will not be reduced during the final stage of implosion, and the neutron yields will be unaffected by this selective adiabat increase (adiabat shaping). New direct-drive designs proposed in the current work use adiabat shaping to improve the performance of the imploding shells. The idea of adiabat shaping using radiation preheat has already been implemented in an ignition target presented in Ref. 2. The designs described in this article use a different approach. The shell adiabat is shaped by launching a shock whose strength decreases as it propagates through the shell. This places an adiabat gradient directed toward the ablation front. Time variation in the shock strength is imposed by using an intensity picket in front of the main-drive pulse. The picket launches a strong shock that propagates through the shell. As the laser intensity drops at the end of the picket, the shocked material starts to expand and a rarefaction wave is launched toward

the shock. After the rarefaction and the shock coalesce, the shock strength decays, reducing the adiabat of the shock-compressed material.

The picket pulse shapes for the direct-drive (DD) ignition target designs were first proposed in Ref. 6. The main motivation for such pulses was to replace a continuous shell acceleration with an impulsive acceleration. The impulsive acceleration leads to a linear-in-time growth, replacing the exponential RT growth.

It would be premature, however, to make a conclusion about the shell stability based only on an analysis of the ablation velocity. A careful account of all additional sources of the perturbation growth prior to and during the shell acceleration is required. The analysis reported in this article reveals that introducing an adiabat gradient creates conditions for an additional instability. In the shaped-adiabat designs, the gradient in the entropy has the same sign as the effective acceleration, which excites the convective instability.⁷ It is well known,⁷ however, that the convective instability modes are internal modes (the eigenmode maximum is localized inside the shell), and the instability growth rates are lower than those of the classical RT instability. Although our analytical calculations and numerical simulations show that such an instability makes no significant contribution to the overall shell nonuniformity balance in the designs described here, care must be taken to control the seeding and the growth of the internal convective modes. In addition, the analysis reveals an “early time” RT growth (prior to the acceleration RT growth) at the ablator/main fuel interface during the transitional phase between the picket and the main drive pulse. Such a growth leads to a modification in the mode structure prior to the acceleration phase.

This article identifies the main advantages and possible disadvantages in using adiabat shaping in ICF target designs. The following sections (1) derive a time history of the material flow in a decaying shock configuration; (2) describe new DD designs for the OMEGA⁸ and the National Ignition Facility’s⁹ laser systems and present the results of stability analysis of such designs; and (3) summarize the results of the experiments performed with the shaped-adiabat warm plastic targets.¹⁰

Propagation of a Decaying Shock

As described in the **Introduction**, new target designs are proposed using an intensity picket to shape the adiabat inside the shell. In this section we determine the adiabat profile by solving a simplified problem of shock propagation in the case

of an impulsive applied pressure. We assume that a finite pressure p_p is applied during a time interval $0 < t < t_p$. At $t > t_p$ the applied pressure goes to zero. During the picket duration, a strong shock is launched into the shell. As the external pressure goes to zero, the shocked material starts to expand, launching a rarefaction wave in the direction of the initial shock. At $t = t_p + t_{rw}$ the rarefaction wave catches up with the shock, and the shock strength starts to decay. Therefore, by the time the shock breaks out at the rear surface, the adiabat at the shell’s rear surface will be lower than the adiabat at the front surface. The problem of shock propagation in the case of the impulsive load has been considered previously,^{11,12} and the solution was obtained using a self-similar analysis.¹¹ Such an analysis, however, is only valid asymptotically ($t \gg t_p$). Since there is a finite decrease in the entropy prior to the time when the solutions of Ref. 11 become valid, the self-similar treatment cannot predict the total entropy variation across the shell, so we must use a different approach to determine the adiabat profile.

Assuming that in the laboratory frame of reference the shock moves in the negative x direction with the velocity $U_s = \sqrt{(\gamma + 1)p_s / (2\rho_0)}$, the hydrodynamic conservation equations can be combined to determine the time evolution of the pressure p_s at the shock front:

$$\frac{dp_s}{dt} = \frac{\gamma - 1}{2\gamma - 1} U_s (\partial_x p)_s, \quad (1)$$

where γ is the ratio of specific heats and ρ_0 is the initial shell density. In writing Eq. (1) we used a strong-shock limit $p_s/p_0 \gg 1$, where p_0 is the initial shell pressure. Next, we must calculate the pressure gradient at the shock front. We accomplish this by considering a physically equivalent problem: instead of a decaying shock propagating through a uniform density (first problem), we consider a rarefaction wave propagating along the hydrodynamic profiles with finite density, pressure, and entropy gradients (second problem). These two problems will be equivalent if the hydrodynamic profiles of the second problem will satisfy the Hugoniot relations⁷ at the shock position in the first problem. If the shock remains strong at all times, the compressed density right after the shock front remains constant, $\rho_s = (\gamma + 1)/(\gamma - 1)\rho_0$. Therefore, the Hugoniot relations must be satisfied in the second problem at the point where the local density is equal to ρ_s . To simplify the solution of the second problem near the shock front, we order $L_s^{-1} = \partial_x s/s \ll \gamma \partial_x \rho/\rho = \gamma L_p^{-1}$ (the large γ limit), where s is the shell entropy. This leads to an intro-

duction of the long-scale variables $T = t\delta$ and $X = x\delta$, where $\delta \sim L_p/(\gamma L_s) \ll 1$. Next, we expand the mass and momentum equations and all hydrodynamic functions in powers of δ and perform a multiscale analysis. Keeping only the zero-order terms in δ in the conservation equations yields the system $(v - \xi)\partial_\xi \rho + \rho \partial_\xi v = 0$, $(v - \xi)\partial_\xi v + c_s^2 \partial_\xi \rho/\rho = 0$, where $\xi = x/(t - t_p)$ [the rarefaction wave is launched at $t = t_p$]. Solving the last system gives $(v - \xi)^2 = c_s^2$, where $c_s = \sqrt{\gamma p/\rho}$. For the rarefaction wave propagating in the negative x direction, we obtain $v = \xi + c_s$. Then, the pressure profile inside the rarefaction wave becomes

$$p = p_p (s_p/s)^{1/(\gamma-1)} \left[2c(X,T)/c_p(\gamma+1) - (\gamma-1)/(\gamma+1) \xi/c_p \right]^{2\gamma/(\gamma-1)},$$

where $c_p = \sqrt{\gamma p_p/\rho_s}$, $s_p = p_p/\rho_s^\gamma$, and $c(X,T)$ is an undefined function of the long-scale variables. Taking the spatial derivative of pressure at the shock front, $\partial_x p \approx \partial_\xi p/(t - t_p)$, yields

$$\partial_x \frac{p_s}{p_p} \approx - \sqrt{\frac{p_s}{p_p}} \frac{2\gamma}{\gamma+1} \frac{1}{c_p(t-t_p)}. \quad (2)$$

Observe that the gradient does not explicitly depend on the unknown function $c(X,T)$; this significantly simplifies the analysis. Substituting Eq. (2) back into Eq. (1) gives $dp_s/dt = -\beta p_s/(t - t_p)$ and $\beta = \sqrt{2\gamma(\gamma-1)}/(2\gamma-1)$, which leads to

$$\frac{p_s}{p_p} = \frac{\alpha_s}{\alpha_f} = \left(\frac{t-t_p}{t_{\text{rw}}} \right)^{-\beta}, \quad (3)$$

where t_{rw} is the rarefaction wave's propagation time from the outer surface of the foil to the shock front and α_f and α_s are the adiabat¹ at the front surface of the shell and shock front, respectively. It can be shown that the corrections to Eq. (3) due to the long-scale variations are small when $\gamma > 1.2$. Figure 93.14 compares Eq. (3) (dashed curve) with the results of numerical simulation (solid curve) using the one-dimensional Lagrangian code *LILAC*.¹³ The figure shows evolution of the pressure at the shock front calculated for a 200- μm -thick DT foil driven by a 300-ps, 3.3×10^{14} W/cm² laser pulse ($t_p + t_{\text{rw}}$

= 440 ps in this case). A good agreement between theoretical predictions and numerical results confirms the accuracy of Eq. (3). Figure 93.14 also plots the results obtained using the self-similar solution of Ref. 11 ($\beta = 0.78$) (dotted curve). Although the self-similar solution accurately predicts the shock pressure's decaying rate after $t = 1$ ns, the absolute value of the pressure (and the adiabat) is ~40% lower than the value obtained in the simulation.

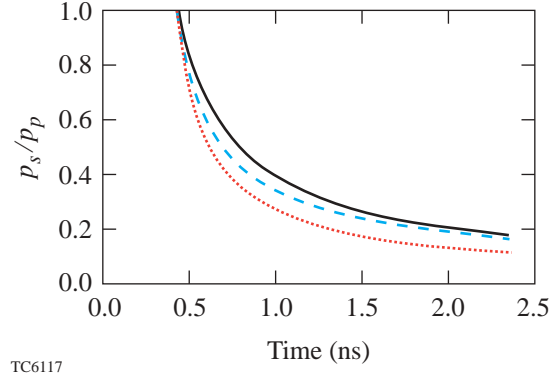


Figure 93.14

Pressure at the shock front calculated using Eq. (3) (dashed curve), results of one-dimensional code *LILAC* (solid curve), and the self-similar solution of Ref. 11 (dotted curve). Calculations are performed for a 200- μm -thick DT foil driven by a 300-ps intensity picket.

Next, using Eq. (3) we calculate the entropy distribution inside the shell in terms of the mass coordinate. First, we introduce the mass m^* per unit area compressed by the shock during time interval $t = t_{\text{rw}} + t_p$, $m^* = \rho_0 U_s^p (t_p + t_{\text{rw}})$, where $U_s^p = \sqrt{(\gamma+1)p_p/(2\rho_0)}$. The rarefaction-wave propagation time t_{rw} can be related to the picket duration time t_p by equating the distance traveled by the shock (in the frame of reference of the compressed material) $d_s = (t_p + t_{\text{rw}})U_{\text{sh}}^p(\gamma-1)/(\gamma+1)$ to the distance traveled by the rarefaction wave $d_s = c_p t_{\text{rw}}$. This gives $t_p/t_{\text{rw}} = \sqrt{2\gamma(\gamma-1)} - 1$. The fraction of mass dm overtaken by the shock during time dt is $dm = \rho_0 U_s dt$. This gives $dm/dt = (m^*/t_{\text{rw}}) \sqrt{\alpha_s/\alpha_f} / (1 + t_p/t_{\text{rw}})$. With the help of Eq. (3), the solution of the last equation becomes

$$\alpha(m) = \alpha_f \left[\frac{2-\beta}{2} \sqrt{\frac{2\gamma}{\gamma-1}} \left(\frac{m}{m^*} - 1 \right) + 1 \right]^{-2\beta/(2-\beta)}. \quad (4)$$

For a practical application, it is important to determine the duration t_p and the height p_p of the picket that gives the maximum adiabat ratio α/α_b at the beginning of the shell

acceleration (the onset of the RT-instability growth), where $\alpha_b = \alpha(m_{\text{sh}})$ is the adiabat at the shell's rear surface and m_{sh} is the total shell mass. The target starts to accelerate soon after the shock breakout at the shell's rear surface. Therefore, to calculate the adiabat at the position of the ablation front at the beginning of the shell acceleration, we must calculate the fraction of the shell material ablated during the shock transit. For a constant applied pressure p_p , the shock transit time across the shell of thickness Δ_0 is $t_{\text{shock}} = \Delta_0 / \sqrt{(\gamma+1)p_p/(2\rho_0)}$. Then, using the scaling of the mass ablation rate

$$\dot{m}(\text{g/cm}^2/\text{s}) = 1.05 \times 10^6 I_{15}^{1/3}$$

and the ablation pressure¹ $p_p(\text{Mbar}) = 80.5 I_{15}^{2/3}$, we obtain the ablated DT mass during the shock propagation, $\Delta m = 0.2 m_{\text{sh}}$. Here, I_{15} is the laser intensity in units of 10^{15} W/cm^2 . Observe that since Δm does not depend on the applied pressure, we can use the derived ablated fraction also in the case of the picket pulse. Substituting $m = \Delta m$ into Eq. (4) we obtain the ablation-front adiabat α_{abl} at the beginning of shell acceleration:

$$\frac{\alpha_{\text{abl}}}{\alpha_b} = \left[\frac{(1-\beta/2)\sqrt{2\gamma/(\gamma-1)}(m_{\text{sh}}/m^* - 1) + 1}{(1-\beta/2)\sqrt{2\gamma/(\gamma-1)}(0.2m_{\text{sh}}/m^* - 1) + 1} \right]^{2\beta/(2-\beta)}. \quad (5)$$

Observe that α_{abl} is a monotonically growing function of m^* . Equation (4), however, is valid only for $m \geq m^*$, thus α_{abl} reaches the maximum value at $m^* = 0.2 m_{\text{sh}}$,

$$\max(\alpha_{\text{abl}}) = \alpha_b \left[2(2-\beta) \sqrt{\frac{2\gamma}{\gamma-1}} + 1 \right]^{2\beta/(2-\beta)} = 6.3 \alpha_b$$

for $\gamma = 5/3$. This shows that at the onset of the RT instability, the maximum ratio of the ablation front and rear-surface adiabat that can be achieved with a single picket pulse is 6. Taking into account that $V_a \sim \alpha^{3/5}$, this gives an increase in the ablation velocity by a factor of 3 at the beginning of the shell acceleration. The ablation velocity, however, decays in time since the ablation front moves into a region with a lower adiabat. Using

$$m^* = \rho_0 U_{\text{sh}}^p t_{\text{rw}} \sqrt{2\gamma/(\gamma-1)} = 0.2 m_{\text{sh}} = 0.2 \rho_0 \Delta_0$$

leads to a relation between the applied impulsive pressure p_p , duration of the picket t_p , and the shell thickness Δ_0 , $p_p t_p^2 \approx 9 \times 10^{-3} \rho_0 \Delta_0^2$. For DT shells, $\rho_0 = 0.25 \text{ g/cm}^3$, and the picket pressure is $p_p = 6.3 p_b$, where $p_b(\text{Mbar}) = 2.14 \rho_s^{5/3} \alpha_b$ is the pressure at the shell's rear surface. Therefore, the optimum pulse duration becomes $t_p(\text{ns}) \sim 10^{-3} \Delta_0(\mu\text{m}) / \sqrt{\alpha_b}$. For a typical OMEGA cryo design $\Delta_0 \sim 80 \mu\text{m}$, and the optimum picket duration for $\alpha_b = 3$ is $t_p = 50 \text{ ps}$. For the NIF DD designs with $\Delta_0 \approx 350 \mu\text{m}$, $t_p \approx 200 \text{ ps}$. This estimate shows that the new target designs require short picket pulses to optimize the adiabat shape inside the shell. In the next section we study the effect of adiabat shaping on the perturbation growth in the OMEGA and NIF cryogenic target designs.

NIF and OMEGA Target Designs with Adiabat Shaping

Adiabat shaping is expected to reduce the growth rates of the RT-instability modes. The final mode amplitudes, however, depend not only on the growth rates but also on the initial seeds. Such seeds are determined by the surface roughness and the laser imprint amplified/reduced by the perturbation evolution during the early stage of the implosion when the first shock launched at the beginning of the laser pulse propagates through the shell. The perturbation amplification factor at the early stage depends on the details of a particular target design. In this section we study the effects of adiabat tailoring (in both the seeding and the RT-growth rates) in the cryogenic $\alpha = 3$ targets designed for the OMEGA and the NIF laser facilities. Here, α stands for the adiabat at the back of the shell. To avoid confusion, we refer to the OMEGA and NIF $\alpha = 3$ designs previously described in Ref. 14 as the standard designs. The designs presented in the current work will be referred to as picket designs. The standard designs have a very thin ($1 \mu\text{m}$ for the OMEGA shells and $3 \mu\text{m}$ for the NIF shells) plastic overcoat required for DT-shell fabrication. These targets are driven by a laser pulse that consists of a constant-intensity foot ($I \sim 10^{13} \text{ W/cm}^2$) followed by the main drive pulse with $I_{\text{max}} \sim 10^{15} \text{ W/cm}^2$. The requirement for the very thin overcoat layers comes from the minimization of the early-stage perturbation growth factors. Such a growth is due to an impedance mismatch between plastic and DT ice that leads to an additional perturbation growth by a factor¹⁵ $\sim e^{1.5\sqrt{k d_{\text{CH}}}}$, where k is the perturbation wave number and d_{CH} is the overcoat thickness. In the picket designs, such a requirement, as shown later, can be relaxed, and a thicker polymer overcoat is used to facilitate shell manufacturing and to increase the laser absorption. The overcoat thickness is determined by the requirement that the plastic layer be ablated by the beginning of the acceleration phase. This is done to take advantage of the higher ablation velocity of the lower-density DT ice. There is a negative side,

however, in an increased overcoat thickness: when the DT ice becomes the ablator, radiation from the plastic present in the hot corona streams through the ablator, preheating the main fuel. The picket designs, nevertheless, use thicker polymer layers ($5\ \mu\text{m}$ for OMEGA and $17\ \mu\text{m}$ for the NIF) since our calculations show the beneficial overall effects of an increased overcoat thickness. The picket designs for OMEGA and the NIF are presented in Fig. 93.15. The laser pulse in both cases consists of a picket [we assume a Gaussian picket with FWHM (full width at half maximum) = t_p], an intensity rise, and the main-drive pulse with the maximum power P_{max} .

Shell thickness is determined by the implosion velocity and the laser energy. The minimum implosion velocity¹ required for ignition of large-aspect-ratio cryogenic targets is $\min(V_{\text{imp}}) \sim 3 \times 10^7\ \text{cm/s}$. The implosion velocity in a robust ignition design must exceed this value in order to have excess kinetic energy at the time of ignition. Such a margin^{14,16} helps to compensate for the effects of the shell nonuniformity. A larger value of the implosion velocity is also required to reduce the perturbation growth rates during the deceleration phase of implosion. As shown in Ref. 17, the ablation velocity during the deceleration phase is proportional to the hot-spot temperature to the power 5/2. The larger implosion velocity leads to a higher hot-spot temperature¹⁶ ($T_{\text{hs}} \sim V_{\text{imp}}$) and larger ablative stabilization of the RT modes during the shell deceleration. Based on results of the stability analysis, we found that the implosion velocity for the direct-drive NIF targets should not be less than $4 \times 10^7\ \text{cm/s}$. For the current design we choose

$V_{\text{imp}} = 4.3 \times 10^7\ \text{cm/s}$. A given implosion velocity and the absorbed laser energy (which can be translated into the shell kinetic energy, taking into account the implosion efficiency of $\sim 7\%$) uniquely determine the shell mass.

Shell radius is defined by minimizing the duration of the shell's coasting phase. Soon after the laser is turned off (end of the acceleration phase), the target starts to decompress: the front and rear surfaces expand with a local sound speed. The expansion of the back of the shell lasts until the main shock reflected from the shell center starts to interact with the incoming shell (beginning of the deceleration phase). Minimizing the time of the shell's free expansion (coasting phase) maximizes the final total ρR . This leads to a requirement on the shell radius: by the time the laser is turned off, the main shock must reach the shell center. If the shell radius is too small, on the other hand, the deceleration phase will begin while the laser is still on. The high pressure in the vapor will prevent, in this case, the shell from gaining the required implosion velocity; therefore, an effective transfer of the absorbed laser energy to the shell's kinetic energy will not be possible.

Laser pulse shape in the picket design is determined by several parameters: (1) rear-surface adiabat, which affects the target neutron yield and shell ρR (it also controls the stability during the deceleration phase), (2) the adiabat shape inside the shell, and (3) proper timing of all shocks and compression waves developed during the implosion. The first two parameters determine the picket peak intensity and picket duration

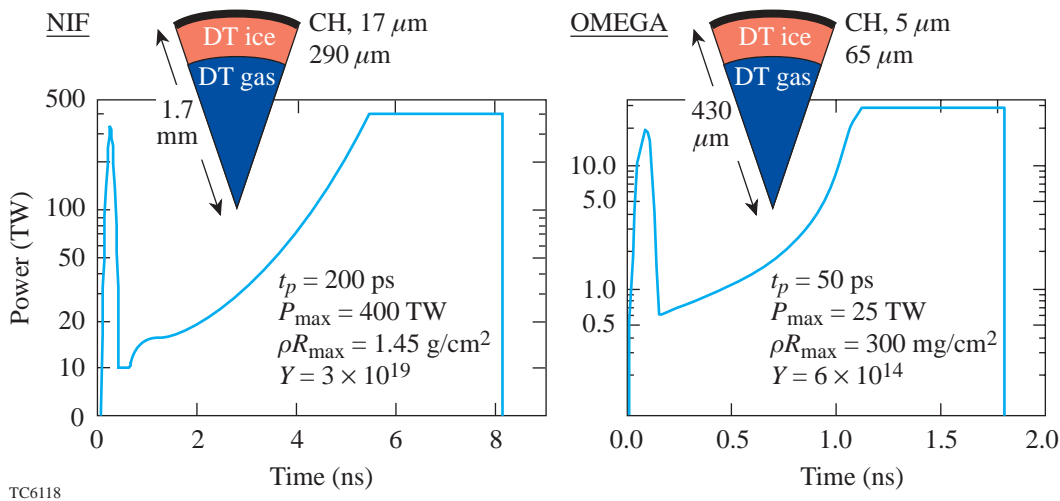


Figure 93.15
Direct-drive, $\alpha = 3$ cryogenic target designs for the OMEGA and NIF laser systems.

(see the previous section). Meeting the third constraint on the pulse shaping requires accounting for all hydrodynamic waves that are launched during the implosion. Next, we summarize the main waves. First, a strong shock wave (SW_1) is launched by the picket at the beginning of the pulse. Then, as the intensity drops to a much lower level after $t = t_p$, a rarefaction wave (RW_p) starts to propagate through the shock-compressed material, and, as soon as the rarefaction catches the shock, the shock strength starts to decrease. The SW_1 sets up the shell adiabat for the entire acceleration phase (with a minor increase due to a radiation preheat and additional hydrodynamic waves). Later, the laser power ramps up to reach the maximum value P_{\max} , and a compression wave or a weak shock is formed at the ablation front. To emphasize that such a wave should not turn into a strong shock (this limits the slopes of the intensity rise), we denote this wave as a compression wave (CW). As the SW_1 breaks out at the shell's rear surface, the surface starts to expand, launching a rarefaction wave (RW_b). While the RW_b travels from the rear surface toward the ablation front, it establishes some velocity, pressure, and density gradients. Each fluid element inside the RW_b is accelerated according to $dv/dt = -\partial_x p/\rho$, where p and ρ are the pressure and density of the fluid element. At the head of the rarefaction, ρ is equal to the shell density compressed by the SW_1 and CW . When RW_b reaches the ablation front, the density suddenly drops, creating a large acceleration gradient. This forms a local excess in the pressure that starts to propagate in the form of a compression wave along decreasing pressure and density profiles. A compression wave propagating along a decaying density turns into a shock (SW_2) inside the shell.¹⁸ We want to stress here that SW_2 cannot be avoided. It will be created even for a constant-intensity pulse. The effect of SW_2 on the target performance, however, can be minimized by appropriately choosing the rise time of the laser pulse: the point where the laser reaches the maximum power must be between the SW_1 breakout at the rear surface and the RW_b breakout at the ablation front (in other words, the laser must reach the peak power while RW_b propagates through the shell). In addition, a proper timing of the pulse requires that, while traveling inside the shell, the SW_1 always be ahead of the CW . The time difference, however, between the breakout of the CW and SW_1 at the rear surface must not be larger than $\Delta t = c_s/(\Delta_0/16)$, where c_s is the average sound speed inside the shell compressed by the SW_1 , and Δ_0 is the initial shell thickness.

Figure 93.15 shows the picket target designs, taking into account all the constraints on the shell size and pulse shape discussed above (for a better shell stability, the coasting phase

in the OMEGA design was extended). The OMEGA design reaches the implosion velocity $V_{\text{imp}} = 4.6 \times 10^7$ cm/s, peak of the total $\rho R_{\max} = 300$ mg/cm², and it produces $Y = 6 \times 10^{14}$ neutrons. The NIF design has, correspondingly, $V_{\text{imp}} = 4.3 \times 10^7$ cm/s, $\rho R_{\max} = 1.45$ g/cm², and $Y = 3 \times 10^{19}$ (gain = 55). Next, we study the stability of the designs presented in Fig. 93.15. We start by analyzing the perturbation growth rates.

1. Reduction in the Rayleigh–Taylor Growth Rates

The main motivation for the adiabat shaping is to increase the ablation velocity of the shell. Such an increase results in a reduction in the RT-growth rates. To separate the effect of the RT-growth-rate reduction from effects of the multiple material interfaces (which will be studied later), we consider a pure-DT shell (no polymer overcoat) driven by both a standard pulse and a picket pulse. The OMEGA all-DT target, equivalent to the design presented in Fig. 93.15, has an outer diameter of 430 μm and a shell thickness $\Delta_0 = 85$ μm . The pulse shape for the standard $\alpha = 3$ OMEGA design is taken from Ref. 14. Averaged over the time of shell acceleration, V_a increases from 4 $\mu\text{m}/\text{ns}$ in the standard design to 6.5 $\mu\text{m}/\text{ns}$ in the picket design. The RT-growth rates are estimated by substituting the ablation-front trajectories R_a obtained from the 1-D simulation into the fitting growth-rate formula,²⁰ $\Gamma_{\text{RT}} = 0.94\sqrt{kg} - 2.6kV_a$. Since the fitting formula uses time-independent planar geometry variables, g , $k = \ell/R_a$, and V_a are averaged over the duration of the acceleration phase. Figure 93.16 shows the results of the fitting formula applied to the two designs. Next, a series of two-dimensional simulations using the Lagrangian code *ORCHID*²¹ was performed to calculate the growth rates of the RT modes. The instability was seeded by applying a 1% laser-intensity modulation.

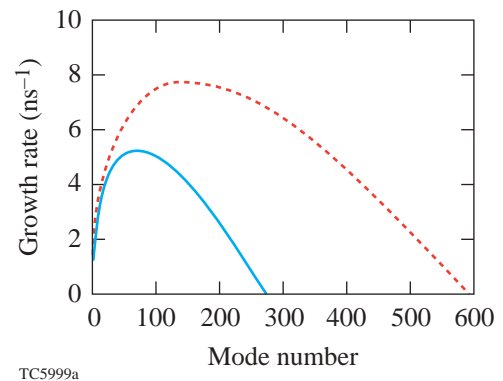


Figure 93.16 Rayleigh–Taylor growth rates for the standard (dashed curve) and the picket (solid curve) OMEGA designs.

Figures 93.17(a) and 93.17(b) compare the results of simulations (solid and dotted lines) with theoretical prediction (dashed straight lines) for mode numbers $\ell = 60$ and $\ell = 100$. Simulations exhibit lower growth rates at the beginning of the acceleration phase and higher growth rates at the end of acceleration. This is mainly due to a wave number variation during shell compression and, in the case of the picket design, lower ablation velocity at the end of the laser pulse. Averaged over the duration of the acceleration phase, however, simulations agree reasonably well with the result of the fitting formula. According to Fig. 93.16, the cutoff mode number is expected to be reduced from $\ell_{\text{cut}} \approx 600$ for the standard pulse to $\ell_{\text{cut}} \approx 280$ for the picket design. In Fig. 93.17(c) we plot the temporal evolution of the mode $\ell = 300$, which is predicted to be stable for the picket case. Indeed, the simulations clearly show the mode growth in the standard design and the mode stabilization in the picket design. Based on the results of 2-D simulations we conclude that the reductions in the growth rates due to adiabat shaping are in good agreement with the analytical predictions. Next, we turn our attention to the seeding of the RT modes in the picket design with multiple layers.

2. Seeding of the Rayleigh–Taylor Modes in Multilayer Targets

To calculate the nonuniformity evolution throughout the implosion, it is essential to accurately predict the initial conditions for the RT-instability growth. Such initial conditions, in turn, depend on how the laser imprint and surface roughness evolve prior to the onset of the RT instability (prior to the RW_b breakout at the ablation front). In this subsection we estimate

the growth factor of the initial perturbation seeds during the early stage of implosion.

The RW_p (see p. 23) launched into the compressed material establishes a pressure profile decaying toward the ablation front. This creates pressure and density gradients of opposite directions at the CH/DT interface. Thus, a short period of the classical RT growth (“early time” RT growth) occurs at the interface. Such a period lasts until the CW reaches the interface and changes the sign of the pressure gradient. The amplification of the interface perturbations (seeded by the distorted SW_1) can be estimated from the following considerations: The interface between the heavier CH and lighter DT is a Lagrangian point moving with a local fluid velocity. Since the pressure profile across the interface is established by the rarefaction wave RW_p , the interface acceleration is an acceleration of a Lagrangian point inside the rarefaction wave. Next, we consider a rarefaction wave traveling along a stationary uniform density $\bar{\rho}$ and pressure \bar{p} . The solution of the hydrodynamic equations in this case written in the Lagrangian coordinates has the form¹⁸ ($\gamma = 5/3$):

$$\rho = \bar{\rho} \left(\frac{x_0}{\bar{c}t} \right)^{3/4}, \quad p = \bar{p} \left(\frac{x_0}{\bar{c}t} \right)^{5/4}, \quad (6)$$

where $\bar{c} = \sqrt{\gamma \bar{p} / \bar{\rho}}$. The time coordinate in the last equation is shifted to the beginning of the rarefaction wave propagation. The acceleration of a Lagrangian point is calculated by taking the derivative of the pressure with respect to the Lagrangian

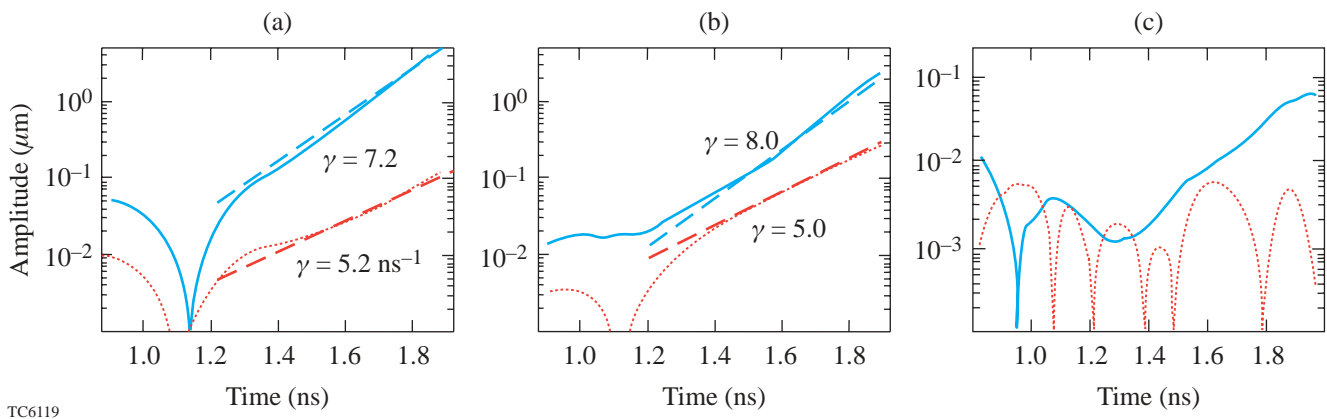


Figure 93.17

Mode evolution for (a) $\ell = 60$, (b) $\ell = 100$, and (c) $\ell = 300$. Numerical results are shown with the solid (standard design) and dotted (picket design) lines; the predictions of the fitting formula²⁰ are indicated by the dashed straight lines. Calculations are performed for the OMEGA $\alpha = 3$ design.

variable x_0 (at time $t = 0$, the rarefaction wave is at $x_0 = 0$):

$$g = -\frac{1}{\bar{\rho}} \frac{\partial p}{\partial x_0} = -\frac{3}{4} \frac{\bar{c}^2 x_0^{1/4}}{(\bar{c}t)^{5/4}}. \quad (7)$$

Next, we take x_0 to be the polymer thickness (Lagrangian position of the CH/DT interface) at the beginning of the RW_p propagation, $x_0 = \Delta_{CH} = c_{CH} t_r$, where t_r is the RW_p breakout time at the CH/DT interface, and c_{CH} is the sound speed of the shock-compressed CH. Simulations show that $\Delta_{CH} \approx d_{CH}/6$, where d_{CH} is the initial overcoat thickness (the SW_1 compresses the plastic layer by a factor of 4; additional reductions in thickness are due to the mass ablation and adiabatic compression of the CH layer during the picket rise). The parameter \bar{c} in this case is $\bar{c} = c_{CH} = \sqrt{\gamma p_{CH}/\rho_{CH}}$, where p_{CH} is the pressure at the shock front in CH and $\rho_{CH} = (\gamma + 1)/(\gamma - 1) \rho_{CH}^0$ is the shock-compressed CH density. Next, to find the perturbation growth factor at the interface, we must solve the RT evolution equation (including decompression effects):

$$\frac{d}{dt} \left[\frac{d_t(\rho\eta)}{\rho} \right] - A_T k g \eta = 0, \quad (8)$$

where η is the CH/DT interface modulation amplitude, k is the wave number, and, according to the *LILAC* simulations, $A_T \approx 1/3$. The Wentzel–Kramers–Brillouin (WKB) solution²² of Eq. (8) has the form

$$\eta = \tau^{11/16} (Ae^\zeta + Be^{-\zeta}),$$

where $\zeta = 4/3 \sqrt{k \Delta_{CH}} \tau^{3/8}$ and $\tau = c_{CH} t / \Delta_{CH}$. Equation (8) is subject to the initial conditions at the onset of the perturbation growth: $\eta(t = t_r) = \eta_0$ and $\dot{\eta}(t_r) = \dot{\eta}_0$. These conditions can be defined from the following considerations: If the interface perturbation is seeded by a nonuniform shock with a modulation amplitude η_s , then η_0 and η_s are related as $\eta_0 = \eta_s U_{ps}^{DT} / U_s^{CH}$, where

$$U_{ps}^{DT} = \sqrt{2/(\gamma + 1) p^{DT} / \rho_{DT}^0}$$

is the post-shock fluid velocity in DT and

$$U_s^{CH} = \sqrt{p_p(\gamma + 1)/2 / \rho_{CH}^0}$$

is the shock velocity in CH. Because of the density jump across the CH/DT interface, the pressure behind the SW_1 drops as the shock crosses the interface. The transmitted pressure p_{DT} must satisfy the following equation derived from the matching conditions across the interface:

$$\sqrt{\Sigma} - \sqrt{\frac{\rho_{DT}^0}{\rho_{CH}^0}} = \sqrt{\frac{2\gamma}{\gamma - 1} \frac{\rho_{DT}^0}{\rho_{CH}^0}} \left(1 - \Sigma^{\frac{\gamma-1}{2\gamma}} \right),$$

where $\Sigma = p_{DT}/p_p$. Substituting $\rho_{DT}^0 = \rho_{CH}^0/4$, the last equation yields $p_{DT} \approx 0.45 p_p$; thus the transmitted pressure is one-half of the initial drive pressure. Thus, the initial interface amplitude becomes $\eta_0 = \eta_s$. It is interesting to observe that the initial interface perturbation is approximately equal to the shock modulation amplitude. To calculate the initial velocity perturbation $\dot{\eta}_0$ we must take into account that the RW_p in the designs presented in Fig. 93.15 catches with the SW_1 inside the plastic, very close to the CH/DT interface. Thus, we can approximate that the interface starts to accelerate with g , defined by Eq. (7), right after the SW_1 crosses the interface. The velocity perturbation gained by the interface during time interval Δt is $\dot{\eta}_0 = g \Delta t$, where $\Delta t = \eta_s / U_s^{CH}$ is the time of the shock propagation across the amplitude η_s ; then, $\dot{\eta}_0 \approx 0.42 \eta_s c_{CH} / \Delta_{CH}$. If the perturbations are seeded by the outer-surface roughness and the initial amplitude of the front ripple is a_0 , then the shock amplitude²³ evolves according to

$$\eta_s(t) = a_0 [J_0(kc_{CH} t/\mu) + 2/3 J_2(kc_{CH} t/\mu)],$$

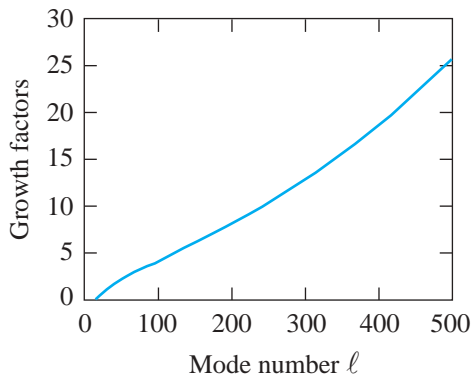
where $J_0(x)$ and $J_2(x)$ are Bessel functions of zero and second orders, respectively, and

$$\mu = 1 / \sqrt{1 - (U_s^{CH} / 4c_{CH})^2} \approx 1$$

in the strong shock limit. Approximating the Bessel functions with their envelopes gives $J_0(z) + 2/3 J_2(z) \approx \sqrt{2/(9\pi z)}$, where z calculated at the SW_1 breakout time at the interface is $z \approx kd_{CH}/2$. Collecting all the terms together, the perturbation growth factor $GF = \eta(t)/a_0$ becomes

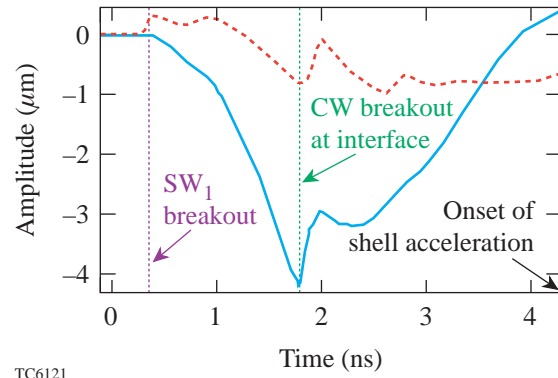
$$\text{GF} = \frac{0.38}{\sqrt{kd_{\text{CH}}}} \left(\frac{t}{t_r} \right)^{11/16} \times \left(\cosh \sigma - \frac{0.8}{\sqrt{kd_{\text{CH}}}} \sinh \sigma \right), \quad (9)$$

where $\sigma = 0.54 \sqrt{kd_{\text{CH}}} \left[(t/t_r)^{3/8} - 1 \right]$. The perturbations imposed at the CH/DT interface by the perturbed SW_1 grow until the CW reaches the interface and changes the sign of the pressure gradient. Figure 93.18 plots the GF calculated for the NIF design presented in Fig. 93.15 ($t/t_r \sim 40$). The mode number ℓ is defined as $k = \ell/R_0$, where $R_0 = 1700 \mu\text{m}$ is the initial outer shell radius. The amplification in the mode amplitude, for the mode numbers of interest to ICF, varies from 1 to 30, but only a fraction of this amplitude seeds the RT mode at the onset of the target acceleration. This is partially due to the interface amplitude compression by the CW. An additional reduction comes from the coupling of the interface ripple to the ablation front, which is stabilized by the dynamic overpressure effect.²⁴ Figure 93.19 illustrates the reduction in the interface amplitude prior to the target acceleration. The interface modulation evolution is calculated using 2-D *ORCHID* simulations with an imposed initial outer-surface perturbation. The dashed line represents the behavior of mode $\ell = 100$ with $a_0 = 0.5 \mu\text{m}$, and the solid line corresponds to $\ell = 300$ with $a_0 = 0.2 \mu\text{m}$. The SW_1 breaks out at the CH/DT interface at 0.4 ns. At this time the interface modulation jumps to the value of the shock ripple amplitude (the shock modulation for $\ell = 300$



TC6120

Figure 93.18
 Growth factors of the “early time” RT instability in the NIF picket design.



TC6121

Figure 93.19

Evolution of the CH/DT interface modulation for $\ell = 100$ (dashed line) and $\ell = 300$ (solid line) prior to shell acceleration.

changes sign at $t = 0.4 \text{ ns}$; therefore the plot shows the growth of this starting from zero amplitude). Although the short wavelengths experience a larger growth due to the early RT instability, their amplitudes are substantially reduced by the time of shell acceleration. The conclusion one can draw from this analysis is that the early RT growth of the CH/DT interface perturbations does not amplify significantly the seeds for the acceleration RT instability. Even if such amplification by a factor of several will occur, the perturbations will be substantially reduced by high ablation velocity (the adiabat has the largest value at the interface) when the ablation front crosses the CH/DT interface.

3. Convective Instability

It is well known that in the presence of the entropy gradient inside the shell, a convective instability develops if the effective acceleration and the entropy gradient are in the same direction.⁷ Such an instability has been studied by several researchers in the past.^{7,25} The following are important results of these studies: (1) In the classical RT case (no ablation) with negligibly small light-fluid density ($A_T \sim 1$), the convective mode is totally decoupled from the RT mode, and the RT-growth rate is $\gamma = \sqrt{kg}$, regardless of the adiabat shape (assuming a sharp interface between lighter and heavier fluids). (2) The growth rate of the convective modes is always smaller than the growth of the RT modes. The growth rates of the modes excited in the shell can be derived by combining the conservation equations into a single differential equation for the x component of the fluid velocity v (x coordinate is chosen in the direction of the acceleration g):

$$\left(\Gamma^2 v - g \frac{dv}{dx}\right) = \left[c_s^2 \frac{d}{dx} + (\gamma - 1)g\right] \times \left(\Gamma^2 + k^2 c_s^2\right)^{-1} \left(\Gamma^2 \frac{dv}{dx} - k^2 g v\right), \quad (10)$$

where k is the wave number, Γ is the perturbation growth rate, and $c_s = \sqrt{\gamma p / \rho}$ is the sound speed. In writing Eq. (10) the ablation effects were neglected. If $x = 0$ at the fluid interface and x is negative inside the shell, the pressure continuity condition at the interface reads as

$$p(\eta) = p_0(0) + \tilde{p}(0) + (dp/dx)\eta = p_0(0),$$

where \tilde{p} is the pressure perturbation, p_0 is the equilibrium pressure, and η is the interface modulation amplitude. The velocity at the interface is related to the distortion amplitude as $v(0) = \Gamma \eta$; in addition, we write $dv/dx|_{x=0} = \mu k v(0)$, where μ is an undetermined constant. The pressure continuity in this case reduces to the simple relation

$$\Gamma = \sqrt{\frac{kg}{\mu}}. \quad (11)$$

It is easy to show that the solution $v \sim e^{kx}$ and $\Gamma = \sqrt{kg}$ ($\mu = 1$) satisfies Eq. (10); thus, the classical RT mode grows with $\Gamma = \sqrt{kg}$, regardless of the entropy profile inside the shell. As shown in Ref. 7, however, for all other modes that can be excited in the shell (the internal convective modes), $\mu > 1$ and the growth rates are smaller than \sqrt{kg} . In the ablative case, the growth rates of the RT instability are significantly reduced by the ablation. For the DT ablator, the fitting formula that reproduces the results of the self-consistent theory has the form²⁰ $\Gamma_{\text{RT}} = 0.94\sqrt{kg} - 2.6 kV_a$. Near the cutoff wave number, where Γ_{RT} vanishes, the growth of the convective modes could exceed the RT growth. It is important, therefore, to study the internal mode growth in such a regime.

We begin the analysis by determining the spatial dependence of the adiabat for the picket designs shown in Fig. 93.15. The shell entropy $s(x)$ calculated using the 1-D simulations can be fitted with a power law $s(x) = s_0 [1 - x/(\beta_s L_{\text{sm}})]^{-\beta_s}$, where L_{sm} (the minimum entropy gradient scale length) and the power index β_s are determined from the fitting procedure. The x coordinate is negative inside the shell, so $s(x)$ decreases

from the interface toward the back of the shell. Next, we solve Eq. (10) to find the eigenvalue μ , imposing the condition of finite v at the back of the shell. Near the RT cutoff, the condition $kL_{\text{sm}} \gg 1$ is satisfied, and Eq. (10) can be greatly simplified:

$$v'' - k^2 Q(x)v = 0, \quad Q(x) = 1 - \frac{\mu}{\gamma k L_s}, \quad L_s = L_{\text{sm}} - \frac{x}{\beta_s}. \quad (12)$$

Here, prime denotes the spatial derivative. In solving Eq. (12) we assume $\mu \gg 1$. This assumption will be verified later. Observe that Q is a decaying function of x ; therefore the solution of Eq. (12) depends on the sign of Q inside the shell. It is easy to show that Q cannot be positive everywhere in the shell. Indeed, to satisfy the boundary condition at the shell's back, we must keep only the exponentially decaying solution

$$v_{\text{WKB}} \sim Q^{-1/4} \exp\left[k \int^x \sqrt{Q(y')} dy'\right],$$

where v_{WKB} is obtained using the WKB approximation. But such a solution does not satisfy the boundary condition at $x = 0$, $v'/v = k\mu$. Thus, Q must be negative somewhere in the shell. Next, we distinguish the following two cases: (1) Q changes sign at point $x = \bar{x}$, (2) Q is negative everywhere. In case (1), solution of Eq. (12) in the region where $Q > 0$ is $v = v_{\text{WKB}}$. In the vicinity of $x = \bar{x}$, the WKB approximation breaks down and Eq. (12) must be solved by expanding Q in the Taylor series,

$$Q = Q_0 - Q_1 k(x - \bar{x}),$$

where $Q_0 = 1 - \mu/[\gamma(kL_{\text{sm}} - k\bar{x}/\beta_s)] = 0$, and $Q_1 = \gamma/(\mu\beta_s)$. Then, the solution of Eq. (12) that matches v_{WKB} at $\tau \rightarrow \infty$ becomes $v_{\text{in}} \sim \text{Ai}(\tau)$, where $\text{Ai}(\tau)$ is the Airy function and $\tau = kQ_1^{1/3}(\bar{x} - x)$. We will show later that $|Q_1 k\bar{x}| \ll 1$ and the Taylor expansion of Q is still valid near $x = 0$. The boundary condition $v'/v = \mu k$ can be applied in this case to v_{in} . Using the expansion of the Airy function for the large negative arguments, the boundary condition reads as

$$\frac{1}{4\tau_0} + \sqrt{\tau_0} \tan\left(\frac{2}{3}\tau_0^{3/2} - \frac{\pi}{4}\right) + \mu^{4/3}(\beta_s/\gamma)^{1/3} = 0, \quad (13)$$

where $\tau_0 = \beta_s^{2/3}(\mu/\gamma - kL_{\text{sm}})(\gamma/\mu)^{1/3}$ is the value of $-\tau$ at the density jump ($x = 0$). Since $\mu \gg 1$ (by assumption), the

right-hand side of Eq. (13) is large, and the equation can be satisfied only if the argument of the tangent is close to $\pi/2$. This defines τ_0 , $(2/3)\tau_0^{3/2} = 3\pi/4 + \pi n$, $n = 0, 1, 2$. Substituting the definition of τ_0 into the last equation leads to $\beta_s^2 \gamma (\mu/\gamma - kL_{sm})^3 = 9\pi^2 (3/4 + n)^2 \mu/4$, which has the following solution:

$$\mu = \gamma k L_{sm} + \frac{\gamma}{4\beta_s} \left[9\pi^2 (3/4 + n)^2 \beta_s k L_{sm} \right]^{1/3}, \quad n = 0, 1, 2. \quad (14)$$

Observe that $\mu \gg 1$ for the short-wavelength modes considered here, in agreement with the initial assumption. Also, $|kQ_1 \bar{x}| \sim (kL_{sm})^{-2/3} \ll 1$, which validates the Taylor expansion of Q near $x=0$. Using Eq. (14), the growth rate $\Gamma = \sqrt{kg/\mu}$ takes the form

$$\Gamma = \frac{g}{\sqrt{\gamma L_{sm} \left\{ 1 + \left[\frac{9\pi(1+4n/3)}{8\beta_s k L_{sm}} \right]^{2/3} \right\}}}. \quad (15)$$

Next, we recall that Eq. (15) is valid only if Q changes sign inside the shell, i.e., $-d < \bar{x} < 0$, where d is the shell thickness. Such a requirement puts an upper limit on values of μ : $\mu < \gamma k (L_{sm} + d/\beta_s)$; using Eq. (14), the last condition reads as $n < (2\beta_s k L_{sm}/3\pi)(d/\beta_s L_{sm})^{3/2}$. The number n has a simple meaning: n indicates how many times the eigenmode changes sign inside the shell. To calculate the number n for the ICF target, we must recall that the internal modes are seeded only by the vorticity inside the shell.⁷ In the ICF experiments the vorticity is induced either by the rippled shock propagating from the ablation front or by the rippled rarefaction wave in the case of the initial inner-surface roughness (feedout). In both cases the imposed vorticity oscillates inside the shell, and the characteristic spatial frequency of such oscillations is of the order of the perturbation wavelength. As an example, let us consider the case of the rippled shock. If a_0 is the initial outer-surface amplitude of the mode with the wave number k , the shock creates the shell vorticity^{23,24} Ω_0 according to

$$\begin{aligned} \Omega_0 &= i(\nabla \times \mathbf{v})_z = -k v_x - i \partial_x v_y \\ &\approx \frac{3}{2} k^2 a_0 c_s \left[J_1(\zeta) + \frac{1}{2} J_3(\zeta) \right], \end{aligned} \quad (16)$$

where $\zeta = k\Delta_0/2(m/m_{sh})$, $J_1(\zeta)$ and $J_3(\zeta)$ are the Bessel functions, m is the mass coordinate inside the shell, m_{sh} is the total shell mass, and Δ_0 is the initial shell thickness. Taking into account that 1/5 of the initial shell material is ablated by the time the shell accelerates (see the **Propagation of a Decaying Shock** section), $\zeta_{max} = 2k\Delta_0/5$. Using Eq. (16) and approximating $J_m(\zeta) \sim \sin(\zeta - m\pi/2 - \pi/4)$, it is easy to calculate the number of zeros in Ω_0 : $N_0 \sim 2k\Delta_0/(5\pi)$. Taking $n = N_0$, the validity condition of Eq. (15) becomes

$$\frac{\Delta_0}{d} < \frac{5}{3} \sqrt{\frac{d}{\beta_s L_{sm}}}. \quad (17)$$

This condition is not satisfied for the target designs presented in Fig. 93.15 [$\Delta_0/d \sim 10$ (shell is compressed by the shock SW₁ and the compression wave CW), $d \approx 8 \mu\text{m}$, $L_{sm} \approx 5.4 \mu\text{m}$, and $\beta_s = 0.5$ for the OMEGA picket design]. Thus, to calculate the convective instability growth rate we must consider the second case when Q is always negative inside the shell.

If $Q < 0$, the WKB solution of Eq. (12) takes the form

$$\begin{aligned} v &= \frac{A}{Q_-^{1/4}} \cos\left(k \int_0^x \sqrt{Q_-(y')} dy'\right) \\ &+ \frac{B}{Q_-^{1/4}} \sin\left(k \int_0^x \sqrt{Q_-(y')} dy'\right), \end{aligned} \quad (18)$$

where $Q_- = -Q > 0$ and A and B are constants of integration. The boundary condition at $x=0$ relates $B = A\mu/\sqrt{Q_-(0)}$. To define the boundary condition at $x=-d$, we must keep in mind that both ρ and c_s vanish at the rear surface. Then, the solution that does not blow up at $x=-d$ must satisfy $v'(-d)/v(-d) = \mu k(\gamma-1)/\gamma$ [this condition can be easily derived directly from Eq. (10)]. Applying the latter condition to solution (18) gives, in the limit of large μ ,

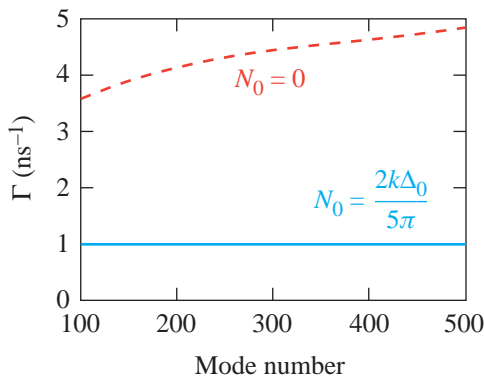
$$k \int_{-d}^0 \sqrt{\frac{\mu}{\gamma k L_s(x)}} - 1 dx = n\pi, \quad n = 1, 2, \dots \quad (19)$$

Performing integration in the last equation and substituting $n = N_0$, we determine μ . Then, the growth rate $\Gamma = \sqrt{kg/\mu}$ becomes

$$\Gamma \approx \sqrt{\frac{g}{\gamma L_{sm} \Sigma}}, \quad (20)$$

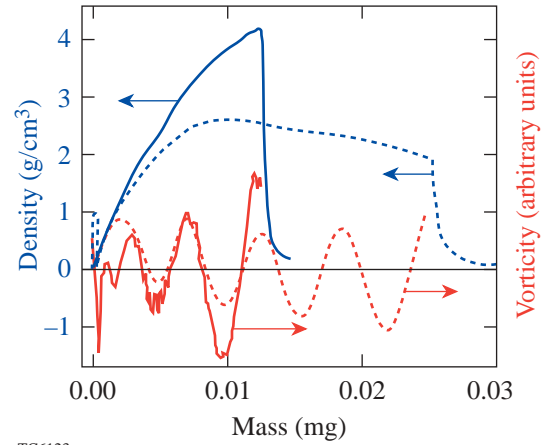
$$\Sigma = \frac{(d/\sqrt{2}\beta L_{sm})^2 + (\Delta_0/5\beta L_{sm})^2}{(\sqrt{1+d/\beta L_{sm}} - 1)^2} - \frac{1}{2} \sqrt{1 + \frac{d}{\beta L_{sm}}}.$$

Figure 93.20 plots the growth rates calculated for the OMEGA picket design using Eqs. (15) ($n = 0$, dashed line) and (20) (solid line). Observe a strong reduction in the growth rate due to the vorticity oscillations. We want to emphasize here that Eq. (20) is valid only if condition (17) is not satisfied. It is possible, however, to steepen the adiabat profile (by introducing a second picket in the laser pulse, for example), reducing the minimum scale length L_{sm} and increasing the compressed shell thickness d (the larger adiabat at the ablation front will lead to a decrease in the shell density). Equation (17) will be satisfied in this case, and Eq. (15) with $n = N_0$ must be used to calculate the growth rate. To validate the result of the performed analysis of the convective mode evolution, we carried out a series of single-mode 2-D *ORCHID* simulations imposing modulation on the outer surface of the shell. Figure 93.21 shows a plot of the density and vorticity as functions of the mass for $\ell = 300$ in the OMEGA picket design (Fig. 93.15). The dashed line represents the beginning of acceleration phase, and the solid line corresponds to the end of the acceleration phase (the mass is reduced because of the ablation). The vorticity amplitude has grown by a factor of 2 during the shell acceleration, which is in agreement with Eq. (20) (the acceleration phase in the OMEGA design lasts for 0.8 ns).



TC6122

Figure 93.20
Growth rate of the internal convective mode with (solid line) and without (dashed line) vorticity oscillation inside the shell.



TC6123

Figure 93.21
Mass density and vorticity calculated at the beginning (dashed line) and the end (solid line) of the acceleration phase.

In conclusion, Fig. 93.20 suggests that there is no significant amplification of the outer-surface distortions due to the convective instability (the growth factor is less than 3 for the entire mode spectrum). One needs to take the results of the present analysis with great caution. We did not address the question of how the internal mode can affect the growth of the RT modes. This issue will be studied in future work. Our simulations, however, indicate that even if such coupling exists, it does not significantly modify the RT growth for the designs described in Fig. 93.15. The conclusions could be different for other shaped-adiabat designs.

4. Multimode Results

The analysis performed in Subsections 1–3 gives an estimate for only the single-mode growth factors experienced by the perturbations during the implosion. To make a conclusion about the shell integrity for a particular target design, one must carry out multimode calculations, taking into account the realistic spectra of the surface roughness and the laser-intensity nonuniformity. Stability analyses of the direct-drive cryogenic targets reported in the past^{14,19} reveal that the laser imprint is the dominant source for a potential shell breakup during the acceleration phase. To study the effect of the adiabat shaping on the shell integrity, we performed a set of multimode *ORCHID* simulations. First, we discuss the simulation results for the OMEGA cryogenic targets (dimensions are shown in Fig. 93.15) driven by the standard and picket pulses. A single-beam laser nonuniformity spectrum is evaluated for a static DPP (distributed phase plate) speckle. Then, an overlap of 12 OMEGA beams and two polarizations at any spot on the capsule are assumed. The effect of the two-dimensional SSD

(smoothing by spectral dispersion) beam-smoothing technique²⁶ is modeled by employing a “flipping” approximation: the sign of the laser perturbation is randomly chosen every correlation time t_c , where $t_c = [\Delta\nu \sin(k\delta/2)]^{-1}$, δ is the speckle size ($\delta = 2.35 \mu\text{m}$ for the OMEGA), $\Delta\nu = 1 \text{ THz}$ is the laser bandwidth, and k is the perturbation wave number. Averaged over time T , the single-beam rms nonuniformity σ for a constant-intensity laser pulse decays in time as $\sigma \sim \sigma_0 \sqrt{t_c/T}$. Because of a finite maximum angular spread $\Delta\theta$ of the light propagating through the laser, the averaged mode amplitude cannot be reduced to the levels below the asymptotic limit. This limit is inversely proportional to the square root of the number of statistically independent speckle patterns

$$N_{\text{stat}}(\lambda) = \left(4S_{\text{max}}^x/\lambda\right)\left(4S_{\text{max}}^y/\lambda\right),$$

where λ is the nonuniformity wavelength, $S_{\text{max}}^{x(y)} = F\Delta\theta^{x(y)}$ is the maximum spatial shift in the $x(y)$ direction, $F = 180 \text{ cm}$ is the focal length, and $\Delta\theta^x = 50 \mu\text{rad}$ and $\Delta\theta^y = 100 \mu\text{rad}$ for the OMEGA laser system. The asymptotic limits are modeled in the flipping approximation by selecting only N_{stat} independent choices for the sign of the nonuniformity amplitude. Snapshots of the shell isodensity contours for the standard and the picket designs are shown in Figs. 93.22(a) and 93.22(b), respectively. The shell has moved the same distance ($\sim 100 \mu\text{m}$) in both designs. The plots reveal a dramatic reduction in shell

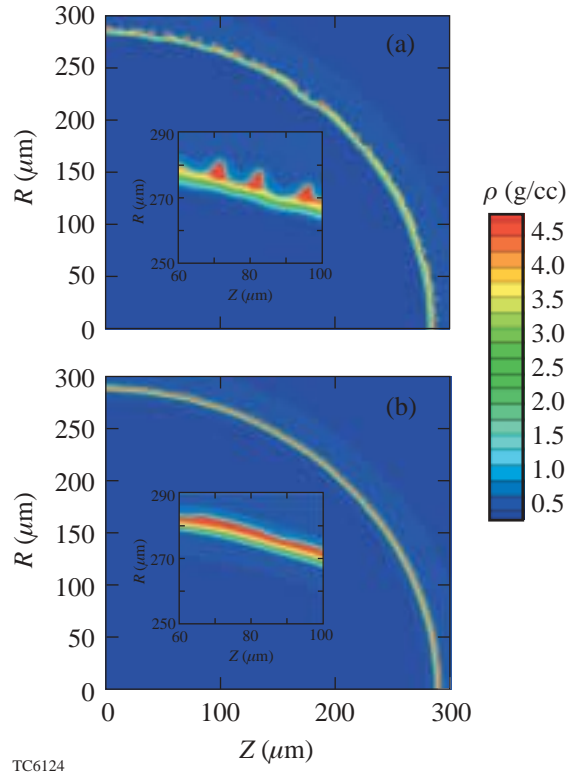


Figure 93.22 Isodensity contours of the (a) standard and (b) picket OMEGA $\alpha = 3$ designs. At the time shown on the plots, the shell has moved $100 \mu\text{m}$ in both designs.

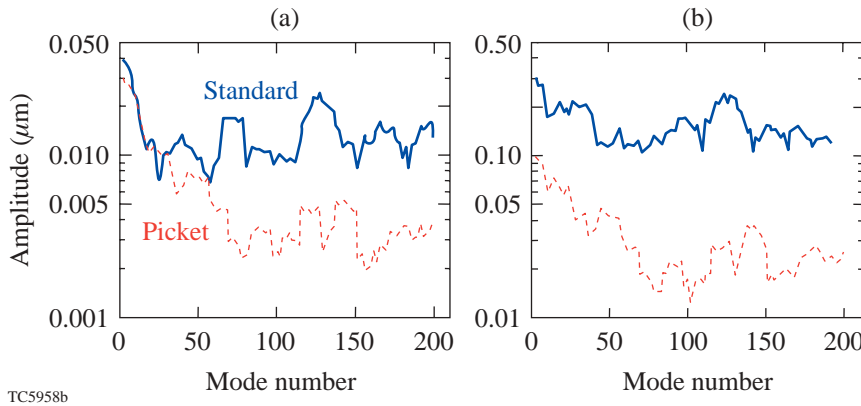


Figure 93.23 Mode spectra for the standard (solid line) and picket (dashed line) OMEGA $\alpha = 3$ designs (a) at the beginning of acceleration phase and (b) at the time shown on Fig. 93.22(b).

nonuniformity in the picket design. We also emphasize that the picket reduces not only the perturbation growth rates but also the laser imprint.²⁷ Figure 93.23(a) plots the mode spectrum at the beginning of the acceleration phase for both designs. As shown in the plot, the picket reduces the initial amplitudes by a factor of 2.5 to 3 for the modes with $\ell > 50$. Comparing the mode amplitudes for the picket and standard designs at the time shown in Fig. 93.22 [see Fig. 93.23(b)], we observe that the separation between the two spectral lines is clearly increased (amplitudes in the picket designs are smaller by a factor of 10 for $\ell > 50$), indicating a slower RT growth in the picket design. A reduction in the growth of the low- ℓ modes is also noticeable. This is due to the ablation effects in a finite-thickness shell (for details see Ref. 28). The numerical simulations of the NIF cryogenic target design show a similar trend: shell nonuniformities are highly reduced in the picket design compared to the standard design. Although detailed multimode simulations including all the nonuniformity sources (surface roughness, laser imprint, and power imbalance) are still in progress, a preliminary analysis reported in this article indicates a substantial improvement in the shell uniformity by using laser-induced adiabat shaping.

Picket Pulse Experiments

To test the effect of the adiabat shaping on the performance of the imploding shells, a series of experiments¹⁰ were carried out on the OMEGA laser system. The experiments were performed on 33- μm thick, 905- μm -diam, D_2 -filled polysty-

rene shells, filled to a pressure of 3 and 15 atm. Two pulse shapes [Fig. 93.24(a)] were used to compress the shells with a low adiabat ($\alpha = 2$) at the fuel/pusher interface. The standard pulse has a 1-TW, 700-ps-long foot followed by the main pulse with a peak power of 20 TW. The picket design has a narrow, 100-ps-FWHM (full width at half maximum) Gaussian picket combined with the main drive pulse described above. The adiabat in the standard pulse varies from 2 to 2.5; the adiabat at the ablation front in the picket design was raised to 4. There was also an increase in the adiabat at the rear surface in the picket design. Analysis performed using the stability post-processor²⁸ indicated that the shell in the standard design was broken due to the perturbation growth, while the shell in the picket design remained intact during the shell implosion. The experimental results are summarized in Fig. 93.24(b). The plot compares the experimental yield against the 1-D *LILAC* prediction. Observe that the predicted yields for the picket design were slightly reduced for both fill pressures, while the experimental yields grew by a factor of 2.5 for the 15-atm fill and by a factor of 2 for the 3-atm fill. The ratio of the experimental yield to the predicted 1-D yield grew from 4% to 18% for the 15-atm fill and from 3% to 15% for the 3-atm fill. A significant improvement in neutron yields indicates a better stability of the implosion shells when a picket was added to the drive laser pulse. A detailed analysis has revealed, however, that the radiation transport in CH shells leads to an additional shaping of the shell adiabat. The effect of such additional shaping will be addressed in future work.

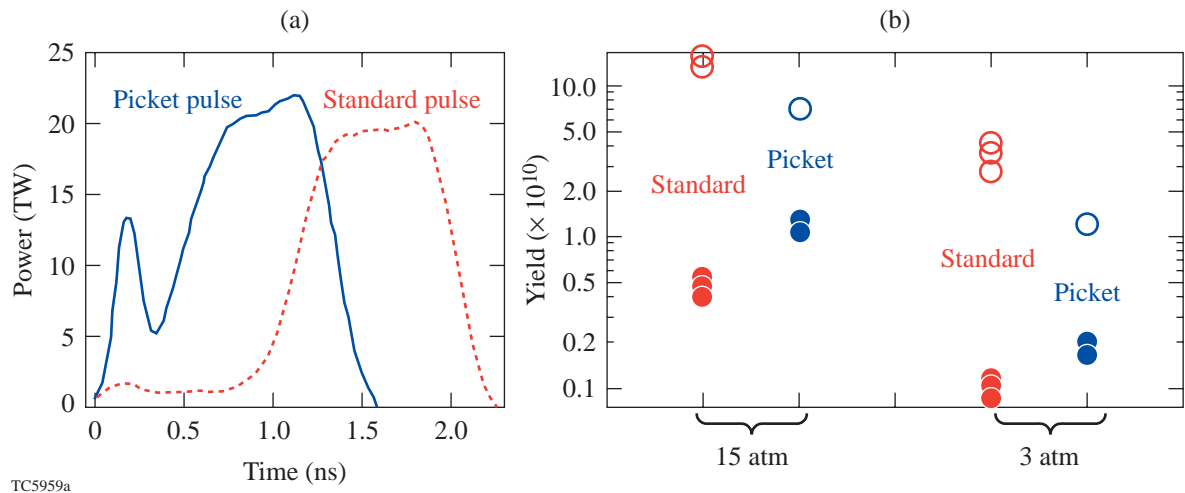


Figure 93.24

(a) Experimental laser pulses for the standard (dashed line) and picket (solid line) $\alpha = 2$, 33- μm -CH-shell target designs. (b) Neutron yield for the standard and picket pulses as predicted by the 1-D code *LILAC* (open circles) and obtained in the experiments (solid circles).

ACKNOWLEDGMENT

One of the authors (V. G.) thanks Dr. A. Velikovich for many helpful discussions. This work was supported by the U.S. Department of Energy Office of Inertial Confinement Fusion under Cooperative Agreement No. DE-FC03-92SF19460, the University of Rochester, and the New York State Energy Research and Development Authority. The support of DOE does not constitute an endorsement by DOE of the views expressed in this article.

REFERENCES

1. J. D. Lindl, *Inertial Confinement Fusion: The Quest for Ignition and Energy Gain Using Indirect Drive* (Springer-Verlag, New York, 1998).
2. S. E. Bodner, D. G. Colombant, J. H. Gardner, R. H. Lehmborg, S. P. Obenschain, L. Phillips, A. J. Schmitt, J. D. Sethian, R. L. McCrory, W. Seka, C. P. Verdon, J. P. Knauer, B. B. Afeyan, and H. T. Powell, *Phys. Plasmas* **5**, 1901 (1998).
3. S. E. Bodner, *Phys. Rev. Lett.* **33**, 761 (1974); J. Sanz, *Phys. Rev. Lett.* **73**, 2700 (1994); V. N. Goncharov, R. Betti, R. L. McCrory, P. Sorotokin, and C. P. Verdon, *Phys. Plasmas* **3**, 1402 (1996); J. D. Kilkenny, S. G. Glendinning, S. W. Haan, B. A. Hammel, J. D. Lindl, D. Munro, B. A. Remington, S. V. Weber, J. P. Knauer, and C. P. Verdon, *Phys. Plasmas* **1**, 1379 (1994); S. G. Glendinning *et al.*, *Phys. Plasmas* **7**, 2033 (2000); C. Cherfils *et al.*, *Phys. Rev. Lett.* **83**, 5507 (1999); J. Grun *et al.*, *Phys. Rev. Lett.* **53**, 1352 (1984); J. P. Knauer, R. Betti, D. K. Bradley, T. R. Boehly, T. J. B. Collins, V. N. Goncharov, P. W. McKenty, D. D. Meyerhofer, V. A. Smalyuk, C. P. Verdon, S. G. Glendinning, D. H. Kalantar, and R. G. Watt, *Phys. Plasmas* **7**, 338 (2000).
4. S. Chandrasekhar, in *Hydrodynamic and Hydromagnetic Stability* (Oxford University Press, Glasgow, 1961).
5. S. E. Bodner, *J. Fusion Energy* **1**, 221 (1981).
6. J. D. Lindl and W. C. Mead, *Phys. Rev. Lett.* **34**, 1273 (1975).
7. L. D. Landau and E. M. Lifshitz, *Fluid Mechanics*, 2nd ed. (Butterworth-Heinemann, Newton, MA, 1987); D. L. Book and I. B. Bernstein, *J. Plasma Phys.* **23**, 521 (1980).
8. T. R. Boehly, D. L. Brown, R. S. Craxton, R. L. Keck, J. P. Knauer, J. H. Kelly, T. J. Kessler, S. A. Kumpan, S. J. Loucks, S. A. Letzring, F. J. Marshall, R. L. McCrory, S. F. B. Morse, W. Seka, J. M. Soures, and C. P. Verdon, *Opt. Commun.* **133**, 495 (1997).
9. J. Paisner *et al.*, *Laser Focus World* **30**, 75 (1994).
10. J. P. Knauer, V. N. Goncharov, P. W. McKenty, T. C. Sangster, R. Betti, V. Yu. Glebov, T. J. B. Collins, D. D. Meyerhofer, P. B. Radha, C. Stoeckl, J. A. Frenje, C. K. Li, R. D. Petrasso, and F. H. Séguin, "Improved Performance of Direct-Drive Implosions with a Laser-Shaped Adiat," submitted to *Physical Review Letters*.
11. Ya. B. Zel'dovich and Yu. P. Raizer, *Physics of Shock Waves and High-Temperature Hydrodynamic Phenomena*, edited by W. D. Hayes and R. F. Probstein (Dover Publications, Mineola, NY, 2002).
12. R. J. Trainor and Y. T. Lee, *Phys. Fluids* **25**, 1898 (1982).
13. J. Delettrez and E. B. Goldman, Laboratory for Laser Energetics Report No. 36, University of Rochester (1976).
14. P. W. McKenty, V. N. Goncharov, R. P. J. Town, S. Skupsky, R. Betti, and R. L. McCrory, *Phys. Plasmas* **8**, 2315 (2001).
15. V. N. Goncharov, S. Skupsky, T. R. Boehly, J. P. Knauer, P. McKenty, V. A. Smalyuk, R. P. J. Town, O. V. Gotchev, R. Betti, and D. D. Meyerhofer, *Phys. Plasmas* **7**, 2062 (2000).
16. W. K. Levedahl and J. D. Lindl, *Nucl. Fusion* **37**, 165 (1997).
17. V. Lobatchev and R. Betti, *Phys. Rev. Lett.* **85**, 4522 (2000).
18. R. Betti, V. Lobatchev, and R. L. McCrory, *Phys. Rev. Lett.* **81**, 5560 (1998).
19. Laboratory for Laser Energetics LLE Review **79**, 121, NTIS document No. DOE/SF/19460-317 (1999). Copies may be obtained from the National Technical Information Service, Springfield, VA 22161.
20. R. Betti, V. N. Goncharov, R. L. McCrory, and C. P. Verdon, *Phys. Plasmas* **5**, 1446 (1998).
21. R. L. McCrory and C. P. Verdon, in *Computer Applications in Plasma Science and Engineering*, edited by A. T. Drobot (Springer-Verlag, New York, 1991), Chap. 11, pp. 291–325.
22. C. M. Bender and S. A. Orszag, *Advanced Mathematical Methods for Scientists and Engineers* (McGraw-Hill, New York, 1978).
23. R. Ishizaki and K. Nishihara, *Phys. Rev. Lett.* **78**, 1920 (1997).
24. V. N. Goncharov, *Phys. Rev. Lett.* **82**, 2091 (1999).
25. S. J. Han and B. R. Suydam, *Phys. Rev. A* **26**, 926 (1982); A. I. Kleeov and A. L. Velikovich, *Plasma Phys. Control. Fusion* **32**, 763 (1990).
26. S. Skupsky, R. W. Short, T. Kessler, R. S. Craxton, S. Letzring, and J. M. Soures, *J. Appl. Phys.* **66**, 3456 (1989).
27. T. J. B. Collins and S. Skupsky, *Phys. Plasmas* **9**, 275 (2002).
28. V. N. Goncharov, P. McKenty, S. Skupsky, R. Betti, R. L. McCrory, and C. Cherfils-Clérouin, *Phys. Plasmas* **7**, 5118 (2000).

High-Conversion-Efficiency Optical Parametric Chirped-Pulse Amplification System Using Spatiotemporally Shaped Pump Pulses

Since its invention in the early 1990s,¹ optical parametric chirped-pulse amplification (OPCPA) has become an attractive alternative to Ti:sapphire-based regenerative amplifiers for producing millijoule-level broadband laser pulses for injection of high-energy, short-pulse lasers that operate at a 1- μm wavelength.²⁻⁴ The primary advantage of OPCPA is the fact that only a single pass through several (~ 3 to 7) centimeters of material is required to provide broadband pulse-amplification factors as large as 10^8 with little or no gain narrowing. Due to its single-pass nature, pulses amplified using OPCPA do not have the prepulses that are commonly associated with regenerative amplifiers, and the fact that a minimal amount of material is required means that there is little *B*-integral accumulation in the amplification process. It has been noted, however, that the pump-to-signal conversion efficiency of the OPCPA process can be quite poor, especially for systems pumped by commercial, *Q*-switched lasers.⁵ Thus if several hundred millijoules of OPCPA output are desired at moderate repetition rates (1 to 10 Hz), pump lasers providing of the order of 5 J of energy at these repetition rates would be required. In addition, if high OPCPA output stability is also required, the fact that OPCPA involves a nonlinear amplification process means that the pump laser must also have very good energy stability.

One approach to overcoming these concerns is to use a pump laser that is better suited to the OPCPA process. Since this process involves no energy storage, the amplification factor for a pulse at a given temporal and spatial position is determined by the pump intensity at that particular spatiotemporal location. This has several implications: First, careful tailoring of the pump and seed spatiotemporal profiles is required to achieve high optical parametric amplification (OPA) conversion efficiency.^{6,7} Second, even slight variations in the pump intensity can result in large amplification-factor fluctuations, potentially leading to significant spatial and spectral modulation and large overall energy fluctuations in the amplified broadband output pulse. It has been shown that, for a narrow range of pump intensities and a particular interaction length, saturation in the OPA process can be observed, reduc-

ing the amplification-factor fluctuations to a value similar to or lower than that of the pump.^{8,9} As a consequence, in addition to careful design of the OPA itself, it is also important that the pump intensity profile be carefully controlled in both space and time to achieve efficient and stable operation of the parametric amplifier.

Much of the previous OPCPA work reported in the literature was conducted using pump lasers that offered limited control over the pumping pulse characteristics.^{3,4,10,11} In this article, we experimentally demonstrate that improved control over the temporal and spatial profiles of the pump laser significantly increases the efficiency of the OPA process. We emphasize the temporal and spatial aspects of the pump that provide optimal pumping conditions, leading to both efficient and stable OPCPA output characteristics.

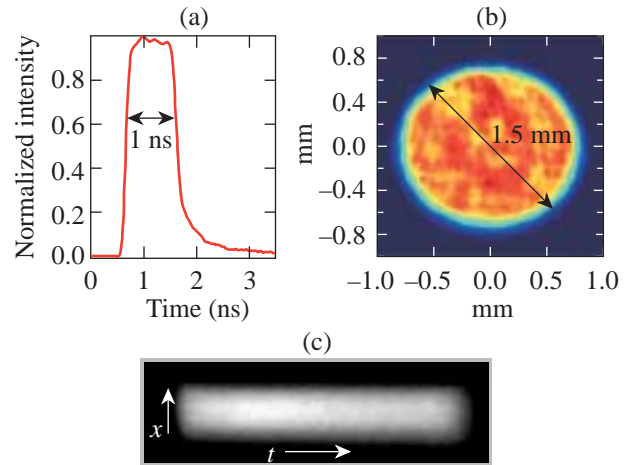
To optimize the OPCPA conversion efficiency and stability, a three-dimensional modeling code was developed that predicts the output of an OPCPA system given arbitrary pump and seed input energies and spatiotemporal profiles. This model, the details of which are described elsewhere,¹² was used to determine both the optimal pump spatiotemporal profile and the OPCPA configuration. Optimal conversion efficiency can be obtained with a uniform rate of energy transfer from the pump to the signal and idler, homogeneously depleting the pump in space and time. In our setup, a pump temporal profile that is flat in time with fast rise and fall times and a full width at half maximum (FWHM) that is roughly equivalent to that of the seed pulse is required. The spatial profile of the pump laser should be high-order super-Gaussian with a FWHM that is comparable to that of the seed pulse. As it is amplified, the originally Gaussian spatiotemporal profile of the seed is significantly sharpened due to the high gain of the OPA process. Thus when the amplification process begins to saturate, the spatiotemporal profiles of the seed and pump are well matched, improving energy extraction. Lithium triborate (LBO) was chosen as the OPA nonlinear medium because of its relatively high nonlinearity, high angular acceptance, and low walkoff between the pump beam (extraordinary wave) and the seed

beam (ordinary wave). The input pump intensity was limited primarily by the measured damage threshold of the antireflective coatings on the OPA crystals, so the model was used to select the crystal lengths that provided both high conversion efficiency and an amplified broadband pulse whose energy and spatial profile fluctuations were minimized.

A diagram of the experimental OPCPA setup is shown in Fig. 93.25. The OPA pump laser, shown in the shaded box, consists of a master oscillator, a temporal pulse-shaping system, a diode-pumped Nd:YLF regenerative amplifier, spatial beam shaping, a double-passed Nd:YLF power amplifier, and frequency doubling. The oscillator is a diode-pumped, single-longitudinal-mode Nd:YLF laser producing ~ 100 -nJ pulses at $1.053 \mu\text{m}$ with a 300-Hz repetition rate.¹³ The output of the oscillator is sent into an aperture-coupled-stripline (ACSL) temporal-pulse-shaping system, which can be configured to provide nearly arbitrary temporal pulse shapes for pulses up to 4 ns in duration.¹⁴ The temporally shaped pulse is then amplified from ~ 50 pJ to 3 mJ in a diode-pumped, Nd:YLF regenerative amplifier.¹⁵ The output of the regenerative amplifier is spatially expanded and apodized using a serrated-tooth apodizer to produce a 5-mm-FWHM beam that has a flat spatial profile at the output of the pump laser. The apodized pulse is then amplified from $\sim 400 \mu\text{J}$ to 40 mJ in a two-pass, flashlamp-pumped, 7-mm Nd:YLF power amplifier operating at 5 Hz. The output of the amplifier is relay imaged to a 3-mm beta-barium borate (BBO) frequency-doubling crystal, producing 526.5-nm pulses with energies as high as 25 mJ. A Pellin–Broca prism separates the second-harmonic light from the unconverted $1.053\text{-}\mu\text{m}$ light so that the latter does not

serve as a seed for the OPA. The output of the BBO is then relay imaged to the OPA crystals.

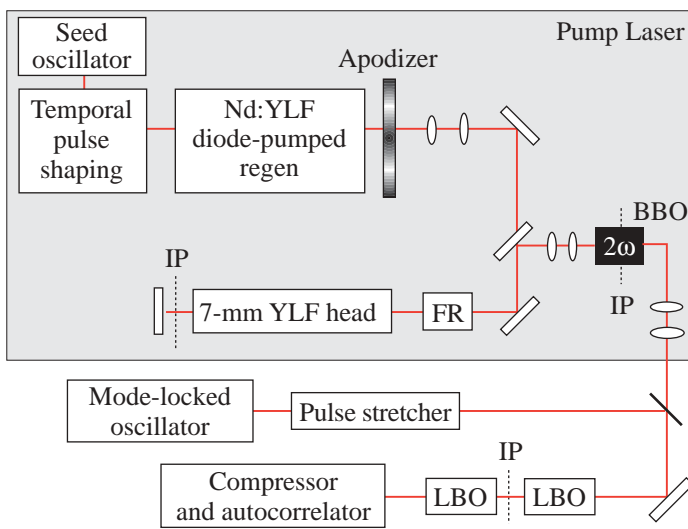
As discussed above, optimizing the conversion efficiency of our OPCPA system requires a constant-intensity pump pulse with a temporal duration that is of the order of that of the seed. As shown in Fig. 93.26(a), temporally flat, 1-ns pulses with a 10 to 90 rise time of ~ 160 ps are produced at the output of the BBO doubling crystal. The time-integrated spatial profile of the pump laser, measured at the input to the OPA, is presented



G5617a

Figure 93.26

(a) 1-ns FWHM square temporal profile of the OPA pump laser; (b) spatial profile of the OPA pump laser; (c) streak camera measurement of the spatiotemporal profile of the pump showing little spatiotemporal coupling.



E11819a

Figure 93.25

Diagram of the OPCPA experimental setup. The shaded box includes all of the components of the OPA pump laser. FR: Faraday rotator; IP: image plane; BBO: beta-barium borate; LBO: lithium triborate.

in Fig. 93.26(b). This beam has a tenth-order super-Gaussian spatial profile with a FWHM that is approximately equal to the spatial FWHM of the seed pulse. Because OPCPA is an instantaneous process, variations in the spatial profile of the pump over its temporal duration (spatiotemporal coupling) can lead to a reduction in conversion efficiency.⁴ Figure 93.26(c) shows the spatiotemporal profile of the pump pulse as measured by a streak camera, demonstrating that there is no spatiotemporal coupling in the OPA pump pulse.

The broadband seed laser for the OPCPA system is a mode-locked, Nd:glass laser (Time-Bandwidth Products, Inc.) producing pulses with a center wavelength of 1.053 μm and a FWHM bandwidth of ~ 6 nm. The laser operates at a repetition rate of 76 MHz and is synchronized to an external master clock that also controls the OPA pump laser's master oscillator and pulse-shaping system. The jitter between the broadband seed and pump lasers, which can lead to output energy and temporal profile fluctuations, was measured to be less than 23 ps peak-to-valley and thus does not affect the stability of the OPCPA output. The 160-mW output of the seed laser is temporally stretched to ~ 700 ps in a double-passed, Öffner-triplet-based pulse stretcher,^{16,17} providing ~ 800 pJ of seed energy at the OPA input with a Gaussian spatial and temporal profile.

The OPA consists of two wedged (2°), 5×5 -mm-clear-aperture LBO crystals with lengths of 25 and 23 mm cut at 11.8° to allow type-I angular phase matching. The crystals have dielectric antireflective coatings provided by the vendor (Conex Systems, Inc.). The pump and temporally stretched seed beams have a FWHM of ~ 1.5 mm, providing a maximum pump intensity of ~ 1.1 GW/cm². The two LBO crystals are used in a walkoff-compensated configuration¹⁸ with a ~ 4 -mm

air gap between them. This gap introduces a negligible amount of dephasing that does not affect the conversion process. The angle between the pump and seed pulses is 0.5° , which allows the signal and idler beams to be separated after the OPA process.

Figure 93.27 shows the conversion efficiency of the two-crystal OPCPA system as a function of pump energy. At maximum conversion efficiency, 17.7 mJ of pump energy produces 5.1 mJ of amplified signal energy, providing an overall gain of greater than 6×10^6 and a conversion efficiency of 29%. As demonstrated by the solid curve in Fig. 93.27, there is excellent agreement between modeling and experimental results. In addition to maximizing conversion efficiency, the OPCPA system was designed to minimize output-energy fluctuations. As shown in the inset table in Fig. 93.27, at the point of maximum conversion efficiency, the energy stability of the OPCPA output is 1.6% rms (measured over 100 shots) and is actually better than that of the pump. This improvement in output stability over that of the pump was predicted previously⁸ and was achieved by carefully designing our OPA so that, at its output, energy in the signal just begins to reconvert into pump energy. We believe that this system demonstrates a significant improvement in output stability beyond systems previously reported in the literature.

The spectra of the input, stretched seed pulse and the amplified signal pulse are shown in Fig. 93.28(a). The FWHM of the amplified signal spectrum is approximately 8 nm, centered at ~ 1055 nm. Whereas the spectrum of the unamplified seed pulse is roughly Gaussian in shape, the shape of the amplified spectrum is square due to saturation in the OPCPA process. The amplified output of the OPCPA system is compressed in a double-passed, single-grating compressor.

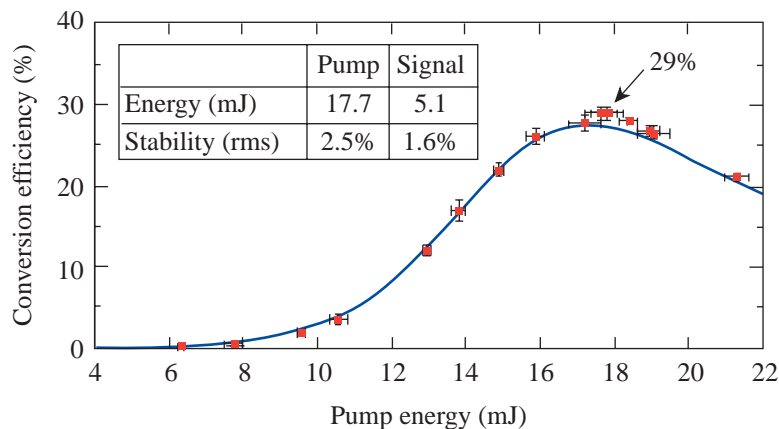


Figure 93.27

Conversion efficiency as a function of pump energy. Solid curve shows model predictions with the squares representing experimentally measured values. Error bars show fluctuations in measured energies. Inset chart shows pump and signal energies and stabilities at the 29% conversion efficiency point.

G5677a

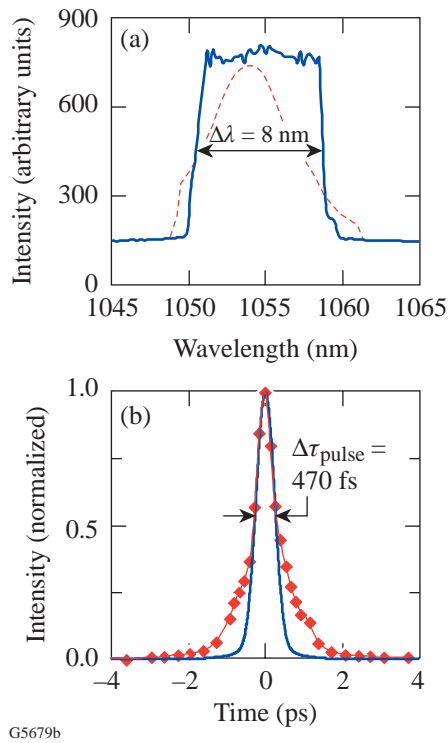


Figure 93.28

(a) Spectra of stretched seed pulse (dashed) and amplified signal pulse (solid). Clipping in the seed-pulse spectrum is due to the finite extent of the stretcher optics. (b) Measured autocorrelation (diamonds) of the amplified signal shown along with an autocorrelation trace (solid line) calculated from a fast Fourier transform (FFT) of the spectrum of the amplified signal shown in part (a). The wings in the measured autocorrelation are also present without OPCPA amplification, indicating that they are due to spectral phase errors in the stretcher-compressor combination.

The autocorrelation at the output of the pulse compressor, as measured with a scanning autocorrelator, is shown in Fig. 93.28(b). Using the measured spectra to estimate the transform-limited pulse width, we estimate the temporal duration (FWHM) of the compressed, amplified signal to be 470 fs, which is approximately 1.3 times the Fourier transform limit. Without amplification, the stretched and recompressed seed autocorrelation trace contains wings that are similar to those shown in Fig. 93.28(b). We thus believe that these wings are due to the uncompensated spectral phase in our stretcher-compressor combination and not the OPCPA process itself.

One of the advantages of an OPA is the fact that any aberrations in the pump spatial profile are transferred to the idler beam. Thus, the signal-beam quality is not degraded in the OPA. We measured the far field of our amplified signal

beam at the focus of a 500-mm-focal-length lens with a 12-bit beam analyzer (Spiricon LBA 500PC and CoHu 4800 CCD camera). By comparing the FWHM of the Fourier transform of the measured near-field profile with that of the measured far field, we determined that the amplified-signal-beam FWHM is ~ 1.3 times the diffraction limit in the horizontal direction and ~ 1.1 times the diffraction-limited width in the vertical direction. These numbers match closely with those measured for the stretched seed pulse, indicating that the OPA did not introduce additional phase errors to the spatial profile of the amplified pulse.

The maximum pump-to-signal conversion efficiency possible in a degenerate OPA such as the one presented here is 50%. In our experiment, the conversion efficiency is limited by a number of factors including the finite slopes of the spatiotemporal profile of the pump pulse, walk-off between the seed and pump, and noise in the spatiotemporal profile. Our simulations show that if we are able to decrease the rise time of the temporal profile to ~ 50 ps and increase the order of the super-Gaussian spatial profile to 30, we could increase the conversion efficiency of our system to approximately 40%. We have also designed a new OPCPA system containing a two-crystal preamplifier and a single-crystal power amplifier that will be able to generate higher energies while increasing the overall system conversion efficiency to greater than 40%.¹²

We have demonstrated an OPCPA system that uses a spatiotemporally shaped pump pulse to maximize the conversion efficiency of the OPCPA process. This system produces 5 mJ of amplified signal at a 5-Hz repetition rate with a pump-to-signal conversion efficiency of 29%. To our knowledge, this is the highest conversion efficiency ever achieved in an OPCPA system. In addition to high conversion efficiency, the system output is highly stable with an rms stability of 1.6%, which is actually better than that of the pump laser.

ACKNOWLEDGMENT

This work was supported by the U. S. Department of Energy Office of Inertial Confinement Fusion under Cooperative Agreement No. DE-FC03-92SF19460, the University of Rochester, and the New York State Energy Research and Development Authority. The support of DOE does not constitute an endorsement by DOE of the views expressed in this article.

REFERENCES

1. A. Dubietis, G. Jonusauskas, and A. Piskarskas, *Opt. Commun.* **88**, 437 (1992).
2. I. N. Ross *et al.*, *Opt. Commun.* **144**, 125 (1997).

3. J. Collier *et al.*, *Appl. Opt.* **38**, 7486 (1999).
4. I. Jovanovic *et al.*, *Appl. Opt.* **41**, 2923 (2002).
5. I. Jovanovic, C. A. Ebberts, and C. P. J. Barty, *Opt. Lett.* **27**, 1622 (2002).
6. I. A. Begishev *et al.*, *Sov. J. Quantum Electron.* **20**, 1100 (1990).
7. I. A. Begishev *et al.*, *Sov. J. Quantum Electron.* **20**, 1104 (1990).
8. S. K. Zhang *et al.*, *Opt. Commun.* **184**, 451 (2000).
9. M. J. Guardalben, J. Keegan, L. J. Waxer, and J. D. Zuegel, presented at the 2002 OSA Annual Meeting, Orlando, FL, 29 September–3 October 2002 (paper TuC5).
10. I. N. Ross *et al.*, *Appl. Opt.* **39**, 2422 (2000).
11. X. Yang *et al.*, *Opt. Lett.* **27**, 1135 (2002).
12. M. J. Guardalben, J. Keegan, L. J. Waxer, and J. D. Zuegel, “Optimization of a High-Conversion-Efficiency Optical Parametric Chirped-Pulse Amplification System” (in preparation).
13. A. V. Okishev and W. Seka, *IEEE J. Sel. Top. Quantum Electron.* **3**, 59 (1997).
14. M. D. Skeldon, A. V. Okishev, R. L. Keck, W. Seka, and S. Letzring, in *Third International Conference on Solid State Lasers for Application to Inertial Confinement Fusion*, edited by W. H. Lowdermilk (SPIE, Bellingham, WA, 1999), Vol. 3492, pp. 131–135.
15. A. V. Okishev, D. Battaglia, I. Begishev, and J. D. Zuegel, in *OSA Trends in Optics and Photonics (TOPS) Vol. 73, Conference on Lasers and Electro-Optics*, OSA Technical Digest (Optical Society of America, Washington, DC, 2002), pp. 365–366.
16. G. Cheriaux *et al.*, *Opt. Lett.* **21**, 414 (1996).
17. D. Du *et al.*, *Opt. Lett.* **20**, 2114 (1995).
18. D. J. Armstrong *et al.*, *J. Opt. Soc. Am. B* **14**, 460 (1997).

Ultrafast Superconducting Single-Photon Optical Detectors and Their Applications

Introduction

Single-photon detectors (SPD's) represent the ultimate sensitivity limit for any quantum radiation detectors. In the visible light range, the best known and most widely used are Si avalanche photodiodes (APD's)¹ and photomultiplier tubes (PMT's).² The operation of photomultiplier/avalanche devices is based on the electron cascade and multiplication effect, which significantly amplifies the response and allows for an easy measurement of the response pulses. Unfortunately, this method of registration leads to a large time lag and jitter of the device response. In addition, the counting rates of APD's and PMT's are well below 100 MHz. Their actual speed is even more limited since, for noise reduction purposes, they have to be used in a time-gated mode, which reduces their counting rates to 10 MHz or below.

Detection of single-photon infrared (IR) radiation remains a major technological challenge because IR photons carry significantly less energy than those of visible light, making it difficult to engineer an efficient electron cascade. The most successful Si APD's have their sensitivity restricted by the band gap, while APD's based on narrow-gap semiconductors exhibit unacceptably large dark counts.³ The best quantum efficiency (QE) reported for InGaAs APD's is ~16% at 1.2 μm , but the large, ~0.5-ns jitter and high, $>10^4$ -per-second dark counts³ make them unattractive for several important applications, including practical quantum communication systems.^{2,4} The PMT's are bulky and demonstrate $\text{QE} < 0.001\%$ at 1.2 μm and ~150-ps jitter.² Finally, the most recently proposed far-IR detectors based on single-electron transistors⁵ are very slow and require millikelvin temperatures.

In this article, we review our most recent research on superconducting SPD's (SSPD's). We demonstrate their excellent operating parameters and show that in many areas they drastically outperform their semiconductor counterparts. Applications ranging from visible free-space and IR fiber-based quantum communications⁴ to nondestructive testing of very-large-scale-integrated (VLSI) devices⁶ require SPD's with very high counting rates, very low jitter, and negligible

dark counts. Effective operation in the mid-IR spectrum range is also very important. Our nanostructured, NbN SSPD's,^{7,8} based on the nonequilibrium hot-electron effect in ultrathin superconducting films,⁹ offer picosecond time resolution and jitter, experimental QE ranging from $>10\%$ for visible light to 5% to 3% in the 1.3- μm to 1.55- μm IR range, and very low dark counts.

The following sections will (1) present an overview of the physics of operation of SSPD's; (2) briefly discuss our fabrication methods; (3) present the experimental results and show the SSPD performance; (4) review already identified applications of SSPD's for VLSI chip testing and quantum cryptography; and (5) present our conclusions, including the direct comparison with other SPD's.

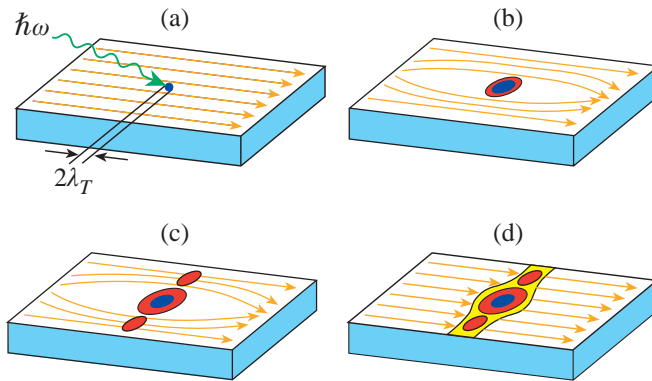
Physics of Operation of SSPD

Superconducting devices have already become practical as radiation sensors because of their quantum nature and low-noise cryogenic operation environment.⁹ The superconducting energy gap 2Δ is typically two to three orders of magnitude lower than the gap in semiconductors; thus, individual optical photons are able to generate a large number of excited carriers when hitting a superconductor.¹⁰ Measuring the resulting electrical pulse allows precise detection of the photon arrival. The efficient avalanche also results in an enhanced resolution of energy-resolving devices, such as superconducting tunnel junctions,¹¹ and extends the range of detectable energies well into the IR range for photodetectors. Finally, energy relaxation time constants of excited electrons in superconductors are in the picosecond range for both the low-temperature¹² and high-temperature¹³ superconductors, ensuring the gigahertz repetition rates for superconducting photon counters.

Our SSPD consists of a superconducting stripe whose thickness is less than the electron thermalization length. The device is operated at a temperature far below the material's critical temperature T_c , in a regime where the bias current I is close to the critical value I_c . Absorption of a photon leads to

the formation of a hotspot region¹⁴ where superconductivity is suppressed or even destroyed [Fig. 93.29(a)]. During the initial thermalization, the hotspot grows in size [Fig. 93.29(b)] as hot electrons diffuse out of the hotspot core. The supercurrent, which biases the device, is expelled from the resistive hotspot volume and is concentrated in the “sidewalks” near the edges of the film [Fig. 93.29(c)]. If the current density after this redistribution exceeds the critical value outside the hotspot, phase-slip centers are created in the sidewalks, the superconductivity is destroyed, and the resistive barrier is formed across the entire width of the device [Fig. 93.29(d)], which, in turn, gives rise to a voltage signal with the amplitude proportional to I . The hotspot growth is followed by its healing, due to the relaxation/cooling of excited electrons and their out-diffusion. Thus, after an ~ 30 -ps-long quasiparticle relaxation time,¹² the hotspot collapses, superconductivity (zero voltage state) is restored, and the detector is ready to register another photon.

The SSPD operation principle outlined above depends directly on the superconductor characteristics, including 2Δ , diffusivity, electron–electron, and electron–phonon interaction times, as well as on the device geometry. Our material-of-choice is NbN, characterized by the picosecond quasiparticle relaxation; it is suitable for photon counting in the <0.4 - μm -to 3.5 - μm -wavelength range. Photons with a wavelength of $1 \mu\text{m}$ create in a 10-nm-thick NbN stripe a hotspot of ~ 20 -nm diameter.⁸ This means that the single-quantum mode of the SSPD operation requires that the width of our NbN superconductive stripe should be 200 nm or narrower.



Z2509a

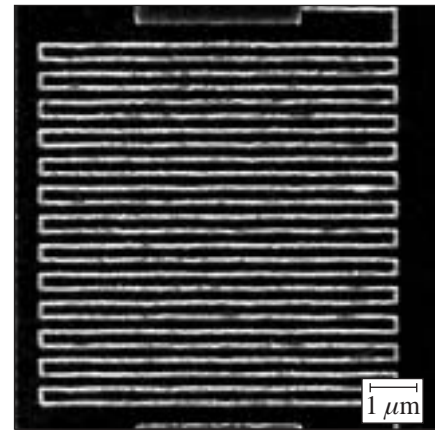
Figure 93.29

Schematics of the hotspot-generated and supercurrent-assisted formation of a resistive barrier in an ultrathin and submicrometer-width superconducting stripe, kept at a temperature far below T_c . The arrows indicate the flow direction of a supercurrent biasing the stripe.

SSPD Fabrication

NbN superconductive films that we use to fabricate our SSPD's have a thickness of 3.5 nm to 10 nm and are deposited on sapphire substrates by dc reactive magnetron sputtering in an Ar and N_2 mixture.¹⁵ The films are characterized by $T_c = 10$ to 11 K, the superconductive transition width $\Delta T_c \sim 0.3$ K, and the critical current density $j_c = 6$ to 7×10^6 A/cm² at 4.2 K. To implement a detector, we have chosen meander-type geometry with characteristic sizes ranging from $10 \times 10 \mu\text{m}^2$ to $4 \times 4 \mu\text{m}^2$ and a filling factor f (the ratio of the area occupied by the superconducting meander to the detector nominal area) up to 0.5. The width of the superconductive stripe varies from 80 nm to 200 nm. Our patterning and etching procedures are presented in detail in Ref. 15; here we mention only that our fabrication process includes an electron-beam lithography, followed by either ion milling through a Ti mask layer or reactive ion etching through a photoresist.

Figures 93.30 and 93.31 present scanning electron microscope images of two SSPD's that are fabricated according to two different patterning procedures described in Ref 15. Figure 93.30 shows a 10×8 - μm^2 , 10-nm-thick meander device, fabricated using the Ti mask and ion milling. We note that in this technology, although we can fabricate devices with very narrow (0.1 μm to 0.2 μm in width) meander stripes, f is always much lower than 1, as the separation between the lines remains significantly larger than the line width. Figure 93.31 presents the center part of our latest-generation, interdigitated structures with $f = 0.4$ to 0.5, etched in a 3.5-nm-thick NbN film. Using ultrathin films and direct reactive ion etching, we



Z2580

Figure 93.30

A scanning-electron-microscope image of a 10×8 - μm^2 , 10-nm-thick meander-type SSPD. The superconducting stripe width is ~ 130 nm and $f \approx 0.2$.

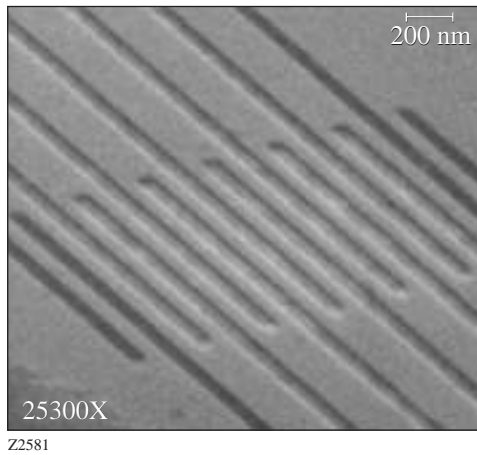


Figure 93.31

A scanning-electron-microscope image of an interdigitated, 3.5-nm-thick SSPD. The width of superconducting stripes (center of the picture) is ~ 80 nm and $f = 0.5$.

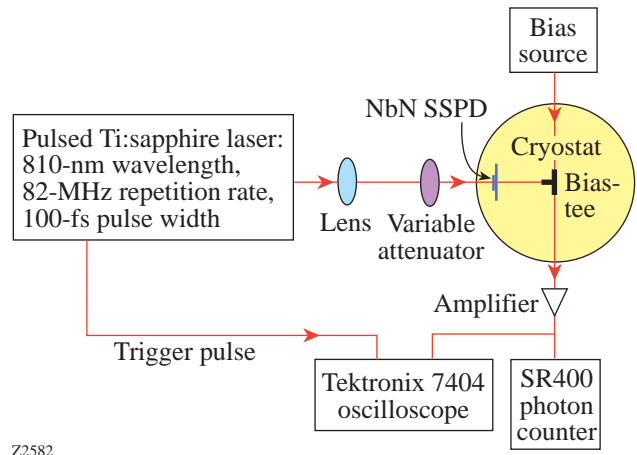


Figure 93.32

Experimental setup for free-space detection of single photons.

not only increased f but also drastically reduced our SSPD stripe edge nonuniformities. This latter factor seems to be dominant in the device performance since, as will be presented later, the 3.5-nm-thick structures exhibited over-an-order-of-magnitude-higher experimental QE, despite having significantly decreased the photon absorption coefficient η .⁷

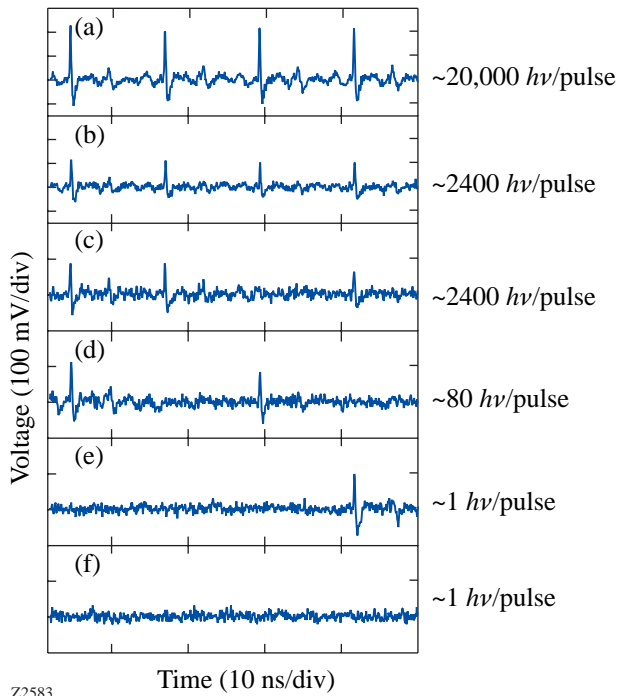
Experimental Results and the SSPD Performance

A schematic diagram of our experimental setup is shown in Fig. 93.32. The SSPD was placed on a cold plate inside an optical, liquid-helium cryostat and maintained at 4.2 K. The device was wire bonded to a microstrip transmission line and connected to the dc bias and rf output circuitry via a broadband, cryogenic bias-tee. The output signal, generated as a result of the photon capture, was amplified by a 20-dB-gain, room-temperature broadband amplifier and either fed into a Tektronix 7404 single-shot digital oscilloscope (synchronously triggered by a Ti:sapphire laser) or counted by an SR400 photon counter. The room-temperature amplifier and the oscilloscope were characterized by a bandwidth of 0.01 to 12 GHz and 0 to 4 GHz, respectively.

As a photon source, we used 100-fs-wide, 82-MHz-repetition-rate pulses from a self-mode-locked Ti:sapphire laser. The incident radiation was focused on the device and attenuated to the picowatt level, using banks of neutral-density filters. The optical beam diameter was typically ~ 50 μm to ensure the SSPD uniform illumination. In addition, the QE spectral sen-

sitivity dependence of the SSPD was measured using a continuous-wave (cw) blackbody radiation source and cw and pulsed laser diodes.

Figure 93.33 shows a collection of real-time “snapshots” recorded by the single-shot oscilloscope for different numbers of photons per laser pulse, incident on a 4×4 - μm^2 -area, 10-nm-thick SSPD, and is intended to illustrate the physical response of our devices. Each snapshot presents a 50-ns-long record of the response to four successive 100-fs-wide optical pulses, randomly selected out of a real-time detector output data stream. Trace (a) in Fig. 93.33 corresponds to essentially a macroscopic signal with $\sim 20,000$ photons per pulse hitting the detector. In this case, the device responded to each optical pulse in the laser train; however, as the incident laser intensity was decreased (with other experimental conditions unchanged), the quantum nature of the detector response started to emerge. For ~ 2400 photons per pulse [traces (b) and (c)], the amplitude of the response pulses was decreased, but, most interestingly, some of the signals were absent in the response train [trace (c)]. Further, over-an-order-of-magnitude decrease in the photon flux did not lead to the decrease of the output signal amplitude, which is characteristic of classical intensity detectors, but many of the response pulses were missing [trace (d)] due to both the limited QE of the device and fluctuations in the number of photons incident on the detector. The quantum nature of our device response was most apparent in the bottom pair of traces: (e) and (f) (1 photon/pulse). We note that



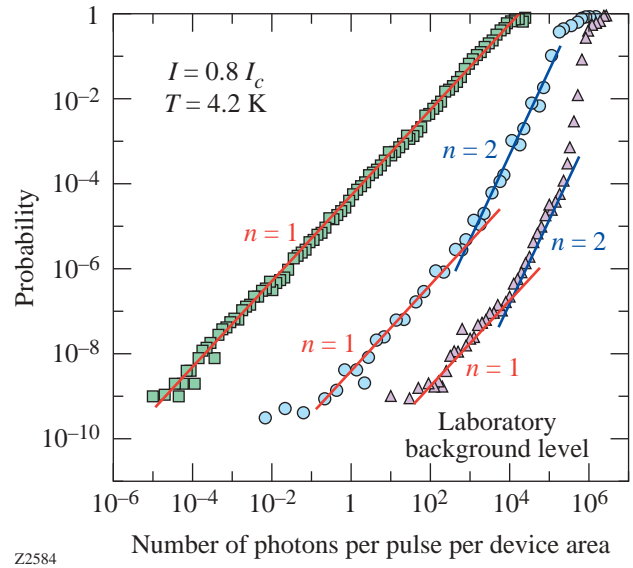
Z2583

Figure 93.33

Real-time responses of a SSPD to trains of 100-fs optical pulses with different numbers of photons per pulse per device area. The presented records illustrate the quantum nature of our device responses at low photon fluxes. Radiation wavelength was 810 nm.

in each case, the detector response is very different and its actual performance has to be judged, based on the response averaged over the recording time much longer than 50 ns. We also note that within the time resolution of our electronics, the width of the SSPD response pulses remained constant for all tested photon fluxes.

Records like the ones shown in Fig. 93.33, but averaged over almost 5×10^9 optical pulses (accumulated over a period of 60 s using the SR400 counter), allowed us to perform statistical analysis of the SSPD response. We observed that for weak photon fluxes (< 100 photons per pulse), both the average number of captured pulses for a given photon flux and the signal amplitude remained constant. Figure 93.34 shows the probability of photon counting (the ratio of the average number of photons captured per second to the repetition rate of laser pulses) as a function of the average number per pulse of 405-nm, 810-nm, and 1550-nm photons from our Ti:sapphire laser, incident on a $10 \times 10\text{-}\mu\text{m}^2$ -area, 10-nm-thick device. The device was biased at $I = 0.8 I_c$, which was low enough to remain subcritical even when I_c was thermally suppressed at the highest incident light intensities. We note



Z2584

Figure 93.34

Probability of photon counting versus the incident photon radiation flux for a $10 \times 10\text{-}\mu\text{m}^2$, 10-nm-thick SSPD at 405-nm (squares), 810-nm (circles), and 1550-nm (triangles) wavelengths. The bias current was $I/I_c = 0.8$ and temperature was 4.2 K. The solid lines illustrate the slope exponents $n = 1$ and $n = 2$.

that for 405-nm photons we have a linear dependence over ten orders of magnitude of the photon flux intensity. At wavelength $\lambda = 810$ nm, we observe the linear response at low photon counts and the quadratic law for higher photon fluxes. Finally, for $\lambda = 1550$ nm, the photon counting rate is a highly nonlinear function of the photon flux, with the linear dependence observed only in the range of 10^2 to 10^4 photons per pulse. We also observe that for the lowest photon fluxes, our experimental data points, for every wavelength, level off at the same $\sim 10^{-9}$ probability value (~ 0.1 counts per second). We interpret this response as the laboratory photon background, resulting from accidental photon absorption by our detector. On the other hand, the saturation (probability approaching 1) observed at the highest incident photon flux levels represents the transition of our quantum device into a classical detector [see also Fig. 93.33(a)].

SSPD's are passive devices, and the main sources of dark or false counts are either extrinsic bias-current instabilities or intrinsic fluctuations. The supercurrent fluctuations are dominating at I very close to I_c and rapidly (exponentially) decrease with the I decrease,¹⁶ while thermally activated phase-slip centers are typically negligible since we operate our devices at $T \ll T_c$. Thus, long-term stability of I when the detector is biased close to I_c is crucial for minimizing dark counts. One

must remember, however, that SSPD's are very broadband sensors and they have to be properly screened from unwanted "photon noise." Large values of dark counts were observed in SSPD implementations, where thermal background radiation from room-temperature objects was inadvertently coupled into the detector.⁶ Measurements of dark counts performed in the setup shown in Fig. 93.32 with the SSPD blocked by a cold load lead to an average of <0.01 counts per second for $I \leq 0.95 I_c$ and were, apparently, limited by our biasing electronics.

The behavior observed in Fig. 93.34 results from the direct linear dependence of the hotspot size on the photon energy.⁸ Thus, for a fixed I , low-energy photons generate hotspots too small to ensure efficient SSPD operation, leading to enhanced probability of multiphoton detection with the increase of the photon flux.

For a mean number of m photons per pulse, the probability $P(n)$ of absorbing n photons from a given pulse is given by the Poisson distribution:

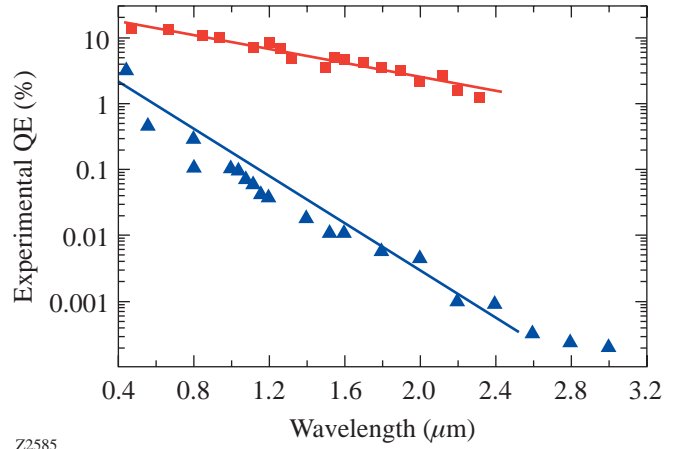
$$P(n) \sim \frac{e^{-m} (m)^n}{n!}. \quad (1)$$

For very weak ($m \ll 1$) photon fluxes, the probability of detecting one photon, two photons, three photons, etc., is

$$P(1) \sim m, P(2) \sim \frac{m^2}{2}, P(3) \sim \frac{m^3}{6}, \text{ etc.} \quad (2)$$

Based on Eq. (2), we can conclude that for a very low number of photons per pulse incident on the SSPD, we clearly observe in Fig. 93.34 a single-photon detection regime (exponent $n = 1$) for each studied wavelength. While for 405-nm radiation, the presence of at least one photon in the optical pulse was sufficient to trigger the detector response, for $\lambda = 1550$ nm, the multiphoton absorption ($n \geq 2$) was dominant.

The probability of photon counting measured at the one-photon-per-pulse level incident upon the SSPD and expressed in percent can be defined as its *experimental QE* [more rigorously: detection efficiency (DE)] for a given photon energy. We must stress that QE is a function of I and the highest values are measured for I very close to I_c as shown in Refs. 8 and 16. Typically, we operate our SSPD's with $I \leq 0.95 I_c$ since, as we mentioned before, higher I values result in excessive dark counts. Figure 93.35 presents experimental QE spectral de-



Z2585

Figure 93.35

Spectral dependences of QE for $10 \times 10\text{-}\mu\text{m}^2$ SSPD's, with NbN stripe thickness of 10 nm (triangles) and 3.5 nm (squares), respectively. The solid lines are guides to the eye, illustrating the exponential dependence of the QE on wavelength.

pendence for two representative $10 \times 10\text{-}\mu\text{m}^2$ -area devices. The 3.5-nm-thick SSPD (squares) was an interdigitated device (see Fig. 93.31) with 80-nm-wide NbN fingers and $f = 0.5$, while the 10-nm-thick, 200-nm-wide-stripe SSPD (triangles) was a meander-type structure (see Fig. 93.30) with $f \approx 0.2$. We observe that in both cases, the DE spectral dependence exhibited an exponential, activated-type character with the slope value characteristic for all devices with the same thickness.⁸ We associate the activation-type behavior with the presence of fluctuations, both extrinsic (stripe width) and intrinsic (superconducting). Simultaneously, we note the drastic improvement in the performance of the 3.5-nm-thick device, as compared to the 10-nm structure, in terms of both the much smaller slope value and the much higher experimental QE.¹⁶

As we mentioned in the **SSPD Fabrication** section, this performance improvement is the result of significant improvements in our fabrication technology.¹⁵ The interdigitated devices implement the ultrathin NbN stripe (larger hotspot dimension) and are truly nanostructured in terms of their physical dimensions. Our best 10-nm-thick SSPD's exhibit experimental QE of $\sim 3\%$ at $\lambda = 405$ nm, decreasing to $\sim 0.01\%$ at $\lambda = 1550$ -nm wavelength. At the same time, the 3.5-nm devices reach over-an-order-of-magnitude-higher QE, ranging from $>10\%$ at $\lambda = 405$ nm to 3.5% at $\lambda = 1550$ nm.

Proper coupling of our devices to the incident photon flux is another, besides I , limiting factor of the SSPD's experimental QE value. Unlike semiconductor SPD's, the SSPD's have a

relatively small active area, and only a certain percentage of incident photons is actually absorbed in the ultrathin NbN stripe. The above limitations are extrinsic; thus, in order to estimate the SSPD ultimate performance, defined as the *intrinsic* QE of the superconducting stripe,^{7,8} one needs to factor in both the filling factor and the photon absorption coefficient. For 10-nm-thick devices, $f \approx 0.2$ and $\eta \approx 0.3$, leading to the intrinsic QE = $DE/(f\eta)$, indicating that the possible improvement can reach up to a factor of 20. In the case of the 3.5-nm SSPD's, similar calculations indicate that the intrinsic QE should reach the theoretical maximum of 100% for all visible-light wavelengths. The above approach is questionable, however, since for our ultrathin, nanostructured devices, the NbN optical conductivity can be quite different from the dc value used in Eq. (1) in Ref. 7 to calculate η . The best approach to further increase the QE of our detectors is, we believe, not by changing the interdigitated SSPD geometry, but by adding a backside mirror to reflect the transmitted photons back into the detector. It would be even more effective to form a $\lambda/4$ resonator with the detector acting as one of the resonator mirrors. In this case, however, the SSPD would lose its broadband sensitivity.

Finally, one can define a *system* QE as the number of photons falling at input on the fiber or other coupling optics, divided by the number of photon counts recorded by the detector. This QE definition includes the impact of the detector coupling optics rather than the SSPD size, and it was used in Ref. 6 to describe the performance of the early SSPD-based system designed for noninvasive testing of the VLSI chips. The system QE value reported in Ref. 6 for one of the first 10-nm-thick, meander-type SSPD's was 0.002% at 1.3- μm wavelength. The latest 3.5-nm devices in the same fiber-based system (although with significantly modified/improved optics) exhibit a system QE of 2% at the same wavelength—a four-orders-of-magnitude improvement over a two-year period.

We have also performed extensive time-domain characterization of our SSPD's, which are presented in Ref. 17. Here we want only to mention that the 10-nm-thick SSPD's have a time resolution <100 ps and a device jitter <35 ps. Thus, they are able to detect photons with at least 10-Gbit/s counting rate and are more than three orders of magnitude faster than any semiconductor SPD. The 3.5-nm devices are expected to have even better time resolution, reaching values close to the intrinsic electron-phonon cooling time in ultrathin NbN films of 30 ps.¹² Their jitter has been already measured and is below 20 ps.

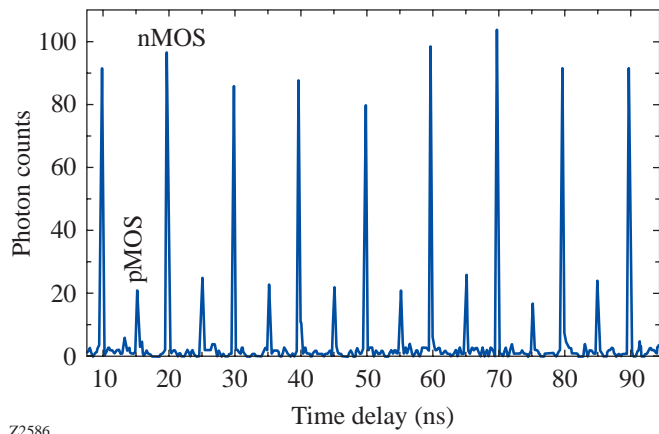
Applications of SSPD's

1. Noncontact VLSI Chip Testing

Modern, high-performance, electronic VLSI circuits are extremely difficult to test on both the functional and logic levels because of their complexity, density of packaging, and the use of flip-chip bonding. Devices are increasingly more sensitive and can be easily perturbed during testing, skewing results and slowing the design and development time. Thus, in complex circuits such as microprocessors, nonperturbing methods of testing the chip functionality while it operates are most desirable.

A normally operating silicon complementary metal oxide semiconductor (CMOS) transistor has a nonzero probability of emitting near-IR (0.9 μm to 1.4 μm) photons when current passes through the channel. This is the spontaneous photon emission associated with intraband transitions as the hot carriers move across the transistor channel.^{18,19} Thus, this photon emission is time-correlated with the transistor switching event and measures directly the transistor switching time, as well as the entire circuit timing characteristics. This intrinsic transistor/circuit information is ideal for timing data acquisition and fault analysis (e.g., leaky transistors tend to emit more photons). The use of near-IR emission from CMOS integrated circuits as a way of diagnosing timing and flaws of VLSI chips has been implemented in the IDS PICA probe system, manufactured by NPTest, San Jose, CA. The IDS PICA system can be equipped with an imaging near-IR detector, the Mepsicon II PMT (Quantar Tech., Inc) or with the SSPD device.⁶ The imaging PMT camera enables light emission from many devices on a test circuit to be simultaneously analyzed, but its IR efficiency is extremely low, leading to hour-long acquisition times and poor noise-to-signal ratio. The SSPD can analyze emission from a single CMOS device only, but its superior IR QE cuts acquisition times to minutes or seconds.

The 3.5-nm-thick NbN SSPD sensors are currently being implemented in the latest IDS PICA version. Test results from a 0.18- μm -linewidth, 1.6-V-bias CMOS integrated circuit running at 100 MHz are shown in Fig. 93.36. The collected histogram has an extremely high signal-to-noise ratio and the time between transistor switching events can be measured with 10-ps accuracy. In addition to the peaks coming from photon emission from nMOS transistors, we can also observe weak signals collected from pMOS inverters. Holes in pMOS devices have lower mobility and emit IR photons much less frequently. We need to stress that the integrated circuit under test and the photon-collecting microscope are at room tem-



Z2586

Figure 93.36

Histogram of single-photon emissions from a CMOS VLSI chip, collected by the NbN SSPD. Signals from both nMOS and pMOS transistors are clearly visible. The picture was copied directly from the PICA screen.

perature, and the microscope is connected to the SSPD via a multimode fiber. Physically, the chip-testing apparatus is approximately 2 to 3 m away from the detector, which is placed inside a commercial cryocooler, operating at 3.5 K.

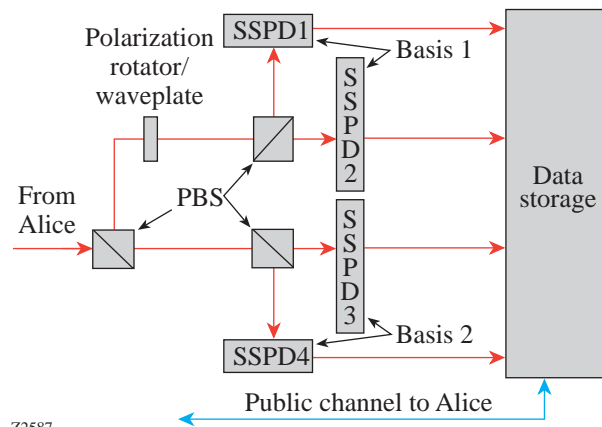
2. Quantum Cryptography

Quantum cryptography (QC) provides a radical improvement over today's methods for secure communications. Unconditionally secret communication is possible in actual physical environments due to the Heisenberg indeterminacy principle: it is impossible to measure the state of a quantum bit without altering it. In QC, the data transport is performed as an exchange of individual photons with their polarization used to code the logic information for the communication protocol. QC is based on the real-time Vernam encryption scheme (so-called "one-time pad").²⁰ The quantum key is formed during the photon transmission (there is no pre-existing key), and the Vernam cipher is invulnerable to any computer attack of any strength, including quantum computations.

A recent theoretical paper by Gilbert and Hamrick²¹ proves that QC is practical, providing that the data transmission rate is high enough to overcome the intrinsic system losses. Both the transceiver (Alice) and the receiver (Bob) must operate at transmission rates of at least 1 Gbit/s for the practical quantum key distribution operation. A GHz-repetition-rate, actively mode-locked laser can be used as the high-speed source of coherent single photons,²² so Alice can readily operate at the GHz range. A serious problem, however, exists at the Bob end,

which should count photons not only very efficiently, but also with negligible dark counts and very low jitter.

Figure 93.37 presents a possible QC receiver, containing four SSPD's for independent counting of photons with four different polarizations imprinted by Alice. The NbN SSPD's are the most promising for practical QC since, as we have already presented, they exhibit sufficiently high QE and are able to reach GHz-range counting rates with very low jitter and negligibly low dark counts. The SSPD's can successfully operate from ultraviolet to IR; thus, they can be implemented in both optical free-space and fiber-based transmission schemes.



Z2587

Figure 93.37

Quantum cryptography receiver (Bob) based on four NbN SSPD's. PBS stands for polarization beamsplitter.

Conclusions

Table 93.II presents the main characteristics of our SSPD's, in direct comparison with other modern single-photon detectors. Experimental QE, ultimate counting rate, jitter, and dark counting rates are compared for 1.3- μm photons, which is the most-interesting wavelength for applications ranging from noninvasive VLSI chip testing to fiber-based optical communications. As can be seen, superconducting detectors significantly outperform even the best semiconductor devices.

ACKNOWLEDGMENT

This work was supported by the AFOSR grant F49620-01-1-0463 (Rochester), by RFBR grant 02-02-16774 (Moscow), and by NPTTest, San Jose, CA. The authors would like to thank their colleagues from the University of Rochester, Moscow State Pedagogical University, and NPTTest for their contributions to the SSPD research. We are also very grateful to Dr. Deborah Van Vechten and the U.S. Office of Naval Research for fostering the Rochester–Moscow collaboration.

Table 93.II: Performance of different SPD's operating at $\lambda = 1.3 \mu\text{m}$.

| Detector Model | Counting Rate | QE | Jitter | Dark Counts |
|---------------------------------|----------------------------------|-------|--------|---------------------|
| | (Hz) | (%) | (ps) | (s^{-1}) |
| InGaAs APD (Fujitsu) | 5.0×10^6 ^(a) | 16 | 200 | 500 ^(b) |
| IR PMT (Hamamatsu) | 9.0×10^6 | 0.5 | 150 | 2.0×10^4 |
| Si APD (EG&G) | 5.0×10^6 | 0.01 | 350 | 25 |
| Mepsicron (Quantar, Inc.) | 1.0×10^6 ^(c) | 0.001 | 100 | 0.1 |
| Superconducting tunnel junction | 5.0×10^3 | 60 | N/A | N/A |
| SSPD (measured) | 10×10^9 | 5 | 35 | 0.1 ^(d) |
| SSPD (projected) | 30×10^9 | >10 | <20 | <0.01 |

^(a)Gated regime with 0.1%-per-gate after-count probability.
^(b)Calculated with 10^{-4} -per-gate probability.
^(c)Data for a high-speed version; standard devices exhibit $1 \times 10^5 \text{ s}^{-1}$.
^(d)Room-temperature input.

REFERENCES

1. T. Isoshima *et al.*, Rev. Sci. Instrum. **66**, 2922 (1995).
2. A. Karlsson *et al.*, IEEE Circuits and Devices Mag. **15**, 34 (1999).
3. F. Zappa *et al.*, Opt. Eng. **35**, 938 (1996).
4. A. A. Verevkin, J. Zhang, W. Slysz, R. Sobolewski, A. P. Lipatov, O. Okunev, G. Chulkova, A. Korneev, and G. N. Gol'tsman, in *Free-Space Laser Communication and Laser Imaging II*, edited by J. C. Ricklin and D. G. Voelz (SPIE, Bellingham, WA, 2002), Vol. 4821, pp. 447–454.
5. O. Astafiev *et al.*, Appl. Phys. Lett. **80**, 4250 (2002).
6. S. Somani, S. Kasapi, K. Wilsher, W. Lo, R. Sobolewski, and G. Gol'tsman, J. Vac. Sci. Technol. B, Microelectron. Nanometer Struct. **19**, 2766 (2001).
7. G. N. Gol'tsman, O. Okunev, G. Chulkova, A. Lipatov, A. Semenov, K. Smirnov, B. Voronov, A. Dzardanov, C. Williams, and R. Sobolewski, Appl. Phys. Lett. **79**, 705 (2001).
8. A. Verevkin, J. Zhang, R. Sobolewski, A. Lipatov, O. Okunev, G. Chulkova, A. Korneev, K. Smirnov, G. N. Gol'tsman, and A. Semenov, Appl. Phys. Lett. **80**, 4687 (2002).
9. A. D. Semenov, G. N. Gol'tsman, and R. Sobolewski, Supercond. Sci. Technol. **15**, R1 (2002).
10. K. S. Il'in, I. I. Milostnaya, A. A. Verevkin, G. N. Gol'tsman, E. M. Gershenzon, and R. Sobolewski, Appl. Phys. Lett. **73**, 3938 (1998).
11. A. Peacock *et al.*, Nature **381**, 135 (1996); R. J. Schoelkopf *et al.*, IEEE Trans. Appl. Supercond. **9**, 2935 (1999).
12. K. S. Il'in, M. Lindgren, M. Currie, A. D. Semenov, G. N. Gol'tsman, R. Sobolewski, S. I. Cherednichenko, and E. M. Gershenzon, Appl. Phys. Lett. **76**, 2752 (2000).
13. M. Lindgren, M. Currie, C. Williams, T. Y. Hsiang, P. M. Fauchet, R. Sobolewski, S. H. Moffat, R. A. Hughes, J. S. Preston, and F. A. Hegmann, Appl. Phys. Lett. **74**, 853 (1999).
14. A. M. Kadin and M. W. Johnson, Appl. Phys. Lett. **69**, 3938 (1996).
15. G. N. Gol'tsman, K. Smirnov, P. Kouminov, B. Voronov, N. Kurova, V. Drakinsky, J. Zhang, A. Verevkin, and R. Sobolewski, "Fabrication of Nanostructured Superconducting Single-Photon Detectors," to be published in IEEE Transactions on Applied Superconductivity.
16. A. Lipatov, O. Okunev, K. Smirnov, G. Chulkova, A. Korneev, P. Kouminov, G. Gol'tsman, J. Zhang, W. Slysz, A. Verevkin, and R. Sobolewski, Supercond. Sci. Technol. **15**, 1689 (2002).
17. J. Zhang, W. Slysz, A. Verevkin, G. Chulkova, A. Korneev, A. Lipatov, O. Okunev, G. Gol'tsman, and R. Sobolewski, "Response Time Characterization of NbN Superconducting Single-Photon Detectors," to be published in IEEE Transactions on Applied Superconductivity.
18. J. C. Tsang and J. A. Kash, Appl. Phys. Lett. **70**, 889 (1997).
19. M. Pavesi *et al.*, Phys. Rev. B **65**, 195209 (2002).
20. G. S. Vernam, J. Amer. Inst. Elec. Eng. **XLV**, 109 (1926).
21. G. Gilbert and M. Hamrick, "Practical Quantum Cryptography: A Comprehensive Analysis (Part One)," MITRE Technical Report MTR00W0000052 (September 2000), <http://xxx.lanl.gov/abs/quant-ph/0009027>; also to be published in Physics Reports.
22. T. R. Clark *et al.*, Electron. Lett. **35**, 720 (1999).

Very Fast Metal–Semiconductor–Metal Ultraviolet Photodiodes on GaN with Submicron Finger Width

Metal–semiconductor–metal (MSM) photodiodes made on GaN are attractive candidates for fast ultraviolet (UV) signals due to the simplicity of fabrication and the visible blind feature (no response for $\lambda > 365$ nm). The temporal response of a MSM photodetector fabricated on GaN has been examined both theoretically¹ and experimentally.^{2–4} While the theoretical modeling for a 0.25- μm MSM interdigitated structure predicted a small time constant of 3.5 ps, experimental measurements have been limited to feature dimensions no smaller than 2 μm . More recently T. Palacios *et al.*⁵ reported on the responsivity of submicron (0.5- μm) MSM UV detectors on GaN; however, the temporal response was not characterized. In this article, we present the results of temporal measurements of a MSM photodiode on GaN with finger width and pitch ranging from 0.3 μm to 5 μm . These detectors were packaged with a specially designed fast circuit. The minimum temporal resolution between consecutive optical pulses was measured to be 26 ps. At high illumination levels, broadening of the detector response was observed and can be attributed to space-charge screening.

The GaN wafers (2- μm thickness) grown on *c*-plane sapphire were purchased from Technologies and Devices International, Inc.⁶ The residual impurities produced a free-electron concentration below $1 \times 10^{16} \text{ cm}^{-3}$. The MSM detectors were fabricated at Cornell Nanofabrication Facilities (CNF) using electron-beam lithography. A 15-nm Au layer was deposited prior to the exposure of the electron beam due to the low conductivity of the material. Native oxide on the surface was removed with a diluted HF (hydrofluoric acid) solution prior to metallization, Ti/Pt (5 nm/80 nm). The finger spacing and width, which were equal, ranged from 0.3 μm to 5 μm . The active area was either $50 \times 50 \mu\text{m}^2$ or $25 \times 25 \mu\text{m}^2$. After fabrication of the fingers, a FOX-12 (field oxide) negative resist layer with 450-nm thickness was deposited and exposed with the *e* beam to form a SiO_2 passivation layer over the entire device.

Unlike other high-speed measurements that used microwave techniques,^{7,8} our time-domain experiments used a

broadband circuit to directly couple out the electrical pulse generated in the active area. The top view of this fixture is shown in Fig. 93.38. The backside of the circuit board is grounded. The transmission line width was designed to be 1.1 mm to match the 50- Ω impedance of the 34-GHz digitizing oscilloscope. A large bias resistor R_c was used to block out reflections from the charging circuit. To avoid an abrupt width change, a pad with a curved taper, calculated⁹ to reduce the impedance mismatch between the transmission line and the active area, was fabricated on the device. An ultrabroadband (12 KHz to 40+ GHz) optical capacitor (“Opt-Cap” in Fig. 93.38) is soldered on the edge of the board to produce a high-speed electrical connection to the backside ground plane. The sample is glued on the gap between the transmission line and the Opt-Cap and electrically connected by silver paste. The impulse response of the whole detector was simulated numerically.¹⁰

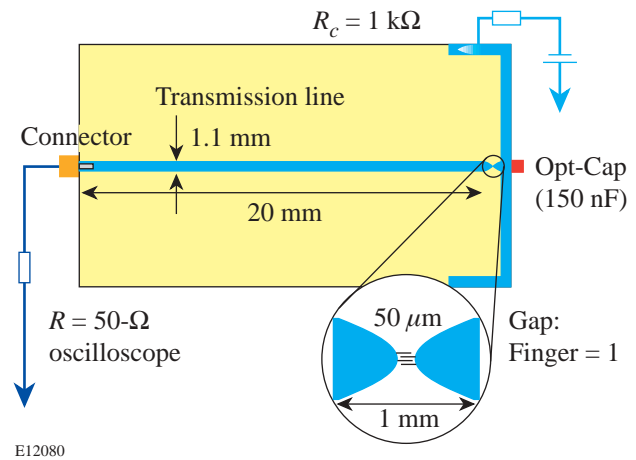


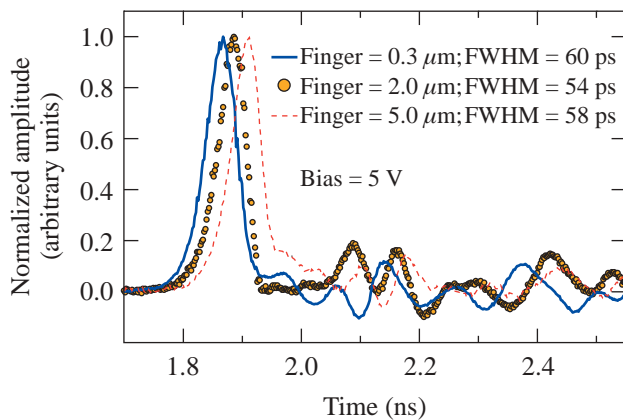
Figure 93.38

Top view of the broadband circuit designed for the MSM photodiode. R_c (1 k Ω) isolates the electrical pulse from bias circuit. An ultrabroadband optical capacitor (Opt-Cap) was soldered to the device and the ground. To avoid an abrupt width change, a pad with a calculated curve tapers the transmission line down to the active area.

The temporal response measurement was implemented with a mode-locked Ti:sapphire laser ($\lambda \sim 810$ nm). The output of the femtosecond laser was coupled into a custom-built third-harmonic generator to produce a UV beam ($\lambda \sim 270$ nm). The beam was then focused onto the active area of the sample by a UV-grade fused-silica lens with a 2-cm focal length. The focal spot was measured to be smaller than $10 \mu\text{m}$. The electrical pulse was displayed on a 34-GHz digital oscilloscope and recorded by a computer.

The device was plugged directly into the oscilloscope to eliminate the dispersion from connecting cables. Figure 93.39 is a plot of the normalized signal from devices with different fingers widths ($0.3 \mu\text{m}$, $2 \mu\text{m}$, and $5 \mu\text{m}$) under 5-V bias. The curves have been shifted in time for visual convenience. The optical energy is about 6 pJ/pulse. The main peaks are followed by ringing reflections from the circuit. It is interesting to compare our data on the $5 \mu\text{m}$ with those in Ref. 2: they reported a full width at half maximum (FWHM) of longer than 100 ps at 5-V bias, almost twice the pulse duration we measured. The slower response was attributed² to carrier transit time, which is contradicted by our experiments.

Further, our data show that the fall time is even faster than the rise time for all the samples at low illumination level, and the FWHM's of the impulse response from different fingers (60 ps for $0.3 \mu\text{m}$, 54 ps for $2 \mu\text{m}$, and 58 ps for $5 \mu\text{m}$) are similar (Fig. 93.39).



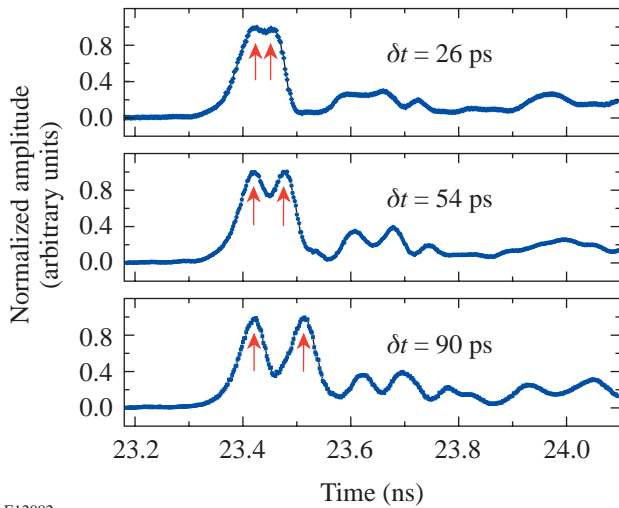
E12081

Figure 93.39 Time response of the detectors with different fingers ($0.3 \mu\text{m}$, $2 \mu\text{m}$, and $5 \mu\text{m}$) under 5-V bias. The amplitudes of the signal have been normalized to the peak values, and the dc background has been subtracted.

To study the relationship between electric field and temporal response time, we changed the bias voltage from 1 V to 10 V while maintaining the same illumination level. The pulse durations remained essentially the same. Another sample, with a $0.3\text{-}\mu\text{m}$ finger spacing and a $25 \times 25\text{-}\mu\text{m}^2$ active area, was examined. Its FWHM was measured at 58 ps, almost the same as the larger samples, thus eliminating device capacitance as the dominant factor contributing to the pulse width. This led us to examine the measurement test fixture, including the silver paste, the discontinuity of the connector, the surface roughness, and the width variation of the transmission line. The combined effect could cause the charging and discharging of the device to experience different impedances. For the device with $0.3 \mu\text{m}$, using reflection (ringing) in the response signal, which is 12% of the peak, we estimate the discharging impedance to be 63Ω . If the charging time is determined by the $Z_C = 63 \Omega$ and discharging time is determined by oscilloscope impedance, 50Ω , the ratio of them should be $63:50 = 1.26$. This matches well with the experimental results of 58-ps rise time and 45-ps fall time. Overall we believe that at a low illumination level the very short electrical pulse generated in our detectors was broadened by the measurement system and the real impulse response of the samples should be faster than the measured pulse duration.

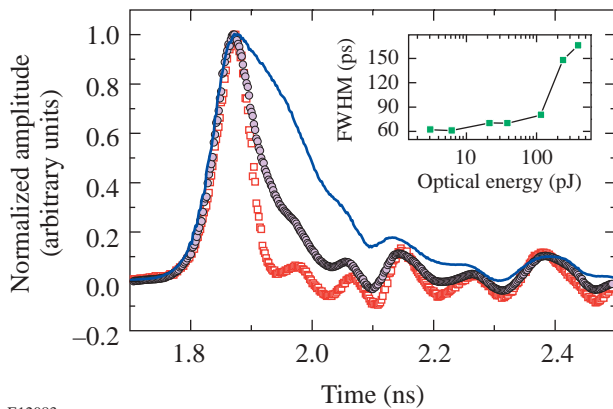
To explore further the inherent device response, a split-beam technique was used. In these experiments, the UV beam was split into two parts with an adjustable delay. The two pulses were then used to excite the detector. Figure 93.40 shows the results of the double-pulse measurement for a device with $0.3\text{-}\mu\text{m}$ finger and $25 \times 25\text{-}\mu\text{m}^2$ active area at 5-V bias. Separable responses began to be discernible at a time delay of 26 ps. This indicates that our devices had an inherent response time of less than 26 ps. When one optical pulse was delayed by 54 ps, the two pulses were well resolved: the value of the valley was about 70% of the value of the peak. This is consistent with our measured pulse duration. If delayed further to 90 ps, the two pulses were clearly separated, as can be seen in the plot.

The power dependence of the response speed was studied by tuning the UV output from the custom-built tripling system from 3 pJ to 391 pJ. In Fig. 93.41 we plot the temporal response data of a sample with $0.3\text{-}\mu\text{m}$ finger width for optical pulse energies of 3, 116, and 391 pJ, respectively. Again the signal amplitudes have been normalized to their peak values. The applied bias is 5 V for all measurements. As the incident optical energy increases, the rise time remains almost constant; however, the fall time increases significantly. This is attributed



E12082

Figure 93.40 Time resolution of the detector in free space. The beam was split into two parts, and one of them was delayed. When the delay was 26 ps, two main peaks started to be discernable. The reflections of the circuit can also be clearly seen.



E12083

Figure 93.41 Impulse response of MSM devices under different illumination energies of 3 pJ (squares), 116 pJ (circles), and 391 pJ (solid line). The insert shows the dependence of pulse width on the incident optical energy. The pulse duration remains constant below 6 pJ.

to screening of the internal field (dark electric field) between the finger electrodes by the space-charge field created by the field-induced separation of photogenerated electrons and hole at high illumination conditions.^{9,11,12} The

measured FWHM's under a different optical energy are plotted in the inset of Fig. 93.41. As can be seen, the FWHM remains flat (60 ps) for optical energy up to 6 pJ, after which the FWHM increases by approximately 10 ps up to 110 pJ and then to 166 ps for optical energy of 391 pJ. The condition on which the space-charge effect does not affect the pulse shape of impulse response was calculated in Refs. 11 and 12 and given as

$$E < \frac{\epsilon_0(\epsilon_s + 1)L^2V(t + D)hc}{4\lambda qt^2(1 - r)[1 - \exp(-\alpha d)]}, \quad (1)$$

where E is the incident optical pulse energy, ϵ_s is the relative permittivity of the semiconductor, L^2 is the active area, V is the applied bias, t is the finger width, D is the interelectrode spacing, λ is the incident wavelength, r is the reflection coefficient, α is the optical absorption coefficient, and d is the thickness of the GaN film. Based on all the parameters used in fabrication and experiment, we obtained a pulse energy of 6.54 pJ for our devices. This is in close agreement with our experimental results (FWHM starts increasing after 6 pJ).

In summary, MSM photodiodes have been fabricated on GaN with finger width and pitch ranging from 0.3 μm to 5 μm , and the impulse responses have been measured at $\lambda = 270$ nm under both low and high illumination conditions with a fast, broadband circuit. For an optical pulse energy less than 6 pJ, the response speed of the detectors was about 60 ps, regardless of the bias voltages (up to 10 V) and finger dimensions. Analysis of the rise and fall times indicates that the very short photogenerated electric pulse was broadened by the measurement system. The inherent device response was determined to be less than 26 ps by the double-pulse measurements. At higher incident optical energies, the pulse width increased significantly due to the screening of the dark electric field between the finger electrodes. The experimental results are in close agreement with theory.

ACKNOWLEDGMENT

One of the authors (JL) thanks Ms. Lu Chen for her help at CNF. This work was supported by the U.S. Department of Energy Office of Inertial Confinement Fusion under Cooperative Agreement No. DE-FC03-92SF19460, the University of Rochester, and the New York State Energy Research and Development Authority. The support of DOE does not constitute an endorsement by DOE of the views expressed in this article.

REFERENCES

1. R. P. Joshi, A. N. Dharamsi, and J. McAdoo, *Appl. Phys. Lett.* **64**, 3611 (1994).
2. J. C. Carrano *et al.*, *J. Electron. Mater.* **28**, 325 (1999).
3. J. C. Carrano *et al.*, *Appl. Phys. Lett.* **73**, 2405 (1998).
4. D. Walker *et al.*, *Appl. Phys. Lett.* **74**, 762 (1999).
5. T. Palacios *et al.*, *Appl. Phys. Lett.* **81**, 1902 (2002).
6. TDI, Inc., Silver Spring, MD 20904.
7. B. C. Wadell, *Transmission Line Design Handbook* (Artech House, Boston, 1991).
8. N. Biyikli *et al.*, *Appl. Phys. Lett.* **79**, 2838 (2001).
9. K. Aliberti *et al.*, *Appl. Phys. Lett.* **80**, 2848 (2002).
10. The details will be reported in a subsequent publication.
11. S. V. Averine and R. Sachot, *Solid-State Electron.* **44**, 1627 (2000).
12. S. V. Averine and R. Sachot, *IEE Proc., Optoelectron.* **147**, 145 (2000).

Glassy Liquid Crystals for Tunable Reflective Coloration

Amorphous Molecular Glasses

Glasses have been in existence for thousands of years, and yet they still represent one of the frontiers in materials science today.¹ They are traditionally classified as amorphous solids exhibiting isotropic properties. Cooled at a sufficiently rapid rate, all liquids should bypass crystallization to form glass. It is well known that liquid viscosity increases exponentially with decreasing temperature. Phenomenologically, the glass transition temperature T_g is defined on the basis of viscosity reaching a value of 10^{13} poise.² Despite intensive efforts over several decades, understanding of molecular processes accompanying glass transition has remained largely qualitative.^{1,2}

Glassy films are characterized by their superior optical quality over a large area with no grain boundaries and, therefore, are ideally suited for electronics, optics, photonics, and optoelectronics.³ Glass formation is ubiquitous among polymeric materials. To take advantage of the ease of film processing due to low melt viscosity and the feasibility of vacuum deposition, considerable efforts have been devoted in recent years to developing low-molar-mass organic materials. Existing amorphous molecular glasses can be categorized as follows: (a) bulky, odd-shaped or twin molecules;⁴⁻⁶ (b) star-

burst molecules and dendrimers;⁷⁻⁹ (c) spiro-linked molecules;¹⁰⁻¹² and (d) tetrahedrally configured molecules.¹³ In general, an elevated T_g relative to the application temperature is desired for stability against recrystallization. Representative structures are presented in Fig. 93.42, where G $x^\circ C$ I expresses a T_g at $x^\circ C$.

Glassy Liquid Crystals

It is arguable that glasses are not necessarily amorphous or isotropic. In principle, mesomorphic organic glasses can be realized by vitrifying liquid crystals through thermal quenching. Liquid crystals are a class of self-organizing fluids characterized by a uniaxial, lamellar, helical, or columnar arrangement in nematic, smectic, cholesteric, and discotic liquid crystalline order,¹⁴ respectively, as depicted in Fig. 93.43.

Each type of liquid crystal has found its respective niche in optics, photonics, or optoelectronics. With these molecular arrangements frozen in the solid state, glassy liquid crystals (GLC's) represent a novel material class that combines properties intrinsic to liquid crystals with those common to polymers, such as glass transition and film- and fiber-forming abilities. The preparation of defect-free GLC films requires

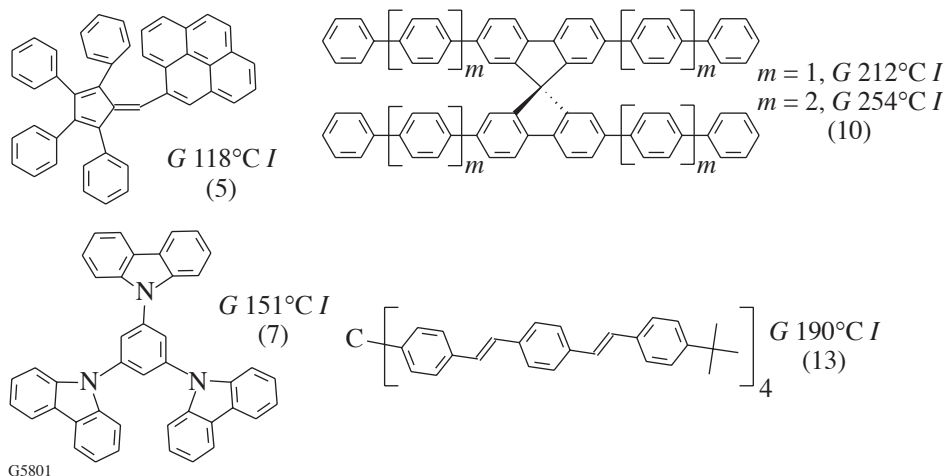


Figure 93.42
Representative amorphous molecular glasses.

slow cooling from mesomorphic melts without encountering crystallization, a challenge to thermal quenching as a conventional means to vitrification. From a fundamental perspective, transition of liquid crystal into mesomorphic solid adds a new dimension to the traditional view of transition from isotropic liquid into isotropic solid. The differential scanning calorimetric thermograms compiled in Fig. 93.44 serve to distinguish a GLC from a conventional liquid crystal.

Heating a conventional liquid crystal causes a first-order transition from crystalline solid to liquid crystal at its melting point T_m followed by a transition into isotropic liquid at its clearing point T_c . In contrast, a stable GLC undergoes a second-order transition from mesomorphic solid into liquid crystal at T_g , without modifying the molecular order, followed by a transition into isotropic liquid at T_c . Intermediate between a conventional liquid crystal and a stable GLC lies an unstable GLC, which tends to recrystallize from mesomorphic melt above T_g upon heating with subsequent melting to liquid crystal at T_m and clearing at T_c . Empirically, T_g/T_m was found to fall between 2/3 and 3/4 on an absolute temperature scale.

The very first attempt to synthesize GLC's in 1971 yielded materials with a low T_g and poor morphological stability.¹⁵ In

parallel to low-molar-mass GLC's, liquid crystalline polymers have been explored for the past three decades.^{16–18} In essence, GLC's are advantageous in their superior chemical purity and favorable rheological properties.¹⁹ Existing GLC's can be categorized into (a) laterally or terminally branched, one-string compounds with a T_g mostly around room temperature;²⁰ (b) twin molecules with an above-ambient T_g , but generally lacking morphological stability;^{21–24} (c) cyclo-siloxanes functionalized with mesogenic and chiral pendants;^{25–27} (d) carbosilane dendrimers exhibiting a low T_g ,^{28–30} and (e) macrocarbocycles with mesogenic segments as part of the ring structure.³¹

Representative structures are presented in Fig. 93.45, where $Gx^\circ C Nm$ or $Chy^\circ C I$ expresses a T_g and a T_c (for a nematic or cholesteric to isotropic transition) at x and $y^\circ C$, respectively. Based on the previously reported structures, there does not seem to be a systematic approach to the design of glassy liquid crystals. Specifically, the structural factors determining the type of mesomorphism, T_g and T_c , and the stability against recrystallization from the glassy state have remained largely elusive. Glassy cholesteric liquid crystals capable of selective wavelength reflection are of particular interest because of the relevance to tunable reflective coloration.

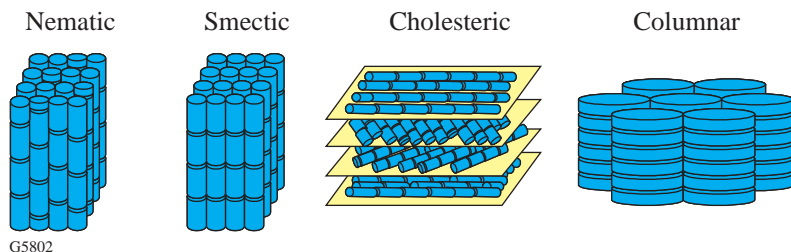


Figure 93.43
Liquid crystalline order via molecular self-organization.

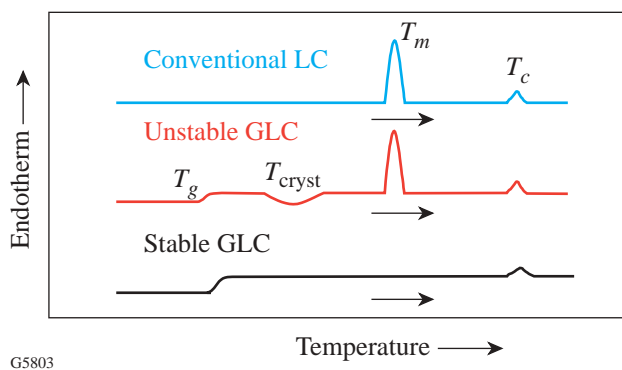


Figure 93.44
DSC thermograms of liquid crystals.

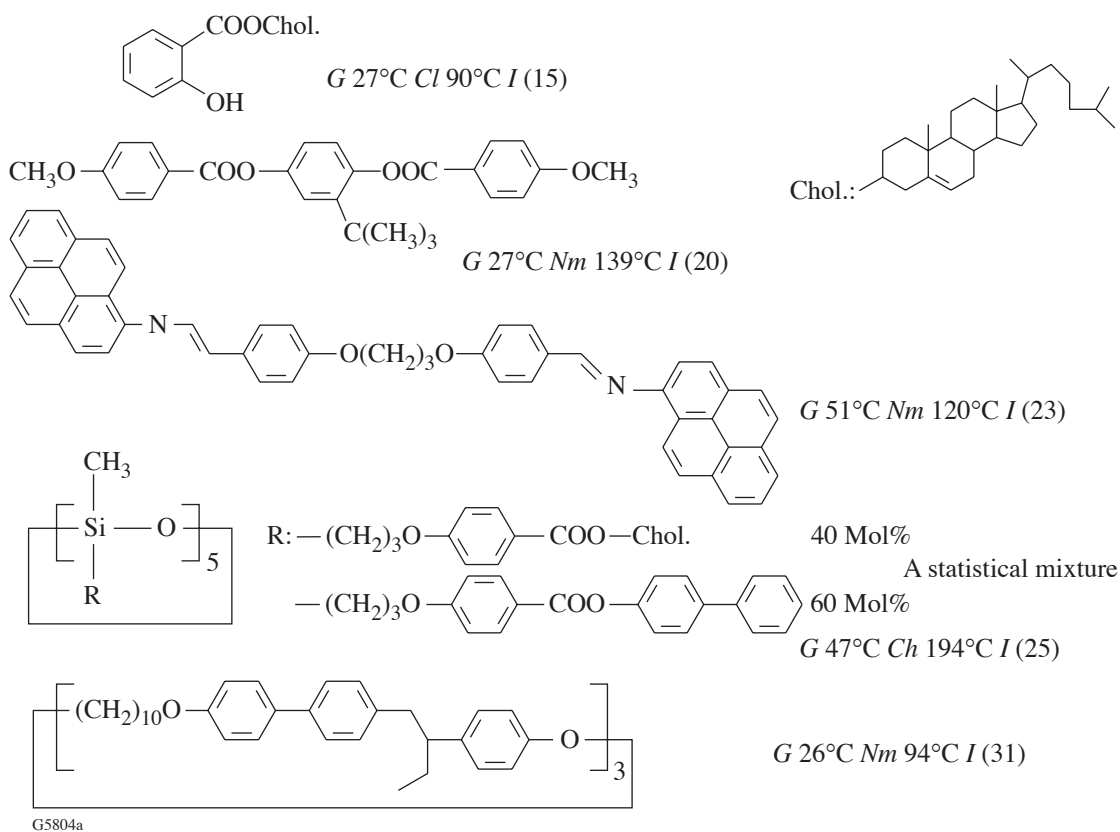


Figure 93.45
Representative glassy liquid crystals reported previously.

Optical Properties of Cholesteric Liquid Crystal Films

A cholesteric liquid crystal contains both nematic and chiral moieties in a single molecular entity or as a binary mixture. Consisting of a helical stack of quasineematic layers, a well-aligned cholesteric film can be characterized by handedness and helical pitch length p , as depicted in Fig. 93.46.

Handedness describes the direction in which twisting of the nematic director occurs from one layer to the next, and p is defined as the distance over which the director rotates by 360° . The property of selective reflection can be described in terms of $\lambda_R = p(n_e + n_o)/2$, in which n_e and n_o are the extraordinary and ordinary refractive indices of the quasi-nematic

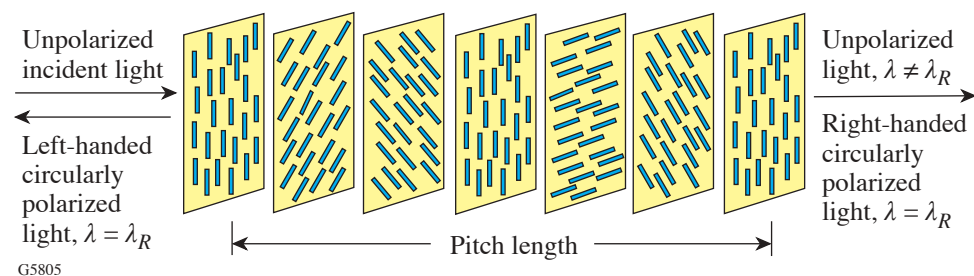


Figure 93.46
Selective reflection by a left-handed cholesteric film.³²

layer, respectively. The other parameter of interest is the helical twisting power, a measure of the ability of a chiral moiety to generate a given helical pitch length. Let us consider incident unpolarized white light propagating through a left-handed film as illustrated in Fig. 93.46. Natural (i.e., unpolarized) light consists of equal amounts of left- and right-handed (LH and RH) circularly polarized components. The LH circularly polarized component in the neighborhood of λ_R is selectively reflected, while the RH component is completely transmitted. The selective reflection bandwidth is determined by optical birefringence, $\Delta n = n_e - n_o$. A sufficiently thick, single-handed cholesteric film is capable of reflecting 50% of incident unpolarized light within the selective reflection band. Outside the selective reflection band, incident light is transmitted regardless of its polarization state. It follows that a stack of RH and LH films tuned at the same λ_R will reflect 100% of incident unpolarized light within the selective reflection band without attenuating the rest of the spectrum.

A New Approach to Glassy Liquid Crystals with Elevated Phase Transition Temperatures and Superior Morphological Stability

Most existing liquid crystals tend to crystallize when cooled to below their melting points, thus losing the desired molecular order characteristic of liquid crystals and resulting in polycrystalline films that scatter light or limit charge transport. As an emerging class of advanced materials, GLC's preserve varied forms of molecular order characteristic of liquid crystals in the solid state. To prevent spontaneous crystallization, we have implemented a molecular design strategy in which mesogenic and chiral pendants are chemically bonded to a volume-excluding core. While the core and the pendant are crystalline as separate entities, the chemical hybrid with a proper flexible spacer connecting the two readily vitrifies into a GLC when cooled. A definitive set of GLC's has been synthesized and characterized³³⁻⁴³ as summarized in Fig. 93.47, where G x°C (Nm , S_A , or Ch) y°C I expresses a T_g and a T_c (for a nematic,

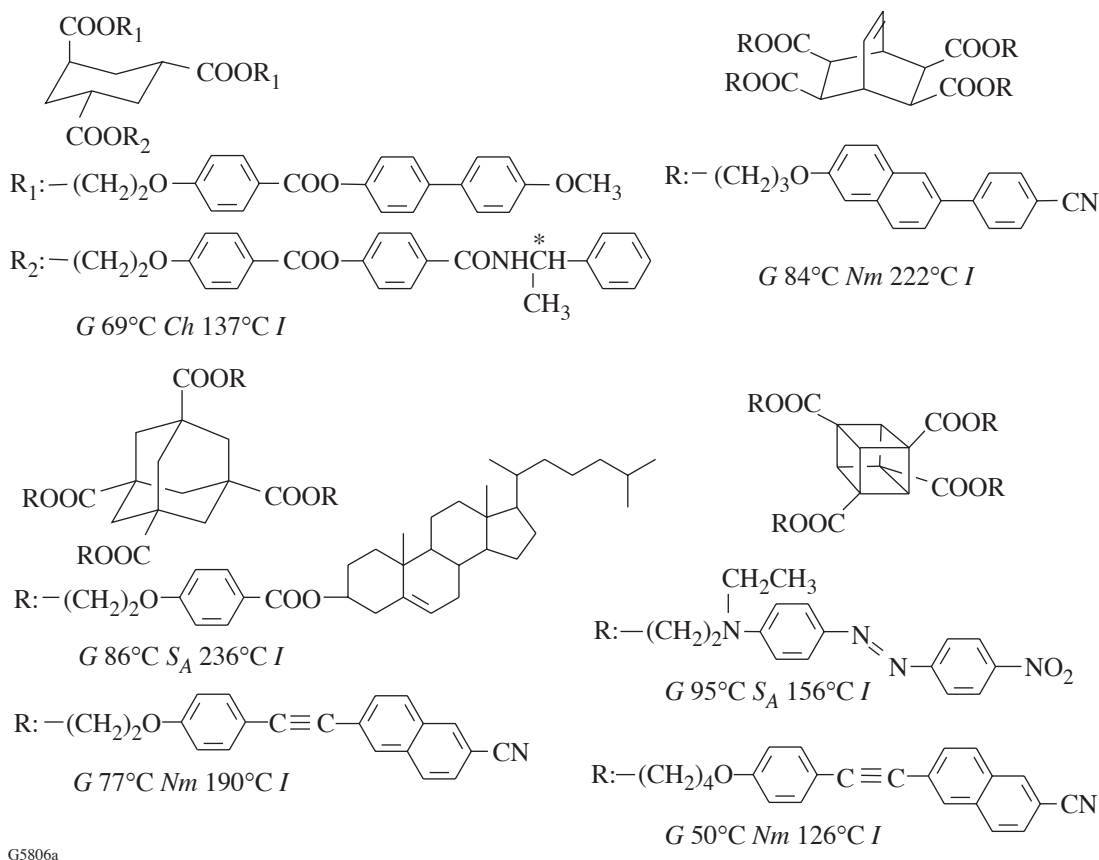


Figure 93.47
Representative morphologically stable glassy liquid crystals.

smectic A, or cholesteric to isotropic transition) at x and $y^\circ\text{C}$, respectively. Cyclohexane, bicyclooctene, adamantane, and cubane serve as the cores to which nematic and chiral pendants are attached, a manifestation of the versatility of our design concept. A spacer length of two to four methylene units was found to be optimum for vitrification with an elevated T_g .

Major advances have been made recently using a cyanoterphenyl nematogen, with an exceptionally high T_m and T_c , in the construction of GLC's with substantially elevated transition temperatures without compromising morphological stability. Note the glassy nematics with a T_g close to 130°C and a T_c close to 350°C ,⁴⁴ the highest values ever achieved in GLC's. As shown in Fig. 93.48, a linear nematogen is superior to an angular one in terms of phase transition temperatures. Glassy cholesterics have been synthesized in the past via a statistical approach, which requires intensive purification of a multicomponent reaction product.⁴⁵ A determinis-

tic synthesis strategy, as described in Reaction Scheme 1, produced enantiomeric glassy cholesterics with an identical molecular structure except opposite chirality.⁴⁶

The mixture of (I) and (II) in Reaction Scheme 1 at a mass ratio of 42 to 58 showed a T_g at 67°C and a T_c at 131°C . The polarization spectra of single-handed glassy cholesteric films are shown in Fig. 93.49. An unpolarized incident beam is decomposed into two circularly polarized components of equal intensities propagating in opposite directions. Since handedness of circularly polarized light can be reversed via reflection from a specular surface, essentially 100% circular polarization of an unpolarized light source can be accomplished. An optical notch filter consisting of a stack of glassy cholesteric films of opposite handedness is shown in Fig. 93.49 to yield an attenuation of 3.75 optical density units, equivalent to a contrast ratio of better than 5000 to 1, representing the best performance of organic materials to date. The spectral range intended for

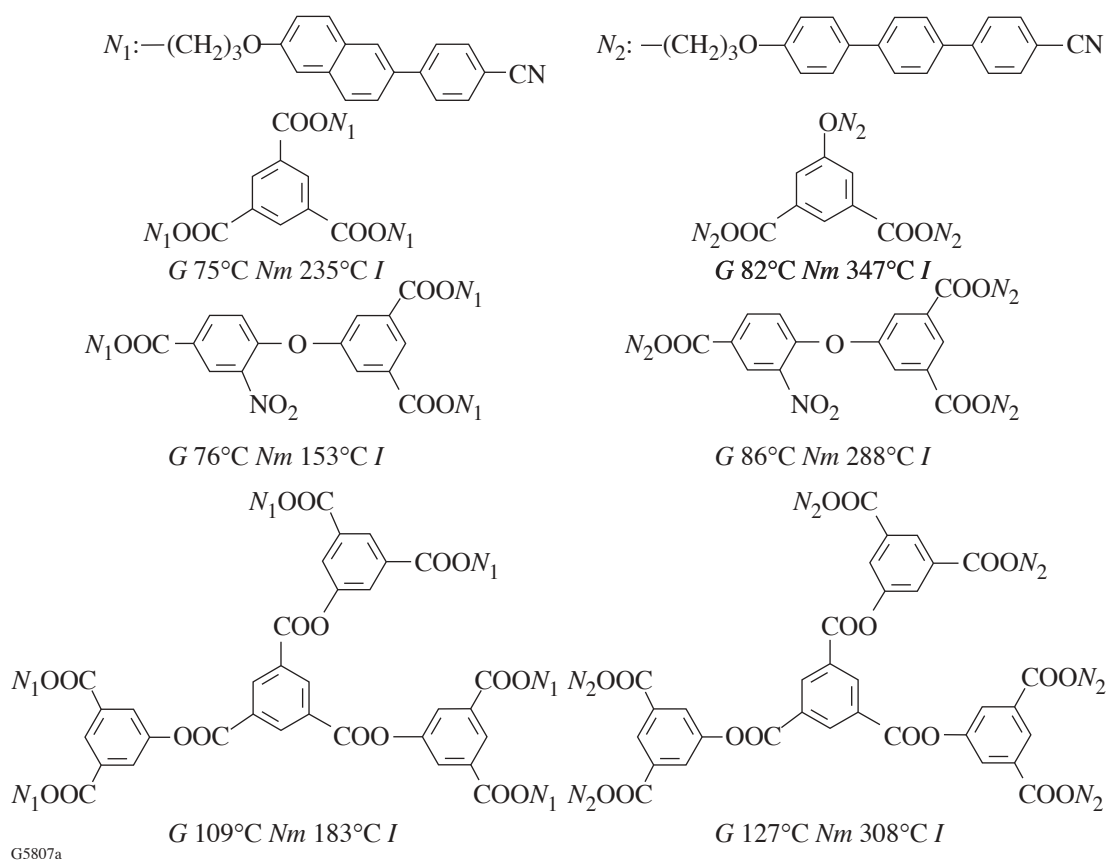
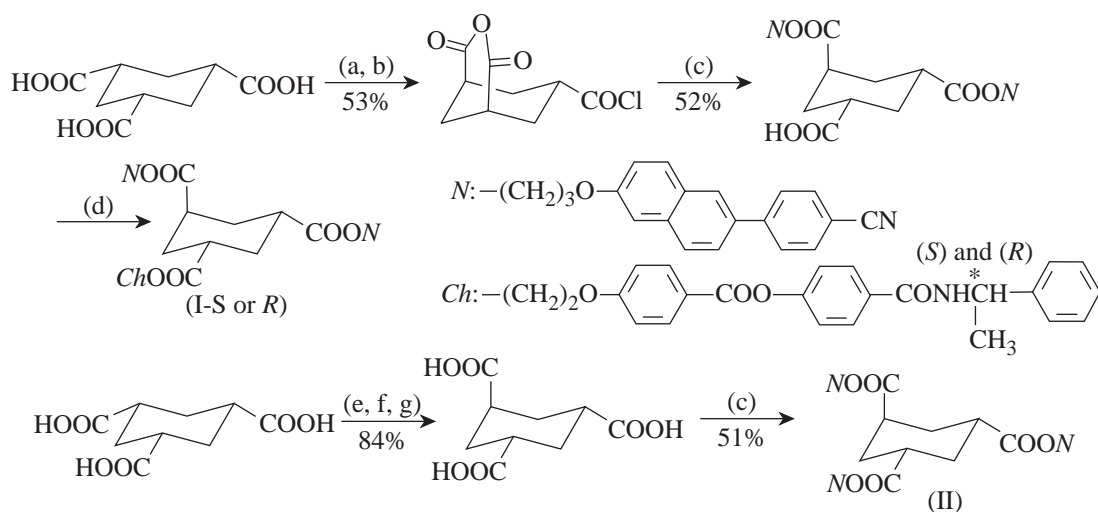


Figure 93.48
High-temperature glassy nematics.

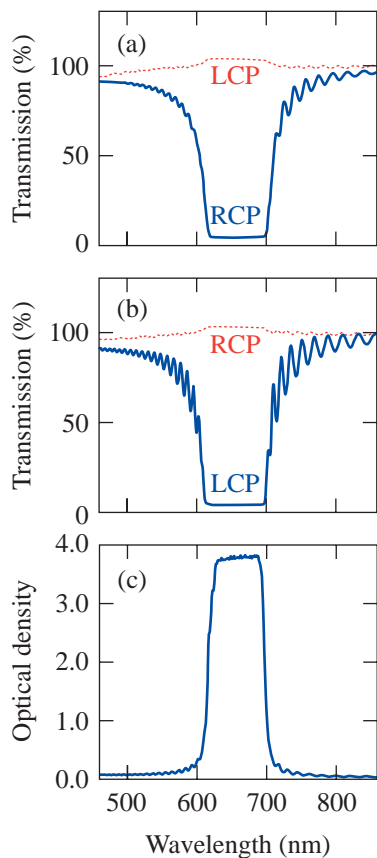


(a) $(\text{CH}_3\text{CO})_2\text{O}/\text{reflux}$; (b) $\text{SOCl}_2/\text{reflux}$; (c) $\text{NOH}/\text{DMAP}/\text{Et}_3\text{N}$; (d) $Ch\text{OH}/\text{DEADC}/\text{PPh}_3$;

(e) $(\text{CH}_3\text{CO})_2\text{O}$, $\text{CH}_3\text{CO}_2\text{Na}$; (f) CH_3COCl ; (g) H_2O

DMAP: 4-(dimethylamino)pyridine; DEADC: diethyl azodicarboxylate; PPh_3 : triphenylphosphine

G5808



G5809

Figure 93.49

Optical spectra of an unpolarized beam through (a) a right-handed, (b) a left-handed glassy cholesteric film, and (c) a notch filter comprising the two single-handed films (reproduced with permission from Ref. 46; copyright 2000 Wiley-VCH).

polarization and reflection can be readily tuned by varying the chemical composition.

The cyanoterphenyl group has also been successfully implemented in high-temperature glassy cholesterics synthesized in a deterministic fashion using the 5-oxyisophthalate linking unit, as shown in Fig. 93.50. Note that $G\ x^{\circ}\text{C}\ Ch\ y^{\circ}\text{C}\ I$ expresses a T_g and a T_c (for cholesteric to isotropic transition) at x and $y^{\circ}\text{C}$, respectively, determined from a differential scanning calorimetry (DSC) heating scan. The DSC cooling scan is presented as $I\ w^{\circ}\text{C}\ Ch\ z^{\circ}\text{C}\ G$, indicating a T_c (for isotropic to cholesteric transition) and a T_g at w and $z^{\circ}\text{C}$, respectively.

Tunable Reflective Coloration by Glassy Cholesteric Films

Two distinct modes of coloration exist in nature: *pigmentary*, involving electronic transitions of chromophores underlying light absorption and emission; and *structural*, involving interference, diffraction, or scattering of ambient light by nanostructures.⁴⁷ Examples of structural colors include butterfly wings, bird feathers, and beetle cuticles. In particular, beetles' exocuticles resemble cholesteric liquid crystalline films capable of selective wavelength reflection with simultaneous circular polarization, giving rise to long-lasting brilliant colors. A wide variety of cholesteric liquid crystalline materials have been developed, such as low-viscosity liquids, lyotropic and thermotropic polymers, liquid crystal/polymer composites, and glassy liquid crystals. Of particular interest are glassy liquid crystals that resist spontaneous crystallization through heating-cooling cycles, such as mixtures of Compounds (III) and (IV) depicted in Fig. 93.51. Although (IV) crystallizes upon heating to 95°C , both (III) and its binary mixtures with (IV) form stable glassy cholesteric films.⁴⁵ Also

shown in Fig. 93.51 are the selective reflection bands ranging from blue to green, red, and the infrared region with mixtures at an increasing ratio of (IV) to (III).

Furthermore, the selective reflection band and its width were shown to be tunable, albeit irreversibly, via photo-racemization of a bridged binaphthyl dopant.⁴⁸ In particular, phototunability is demonstrated in Fig. 93.52, where UV irradiation of a cholesteric film at a temperature above its T_g (i.e., 120°C versus 68°C) over an increasing time period followed by cooling to room temperature is shown to result in an increasing selective reflection wavelength. Morphologically stable GLC's that resist crystallization upon heating and cooling are the key to the successful implementation of this device concept.

Reversible Tunability of Reflective Coloration

Reversible tunability of reflective coloration has been extensively explored with temperature, pressure, electric field, and light as the external stimuli.^{49–57} The approach based on photoisomerization appears to be the most promising. The concept was first demonstrated by Sackman,⁵⁴ and revisited recently by Ikeda *et al.*,⁵⁵ based on *cis-to-trans* isomerization of azobenzene dopants in cholesteric fluid films. Shibaev *et al.*⁵⁶ employed a chiral azobenzene, both as a dopant and as a comonomer, in a polymer system with an ambient T_g and a response time of tens of minutes. Tamaoki *et al.*⁵⁷ used a glassy cholesteric matrix containing an azobenzene dopant, a material system allowing for photomodulation of pitch length at temperatures above T_g followed by cooling to below T_g to preserve the modified pitch in the solid state. All these approaches employing azobenzenes to tune reflective coloration suffer from fatigue and thermally activated *cis-to-trans* isomerization. Photoinduced interconversion between nematic and

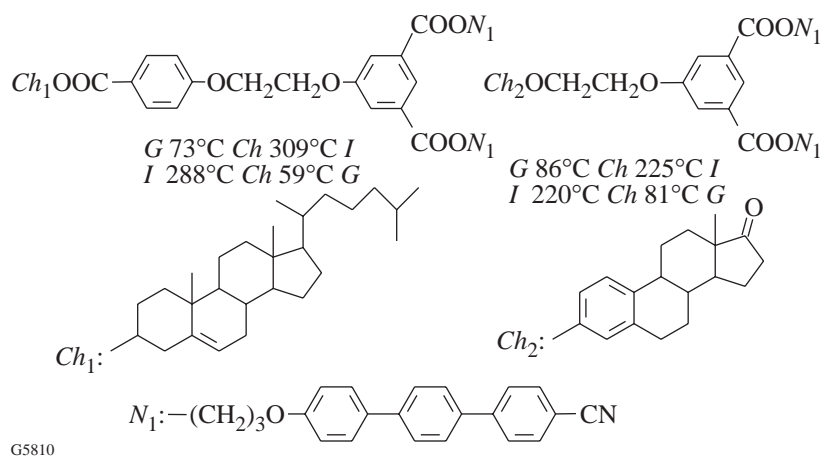


Figure 93.50
High-temperature glassy cholesterics.

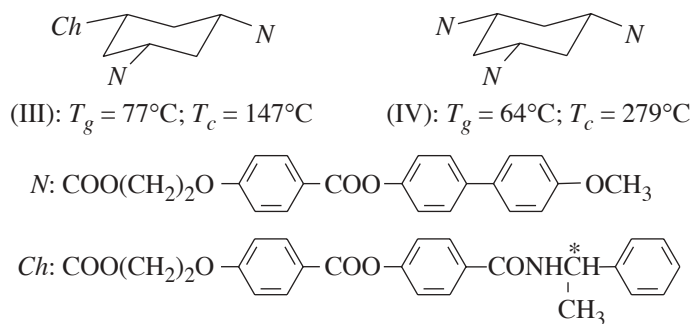
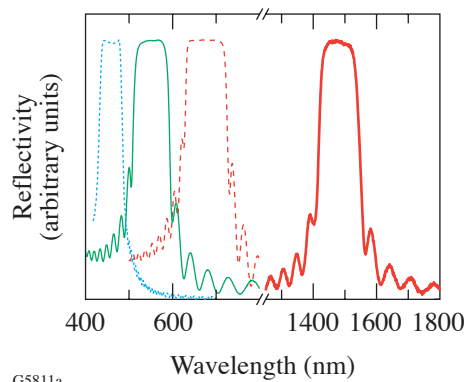


Figure 93.51
Reflective coloration by glassy cholesteric films.

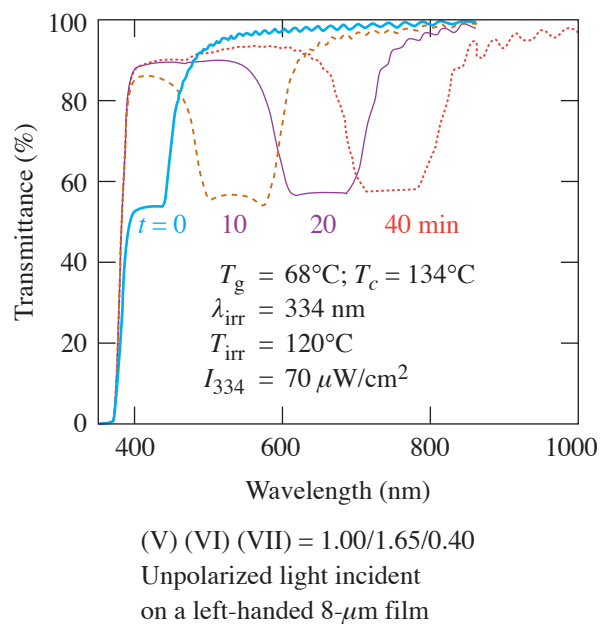
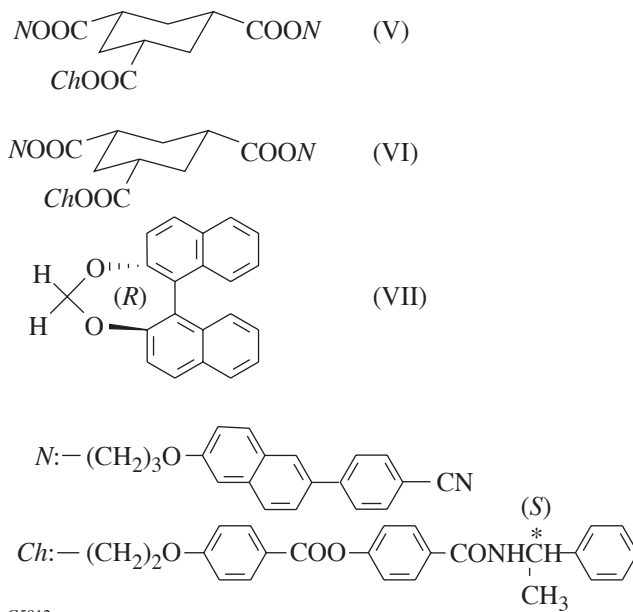


Figure 93.52
A phototunable glassy cholesteric film.

cholesteric mesomorphism and that between the right- and left-handed cholesteric mesomorphism have also been reported,^{58–63} where a helical pitch length of the order of 10 μm was observed.

Of all the photoresponsive moieties that have been explored, diarylethenes⁶⁴ appear to be the most promising in terms of thermal stability and fatigue resistance. The premise is that the two interconvertible isomers, viz., the open and closed forms, present disparate helical twisting powers in a liquid crystal matrix. Indeed, the closed form of chiral diarylethenes was found to have a stronger helical twisting power than the open form in nematic liquid crystal hosts with a helical pitch length of the order of 10 μm in all cases.^{62,63} To accomplish tunable reflective coloration in the visible region, a cholesteric liquid crystal with a short pitch length must be used as the host to define the base case. Moreover, glassy liquid crystal films are much preferred over liquid crystal films in practical application. Isomerization of diarylethenes was found to take place not only in liquid but also in single-crystalline⁶⁴ and amorphous^{65,66} solids without altering the morphology. Modulation of pitch length, however, requires a relative rotation between quasi-nematic layers as depicted in Fig. 93.46, a macroscopic rearrangement allowable only in the liquid state; therefore, we aim at cholesteric GLC's containing diarylethene moieties.

A Novel Class of Photoresponsive GLC's

Reversible tunability of reflective coloration using diarylethene-containing GLC's is envisioned in Fig. 93.53. A glassy cholesteric film comprising the open form of a diarylethene moiety with a predetermined reflection wavelength λ_R^0 is heated to above its T_g , where irradiation at λ_1 is performed to afford the closed form. This treatment results in a shorter reflection wavelength λ_R^c , which can be preserved in the solid state with subsequent cooling to below T_g . The more-extended conjugation of the closed form could cause light absorption in the visible region. With λ_R^c frozen in the solid state, irradiation of the closed form at λ_2 will regenerate the open form, thereby bleaching the undesired absorptive color without altering λ_R^c , a clear advantage over the use of liquid films. As dictated by the open form, subsequent heating to above T_g will recover λ_R^0 , which can then be frozen in the solid state by cooling through T_g . To attain the envisioned phototunability, we have developed the first diarylethene-containing nematic and chiral glasses. The molecular structures are depicted in Fig. 93.54, where *N* and *Ch* denote a nematic and a chiral moiety, respectively. Work is in progress to take advantage of these novel glassy materials together with the high-temperature GLC's shown in Figs. 93.48 and 93.50 for reversible tunability of reflective coloration with superior thermal stability and fatigue resistance.

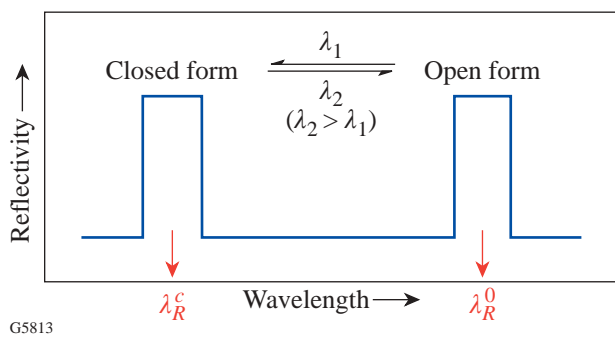


Figure 93.53
Reversible phototunability of reflective coloration.

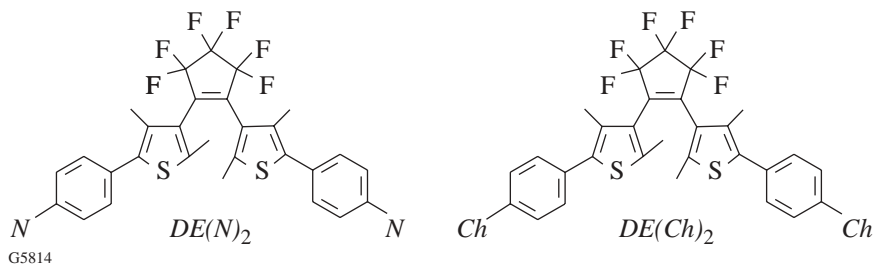


Figure 93.54
Novel glassy materials containing photoresponsive diarylethenes.

Conclusions

Glassy liquid crystals with elevated glass transition and clearing temperatures, a broad mesomorphic fluid temperature range, and excellent morphological stability have been developed for a diversity of photonic applications. In particular, glassy cholesteric films have been demonstrated for high-performance circular polarizers, optical notch filters, and reflectors across a spectral range that can be tuned by varying the chemical composition or by UV irradiation, albeit irreversibly. The molecular design concept governing glassy liquid crystals has been generalized to photoresponsive material systems containing diarylethenes, thereby enabling reversible tunability of reflective coloration with superior thermal stability and fatigue resistance.

ACKNOWLEDGMENT

The authors wish to thank F. Fan for synthesizing some of the materials reported herein, and S. D. Jacobs and K. L. Marshall at the University of Rochester's Laboratory for Laser Energetics for technical advice and helpful discussions. They are grateful for the financial support provided by the Multidisciplinary University Research Initiative, administered by the Army Research Office, under DAAD19-01-1-0676, the National Science Foundation under Grants CTS-9818234 and 0204827, and Eastman Kodak Company. Additional funding was provided by the U.S. Department of Energy Office of Inertial Confinement Fusion under Cooperative Agreement No. DE-FC03-92SF19460, the University of Rochester, and the New York State Energy Research and Development Authority. The support of DOE does not constitute an endorsement by DOE of the views expressed in this article.

REFERENCES

1. C. A. Angell, *Science* **267**, 1924 (1995).
2. P. G. Debenedetti and F. H. Stillinger, *Nature* **410**, 259 (2001).
3. G. Zerbi, ed. *Organic Materials for Photonics: Science and Technology*, European Materials Research Society Monographs, v. 6 (North-Holland, Amsterdam, 1993).
4. D. Braun and R. Langendorf, *J. Prakt. Chem.-Chem. Ztg.* **341**, 128 (1999).
5. I. Alig *et al.*, *J. Mater. Chem.* **8**, 847 (1998).
6. D. F. O'Brien *et al.*, *Adv. Mater.* **10**, 1108 (1998).
7. K. Naito and A. Miura, *J. Phys. Chem.* **97**, 6240 (1993).
8. K. Katsuma and Y. Shirota, *Adv. Mater.* **10**, 223 (1998).
9. M. Halim *et al.*, *ibid.*, **11**, 371 (1999).
10. N. Johansson *et al.*, *ibid.*, **10**, 1136 (1998).
11. U. Bach *et al.*, *ibid.*, **12**, 1060 (2000).
12. B. Schartel, T. Damerau, and M. Hennecke, *Phys. Chem. Chem. Phys.* **2**, 4690 (2000).
13. S. Wang *et al.*, *J. Am. Chem. Soc.* **122**, 5695 (2000).
14. P. J. Collings and J. S. Patel, eds. *Handbook of Liquid Crystal Research* (Oxford University Press, New York, 1997).
15. K. Tsuji, M. Sorai, and S. Seki, *Bull. Chem. Soc. Jpn.* **44**, 1452 (1971); M. Sorai and S. Seki, *ibid.*, 2887 (1971).
16. C. B. McArdle, ed. *Side Chain Liquid Crystal Polymers* (Chapman and Hall, New York, 1989).
17. N. A. Platé and S. L. Schnur, eds. *Liquid-Crystal Polymers*, Specialty Polymers (Plenum Press, New York, 1993).
18. A. Ciferri, ed. *Liquid Crystallinity in Polymers* (VCH Publishers, New York, 1991).
19. H. Shi, S. H. Chen, M. E. De Rosa, T. J. Bunning, and W. W. Adams, *Liq. Cryst.* **20**, 277 (1996).
20. W. Wedler *et al.*, *J. Mater. Chem.* **1**, 347 (1991).
21. G. Attard and C. T. Imrie, *Liq. Cryst.* **11**, 785 (1992).
22. H. Dehne *et al.*, *Liq. Cryst.* **6**, 47 (1989).
23. G. S. Attard, C. T. Imrie, and F. E. Karasz, *Chem. Mater.* **4**, 1246 (1992).
24. N. Tamaoki, G. Kruk, and H. Matsuda, *J. Mater. Chem.* **9**, 2381 (1999).
25. F.-H. Kreuzer *et al.*, *Mol. Cryst. Liq. Cryst.* **199**, 345 (1991).
26. F.-H. Kreuzer, R. Maurer, and P. Spes, *Makromol. Chem., Macromol. Symp.* **50**, 215 (1991).
27. K. D. Gresham *et al.*, *J. Polym. Sci. A, Polym. Chem.* **32**, 2039 (1994).
28. K. T. Lorenz *et al.*, *Adv. Mater.* **8**, 414 (1996).
29. S. A. Ponomarenko *et al.*, *Macromolecules* **33**, 5549 (2000).
30. I. M. Saez, J. W. Goodby, and R. M. Richardson, *Chem. Eur. J.* **7**, 2758 (2001).
31. V. Percec *et al.*, *Macromolecules* **25**, 3851 (1992).
32. R. Dreher and G. Meier, *Phys. Rev. A* **8**, 1616 (1973).
33. H. Shi and S. H. Chen, *Liq. Cryst.* **17**, 413 (1994).
34. *ibid.*, **18**, 733 (1995).
35. J. C. Mastrangelo, T. N. Blanton, and S. H. Chen, *Appl. Phys. Lett.* **66**, 2212 (1995).
36. H. Shi and S. H. Chen, *Liq. Cryst.* **19**, 785 (1995).
37. S. H. Chen, J. C. Mastrangelo, H. Shi, A. Bashir-Hashemi, J. Li, and N. Gelber, *Macromolecules* **28**, 7775 (1995).

38. H. Shi and S. H. Chen, *Liq. Cryst.* **19**, 849 (1995).
39. M. E. De Rosa, W. W. Adams, T. J. Bunning, H. Shi, and S. H. Chen, *Macromolecules* **29**, 5650 (1996).
40. S. H. Chen, J. C. Mastrangelo, T. N. Blanton, A. Bashir-Hashemi, and K. L. Marshall, *Liq. Cryst.* **21**, 683 (1996).
41. S. H. Chen, H. Shi, B. M. Conger, J. C. Mastrangelo, and T. Tsutsui, *Adv. Mater.* **8**, 998 (1996).
42. S. H. Chen, J. C. Mastrangelo, H. Shi, T. N. Blanton, and A. Bashir-Hashemi, *Macromolecules* **30**, 93 (1997).
43. S. H. Chen, D. Katsis, A. W. Schmid, J. C. Mastrangelo, T. Tsutsui, and T. N. Blanton, *Nature* **397**, 506 (1999).
44. F. Y. Fan, S. W. Culligan, J. C. Mastrangelo, D. Katsis, S. H. Chen, and T. N. Blanton, *Chem. Mater.* **13**, 4584 (2001).
45. D. Katsis, P. H. M. Chen, J. C. Mastrangelo, S. H. Chen, and T. N. Blanton, *ibid.*, **11**, 1590 (1999).
46. H. P. Chen, D. Katsis, J. C. Mastrangelo, S. H. Chen, S. D. Jacobs, and P. J. Hood, *Adv. Mater.* **12**, 1283 (2000).
47. M. Srinivasarao, *Chem. Rev.* **99**, 1935 (1999).
48. S. H. Chen, J. C. Mastrangelo, and R. J. Jin, *Adv. Mater.* **11**, 1183 (1999).
49. P. Pollmann and B. Wiege, *Mol. Cryst. Liq. Cryst.* **150B**, 375 (1987).
50. H. Kimura, M. Hosino, and H. Nakano, *J. Phys. Colloq.* **40**, 174 (1979).
51. R. B. Meyer, *Appl. Phys. Lett.* **14**, 208 (1969); H. Baessler and M. M. Labes, *Phys. Rev. Lett.* **21**, 1791 (1968).
52. R. A. M. Hikmet and H. Kemperman, *Nature* **392**, 476 (1998).
53. Y. Nishio *et al.*, *Macromolecules* **31**, 2384 (1998).
54. E. Sackmann, *J. Am. Chem. Soc.* **93**, 7088 (1971).
55. H.-K. Lee *et al.*, *J. Phys. Chem. B* **104**, 7023 (2000).
56. A. Yu. Bobrovsky *et al.*, *Adv. Mater.* **12**, 1180 (2000).
57. N. Tamaoki *et al.*, *ibid.*, **12**, 94 (2000); N. Tamaoki, *ibid.* **13**, 1135 (2001).
58. B. L. Feringa, P. M. Huck, and H. A. van Doren, *J. Am. Chem. Soc.* **117**, 9929 (1995).
59. M. Suarez and G. B. Schuster, *ibid.*, 6732 (1995).
60. C. Denekamp and B. L. Feringa, *Adv. Mater.* **10**, 1080 (1999).
61. B. L. Feringa *et al.*, *Chem. Rev.* **100**, 1789 (2000).
62. T. Yamaguchi *et al.*, *Chem. Mater.* **12**, 869 (2000).
63. T. Yamaguchi *et al.*, *J. Mater. Chem.* **11**, 2453 (2001).
64. M. Irie, *Chem. Rev.* **100**, 1685 (2000).
65. T. Kawai, T. Koshido, and K. Yoshino, *Appl. Phys. Lett.* **67**, 795 (1995).
66. T. Kawai *et al.*, *Jpn. J. Appl. Phys.* **38**, L1194 (1999).

High-Resolution Near-Field Raman Microscopy of Single-Walled Carbon Nanotubes

Introduction

Recent rapid advances in nanotechnology and nanoscience are largely due to our newly acquired ability to measure and manipulate individual structures on the nanoscale. Among the new methods are scanning probe techniques, optical tweezers, and high-resolution electron microscopes. A recently demonstrated near-field optical technique allows spectroscopic measurements with 20-nm spatial resolution.¹ This method makes use of the strongly enhanced electric field close to a sharp metal tip under laser illumination and relies on the detection of two-photon excited fluorescence. Fluorescence imaging, however, requires a high fluorescence quantum yield of the system studied or artificial labeling with fluorophores. Furthermore, fluorescence quenching by the metal tip competes with the local field enhancement effect and therefore limits the general applicability. On the other hand, Raman scattering probes the unique vibrational spectrum of the sample and directly reflects its chemical composition and molecular structure. A main drawback of Raman scattering is the extremely low scattering cross section, which is typically 14 orders of magnitude smaller than the cross section of fluorescence. Surface-enhanced Raman scattering (SERS), induced by nanometer-sized metal structures, has been shown to provide enormous enhancement factors of up to 10^{15} , allowing for Raman spectroscopy even on the single-molecule level.^{2,3} Controlling SERS with a sharp metal tip that is raster scanned over a sample surface has been proposed in Refs. 1 and 4, and near-field Raman enhancement has been experimentally demonstrated in Refs. 5–9. Here, we show the chemical specificity of this near-field technique and demonstrate an unprecedented spatial resolution.

Single-walled carbon nanotubes (SWNT's) have been the focus of intense interest due to a large variety of potential nanotechnological applications. The unique properties of SWNT's arise from their particular one-dimensional structure, which is directly linked to the characteristic Raman bands. Raman scattering on SWNT's has been studied intensively in the literature (see, e.g., Refs. 10–13), and Raman enhancements of up to 10^{12} have been reported for tubes in contact with fractal silver colloidal clusters.¹⁴ In this article, near-field

Raman imaging of SWNT's is demonstrated using a sharp silver tip as a probe. We show, for the first time, that single isolated SWNT's can be detected optically with a spatial resolution of better than 30 nm. This high-resolution capability is applied to resolve local variations in the Raman spectrum along a single SWNT that would be hidden in far-field measurements. The near-field origin of the Raman enhancement is proven by tip-to-sample-distance measurements.

Experimental

Our experimental setup is based on an inverted optical microscope with an x,y scan stage for raster scanning a transparent sample with SWNT's. A laser beam ($\lambda = 633$ nm, 30 to 100 μW) is reflected by a dichroic beam splitter and focused by a high numerical aperture objective (1.4 N.A.) on the sample surface. A sharp silver tip is positioned near the focus of the beam and maintained above the sample surface at a distance ≈ 1 nm by means of a sensitive shear-force feedback mechanism.¹⁵ Raman-scattered light is collected with the same objective, transmitted by the beam splitter, and filtered by a long pass filter. The signal is detected either by a combination of a spectrograph and a thermoelectrically cooled charge-coupled device (CCD) or by a narrow bandpass filter (FWHM = 10 nm) centered at 760 nm (or 700 nm), followed by a single-photon counting avalanche photodiode. A near-field Raman image is established by raster scanning the sample and continuously recording the scattered Raman signal. Sharp silver tips with a radius of 10 to 15 nm are produced by electrochemical etching followed by focused-ion-beam (FIB) milling with a dual-beam FIB system (FEI Strata-235) and applying a similar procedure as used for STM/AFM tip sharpening.¹⁶

To establish a strong field enhancement at the tip, the electric field of the exciting laser beam needs to be polarized along the tip axis.¹⁷ To achieve this condition in our on-axis illumination scheme, we displace the tip from the center of the beam in the direction of polarization into one of the two longitudinal field lobes characteristic of strongly focused Gaussian beams.¹⁸ The strength of this longitudinal field increases with increasing N.A. of the focusing lens and, in our

configuration, is only five times weaker than the transverse field strength at the center of the focus.

Results and Discussion

Two different types of SWNT samples were studied. The first sample consists of nearly monodisperse SWNT's grown by chemical vapor deposition (CVD) on SiO₂ substrates. The substrates were first cleaned by solvent washing, then heated to 700°C in a tube furnace for 30 min while being exposed to air. Next, 50 μL of Ferritin solution [Sigma-Aldrich; diluted in deionized (DI) water, 1:10 ratio (Ferritin: H₂O)] was applied to the clean substrate, which was left for 30 s, then rinsed with DI water and placed in the tube furnace using growth parameters similar to commonly known SWNT growth methods.¹⁹ The material for the second sample was purchased from Bucky USA and consists of purified SWNT's with a diameter distribution from 1.0 to 1.8 nm, produced by arc discharge using Ni/Y catalyst particles. The material was dispersed in dichloroethane, sonicated for 1 h, and spin-cast onto a microscope cover glass. AFM measurements were performed to determine sample coverage and to distinguish spatially isolated tubes from nanotube bundles.

The far-field Raman spectra of the SWNT samples (not shown) are dominated by the sharp tangential stretching mode at 1596 cm⁻¹ (*G* band) and a broader band around 2615 cm⁻¹ (*G'* band), which arises from an overtone of the disorder-induced mode around 1310 cm⁻¹.²⁰ Figure 93.55 shows confocal far-field Raman images of SWNT bundles produced by

arc discharge that were recorded by integrating the signal intensity of the *G'* band [760-nm bandpass filter (see above)] for vertical (a) and horizontal (b) polarization of the incident laser beam. Similar Raman images are obtained by detecting the intensity of the *G* band using the 700-nm bandpass filter. The Raman images clearly demonstrate that tubes oriented completely perpendicular to the respective light polarization do not produce any signal (see arrows in Fig. 93.55). This polarization contrast is a consequence of the polarization properties of the *G* and *G'* Raman bands reported for *G* in the literature.^{11,12,21} AFM measurements of the same area reveal that the diameter of the nanotube bundles varies between 5 and 15 nm, which corresponds to 10 to 100 individual nanotubes per bundle.

Confocal Raman imaging of SWNT's grown by CVD was not possible within feasible acquisition times because the sample consists mostly of separated individual SWNT's for which the Raman scattering strength is much weaker. However, as shown in Fig. 93.56(a) for CVD-grown SWNT's, the contrast and resolution of Raman images can be greatly increased by positioning a sharp silver tip near the laser focus. The simultaneously recorded topographic image is presented in Fig. 93.56(b). The lower portions [Figs. 93.56(c) and 93.56(d)] show cross sections taken along the dashed white lines. Besides SWNT's, the topographic image shows a large number of small circular features with a height ≈ 2 nm, which are due to condensating water and can be removed by sample heating to 70°C. Comparison of the widths (FWHM) of SWNT's in the topographic and Raman images indicates that the resolution of the Raman image is better than the resolution of the topographic image (25 nm versus 30 nm). This high spatial resolution is unprecedented and clearly indicates the near-field origin of the Raman signal. The width of the optical features and the topographical features results from the convolution of the tip shape with the object studied and is therefore limited by the finite size of the tip apex. Both images are closely correlated and the SWNT's are clearly identified. The small topographic features formed by condensation do not show up, however, in the Raman image, which proves the chemical specificity of the method. The diameter of SWNT's grown by CVD can be controlled by growth parameters. The sample used in Fig. 93.56 consists mostly of SWNT's with a diameter ≈ 1.4 nm, which is verified by the topographic data in Figs. 93.56(b) and 93.56(d) and also by independent AFM measurements in the absence of water condensation. Thus, we observe near-field Raman scattering from spatially separated single SWNT's. It is important to notice that vertically *and* horizontally oriented SWNT's are observed in the Raman

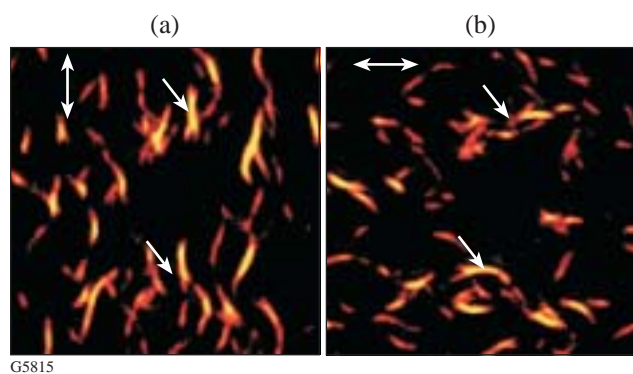
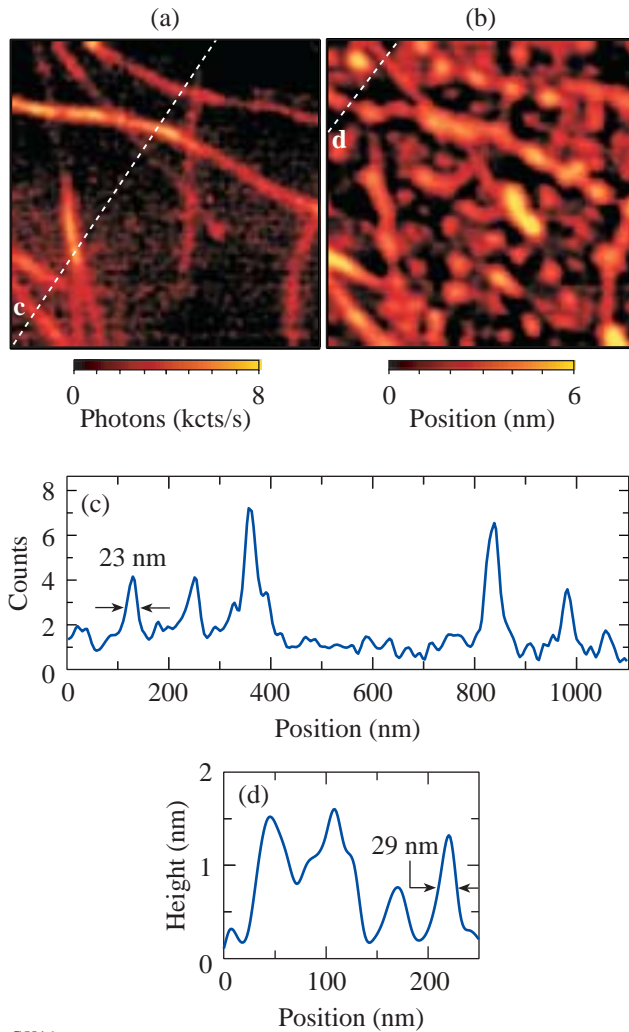


Figure 93.55 Confocal Raman images of SWNT bundles produced by arc discharge on glass acquired by detecting the intensity of the *G'* band ($\nu = 2615 \text{ cm}^{-1}$) while raster-scanning the sample (without metal tip, scan area $15 \times 15 \mu\text{m}$) for vertical (a) and horizontal polarization (b) of the laser excitation at 633 nm. The arrows indicate tubes that are oriented completely perpendicular to one polarization direction, demonstrating the polarization contrast.

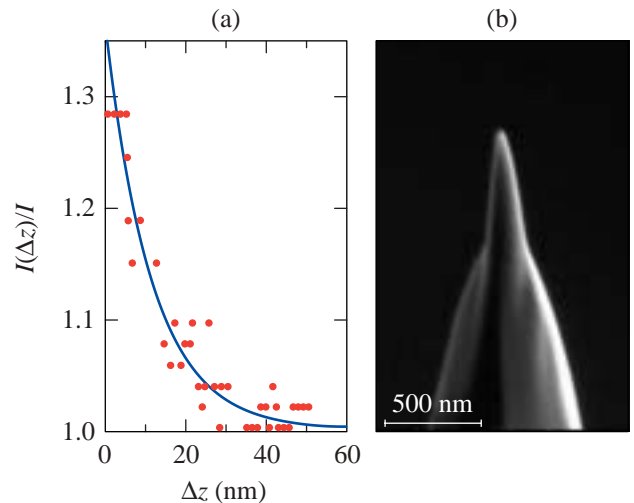
image with similar signal intensity, even though the incident laser light is oriented vertically. This observation is in strong contrast to the polarization contrast observed in the far-field measurements shown in Fig. 93.55. Accordingly, the polarization of the enhanced field has to be radially symmetric with respect to the tip axis. This finding is in agreement with theoretical calculations¹⁷ and confirms the unique properties of the near field.



G5816

Figure 93.56 Simultaneous near-field Raman image (a) and topographic image (b) of SWNT's grown by CVD on glass (scan area $1 \times 1 \mu\text{m}$). The Raman image is acquired by detecting the intensity of the G' band upon laser excitation at 633 nm. No Raman scattering signal is detected from humidity-related circular features present in the topographic image (see text). (c) Cross section taken along the indicated dashed line in the Raman image. (d) Cross section taken along the indicated dashed line in the topographic image. The height of individual tubes is ≈ 1.4 nm. Vertical units are photon counts per second for (c) and nanometer for (d).

The optical resolution apparent in Fig. 93.56 shows that the enhanced field is laterally confined to the size of the metal tip. To demonstrate the confinement of the enhanced fields in the longitudinal direction, the tip is positioned above a SWNT and the Raman scattering strength is recorded as a function of tip-to-sample distance Δz . The result, shown in Fig. 93.57, has been fitted with an exponential curve and normalized with the Raman scattering strength in the absence of the tip, i.e., with the far-field Raman signal. For distances $\Delta z < 30$ nm, the increase of the signal clearly indicates a distance-dependent near-field contribution with a decay length of 11 nm. This longitudinal confinement is in agreement with the lateral confinement observed in the near-field Raman images and consistent with the tip radius of 10 to 15 nm as determined by a scanning electron microscopy [cf. Fig. 93.57(b)]. All of the tips used in our experiments were fabricated by the same procedure and rendered similar SEM images; however, only about 30% to 40% of the tips produced a measurable signal enhancement. The reason for this behavior is the subject of ongoing studies. The highest Raman enhancement factors observed so far were estimated to be around 10^3 . These numbers follow from the detected ratio of near-field to far-field signals and from a comparison of the different volumes probed by the near field and the far field.



G5817

Figure 93.57 (a) Dependence of the Raman-scattering strength of the G' band (I) on the longitudinal separation (Δz) between a single SWNT and the tip. The solid line is an exponential fit with a decay length of 11 nm. The signal is normalized with the far-field signal. (b) Scanning electron micrograph of a sharp silver tip fabricated by focused-ion-beam milling.

To demonstrate the high-resolution spectroscopic capabilities of the near-field technique presented here, we investigate the Raman spectrum along a SWNT with a diameter of 1.7 nm grown by arc discharge. Figure 93.58(a) shows the topography near the end of a SWNT produced by this technique. Three bumps with a height ≈ 5 nm can be recognized on top of the SWNT. Because of their size, these bumps are presumably Ni/Y-catalyst particles, indicating the initial point of growth.²² The labels 1 to 4 in Fig. 93.58(a) mark the positions at which Raman spectra were taken in the presence of the metal tip. At the very beginning of the SWNT (positions 1 and 2) the G band at 1596 cm^{-1} (FWHM = 17 cm^{-1}) dominates the spectra and is significantly stronger than the G' band at 2619 cm^{-1} (FWHM = 35 cm^{-1}) with an amplitude ratio $G/G' \approx 1.3$ [see Fig. 93.58(b)]. Moving along the SWNT to position 3 and farther to position 4 (separated by 35 nm and 85 nm, respectively), however, the amplitude of the G band decreases with respect to the G' band and the ratio G/G' reduces to ~ 0.7 . Simultaneously, the shape of the G' band changes and its center frequency is shifted to 2610 cm^{-1} , whereas the G band re-

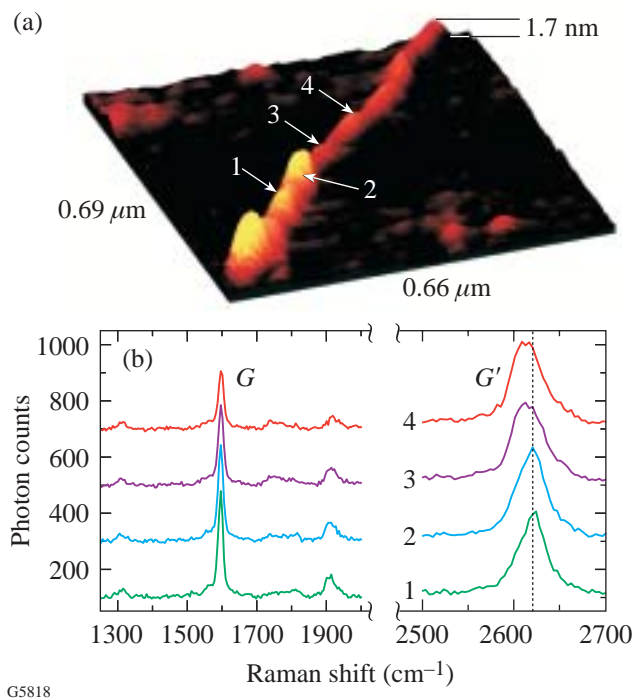


Figure 93.58

(a) Three-dimensional topographic image of a SWNT on glass grown by arc discharge. The three bumps are presumably enclosed Ni/Y catalyst particles and indicate the initial point of growth. (b) Near-field Raman spectra detected at the marked positions 1 to 4 in (a). The distance between positions 2 and 3 is 35 nm. The spectra are offset for clarity.

mains at 1596 cm^{-1} . For 1 and 2, the G' band has a Lorentzian shape, while for 3 and 4, two Lorentzian peaks are needed to model its shape. Raman spectra recorded beyond point 4 in Fig. 93.58(a) remain unchanged.

Variations in the Raman spectrum reflect changes in the molecular structure that can have several origins such as external stress, due to the catalyst particles, or local defects in the tube structure. The observed spectral variations between 2 and 3 can also be explained by a change of the tube structure, described by $(n,m) \rightarrow (n',m')$, which modifies the electronic-state energies of the tube and therefore the resonance enhancement of the Raman bands at a fixed excitation energy. A decrease of the resonance enhancement between positions 2 and 3 would lead to a lower G -band amplitude and could cause a splitting of the G' band into a double peak.²⁰

Recent experiments have shown that huge surface enhancement of Raman signals can be accompanied by fluctuating white-light emission.^{3,23} According to Ref. 23, huge SERS enhancement and strong white-light emission require chemisorption of the Raman scatterer to the metal surface. Since we maintain a well-defined separation (≈ 1 nm) between tip and sample in our experiments, we do not expect a significant white-light contribution. Moreover, white-light emission is observed for Raman enhancement factors more than ten orders of magnitude stronger than the enhancements determined in our experiments. Indeed, our near-field Raman spectra show no indication for a significant broadband background [see Fig. 93.58(b)]. To exclude any contributions to the image contrast arising from background signals, we recorded for each image pixel the full spectrum and integrated the intensity of the G' band and the G band while subtracting the background. The resulting images were virtually identical to those shown in Fig. 93.56(a). We also note that by comparing the near-field and far-field Raman spectra of SWNT's, we find, within the noise limit, no indication for the gradient-field Raman effect discussed in Ref. 24.

Conclusion

We have demonstrated a method for nanoscale Raman spectroscopy with sub-30-nm spatial resolution. This method extends our abilities to characterize weakly fluorescent structures on the nanoscale. Near-field Raman spectroscopy combined with simultaneous AFM measurements appears to be extremely useful for investigations of carbon nanotubes. This method holds promise for the experimental investigation of special structural nanotube features, such as kinks, intertube junctions, or even tubes loaded with C_{60} molecules.

ACKNOWLEDGMENT

The authors wish to thank M. Beversluis and A. Bouhelier for stimulating discussions. Assistance on the CVD of SWNT's by Dr. T. Rueckes and Dr. B. Segal of Nantero (Woburn, MA) is gratefully acknowledged. This research was supported by NSF through grant BES-0086368.

REFERENCES

1. E. J. Sánchez, L. Novotny, and X. S. Xie, *Phys. Rev. Lett.* **82**, 4014 (1999).
2. K. Kneipp *et al.*, *Phys. Rev. Lett.* **78**, 1667 (1997).
3. S. Nie and S. R. Emory, *Science* **275**, 1102 (1997).
4. J. Wessel, *J. Opt. Soc. Am. B* **2**, 1538 (1985).
5. C. L. Jahncke, H. D. Hallen, and M. A. Paesler, *J. Raman Spectrosc.* **27**, 579 (1996).
6. R. M. Stöckle *et al.*, *Chem. Phys. Lett.* **318**, 131 (2000).
7. N. Hayazawa *et al.*, *Chem. Phys. Lett.* **335**, 369 (2001).
8. L. T. Nieman, G. M. Krampert, and R. E. Martinez, *Rev. Sci. Instrum.* **72**, 1691 (2001).
9. N. Hayazawa *et al.*, *J. Chem. Phys.* **117**, 1296 (2002).
10. A. Jorio *et al.*, *Phys. Rev. Lett.* **86**, 1118 (2001).
11. Z. Yu and L. Brus, *J. Phys. Chem. B* **105**, 1123 (2001).
12. G. S. Duesberg *et al.*, *Phys. Rev. Lett.* **85**, 5436 (2000).
13. J. Maultzsch, S. Reich, and C. Thomsen, *Phys. Rev. B* **65**, 233402 (2002).
14. K. Kneipp *et al.*, *Phys. Rev. Lett.* **84**, 3470 (2000).
15. K. Karrai and R. D. Grober, *Appl. Phys. Lett.* **66**, 1842 (1995).
16. M. J. Vasile, C. Biddick, and H. Huggins, *Appl. Phys. Lett.* **64**, 575 (1994).
17. L. Novotny, E. J. Sánchez, and X. S. Xie, *Ultramicroscopy* **71**, 21 (1998).
18. B. Sick, B. Hecht, and L. Novotny, *Phys. Rev. Lett.* **85**, 4482 (2000).
19. J. H. Hafner, C. L. Cheung, and C. M. Leiber, *J. Am. Chem. Soc.* **121**, 9750 (1999).
20. A. G. Souza Filho *et al.*, *Phys. Rev. B* **65**, 085417 (2002).
21. A. Jorio *et al.*, *Phys. Rev. Lett.* **85**, 2617 (2000).
22. C. Journet *et al.*, *Nature* **388**, 756 (1997).
23. A. M. Michaels, M. Nirmal, and L. E. Brus, *J. Am. Chem. Soc.* **121**, 9932 (1999).
24. E. J. Ayars, H. D. Hallen, and C. L. Jahncke, *Phys. Rev. Lett.* **85**, 4180 (2000).

Optimization of Deposition Uniformity for Large-Aperture NIF Substrates in a Planetary Rotation System

Introduction

Large substrates for precision optical applications require the accurate, uniform deposition of multilayer thin-film coatings. Typically, this results in the use of electron-beam evaporation in a “box-coater” configuration, utilizing either simple or planetary rotation of the substrates. Simple rotation of the substrate minimizes the size of the necessary coating chamber but generally results in films with nonuniformity of 2% or greater,¹ an unacceptable level for the precise requirements of the National Ignition Facility (NIF). Typical planetary rotation systems, containing four to five individual substrate holders, or planets, tend to produce relatively uniform coatings but would necessarily be quite large in order to process optics of a significant size. To process large optics for the NIF, a counter-rotating planetary geometry was developed and implemented in a 72-in. electron-beam deposition system.² Although this rotation system utilizes planetary motion to reduce the effect of deposition fluctuations, the large optic sizes relative to the overall chamber size and geometry result in coatings with a significant degree of nonuniformity if regions of the vapor plume are not masked.

To achieve the goal of producing optical coatings with nonuniformities of approximately 0.5% (peak-to-valley) over apertures of 0.85 m, a careful model needs to be constructed to account for deposition sources, planetary configuration, planetary gearing, and uniformity masking. The model assumes that the chamber and source conditions are quite stable throughout the length of the deposition, requiring a highly deterministic process. The process uses metallic hafnia for high-index layers and granular silica for low-index layers to produce coatings with exceptional resistance to high-peak-power laser irradiation.^{3,4} The use of hafnium metal as an evaporant is ideal due to the smooth melt surface, the low occurrence of nodular defects in the growing film, and the stable chemical composition of the melt throughout the length of the deposition. Silica deposition tends to pose some difficulties, but its use is necessitated by the lack of a suitable substitute for precision laser coatings; electron-beam sweep parameters,

deposition rate, and oxygen backfill pressure were optimized to minimize process variability.

Background

The uniform deposition of a thin film applied over a surface from a point or surface source can essentially be characterized as an illumination problem, with the appropriate type of source characterization. The theoretical equations governing the amount of material deposited on a given area have been well established;^{5–9} therefore the results specific to a given chamber configuration simply become a summation of incremental thickness contributions as the planet position is indexed through the chamber. Since the system under study uses electron-beam sources, the source may be considered to be of the directed surface source type, with

$$t = \left(\frac{m}{\pi\mu} \right) \left(\frac{\cos\phi \cos\theta}{r^2} \right), \quad (1)$$

where t is the thickness of the film deposited, m is the total mass of the material emitted from the source, μ is the density of the film being deposited, ϕ is the angle normal to the surface of the source, θ is the angle normal to the substrate surface, and r is the distance from the source to the point on the substrate under evaluation (see Fig. 94.1). However, since the primary concern is uniformity of the deposited film, once the summation is performed for all of the incremental planar positions, the relative thicknesses will be normalized over the surface of the substrates being coated. When the thicknesses are normalized, the constants in Eq. (1) will cancel, resulting in the simplified expression

$$t = \frac{\cos\phi \cos\theta}{r^2}. \quad (2)$$

The geometry may be further simplified to reflect that the source surface is parallel to that of the surface being coated; such a condition would not be appropriate for a tilted-planet

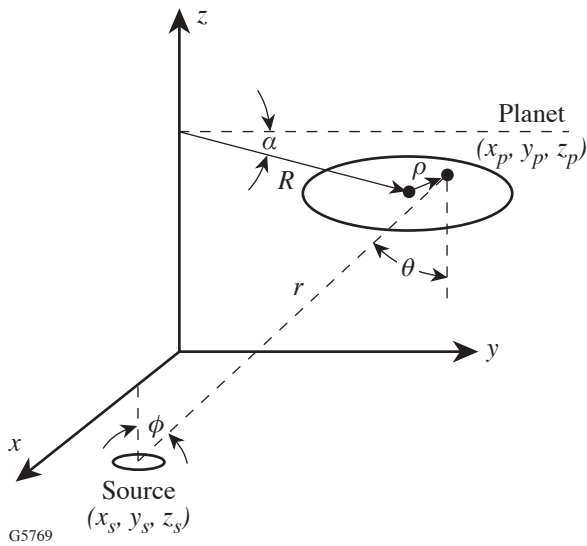


Figure 94.1
Basic planetary configuration as substrate undergoes rotations/revolution.

rotation but is applicable for a standard planetary with all surfaces being coated rotating in a plane. In this case,

$$t = \frac{\cos^2 \theta}{r^2}. \quad (3)$$

This expression is appropriate for an ideal directed-surface source, but measurements of film uniformity indicate factors such as the form of the material being evaporated, the electron-beam sweep parameters, and the proximity of the source to the walls of the coating chamber possibly affecting the accuracy of this formula. In practice, the formula may be modified to⁹

$$t = \frac{\cos^n \theta}{r^2}, \quad (4)$$

where n is now a variable allowing the theoretical thickness distribution to be fit to that of the measured distribution. Converting this to coordinate geometry,

$$r = \sqrt{(x_p - x_s)^2 + (y_p - y_s)^2 + (z_p - z_s)^2} \quad (5)$$

and

$$\cos \theta = \frac{z_p - z_s}{\sqrt{(x_p - x_s)^2 + (y_p - y_s)^2 + (z_p - z_s)^2}}, \quad (6)$$

where the subscript “ p ” denotes the point on the planet and “ s ” denotes the source. Substitution and simplification then yield

$$t = \left\{ \frac{(z_p - z_s)^n}{\left[(x_p - x_s)^2 + (y_p - y_s)^2 + (z_p - z_s)^2 \right]^{\frac{n+2}{2}}} \right\}. \quad (7)$$

The coordinates of the source(s), as well as the height of the substrates, will be measured quantities to be inserted into the deposition model. The x and y coordinates of a given point being tracked in the planetary must be calculated, based on Fig. 94.1. Given the relation as shown, the primary factor in determining the motion of a point on the planet will be the relative angular rotation of the planet to that of the revolution of the system, which is simply a function of the relative gear sizes for the solar and planet gears. This will be explored in greater detail later, but the motion of a point on the planet undergoing planetary rotation will trace out the path described by

$$x(\alpha) = R \cos \alpha + \rho \cos \left(\frac{\alpha N_s}{N_p} \right) \quad (8)$$

and

$$y(\alpha) = R \sin \alpha + \rho \sin \left(\frac{\alpha N_s}{N_p} \right), \quad (9)$$

where R is the radius of the planet orbit, ρ is the radial position of the point on the planet, α is the angular position of the planet in its orbit, and N_s and N_p are the number of teeth on the solar and planet gears, respectively. Since the planets are rotating in-plane, z_p will remain constant and the thickness contribution at any point in the planetary motion can now be calculated as a function of only α . A summation of the individual contributions throughout a number of revolutions, where α is incremented from 0 to 2π , and for a range of ρ from the center to the edge of the planet, will provide an overall uniformity distribution over the surface of the planet.

Coating efficiency is also of interest when configuring the planetary rotation system since configurations can be conceived that provide nearly ideal uniformity, but due to signifi-

cant offsets of the source from the center of rotation or excessive distances between the substrate and the source, the percentage of vaporized material condensing on the substrates is negligible. Therefore, since the desired result is to achieve a high degree of film uniformity while maximizing source material utilization, it is necessary to calculate the percentage of evaporated material being deposited on the substrate.

The motion of a typical planetary rotation describes an annulus in the plane of rotation since the planets orbit at a constant radius without crossing the center of the chamber. Since the planets in the counter-rotating configuration cross the center of the chamber, a disk replaces the annulus and the efficiency becomes the percentage of deposited material within this disk. The efficiency with which evaporated source material is used is equal to the integral of Eq. (4) over the area defined by the disk, divided by the integral of Eq. (4) over the hemisphere above the source, i.e., the range of θ from 0 to $\pi/2$. The integration over a hemisphere is straightforward, resulting in a normalization value of π .

$$\text{Efficiency} = \frac{1}{\pi} \int_{\text{over disc}} \int \frac{\cos^{n+1} \theta}{r^2} d\gamma d\theta. \quad (10)$$

The integration of an off-axis source, as shown in Fig. 94.2, is transformed to that of an on-axis source in order to easily and

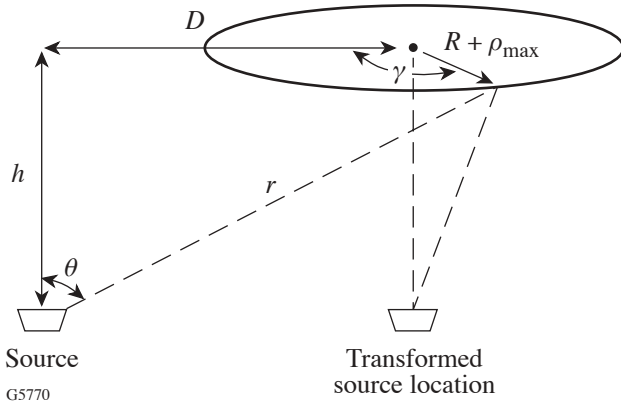


Figure 94.2
Deposition efficiency is calculated by transforming the source location to a position on-axis with the rotation and integrating over the maximum area described by the planetary motion, a disk with radius $R + \rho_{\max}$.

accurately express the limits of integration. Performing the transformation, the efficiency of the source is found to be

$$\text{Efficiency} = \frac{1}{\pi} \int_0^{2\pi} \int_0^{R+\rho_{\max}} \frac{h^{n+1} r' dr' d\gamma}{[r'^2 + 2r'D \cos \gamma + h^2 + D^2]^{\frac{n+3}{2}}}, \quad (11)$$

where n is the exponent of the cosine as in Eq. (4), ρ_{\max} is the maximum radial extent of the planet, and all other variables are as shown in Fig. 94.2. The efficiency can then be calculated for a range of source offsets for a given planetary geometry. The results of these efficiency calculations are shown for the counter-rotating geometry in Fig. 94.3.

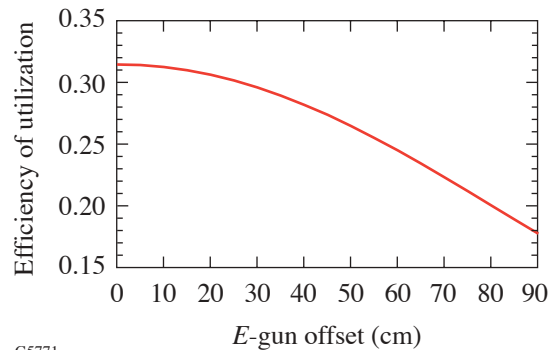


Figure 94.3
Efficiency of material utilization as a function of the offset of the source from the center of the coating chamber. An offset of 0 is for source location $(0, 0, z_s)$ in Fig. 94.1, with increasing offsets representing the movement of the source along the x axis. While there is a significant reduction in the efficiency of the material being evaporated, the reduction in the size of secondary masking may offset this loss.

The efficiency of material utilization may be somewhat misleading since this considers only whether the material is available for use, not where the material would condense on the substrate and its impact on the film uniformity. To make an informed analysis of the actual material utilization, one must take into account any masking required to achieve a uniform deposition.

Measurement of Film Uniformity

Many different coating designs are required for the NIF, but all use the same evaporant materials with layer deposition times greater than 4 min, with a planetary revolution period of approximately 6 s. Therefore, the uniformity of the deposition process will be qualified for NIF specifications, assuming the deposition of similar layers will not deviate substantially from the measured uniformity.

To improve film uniformity, it is first necessary to accurately measure the achieved uniformity. A large-aperture scanning laser photometer installed at LLE is capable of mapping transmission and reflection performance of a NIF-sized (525×807 -mm) optic (Fig. 94.4). Since this instrument measures photometric performance at a single wavelength, it is necessary to develop a correlation between transmission of the coating and film uniformity. Furthermore, to increase the accuracy of the measurement, the transmitted light should be highly sensitive to thickness nonuniformities, with a maximum range of transmitted light.



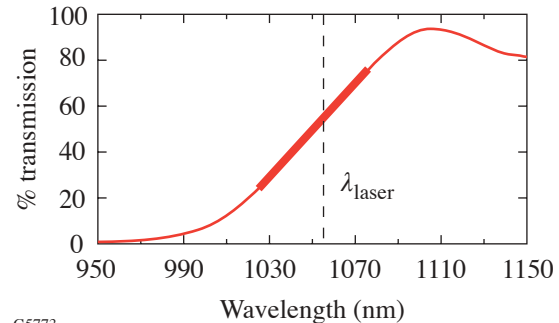
G5772

Figure 94.4

Scanning laser photometer at LLE. This system is capable of simultaneously measuring % T and % R over a 525×807 -mm aperture, from 8° to 60° , at wavelengths of 1053, 527, and 351 nm. Results are presented as a 2-D intensity map of the surface, digitized to pixels of 1 to 5 mm.

A modified quarter-wave reflector was designed such that the edge of the reflectance band is approximately linear with respect to wavelength (Fig. 94.5). Since the photometer operates at 1053 nm, a slope of 1% T per nanometer correlates to a relationship of 1% T per 0.1% thickness nonuniformity. When a large coated substrate is then mapped on the photometer, changes in transmittance will indicate the shifting of the spectral performance of the coating to the left or right in

Fig. 94.5, for higher or lower values of % T respectively. If the slope of the reflectance band is verified on a spectrophotometer, the precise correlation of transmittance to thickness change can then be established for a given coating deposition since the percent wavelength shift of the coating performance will be equal to the percent change in coating thickness. This is typically adequate for initial uniformity efforts, although further reduction of nonuniformity may require coatings that have a more steeply sloped transmission profile and therefore are more sensitive to slight film nonuniformities.



G5773

Figure 94.5

Modified quarter-wave reflector with linear transmission with respect to wavelength over the range $\lambda_0 \pm 2\%$. Provided the coating is deposited properly and all nonuniformities are less than 4% peak-to-valley, the resulting photometer transmittance map will directly correlate to film-thickness uniformity.

Planetary Gearing

The essence of a planetary rotation system in a vacuum coating chamber is that the substrate holder, or planet, will undergo planetary motion by rotating about its center axis while revolving about the center axis of the coating chamber. The planet will continue to move through the vapor plume of the evaporation source in this manner, allowing the deposited film thickness to become more uniform by averaging the different regions of the plume incident on each portion of the planet. The most basic system is a two-gear system, as depicted in Fig. 94.1. The center “solar gear” remains stationary, and the outer “planet gear” rotates while revolving about the center of the system.

Many thin-film-uniformity calculations assume that a sufficient number of revolutions take place during a layer deposition that the calculations of thickness uniformity can be reduced to an integration over the planet radius,⁷ with the corresponding assumption that the film is “perfectly uniform” for constant planet radius. This would mean that all film nonuniformity would be only in the radial direction in a polar coordinate

system. In reality, the relative sizes of planetary and solar gears are critical to achieving high degrees of thickness uniformity. If the solar gear has a number of teeth equal to “ N_s ” and the planet gear has a number of teeth equal to “ N_p ,” then the gear ratio is given by

$$\text{Gear ratio} = \frac{N_s}{N_p}. \quad (12)$$

This gear ratio determines the number of rotations the planet will make for each revolution of the planetary fixture, causing each point on the planet to trace out a cycloid during each revolution based on Eqs. (8) and (9). Beginning with the simplest case of a gear ratio equal to 1, it is apparent that successive revolutions of the planetary will trace identical circles since each revolution of the planet also corresponds to a single rotation; this eliminates the benefit of planetary motion since a given point will travel an identical path through the vapor plume, failing to average differing plume conditions [Fig. 94.6(a)]. Typically, the gear ratio is not equal to 1, but instead, due to planetary geometry, $N_s > N_p$. If the gear ratio is an integer greater than 1, identical cycloids will be traced out for each successive revolution, severely limiting the degree of random motion [Figs. 94.6(b)–94.6(f)]. It has been known for some time that the gear ratio must be non-integral,⁵ such that the cycloid traced out is no longer a closed figure and therefore will not be repeated with each successive revolution.

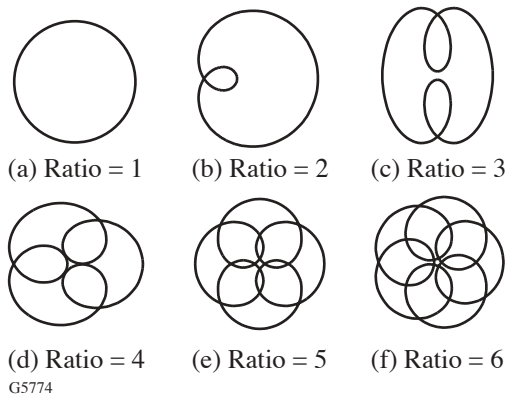


Figure 94.6

Cycloids traced out by an off-center point in a planetary rotation after one revolution with different integral gear ratios. Note that all figures are closed, requiring that the point will trace out an identical path for all successive revolutions.

The limitations on this next level of randomization can also be expanded by examining how quickly a given cycloid will be repeated. If the gear ratio is non-integral, this indicates that

the planet will not reach its starting angular orientation at the conclusion of one revolution of the planetary. Therefore, the cycloid traced out by the previous revolution cannot be repeated in the next revolution since the revolution did not trace out a closed figure. Each successive revolution will provide an opportunity for the planet orientation to achieve its starting position and therefore repeat its path through the vapor plume. The path will not repeat until

$$m \left(\frac{N_s}{N_p} \right) = \text{an integer} \quad m = 1, 2, 3, \dots, \quad (13)$$

where m is the number of revolutions of the planetary, since this represents an integral number of rotations of the planet and therefore closes the figure traced by the cycloid. Since N_s and N_p are both integers, the maximum possible number of revolutions before the system repeats is $m = N_p$. In the event that N_p and N_s have common factors, the ratio simplifies and repetition of the path through the vapor plume will occur at

$$m = \frac{N_p}{g}, \quad (14)$$

where g is the greatest common factor of N_p and N_s .

The previous condition requiring no common factors is sufficient to establish unique paths through the vapor plume, but again it is insufficient to minimize film nonuniformities in practice. Since the maximum number of paths is equal to N_p , every path will be used exactly once only for those layers of the appropriate thickness such that the deposition time is equal to N_p multiplied by the period of revolution of the planetary, or an integer multiple thereof. In practice, this condition is rarely if ever met due to variations in deposition rate, design layer thickness, and material being deposited. In this event, paths that are similar to one another are sufficient to cause greater degrees of nonuniformity, and the fewer the number of revolutions of the planetary, the greater the observed impact on uniformity. If the angular orientation of the planet is tracked and plotted at a fixed point in the revolution, such as the center of the door of the chamber, it can be shown how the paths relate to one another. As shown in Fig. 94.7 for the given values of $N_s = 237$ and $N_p = 71$, the planet starts with the arrow denoting its orientation at 0° . After one revolution, the planet has undergone 3 full rotations plus an additional partial rotation, resulting in a change in orientation of 121.69° . After the second revolution, the planet will again have undergone 3 complete rotations plus an additional 121.69° , resulting in an orientation

of 243.38°. The third revolution will nearly return the planet to its starting orientation, differing only by 5.1°. This will repeat for successive revolutions such that, for the given configuration, every 3 revolutions the planet will return to almost the same orientation. The graphs in Fig. 94.8, I(a)–I(c), plot the angular orientation of a planet as a function of the number of

revolutions the planetary has undergone for different gear configurations. Tracking the planet in such a manner, it is possible to see that the planet assumes approximately the same angular orientation every 3 revolutions for configuration (a), every 4 revolutions for configuration (b), and every 13 revolutions for configuration (c). The graphs labeled II(a)–II(c) show the path traced by a point on the planet through 30 revolutions of the planetary rotation. Especially when depositing thin layers, this near-repetition is evident in the symmetry observed in the measured film uniformity. The surface plots in Row III of Fig. 94.8 provide experimental evidence of rotational nonuniformity due to inappropriate gearing, and 3-, 4-, and 13-way symmetries are apparent in the measured film thickness. As higher degrees of symmetry are reached, it becomes much more difficult to resolve these effects and the uniformity is significantly improved.

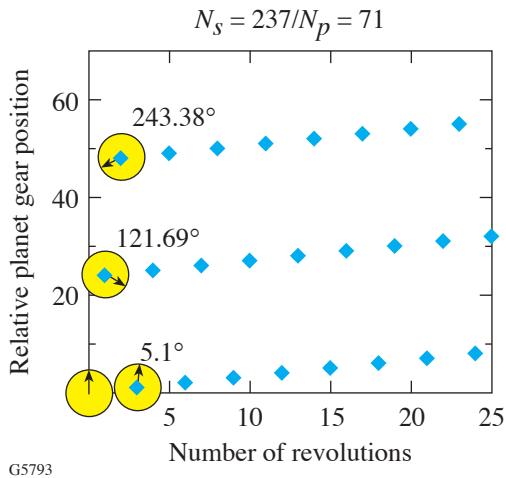


Figure 94.7
Relative planar orientations versus revolutions of the planetary rotation. Every 3 revolutions, the planet assumes almost the same angular orientation, differing only by 5.1°.

Uniformity Masking

Once a stable deposition system has been configured, with optimized planetary gearing, the residual thickness non-uniformities can be removed through the use of masking. Most planetary rotation geometries will result in the center of the planet having a thicker film deposited than the periphery; therefore the mask will be required to obscure a greater percentage of the center each revolution. There are multiple methods of masking the vapor plume, including large masks rotating in the opposite direction as that of the planetary,

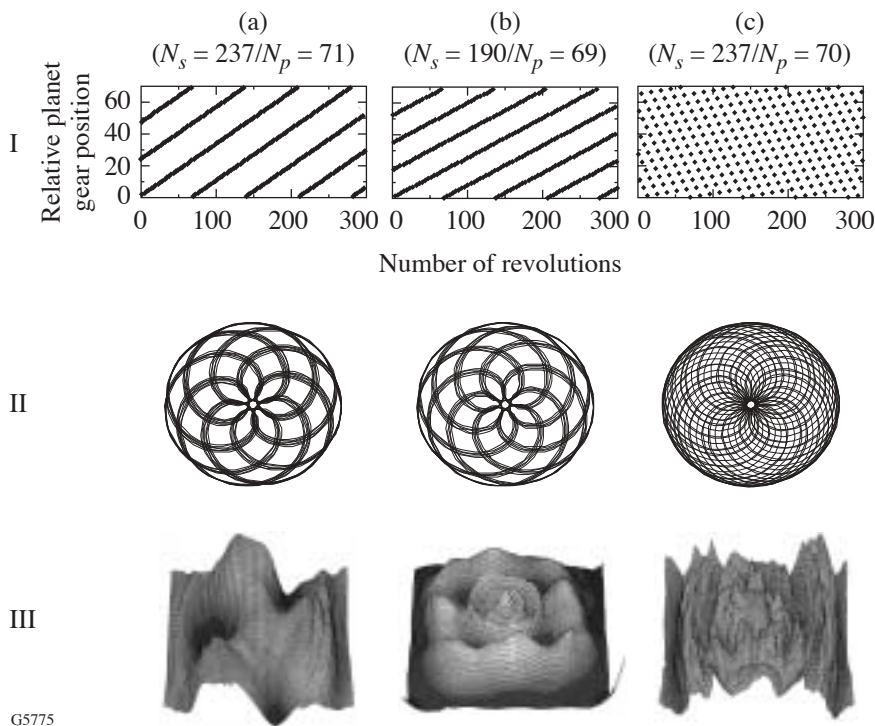


Figure 94.8
Comparison of the effects of different planetary gear ratios. The graphs in Row I track the angular orientation of a planet each time it passes a fixed point in the chamber, such as the center of the door, as a function of the number of revolutions of the planetary. Since a geared system is being analyzed, the possible angles correspond to a specific gear tooth number. Row II depicts the path of an off-center planetary point through 30 revolutions of the planetary. Row III depicts the measured film uniformity pattern on the mapping laser photometer. Gearing configuration (c) provides a greater degree of randomization through the vapor plume, yielding significant improvements in film uniformity.

GS775

individual masks for each planet that are rotated with the planetary, and fixed-position uniformity masks. The fixed-position masking is the lowest-maintenance, highest-mechanical-reliability system so is therefore preferred, provided it is capable of meeting the nonuniformity requirements of the coatings. A critical aspect of this masking system is the proper mounting of the masks in the coating chamber; the masks must be placed precisely in the position defined by the model, using a mounting structure that is stable and repeatable and that takes thermal expansion into account if the effect on mask placement warrants. Small changes in the mask shape can have a significant impact on the film uniformity, and care must be taken to avoid changes due to poor mounting.

A model was created to sum thickness contributions over the aperture of a planet as it undergoes planetary rotation, according to Eqs. (4)–(9) above. The model accounts for the motion of the planet due to the gearing and relies on plume shape fitting by varying n in Eq. (4). Masks are projected onto the plane in which the planet surface moves, providing a binary multiplier to the thickness contribution at that point. Mask shapes are determined by evaluating the film distribution and altering the mask width as needed at the appropriate radii in the planetary.

We have found that the optimal mask shapes for a standard planetary rotation system have a very smooth, continuous shape, providing minimal difficulty in manufacture, installation, or usage; this also results in an absence of high-frequency, high-gradient thickness changes. The primary focus of this work, however, was to improve uniformity over a large-aperture optic for the NIF laser system suspended in a counter-rotating planetary, as shown in Fig. 94.9. The fact that the optic crosses the center of the coating chamber, and may experience masking effects intended for a different radius on the optic, poses significant challenges in creating a suitable mask shape. In spite of this, the basic model is identical to that used for a standard planetary system, although the aperture over which the coating must be uniform is significantly larger.

The source placement and characteristics have a significant impact on the uniformity of the film thickness prior to the use of masking. As shown in Fig. 94.10, changes in the source placement can vary the degree of nonuniformity over a range of 17.6% to 2.4% for source positions of 0 to 90-cm offset from the center of the planetary, respectively, for a 90-cm-aperture optic in the counter-rotating planetary. Exact performance will be highly dependent upon the geometry of the particular planetary rotation. A source offset of 90 cm was the

maximum considered since this would correspond to placing the source in the corner of the 72-in. coating chamber. Some of the standard arguments against placing the source a significant distance off-center in a planetary include the following:

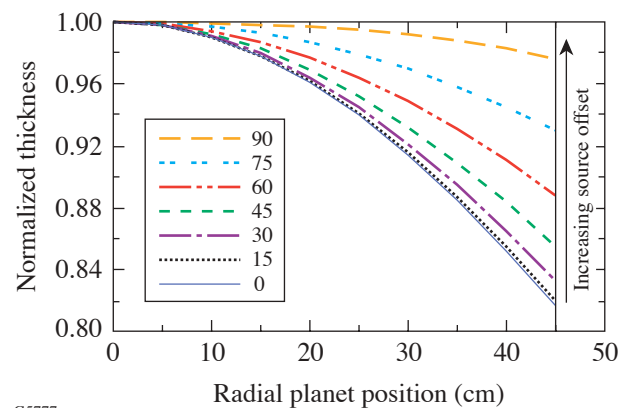
1. The material utilization of the source will be significantly decreased.
2. The chamber walls will influence the vapor plume, causing undesirable effects.
3. The higher angles of the vapor plume, which are more erratic, will be used, resulting in reduced consistency of the uniformity.



G5789

Figure 94.9

Mask configuration implemented in a 72-in. coating chamber for a counter-rotating planetary. Multi-point quartz crystal monitoring is installed in the mask mounts, providing six thickness/rate measurements.



G5777

Figure 94.10

Theoretical uniformity of film deposition over the radius of the planet versus offset of the source position from the center of the coating chamber, for $z_p - z_s = 1200$ mm, $R = 391$ mm, and $n = 1.6$. By minimizing the nonuniformity of the deposited film, the degree of secondary masking may also be minimized.

While the material utilization is decreased, as shown in Fig. 94.3, the decrease in the amount of masking required to produce a uniform deposition results in an equivalent, or even improved, material utilization once the masked configuration is considered. Wall effects are possible, but it was decided to proceed with the configuration change and experimentally determine if this effect is significant. As demonstrated in the uniformity results shown below, as well as by laser-damage testing, the influence of the wall proximity was not an issue. As for the possibility of increased sensitivity, thickness uniformity was modeled for differing plume shapes once a masked configuration was developed for different radial offsets of the source. The model indicates that the uniformity is actually more stable for the source positions that are farther off-axis in the planetary, as shown in Fig. 94.11.

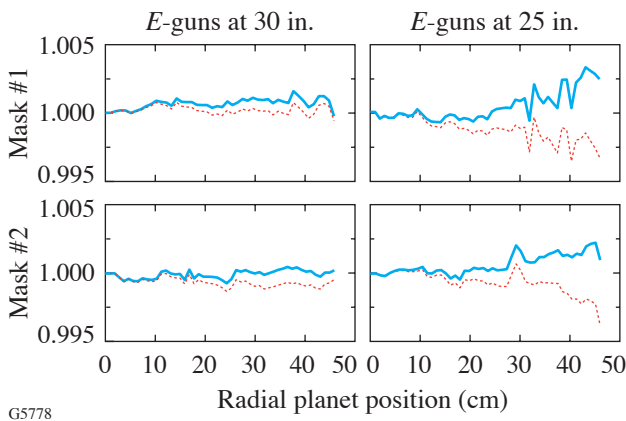


Figure 94.11

Theoretical influence of source offset on the sensitivity of film uniformity to changes in the vapor plume distribution. Source distribution modeled as $\cos^{1.6}\theta$, with n varying ± 0.2 . Two significantly different mask designs are modeled, each with two source offsets, showing that the greater source offset is actually less sensitive to variations in the vapor plume.

Results

Uniformity masks have been produced for a number of different chamber configurations, and the experimental results have been mapped on the scanning laser photometer. First, a value of n in Eq. (4) is assumed in the model, appropriate masking is designed to correct the thickness nonuniformities, and a deposition is performed on a large-aperture substrate. The transmittance is then mapped on the laser photometer, the correlation of transmittance to thickness is determined based on a spectral measurement at one point in the planet, and the resulting nonuniformity is calculated. In order to improve

upon this result, the variable n must now be adjusted to best-fit the model to the experimentally determined nonuniformity. All other quantities, such as the source and substrate locations, mask shapes and locations, and planetary gearing, are physically measured quantities known to a high degree of precision. Once the model accurately predicts the results achieved, the model may be used to redesign the masks to correct the remaining nonuniformities, repeating the process until the degree of nonuniformity is acceptable. Typically, deviations in the best-fit process were found to be less than 0.1% except at the extremes of the substrates, where variations could reach 0.15%. Figure 94.12 illustrates the nonuniformity achieved for a 24-layer coating with layer thicknesses of approximately $\lambda/4$ at 900 nm in a 72-in. counter-rotating planetary. Edge roll-off is evident in the data due to shadowing of the coating tooling along the edges of the substrate. Typical model performance has yielded nonuniformity of less than 1% over the aperture of interest in one to two masking iterations. The primary goal—to achieve good uniformity over a full NIF aperture—was completed in two mask iterations, with a final film nonuniformity of 0.45% peak-to-valley, after removal of roll-off. Correction of tilt in the planet would allow this to be further reduced to 0.30%; while this is a 33% reduction in the nonuniformity, it is relatively insignificant compared to optic specifications, and the necessary modifications cannot be justified.

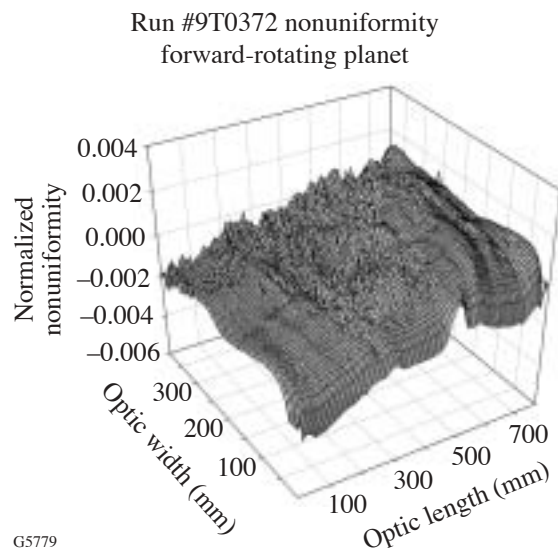
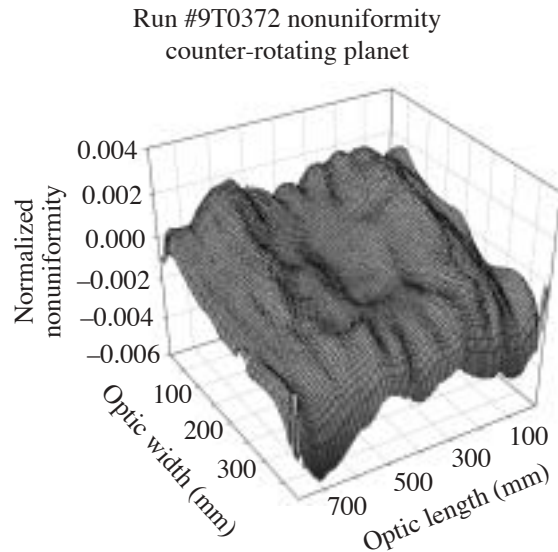
Conclusions

Highly uniform thin films for large-aperture, high-precision optical coatings have been deposited with stationary masking and planetary rotation utilizing the two-gear, counter-rotating configuration. Impacts on nonuniformity due to planetary gearing have been measured, the causes investigated, and appropriate corrections applied to minimize rotational nonuniformities in film thickness. The model developed has been shown to be effective in designing suitable masks to correct thickness nonuniformities. While further improvements are certainly possible through the use of rotating masks, friction-drive planetary rotation, or three-gear configurations, the simplicity and reliability of the current system make its continued use highly desirable. Furthermore, the results achieved significantly exceed the uniformity requirements for NIF laser coatings, despite the complexities of the counter-rotating planetary.

Further improvements to the uniformity masking model are planned in two primary areas: (1) a better description of the vapor plume to more accurately fit the measured results at higher angles and (2) automated optimization of the mask shape. The masking concept can also be further improved by

making the masks asymmetric, to account for differences in the shapes of the vapor plumes of the individual sources. The described configuration has been shown to work well for the

deposition of layers >4-min duration, with a planetary period of approximately 6 s. It is expected that layers with significantly shorter deposition times will require higher planetary speeds or will necessitate the use of additional enhancements to the planetary/masking system, such as the use of rotating masks.



G5779

Figure 94.12

Film nonuniformity in both the counter-rotating and forward-rotating planets for a masked configuration with electron-beam sources at 76-cm offset from chamber center. Roll-off is evident along the length of the coating due to shadowing effects of the coating tooling. Discounting this effect, which may be eliminated by modification of the coating tooling, both uniformity maps exhibit 0.45% nonuniformity peak-to-valley. Furthermore, if the tilt evident in both surface plots is subtracted, since this is a result of the optic rotating out-of-plane, nonuniformity is reduced to 0.30%.

ACKNOWLEDGMENT

This work was supported by the U. S. Department of Energy Office of Inertial Confinement Fusion under Cooperative Agreement No. DE-FC03-92SF19460, the University of Rochester, and Lawrence Livermore National Laboratories under subcontract B399901. The support of DOE does not constitute an endorsement by DOE of the views expressed in this article.

REFERENCES

1. I. C. Stevenson and G. Sadkhin, in *Proceedings of the 44th Annual Technical Conference of the Society of Vacuum Coaters* (Society of Vacuum Coaters, Albuquerque, NM, 2001), pp. 306–313.
2. D. J. Smith *et al.*, in *Proceedings of the 41st Annual Technical Conference of the Society of Vacuum Coaters* (Society of Vacuum Coaters, Albuquerque, NM, 1998), pp. 193–196.
3. B. Andre, L. Poupinet, and G. Ravel, *J. Vac. Sci. Technol. A* **18**, 2372 (2000).
4. R. Chow *et al.*, *Appl. Opt.* **32**, 5567 (1993).
5. B. S. Ramprasad and T. S. Radha, *Thin Solid Films* **15**, 55 (1973).
6. K. H. Behrndt, in *Transactions of the Tenth National Vacuum Symposium of the American Vacuum Society*, edited by G. H. Bancroft (The Macmillan Company, New York, 1963), pp. 379–384.
7. A. G. Zhiglinskiy and E. S. Putilin, *Opt.-Mekh. Prom.* **38**, 46 (1971).
8. H. A. Macleod, *Thin-Film Optical Filters*, 3rd ed. (IOP Publishing, Bristol, England, 2001), pp. 488–497.
9. A. Musset and I. C. Stevenson, in *Proceedings of the 31st Annual Technical Conference of the Society of Vacuum Coaters* (Society of Vacuum Coaters, Albuquerque, NM, 1988), pp. 203–209.

Multibeam Effects on Fast-Electron Generation from Two-Plasmon-Decay Instability

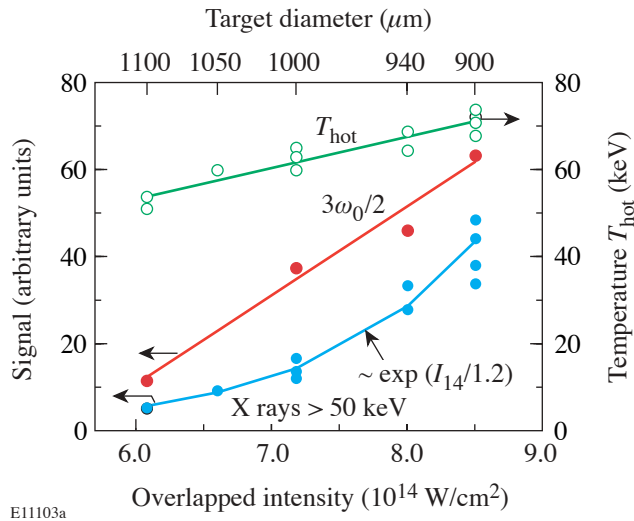
Two-plasmon-decay (TPD) instability has long been identified as a potential source for suprathermal electrons that can pre-heat the target fuel in direct-drive inertial confinement fusion (ICF) experiments, potentially impeding the assembly of sufficient fuel areal density for ignition.¹⁻⁴ TPD is a three-wave parametric instability in which an incident photon at frequency ω_0 decays into two electron-plasma waves (plasmons) with frequencies near $\omega_0/2$. Because of the resonant nature of this process, it is restricted to a small range of electron densities near the quarter-critical density. The instability threshold intensity is known to decrease and the saturation levels increase as the plasma density scale length increases.⁵⁻⁸

The basic theory of TPD was developed long ago^{5,6} along with a number of numerical simulations;⁷⁻¹³ however, experimental verification has been of a qualitative nature at best. Quantitative predictions for the suprathermal-electron generation are only now starting to emerge from simulations but have not yet been compared with experimental data.¹³ Even though some experiments used multiple overlapping beams,¹ their analysis has always been made in the single-beam approximation. This was based on the belief that the single-beam intensity dominates the scaling of the TPD instability even in experiments with multiple overlapping beams.

This article presents for the first time clear evidence for strong overlapping-beam effects on suprathermal-electron generation in both spherical and planar experiments. TPD instability was found to scale predominantly with overlapped intensity, which is defined as the incoherent sum of the interaction-beam intensities. The single-beam intensity and the number of overlapped beams did not significantly affect the observed scaling. There are several characteristic signatures for TPD instability: $3\omega_0/2$ and $\omega_0/2$ emission in the scattered light,^{4,14} a hard component (>20 keV) in the continuum x-ray bremsstrahlung spectrum,¹⁵ an energetic tail in the suprathermal electron spectrum,¹⁶ and K_α emission from cold material due to preheat.^{17,18} On the OMEGA laser system¹⁹ TPD instability is monitored using a $3\omega_0/2$ spectrometer and a time-resolved, scintillator-based, four-channel hard-x-ray detector

system.²⁰ The observed hard x rays can be attributed only to TPD instability since competing production mechanisms such as stimulated Raman scattering (SRS) are not seen in significant amounts in these experiments.^{21,22} In addition, the electron temperatures inferred from the hard-x-ray signals are well above those measured for SRS,²³ and the $3\omega_0/2$ signature is seen in all of the reported experiments.

The experiments in spherical geometry used targets of varying diameters similar to those described in Ref. 24. Gas-filled CH targets (900- to 1100- μm diameter, ~ 27 - μm wall thickness, and 20 atm of D_2 fill) were irradiated with 60 beams at 351-nm wavelength, with 1-ns square pulses and ~ 23 -kJ total energy. All beams were smoothed by two-dimensional smoothing by spectral dispersion²⁵ with 1-THz bandwidth in the UV and polarization smoothing.²⁶ Standard OMEGA phase plates²⁷ were used throughout with a spot size of ~ 0.5 -mm FWHM and a speckle-averaged peak intensity of $\sim 2 \times 10^{14}$ W/cm². The total overlapped intensity on target varied between 6.0×10^{14} W/cm² and 8.5×10^{14} W/cm², due to the varying target surface area, while the peak single-beam intensity on target was virtually unchanged. One-dimensional *LILAC*²⁸ hydrodynamic simulations show a rapidly growing radial density scale length at a quarter-critical density that reaches ~ 100 μm midway through the pulse. This is followed by a slower growth to ~ 150 μm at the end of the pulse. The coronal electron temperature is predicted to be relatively constant, with a typical value of ~ 2.5 keV. Figure 94.13 shows the hard-x-ray and $3\omega_0/2$ signatures of the TPD instability from the spherical experiments as a function of overlapped intensity. The suprathermal-electron temperature as inferred from the hard-x-ray spectrum²⁰ changes very little, which is consistent with earlier observations.^{2,3} In contrast, the measured hard-x-ray energy scales exponentially with overlapped intensity as $\exp(I_{14}/1.2)$, where I_{14} is the intensity in units of 10^{14} W/cm². This behavior strongly suggests that the TPD instability in the OMEGA implosion experiments scales primarily with the overlapped intensity rather than the single-beam intensity. Even though the overlapped intensity varies by only 30%, the hard-x-ray signature from the suprathermal elec-



E11103a

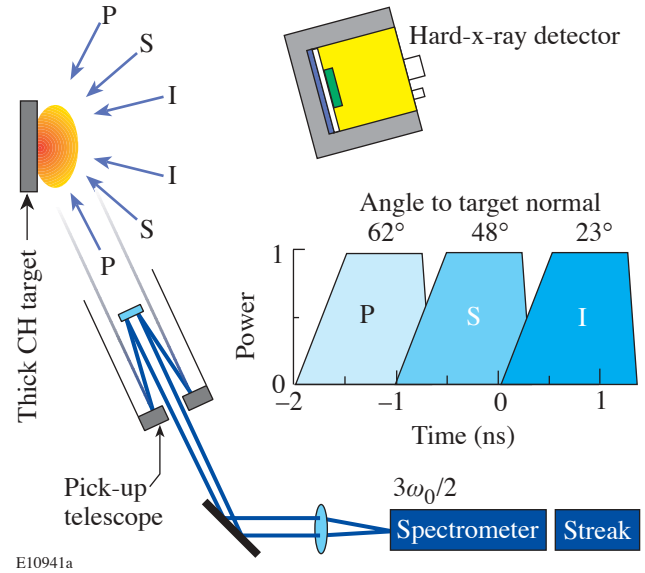
Figure 94.13

Signatures from TPD instability observed in a spherical implosion experiment on OMEGA using targets of varying diameter. The hard-x-ray (>50-keV) signal, the $3\omega_0/2$ emission, and the suprathermal-electron temperature inferred from the hard-x-ray spectrum scale with the total overlapped intensity. The peak single-beam intensity is kept constant.

trons changed by a factor of 10 and the $3\omega_0/2$ signature varied by a factor of 5.

Future direct-drive ignition experiments on the National Ignition Facility (NIF)²⁹ are expected to generate longer scale lengths ($\sim 500 \mu\text{m}$) at a higher overlapped laser intensity ($1.3 \times 10^{15} \text{ W/cm}^2$). Since these conditions are potentially more vulnerable to suprathermal-electron generation, a set of dedicated planar experiments was carried out at longer scale lengths closer to those expected on the NIF. The experimental layout (Fig. 94.14) was similar to that of Ref. 30. CH targets of $100\text{-}\mu\text{m}$ thickness and 5-mm diameter were sequentially irradiated with nine primary (P) beams, followed by six secondary (S) beams and two to six interaction (I) beams. The interaction beams were incident at $\sim 23^\circ$ to the target normal, and the P and S beams were at $\sim 62^\circ$ and $\sim 48^\circ$, respectively. The beam-smoothing conditions were identical to the spherical experiments. The P and S beams had standard phase plates that were defocused ($\sim 1\text{-mm}$ FWHM) with speckle-averaged peak intensities of $\sim 5 \times 10^{13} \text{ W/cm}^2$. The six interaction beams used either standard phase plates at nominal focus ($\sim 2 \times 10^{14} \text{ W/cm}^2$) or high-intensity phase plates ($\sim 0.25\text{-mm}$ FWHM) at $8 \times 10^{14} \text{ W/cm}^2$. The individual beam energies were varied between 180 and 360 J, and the laser pulse shape was well approximated by a 500-ps ramp followed by a 1-ns flat portion. Two-dimensional hydrodynamic *SAGE*³¹ simulations, which

generally replicate these experimental configurations very well,²¹ predict typical electron temperatures of $\sim 2.5 \text{ keV}$ and a relatively constant electron-density scale length of $\sim 350 \mu\text{m}$ for six overlapped interaction beams with standard phase plates. For six high-intensity interaction beams, the predicted electron temperatures rise to $\sim 4.5 \text{ keV}$ with density scale lengths reduced to $\sim 180 \mu\text{m}$. Simulations for fewer than six overlapped beams generally show similar scale lengths at lower temperatures.

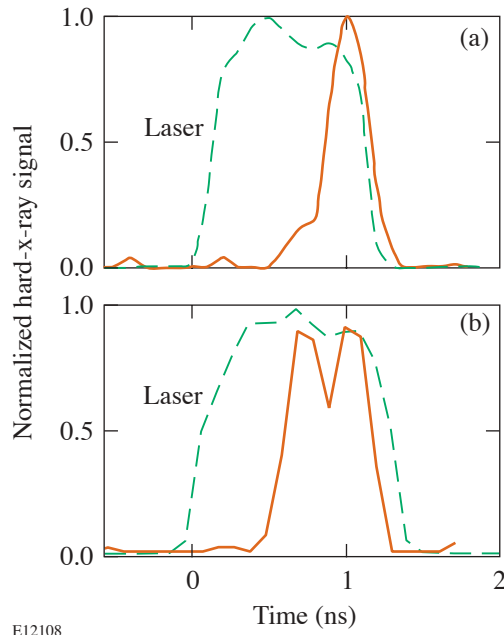


E10941a

Figure 94.14

Schematic layout of planar experiments using three sets of laser beams: nine primary (P) beams, six secondary (S) beams, and two to six interaction (I) beams. The pulse sequence, pulse shape, and approximate angles of incidence are indicated. The TPD instability is monitored using a streaked optical $3\omega_0/2$ spectrometer and a time-resolved, scintillator-based, four-channel hard-x-ray detector system (only one channel is shown).

Figure 94.15 shows the time-resolved hard-x-ray signal (>50 keV) from a spherical implosion (a) and a planar experiment using six overlapped beams with standard phase plates (b), with the same overlapped intensity of $\sim 10^{15} \text{ W/cm}^2$. In both cases the signal is significantly delayed with respect to the laser pulse and vanishes rapidly at the end of the laser pulse. This delay is not fully understood, but the difference between the spherical and planar experiments is probably due to the pre-existing scale length at the start of the interaction beam for the planar case. The highly nonlinear scaling of the TPD instability with intensity can be observed in the strong amplification of the laser-intensity variations.



E12108

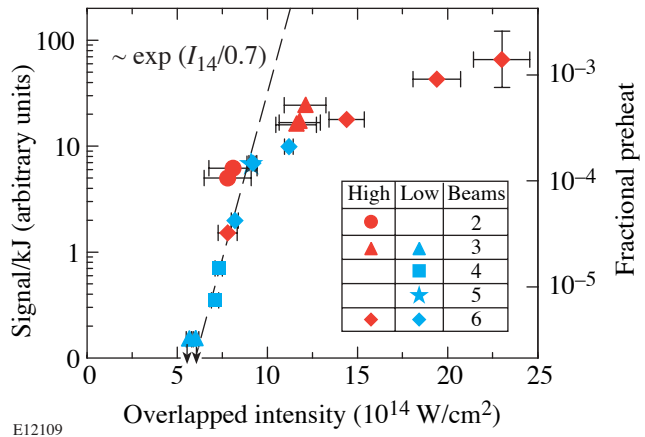
Figure 94.15

Time-resolved hard-x-ray (>50 -keV) emission (solid line) from a spherical implosion experiment (a) and a planar long-scale-length experiment using six beams with standard phase plates (b). The time history of the laser pulse (dashed line) is shown for comparison. The overlapped laser intensity was $\sim 10^{15}$ W/cm 2 in both cases.

Figure 94.16 shows time-integrated hard-x-ray signals for $E_x > 50$ keV (normalized to the total interaction-beam energy for the planar experiments with both standard and high-intensity phase plates). The pointing accuracy (~ 50 - μ m rms) of the overlapping beams is the dominant contribution to the error for the overlapped intensity. The measurement error of the hard-x-ray signal is $<10\%$, about the size of the symbols used. Even though the plasma conditions vary considerably in both scale length and temperature, the hard-x-ray signal is primarily a function of overlapped interaction-beam intensity. The number of overlapped beams and the single-beam intensity seem to be of almost no importance. Remarkably all data can be fit to a universal exponential scaling $\sim \exp(I_{14}/0.7)$ below an intensity of 10^{15} W/cm 2 , even stronger than that observed in spherical geometry. Above 10^{15} W/cm 2 the scaling of the hard-x-ray signal with intensity changes significantly and is much weaker. The fact that the overlapped intensity governs the scaling of TPD is most easily seen by comparing the signals from six overlapped beams with standard phase plates at an intensity of 11.2×10^{14} W/cm 2 to those of three beams with standard phase plates at an intensity of 5.7×10^{14} W/cm 2 . If single-beam intensity were to govern suprathermal-electron

generation, three beams would produce the same hard-x-ray signal per kJ of laser energy as six beams, but actual experiments show $>60\times$ reduction, which means that the hard-x-ray signals are actually below the detector threshold.

An absolute measurement of the hard x rays is necessary to infer the heating of the targets from suprathermal electrons. Because the absolute calibration of the hard-x-ray detectors is not very accurate,²⁰ the detectors have been cross-calibrated with preheat measurements using K_α spectroscopy^{32,33} on CH targets with embedded high-Z layers. These layers consisted of 5 μ m of titanium followed by 40 μ m of vanadium, covered with 20 μ m of CH on all sides to avoid direct laser interaction. Consequently the generation of suprathermal electrons is the same as in the primary experiments. The titanium layer absorbs the coronal x radiation without significantly affecting the suprathermal electrons, which then excite K_α radiation in the vanadium layer. The total energy in the vanadium K_α line observed on the back of the target is a good measure of the energy deposited by the electrons and thus the preheat.³² Thus calibrated, the signals from the hard-x-ray detectors can be used to infer the level of preheat of the CH planar targets. The inferred fractional preheat (preheat energy



E12109

Figure 94.16

Time-integrated hard-x-ray signals ($E_x > 50$ keV) as a function of overlapped interaction-beam intensity for planar experiments. Two to six beams are used with both standard and high-intensity phase plates at beam energies between 180 and 360 J. The error for the intensity is determined by the beam-pointing accuracy of ~ 50 - μ m rms of the overlapping beams. The relative error of the hard-x-ray signal is about the size of the symbols used ($<10\%$). An exponential scaling $\sim \exp(I_{14}/0.7)$ below an overlapped intensity of 10^{15} W/cm 2 (dashed line) is shown for comparison. The axis on the right corresponds to the estimate of the target preheat based on the calibration using K_α spectroscopy. The uncertainty of the calibration ($\sim 50\%$) is indicated with the error bar on the far-right data point.

normalized to incident laser energy) is shown on the right axis of Fig. 94.16. The uncertainty of these numbers is determined by the accuracy of the K_α cross-calibration of $\sim 50\%$. It is encouraging that the preheat level lies below 0.1% for intensities around 1.3×10^{15} W/cm², the peak intensity required for NIF direct-drive experiments.

In conclusion, experimental evidence from both spherical and long-scale-length planar experiments shows clearly that the total overlapped intensity governs the scaling of the suprathermal-electron production while the single-beam intensity is of lesser importance. Presently no theoretical explanation of this behavior exists, but simulations of the nonlinear saturated stage of the TPD instability¹² suggest that the spectrum of the plasma waves broadens considerably, which makes it conceivable that overlapping beams might act on the same plasmon. The exponential scaling seen in both experiments at overlapped intensities below 10^{15} W/cm² is even stronger in the planar case than that observed in the spherical experiments. This may be due to the presence of a long ($>100 \mu\text{m}$) and slowly evolving density scale length right from the start of the interaction beam in the planar experiments, which is correlated with an earlier onset of hard-x-ray emission, as compared to the spherical experiments. The origin of the consistently observed change in scaling with intensity of the fractional-preheat levels above 10^{15} W/cm² for all studied plasma density scale lengths and temperatures remains unclear at this time. There could potentially be a correlation with the filamentation instability, which has a similar threshold.³⁴ Nevertheless, this observation increases the confidence that the preheat levels from suprathermal electrons are manageable for direct-drive ignition experiments on the NIF.

ACKNOWLEDGMENT

This work was supported by the U.S. Department of Energy Office of Inertial Confinement Fusion under Cooperative Agreement No. DE-FC03-92SF19460, the University of Rochester, and the New York State Energy Research and Development Authority. The support of DOE does not constitute an endorsement by DOE of the views expressed in this article.

REFERENCES

1. D. W. Phillion *et al.*, Phys. Rev. Lett. **49**, 1405 (1982).
2. D. M. Villeneuve, R. L. Keck, B. B. Afeyan, W. Seka, and E. A. Williams, Phys. Fluids **27**, 721 (1984).
3. C. Rousseaux *et al.*, Phys. Fluids B **4**, 2589 (1992).

4. W. Seka, R. E. Bahr, R. W. Short, A. Simon, R. S. Craxton, D. S. Montgomery, and A. E. Rubenchik, Phys. Fluids B **4**, 2232 (1992).
5. C. S. Liu and M. N. Rosenbluth, Phys. Fluids **19**, 967 (1976).
6. A. Simon, R. W. Short, E. A. Williams, and T. Dewandre, Phys. Fluids **26**, 3107 (1983).
7. A. B. Langdon, B. F. Lasinski, and W. L. Kruer, Phys. Rev. Lett. **43**, 133 (1979).
8. B. F. Lasinski and A. B. Langdon, Lawrence Livermore National Laboratory, Livermore, CA, UCRL-50021-77, 4-49 (1978).
9. L. V. Powers and R. L. Berger, Phys. Fluids **27**, 242 (1984).
10. *Ibid.*, **28**, 2419 (1985).
11. R. L. Berger and L. V. Powers, *ibid.*, 2895 (1985).
12. D. F. DuBois, D. A. Russell, and H. A. Rose, Phys. Rev. Lett. **74**, 3983 (1995).
13. D. A. Russell and D. F. DuBois, Phys. Rev. Lett. **86**, 428 (2001).
14. J. Meyer and Y. Zhu, Phys. Rev. Lett. **71**, 2915 (1993).
15. R. L. Keck, L. M. Goldman, M. C. Richardson, W. Seka, and K. Tanaka, Phys. Fluids **27**, 2762 (1984).
16. N. A. Ebrahim *et al.*, Phys. Rev. Lett. **45**, 1179 (1980).
17. B. Yaakobi, I. Pelah, and J. Hoose, Phys. Rev. Lett. **37**, 836 (1976).
18. J. D. Hares *et al.*, Phys. Rev. Lett. **42**, 1216 (1979).
19. T. R. Boehly, D. L. Brown, R. S. Craxton, R. L. Keck, J. P. Knauer, J. H. Kelly, T. J. Kessler, S. A. Kumpan, S. J. Loucks, S. A. Letzring, F. J. Marshall, R. L. McCrory, S. F. B. Morse, W. Seka, J. M. Soures, and C. P. Verdon, Opt. Commun. **133**, 495 (1997).
20. C. Stoeckl, V. Yu. Glebov, D. D. Meyerhofer, W. Seka, B. Yaakobi, R. P. J. Town, and J. D. Zuegel, Rev. Sci. Instrum. **72**, 1197 (2001).
21. S. P. Regan, D. K. Bradley, A. V. Chirikikh, R. S. Craxton, D. D. Meyerhofer, W. Seka, R. W. Short, A. Simon, R. P. J. Town, B. Yaakobi, J. J. Carroll III, and R. P. Drake, Phys. Plasmas **6**, 2072 (1999).
22. R. L. McCrory, R. E. Bahr, T. R. Boehly, T. J. B. Collins, R. S. Craxton, J. A. Delettrez, W. R. Donaldson, R. Epstein, V. N. Goncharov, R. Q. Gram, D. R. Harding, P. A. Jaanimagi, R. L. Keck, J. P. Knauer, S. J. Loucks, F. J. Marshall, P. W. McKenty, D. D. Meyerhofer, S. F. B. Morse, O. V. Gotchev, P. B. Radha, S. P. Regan, W. Seka, S. Skupsky, V. A. Smalyuk, J. M. Soures, C. Stoeckl, R. P. J. Town, M. D. Wittman, B. Yaakobi, J. D. Zuegel, R. D. Petrasso, D. G. Hicks, and C. K. Li, in *Inertial Fusion Sciences and Applications 99*, edited by C. Labaune, W. J. Hogan, and K. A. Tanaka (Elsevier, Paris, 2000), pp. 43–53.
23. R. P. Drake *et al.*, Phys. Rev. A **40**, 3219 (1989).

24. D. D. Meyerhofer, J. A. Delettrez, R. Epstein, V. Yu. Glebov, V. N. Goncharov, R. L. Keck, R. L. McCrory, P. W. McKenty, F. J. Marshall, P. B. Radha, S. P. Regan, S. Roberts, W. Seka, S. Skupsky, V. A. Smalyuk, C. Sorce, C. Stoeckl, J. M. Soures, R. P. J. Town, B. Yaakobi, J. D. Zuegel, J. Frenje, C. K. Li, R. D. Petrasso, D. G. Hicks, F. H. Séguin, K. Fletcher, S. Padalino, M. R. Freeman, N. Izumi, R. Lerche, T. W. Phillips, and T. C. Sangster, *Phys. Plasmas* **8**, 2251 (2001).
25. S. Skupsky, R. W. Short, T. Kessler, R. S. Craxton, S. Letzring, and J. M. Soures, *J. Appl. Phys.* **66**, 3456 (1989).
26. T. R. Boehly, V. A. Smalyuk, D. D. Meyerhofer, J. P. Knauer, D. K. Bradley, R. S. Craxton, M. J. Guardalben, S. Skupsky, and T. J. Kessler, *J. Appl. Phys.* **85**, 3444 (1999).
27. T. J. Kessler, Y. Lin, J. J. Armstrong, and B. Velazquez, in *Laser Coherence Control: Technology and Applications*, edited by H. T. Powell and T. J. Kessler (SPIE, Bellingham, WA, 1993), Vol. 1870, pp. 95–104.
28. M. C. Richardson, P. W. McKenty, F. J. Marshall, C. P. Verdon, J. M. Soures, R. L. McCrory, O. Barnouin, R. S. Craxton, J. Delettrez, R. L. Hutchison, P. A. Jaanimagi, R. Keck, T. Kessler, H. Kim, S. A. Letzring, D. M. Roback, W. Seka, S. Skupsky, B. Yaakobi, S. M. Lane, and S. Prussin, in *Laser Interaction and Related Plasma Phenomena*, edited by H. Hora and G. H. Miley (Plenum Publishing, New York, 1986), Vol. 7, pp. 421–448.
29. P. W. McKenty, V. N. Goncharov, R. P. J. Town, S. Skupsky, R. Betti, and R. L. McCrory, *Phys. Plasmas* **8**, 2315 (2001).
30. W. Seka, H. A. Baldis, J. Fuchs, S. P. Regan, D. D. Meyerhofer, C. Stoeckl, B. Yaakobi, R. S. Craxton, and R. W. Short, *Phys. Rev. Lett.* **89**, 175002 (2002).
31. R. S. Craxton and R. L. McCrory, *J. Appl. Phys.* **56**, 108 (1984).
32. B. Yaakobi, C. Stoeckl, T. Boehly, D. D. Meyerhofer, and W. Seka, *Phys. Plasmas* **7**, 3714 (2000).
33. B. Yaakobi, C. Stoeckl, T. R. Boehly, R. S. Craxton, D. D. Meyerhofer, and W. D. Seka, in *26th European Conference on Laser Interaction with Matter*, edited by M. Kalal, K. Rohlena, and M. Siñor (SPIE, Bellingham, WA, 2001), Vol. 4424, pp. 392–401.
34. Laboratory for Laser Energetics LLE Review **91**, 93, NTIS document No. DOE/SF/19460-458 (2002). Copies may be obtained from the National Technical Information Service, Springfield, VA 22161.

On the Bell–Plesset Effects: The Effects of Uniform Compression and Geometrical Convergence on the Classical Rayleigh–Taylor Instability

Introduction

This article considers a simple treatment of the Rayleigh–Taylor (RT) instability of incompressible perturbations of the interface between two homogeneous fluids undergoing acceleration due to a pressure gradient, including the effects of uniform compression and geometrical convergence. The growth rate for incompressible linear perturbations of a planar interface between incompressible fluids is well known from the work of Rayleigh¹ and Taylor² and has become a classic textbook result.^{3,4} When the perturbed interface undergoes compression or geometrical convergence, such as in the case of an interface embedded in a collapsing cylinder or sphere, the perturbation growth is modified. These modifications have been referred to collectively^{5,6} as Bell–Plesset (BP) effects.^{7,8} Both RT and BP effects are known to be important to the outcome of implosion experiments in inertial confinement fusion (ICF).^{9–11} The purpose of this article is to formulate and analyze BP effects in a simple way that reveals a wide range of behavior in a variety of geometries.

The term “accelerationless growth” has also been used for BP effects. This terminology acknowledges that interface perturbations would evolve due to convergence and compression in the absence of the buoyant force that drives the RT instability, but, as will be shown below, the modified RT growth does not separate naturally into an acceleration-driven RT contribution and an accelerationless contribution. Nevertheless, the chosen formulation clarifies the physical distinction between RT and BP effects. To be precise, the term “accelerationless” will be used below only to denote perturbation growth in the limit of no RT growth.

The description developed in this article is based on the very similar methods of Bell² and Plesset,³ combining Plesset’s treatment of interfaces with an arbitrary density jump, rather than only free surfaces, and Bell’s inclusion of uniformly compressible background flow. We also adopt Bell’s choice of a mass perturbation amplitude in order to obtain perturbation equations of a particularly simple and useful form. In cases where the local convergence and compression rates are con-

stant over useful time intervals, the perturbation solutions evolve exponentially, and scaling of the perturbation with the interface density and radius can be derived.

The Background Flow

To begin the perturbation calculation describing RT growth, we postulate one-dimensional irrotational unperturbed background flow in planar, cylindrical, and spherical geometries where an interface separates homogeneous fluids of contrasting uniform densities $\rho_1(t)$ and $\rho_2(t)$. The interface is at coordinate position $R(t)$, and the subscripts 1 and 2 denote the half-spaces at coordinate values less than or greater than $R(t)$, respectively. The fluid motion is fully specified by the interface history $R(t)$ and the rate of compression $\gamma_\rho(t)$. From this point on, $R(t)$, $\gamma_\rho(t)$, and other functions of time alone will be written without explicitly indicating the time dependence. This rate of compression is assumed to apply everywhere, or, in other words,

$$\gamma_\rho = \dot{\rho}_1/\rho_1 = \dot{\rho}_2/\rho_2. \quad (1a)$$

Similarly, the convergence rate is written as

$$\gamma_R = \dot{R}/R. \quad (1b)$$

For the cylindrical and spherical cases, R is the radius of the surface, while for a planar interface, the radius is effectively infinite, and $\gamma_R = 0$.

The unperturbed flow velocity is

$$v(x, t) = -(x - R)\gamma_\rho + \dot{R} \quad (2a)$$

in planar geometry,

$$v(r, t) = \dot{R}\left(\frac{R}{r}\right) + \left(\frac{\gamma_\rho}{2}\right)\left(\frac{R^2}{r^2} - 1\right)r \quad (2b)$$

in cylindrical geometry, and

$$v(r, t) = \dot{R} \left(\frac{R^2}{r^2} \right) + \left(\frac{\gamma_\rho}{3} \right) \left(\frac{R^3}{r^3} - 1 \right) r \quad (2c)$$

in spherical geometry. These velocities can be derived from the velocity potential functions

$$\Phi(x, t) = \Phi_0(t) - (x - R)\dot{R} + (x - R)^2 \gamma_\rho / 2 \quad (3a)$$

in planar geometry,

$$\Phi(r, t) = \Phi_0(t) - (R\dot{R} + \gamma_\rho R^2 / 2) \ln r + (\gamma_\rho / 4) r^2 \quad (3b)$$

in cylindrical geometry, and

$$\Phi(r, t) = \Phi_0(t) + \frac{R^2 \dot{R}}{r} + \left(\frac{\gamma_\rho}{3} \right) \left(\frac{r^2}{2} + \frac{R^3}{r} \right) \quad (3c)$$

in spherical geometry using

$$\vec{v} = -\vec{\nabla}\Phi. \quad (4)$$

These flows can be obtained from the Euler equation in one dimension

$$\frac{\partial v}{\partial t} + v \frac{\partial v}{\partial x} = -\frac{\partial U(x)}{\partial x} - \frac{1}{\rho} \frac{\partial p(x, t)}{\partial x}, \quad (5)$$

given the appropriate pressure $p(x, t)$ and external potential field $U(x, t)$. In planar geometry, it is easy to verify that the desired flow is obtained from the pressure

$$p(x, t) = p_0 - \rho g_P (x - R) + \rho (\dot{\gamma}_\rho - \gamma_\rho^2) (x - R)^2 / 2 \quad (6a)$$

and the external potential field

$$U(x, t) = U_0 - g_U x, \quad (7)$$

where

$$g_P = -\frac{1}{\rho} \frac{\partial p(R, t)}{\partial x}$$

and

$$g_U = -\frac{\partial U(R)}{\partial x}$$

are the separate components of the fluid acceleration at the unperturbed interface position due to pressure and the external potential, respectively. Using

$$\dot{R} = v(R, t), \quad (8)$$

the Euler equation gives

$$\ddot{R} = g_U + g_P. \quad (9)$$

In cylindrical geometry, the required combination of pressure and potential field is

$$\begin{aligned} U + \frac{p}{\rho} &= \left(U + \frac{p}{\rho} \right)_{r=R} - [R\ddot{R} + \dot{R}^2 + \gamma_\rho R\dot{R}] \ln r \\ &+ \left[\frac{\dot{\gamma}_\rho}{2} - \left(\frac{\gamma_\rho}{2} \right)^2 \right] r^2 \\ &- \frac{1}{2} \left[\frac{\dot{R}^2}{2} + \gamma_\rho R\dot{R} - \left(\frac{\gamma_\rho}{2} \right)^2 R^2 \right] \left(\frac{R^2}{r^2} \right), \end{aligned} \quad (6b)$$

and in spherical geometry, the required combination is

$$\begin{aligned} U + \frac{p}{\rho} &= \left(U + \frac{p}{\rho} \right)_{r=R} + \frac{\ddot{R}R^2}{r} - \left(\frac{2R\dot{R}^2}{r} - \frac{4}{3} \gamma_\rho \frac{R^2 \dot{R}}{r} \right) \\ &\times \left(1 - \frac{R^3}{4r^3} \right) - \left(\frac{\gamma_\rho}{3} \right)^2 \frac{r^2}{2} \left(1 - \frac{R^3}{r^3} \right)^2 \\ &+ \left(\frac{\dot{\gamma}_\rho}{3} \right) \frac{r^2}{2} \left(1 + \frac{2R^3}{r^3} \right). \end{aligned} \quad (6c)$$

Again, in both the latter cases, Eq. (9) is obtained from the Euler equation.

The one-dimensional background flow in planar geometry conserves mass everywhere according to

$$\bar{\nabla} \cdot \bar{v} = -\gamma_\rho, \quad (10a)$$

but, for arbitrary convergence and compression rates, a line source is required for cylindrical flow,

$$\bar{\nabla} \cdot \bar{v} = -\gamma_\rho + \dot{m}\delta^{(2)}(r), \quad (10b)$$

where

$$\frac{\dot{m}}{\pi\rho R^2} = 2\gamma_R + \gamma_\rho, \quad (11a)$$

and a point source is required for spherical flow,

$$\bar{\nabla} \cdot \bar{v} = -\gamma_\rho + \dot{m}\delta^{(3)}(r), \quad (10c)$$

where

$$\frac{3\dot{m}}{4\pi\rho R^2} = 3\gamma_R + \gamma_\rho. \quad (11b)$$

The cylindrical and spherical velocities given by Eqs. (2b) and (2c) can be written simply in terms of \dot{m} as

$$v(r,t) = \frac{\dot{m}}{2\pi r\rho} - \gamma_\rho \frac{r}{2} \quad (12a)$$

and

$$v(r,t) = \frac{\dot{m}}{4\pi r^2\rho} - \gamma_\rho \frac{r}{3}. \quad (12b)$$

To consider a broad range of BP effects, it is important to be able to specify the compression and convergence rates independently, and this requires the mass source \dot{m} at $r = 0$. Imposing $\dot{m} = 0$ restricts the problem to either constant cylindrical mass, $2\gamma_R + \gamma_\rho = 0$, or constant spherical mass, $3\gamma_R + \gamma_\rho = 0$. According to Eqs. (6), placing a mass source at $r = 0$ to create desired background flows introduces unphysical pressures at $r = 0$. These flows are unlikely to resemble any intended application globally, but they suffice for the perturbation calculations if they are reasonably descriptive of conditions in the neighborhood of the density jump because discrepant

flow beyond a few perturbation wavelengths from the density jump will be largely decoupled from the perturbations.

It is worth noting a curious property of Eq. (6a) for the pressure driving the planar flow. For planar flow that is either converging or diverging at a constant rate $\dot{\gamma}_\rho = 0$, the pressure does not depend on the sign of γ_ρ ; in both cases, the pressure driving the flow exerts a diverging force, even if the flow is converging. In both cases, the distinction between diverging and converging flow comes from the initial conditions of the flow, not the pressure.

Perturbation Equations

To obtain the equations of motion for the incompressible perturbations of these interfaces, we follow the calculation of Plesset for a spherical interface.⁸ Following the work of Bell,⁷ we generalize Plesset's method to include cylindrical and planar geometries and to include compression of the unperturbed background flow at a spatially uniform rate.

The velocity potential function Φ describing irrotational flow with uniform mass density is governed by the Bernoulli theorem^{4,12}

$$\frac{p}{\rho} + U + \frac{1}{2}|v^2| - \frac{\partial\Phi}{\partial t} = 0, \quad (13)$$

where all the quantities have been defined above. The velocity potential includes the potential for the background flow plus the potential perturbation $\Phi_{\text{total}} = \Phi + \phi_\ell(\bar{x}, t)$. The subscript ℓ denotes the harmonic order of the perturbation mode corresponding to $\cos(2\pi\ell y/L)$, $\cos(\ell\theta)$, or $Y_\ell^m(\theta, \phi)$ transverse harmonic dependence in planar, cylindrical, and spherical geometry, respectively. The perturbation is assumed to be incompressible, which requires

$$\nabla^2\phi_\ell = 0. \quad (14)$$

Imposing vanishing boundary conditions on ϕ_ℓ at large distances from the interface and continuity at the origin, if applicable, we obtain solutions for each side of the interface for planar, cylindrical, and spherical geometries:

$$\phi_{\ell\pm}(\bar{x}, t) = b_{\ell\pm}(t)e^{\pm 2\pi\ell x/L} \cos(2\pi\ell y/L), \quad (15a)$$

$$\phi_{\ell\pm}(\bar{x}, t) = b_{\ell\pm}(t)r^{\pm\ell} \cos(\ell\theta), \quad (15b)$$

and

$$\phi_{\ell\pm}(\bar{x}, t) = b_{\ell\pm}(t)r^{\ell, -(\ell+1)}Y_{\ell}^m(\theta, \phi). \quad (15c)$$

For the planar perturbation, we have imposed a zero boundary condition at $y = 0$ and $y = L$ so that the set of perturbation modes would form a discrete spectrum with an integer index ℓ , preserving a unity of notation among the three geometries with no loss of generality. For planar and cylindrical geometry, we have disregarded z -dependent perturbations.

The position of the perturbed interface is $r = r_s(t)$, where

$$r_s(t) = R + a_{\ell}(t)\cos(2\pi\ell y/L), \quad (16a)$$

$$r_s(t) = R + a_{\ell}(t)\cos(\ell\theta), \quad (16b)$$

and

$$r_s(t) = R + a_{\ell}(t)Y_{\ell}^m(\theta, \phi) \quad (16c)$$

for planar, cylindrical, and spherical geometries, respectively. The interface displacement a_{ℓ} is the spatial amplitude of the perturbation.

Whenever it is clear in the following development that a coordinate-dependent expression applies to all three geometries, the symbol r will be used to denote the coordinate in the direction of the unperturbed flow, rather than repeat the exact same expression using the Cartesian coordinate symbol x for planar flow.

An ordinary second-order differential equation for a_{ℓ} is obtained from Eq. (13), first by evaluating P on both sides of the interface in terms of the perturbed velocity potential to first order in small distances from the unperturbed interface. These expressions for P are then matched at the interface $r = r_s$. A required expression for the function $b_{\ell\pm}$ in terms of the amplitude a_{ℓ} is obtained by equating the interface velocity to the fluid velocity at the interface:

$$\frac{dr_s}{dt} = -\frac{\partial[\Phi(r_s, t) + \phi_{\ell\pm}(r_s, t)]}{\partial r}. \quad (17)$$

This matching of pressures eliminates δp_{ℓ} , leaving an ordinary homogeneous second-order differential equation for a_{ℓ} .

Equations (6) show that one can write a pressure that produces the desired background flow. For the purposes of constructing linear equations for flow perturbations near $r = R$, the linear approximation

$$U(x, t) \approx U_0 - rg_U, \quad p(x, t) \approx p_0 - (r - R)\rho g_p \quad (18)$$

suffices. As Eq. (9) for the interface acceleration suggests, the background flow does not depend on the potential and the pressure gradients separately, only their sum. The RT growth rate, however, depends most directly on g_p and not g_U . In the absence of pressure gradients $g_p = 0$, the fluid is in a state of free fall, where there are no buoyant forces to drive the RT instability.

To begin constructing the expression for pressure continuity at the perturbed interface, we begin by rewriting Eq. (13) as

$$\frac{P(r, t) + \delta p_{\ell}}{\rho} = -U_0 + rg_U - \frac{1}{2}|v^2| + \frac{\partial\Phi}{\partial t}. \quad (19)$$

All quantities are evaluated at $r = r_s$ by expanding them to first order in the perturbation about the unperturbed interface position $r = R$. We evaluate the pressures in the fluid half-spaces $r < R$ and $r > R$, denoted by subscripts 1 and 2, respectively. Matching the harmonic components of the pressure perturbation $\delta p_{\ell 1} = \delta p_{\ell 2}$ gives the perturbation equations, which are

$$\left(-\gamma_{\rho} + \frac{d}{dt}\right)\frac{d}{dt}(a_{\ell}\rho) = \gamma_0^2(a_{\ell}\rho), \quad (20a)$$

$$\left(-\gamma_{\rho} + \frac{d}{dt}\right)\frac{d}{dt}(a_{\ell}\rho R) = \gamma_0^2(a_{\ell}\rho R), \quad (20b)$$

and

$$\left(-\gamma_{\rho} - \gamma_R + \frac{d}{dt}\right)\frac{d}{dt}(a_{\ell}\rho R^2) = \gamma_0^2(a_{\ell}\rho R^2) \quad (20c)$$

for planar, cylindrical, and spherical geometry, respectively. The resulting perturbation equations assume this simple and transparent form when written in terms of the “mass” amplitude z_ℓ , where

$$z_\ell = a_\ell \rho, \quad z_\ell = a_\ell \rho R, \quad \text{or} \quad z_\ell = a_\ell \rho R^2 \quad (21)$$

for the three chosen geometries. The interface density ρ can be the mean density $\rho = (\rho_1 + \rho_2)/2$ or any other fixed linear combination of ρ_1 and ρ_2 . Since a uniform compression rate applies everywhere, according to Eq. (1a), the only effect of alternative choices for the interface density is to introduce a constant factor into the definition of the mass amplitude [Eq. (21)]. The units of z_ℓ are mass only for spherical geometry. They are mass per area for planar geometry and mass per axial length for cylindrical geometry. In this form, the “driving” terms are proportional to the RT growth rates γ_0 , where

$$\gamma_0^2 = k \frac{(\rho_2 - \rho_1)}{(\rho_2 + \rho_1)} g_p, \quad (22a)$$

$$\gamma_0^2 = \frac{\ell}{R} \frac{(\rho_2 - \rho_1)}{(\rho_2 + \rho_1)} g_p, \quad (22b)$$

and

$$\gamma_0^2 = \frac{\ell(\ell + 1)}{R} \frac{(\rho_2 - \rho_1)}{[\ell\rho_2 + (\ell + 1)\rho_1]} g_p \quad (22c)$$

for the three geometries. Equation (22a) is the familiar “classical” RT growth rate for incompressible planar flow. The spherical results [Eqs. (20c) and (22c)] are equivalent to the result of Plesset⁸ for incompressible fluid ($\gamma_\rho = 0$), even though they are not easily recognized as such. For the special case of a free surface (either $\rho_1 = 0$ or $\rho_2 = 0$), Eqs. (20) and (22) become Bell’s⁷ final result.

The driving terms are easily identified as being the only terms containing either an acceleration or a density jump, both of which are required for the buoyant force driving the RT effect. Compared with alternative formulations,^{8,11} Eqs. (20) and (22) display a more physically meaningful isolation of the RT effect into a single term. Even though the RT effect can be

isolated in this way, the total perturbation growth rates do not separate naturally into RT and BP contributions. The form of Eqs. (20) does allow equations governing accelerationless growth to be obtained by setting $\gamma_0 = 0$, but the accelerationless limit cannot be simply combined with the classical RT growth rate to obtain a correct result.

Equations (20) are easily solved over time intervals where the compression and convergence rates, γ_ρ and γ_R , respectively, and the RT growth rate γ_0 are constant. The resulting solution pairs are exponential in time with constant growth rates,

$$\gamma_\pm = \frac{1}{2} \gamma_\rho \pm \sqrt{\gamma_0^2 + \frac{1}{4} \gamma_\rho^2} \quad (23a)$$

for both planar and cylindrical geometry and

$$\gamma_\pm = \frac{1}{2} (\gamma_\rho + \gamma_R) \pm \sqrt{\gamma_0^2 + \frac{1}{4} (\gamma_\rho + \gamma_R)^2} \quad (23b)$$

for spherical geometry. Since γ_0^2 can be negative, the growth rates can be complex, giving perturbations exhibiting exponential or sinusoidal behavior, or both. In characterizing an interface as stable or unstable, Plesset argues that exponential behavior suggests unbounded growth of one of the solutions, which indicates instability. Conversely, oscillation suggests stability. Even though Eqs. (20c) and (22c) are consistent with the corresponding equations of Plesset,⁸ one can draw different conclusions about the criteria for stability based solely on the inspection of the respective equations. Except for the case of planar incompressible flow, exponential growth, for example, does not necessarily imply net growth. Equations (23) can be a guide in formulating general stability criteria for intervals where γ_ρ , γ_R , and γ_0 are constant, but there are other approaches. In the next section where BP effects in the large- γ_0 limit are considered, the solutions appear as products of power-law factors of R and ρ and a factor that is exponential in $\gamma_0 t$. If one does not regard power-law density and radius scaling behavior as either stable or unstable, then the question of stability is simply the question of the sign of γ_0^2 , without regard for BP effects.

Solving fully time-dependent perturbation equations [Eqs. (20) and (22)] provides a more complete and thus more correct description of RT growth than the common practice of

estimating unstable growth from an exponential growth factor, such as

$$a(t) = a(0) \exp \left[\int_0^t \gamma(t') dt' \right], \quad (24)$$

where the positive growth rate is used in the integrand. The fully time-dependent solution permits specifying amplitudes with arbitrary initial values and time derivatives, while the growth factor implies a particular initial condition. For example, the solution pair for incompressible planar flow has equal and opposite growth rates, so a solution with a static initial amplitude is composed initially of equal parts of the growing and decaying components of the general solution. Equation (24), on the other hand, attributes the entire initial amplitude to the growing component of the full solution. As a result, the growth-factor solution will become too large by a factor of 2 if it is used to represent growth of a perturbation that is initially static. More generally, if the acceleration changes abruptly from one constant value to another, matching the solutions before and after the change cannot be done without considering the fully time-dependent solution. A second advantage of the fully time-dependent formulation is that Richtmyer–Meshkov–like¹³ behavior is obtained for impulsive acceleration. For an acceleration with an appropriate oscillating component, the fully time-dependent formulation exhibits the dynamic stabilization effect obtained by Betti *et al.*,¹⁴ another effect that cannot be described by an exponential growth factor.

Equations (20) and (22) were originally derived for use in a perturbation growth model for a saturable multimode model of RT instability¹⁶ applicable to simulations of inertial confinement fusion experiments.¹⁵

Scaling

In this section, we shall examine both the mass and spatial perturbation amplitudes in two limits where the BP effects appear entirely as scaling factors with power-law dependences on the interface density and radius. The first is the accelerationless limit of small γ_0 , and the second is the limit of rapid RT growth, relative to the compression and convergence rates. As will be shown below, the accelerationless BP effects are different from BP effects occurring in combination with the RT instability.

In the limit where the interface acceleration vanishes, or when the density jump at the interface vanishes, γ_0 approaches

zero. In this limit, assuming constant compression and convergence rates, the pairs of solutions are of the form $z_{\pm} \propto \exp(\gamma_{\pm} t)$, where

$$\gamma_{\pm} = [\gamma_{\rho}, 0] \quad (25a)$$

for both planar and cylindrical geometry and

$$\gamma_{\pm} = [\gamma_{\rho} + \gamma_R, 0] \quad (25b)$$

for spherical geometry. The leading-order RT corrections to Eqs. (25) are second order in γ_0 . From assuming that γ_{ρ} and γ_R are constants, we have $R \propto \exp(\gamma_R t)$ and $\rho \propto \exp(\gamma_{\rho} t)$ and the solution pairs are

$$z_{\pm} \propto [\rho, 1] \quad (26a)$$

for planar and cylindrical geometry and

$$z_{\pm} \propto [\rho R, 1] \quad (26b)$$

for spherical geometry. For uniform compression of a constant cylindrical mass $M = \rho R^2$ or spherical mass $M = \rho R^3$, the solutions $z_{M\pm}$ are

$$z_{M\pm} = [R^{-2}, 1] \quad (27)$$

for both cylindrical and spherical geometry. The spatial amplitudes are related to the mass amplitudes according to Eq. (21), which gives

$$a_{\pm} = [1, \rho^{-1}], \quad (28a)$$

$$a_{\pm} = [R^{-1}, (\rho R)^{-1}], \quad (28b)$$

and

$$a_{\pm} = [R^{-1}, (\rho R^2)^{-1}]. \quad (28c)$$

For uniform compression of a constant cylindrical mass or spherical mass, the solutions $a_{M\pm}$ are

$$a_{M\pm} = [R^{-1}, R] \quad (29)$$

for both cylindrical and spherical geometry.

While the accelerationless limit gives a view of the BP effects in the absence of RT growth, a more interesting limit is that of a dominant RT effect or, equivalently, of large ℓ where we have $\gamma_0 \gg \gamma_\rho$, $\gamma_0 \gg \gamma_R$, and $\gamma_0^2 \gg \dot{\gamma}_0$. In this limit, Eqs. (23) become, to leading order in the small numbers γ_ρ/γ_0 and/or γ_R/γ_0 ,

$$\gamma_\pm \approx \frac{1}{2} \gamma_\rho \pm \gamma_0 \quad (30a)$$

for both planar and cylindrical geometry and

$$\gamma_\pm \approx \frac{1}{2} (\gamma_\rho + \gamma_R) \pm \gamma_0 \quad (30b)$$

for spherical geometry. In an imploding sphere, such as in the deceleration phase of an ICF implosion experiment,^{17,18} for example, we estimate the magnitude of the small parameter of this limit by writing the classical growth rate as

$$\gamma_0^2 \approx \ell A \frac{\ddot{R}}{R}, \quad (31)$$

where A is the Atwood number

$$A \equiv \frac{(\rho_2 - \rho_1)}{(\rho_2 + \rho_1)}. \quad (32)$$

For the purpose of characterizing a large- ℓ limit, it is sufficient to assign a single time scale τ to all time derivatives,

$$\ddot{R} \sim R/\tau^2, \quad \dot{R} \sim R/\tau, \quad \dot{\rho} \sim \rho/\tau, \quad (33)$$

so that the small number in this limit is

$$\gamma_\rho/\gamma_0 \sim \gamma_R/\gamma_0 \sim (\ell A)^{-1/2}, \quad (34)$$

which is small for the large mode numbers of interest in ICF implosions.¹⁷ In this limit, the solution pairs are

$$z_\pm \propto \rho^{1/2} e^{\pm\gamma_0 t} \quad (35a)$$

for planar and cylindrical geometry and

$$z_\pm \propto \rho^{1/2} R^{1/2} e^{\pm\gamma_0 t} \quad (35b)$$

for spherical geometry. For uniform compression of a constant cylindrical mass or spherical mass, the solutions $z_{M\pm}$ are

$$z_{M\pm} = R^{-1} e^{\pm\gamma_0 t} \quad (36)$$

for both cylindrical and spherical geometry. The corresponding spatial amplitudes are

$$a_\pm = \rho^{-1/2} e^{\pm\gamma_0 t}, \quad (37a)$$

$$a_\pm = \rho^{-1/2} R^{-1} e^{\pm\gamma_0 t}, \quad (37b)$$

and

$$a_\pm = \rho^{-1/2} R^{-3/2} e^{\pm\gamma_0 t}. \quad (37c)$$

For uniform compression of a constant cylindrical mass or spherical mass, the solutions $a_{M\pm}$ are

$$a_{M\pm} = e^{\pm\gamma_0 t}, \quad (38)$$

which is an interesting example of a spatial amplitude evolving virtually free of any BP effects.

In this large- ℓ limit, the BP effects appear separately from the RT growth factors as scaling factors in powers of ρ and/or R that are the same for both solutions of each pair. The fact that the BP effects are the same for both solutions is a property unique to the large- ℓ limit. Except in this one limit, Eqs. (23) predict different BP effects for the two solutions.

Discussion

In the accelerationless limit where $\gamma_0 = 0$, the density and radius scaling of the perturbation solutions of constant mass amplitude are readily visualized. These solutions are the second solutions of Eqs. (26) and (27) and their spatial-amplitude

counterparts in Eqs. (28) and (29). The spherical cases are illustrated schematically in Fig. 94.17, where a layer of fluid is highlighted to suggest the “peak-to-valley” extent of the perturbation. Figure 94.17(a) shows an incompressible spherical layer thickening as it converges to maintain constant density, and Fig. 94.17(b) shows the same layer compressing in proportion to the radius of the uniformly compressing homogeneous sphere in which it is embedded. It is important to remember that this solution of constant mass amplitude is obtained only with appropriate initial conditions. The general solution for arbitrary initial conditions exhibits a more complicated mixture of behaviors. The fact that the convergence and compression effects are different for the two solutions in each pair is the rule, not the exception. It is a unique property of the opposite limit, where the RT rate is much larger than the compression and convergence rates, that both solutions exhibit the same BP scaling with density and radius.

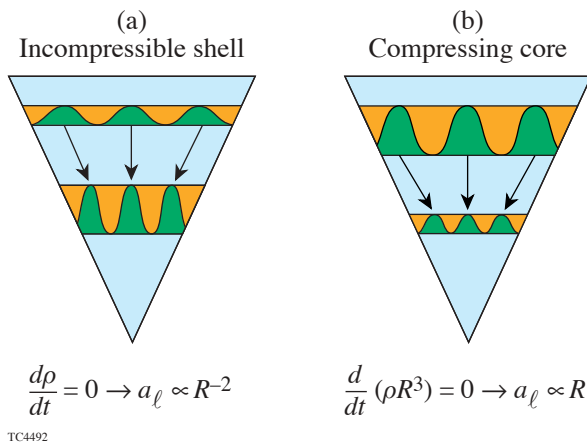


Figure 94.17

The cases of a perturbed surface embedded in an incompressible shell and a compressible sphere suggest, respectively, $a_\ell \propto R^{-2}$ and $a_\ell \propto R$ scaling of the spatial amplitude in the absence of a Rayleigh–Taylor growth term. Each of these solutions are paired with another independent solution, however, and the scaling behavior is more complicated if contributions from these other solutions are introduced by the initial conditions of the amplitude.

A simple demonstration of the importance of BP effects and the differences obtained from alternative initial conditions are shown in Fig. 94.18. The two plots show the growth of the spatial amplitude of a perturbation of an imploding, decelerating spherical interface. The implosion parameters correspond roughly to those of ICF capsule implosions near peak compression. The surface is assumed to compress by a radial factor of 10 while decelerating uniformly at 2.0×10^{16} cm/s² from a radius of 400 μm . The perturbation growth was calculated by direct integration of Eq. (20c). Each plot shows the amplitude

growth for an incompressible spherical shell ($\gamma_\rho = 0$), for a uniformly compressing sphere ($3\gamma_R + \gamma_\rho = 0$), and for the incompressible planar limit ($\gamma_R = \gamma_\rho = 0$) with no BP effects. Figure 94.18(a) shows results obtained by applying a static initial condition to the spatial amplitude, and Fig. 94.18(b) shows the same results obtained by applying a static initial condition to the mass amplitude. The RT growth rate was set to $\gamma_0^2 = 4\dot{R}/R$, choosing $\ell A = 4$ to create an intermediate case between the accelerationless and the large-growth limits. The results show that BP effects vary in importance, depending on which compressibility assumption is made, and that they are sensitive to the choice of initial condition. If the amplitude is initialized as a static mass amplitude, the incompressible shell growth is particularly large. These results should not be ex-

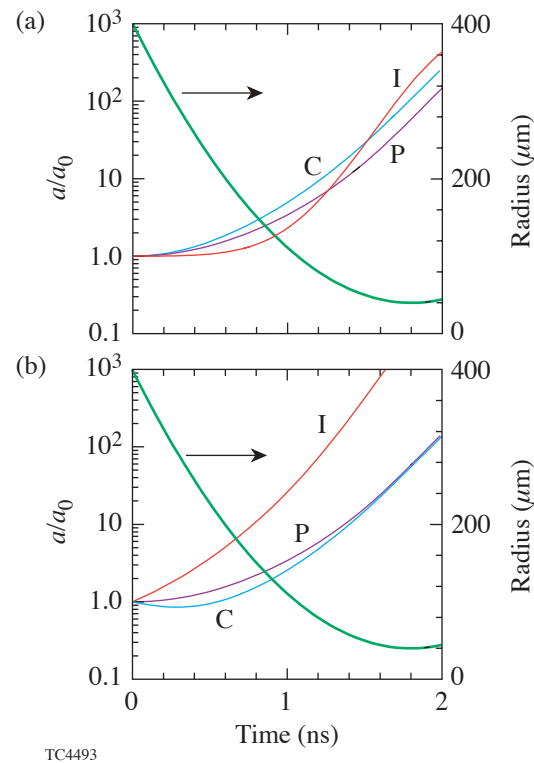


Figure 94.18

Significant differences in perturbation growth are obtained for different compressibility cases and with different initializations. Results for perturbations of an incompressible shell (I) and a compressible sphere (C) are shown, compared with the results of the “classical” Rayleigh–Taylor model, or the incompressible planar approximation (P), where convergence and compression effects are ignored. The importance of initial conditions is seen by comparing results obtained using (a) static initial spatial amplitudes and (b) static initial mass amplitudes.

pected to conform closely to the scaling results [Eqs. (37c) and (38)] because the compression, convergence, and RT rates are not constant and γ_0^2 does not occur close to either of the scaling limits of the previous section, but Eq. (38) does suggest that the amplitudes from the compressible sphere and incompressible planar models should tend to agree as they seem to do in both plots. Also, Eq. (37c) suggests that the BP effect on the amplitude of a spatial perturbation of a spherical surface converging by a factor of 10 should increase the amplitude over the other two cases by about 1.5 decades, which is approximately what is seen in Fig. 94.18(b).

Actual ICF implosions are, of course, more complicated than this simple illustration. The deceleration of the compressing core occurs during a brief “deceleration” phase following a longer “coasting” phase between the period of acceleration due to the driver and the onset of deceleration by the compressing core. The coasting phase can be characterized crudely by an incompressible shell in the accelerationless limit ($\gamma_\rho = 0$ and $\gamma_0 = 0$), and the deceleration phase would resemble, in contrast, the case of the uniformly compressing sphere ($3\gamma_R + \gamma_\rho = 0$). In a realistic simulation, the convergence and compression rates vary continuously, and the true description of an unstable surface will be somewhere between the limits of an incompressible shell and a uniformly compressible sphere of constant mass.

Overall, BP effects in the accelerationless limit and in the limit where the RT growth is dominant exhibit distinct differences in the nature of the effects and in their importance. Between these two scaling limits, the latter is the more applicable limit when analyzing observations of hydrodynamic instability in ICF implosion experiments.

The BP effects have been called the “Bell–Plesset instability,”⁶ which is not a correct description. They may be better described as a scaling behavior, for example, but they are certainly not a true instability in the sense that the RT instability is a true instability whose growth is driven by positive feedback that grows in proportion to its amplitude.

Summary and Conclusion

A formal description of the BP effects of compression and geometric convergence on the RT instability has been obtained. Even though the chosen model is restricted to incompressible perturbations of an interface separating homogeneous fluids and to a spatially uniform compression rate for the entire fluid, the model is general enough to encompass a usefully broad range of behavior. Results for three geometries (planar,

cylindrical, and spherical) are presented in parallel, and the fluid is allowed to compress and converge independently. The governing perturbation equations [Eqs. (20) and (22)] are only slightly modified from the classical RT equations as given by Eqs. (20a) and (22a) for incompressible ($\gamma_\rho = 0$) planar flow whose solutions exhibit simple exponential or sinusoidal evolution of the interface distortion. The RT growth rates for the three chosen geometries are very similar and, as expected, become identical in the limit of large harmonic order ℓ or k , where $k = \ell/L$. The first of two modifications of the planar incompressible RT equation that add the BP effects is to write it in terms of a mass amplitude. It is not surprising that the perturbation equations would be simplified by writing them in terms of a mass amplitude because an embedded perturbed interface would simply compress and converge with the flow, with the peak-to-valley displacement of the interface demarcating a layer of constant mass. The second modification is to add a first-time-derivative term appropriate for the chosen geometry, which results in a pair of growth rates that differ by more than just a sign flip.

With constant compression, convergence, and growth rates, the simple form of Eqs. (20) leads to BP effects expressible as power-law scaling with density and radius. These scalings vary, depending on the underlying geometry, the assumed interdependence of the compression and convergence rates, and which limit of either slow [Eqs. (25)–(29)] or rapid [Eqs. (30)–(33)] RT growth applies. In the limit of slow RT growth or, equivalently, in the limit of true accelerationless growth, each solution in a pair has its own distinct BP scaling, and only one solution of the pair exhibits the constant mass amplitude expected for an embedded surface. The scaling behavior is distinctly different for RT growth that is much faster than the convergence and/or compression. While rapid RT growth might amount to several e foldings in, for example, an ICF implosion, the BP effects can be much smaller and still amount to a significant effect. In this limit, the BP scaling becomes identical for each of the pair of solutions. While the variety of scalings among the solutions is simpler where RT growth dominates, the scaling is neither as intuitive nor as recognizable as the constant mass amplitude solution of the accelerationless limit. Perhaps the most surprising result is Eq. (38), indicating no first-order BP effect at all for the uniform compression of a constant spherical or cylindrical mass.

Even though the underlying assumptions behind the results shown here are somewhat restrictive, this presentation of a unified body of results for several geometries and flow characteristics hopefully has conveyed a clearer sense of the origin,

nature, and the surprising diversity of BP effects and their tendency to defy any simple characterization applicable over a wide range of circumstances.

ACKNOWLEDGMENT

This work was supported by the U.S. Department of Energy Office of Inertial Confinement Fusion under Cooperative Agreement No. DE-FC03-92SF19460, the University of Rochester, and the New York State Energy Research and Development Authority. The support of DOE does not constitute an endorsement by DOE of the views expressed in this article.

REFERENCES

1. Lord Rayleigh, Proc. London Math Soc. **XIV**, 170 (1883).
2. G. Taylor, Proc. R. Soc. London Ser. A **201**, 192 (1950).
3. S. Chandrasekhar, *Hydrodynamic and Hydromagnetic Stability*, International Series of Monographs on Physics (Dover Publications, New York, 1981), Chap. X, pp. 428–480.
4. L. D. Landau and E. M. Lifshitz, *Fluid Mechanics* (Pergamon Press, London, 1959).
5. J. B. Beck, “The Effects of Convergent Geometry on the Ablative Rayleigh–Taylor Instability in Cylindrical Implosions,” Ph.D. thesis, Perdue University, 1996.
6. W. W. Hsing and N. M. Hoffman, Phys. Rev. Lett. **78**, 3876 (1997).
7. G. I. Bell, Los Alamos National Laboratory, Report LA-1321 (1951).
8. M. S. Plesset, J. Appl. Phys. **25**, 96 (1954).
9. W. W. Hsing *et al.*, Phys. Plasmas **4**, 1832 (1997).
10. V. N. Goncharov, P. McKenty, S. Skupsky, R. Betti, R. L. McCrory, and C. Cherfils-Clérouin, Phys. Plasmas **7**, 5118 (2000).
11. P. Amendt *et al.*, Phys. Plasmas **10**, 820 (2003).
12. A. L. Fetter and J. D. Walecka, *Theoretical Mechanics of Particles and Continua*, International Series in Pure and Applied Physics (McGraw-Hill, New York, 1980).
13. R. D. Richtmyer, Commun. Pure. Appl. Math. **XIII**, 297 (1960).
14. R. Betti, R. L. McCrory, and C. P. Verdon, Phys. Rev. Lett. **71**, 3131 (1993).
15. R. Epstein, J. A. Delettrez, and C. P. Verdon, presented at the 27th Annual Anomalous Absorption Conference, Vancouver, BC, Canada, 1–5 June 1997.
16. S. W. Haan, Phys. Rev. A **39**, 5812 (1989).
17. P. W. McKenty, V. N. Goncharov, R. P. J. Town, S. Skupsky, R. Betti, and R. L. McCrory, Phys. Plasmas **8**, 2315 (2001).
18. D. D. Meyerhofer, J. A. Delettrez, R. Epstein, V. Yu. Glebov, V. N. Goncharov, R. L. Keck, R. L. McCrory, P. W. McKenty, F. J. Marshall, P. B. Radha, S. P. Regan, S. Roberts, W. Seka, S. Skupsky, V. A. Smalyuk, C. Sorce, C. Stoeckl, J. M. Soures, R. P. J. Town, B. Yaakobi, J. Frenje, C. K. Li, R. D. Petrasso, F. H. Séguin, K. Fletcher, S. Padalino, C. Freeman, N. Izumi, R. A. Lerche, T. W. Phillips, and T. C. Sangster, Plasma Phys. Control. Fusion **43**, A277 (2001).

Laser-Induced Adiabatic Shaping by Relaxation in Inertial Confinement Fusion Implosions

Introduction

In direct-drive inertial confinement fusion (ICF), a spherical shell of cryogenic deuterium–tritium is imploded by direct laser irradiation. As the shell accelerates inward, the outer surface is unstable due to the Rayleigh–Taylor (RT) instability, which causes a large shell distortion leading to significant degradation in capsule performance. Controlling the seeds and the growth rates of the RT instability during the acceleration phase is essential for the success of ICF implosions. The main damping mechanism of the instability growth during the acceleration phase is the ablative mass flow^{1,2} off the shell’s outer surface since the RT growth rates for cryogenic DT can be approximated as² $\Gamma \approx 0.94\sqrt{kg} - 2.7 kV_a$, where g is the shell acceleration, k is the instability wave number, and V_a is the ablation velocity. The latter represents the propagation speed of the heat front into the imploding shell and is inversely proportional to the shell density at the ablation front, $V_a = \dot{m}/\rho_a$, where \dot{m} is the mass ablation rate per unit area and ρ_a is the shell density at the ablation front. While the ablation rate is solely dependent on the laser intensity ($\dot{m} \sim I^{1/3}$), the density is related to the local value of the entropy (also referred to as the “adiabat”) $\rho_a = (p_a/S_a)^{1/\gamma}$, where p_a is the ablation pressure, S_a is the ablation-front adiabat, and $\gamma = 5/3$ is the adiabatic index. For a fixed laser wavelength, the ablation pressure depends on the laser intensity $p_a \sim I^{2/3}$, leading to a scaling of the ablation velocity $V_a \sim S_a^{3/5} I^{-1/15}$, which is almost solely dependent on the ablation-front adiabat. The ablation velocity increases for larger values of the adiabat, leading to lower growth rates and improved stability. The 1-D capsule performance degrades, however, as the adiabat increases. Indeed, the energy required for ignition³ in a 1-D implosion is approximately proportional to S_{dec}^2 , and the shell areal density at stagnation decreases for larger S_{dec} (here S_{dec} is the in-flight shell adiabat at the beginning of the deceleration phase).

It is important to emphasize that the 1-D capsule performance is affected by the shell adiabat at the beginning of the deceleration phase (S_{dec}) only when the laser is turned off and mass ablation off the outer shell surface has ceased. Since a

large portion of the shell mass is ablated off during the acceleration phase, the 1-D shell performance during the deceleration phase depends on the adiabat of the unablated shell. On the contrary, the ablative stabilization during the acceleration phase depends on the adiabat at the ablation front (S_a), that is, the adiabat of the ablated portion of the shell. It follows that a desirable adiabat shape would exhibit a minimum on the rear surface and a maximum on the ablation front. The idea of adiabat shaping was first introduced in Ref. 4, where the shaping is induced by the interaction of soft x rays with an ablator material having multiple absorption lines and radiation penetration depths. The first target design of such kind⁵ makes use of the x rays produced by a thin gold overcoat and by the carbon radiation in a wetted-foam ablator. Even though such a clever design^{4,5} can produce the desired shaping, significant complications arise from the target-manufacturing aspect, based on wetted-foam technology.

In this article, we show that it is possible to shape the shell adiabat with only a minor modification of the laser pulse without requiring any change to the shell structure. Adiabatic shaping can easily be performed by relaxing the density profile of the shell with a weak laser prepulse followed by a power shutoff. The adiabat is shaped when the main pulse is turned on, driving a strong shock through the relaxed profile. The adiabat profiles are usually steep, leading to a large increase in the ablation velocity. We refer to this technique as relaxation (RX). A good degree of adiabat shaping can also be accomplished by using a strong prepulse driving a very strong shock in the shell. When the laser power is lowered, the shock decays, leaving behind a shaped-adiabat profile. Shaping by a decayed shock (DS) was first proposed in Ref. 6 by Goncharov *et al.* and is described only briefly here for the purpose of comparison. We refer to Ref. 6 for a more detailed description of the DS technique. Instead, we focus our attention primarily on the RX adiabat shaping requiring only a weak prepulse and therefore easily implementable on current laser systems. Another advantage of the RX technique is that the main pulse starts with a high-intensity foot leading to a low contrast ratio for the main pulse laser power, better conversion efficiency, and therefore

more energy on target. Unlike the DS, the RX-induced adiabat shape is not unique and can be tuned by changing the laser prepulse and main pulse. The benefits of RX shaping have also been confirmed by a series of recent simulations by Perkins⁷ *et al.* and may also explain the improved stability observed in the simulations of Lindl and Mead.⁸ Furthermore, the use of a laser prepulse may also lead to a reduced level of imprinting.⁹

Analysis of Adiabatic Shapes

Both the DS and RX techniques require a prepulse (strong and weak, respectively) launching a decaying strong shock in the shell. We assume that the prepulse produces a constant pressure (P_{prep}) of duration (t_{prep}). The strong shock launched by the pressure $p_* = P_{\text{prep}}$ compresses the shell material to a density $\rho_* \approx 4 \rho_0$ (here ρ_0 is the initial shell density) and sets the adiabat of the shocked material to a constant value $S_* = p_*/\rho_*^{5/3}$. After the interval t_{prep} , the laser intensity (and therefore the applied ablation pressure) is greatly reduced, causing a rarefaction wave to propagate from the ablation front toward the shock front. We define with $t = 0$ the time corresponding to the end of the prepulse and launching of the rarefaction wave. Since the leading edge of the rarefaction wave travels faster than the shock, the shock front is overtaken by the rarefaction wave at time $t_* \approx 0.81 t_{\text{prep}}$ corresponding to an areal density $m_* = t_* \sqrt{\gamma p_* \rho_*}$. After the shock is overtaken by the rarefaction wave ($t > t_*$), both the shock strength and the adiabat of the shocked material decrease. The analysis is greatly simplified by working in the Lagrangian frame of reference and by using the areal density $m = \int_{r_0}^r \rho(r', t) dr'$ as the spatial coordinate, with r and r_0 representing the position of the fluid elements and the outermost Lagrangian point, respectively.

For the DS case, it is important to determine the entropy shape caused by the decaying shock. Using the normalized variables ρ/ρ_* , p/p_* , t/t_* , $u/\sqrt{\gamma p_*/\rho_*}$, and m/m_* , it is easy to show that the equations of motion and the initial and boundary conditions depend only on γ , suggesting that the normalized adiabat $\hat{S} = S/S_*$ is a universal function of $z = m/m_*$ with a shape depending only on γ . It follows that $\hat{S}(z)$ can be determined once and for all from a single one-dimensional simulation. For $\gamma = 5/3$, the normalized adiabat $\alpha \equiv P(\text{Mb})/2.18 \rho(\text{g/cm}^3)^{5/3}$ is flat for $m < m_*$ and follows approximately a power law for $m > m_*$:

$$\alpha_{m_* < m < m_{\text{sh}}} \approx \alpha_b (m_{\text{sh}}/m)^{1.3}, \quad (1)$$

where m_{sh} is the total shell areal density and α_b is the rear-surface adiabat that determines the 1-D performance. It is

important to notice that while the adiabat shape is independent of the prepulse characteristics, the front-surface adiabat $\alpha_f = \alpha_b (m_{\text{sh}}/m_*)^{1.3}$ increases by lowering m_* . This can be accomplished by a short, intense prepulse. After the strong prepulse, the standard main pulse immediately follows, driving the shell to the desired implosion velocity.

For the RX case, the prepulse shock is weaker than the DS case, leading to a negligible entropy variation. During the power shutoff, the rarefaction trailing edge expands outward and the shocked material relaxes. Both the pressure and density profiles develop a monotonically increasing profile up to the shock front. The adiabat shaping occurs later in time when the laser is turned on again and the foot of the main pulse starts (see Fig. 94.19 for a typical laser pulse). At this time (t_{foot}) a strong shock is launched and supported by the pressure of the foot of the main pulse (P_{foot}). The shock travels through the relaxed profiles and initially interacts with the low-pressure material of the rarefaction trailing edge. Because of the large pressure ratio before and after the shock front, the shock strength is initially very high and the shell's outer surface is set on a high adiabat. As the shock travels up the pressure (and density) profile, the pressure of the unshocked material increases and the shock strength decreases, leading to a lower adiabat. When the shock driven by the main pulse merges with the shock launched by the prepulse at the shell's rear surface, the adiabat acquires the desired shape with large values on the outer surface and low values on the inner surface.

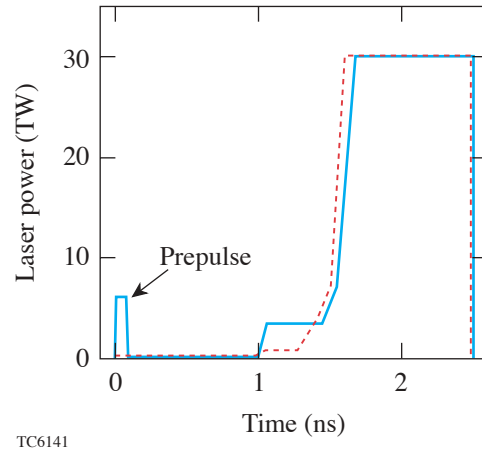


Figure 94.19

Laser pulse for a flat adiabat (dashed) and for adiabat shaping by relaxation (RX) (solid).

The adiabat shape can be calculated analytically for the two limiting cases: (a) a long prepulse launching a rarefaction wave that catches the shock just before the shell's rear surface ($m_* \approx m_{\text{sh}}$) and (b) a short prepulse with a rarefaction wave catching the shock near the front surface ($m_* \ll m_{\text{sh}}$). In case (a), the relaxed density profile just before the main shock launch follows a power law of the areal density $\rho \sim m^{0.75}$. The propagation of the main shock through such a profile can be calculated analytically, leading to the following entropy profile after the main shock:

$$\alpha \approx \alpha_b (m_{\text{sh}}/m)^{1.25}. \quad (2)$$

Observe that the adiabat shape follows a power law similar to the decaying shock case [Eq. (1)] except for the absence of the flat-adiabat region for $m < m_*$, therefore extending the large adiabat profile through the entire shell. In case (b), the relaxed density profile just before the main shock can also be approximated with a power law of the areal density but with a higher exponent $\rho \sim m^{1.45}$ for $m > m_*$ (here $m_* \ll m_{\text{sh}}$). When the exponent exceeds unity, the hydro equations for the main shock propagation cannot be solved exactly. Instead, an approximate solution can be found by assuming that the pressure profile behind the shock is linear in the areal density. A straightforward manipulation of the hydro equations leads to the following adiabat shape behind the main shock:

$$\alpha = \alpha_b \left(\frac{m_{\text{sh}}}{m} \right)^{2.4} \frac{1 + \Theta(m/m_*)}{1 + \Theta(m_{\text{sh}}/m_*)}, \quad (3)$$

$$\Theta(\xi) = \frac{2.64 \xi^2 - 8.1 \xi^{1.45} + 6.4 \xi - 1}{(1 - \xi)^2}.$$

Observe that the adiabat profile given by Eq. (3) approaches the power law $\alpha \sim m^{-2.4}$ for $m_* \rightarrow 0$ and is quite steeper than the one produced by the decaying shock [Eq. (1)], leading to larger values of the adiabat at the ablation front and larger ablation velocities.

Prepulse Design Formulas

The shock-merging condition on the rear surface is a necessary condition for an optimum RX shaping. Indeed, it is easy to show that when the two shocks (main and prepulse) merge inside the shell, the transmitted shock sets the rear surface on

an adiabat that is about five times larger than the desired value. Furthermore, if the prepulse shock reaches the rear surface before the main shock, then the back of the shell relaxes and the main shock travels through a decreasing pressure profile, acquiring strength and setting the rear surface on a very high adiabat. The condition of shock merging on the rear surface is an important constraint for a successful adiabat shaping. Assigning the rear-surface adiabat and satisfying the shock-merging requirement are the two conditions needed to determine the starting time and the intensity (i.e., pressure) of the foot of the main laser pulse. A dimensional analysis indicates that four dimensionless parameters can be identified: $\hat{T} = t_{\text{foot}}/t_{\text{prep}}$, $\hat{P} = P_{\text{foot}}/P_{\text{prep}}$, $\hat{m} = m_*/m_{\text{sh}}$, and $\hat{S} = S_*/S_b$, where $S_* = p_*/\rho_*^{5/3}$ and the * indicates the prepulse hydrodynamic variables. Using the two constraints and a set of numerical simulations in the strong shock regime with different prepulse durations and prepulse pressures, we have constructed a power-law relation among the dimensionless parameters ($\hat{P} \sim \hat{m}^{0.26} \hat{S}^{0.95}$ and $\hat{T} \sim \hat{S}^{0.08} / \hat{m}^{1.76}$), leading to the following simple formulas:

$$P_{\text{foot}}^{\text{Mb}} \approx 22.5 \left[\frac{100}{\Delta_{\text{sh}}^{\mu\text{m}}} \right]^{0.26} \left(\frac{\alpha_b}{3} \right)^{0.95} \left[\frac{t_{\text{prep}}^{\text{ns}}}{0.1} \right]^{-0.26} \left[\frac{P_{\text{prep}}^{\text{Mb}}}{10} \right]^{-0.18} \left[\frac{\rho_0^{\text{g/cm}^3}}{0.25} \right]^{1.45}, \quad (4)$$

$$t_{\text{foot}}^{\text{ns}} \approx 2.5 \left[\frac{\Delta_{\text{sh}}^{\mu\text{m}}}{100} \right]^{1.76} \left(\frac{\alpha_b}{3} \right)^{0.08}$$

$$\left[\frac{0.1}{t_{\text{prep}}^{\text{ns}}} \right]^{0.76} \left[\frac{10}{P_{\text{prep}}^{\text{Mb}}} \right]^{0.96} \left[\frac{\rho_0^{\text{g/cm}^3}}{0.25} \right].$$

Observe that the prepulse characteristics can be arbitrarily chosen. For a given prepulse (P_{prep} and t_{prep}) and assigned shell thickness Δ_{sh} , density, and rear-surface adiabat (α_b), Eqs. (4) yield the starting time and initial intensity of the foot of the main pulse to within 20%.

Rayleigh–Taylor Growth Rates

1. Analytic Results

The growth rates Γ of the ablative RT in the presence of finite shell entropy gradients can be calculated using a sharp boundary approximation¹⁰ that is valid for $kL_s \sim kd \gg 1$, where $k = \ell/R$ is the mode wave number, R is the in-flight radius, d is the target thickness, and $L_s = -S/S'$ is the entropy gradient scale length. The main difference from the standard ablative RT analysis^{1,2,10} is in the spatial behavior of the perturbation, which decays slower in the overdense shell as a result of the finite entropy gradient $\tilde{v} \sim \exp(-k\hat{h}x)$ [instead of the standard $\exp(-kx)$], where x is the distance from the ablation front and \hat{h} is the solution to the following transcendental equation:

$$\hat{h}^2 \approx 1 - \frac{g/\gamma L_s}{(\Gamma + k\hat{h}V_a)^2} + \frac{1}{\gamma k L_s}. \quad (5)$$

The last term on the right-hand side is negligible for $kL_s \gg 1$. It has been introduced *ad hoc* to recover the growth rates of long wavelengths that are not affected by either ablation or entropy gradients. Observe that the effect of finite entropy gradients *per se* is destabilizing ($\hat{h} < 1$); however, the overall effect of adiabat shaping is stabilizing due to the large increase in ablation velocity. In the limit of $kd \gg 1$, the RT relation reduces to

$$A\Gamma^2 + B\Gamma kV_a + Ck^2V_a^2 - D(kg - k^2V_aV_b) = 0, \quad (6)$$

where $A = \hat{h} + \hat{\rho}_b$, $B = (1 + \hat{h})^2$, $C = \hat{h}(1 + \hat{h})$, and $D = (1 - \hat{\rho}_b)$ with V_b and $\hat{\rho}_b$ representing the blowoff velocity and normalized density as defined in Eq. (6) of Ref. 2. Equations (5) and (6) must be solved simultaneously to determine the growth rate. It is important to note that an additional instability develops for finite L_s . This is a convective instability driven by the entropy gradients. The convective mode is internal to the shell and poses a serious threat to shell stability only when it grows sufficiently fast and develops the eigenfunction of a wide vortex stretching over a large portion of the shell. Its growth is typically much slower than the RT growth except for short wavelengths when $\Gamma \rightarrow \sqrt{g/\gamma L_s}$. Two-dimensional simulations (below) have indicated, however, that this mode grows to a very low amplitude simply because wide vortices are not seeded in the short-wavelength regime. Nevertheless, it is important to investigate the growth of the convective mode on a case-by-case basis since some target designs with extreme adiabat shaping may develop stronger convective instabilities.

2. Simulation Results

The results above are applied to a typical OMEGA cryogenic shell with an inner radius of 345 μm and a DT-ice layer of 85 μm . The shell is driven by a 30-kJ laser pulse (dashed curve in Fig. 94.19) yielding approximately 5.4×10^{14} neutrons on a flat, $\alpha \approx 3$ adiabat according to a one-dimensional simulation performed with the code *DRACO*.¹¹ We apply adiabat shaping to the same shell through relaxation, keeping $\alpha_b \approx 3$ on the rear surface. We use an 85-ps square prepulse with a pressure of 20 Mb and derive the corresponding main-pulse time and foot pressure from Eq. (4), yielding $P_{\text{foot}} \approx 25$ Mb and $t_{\text{foot}} \approx 1.2$ ns. The pulse in Fig. 94.19 (solid) shows approximately such characteristics when simulated with *DRACO*. The resulting shaped adiabat is shown in Fig. 94.20 (solid) and compared with the theoretical predictions (dotted) from Eq. (3). The 1-D performances of the flat- and shaped-adiabat implosions in terms of yield and peak areal density are within 30% and 7%, respectively. The ablation velocity during the flattop portion of the laser pulse is shown in Fig. 94.21 indicating that the shaped-adiabat implosion exhibits a considerably larger ablation velocity. Figure 94.22 shows the reduction in growth rate versus the mode number ℓ , as given by a series of 2-D *DRACO* simulations. The growth rates are calculated toward the end of the laser flattop when the growth is clearly exponential. Figure 94.22 also shows a comparison with the theoretical growth rates from Eqs. (5) and (6) calculated with 1-D average values obtained from *DRACO*: $\langle g \rangle = 345 \mu\text{m}/\text{ns}^2$ and $\langle V_a \rangle = 4.2 \mu\text{m}/\text{ns}^2$ for the flat adiabat, and $\langle g \rangle = 345 \mu\text{m}/\text{ns}^2$, $\langle V_a \rangle = 6.4 \mu\text{m}/\text{ns}$ and $L_s = 6 \mu\text{m}$ for the

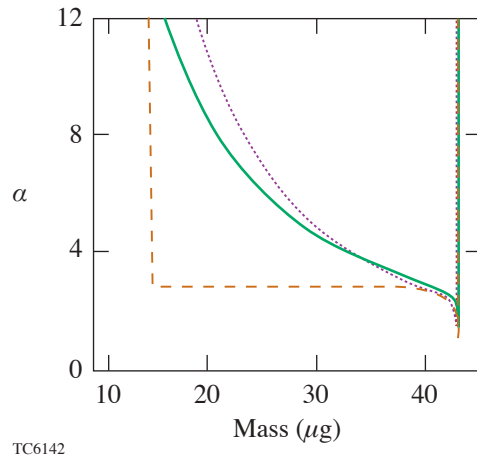


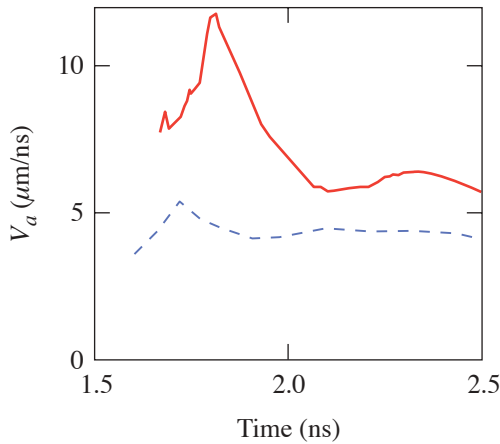
Figure 94.20

Flat adiabat (dashed) and shaped adiabat (solid) profiles induced by the pulses of Fig. 94.19. The dotted curve is the result of Eq. (3).

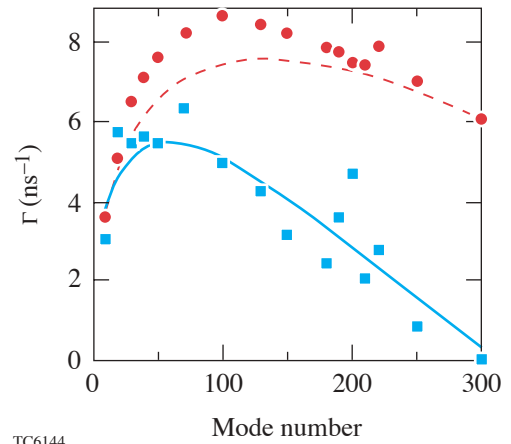
shaped adiabat. The large reduction in growth rates induced by the high ablation velocity indicates that adiabat shaping can significantly improve the stability of imploding shells.

The anomalous behavior of the growth rate in modes $\ell \sim 200$ shown in Fig. 94.22 is due to a resonant interaction of the RT mode with the convective mode. When the vorticities of the convective and RT modes have the same sign, they add constructively, thereby amplifying the growth rate of the surface perturbation. Figure 94.23 shows radial lineouts of the vortic-

ity for the shaped mode $\ell = 200$ case at two times. The first snapshot (a) is at the beginning of the convective–RT interaction. One can clearly see the RT mode at the ablation front and a larger amplitude convective mode just inside the ablation front. The second snapshot (200 ps later) shows a significant amplification of the RT vorticity as the ablation surface penetrates into the convective cell. This interaction occurs to varying extents at modes of all wavelengths; however, it is most noticeable in regimes where neither mode dominates. Note that under the right circumstance, this convective–RT



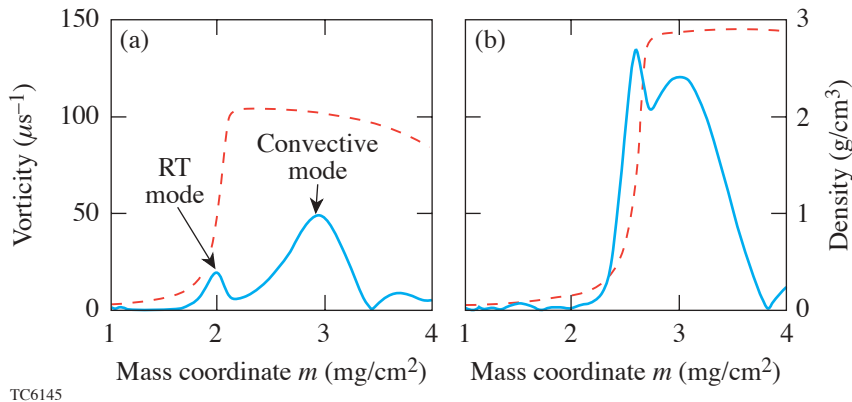
TC6143



TC6144

Figure 94.21
Time evolution of the ablation velocities during the power flattop for the flat-adiabat (dashed) and shaped-adiabat (solid) implosions.

Figure 94.22
RT growth rates versus mode number ℓ for the flat adiabat from DRACO (circles) and from Eqs. (5) and (6) (dashed) and for the shaped adiabat from DRACO (squares) and from Eqs. (5) and (6) (solid).



TC6145

Figure 94.23
Vorticity (solid line) and density (dashed line) for the shaped-adiabat, $\ell = 200$ case (a) at the beginning of the convective–RT mode interaction and (b) 200 ps later.

interaction may also be destructive, leading to lower-than-expected growth rates.

We have developed the theoretical basis (adiabat profiles, laser pulses, RT-growth rates) for laser-induced adiabat shaping by relaxation and have shown that RT growth rates can be reduced without significantly degrading 1-D capsule performances.

ACKNOWLEDGMENT

The authors would like to thank Profs. V. Goncharov and J. Sanz for many useful discussions on adiabat shaping and ablative RT. This work was supported by the U.S. Department of Energy Office of Inertial Confinement Fusion under Cooperative Agreement No. DE-FC03-92SF19460, the University of Rochester, and the New York State Energy Research and Development Authority. The support of DOE does not constitute an endorsement by DOE of the views in this article.

REFERENCES

1. S. E. Bodner, Phys. Rev. Lett. **33**, 761 (1974); H. Takabe *et al.*, Phys. Fluids **28**, 3676 (1985); J. Sanz, Phys. Rev. Lett. **73**, 2700 (1994).
2. R. Betti, V. N. Goncharov, R. L. McCrory, and C. P. Verdon, Phys. Plasmas **5**, 1446 (1998).
3. M. C. Herrmann, M. Tabak, and J. D. Lindl, Nucl. Fusion **41**, 99 (2001); A. Kemp, J. Meyer-ter-Vehn, and S. Atzeni, Phys. Rev. Lett. **86**, 3336 (2001); R. Betti, K. Anderson, V. N. Goncharov, R. L. McCrory, D. D. Meyerhofer, S. Skupsky, and R. P. J. Town, Phys. Plasmas **9**, 2277 (2002).
4. J. H. Gardner, S. E. Bodner, and J. P. Dahlburg, Phys. Fluids B **3**, 1070 (1991).
5. S. E. Bodner *et al.*, Phys. Plasmas **7**, 2298 (2000); L. Phillips *et al.*, Laser Part. Beams **17**, 225 (1999).
6. V. N. Goncharov, "Improved Performance of Direct-Drive ICF Target Designs with Adiabat Shaping Using an Intensity Picket," to be published in Physics of Plasmas.
7. L. J. Perkins, M. Tabak, J. Lindl, D. Bailey, J. Harte, A. Schmitt, S. Obenschain, and R. Betti, Bull. Am. Phys. Soc. **47**, 101 (2002).
8. J. D. Lindl and W. C. Mead, Phys. Rev. Lett. **34**, 1273 (1975).
9. T. J. B. Collins and S. Skupsky, Phys. Plasmas **9**, 275 (2002).
10. A. R. Piriz, J. Sanz, and L. F. Ibañez, Phys. Plasmas **4**, 1117 (1997).
11. D. Keller, T. J. B. Collins, J. A. Delettrez, P. W. McKenty, P. B. Radha, B. Whitney, and G. A. Moses, Bull. Am. Phys. Soc. **44**, 37 (1999).

Demonstration of a Room-Temperature Single-Photon Source for Quantum Information: Single-Dye-Molecule Fluorescence in a Cholesteric Liquid Crystal Host

Introduction

Quantum information in the form of quantum communications and quantum computing (see Refs. 1–33) is currently an exceedingly active field. Numerous theoretical concepts promise powerful quantum-mechanics-based tools³⁴ that, to date, wait for realization pending the arrival of reliable hardware.^{1–33} A *single-photon source* (SPS)³⁵ that efficiently produces photons with *antibunching* characteristics^{36–38} is one such pivotal hardware element for quantum information technology. Using an SPS, secure quantum communication will prevent any potential eavesdropper from intercepting a message without the receiver noticing.^{25,30,39–41} In another implementation, an SPS becomes the key hardware element for quantum computers with linear optical elements and photodetectors.^{42–52} Again, its practical realization is held back in part because of the difficulties in developing robust sources of antibunched photons on demand. In spite of several solutions for SPS's presented in the literature, significant drawbacks remain. The drawbacks are the reason for current quantum communication systems being baud-rate bottlenecked, causing photon numbers from ordinary photon sources to attenuate to the single-photon level (~ 0.1 photon per pulse on average).^{25,39,41} An efficient (with an order-of-magnitude-higher photon number per pulse) and reliable light source that delivers a train of pulses containing one, and only one, photon is a very timely challenge. To meet this challenge, several issues need to be addressed, from achieving full control of the quantum properties of the source to easy handling and integrability of these properties in a practical quantum computer and/or communication setup. In addition, in quantum information systems it is desirable to deal with single photons synchronized to an external clock, namely, *triggerable* single photons.⁵³ *Polarization states* of single photons are also important since they enable polarization-qubit encoding of information.

The critical issue in producing single photons in another way than by trivial attenuation of a beam is the *very low concentration of photon emitters* dispersed in a host, such that within a laser focal spot only one emitter becomes excited, emitting only one photon at a time. In initial demonstrations of

resonance-fluorescence photon antibunching,⁵⁴ SPS's possessed a random photon-emission time.^{54–63} Single photons “on demand,” i.e., triggerable single photons, were obtained only recently.^{53,64–76} De Martini *et al.*⁶⁴ used an active microcavity excited by a mode-locked laser. In experiments by Kim *et al.*,⁶⁵ Imamoglu *et al.*,⁶⁶ and Moreau *et al.*,⁶⁷ a single-photon turnstile device utilized Coulomb blockade of tunneling for electrons and holes in a mesoscopic double-barrier p - n junction. Single photons were generated at the modulation periodicity of the junction voltage. Michler *et al.*⁶⁸ and Santory *et al.*⁶⁹ demonstrated single-photon devices using pulsed-laser excitation of a single AlGaAs quantum dot. Electrically driven single photons (also at cryogenic temperatures as in Refs. 65–69) were obtained by Yuan *et al.*^{70,71} Experiments by Brunel *et al.*,⁷² Lounis and Moerner,⁷³ and Treussart *et al.*⁷⁴ were based on an entirely different system, namely single dye molecules embedded at low concentration within organic single-crystal platelets or covered by a polymer layer. Single photons were triggered either by a combination of cw laser excitation and an electronic signal⁷² or by short-pulse laser irradiation.^{73,74} Most of these sources, e.g., Refs. 65–71, operate reliably only at liquid He temperature—a major impediment to widespread use. To date, three approaches are known to be eligible for *room-temperature* SPS implementation, two inorganic and one organic. The first inorganic, room-temperature approach involves a mono-/polycrystal diamond and one of its color centers.^{59–61,75,76} The second inorganic approach uses single-colloidal CdSe/ZnS quantum dots (Michler *et al.*,⁷⁷ Lounis *et al.*,⁷⁸ and Messin *et al.*⁷⁹). The alternative, organic approach,^{58,62,63,72–74} based on numerous previous experiments around liquid-He temperature,^{80–83} uses a vapor-phase-sublimated host crystal of para-terphenyl doped with an emitting species, terrylene.^{62,73}

As acceptable as these approaches may be strictly on quantum-optics grounds, all suffer from shortcomings that will delay quantum information from gaining a technology foothold in the near future. None of these sources is used in practical, civilian systems. Their specific shortcomings include the following: (1) Polarization of single photons varies

from one emitter to another (nondeterministic); (2) single photons are produced with *very low efficiency* and *polluted* by additional photons at about the same frequency from the host material;⁵³ and (3) alternatives such as color centers in diamond and colloidal CdSe/ZnS quantum dots possess unacceptably long fluorescence lifetimes (for instance, the diamond color center has a 11.6-ns and 22.7-ns fluorescence lifetime in mono- and polycrystal, and CdSe-ZnS quantum dots have a fluorescence lifetime of ~ 22 ns).

The organic, room-temperature SPS approach is based on using a chromophore molecule as the single emitter. The key advantage of chromophore molecules is that their excited-state lifetime of only a few nanoseconds permits excitation repetition rates above ~ 100 MHz. In *amorphous* media such molecules tend to be *unstable*: they are blinking at various characteristic time intervals, change their spectral behavior, and can be easily bleached. Recently, however, single terrylene molecules have been doped into *p*-terphenyl molecular crystals (10^{-11} moles of terrylene per mole of *p*-terphenyl) prepared by a sublimation procedure that produced tiny platelets.^{62,73} In this host, the chromophore is protected from exposure to diffusing quenchers (such as oxygen) and benefits from strong phonon emission into the host, preventing rapid thermal decomposition of the chromophore under intense irradiation. In Ref. 73 it was found that for “thick” *p*-terphenyl crystals (~ 10 μm), this system becomes extremely photostable, allowing hours of continuous illumination of individual molecules without photobleaching. It assures long-term spectral stability and reproducibility from one terrylene absorber to the next.^{84,85} Pumped by periodic, short-pulse laser radiation, single photons were generated at predetermined times at pump-pulse-repetition rates within the accuracy of the emission lifetime (~ 3.8 ns). Technical implementation of this system is difficult because these monoclinic, sublimation-produced microcrystals are stress sensitive and fragile. In addition, terrylene’s molecular dipole moment in the *p*-terphenyl host crystal takes on an orientation perpendicular to the platelet’s surface (i.e., perpendicular to the incident light’s E field).⁷³ This, in turn, leads to poor coupling with the polarized excitation light, prompting poor fluorescence emission even at high excitation intensities (saturation intensity is about $1 \text{ MW}/\text{cm}^2$ at room temperature). In spite of the elegance of the terrylene/*p*-terphenyl experiments, this technology must be considered unrealistic for practical application. Its weak point is also a background from “ordinary photons” from out-of-focus molecules or Raman scattering because of the very high pumping intensities required. Emitted photons are not polarized *deterministically* (there is no known efficient method for aligning

rapidly a multitude of micrometer-sized, monoclinic crystal-lites relative to one another). Note that noncrystalline, amorphous hosts, e.g., polymers,⁶³ neither (1) offer the same spectral stability in single-molecule emission even in the case of terrylene, nor (2) provide long-time protection against bleaching. To date, *no crystal hosts* other than the fragile, sublimated *p*-terphenyl flakes have been proposed in *single-molecule room-temperature* experiments.

This article describes some new approaches toward implementing an efficient, deterministically polarized SPS on demand: (1) using *liquid crystal hosts* (including liquid crystal polymers) to preferentially align the emitter molecules for maximum excitation efficiency (deterministic molecular alignment will also provide deterministically polarized output photons); (2) using planar-aligned cholesteric (chiral-nematic) liquid crystal hosts⁸⁶ as 1-D photonic-band-gap microcavities^{87–91} tunable to the dye fluorescence band;^{92–93} and (3) using liquid crystal technology to prevent dye bleaching.

Cholesteric-Liquid-Crystal, 1-D Photonic-Band-Gap Materials

In planar cholesterics (Fig. 94.24) that for visualization purposes can be described as consisting of, but in reality not comprising, a layered structure, the axes of the molecular director (far-right set of arrows in Fig. 94.24) rotate monotonically to form a periodic helical structure with pitch P_0 .⁸⁶ With few exceptions, liquid crystal media are non-chiral and require

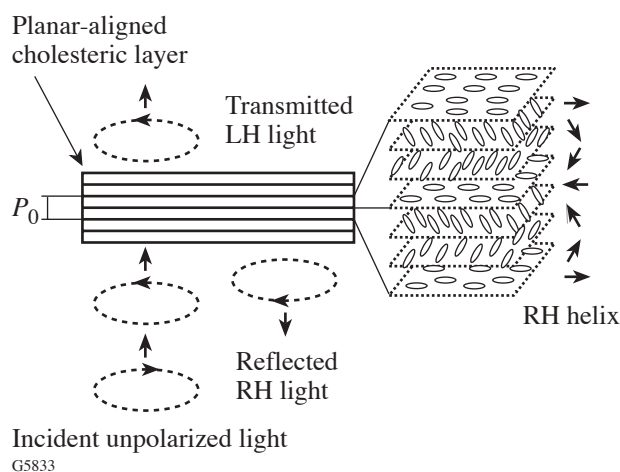


Figure 94.24
Transmission and reflection by a cholesteric liquid crystal layer near selective reflection conditions.

additives to induce the chiral order. Dependent on the chirality-inducing additive, the final structure may show either a right- or a left-handed sense of rotation.

When a solid cholesteric is flipped on its side and inspected by a high-resolution tool such as an atomic force microscope, the periodic pitch becomes observable through height variations along the helical axis. For instance, Fig. 94.25 shows such a topography for a Wacker cyclo-tetrasiloxane-oligomer cholesteric liquid crystal (OCLC)⁹⁴ platelet. Periodic stripes in the image correspond to one-half of the pitch length.

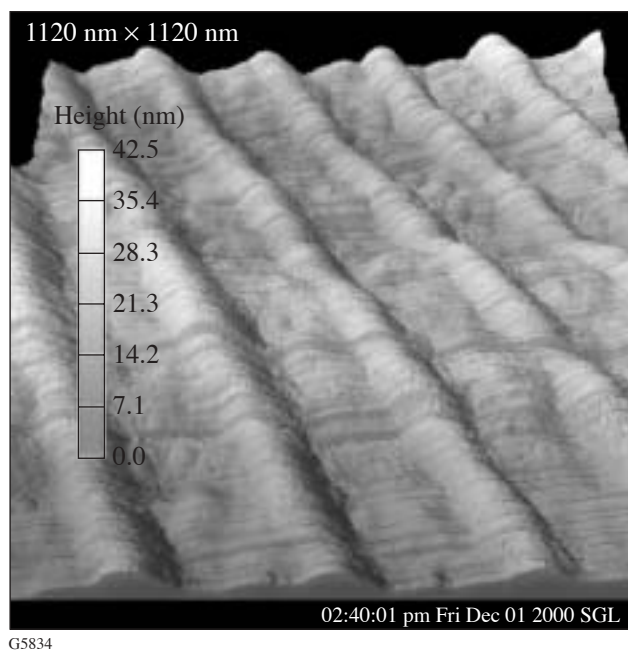


Figure 94.25
Perspective view of the AFM topographical image of a planar-aligned Wacker OCLC layer ($1.12\text{-}\mu\text{m} \times 1.12\text{-}\mu\text{m}$ scan).

For liquid crystal thicknesses $\geq 10\ \mu\text{m}$, the reflectance of normally incident, circularly polarized light with electric-field vector rotation opposite to the rotation of molecules in the helical structure (Bragg condition) approaches 100% within a band centered at $\lambda_0 = n_{\text{av}}P_0$, where $n_{\text{av}} = (n_e + n_o)/2$ is the average of the ordinary and extraordinary refractive indices of the medium. This is the so-called selective reflection of cholesteric liquid crystals. The bandwidth is $\Delta\lambda = \lambda_0\Delta n/n_{\text{av}}$, where $\Delta n = n_e - n_o$. Such a periodic structure can also be viewed as a 1-D photonic crystal, with a bandgap within which propagation of light is forbidden. For emitters located within such a structure, the rate of spontaneous emission is suppressed within the spectral stop band and enhanced near the band

edge.⁹⁵ Several groups have reported lasing in photonic band-gap material hosts, including cholesteric liquid crystals,^{95–98} with spectral emission features underscoring the validity of this concept. Generation of strongly circularly polarized photoluminescence from planar layers of glass-forming chiral-nematic liquid crystals was also reported.^{92–93} Light-emitting dopants at 0.2-wt% concentration were embedded in these liquid crystals. The degree of circularly polarized photoluminescence, i.e., its asymmetry,^{92–93}

$$G_e \equiv 2(I_L - I_R)/(I_L + I_R), \quad (1)$$

where I_R and I_L denote the right- and left-handed emission intensity, respectively (see Fig. 94.26), was found to be equal to maximum value [~ -2 (Refs. 92 and 93)].

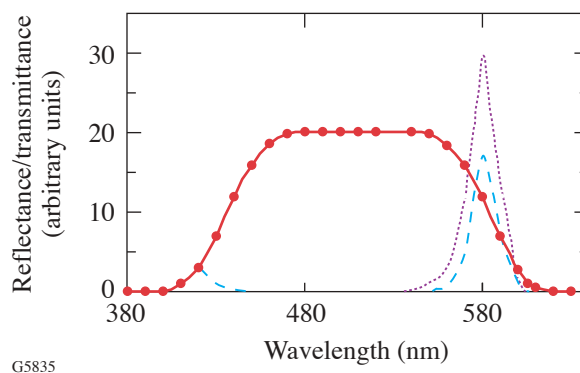


Figure 94.26
Tutorial schematic of the wavelength dependence between the photonic stop-band reflectance (solid line), dye photoluminescence intensity (dotted line), and photoluminescence polarization asymmetry G_e inside the band (dashed line).

Matching of λ_0 of cholesteric liquid crystal with a dye-fluorescence band will be the subject of a future article. In our current experiments, Wacker OCLC (see Fig. 94.27) with λ_0 outside the terrylene-dye-fluorescence band was doped with terrylene (Fig. 94.28) at an extremely low concentration such that the final sample contained only a few molecules per μm^2 irradiation area. Cast from solution on single microscope cover-glass slips, the samples ranged in thickness from $\sim 50\ \text{nm}$ to several micrometers. In some experiments, we also used terrylene-doped layers of monomeric cyanobiphenyl liquid crystal 5CB with chiral additive CB15. The 5CB liquid crystal layers were placed between two microscope cover-glass slips separated by glass-bead spacers.

To minimize false fluorescence contributions by contaminants during single-molecule-fluorescence microscopy, rigorous cleaning of glass substrates is mandatory. For this purpose, the microscope glass slips (Corning, 0.17-mm thickness) were etched in a piranha solution and rinsed in deionized water. Proper terrylene concentration for single-molecule fluorescence microscopy was established by iterative trial and error. In sequential dilution steps of terrylene in chlorobenzene solvent, solutions were spun onto glass slips, and for each concentration, confocal fluorescence microscopy determined the final emitter concentration per irradiation volume. Once single molecules were predominantly observed, the dilution endpoint was reached. This final terrylene solution was mixed with Wacker OCLC starting material (8% weight concentra-

tion of oligomer). For planar alignment, standard buffing procedures could not be employed at the risk of introducing dirt particles. Two alternate methods were found satisfactory: either the film was *flow aligned* by letting the OCLC solution run down a vertically inclined glass slip, or a special glass cylinder was rolled unidirectionally across a spin-coated OCLC layer heated to the isotropic state. Figure 94.29 shows an optical microscope image of a planar-aligned OCLC layer with “oily streak” defects typical for a planar structure of cholesteric liquid crystals (both monomeric and oligomeric).^{99–101} The influence of the oily streak defects on a single-molecule fluorescence will be considered in future work. We mention them here to show evidence of a planar structure of OCLC prepared by our group.

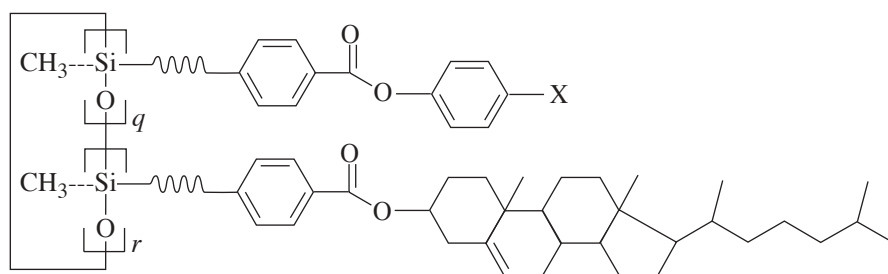
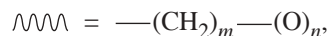
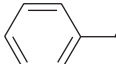
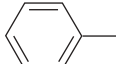


Figure 94.27
Molecular structure of Wacker siloxane OCLC (from Ref. 94).

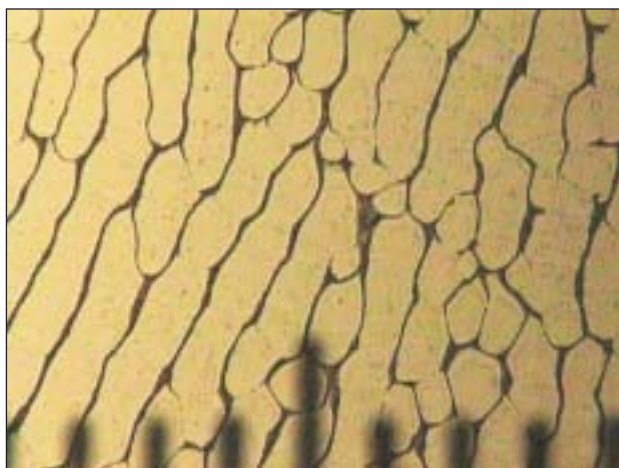


where $m = 3, 4, 5, 6, 8, 10$ and $n = 0, 1$;

$q + r = 3, 4, 5, 6, \text{ or } 7$ and $q/(q + r) = 0 \text{ to } 1$

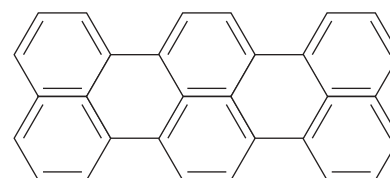
$X = \text{Cl}, \text{OMe}, \text{O}(\text{CH}_2)_3\text{H},$  $\text{---} \text{CN}$ or  $\text{---} (\text{CH}_2)_p\text{H}$, where $p = 2, 4, \text{ or } 5$

G5836



G5838

Figure 94.29
Optical microscopy of “oily streak” defects of planar-aligned Wacker OCLC layer.



G5837

Figure 94.28
Molecular structure of terrylene dye.

Experimental Setup for Single-Dye-Molecule Fluorescence Microscopy and Antibunching Correlation Measurements

Photon antibunching correlation measurements are carried out using the setup shown in Figs. 94.30 and 94.31. The terylene-doped liquid crystal sample is placed in the focal plane of a 0.8-N.A. microscope objective (Witec alpha-SNOM platform). The sample is attached to a piezoelectric, XYZ translation stage. Light emitted by the sample is collected by a confocal setup using a 1.25-N.A., oil-immersion objective together with an aperture formed by the core of a multimode optical fiber. The cw, spatially filtered (through a single-mode

fiber), linearly polarized (contrast $10^5:1$), 532-nm diode-pumped Nd:YAG laser output excites single molecules. In focus, the intensities used are of the order of several kW/cm^2 . The collection fiber is part of a non-polarization-sensitive 50:50 fiber splitter that forms the two arms of a Hanbury Brown and Twiss correlation setup¹⁰² (Fig. 94.31). Residual, transmitted excitation light is removed by two consecutive dielectric interference filters yielding a combined rejection of better than six orders of magnitude at 532 nm. The fluorescence band maximum of terylene molecules used in our experiments lies in a spectral region near 579 nm with a bandwidth of ~ 30 nm.



G5839

Figure 94.30
Witec alpha-SNOM microscope with a laser.

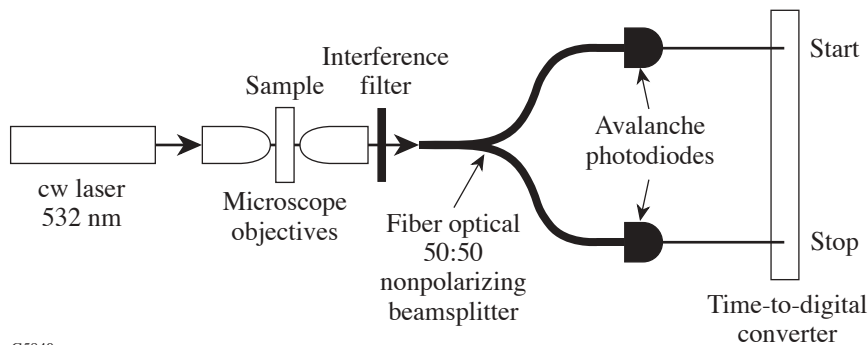
Photons in the two Hanbury Brown and Twiss arms are detected by identical, cooled avalanche photodiodes in single-photon-counting Geiger mode. The time interval between two consecutively detected photons in separate arms is measured by a 68-ns-full-scale time-to-digital converter using a conventional start-stop protocol. Within this converter's linear range, the time uncertainty in each channel corresponds to 25 ps.

It has been proven experimentally (see, e.g., Refs. 62 and 63) that a very good approximation of the autocorrelation function $g^{(2)}(\tau)$ comes directly from the coincidence counts (event distribution) $n(\tau)$, for relatively low detection efficiency and therefore low counting rate. That is why we consider that $n(\tau)$ is proportional to the autocorrelation function $g^{(2)}(\tau)$. For single photons, $g^{(2)}(0) = 0$, indicating the absence of pairs, i.e., antibunching.

Experimental Results

1. Single-Dye-Molecule Fluorescence in a Cholesteric Liquid Crystal Host

Figure 94.32 shows terylene-dye-molecule-fluorescence images obtained by confocal fluorescence microscopy: (a) single terylene molecules embedded in a Wacker OCLC host ($\lambda_0 = 2.2 \mu\text{m}$); (b) clusters of terylene molecules spin



G5840

Figure 94.31
Experimental setup for photon antibunching correlation measurements.

coated from chlorobenzene solution onto a bare cover-glass slip. For both images, the scan direction is from left to right and line by line from top to bottom. The scan dimensions are $10\ \mu\text{m} \times 10\ \mu\text{m}$. Most single molecules in our samples exhibited fluorescence blinking in time, with a period ranging from several milliseconds up to several seconds. In Fig. 94.32, this “blinking” behavior by single molecules manifests itself as bright and dark horizontal stripes in image (a). These features are absent in emission images from clusters (b).

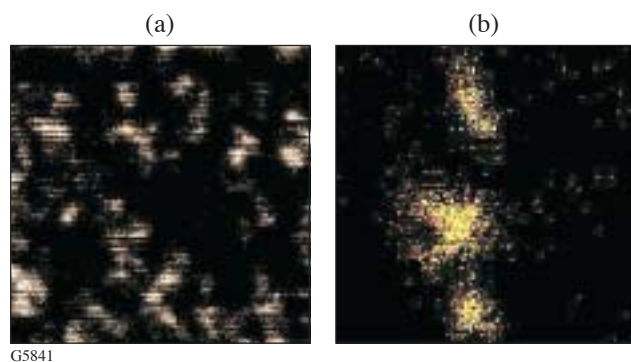


Figure 94.32

Terrylene molecule fluorescence: (a) single-molecule fluorescence from the OCLC host; (b) fluorescent-molecule clusters on a bare surface. Resolution of the optical system is $\sim 0.5\ \mu\text{m}$.

Blinking is a common phenomenon and convincing evidence of the single-photon nature of the source. Several mechanisms are suggested to explain the blinking behavior: for instance, “shelving” (triplet blinking) to the long-living state, and fluctuations in the photo-physical parameters of the molecule and its local environment.¹⁰³ By modeling the molecule as a three-level system (singlet ground state S_0 , excited-state level S_1 , and triplet state T_1) as depicted in Fig. 94.33, “triplet blinking” can be explained by a population of T_1 level that is often a dark state in fluorescent dyes.

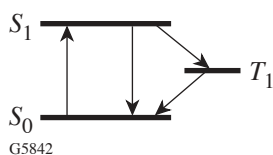


Figure 94.33

Three-level model for molecular fluorescence.

2. Photon Antibunching Correlation Measurements

Figure 94.34 shows a coincidence-count histogram $n(\tau)$ from (a) host-free single terrylene molecules (left) and (b) an

assembly of many uncorrelated molecules within the excitation volume [Fig. 94.32(b)]. The scan speed is $\sim 3\ \text{s}$ per line (512 pixels). The left histogram exhibits a dip at $\tau=0$. The measured signal-to-background ratio of our experiments ranges from 2 to 30, so the probability that a photon from the background triggers a coincidence with a photon from the molecule is very low. Because $n(\tau)$ is proportional to the autocorrelation function $g^{(2)}(\tau)$, $n(0) \sim 0$ means that $g^{(2)}(0) \sim 0$ in our experiments. Two fluorescence photons are not observed within an arbitrarily short time interval. This fluorescence antibunching is due to the finite radiative lifetime of the molecular dipole and is therefore clear proof that we observed the emission of one, and only one, molecule. The histogram on the right from a multiple of uncorrelated molecules shows no such dip at $\tau=0$, i.e., no antibunching.

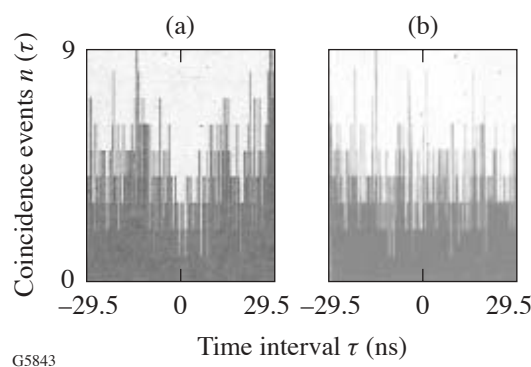


Figure 94.34

Histograms of coincidence events of single-terrylene-molecule fluorescence on a bare glass substrate (a) and from an assembly of several uncorrelated molecules within the excitation volume (b).

To eliminate any potential for leaked excitation light causing the dip at $\tau=0$, the sample was replaced with a bare glass slide and one blocking interference filter was removed. The coincidence histogram for this condition is depicted in Fig. 94.35(b). No antibunching is observed. Two interference filters attenuated excitation light so strongly that no counts other than dark counts of avalanche photodiodes were observed during the same time interval.

Figure 94.36 shows the results of doping terrylene into liquid crystals. The histogram of coincidence events $n(\tau)$ [Fig. 94.36(a)] exhibits a dip at $\tau=0$ indicating photon antibunching in the fluorescence of the single molecules in the Wacker OCLC host; no antibunching is observed in the fluorescence from an assembly of several uncorrelated molecules in the same host, different sample [Fig. 94.36(b)]. The histogram in Fig. 94.36(a) is noteworthy in that it demonstrates that

several *single* molecules can sequentially contribute to an antibunching histogram without loss of $\tau = 0$ contrast, as in practice the long integration time and competing molecule-bleaching events make obtaining an entire, good-contrast histogram from only one molecule too much a matter of luck. When the initial single molecule was bleached, the sample was advanced to another single molecule while the photon-correlation count continued. This finding is crucial for future device implementation.

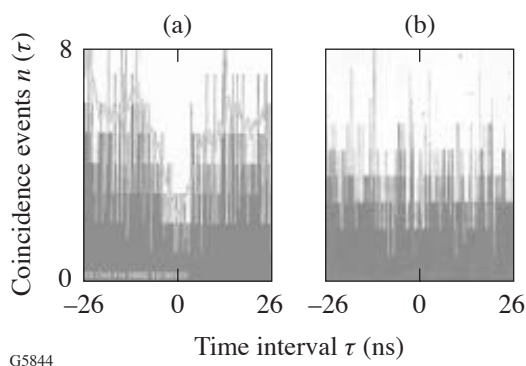


Figure 94.35
The histograms of coincidence events of the single-terrylene-molecule fluorescence on a bare glass substrate (a) and of the radiation of excited green laser beam (b).

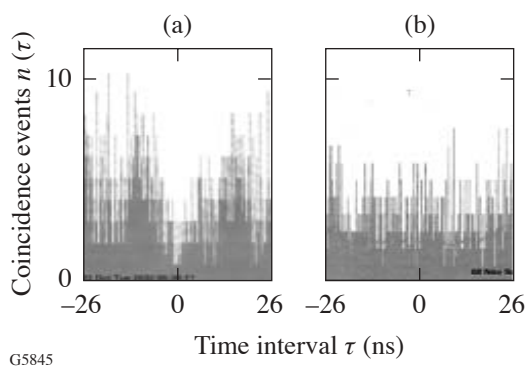


Figure 94.36
The histograms of coincidence events of the single-terrylene-molecule fluorescence in a Wacker OCLC host (a) and of an assembly of several uncorrelated molecules (b).

3. Preventing Dye Bleaching in Liquid Crystal Hosts

Practical device implementation also depends on photochemical stability of both emitters and hosts. We increased terrylene fluorescence stability in monomeric liquid crystal hosts by saturating the liquid crystals with helium in a sealed

glovebox for 1 h. Oxygen, which is mostly responsible for dye bleaching, is displaced by helium during this procedure. Ground-state oxygen can form highly reactive singlet oxygen by quenching a triplet state of the dye. The singlet oxygen can then react with its surroundings, including dye molecules. Figure 94.37 shows fluorescence-bleaching results of terrylene molecules at two-orders-of-magnitude-higher concentration than in single-molecule experiments in different liquid crystal hosts: either immobilized in an oligomer cholesteric liquid crystal or dissolved in monomeric cyanobiphenyl 5CB saturated with helium (both at identical excitation intensity and identical terrylene volume concentration). Over the course of more than 1 h, *no* dye bleaching was observed in the *oxygen-depleted* liquid crystal host (upper curve).

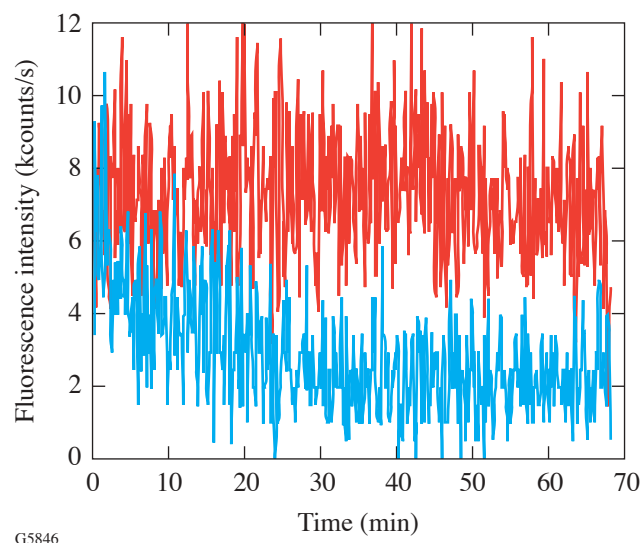


Figure 94.37
Fluorescence bleaching behavior of an assembly of terrylene molecules as a function of time and in two different liquid crystal hosts.

Dye bleaching is not a critical impairment for an efficient SPS, but it is an important factor for device simplicity and cost. When one molecule is bleached, the system can be rapidly realigned to utilize another isolated dye molecule, allowing practically continuous source action (see left histograms on Figs. 94.34–94.36).

Both well-known liquid crystal hosts are photochemically stable and do not absorb excitation light. In addition, incident intensities are too low for two-photon absorption processes. The absorption by a single molecule is insufficient for significant host heating.

Conclusion

A robust, room-temperature single-photon source based on fluorescence from a single dye molecule (fluorescence antibunching) was demonstrated for the first time for liquid crystal hosts. Planar-aligned, 1-D photonic-band-gap structures in dye-doped cholesteric oligomer were prepared. Avoiding bleaching of the terrylene dye molecules for excitation times >1 h was achieved by innovative preparation procedures. Liquid crystal hosts further increase the efficiency of the source (1) by aligning the dye molecules along a direction preferable for maximum excitation efficiency; and (2) by tuning a 1-D photonic-band-gap microcavity of planar-aligned cholesteric liquid crystal to the dye fluorescence band. Source-efficiency issues will be addressed in a subsequent article.

Future work will be directed toward increasing the efficiency, life, and polarization purity of the single-photon source by improved selection of dye, liquid crystal, and the photonic-band-gap structure matching with the dye-fluorescence band. A pulsed laser source will be used to create a real quantum cryptography system with a cholesteric-liquid-crystal, single-photon source on demand.

ACKNOWLEDGMENT

The authors acknowledge the support by the U.S. Army Research Office under Award No. DAAD19-02-1-0285. The work was also supported by the U.S. Department of Energy Office of Inertial Confinement Fusion under Cooperative Agreement No. DE-FC03-92SF19460, the University of Rochester, and the New York State Energy Research and Development Authority. The support of DOE does not constitute an endorsement by DOE of the views expressed in this article. Receipt of OCLC starting material from Dr. F. Kreuzer of Wacker, Munich, is gratefully acknowledged. The authors thank L. Novotny, K. Marshall, J. Shojaie, O. Hollricher, and T. Kosc for advice and help, J. Howell and D. A. Voloshchenko for fruitful discussions, S. Papernov for help with AFM imaging of OCLC, and J. Starowitz for help in the Optical Materials Laboratory.

REFERENCES

- M. A. Nielsen and I. L. Chuang, *Quantum Computation and Quantum Information* (Cambridge University Press, Cambridge, England, 2001).
- J. Gruska, *Quantum Computing*, Advanced Topics in Computer Science Series (McGraw-Hill, London, 1999).
- M. Brooks, ed. *Quantum Computing and Communications* (Springer, London, 1999).
- C. P. Williams and S. H. Clearwater, *Explorations in Quantum Computing* (TELOS, Santa Clara, CA, 1998).
- D. Deutsch, *The Fabric of Reality* (Penguin, London, 1998); T. Siegfried, *The Bit and The Pendulum: From Quantum Computing to M Theory—The New Physics of Information* (Wiley, New York, 2000).
- S. Singh, *The Code Book: The Science of Secrecy from Ancient Egypt to Quantum Cryptography* (Anchor Books, New York, 2000).
- J. R. Brown, *Minds, Machines, and Multiverse: The Quest for the Quantum Computer* (Simon & Schuster, New York, 2000).
- P. Kumar, G. M. D'Ariano, and O. Hirota, eds. *Quantum Communication, Computing and Measurement 2* (Kluwer Academic/Plenum Publishers, New York, 2000).
- D. Bouwmeester, A. K. Ekert, and A. Zeilinger, eds. *The Physics of Quantum Information: Quantum Cryptography, Quantum Teleportation, Quantum Computation*, 1st ed. (Springer, Berlin, 2000).
- H.-K. Lo, T. Spiller, and S. Popescu, eds. *Introduction to Quantum Computation and Information* (World Scientific, Singapore, 1998).
- S. L. Braunstein, *Quantum Computing: Where Do We Want to Go Tomorrow?* (Wiley-VCH, Weinheim, 1999).
- S. L. Braunstein, H.-K. Lo, and K. Pieter, *Scalable Quantum Computers: Paving the Way to Realization*, 1st ed. (Wiley-VCH, Berlin, 2001).
- G. J. Milburn, *The Feynman Processor: Quantum Entanglement and the Computing Revolution*, Frontiers of Science (Perseus Books, Reading, MA, 1998).
- N. Gisin *et al.*, Rev. Mod. Phys. **74**, 145 (2002); S. Ya. Kilin, Usp. Fiz. Nauk **42**, 435 (1999).
- A. Steane, Rep. Prog. Phys. **61**, 117 (1998).
- D. Aharonov, in *Annual Reviews of Computational Physics. VI*, edited by D. Stauffer (World Scientific, Singapore, 1999), pp. 259–346.
- A. Galindo and M. A. Martin-Delgado, Rev. Mod. Phys. **74**, 347 (2002).
- D. P. DiVincenzo, Science **270**, 255 (1995).
- A. K. Ekert and R. Jozsa, Rev. Mod. Phys. **68**, 733 (1996).
- J. Preskill, Course information for Physics 219/Computer Science 219 available at <http://theory.caltech.edu/~preskill/ph229> (California Institute of Technology, Pasadena, CA, 2000).
- A. Y. Kitaev, Russ. Math. Surv. **52**, 1191 (1997).
- The Center for Quantum Computation (Oxford) (<http://www.qubit.org>).
- The International Conference on Quantum Information (ICQI) and the Eighth Rochester Conference on Coherence and Quantum Optics (CQO8) Rochester, NY, 10–16 June 2001; see <http://www.optics.rochester.edu/~stroud/conference>.
- G. Giedke, "What is Quantum Information Processing?," available at www.maqitech.com/products/whatsqip.php.
- P. L. Knight and R. W. Boyd, eds., J. Mod. Opt. (Special Issue: Quantum Communication) **41** (12) (1994); G. Rarity, P. R. Tapster, and P. M. Gorman, eds., J. Mod. Opt. (Special Issue: Technologies for Quantum Communications) **48** (13) (2001); P. G. Kwiat, ed., New J. Phys. (Focus on Quantum Cryptography) **4** (2002).

26. S. Braunstein and H.-K. Lo, eds., *Fortschr. Phys.* (Special Focus Issue: Experimental Proposals for Quantum Computation) **48** (9–11) (2000).
27. I. Chuang, *Nature* **420**, 25 (2002); *Quantum Information and Computation* **1** (1) (2001).
28. C. H. Bennett, *Phys. Today* **48**, 24 (1995).
29. I. Walmsley and P. Knight, *Opt. Photonics News*, November 2002, 42.
30. W. P. Risk and D. S. Bethune, *Opt. Photonics News*, July 2002, 26.
31. A. Zeilinger, *Phys. World* **11**, 35 (1998).
32. M. A. Nielsen, *Sci. Am.* **287**, 67 (2002).
33. See <http://www.sciam.com> for Scientific American articles related to quantum information science.
34. J. A. Wheeler and W. H. Zurek, eds. *Quantum Theory and Measurement*, Princeton Series in Physics (Princeton University Press, Princeton, NJ, 1983).
35. P. Jonsson, “Generation, Detection and Applications of Single Photons,” Ph.D. thesis, Royal Institute of Technology, 2002; “Solid State Sources for Single Photons (S4P),” available at <http://www.iota.u-psud.fr/~S4P/>.
36. D. F. Walls and G. J. Milburn, *Quantum Optics* (Springer-Verlag, Berlin, 1995), p. 42.
37. L. Davidovich, *Rev. Mod. Phys.* **68**, 127 (1996).
38. U. Mets, in *Fluorescence Correlation Spectroscopy: Theory and Applications*, edited by R. Rigler and E. Elson, Springer Series in Chemical Physics, Vol. 65 (Springer, Berlin, 2001), pp. 346–359.
39. R. J. Hughes, G. L. Morgan, and C. G. Peterson, *J. Mod. Opt.* **47**, 533 (2000); R. J. Hughes *et al.*, *New J. Phys.* **4**, 43 (2002); J. G. Rarity *et al.*, *New J. Phys.* **4**, 82 (2002).
40. D. Stucki *et al.*, *New J. Phys.* **4**, 41 (2002); E. Klarreich, *Nature* **418**, 270 (2002).
41. A. V. Sergienko *et al.*, *Phys. Rev. A* **60**, R2622 (1999); B. C. Jacobs and J. D. Franson, *Opt. Lett.* **21**, 1854 (1996).
42. E. Knill, R. Laflamme, and G. J. Milburn, *Nature* **409**, 46 (2001); E. Knill, R. Laflamme, and G. Milburn, “Efficient Linear Optics Quantum Computation” (2000), available at <http://arXiv.org/abs/quant-ph/0006088>.
43. J. Calsamiglia, “Quantum Information Processing and Its Linear Optical Implementation,” Ph.D. thesis, University of Helsinki, 2001.
44. Q. A. Turchette *et al.*, *Phys. Rev. Lett.* **75**, 4710 (1995).
45. C. K. Law, *J. Mod. Opt.* **44**, 2067 (1997).
46. N. J. Cerf, C. Adami, and P. G. Kwiat, *Phys. Rev. A* **57**, R1477 (1998).
47. J. C. Howell and J. A. Yeazell, *Phys. Rev. Lett.* **75**, 198 (2000).
48. *Ibid.*, *Phys. Rev. A* **61**, 052303 (2000).
49. *Ibid.*, 012304 (2000).
50. T. B. Pittman, B. C. Jacobs, and J. D. Franson, *Phys. Rev. Lett.* **88**, 257902 (2002).
51. *Ibid.*, *Phys. Rev. A* **64**, 062311 (2001).
52. A. Shields, *Science* **297**, 1821 (2002).
53. S. Benjamin, *Science* **290**, 2273 (2000).
54. H. J. Kimble, M. Dagenais, and L. Mandel, *Phys. Rev. Lett.* **39**, 691 (1977).
55. C. K. Hong and L. Mandel, *Phys. Rev. Lett.* **56**, 58 (1986).
56. F. Diedrich and H. Walther, *Phys. Rev. Lett.* **58**, 203 (1987).
57. P. Grangier, G. Roger, and A. Aspect, *Europhys. Lett.* **1**, 173 (1986).
58. W. P. Ambrose *et al.*, *Chem. Phys. Lett.* **269**, 365 (1997).
59. C. Kurtsiefer *et al.*, *Phys. Rev. Lett.* **85**, 290 (2000).
60. R. Brouri *et al.*, *Opt. Lett.* **25**, 1294 (2000).
61. S. Mayer, “N/V-Zentren als Einzel-Photonen-Quelle,” Ph.D. thesis, Ludwig-Maximilians-Universität München, 2000.
62. L. Fleury *et al.*, *Phys. Rev. Lett.* **84**, 1148 (2000).
63. F. Treussart *et al.*, *Opt. Lett.* **26**, 1504 (2001).
64. F. De Martini, G. Di Giuseppe, and M. Marrocco, *Phys. Rev. Lett.* **76**, 900 (1996).
65. J. Kim *et al.*, *Nature* **397**, 500 (1999).
66. A. Imamoglu and Y. Yamamoto, *Phys. Rev. Lett.* **72**, 210 (1994).
67. E. Moreau *et al.*, *Appl. Phys. Lett.* **79**, 2865 (2001).
68. P. Michler *et al.*, *Science* **290**, 2282 (2000).
69. C. Santori *et al.*, *Phys. Rev. Lett.* **86**, 1502 (2001).
70. J. Hecht, *Laser Focus World* **38**, 20 (2002).
71. Z. Yuan *et al.*, *Science* **295**, 102 (2001).
72. C. Brunel *et al.*, *Phys. Rev. Lett.* **83**, 2722 (1999).
73. B. Lounis and W. E. Moerner, *Nature* **407**, 491 (2000).
74. F. Treussart *et al.*, *Phys. Rev. Lett.* **89**, 093601 (2002).
75. A. Beveratos *et al.*, *Eur. Phys. J. D* **18**, 191 (2002).
76. A. Beveratos *et al.*, *Phys. Rev. Lett.* **89**, 187901 (2002).
77. P. Michler *et al.*, *Nature* **406**, 968 (2000).
78. B. Lounis *et al.*, *Chem. Phys. Lett.* **329**, 399 (2000).

79. G. Messin *et al.*, *Opt. Lett.* **26**, 1891 (2001).
80. T. Basché *et al.*, eds. *Single-Molecule Optical Detection, Imaging and Spectroscopy* (VCH Publishers, Weinheim, 1997).
81. W. E. Moerner and M. Orrit, *Science* **283**, 1670 (1999).
82. W. E. Moerner, *Science* **277**, 1059 (1997).
83. T. Basché *et al.*, *Phys. Rev. Lett.* **69**, 1516 (1992).
84. L. Fleury *et al.*, *Mol. Phys.* **95**, 1333 (1998).
85. F. Kulzer *et al.*, *Chem. Phys.* **247**, 23 (1999).
86. S. Chandrasekhar, *Liquid Crystals*, Cambridge Monographs on Physics (Cambridge University Press, Cambridge, England, 1977).
87. E. Yablonovitch, *Phys. Rev. Lett.* **58**, 2059 (1987).
88. S. John, *Phys. Rev. Lett.* **58**, 2486 (1987).
89. E. Yablonovitch, *J. Opt. Soc. Am. B* **10**, 283 (1993).
90. P. R. Villeneuve and M. Piché, *Prog. Quantum Electron.* **18**, 153 (1994).
91. G. Kurizki and J. W. Haus, eds., *J. Mod. Opt.* (Special Issue: Photonic Band Structures) **41** (2) (1994).
92. S.-H. Chen, D. Katsis, A. W. Schmid, J. C. Mastrangelo, T. Tsutsui, and T. N. Blanton, *Nature* **397**, 506 (1999).
93. D. Katsis, A. W. Schmid, and S.-H. Chen, *Liq. Cryst.* **26**, 181 (1999).
94. T. J. Bunning and F. H. Kreuzer, *Trends Polym. Sci.* **3**, 318 (1995).
95. V. I. Kopp *et al.*, *Opt. Lett.* **23**, 1707 (1998).
96. I. P. Il'chishin *et al.*, *JETP Lett.* **32**, 24 (1980).
97. B. Taheri *et al.*, *Mol. Cryst. Liq. Cryst.* **358**, 73 (2001).
98. H. Finkelmann *et al.*, *Adv. Mater.* **13**, 1069 (2001).
99. O. D. Lavrentovich and M. Kleman, in *Chirality in Liquid Crystals*, edited by H.-S. Kitzerow and C. Bahr, *Partially Ordered Systems* (Springer, New York, 2001), pp. 115–158.
100. L. Ramos *et al.*, *Phys. Rev. E* **66**, 031711 (2002).
101. Y. Geng, A. Trajkovska, D. Katsis, J. J. Ou, S. W. Culligan, and S. H. Chen, *J. Am. Chem. Soc.* **124**, 8337 (2002).
102. R. Hanbury Brown and R. Q. Twiss, *Nature* **177**, 27 (1956).
103. A. Molski, *Chem. Phys. Lett.* **324**, 301 (2000).

EXAFS Measurements of Laser-Generated Shocks with an Imploded Target as a Radiation Source

Introduction

Recently, great interest has been shown in the study of dynamic material response to shocks of high pressure and high strain rate.^{1,2} Shocks of up to ~ 1 Mbar and strain rates of $\sim 10^7$ to 10^8 s⁻¹ were generated in metals (Al, Cu) by laser irradiation. The laser intensity in those experiments ($\sim 10^{11}$ W/cm²) was high enough to raise the pressure above the Hugoniot elastic limit (HEL) but low enough for the compressed material to remain solid. Using Bragg and Laue x-ray diffraction, the experiments clearly showed the retention of crystallinity during the passage of the shock. Silicon under these conditions was found to compress elastically, i.e., only in the direction of shock compression. Copper, on the other hand, was found to compress equally in all dimensions, indicating the transition to plastic flow. These differences were explained in terms of the different velocity of dislocation propagation that gives rise to the elastic-plastic transition.

The goal of this work is to examine the use of EXAFS³ (extended x-ray absorption fine structure) as a complementary characterization of such laser-shocked metals. EXAFS modulations above an absorption edge are due to the interference of the ejected photoelectron wave with the reflected wave from neighboring atoms. Thus, the interference translates into modulations in the cross section for photon absorption above the edge. The frequency of these modulations relates to the inter-particle distance, hence the density of the compressed material. The decay rate of the modulation with increasing photoelectron energy yields the MSRD (mean-square relative displacement) and can thus serve as a temperature diagnostic. EXAFS had originally been applied to crystalline materials but has since been widely used to study amorphous,⁴⁻⁶ liquid,⁷⁻⁹ heated,^{8,10-17} or compressed^{11,14-16,18,19} materials. In those steady-state experiments, the imposed temperature is known independently and the main emphasis is on studying the chemical structure. In this experiment the emphasis is on measuring the compression and temperature of the shocked material through the EXAFS spectrum itself. There is an important difference between the diffraction experiments and the present EXAFS experiment: EXAFS, which depends only

on short-range order, does not require the use of single-crystal samples, as was the case in the diffraction experiments. In this experiment we use polycrystalline Ti foils in which the number of crystalline grains under the laser focal spot is very large. Thus, the shock direction is randomly distributed with respect to the atomic planes. It is known that the same stress can cause elastic or plastic deformation in the same crystal, depending on the orientation of the shock direction with respect to the crystal planes.²⁰ Since the transition to plastic flow depends on the propagation of dislocations along slip planes, we can expect a plastic response in some or most of the crystalline grains. Like in the shock experiments in silicon and copper cited above,^{1,2} the shock pressure in our experiments (~ 0.4 Mbar) is much higher than the Ti HEL.²¹ *The assumption of three-dimensional compression, required to relate the EXAFS-determined inter-atomic distance to the density, can be tested by comparison with the measurement of shock speed, which yields the compression (through the known Hugoniot).*

Most EXAFS experiments are performed with a synchrotron radiation source, and the spectrum due to a sample in steady state is slowly scanned. In laser experiments²²⁻²⁴ the entire spectrum is recorded simultaneously during the short pulse (\sim ns) of the laser. This makes it challenging to obtain an EXAFS spectrum of high signal-to-noise ratio. In a previous paper²⁵ we have shown that a CH shell imploded by a multi-beam laser system constitutes a source of an intense and smooth spectrum of x-ray radiation, suitable for EXAFS measurements. The high source intensity enables us to work with a thick Ti foil (attenuation $\sim e^{-3}$ above the *K* edge), which increases the relative modulations in the observed signal. Using the 60-beam OMEGA laser,²⁶ the intensity from imploded shells around 5 keV was sufficient to obtain a good EXAFS spectrum above the *K* edge of Ti at 4.96 keV. Fitting a theoretical model to the measured EXAFS spectrum yielded the inter-particle distance and temperature in agreement with synchrotron results.^{27,28} Those absorption experiments were performed on cold, unshocked Ti foils in order to test the reliability of the present method, which is here extended to the shocked case.

Titanium was chosen because of the following considerations: The EXAFS spectrum from a low- Z absorber, because of the high attenuation in our experiment, would be dominated by the second-order crystal diffraction (whose attenuation is much smaller). In Ti the second-order radiation (around ~ 10 keV) is too weak to affect the results. On the other hand, for a higher- Z absorber the imploding-target emission at the corresponding higher photon energy would be too weak. Titanium behavior is complicated, however, by phase transitions:²⁹ at normal conditions Ti crystallizes as hexagonal close packed (α -Ti); as the pressure rises, it transforms to a hexagonal phase (ω -Ti) at low temperatures, or to a body-centered cubic (β -Ti) at high temperatures. For shocked titanium a transition from α -Ti to ω -Ti has been shown³⁰ to occur at a pressure of ~ 0.12 Mbar; this value varies with the sample purity but it is clearly much lower than the pressure in this experiment (~ 0.4 Mbar). Following this transition there may be an additional transition of ω -Ti to β -Ti, but the Hugoniot shows no additional discontinuity up to ~ 1.2 Mbar³¹ and static-pressure studies showed no such transition for pressures as high as 0.87 Mbar.³² Recently, a new Ti phase (γ) has been discovered³³ but it is reached at a higher pressure (~ 1.1 Mbar) than relevant to this experiment. We next address the question of the time constant t_0 for the (α -Ti) to (ω -Ti) phase transition. Although previous phase transitions in Ti have been observed with much lower strain-rate shocks, a pressure dependence of t_0 has been determined³⁴ that can be extrapolated to the pressure (~ 0.4 Mbar) in this experiment. In the range of 0.05 to 0.09 Mbar, the time constant decreases exponentially with the pressure; extrapolating to $P = 0.4$ Mbar yields $t_0 \ll 1$ ns. The phase transition α -Ti to ω -Ti entails a 1.9% decrease in volume,³³ much smaller than the implied volume change due to the compression. However, the change in crystal structure strongly affects the EXAFS spectrum as the geometry of the nearest neighbors is now more complex.³⁵

The theory of EXAFS³ yields an expression for the normalized modulations $\chi(k) = \mu(k)/\mu_0(k) - 1$, where $\mu(k)$ is the absorption coefficient (or opacity) and $\mu_0(k)$ is the absorption of the isolated atom (i.e., without the EXAFS oscillations). $\mu_0(k)$ can be obtained by passing a smooth curve through the EXAFS oscillations. k is the wave number of the ejected photoelectron and is given by the de Broglie relation $\hbar^2 k^2 / 2m = E - E_K$, where E is the absorbed photon energy and E_K is the energy of the K edge. For low disorders and polycrystalline materials, the basic EXAFS theory,³ assuming single-electron scattering and plane electron waves and neglecting multiple scattering, yields the following expression for the normalized modulations $\chi(k)$:

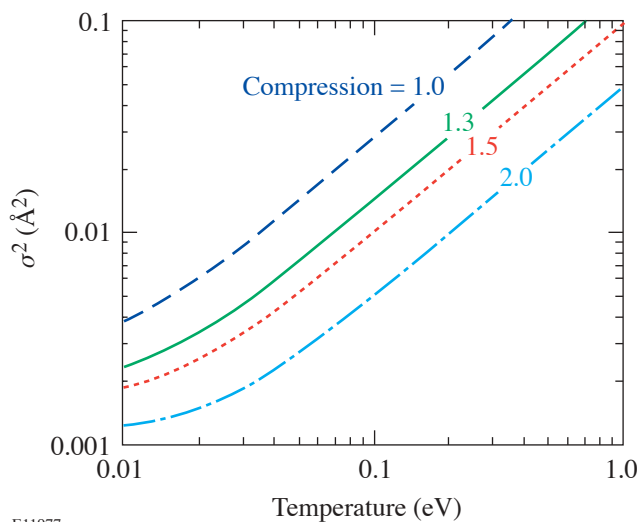
$$\chi(k) = \sum_j N_j S_0^2 F_j(k) \exp[-2\sigma^2 k^2 - 2R_j/\lambda(k)] \times \sin[2kR_j + \phi_j(k)] / kR_j^2, \quad (1)$$

where N_j is the number of atoms surrounding the absorbing atom at a distance R ($N_1 = 12$ in Ti). The sum over j relates to successive shells of atoms around the photo-absorbing atom. Only the first coordination shell will be of interest here because it suffices for determining the density; also, in the shocked material the contribution of higher shells essentially disappears. R is the interparticle distance, and the factor σ^2 (Debye-Waller factor) accounts for thermal vibrations, derived from a harmonic potential. σ^2 can also include static disorder ($\sigma_{\text{total}}^2 = \sigma_{\text{vibration}}^2 + \sigma_{\text{disorder}}^2$), corresponding to a Gaussian distribution of pair distances. The backscattering amplitude $F(k)$ and phase-shift factor $\phi(k)$ for titanium were calculated by Teo and Lee.³⁶ McKale *et al.*³⁷ have improved these calculations by removing the assumption of photoelectron plane waves; their results differ from those of Teo and Lee, primarily for $k \leq 3$. We have averaged the results of McKale *et al.* for scandium and vanadium (their calculations apply to every other element) and have made a minor adjustment to fit the Ti results of Teo and Lee at high wave numbers. The mean free path of the ejected electron for inelastic collisions in titanium, $\lambda(k)$, was taken from Blanche *et al.*²⁷ The vibration amplitude σ^2 and the interatomic distance R are treated as adjustable parameters in fitting Eq. (1) to the experimental EXAFS spectrum. In addition, the adjustable constant $S_0^2 (< 1)$ accounts for multi-electron effects such as relaxation of the core hole and excitation of other than the ejected photoelectron.³ Finally, an adjustable energy shift ΔE is applied to the experimental points to account for uncertainties in chemical-bonding and core-relaxation effects. The edge energy ($k = 0$) is initially determined by the inflection point, i.e., the energy for which the derivative of the falling intensity above the edge is maximal. The distance R can yield the density of the absorber. The temperature can be found from the σ^2 value, which depends also on the density. Beni and Platzman³⁸ have calculated σ^2 as a function of temperature using the Debye model for the phonon density of states, including correlation between the motions of the central and neighboring atoms. We use the first term in their result (including a factor-of-2 correction¹⁰), neglecting the correlation term. Gregor and Lytle¹⁰ have compared the results of Beni and Platzman³⁸ to their measurements (in copper) and have shown that neglecting the correlation term increases σ^2 by about 20%. We therefore reduced the uncorrelated results for Ti by 20%. As a check, we compared

the measured values⁷ of σ^2 for Zn in the temperature range of 0.01 to 0.06 eV with those calculated by the procedure described here, and they agree to within a few percent. σ^2 depends on the density through the Debye temperature. Using an empirical model³⁹ we calculate the density dependence of the Debye temperature (in eV) as

$$\Theta_B = -14.79 + 50.39(\rho/\rho_s) + (\rho/\rho_s)^2, \quad (2)$$

where ρ is the density and ρ_s is the solid density. We show in Fig. 94.38 the calculated σ^2 for Ti as a function of temperature and density. As seen, compression increases the amplitude of the EXAFS signal because of the decrease in σ^2 . This is in addition to the increase because of the explicit $1/R^2$ dependence in Eq. (1). On the other hand, compression reduces the EXAFS signal because $\lambda(k)$ in Eq. (1) depends on the density ρ as $1/\rho$.



E11977

Figure 94.38
Calculated σ^2 due to thermal vibrations for Ti from the model of Beni and Platzman³⁸ making use of the density dependence of the Debye temperature from Ref. 39. Correlation was accounted for by reducing the first, uncorrelated term in Ref. 38 by 20%.

Although advanced EXAFS models have been developed,^{40–42} the use of Eq. (1) is adequate for our experiments: curved-wave effects are included in the calculations³⁷ of phase shift and backscattering amplitude, multi-electron effects are accounted for by the S_0^2 factor, and multiple scattering is negligible for the first coordination shell,⁴³ the only one of interest here.

Experiment

Figure 94.39 shows a schematic view of the target used to measure EXAFS spectrum in laser-shocked targets. Fifty-seven beams of the OMEGA laser, of ~ 21 -kJ total energy, are focused on an empty CH shell whose implosion generates the radiation source for measuring the absorption spectrum in Ti. The three remaining OMEGA beams are stacked and used to irradiate and launch a shock wave in Ti. The laser pulse shape was 1 ns square; thus the three stacked beams formed a 3-ns-long square pulse; these beams were focused onto the plane target in a 3.8-mm-diam focal spot, giving an irradiance of 0.5 TW/cm^2 . A delay time for the three stacked beams with respect to the rest of the beams was adjusted so that peak implosion of the spherical target occurred when the shock had just traversed the Ti layer. The spherical target had a diameter $\sim 940 \mu\text{m}$ and a thickness $\sim 20 \mu\text{m}$. The planar target consisted of $10\text{-}\mu\text{m}$ -thick polycrystalline Ti, coated on both sides with $17 \mu\text{m}$ of CH. The purpose of the front CH layer was to prevent laser heating and ablation of the Ti. The purpose of the back CH layer was to prevent the shock unloading at the back Ti surface. The thickness of the Ti layer d was the highest ($\mu_0 d \sim 3$) that still yielded significant x-ray signal after K -edge absorption. A thicker absorber yields higher EXAFS modulations in the observed intensity I since $(\Delta I/I) \sim (\mu_0 d)(\Delta\mu_0/\mu_0)$. From the point of view of signal-to-noise (S/N) ratio, the optimal value of $\mu_0 d$ depends on the source of noise: for photon noise ($\sim I^{1/2}$) it can be shown to be 2. When the noise is proportional to I , the S/N ratio continuously increases with $\mu_0 d$. We found the latter to be the case here. The CH thickness and laser pulse length were chosen to minimize nonuniformity in the Ti properties in the direction of the shock (see Fig. 94.43 later in article).

The heat shield (0.5-mm-thick CH foil) minimizes the heating of the Ti layer due to radiation from the imploding spherical target. It attenuates the EXAFS-producing radiation at $\sim 5 \text{ keV}$ by a factor of ~ 2.5 while very strongly attenuating the softer radiation, which can heat the Ti foil. The functioning of the heat shield was tested (see below) by measuring the EXAFS spectrum when the three shock-launching beams were not fired.

Two x-ray spectrometers measured the spectrum on calibrated film.⁴⁴ One x-ray spectrometer (XRS-I) measured the EXAFS spectrum, the other (XRS-II) the incident spectrum I_0 . A typical I_0 spectrum is shown in Fig. 2(a) of Ref. 25. To cross-calibrate the two spectrometers, a $10\text{-}\mu\text{m}$ -thick Ti foil was placed on some shots in front of XRS-II, and its EXAFS spectrum was compared with that obtained in XRS-I without launching a shock. The spectral resolution of the spectrometer

is limited by the source size. The FWHM size of the core seen at 5 keV (Fig. 1 in Ref. 25) is $D \sim 100 \mu\text{m}$; this translates to a spectral resolution $\Delta E = ED/tg(\Theta_B)L$, where L is the distance from the target to the film and Θ_B is the Bragg angle. This yields a resolution of ~ 5 eV, much smaller than a typical EXAFS modulation period (~ 60 eV).

Although the EXAFS measurement is time integrated, a meaningful shock diagnosis can be obtained without streaking the spectrum in time because the x-ray pulse width is very short. We previously showed²⁵ that the emission from the spherical target above the Ti K edge (~ 5 keV) comes mostly from the compressed core, whereas the emission from the laser-absorption region is much weaker. This was seen in both the time-resolved spectrum as well as the space-resolved spectrum. The former showed that the pulse width of the x-ray emission at ~ 5 keV was only ~ 120 ps [Fig. 2(b) in Ref. 25], much shorter than the shock transit time through the Ti (~ 2 ns).

The implosion of the spherical target has to be timed so as to probe the Ti layer after it is traversed by the shock. This is because the EXAFS spectrum of a partly shocked foil is dominated by the low-temperature region ahead of the shock front. The delay of the shock-launching beam with respect to the implosion beams is given by the difference $\tau(\text{implosion}) - \tau(\text{Ti})$, where $t(\text{implosion})$ is the compression time of the

spherical target and $\tau(\text{Ti})$ is the shock arrival time at the back of the Ti layer. Both these times have been measured; they are also known from simulations by the hydrodynamic code *LASNEX*.⁴⁵ The implosion time is determined by streaking the soft-x-ray emission from the spherical target. Since the emission above the Ti K edge (~ 5 keV) is completely dominated by the compressed core, in order to see the coronal emission during the rising part of the laser, we streak the spectrum at the softer energy of ~ 3 keV (see Fig. 94.40), where the compressed-core emission is completely saturated. The indicated compression time is ~ 1.7 ns.

The time $\tau(\text{Ti})$ is determined experimentally by the method of active shock breakout (ASBO).⁴⁶ Figure 94.41 shows the corresponding experimental configuration and a sample result. An EXAFS target (Fig. 94.39) was irradiated at the same intensity as in the EXAFS experiment. A frequency-tripled YAG laser, synchronized with OMEGA, irradiated the backside of the target and interfered with the reflected beam. Figure 94.41 shows the interference fringes measured by a streak camera, viewing the central portion of the focal spot. Also shown is a series of simultaneously recorded fiducial time pulses marking the time scale; the time $t = 0$ corresponds to the start of the laser pulse. Initially, the laser is reflected from the backside of the Ti foil. When the shock reaches this surface [at time $\tau(\text{Ti})$], the reflection is seen to be disrupted. This is the

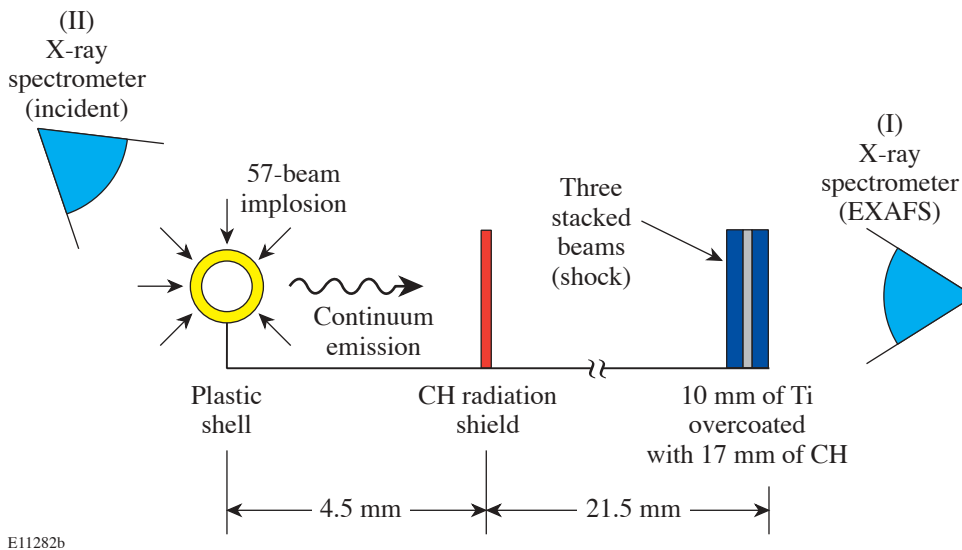
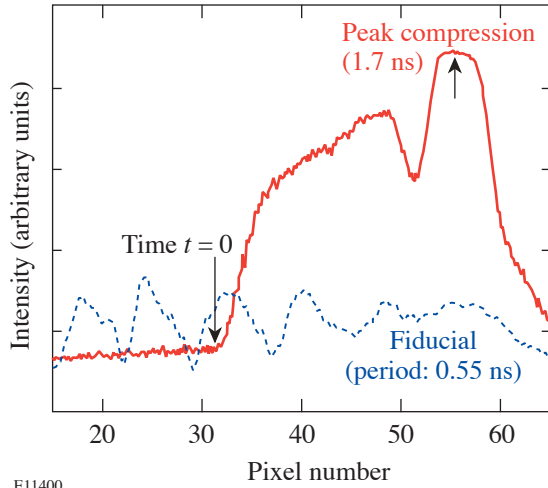


Figure 94.39

Schematic view of the target. The imploding spherical target serves as a radiation source for EXAFS measurements. X-ray spectrometer I measures the EXAFS spectrum; x-ray spectrometer II measures the incident spectrum I_0 . The heat shield minimizes the heating of the shocked Ti layer due to radiation from the imploding spherical target.

optimal time for EXAFS probing. Subsequent to this, a weaker reflection from the backside of the CH layer is seen; when the shock reaches that surface, at time $\tau(\text{CH})$, ablation sets in, the laser is strongly absorbed, and reflection disappears. It is not mandatory to know $\tau(\text{Ti})$ with great precision in setting the



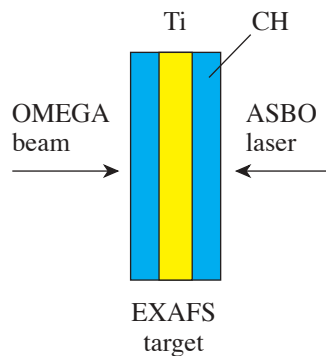
E11400

Figure 94.40
Streaked x-ray spectral intensity around ~ 3 keV emitted by the imploding spherical shell. The streak is used to determine the implosion time, which is required for determining the EXAFS probing time.

delay between the shock-launching beam and the backlighter beams. This is because we repeat the experiment for different time delays around the expected optimal value; when the shock arrives at the back surface of the Ti layer, the EXAFS spectrum clearly changes into a lower-intensity, faster-decaying spectrum.

The ASBO data can also be used to determine the shock velocity, i.e., the shock strength. Since the time $\tau(\text{Ti})$ includes the time of shock travel through the front CH layer, we can use the difference $\tau(\text{CH}) - \tau(\text{Ti})$ to find the net transit time through the Ti layer. For that we assume that the travel time through the two CH layers is the same. This was verified by code simulations to be correct to within a few percent. For an irradiance of 0.5 TW/cm^2 (the case analyzed by EXAFS below) the shock velocity in the Ti layer was found to be $\sim 6.3 \text{ km/s}$, which, according to the Ti Hugoniot,^{31,47} corresponds to a pressure of 0.4 Mbar and compression of 1.28. An agreement of the density as measured by EXAFS and the density derived from the shock speed through the Hugoniot (as is the case below) is a confirmation of the assumption of 3-D compression.

Finally, the ASBO data show the velocity nonuniformity across the shock front to be $\pm 10\%$, which, according to the Hugoniot of Ti, translates into a nonuniformity of $\pm 4\%$ in the pressure as well as in the density. *LASNEX* runs show that the



E11860a

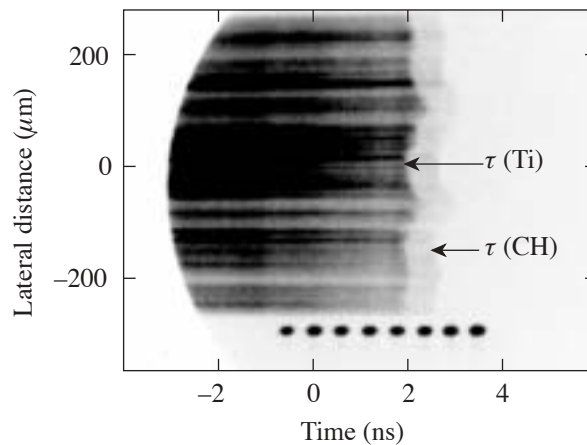


Figure 94.41
Active shock breakout (ASBO) measurement of the arrival time $\tau(\text{Ti})$ of the laser-launched shock at the back surface of the Ti layer. Time $t = 0$ corresponds to the start of the laser pulse. This measurement is also used to assess the shock nonuniformity and to confirm (through the Hugoniot) the EXAFS-measured compression.

average density variation during the probing time interval (~ 120 ps) is less than 2%, as is the density variation along the shock direction (Fig. 94.43). These uncertainties are much smaller than the change in density due to the compression, as shown below.

Hydrodynamic Simulations

To determine the expected shock strength and the properties of the shocked Ti for a given laser irradiation, the hydrodynamic code *LASNEX* was used for one-dimensional simulations. It includes the “quotidian” equation of state³⁹ (QEOS), based on the Thomas–Fermi equation of state with empirical corrections. As an indication of its validity at low temperatures we compare in Fig. 94.42 curves of QEOS pressures at constant Ti compression with experimental points³³ obtained recently for Ti in a diamond anvil cell at room temperature and the same compressions. The agreement is quite good; however, the curves also show the low sensitivity to the temperature, which reduces the precision in the temperature prediction.

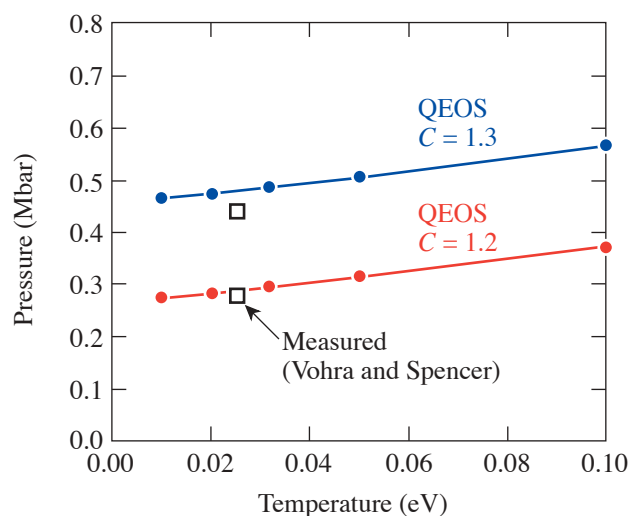


Figure 94.42

QEOS curves for two compression values in Ti. Experimental values obtained in a diamond anvil cell at room temperature for the same compression values are also shown.³³

The *LASNEX*-calculated profiles of density, pressure, and temperature for a laser irradiance of 0.5 TW/cm^2 are shown in Fig. 94.43 at the time of arrival of the shock at the rear surface of the Ti layer, namely 3.5 ns. These simulations correspond to the experimental results discussed below. The profiles, particularly that of the density, are seen to be quite uniform throughout the Ti. The average value of density within the Ti ($\sim 5.6 \text{ g/cm}^2$) and the average value of pressure ($\sim 0.4 \text{ Mbar}$) are

consistent with the measured^{31,47} Hugoniot of Ti. As will be shown in the next section, the measured EXAFS spectrum at about the time 3.5 ns yields a compression of 1.3 (assuming three-dimensional compression), as compared with a compression of 1.25 in these simulations. Code runs with an initial temperature higher than room temperature showed that the temperature due to radiation preheat can simply be added to the calculated temperature profiles.

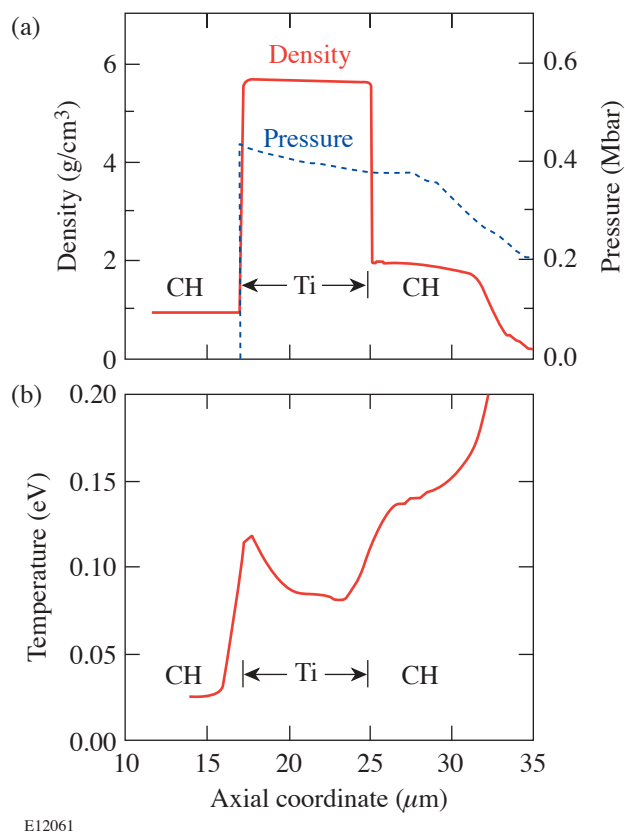


Figure 94.43

LASNEX-calculated profiles of (a) density and pressure and (b) temperature for a laser irradiance of 0.5 TW/cm^2 at the time of arrival of the shock at the back surface of the Ti layer, namely 3.5 ns. The laser is incident from the right.

Results and Analysis

1. Radiation Heating

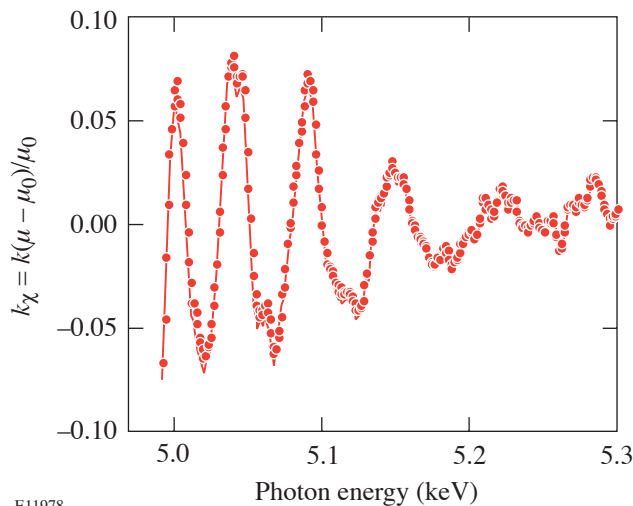
The extraction of the experimental $\chi(k)$ to be compared with Eq. (1) follows the standard procedure.³ First, the absorption coefficient $\mu = \log(I_0/I)$ is computed from the measured intensities. As explained before, no correction for the finite spectral resolution ($\sim 5 \text{ eV}$) was required. Likewise, higher-harmonic contribution to the crystal diffraction could be ignored: the spectrum emitted by the implosion had a characteristic temperature $\sim 1 \text{ keV}$; thus the second-order radiation at 10 keV

was weaker than the first order by a factor of $\sim e^5$, in addition to its lower crystal reflectivity. The normalized EXAFS spectrum $\chi(k)$ was calculated using the McMaster adjustment:⁴⁸

$$\chi(k) = \left\{ \frac{\mu(k) - \mu_0(k)}{\Delta\mu} \right\} \left[\frac{\Delta\mu^{\text{th}}(k=0)}{\Delta\mu^{\text{th}}(k)} \right], \quad (3)$$

where $\Delta\mu$ is the measured jump at the K edge and $\Delta\mu^{\text{th}}(k)$ is the theoretical net K -shell absorption.

To study the effect of shocks on the Ti metal, the effect of radiation heating should be minimal. This was verified by measuring the EXAFS spectrum with the target of Fig. 94.39 but without launching a shock. Figure 94.44 shows the measured normalized EXAFS spectrum $\chi(k)$ for such a shot. Next, the $\chi(k)$ due to the first coordination shell is extracted as explained in Ref. 25: $k\chi(k)$ is Fourier transformed to the real space and the first peak is filtered and transformed back to the k space. We use $k\chi(k)$ to de-emphasize the low- k region, where the theory is imprecise. We next fit Eq. (1) to the filtered spectrum while varying R , σ^2 , S_0^2 , and ΔE_0 . Figure 94.45 shows the best fit. Before performing the fit, the theoretical profile was subjected to the same Fourier filtering as the experimental spectrum (in particular, using the same k range); this increases the quality of the fit. The best fit was obtained with $R = 2.93 \text{ \AA}$, $\sigma^2 = 0.011 \text{ \AA}^2$, $S_0^2 = 0.86$, and $\Delta E = 13 \text{ eV}$. The value of σ^2 corresponds according to Fig. 94.38 to $T = 40 \text{ meV}$. Thus the radiation heating above room temperature amounts to only $\sim 15 \text{ meV}$. As shown below, this is much



E11978

Figure 94.44
Normalized EXAFS spectrum $\chi(k)$ before Fourier filtering for an unshocked shot, used to determine the temperature rise due to radiation heating.

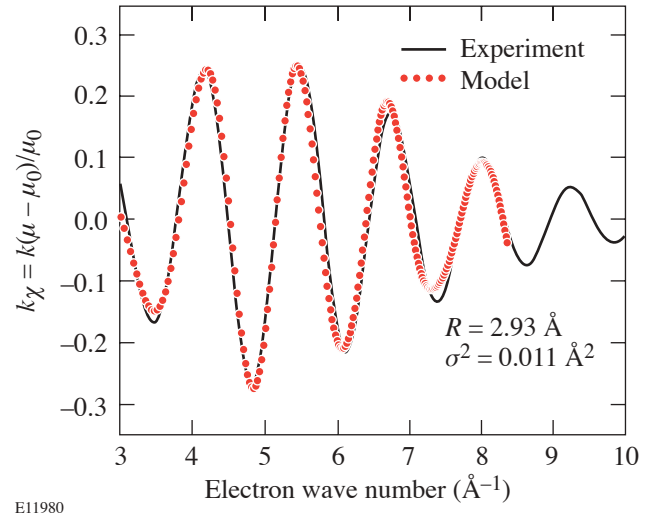


Figure 94.45
Fitting of the model [Eq. (1)] to the observed $k\chi(k)$ EXAFS spectrum from Fig. 94.42. The parameter values (R and σ^2) giving the best fit are shown. The value of R agrees with the known value for Ti at normal conditions. σ^2 corresponds to a temperature of $\sim 40 \text{ meV}$.

smaller than the shock heating. Since the incident x-ray intensity in successive shots is not entirely reproducible, we normalize the heating in each shot by the corresponding intensity of x-ray emission at 5 keV. The explanation of the fitting and the calculation of the error bars are explained in the Appendix.

2. Shock Compression

Shock-compression experiments using the 3-ns, 0.5-TW/cm² laser irradiation have been performed by varying the shock probing time, given by the delay between the shock-launching beams and the compression beams. The appropriate shock probing time for a 3-ns laser pulse, an irradiation of 0.5 TW/cm², and the target described above was found to be $\sim 3.5 \text{ ns}$, both through ASBO measurements and *LASNEX* code simulations. In successive shots we probed the shocked Ti both before and after that time. At around a probing time of $\sim 3.5 \text{ ns}$ the EXAFS clearly changed to a faster-decaying spectrum: the number of clearly visible modulations dropped from ~ 6 to ~ 3 . The results at a probing time $\sim 3.5 \text{ ns}$ indeed show a compression of the Ti layer. To illustrate the compression directly we compare in Fig. 94.46 the measured absorption spectra (before Fourier filtering) for two probing times: before the shock enters the Ti layer (marked “before shock arrival”) and when the shock has just traversed the Ti layer (marked “after shock arrival”). The lengthening of the EXAFS period of modulation in the after-shock case is evidence of compression. The two shots were identical except for the different delay time. The

curve marked before shock is shifted by 5 eV toward higher wave numbers for a clearer demonstration of the lengthening. The effect of the shock is also seen in increasing the damping rate of the modulations. Figure 94.47 shows the fitting of Eq. (1) to the Fourier-filtered experimental spectrum. The value of R for the best fit is $(2.68 \pm 0.05) \text{ \AA}$, which is smaller by a factor of ~ 1.1 than the value $R = 2.92 \text{ \AA}$ for an unperturbed Ti. The difference between the two values is much larger than the uncertainty in R . Assuming the compression is three-dimensional, this corresponds to a volume compression by a factor of ~ 1.3 or a density of 5.8 g/cm^3 . This agrees with the compression value derived above from the measured shock velocity (1.28) as well as with the average compression (1.25) of the profile calculated by *LASNEX* (Fig. 94.43). This agreement supports the assumption of three-dimensionality, which was also postulated above, based on the fact that a polycrystalline Ti sample was used in this experiment.

The value of σ^2 (namely, 0.033) is much higher than in the unshocked case (Fig. 94.45). According to Fig. 94.38, this value would correspond to a temperature of $\sim 0.24 \text{ eV}$, much higher than the value ~ 0.09 predicted by *LASNEX* (Fig. 94.43). We conclude that σ^2 has a contribution from static disorder in addition to thermal vibrations, due possibly to the α -Ti to

ω -Ti phase transformation. A large σ^2 value has also been found in EXAFS measurements applied to various disordered systems.^{5,6,15,17} In particular, it has been shown¹⁵ that a Ge crystal transformation from diamond type to white-tin type at 0.11 Mbar is accompanied by a quadrupling in the value of σ^2 . Similarly, a doubling in the value of σ^2 was found¹⁷ to accompany the order-disorder transition in CuI; finally, we cite measurements¹⁶ on compressed Ga close to room temperature where, because of phase transformation, values of σ^2 comparable to the result of Fig. 94.47 have been measured. It should be emphasized that the increase in σ^2 cannot be due to melting. First, the melting temperature of Ti at normal conditions is $\sim 0.17 \text{ eV}$, but at a compression of 1.3 it rises to $\sim 0.3 \text{ eV}$ as calculated by the Lindemann law,⁴⁹ thus certainly higher than the temperature in the shocked Ti. Moreover, experiments have shown that melting does not cause an increase in σ^2 beyond that associated with the increase in temperature.⁹

In the initial α -Ti crystal each atom is surrounded by 12 atoms at a distance of 2.92 \AA . In the more-complex ω -Ti geometry³⁵ the arrangement of neighboring atoms is of two kinds, described as site A and site B. For every atom in site A there are two atoms in site B. Site-A atoms have 14 nearest neighbors at a distance of 2.92 \AA . Site-B atoms have three

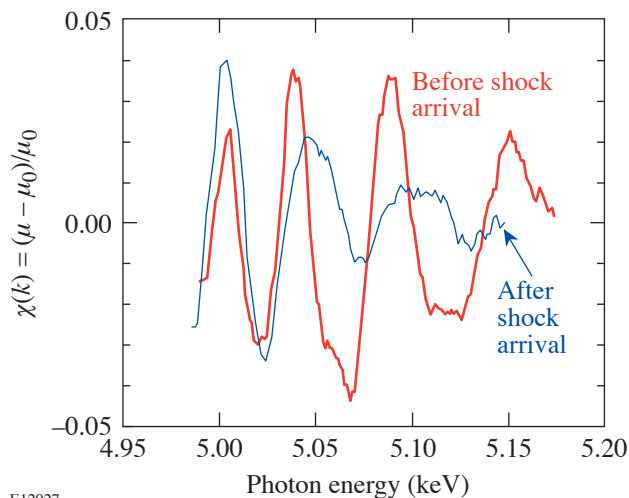


Figure 94.46

Demonstration of shock compression based on the lengthening of the EXAFS period of modulation. The two normalized EXAFS spectra (shown before Fourier filtering) correspond to different probing times from otherwise identical shots. The curve marked "after shock arrival" corresponds to the time when the shock has just traversed the Ti layer. The curve marked "before shock arrival" corresponds to a time before the shock entered the Ti layer.

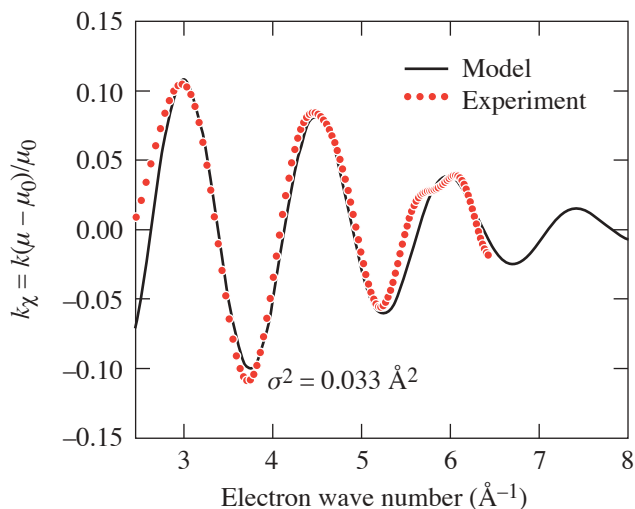


Figure 94.47

Fitting of the model [Eq. (1)] to the observed $k\chi(k)$ EXAFS spectrum (derived from the curve labeled "after shock arrival" in Fig. 94.44, after Fourier filtering). The parameter values giving the best fit are shown. The interatomic distance R yields a compression of 1.3 (assuming to be three-dimensional) and the factor $\sigma^2 = \sigma_{\text{therm}}^2 + \sigma_{\text{stat}}^2$ contains both the temperature-dependent vibrations term and a static disorder term.

neighbors at a distance of 2.667 Å, six neighbors at a distance of 2.845 Å, and two atoms at a distance of 3.023 Å. Thus, there is a spread of ~ 0.3 Å (or $\sim 10\%$) in the first-shell distances. This has the effect of adding a disorder term to the thermal disorder due to crystal vibration. The different distances translate to EXAFS modulation of different frequencies. The beating of these frequencies when calculating the total EXAFS spectrum gives rise to a decreasing amplitude. Thus, EXAFS spectra can be used to study *dynamic* α -Ti to ω -Ti phase transformation in shock compression. On the other hand, to reliably extract the temperature value from the EXAFS spectrum, a metal that does not undergo a phase transformation should be used. For example, in vanadium no phase transformation has been found up to pressures of 1 Mbar.²⁹ A smaller σ^2 value in a comparable shocked vanadium experiment would support the conclusion that a phase transformation in the titanium experiment has actually taken place.

To assess the observability of EXAFS in future titanium experiments we plot in Fig. 94.48 the contours of $\max(|\chi|)$ in the compression-temperature space. We divide the contour-value scale into three regions: (a) $\max(|\chi|) > 0.05$, termed high; (b) $0.03 < \max(|\chi|) < 0.05$, termed marginal; and (c) $\max(|\chi|) < 0.03$, termed low. EXAFS can readily be measured in the first region and only marginally in the second [for solid titanium at room temperature $\max(|\chi|) \sim 0.06$]. To show what part of the compression-temperature space can be ac-

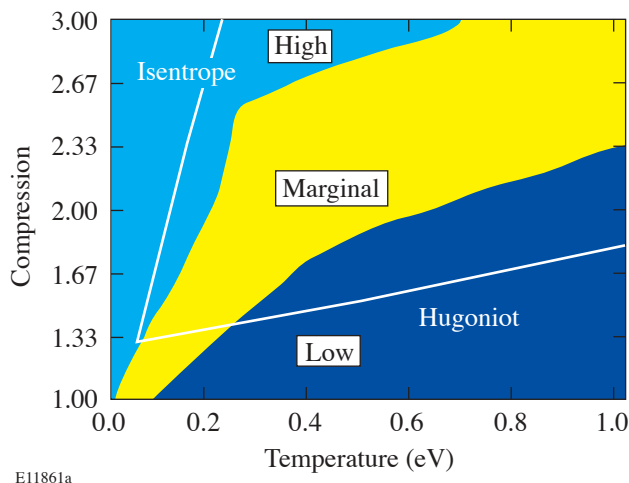


Figure 94.48
Regions of observability of EXAFS in compressed titanium. High: $\max(|\chi|) > 0.05$; marginal: $0.03 < \max(|\chi|) < 0.05$; and low: $\max(|\chi|) < 0.03$. The Hugoniot for Ti^{31,46} is shown as well as the isentrope, both passing through the point corresponding to the present experiment.

cessed by shocks we superimpose on the contours in Fig. 94.48 the values along the principal Hugoniot of Ti.^{31,47} As seen, strong shocks are not readily measurable with EXAFS. On the other hand, isentropic (low-temperature) compressions of metals are much more suitable for EXAFS measurements. Figure 94.48 also shows the calculated isentrope that passes through the Hugoniot point corresponding to the present experiment (Fig. 94.47). It was obtained by using the Cowan model for the density dependence of the Grüneisen (γ) of Ti,³⁹ normalized to the experimental value (~ 1.17) at solid density.³⁰ Obviously, even a near-isentropic compression will be much easier to diagnose with EXAFS than a shock of comparable compression.

Further understanding of high-strain-rate shock compression of metals can be gained in future experiments by (a) performing similar experiments on single-crystal samples and comparing EXAFS and multidirectional diffraction measurements, (b) employing a target material that does not undergo phase transformation below ~ 1 -Mbar pressure (e.g., vanadium²⁹), and (c) performing near-isentropic compression experiments where higher densities at lower temperatures can be achieved.

ACKNOWLEDGMENT

This work was supported by the U.S. Department of Energy Office of Inertial Confinement Fusion under Cooperative Agreement No. DE-FC03-92SF1931,460, the University of Rochester, and the New York State Energy Research and Development Authority. The support of DOE does not constitute an endorsement by DOE of the views expressed in this article.

Appendix A: Fit Optimization and Error Analysis

The fitting of the model [Eq. (1)] to the experimental EXAFS spectrum is achieved by minimizing the X^2 (chi squared) function. To determine the uncertainty in the EXAFS fitting parameters R and σ^2 we use the inverse-Hessian method.⁵⁰ We actually vary two other parameters in the fitting, ΔE_0 and the amplitude multiplier S_0^2 , but since we are mainly interested in the uncertainty in R and σ^2 , we simplify the error calculation to the latter two parameters. The adjustment of S_0^2 and ΔE_0 is done by trial and error, and then the best values of R and σ^2 are determined by minimizing the two-dimensional X^2 . We make use of the definition

$$X^2 = \sum_{j=1}^N \frac{[k\chi(\text{exp}) - k\chi(\text{theory})]^2}{N\delta^2}, \quad (\text{A1})$$

where δ is the mean root square of the noise in the data. The film data are digitized into a 2-D array of pixels s_{ij} . The signal is the average of m rows s_i in the direction of dispersion. As in Fig. 5 of Ref. 25, the noise is obtained by the average over the differences between adjacent pixel rows:

$$\sigma_{\text{noise}} = \sum_{i=1}^{m/2} (s_{2i-1} - s_{2i})/m. \quad (\text{A2})$$

Here the random components of the measured signals add up, whereas the net signal cancels out. The two-dimensional matrix $X^2(R, \sigma^2)$ is used to find the best values of the parameters R and σ^2 as well as to derive the Hessian matrix $H_{ik} = \delta^2 \chi^2 / \delta a_i \delta a_k$, where $a_1 = R$ and $a_2 = \sigma^2$. The standard deviation in the parameters is obtained from C , the inverse matrix of H : $\Delta R = (C_{11})^{1/2}$ and $\Delta \sigma^2 = (C_{22})^{1/2}$. For the unshocked case (Fig. 94.45) we find $\Delta R = \pm 0.013 \text{ \AA}$ or a relative error of $\sim 0.5\%$ and $\Delta \sigma^2 = \pm 0.002 \text{ \AA}^2$ or a relative error of $\sim 20\%$. This is in line with reported uncertainties in synchrotron experiments. The actual uncertainty in R can be higher because of imprecision in the x-ray wavelength scale, which is $\sim 1\%$. This is of no concern here, however, because the interest is in shock-induced changes in R , which are of the order of $\sim 10\%$.

To illustrate the error-calculation results we show in Fig. 94.49 the variation of X^2 with R for the optimal value of σ^2 and with σ^2 for the optimal value of R . The minimum value of X^2 is close to 1, which indicates that the errors in the experimental points are random. The vertical lines show the brackets of uncertainty derived from the two-dimensional Hessian analysis. For shocked-Ti experiments the uncertain-

ties are higher: $R = 2.66 \pm 0.05 \text{ \AA}$ or a relative error of $\sim 2\%$ and $\sigma^2 = 0.033 \pm 0.008 \text{ \AA}^2$ or a relative error of $\sim 25\%$. The poor fit in Fig. 94.47 (mainly in R) indicates the inadequacy of Eq. (1) for the shocked result. Because of the large disorder contribution σ_{stat} (due possibly to a phase transition in Ti), a detailed EXAFS calculation relevant to the crystallographic structure of shocked Ti should be carried out.

REFERENCES

1. D. H. Kalantar *et al.*, Phys. Plasmas **7**, 1999 (2000).
2. L. Loveridge-Smith, A. Allen, J. Belak, T. Boehly, A. Hauer, B. Holian, D. Kalantar, G. Kyrala, R. W. Lee, P. Lomdahl, M. A. Meyers, D. Paisley, S. Pollaine, B. Remington, D. C. Swift, S. Weber, and J. S. Wark, Phys. Rev. Lett. **86**, 2349 (2001).
3. P. A. Lee *et al.*, Rev. Mod. Phys. **53**, 769 (1981).
4. K. Sakurai *et al.*, Appl. Phys. Lett. **57**, 2660 (1990).
5. M. L. Fdez-Gubieda *et al.*, Phys. Rev. B **53**, 620 (1996).
6. M. C. Ridgway *et al.*, Nucl. Instrum. Methods Phys. Res. B **147**, 148 (1999).
7. E. D. Crozier and A. J. Seary, Can. J. Phys. **58**, 1388 (1980); E. D. Crozier, in *EXAFS Spectroscopy: Techniques and Applications*, edited by B. K. Teo and D. C. Joy (Plenum Press, New York, 1981), Chap. 6, pp. 89–101.
8. G. Aquilanti *et al.*, J. Synchrotron Rad. **6**, 251 (1999).
9. Y. Katayama, O. Shimomura, and K. Tsuji, J. Non-Cryst. Solids **250–252**, 537 (1999).
10. R. B. Greegor and F. W. Lytle, Phys. Rev. B **20**, 4902 (1979).
11. K. Tamura *et al.*, J. Non-Cryst. Solids **150**, 351 (1992).
12. Y. Nishihata *et al.*, J. Phys., Condens. Matter **6**, 9317 (1994).

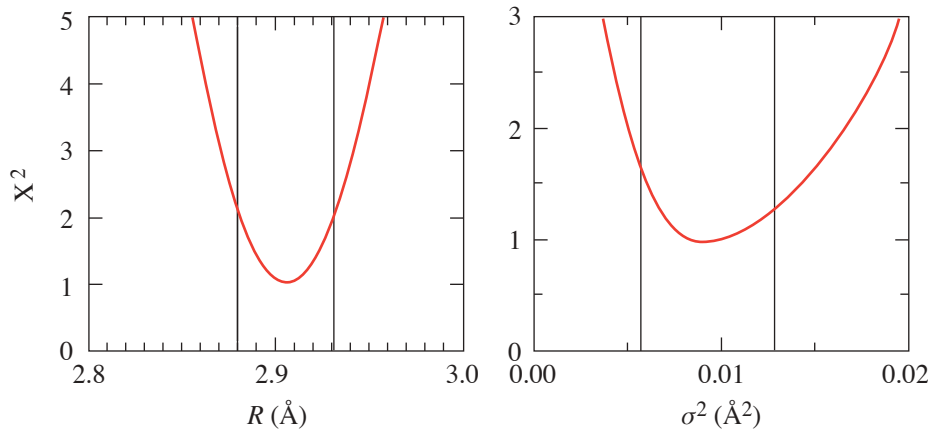


Figure 94.49
EXAFS spectrum fitting for the unshocked case (Fig. 94.43): the variation of X^2 with R for the optimal value of σ^2 and with σ^2 for the optimal value of R . The vertical lines show the standard deviation obtained from an inverse-Hessian analysis of X^2 .

13. G. Dalba and P. Fornasini, *J. Synchrotron Radiat.* **4**, 243 (1997).
14. Y. Soldo *et al.*, *Phys. Rev. B* **57**, 258 (1998).
15. A. Yoshiasa *et al.*, *J. Synchrotron Rad.* **6**, 43 (1999).
16. L. Comez *et al.*, *Phys. Rev. B* **65**, 014114 (2002).
17. A. Trapananti, A. Di Cicco, and M. Minicucci, *Phys. Rev. B* **66**, 014202 (2002).
18. R. C. Albers, A. K. McMahan, and J. E. Müller, *Phys. Rev. B* **31**, 3435 (1985).
19. A. Sadoc, J. P. Itie, and A. Polian, *Philos. Mag. A, Phys. Condens. Matter Struct. Defects Mech. Prop.* **80**, 2057 (2000).
20. P. A. Rigg and Y. M. Gupta, *Phys. Rev. B* **63**, 094112 (2001).
21. A. Hopkins and N. S. Brar, in *Shock Compression of Condensed Matter – 1999, AIP Conference Proceedings 505*, edited by M. D. Furnish, L. C. Chhabildas, and R. S. Hixson (American Institute of Physics, New York, 2000), pp. 423–426.
22. R. W. Eason *et al.*, *J. Phys. C, Solid State Phys.* **17**, 5067 (1984).
23. B. A. Shiwai *et al.*, *Laser Part. Beams* **10**, 41 (1992).
24. B. Yaakobi, F. J. Marshall, D. K. Bradley, J. A. Delettrez, R. S. Craxton, and R. Epstein, *Phys. Plasmas* **4**, 3021 (1997).
25. B. Yaakobi, F. J. Marshall, T. R. Boehly, R. P. J. Town, and D. D. Meyerhofer, *J. Opt. Soc. Am. B* **20**, 238 (2003).
26. T. R. Boehly, R. S. Craxton, T. H. Hinterman, J. H. Kelly, T. J. Kessler, S. A. Kumpan, S. A. Letzring, R. L. McCrory, S. F. B. Morse, W. Seka, S. Skupsky, J. M. Soures, and C. P. Verdon, *Rev. Sci. Instrum.* **66**, 508 (1995).
27. G. Blanche *et al.*, *Ultramicroscopy* **50**, 141 (1993).
28. A. Balzarotti, M. De Crescenzi, and L. Incoccia, *Phys. Rev. B* **25**, 6349 (1982).
29. D. A. Young, *Phase Diagrams of the Elements* (University of California Press, Berkeley, CA, 1991).
30. C. W. Greeff, D. R. Trinkle, and R. C. Albers, *J. Appl. Phys.* **90**, 2221 (2001).
31. R. G. McQueen *et al.*, in *High-Velocity Impact Phenomena*, edited by R. Kinslow (Academic Press, New York, 1970), Chap. VII, pp. 293–417.
32. H. Xia *et al.*, *Phys. Rev. B* **42**, 6737 (1990).
33. Y. K. Vohra and P. T. Spencer, *Phys. Rev. Lett.* **86**, 3068 (2001).
34. A. K. Singh, M. Mohan, and C. Divakar, *J. Appl. Phys.* **53**, 1221 (1982).
35. H. Dammak, A. Dunlop, and D. Lesueur, *Philos. Mag. A, Phys. Condens. Matter Struct. Defects Mech. Prop.* **79**, 147 (1999).
36. B.-K. Teo and P. A. Lee, *J. Am. Chem. Soc.* **101**, 2815 (1979).
37. A. G. McKale *et al.*, *J. Am. Chem. Soc.* **110**, 3763 (1988).
38. G. Beni and P. M. Platzman, *Phys. Rev. B* **14**, 1514 (1976).
39. R. M. More *et al.*, *Phys. Fluids* **31**, 3059 (1988).
40. P. A. Lee and J. B. Pendry, *Phys. Rev. B* **11**, 2795 (1975).
41. J. Mustre de Leon *et al.*, *Phys. Rev. B* **44**, 4146 (1991).
42. J. J. Rehr and R. C. Albers, *Rev. Mod. Phys.* **72**, 621 (2000).
43. E. A. Stern, B. A. Bunker, and S. M. Heald, *Phys. Rev. B* **21**, 5521 (1980).
44. B. L. Henke *et al.*, *J. Opt. Soc. Am. B* **3**, 1540 (1986).
45. G. B. Zimmerman and W. L. Kruer, *Comments Plasma Phys. Control. Fusion* **2**, 51 (1975).
46. P. M. Celliers *et al.*, *Appl. Phys. Lett.* **73**, 1320 (1998).
47. R. F. Trunin, G. V. Simakov, and A. B. Medvedev, *Teplofiz. Vys. Temp.* **37**, 881 (1999).
48. N. Dimakis and G. Bunker, *Phys. Rev. B* **58**, 2467 (1998).
49. J. A. Moriarty, D. A. Young, and M. Ross, *Phys. Rev. B* **30**, 578 (1984).
50. W. H. Press *et al.*, *Numerical Recipes: The Art of Scientific Computing* (Cambridge University Press, Cambridge, England, 1987), Chap. 14, pp. 498–546.

Modeling Temperature and Pressure Gradients During Cooling of Thin-Walled Cryogenic Targets

Introduction

High-quality targets must be provided to achieve successful results from OMEGA cryogenic experiments.¹ One type of target is a thin-walled polymer capsule with a fuel layer of solid deuterium (D_2) or deuterium/tritium (DT) ice, approximately $100\ \mu\text{m}$ thick, uniformly distributed on the inner wall of the capsule.² To create the fuel layer, the capsule is placed in a room-temperature pressure vessel and slowly pressurized, filling the capsule by permeation through the polymer wall.³ The capsule is slowly cooled to the critical point ($\sim 38.3\ \text{K}$ for D_2) to first liquefy the gas, and then further cooled to freeze it. The mass of ice is made uniform through layering techniques.⁴ Because of the capsules' fragile nature and the great amount of time required to fill them, the cooling process is a critical phase of operation for providing cryogenic targets.

The filling and cooling of the capsules takes place in the permeation cell. The permeation cell is a pressure vessel constructed of A-286, a high-strength Ni-based superalloy, which contains an insert bearing the capsules called the target rack. The permeation cell contains two parts: (1) an outer surface that carries the mechanical load designed to contain up to 1500 atm and (2) an inner surface that is the outer wall of the pressure vessel. This inner surface has a heater and silicon-diode temperature sensors bonded to it. The outer surfaces are actively cooled by helium gas at 8 K flowing through a tube wound around the outside of the permeation cell. The temperature inside the permeation cell is measured by silicon temperature sensors imbedded at various locations and is maintained by regulating the helium flow and the power to the heater on the core around the target rack. The capsules are fixed in "C-mounts" between four threads of spider silk and placed into the target rack, which is inserted into the center of the permeation cell.⁵ The target rack is designed to minimize free volume around the capsule and is constructed of high-conductivity copper to minimize temperature gradients.

This article presents the results of both a steady-state analysis and a transient analysis of the pressure differences across the wall of a thin-walled capsule during the cooling

process. The analyses were separated to quantify the effects that each phenomenon contributes. The steady-state contribution to the pressure difference arises from two sources: (1) the different thermal contractions of the materials that comprise the permeation cell and capsule and (2) the room-temperature volume of gas in the line connecting the permeation cell to the isolation valve. An optimum value for the room-temperature volume has been found that minimizes the burst and buckle pressures and allows for 1- and 3- μm -wall capsules to be filled. The transient analysis considered the pressure differences across the capsule wall that arise from temperature changes to the permeation cell. A 3- μm -wall capsule can withstand changes of 1 K at warmer temperatures, while a 1- μm -wall capsule should not be subjected to sudden temperature changes of more than 0.1 K. A cooling program that incorporates permeability at higher temperatures and safely maintains the capsule within the critical burst and buckle pressures allows the time to reach the frozen state to be reduced by over 30%.

Effect of Thermal Contraction and Room-Temperature Volume

Targets to be filled with D_2 or DT are held at room temperature while the pressure is raised at a slow, steady rate, typically to 1000 atm. The pressurization rate is based on the permeability of the capsule wall and its strength against buckling. To assure the capsule's survival, the pressurization rate is kept below P_{buckle}/τ , where P_{buckle} is the buckling pressure and τ is the permeation time constant. For a glow discharge polymer (GDP) capsule of 920- μm diameter with a 3- μm wall, $P_{\text{buckle}} \cong 1\ \text{atm}$ and $\tau \cong 30\ \text{s}$, which allows a 1000-atm fill in 11 h. It is assumed, for safety, that the fill proceeds 30% more slowly than the maximum rate. If the wall thickness is 1 μm , $P_{\text{buckle}} \cong 0.1\ \text{atm}$ and $\tau \cong 10\ \text{s}$, which requires 36 h for a similar fill. When the GDP capsules are fabricated, modifying the deposition conditions for the GDP⁶ can result in increased P_{buckle} along with higher permeability, which should allow slightly more rapid filling. After filling, a valve is closed, which isolates the permeation cell from the compressor, and the permeation cell is slowly cooled. The cooling proceeds slowly in order to (1) minimize thermal gradients in the permeation

cell and (2) allow some permeation through the capsule wall in response to a pressure differential that develops during the cooling process.

The pressure differential across the capsule wall arises partly because of a small room-temperature volume connected to the permeation cell, and partly because of differences in the thermal contraction between the polymer capsule wall and the metals of the permeation cell. The small room-temperature volume formed by the isolation valve and the tube connecting this valve to the permeation cell exists because of the unavailability of a suitable cryogenic valve. This room-temperature volume generates an external pressure on the capsule because the increasing density of the gas, as it cools, draws some of the less-dense room-temperature gas into the permeation cell. Simultaneously, the thermal contraction of both the polymer of the capsule wall, which is nearly four times greater than the contraction of the stainless steel of the permeation cell, and the copper of the target rack tends to create an excess internal pressure in the capsule.

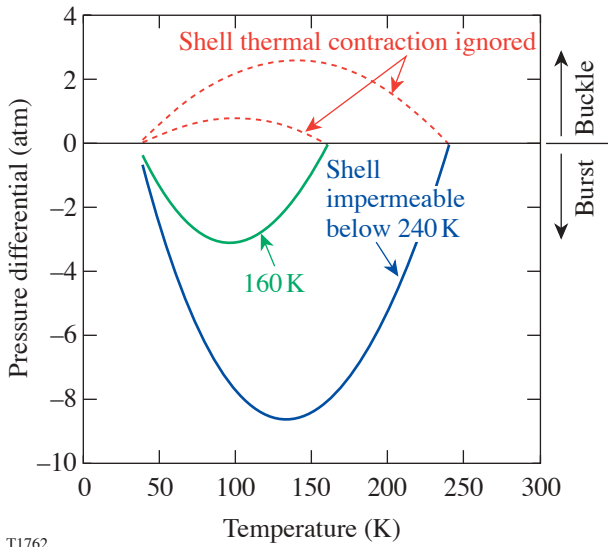
To assess these competing effects, the pressure across the capsule wall during the cooldown is calculated for various values of room-temperature volume. These calculations use the NIST equation of state for deuterium,⁷ which expresses pressure as a 24-term function of density and temperature. Starting with room-temperature volumes for the permeation cell, the copper target rack, and the small external volume, the molar content is calculated, assuming a 1000-atm fill. At each reduced temperature, the volumes of the cooled elements are recalculated based on the thermal contraction values for copper and stainless steel.⁸ The portion of the connecting tube between the room-temperature volume and the permeation cell that has a thermal gradient on it—one-quarter as large as the room-temperature volume—is treated as being part of the room-temperature volume. While varying the temperature of the permeation cell, the pressure and density in the cell are determined by solving three simultaneous equations: (1) conservation of the sum of the molar content of the permeation cell and the room-temperature volume, taking thermal contraction into account; (2) equating the pressure in the permeation cell with that in the room-temperature volume; and (3) applying the deuterium equation of state.

To calculate the pressure in the capsule during the cooldown, a temperature is arbitrarily selected below which the capsule is assumed to be impermeable. This strategy is justified by the sharp decrease in permeability with temperature generally exhibited by polymers, following the Arrhenius

relation. The activation energy for this process has not been measured for the GDP shell material, so the temperature at which the shell becomes effectively impermeable is unknown; however, comparison to polystyrene,⁹ which has a similar value of room-temperature permeability, suggests this temperature is in the range of 160 K to 240 K, depending on wall thickness and cooling rate. Within this temperature range, the permeation time constants of capsules with wall thicknesses of 1 to 3 μm range from 10 to 60 min. At lower temperatures, no significant permeation occurs with practical rates of cooling, such as 0.1 K/min. Vapor-deposited polyimide, which is less permeable,¹⁰ becomes effectively impermeable in the temperature range of 220 K to 290 K, if it is previously unstrained. The thermal contraction of GDP is estimated by scaling the polystyrene data⁹ with a contraction value measured for a GDP sample cooled from room temperature to 77 K. The length of this flat sample was found to decrease by 0.99% when immersed in liquid nitrogen, compared to 1.32% for the polystyrene data. To estimate the GDP contraction as a function of temperature, the polystyrene data are multiplied by 0.75, the ratio of the GDP value to the polystyrene value at 77 K.

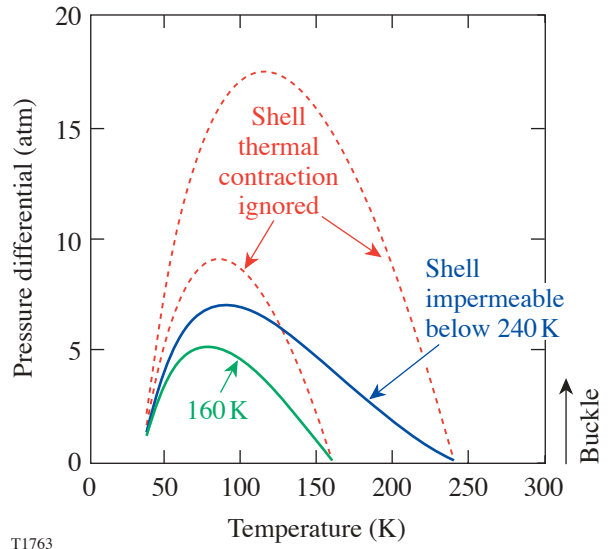
The results of these calculations are shown in Figs. 94.50–94.53. In Fig. 94.50, it is seen that if the room-temperature volume is zero (i.e., if there was a cryogenically cooled isolation valve), a substantial bursting pressure is generated. It is also seen that if there was no shell contraction, the pressure differential generated would be external—a buckling pressure. Comparing Fig. 94.51 to Fig. 94.50, it is seen that adding a relatively small room-temperature volume of 0.3 cc changes the result from a strong bursting pressure to a strong buckling pressure. In Fig. 94.52, an effective compromise between these cases is shown. Reducing the warm volume to 0.11 cc yields a tolerable buckling pressure that a thin-walled capsule should survive and a similarly modest bursting pressure. This conclusion seems to hold regardless of what temperature in the range 160 K to 240 K best represents the effective point at which the capsule becomes impermeable. Other values of warm volume were tried, and 0.11 cc was found to be an optimum value. The volume actually achieved, however, after insertion of volume reducers is estimated to be 0.17 cc. Figure 94.53 plots the pressure differential across the capsule as a function of temperature for various temperatures at which the capsule could become impermeable. A positive pressure differential exceeding 1.5 atm develops, easily buckling a capsule with a 1- μm wall.

The expected buckling pressures shown in Fig. 94.53 for capsules with 1- μm and 3- μm wall thickness are calculated



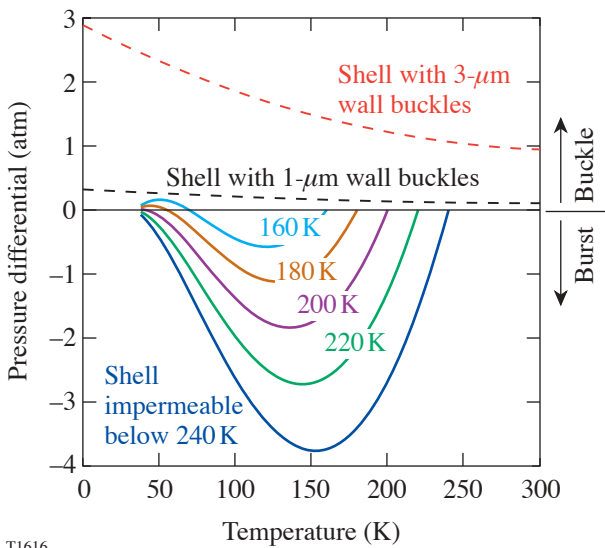
T1762

Figure 94.50
The calculated pressure differential across a capsule wall (assumed inelastic) is plotted for the case of zero room-temperature volume. The capsule is permeated with 1000 atm of D₂ and then cooled slowly to 25 K or lower. The dashed lines indicate the excess external pressure (buckling pressure) that would occur if thermal contraction of the permeation cell is taken into account, but not thermal contraction of the capsule. The solid lines include capsule contraction and show a large bursting pressure. If the capsule becomes impermeable at 240 K, a very large burst pressure is generated, while permeability at temperatures down to 160 K, followed by impermeability at lower temperatures, produces more-modest internal pressures.



T1763

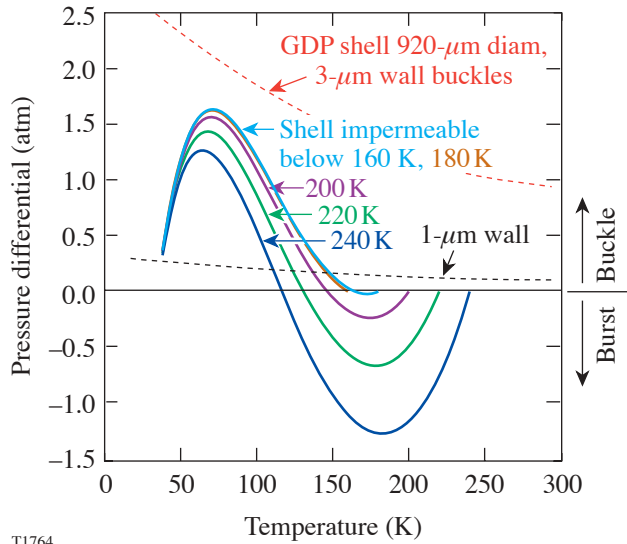
Figure 94.51
The calculated pressure differential across a capsule wall is plotted for a realistic room-temperature volume of 0.3 cc and a permeation cell volume of 5 cc. The dashed lines ignore thermal contraction and the solid lines include it. An excess pressure external to the capsule arises that would cause any thin-walled capsule to buckle. An inelastic capsule is assumed. The room-temperature volume is reduced from this value by insertion of spacers.



T1616

Figure 94.52
The calculated pressure differential across a capsule wall is plotted for a small value of room temperature volume for various temperatures at which the capsule could become impermeable. The dashed lines indicate the buckling pressure of capsules with 1- and 3- μ m walls. Reducing the room-temperature volume to 0.11 cc reduces the buckling pressure to a level that is survivable by an inelastic shell with a 1- μ m wall. While this volume appears optimal, it would be difficult to achieve such a small volume.

using values of Young’s modulus inferred from measuring the buckling pressures of a group of GDP capsules at various temperatures. It is found that Young’s modulus increases significantly upon cooling, reaching a value at 10 K of 2.5× the value at room temperature.



T1764

Figure 94.53
The calculated pressure differential across an inelastic capsule wall is plotted for an achievable room-temperature volume of 0.17 cc for various temperatures at which the capsule could become impermeable. The dashed lines show the buckling pressures for capsules with 1- and 3-μm walls. The thicker-walled capsules would survive, while the thinner-walled ones would not.

Effect of Shell Elasticity

The preceding calculations do not take into account the expansion or shrinkage of the capsule due to internal or external pressure. Taking into account dimensional change due to elasticity reduces the resulting differential pressure on the capsule wall,¹¹ rendering it less vulnerable to bursting or buckling. The calculations assume the capsule wall is perfectly spherical, uniform in thickness, and homogeneous. The fractional change in the radius *r* is given¹² by

$$\frac{\Delta r}{r} = \frac{r \Delta P(1 - \nu)}{2 E w}, \tag{1}$$

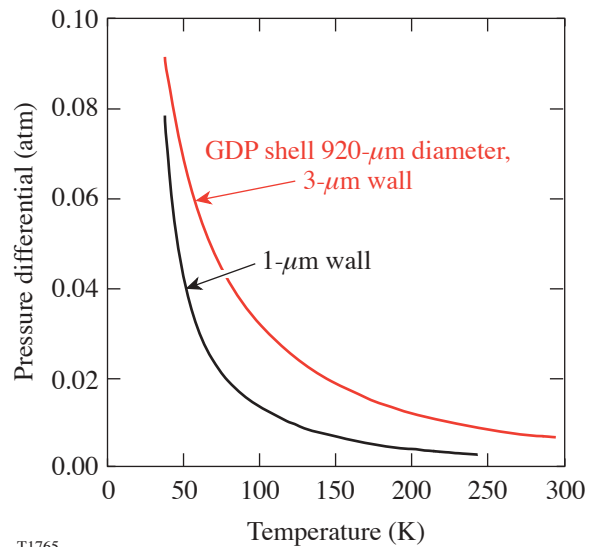
where ΔP is the pressure differential across the wall, ν is Poisson’s ratio of the capsule material (the polystyrene value, 0.35, is used here), E is Young’s modulus, and w is the wall thickness. While deuterium at the densities of a typical target

fill is far from an ideal gas, it is useful to consider the functional dependence of the pressure differential on elasticity for the ideal gas case. If a pressure differential ΔP_i is applied across a capsule wall, which thereupon undergoes elastic expansion or contraction, the final pressure differential is readily found to be, in the ideal gas case, for $\Delta r \ll r$,

$$\Delta P_f \cong \frac{\Delta P_i}{1 + (P + \Delta P_i) \frac{3r(1 - \nu)}{2 E w}}, \tag{2}$$

where P is the initial pressure inside and outside the capsule. This solution is useful as a check on the non-ideal-gas solution at its low-pressure limit.

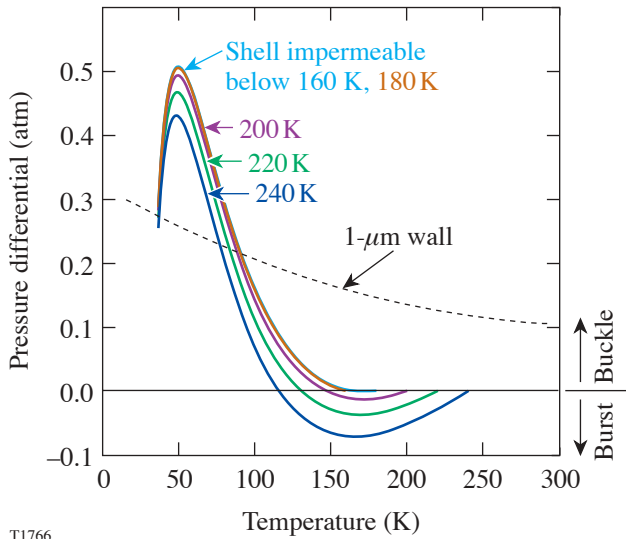
To calculate ΔP resulting from a change in the pressure external to the capsule for the non-ideal-gas case, Eq. (1) is solved by applying the deuterium equation of state along with the requirement that the molar content of the capsule is unchanged. The result, dependent on temperature and wall thickness, is shown in Fig. 94.54 for the case of a 0.1-atm change in the external pressure. Applying this method to the pressure differential that results from thermal contraction and a room-



T1765

Figure 94.54
Pressure differential across the wall of an elastic capsule (GDP) that has expanded or contracted due to a 0.1-atm change in external pressure. The capsule diameter is 920 μm, and the wall thickness is 1 or 3 μm. At such a high gas density (~25 mol/L), external pressure changes are substantially attenuated.

temperature volume, the data in Fig. 94.53 are transformed into Fig. 94.55. For a room-temperature volume of 0.17 cc, the maximum pressure differential is reduced from 1.6 atm to 0.5 atm but is still enough to buckle a shell with a 1- μm wall. The buckling problem could be solved by reducing the warm volume to 0.11 cc or by adjusting thermal gradients in the permeation cell. These calculations, showing reduced vulnerability to failure due to capsule elasticity, assume the capsule is perfectly spherical and of uniform wall thickness, and have not been tested experimentally.



T1766

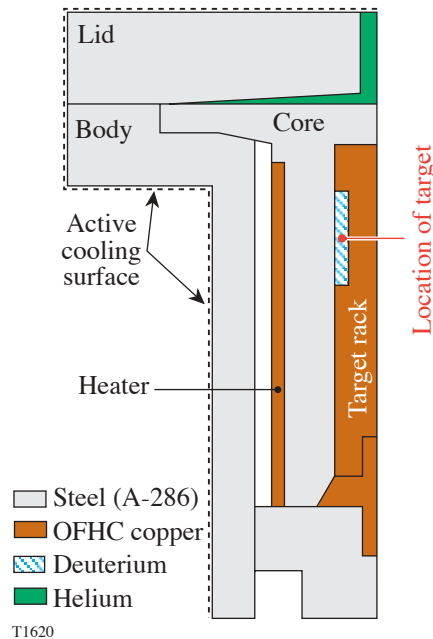
Figure 94.55 Pressure differential across an elastic capsule (GDP) wall of 1- μm thickness and 920- μm diameter, and a room-temperature volume of 0.17 cc. The capsule's buckling pressure (dashed line) is also plotted. While the maximum external pressure is reduced by more than a factor of 3 from the case of the inelastic shell (Fig. 94.53), the capsule's buckling pressure would still be exceeded.

Modeling the Transient Cooling Phase

A computational fluid dynamics (CFD) program is used to calculate the temperature profiles and heat flows inside the permeation cell. Only through modeling can the thermal conditions and the forces on the capsule during the transient cooling phase be quantified. When cooling is enacted, the thermal gradients change inside the permeation cell and therefore across the capsule wall. This temperature difference creates a pressure difference that leads to either a burst or buckling pressure on the capsule. Exceeding the material properties causes the capsule to fail by either bursting or collapsing. As stated previously, the failure pressure of thin-walled capsules is small, and significant pressure differences can occur during transient cooling processes if the cooling rate

is too large. The CFD simulation is used to calculate the resulting pressure difference across the capsule wall caused by cooling steps throughout the temperature range from 294 K to 40 K. These results are used to determine a cooling program that could successfully cool capsules until the fuel freezes while avoiding a pressure difference that may destroy the capsule. Reducing the typically lengthy cooling time increases target production and saves operator effort. A maximized cooling rate is much more important when filling with DT; reducing the cooling time will minimize He³ buildup and capsule deterioration.

The permeation cell and its components are recreated as a two-dimensional axisymmetric model, shown in Fig. 94.56. The model is comprised of the A-286 superalloy body, lid, and core, the copper target rack, and deuterium gas in the space



T1620

Figure 94.56 A two-dimensional axisymmetric representation of the permeation cell. The properties of the temperature-dependent materials are accounted for in the model. The capsule is located in the center of the gas space around the target rack. The boundary conditions are held on the outer cooling surfaces of the model, and the temperatures are implemented by changing the power to the heater. The averages gas temperatures external and internal to the capsule wall are recorded. The corresponding external and internal pressures, which are a function of temperature and density, are calculated from the deuterium equation of state.

surrounding the capsule and target rack. The capsule is located in the center of the deuterium gas space in the notch of the target rack. The solutions are generated using *FLUENT* computational fluid dynamics software.¹³

The following solution procedure is used to determine the pressure difference across the capsule wall. Temperature boundary conditions are set on the outer surfaces of the model (on the lid and body) and on the heater, as shown in Fig. 94.56. The permeation cell is initially considered isothermal. This assumption is applicable for deuterium—not DT, which generates heat—and is an approximation of the actual conditions. The solver uses the temperature-dependent material properties of the components and gas, which are listed in Table 94.I. These properties span a wide range over the temperature range from 294 K to 40 K. To commence the simulation, the temperature setting on the silicon diode is lowered to enact a cooling step. The temperature in each volume element is recorded as the simulation progresses, and a temperature profile in the permeation cell is generated. The simulation is run until a steady-state final temperature profile develops. This is assumed when the average capsule temperature reaches a steady value. From the instantaneous temperature in each volume element of the model, the time instantaneous and volume-averaged temperatures on either side of the capsule wall are calculated. These average temperatures are converted into average gas pressures from the deuterium equation of state. The average internal and external pressures of the capsule yield the bursting pressure as a function of time.

Cooling steps in increments of 0.125, 0.5, and 1 K are performed at temperatures through the temperature range from 294 K to 40 K. The size of the increments was chosen due to the accuracy of the sensors and the magnitude of actual cooling increments. (The temperature resolution of the sensor is 1 K at

300 K and 0.5 K at 100 K.) After a cooling step is made, the temperature of the gas inside the capsule lags behind that of the external gas and the magnitude of the difference depends on the temperature-dependent physical properties of the gas. The thermal diffusivities of the steel and deuterium are plotted in Fig. 94.57. The gas, which has a thermal diffusivity one to two orders of magnitude less than that of the metals, responds more slowly to temperature changes, and the difference increases at lower temperatures. The difference (ΔT) between the average external (to the capsule) and internal temperatures for three

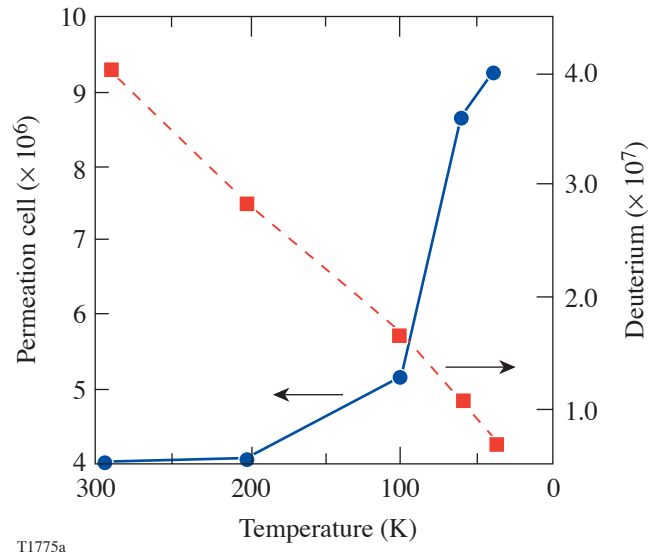


Figure 94.57 The thermal diffusivities of the steel and deuterium as a function of temperature are plotted. The gas, which has a thermal diffusivity one to two orders of magnitude less than that of the metals, responds more slowly to temperature changes, and the difference between the thermal diffusivity of the gas and steel increases at lower temperatures.

Table 94.I: Temperature-dependent properties of materials in the permeation cell model.

| | 294 K | | 100 K | | 40 K | |
|--|-------|------|-------|------|-------|-------|
| | C_p | k | C_p | k | C_p | k |
| Steel | 503 | 16.3 | 216 | 9 | 40 | 3 |
| Copper | 381 | 388 | 253 | 500 | 60 | 1000 |
| Deuterium (1000 atm @ 294 K) | 7790 | 0.32 | 8900 | 0.15 | 14300 | 0.098 |
| C_p = heat capacity (J/kg K) k = thermal conductivity (W/m K) | | | | | | |

different cooling steps is shown as a function of time in Figs. 94.58(a)–94.58(c). The largest average ΔT of about -0.2 K for a temperature change of 1.0 K occurs about 10 to 20 s after the change is made, depending at which temperature it occurs. As the temperature of the gas external to the capsule equilibrates, ΔT approaches zero in less than 100 s. The values of ΔT shown in the figures are negative for the case of cooling. It is possible, however, that ΔT becomes positive if the permeation cell was warmed (for example, a cooling power fluctuation or a control error).

The calculated temperature profiles are converted to pressure differences (ΔP) across the capsule wall. For temperature changes made in increments of 0.125 , 0.5 , and 1.0 K, the temporal pressure difference at temperatures through the cooling cycle are shown in Figs. 94.59(a)–94.59(c), respectively. Since the external temperature is less than the internal temperature, and likewise for the pressures, a burst pressure develops inside the capsule. The pressure gradient reaches a maximum ΔP_{\max} before dissipating as the temperatures across the wall equilibrate and/or permeation takes place. In all three cases, more severe pressure gradients occur at lower temperatures. This is explained by the increase of heat capacity and decrease of thermal conductivity of deuterium at reduced temperatures. The gas responds more slowly to thermal changes as the thermal diffusivity decreases. Therefore, as the difference

between the external and internal temperatures increases, so does the pressure difference. As shown, the induced burst pressure approaches 0.9 atm for a temperature change of 1.0 K. This is well within the limits of thin-walled plastic capsules. As mentioned in the previous paragraph, it is possible that ΔP becomes positive if the permeation cell was warmed. If this occurs, a buckling pressure would be applied on the capsule. For a $1\text{-}\mu\text{m}$ -wall GDP capsule, P_{buckle} is ~ 0.1 to 0.2 atm, and a warming of 0.125 K causes a buckling pressure very near the failure limit. It is therefore essential that $1\text{-}\mu\text{m}$ capsules are not warmed suddenly by more than 0.1 K.

No single cooling step of 1.0 K causes a pressure difference that would burst a capsule of these dimensions. A series of temperature changes, however, in which the next step occurs before the pressures equilibrate can cause ΔP to exceed its bursting pressure. After each cooling step, an amount of time elapses before ΔP vanishes due to temperature equilibration (assuming no permeability). The equilibration times, shown in Fig. 94.60, increase at the colder temperatures of the cooling program. This effect is also attributed to a lower thermal diffusivity of the gas. This suggests that greater consideration must be taken in this temperature regime, namely a slower cooling rate. Likewise, the cooling rate (and associated depressurization rate) may be increased in the initial stages of the cooling program where temperatures are higher.

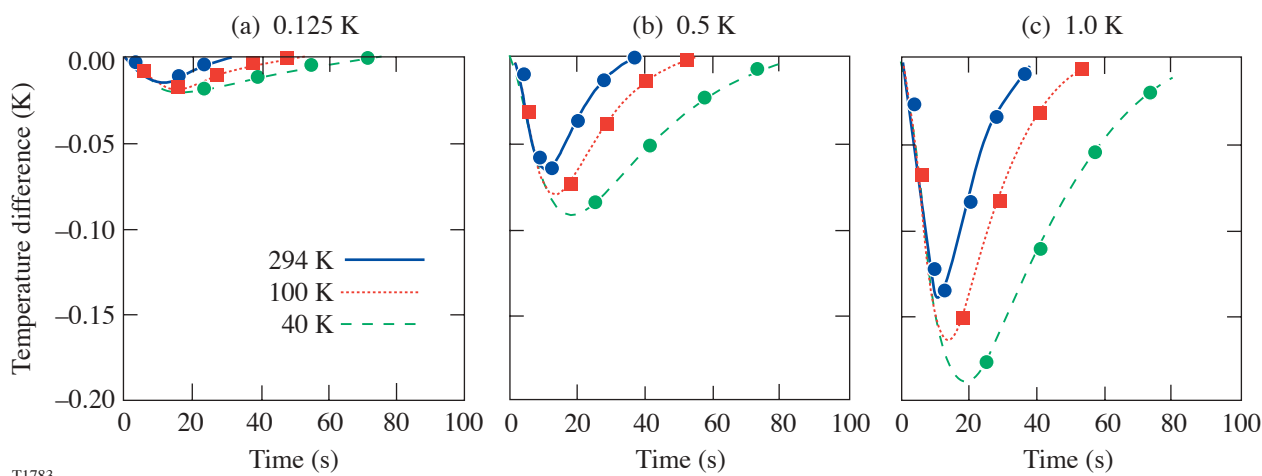


Figure 94.58

The difference (ΔT) between the average external (to the capsule) and internal temperatures for cooling steps of (a) 0.125 K, (b) 0.5 K, and (c) 1.0 K is plotted as a function of time for various temperatures. The largest average ΔT of nearly -0.2 K for a temperature change of 1 K occurs about 10 to 20 s after the change is made, depending at which temperature it occurs. As the temperature of the gas external to the capsule equilibrates, ΔT approaches zero in less than 100 s. The values of ΔT shown in the three figures are negative for the case of cooling. It is possible, however, that ΔT becomes positive if the permeation cell was warmed.

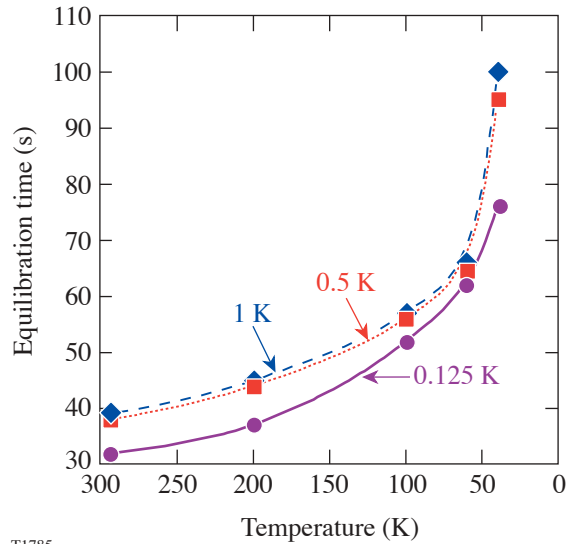
The permeability of the capsule material affects the pressure gradients across its wall. As time elapses, the pressure difference between the external and internal gas will be reduced as the temperatures equilibrate and permeation occurs. Permeation through a polystyrene capsule is temperature dependent and permeability follows the Arrhenius relation:⁹

$$K_p = 1.18 \times 10^{-12} \exp(-1535/T),$$

where K_p is in units of mol/m s Pa and T is in K. The permeation time constant τ of deuterium through polystyrene is given by the equation

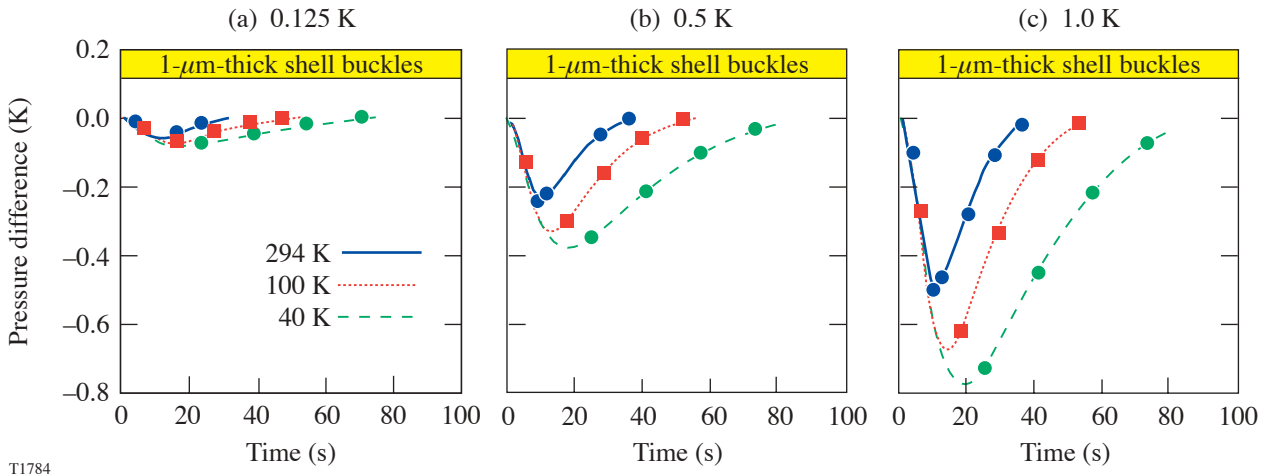
$$\tau = wD/6 K_p RT,$$

where w and D are the capsule's wall thickness and diameter, respectively, and R is the gas constant. (Vapor-deposited polyimide capsules can be less permeable.) Since the gas outside the capsule cools first and reduces pressure, an overpressure inside the capsule occurs for each temperature change. A succession of cooling steps can be viewed as a depressurization rate on the capsule. The maximum-allowable depressurization rate a capsule may experience is expressed as



T1785

Figure 94.60 The amount of time required for the pressure difference to equilibrate across the capsule wall after a cooling step, assuming no permeation, as a function of temperature. Curves for the three different cooling steps are shown. The time increases at lower temperatures due to the increase in thermal diffusivity of the gas.



T1784

Figure 94.59 The difference (ΔP) between the external (to the capsule) and the internal gas pressures that arise from cooling steps of (a) 0.125 K, (b) 0.5 K, and (c) 1.0 K is plotted as a function of time for various temperatures. Negative values of ΔP indicate a burst pressure. The external and internal gas pressures, which are a function of temperature and density, are calculated from the deuterium equation of state. The peak ΔP occurs at 10 to 20 s and is more pronounced at lower temperatures. The values of ΔP shown in the three figures are negative for the case of cooling. It is possible, however, that ΔP becomes positive (representing a buckling pressure) if the permeation cell was warmed. The dashed line indicates the value of ΔP at which a 1- μ m-wall GDP capsule will buckle. Capsules with a 1- μ m-thick wall would easily buckle from positive temperature changes of 0.5 K and 1 K and are near the limit for temperature changes of 0.125 K.

$\sim (P_{\text{burst}}/\tau)$, where P_{burst} is the capsule's bursting pressure. The capsule would fail if the bursting pressure was reached while depressurizing at this rate. Assuming a 920- μm -diam capsule with a 3- μm -thick wall and material properties of GDP, the capsule's bursting pressure is ~ 5.7 atm. Since τ is inversely proportional to temperature and permeability, the maximum-allowable depressurization rate decreases at lower temperatures; thus, cooling should be slowed to prevent capsule breakage. A plot of allowable depressurization rates (dP^*/dt) is shown in Fig. 94.61, where, as a safety concern, (dP^*/dt) is one-half the maximum value. At the temperature at which the capsule becomes impermeable, (dP^*/dt) approaches zero because τ approaches infinity. However, low depressurization rates (~ 0.1 K/min) are possible because the capsule never reaches P_{burst} before the pressures are balanced by temperature equilibration.

Currently, gas-filled capsules are cooled at a rate of 0.1 K/min from room temperature until the fuel liquefies. Thus, it takes about 45 h to complete the process. A faster cooling program may be achieved by analyzing the pressure differ-

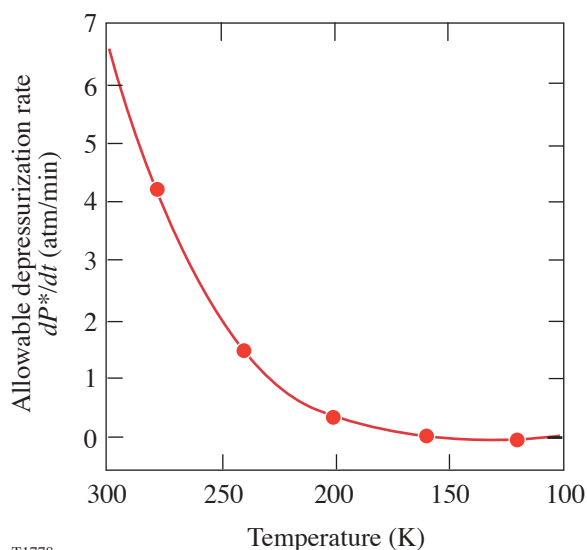
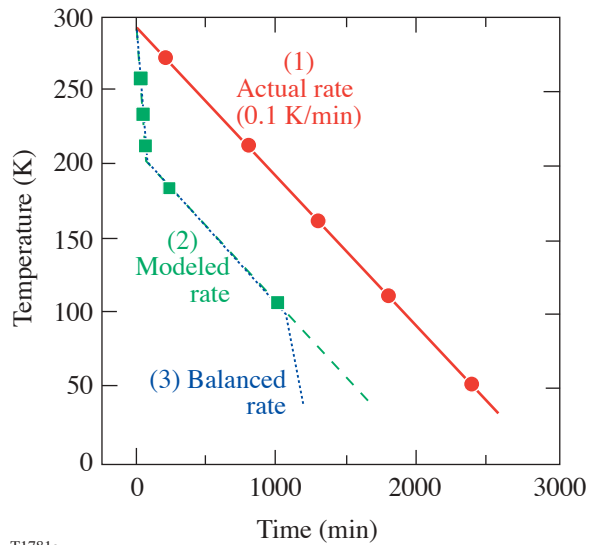


Figure 94.61

Allowable depressurization rates (dP^*/dt) for a 920- μm -diam, 3- μm -thick-wall capsule as a function of temperature. The allowable rate was one-half the maximum rate for safety considerations. The curve is based on the relationship $(dP/dt) \sim (P_{\text{burst}}/\tau)$. The permeability values of polystyrene were used to calculate τ because the temperature-dependent permeability of GDP has not been measured. This approximation is used because of the generally similar Arrhenius behavior of polymers and the similar values of permeability of polystyrene and GDP at room temperature.

ences on the capsule via modeling. From the cooling-induced pressure differences shown in Figs. 94.59(a)–94.59(c), the maximum pressure difference occurs ~ 10 to 20 s after the cooling step. From the initial descent portion of each curve (until ΔP_{max}), one can calculate the depressurization rate of the gas outside the capsule that arises from a temperature change. The goal then is to make cooling steps that maintain the depressurization rate below the allowable value (dP^*/dt) shown in Fig. 94.61 at each temperature. As shown in Fig. 94.59(c), from 294 K to 255 K, a cooling step of 1 K can be made, which results in ΔP_{max} of 0.48 atm in 10 s. This gives a depressurization rate of 2.9 atm/min, which can be converted back into a cooling rate. To minimize the total cooldown time, a subsequent cooling step should be made at the time ΔP_{max} is reached, about 10 s for the 294-K curve in Fig. 94.59(c). Thus a cooling rate of 5 K/min can be performed safely. According to Fig. 94.61, in the temperature range from 255 K to 240 K, it is required that (dP^*/dt) be less than ~ 2 atm/min. From the 294-K curve in Fig. 94.59(b), a cooling step of 0.5 K causes ΔP_{max} of 0.24 atm at 11 s. The use of the 294-K curve at these temperatures is justified because the initial slopes of the 294-K and 200-K curves (the latter is not shown) that cover this temperature range are essentially similar. This corresponds to a depressurization rate of 1.31 atm/min, which is safely within the limit. If another cooling step is made at 11 s (the time when ΔP_{max} is reached), then the subsequent cooling rate is 2.7 K/min. This procedure was continued in a likewise fashion to further choose temperature changes below 240 K that maintain the depressurization rate below (dP^*/dt) as cooling progresses. These calculations yield an acceptable cooling program to 40 K, shown in Fig. 94.62, where the minimum rate of 0.1 K/min is used below 200 K. For comparison, the cooldown program used in actual experiments of 0.1 K/min throughout the entire temperature range from 294 K to 40 K is also plotted in the figure. With the revised cooling program, which takes into account permeation at higher temperatures, the total cooling time has dropped from 2450 min to 1670 min, a savings of over 14 h (34% of the total time).

When considering the buckling pressure caused by the steady-state effects described earlier (thermal contraction mismatch and room-temperature gas volume) and the burst pressure caused by transient cooling, it is conceivable that one could balance these contributions to develop a faster cooling program. Note that capsules are more susceptible to buckling than bursting. As shown in Fig. 94.55, a dangerous buckle pressure of about 0.2 to 0.5 atm arises while cooling from 100 K to 50 K. In this regime, a cooling step of 0.5 K, which causes a burst pressure of about 0.3 atm, may be used to offset



T1781a

Figure 94.62

Temperature program for cooling a gas-filled capsule to freezing. Three different programs are plotted: (1) the currently used experimental rate (0.1 K/min), (2) a faster rate that accounts for permeation at higher temperatures to offset pressure differences, and (3) a proposed faster rate that accounts for permeation at higher temperatures and allows cooling-induced burst pressures and steady-state-effect buckle pressures to counterbalance each other.

buckling pressure. If a step is made every minute, allowing for the pressure to equilibrate, it is plausible that the total cooling time may be halved to ~ 1200 min, as shown in Fig. 94.62.

Summary

An analysis of the temperature and pressure gradients in the permeation cell that occur during the cooling of thin-walled cryogenic targets has been presented. Both steady-state and transient effects may cause the capsule to fail during cooling. The steady-state contribution to the pressure difference arises from three sources: (1) the thermal contraction of the materials that comprise the capsule and the permeation cell, (2) the room-temperature volume of gas in the line connecting the permeation cell to the isolation valve, and (3) elastic deformation of the capsule. An optimum value for the room-temperature volume has been found that minimizes the burst and buckle pressures. The transient analysis considered the pressure differences across the capsule wall that arise from temperature changes to the permeation cell. A $3\text{-}\mu\text{m}$ -wall capsule can withstand changes of 1 K at warmer temperatures, while a $1\text{-}\mu\text{m}$ -wall capsule should not be subjected to sudden temperature changes of more than 0.1 K. A cooling program that incorporates permeability at higher temperatures and safely

maintains the capsule within the critical burst and buckle pressures allows the time to reach the frozen state to be reduced by over 30%.

ACKNOWLEDGMENT

This work was supported by the U.S. Department of Energy Office of Inertial Confinement Fusion under Cooperative Agreement No. DE-FC03-92SF19460, the University of Rochester, and the New York State Energy Research and Development Authority. The support of DOE does not constitute an endorsement by DOE of the views expressed in this article.

REFERENCES

1. Laboratory for Laser Energetics LLE Review **90**, 49, NTIS document No. DOE/SF/19460-437 (2002). Copies may be obtained from the National Technical Information Service, Springfield, VA 22161.
2. D. D. Meyerhofer, C. Chiritescu, T. J. B. Collins, J. A. Delettrez, R. Epstein, V. Yu. Glebov, D. R. Harding, R. L. Keck, S. J. Loucks, L. D. Lund, R. L. McCrory, P. W. McKenty, F. J. Marshall, S. F. B. Morse, S. P. Regan, P. B. Radha, S. Roberts, W. Seka, S. Skupsky, V. A. Smalyuk, C. Sorce, C. Stoeckl, J. M. Soures, R. P. J. Town, J. A. Frenje, C. K. Li, R. D. Petrasso, F. H. Séguin, K. Fletcher, C. Padalino, C. Freeman, N. Izumi, R. Lerche, T. W. Phillips, and T. C. Sangster, presented at the 14th Target Fabrication Meeting, West Point, NY, 15–19 July 2001.
3. Laboratory for Laser Energetics LLE Review **81**, 6, NTIS document No. DOE/SF/19460-335 (1999). Copies may be obtained from the National Technical Information Service, Springfield, VA 22161.
4. M. D. Wittman, D. R. Harding, P. W. McKenty, H. Huang, L. S. Iwan, T. J. Kessler, L. Elasky, and J. Sailer, presented at the 14th Target Fabrication Meeting, West Point, NY, 15–19 July 2001.
5. S. G. Noyes, M. J. Bonino, D. Turner, J. Tidu, and D. R. Harding, presented at the 14th Target Fabrication Meeting, West Point, NY, 15–19 July 2001.
6. A. Nikroo *et al.*, *Fusion Sci. Technol.* **41**, 214 (2002).
7. R. Prydz, K. D. Timmerhaus, and R. B. Stewart, in *Advances in Cryogenic Engineering*, edited by K. D. Timmerhaus (Plenum Press, New York, 1968), Vol. 13, pp. 384–396.
8. G. K. White, *Experimental Techniques in Low-Temperature Physics*, 2nd ed., Monographs on the Physics and Chemistry of Materials (Clarendon Press, Oxford, 1968), p. 377.
9. L. A. Scott, R. G. Schneggenburger, and P. R. Anderson, *J. Vac. Sci. Technol. A* **4**, 1155 (1986).
10. F.-Y. Tsai, D. R. Harding, S. H. Chen, T. N. Blanton, and E. L. Alfonso, *Fusion Sci. Technol.* **41**, 178 (2002).
11. R. Stephens, General Atomics, private communication (2001).
12. W. C. Young, in *Roark's Formulas for Stress & Strain*, 6th ed. (McGraw-Hill, New York, 1989), p. 523.
13. *FLUENT* (version 6.0.20), Fluent USA Inc., Lebanon, NH 03766.

Development of an Elementary Climate Model: Two-Layer Cellular Case

Introduction

The recent gradual increase in Earth's average temperature¹ is generating intense interest in both public and scientific circles. It is important that physicists understand the basic energetics in climatology. While excellent climatology texts such as Hartmann's² exist, materials generally available to the undergraduate physics major and instructor lack a systematic physical treatment and an unavoidable terminology barrier exists. The comprehensive and readable work of Peixoto and Oort,³ written by and for physicists, is at a level too demanding for introductory study. We concentrate solely on some aspects of the basic energy transfer to establish a level suitable for undergraduate teaching; more sophisticated treatments do exist.⁴⁻⁷

Despite the complexities of the real atmosphere, the global average temperature of 288 K (Ref. 2, p. 2) may be estimated with remarkably few modifications of the classic homogeneous blackbody model of Earth.^{2,8-11} One purpose of developing this article has been to build on our earlier elementary model⁹ as realistically as possible, retaining both a physics style and a reasonable mathematical and computational level. We thought it would be of interest to see whether the two-layer model of the energy fluxes could be employed on a regional basis, for which we consider Earth's surface covered by a layer of 864 noninteracting cells. Here we will show that it does appear to be a consistent theory that can provide certain insights. In particular, we find that the cellular radiative energy transports clearly dominate the cellular nonradiative energy flux. We show that this flux has a strong systematic dependence on latitude and time of year. Thus, for this article we wish to avoid using a more precise radiative model of the atmosphere. Also, all heat transmission through the earth's surface is neglected. This precludes a quantitative prediction of the phase difference between the cyclical variations of the solar flux and the surface temperature.

We first briefly review the two-layer model in order to set up notation. In our earlier work⁹ the two layers of the Arrhenius model were called, informally, the atmosphere and the surface. Except for one nonradiative flux S_{NR} , all energy transfers were

modeled as radiative. The model makes use of the fact that the incoming solar radiation and the outgoing terrestrial radiation occupy distinct spectral regions called respectively, for convenience, UV and IR. The upper layer, at temperature T_A , has a UV reflectivity and absorptivity, r_A and a , respectively, and an IR absorptivity ϵ . The symbols a and ϵ are used here in place of f and g in the original article but all other notation is preserved. The surface, at temperature T_E , has a UV reflectivity r_S and is assumed to absorb all incident IR. The solar radiation has a flux $S_0 = 342 \text{ W/m}^2$ when averaged over time and over the surface of the earth. When the UV radiation hits the upper layer, a part r_A is reflected and the part that enters the layer is $(1-r_A)$. Of this part, $a(1-r_A)$ is absorbed. In this first pass, the surface therefore receives $(1-r_A)(1-a)$, of which r_S is reflected, leaving $(1-r_A)(1-a)(1-r_S)$ as the fraction of original incident solar flux to be absorbed at the surface. Following this logic, a diagram can be constructed showing all the fractions of absorbed and reflected radiation including the term S_{NR} for nonradiative energy transfer (Fig. 94.63). When multiple reflections are included, a factor $k_M = (1-r_A r_S)^{-1}$ appears in terms involving reflections between the surface and atmosphere. The nonradiative flux S_{NR} , which served as an arbitrary model parameter in the global calculation, will be seen to play a much greater role in the current work.

The energy-balance equations for the upper and surface layers take the form

$$2\epsilon S_A - \epsilon S_E = AS_0 + S_{\text{NR}} \quad (1a)$$

and

$$-\epsilon S_A + S_E = BS_0 - S_{\text{NR}}, \quad (1b)$$

respectively. These equations express net incoming UV and nonradiative flux on the right-hand sides and net outgoing IR flux on the left. Here S_A and S_E are defined as the ideal Stefan-Boltzmann fluxes $S_A = \sigma T_A^4$ and $S_E = \sigma T_E^4$, where $\sigma = 5.67 \times 10^{-8} \text{ W/m}^2 \text{ K}^{-4}$. The quantities A and B correspond to the fractions of S_0 ultimately absorbed by the atmosphere and

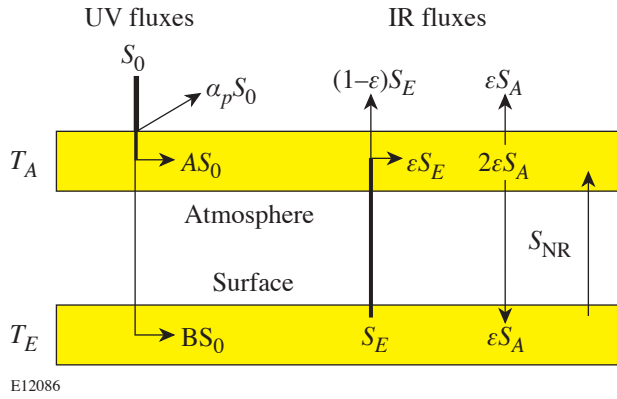


Figure 94.63
Movement of radiative and nonradiative energy in the two-layer scheme. Horizontal arrows indicate deposition in the layer. Lighter arrows represent radiation that is either reflected or passed through a layer unabsorbed. Multiple reflections of UV radiation are accounted for by the factor k_M in Eqs. (1a) and (1b) in the text. The factors α_p , A , and B are the overall fractions of S_0 that are reflected, absorbed by the upper layer, and absorbed by the lower layer, respectively. Other symbols are defined in the text.

surface, respectively,

$$A = a(1 - r_A) + ak_M(1 - r_A)^2(1 - a)r_S \quad (2a)$$

and

$$B = k_M(1 - r_A)(1 - r_S)(1 - a) \quad (2b)$$

Global and time averages of all the parameters are inserted, and Eqs. (1) are easily solved for S_A and S_E , from which temperatures T_A and T_E are then obtained. This original model was used to investigate broadly the effect of non-solar-related energy sources at the surface.

The following sections (1) extend the model by introducing coarsely grained surface features and locally time averaged fluxes in 864 noninteracting cells; (2) compute and discuss zonal (latitudinal) averages; and (3) summarize and discuss the limitations of the model and possibilities for its further development.

Cellular Model

1. Rationale and Design

We choose the grid scheme used by Hansen *et al.*¹² in which the earth's surface is divided into 864 cells of dimension $8^\circ \times 10^\circ$ (latitude by longitude). We then assume that Eqs. (1) are satisfied within each cell. The next step is to extend the computations from globally time-averaged to locally time-

averaged parameters. For each of the 864 cells, the land fraction and the annually averaged parameters for observed total cloud cover fraction, calculated incoming annual average solar radiation, and land and sea reflectivities are stored. All parameters are determined at the center of the cell, and the values are applied to the entire area of the cell. The energy-balance equations are then solved at each location. For comparison to global values, the local values are weighted by fractional cell area and summed. Our model does not take into account changes in atmospheric components, the parameters' temperature dependence,¹¹ or any geothermal variations.

All programming is done using MATLAB[™], an array-based language with simple commands. In the MATLAB environment, each computation is performed simultaneously on each cell in an identical manner. A very useful source for MATLAB programming styles is the Appendix of a text by Borse.¹³

Before solving the energy-balance equations for the temperatures and emissions of the two layers, the input parameters must be specified. These values have been gathered from different sources. The land fraction $f_{\text{land}}(n)$ is taken directly from Hansen *et al.*¹² It is shown by the contours in Fig. 94.64, which establishes the scale and resolution of subsequent maps.

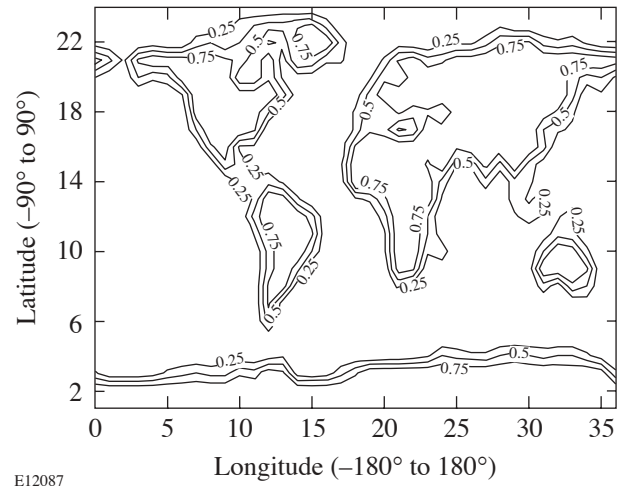


Figure 94.64
Global land fraction plotted with contours at 0.25, 0.5, and 0.75. This map may be used as a template in the study of Figs. 94.66, 94.67, and 94.69. It also gives a good indication of the resolution afforded by our 864-cell calculations. Horizontal axis: ticks correspond to centers of 10° cells located (centered) at longitudes $-180^\circ(1)$, $-170^\circ(2)$, ..., $0^\circ(19)$, ..., $+170^\circ(36)$. Vertical axis: ticks correspond to centers of 8° cells at latitudes $-84^\circ(2)$, $-76^\circ(3)$, ..., $-4^\circ(12)$, $+4^\circ(13)$, ..., $+84^\circ(23)$. The bottom and top rows correspond to centers of 2° cells at $-89^\circ(1)$ and $+89^\circ(24)$, respectively.

The 18-year-average annual cloud fraction coverage was taken from data collected by satellites from 1983 to 2001 under the International Satellite Cloud Climatology Project.¹⁴ Similarly, surface reflectivities (r_S) were estimated by using the ISCCP surface reflectivities in coordination with Table 4.2 in Hartmann.² Hartmann specifies albedo ranges and typical values for distinct land types. Table 94.II shows the land types, albedo ranges, and typical albedo values. The estimates of r_S are shown in Table 94.III.

It might appear that a serious approximation is being made in neglecting net annual lateral transport of energy. Lateral heat flows, however, will be effectively redirected into a vertical heat flux; the quantity S_{NR} will contain this contribution. Consider, for example, a horizontal wind, carrying water vapor from one cell to the next. When the vapor precipitates in the

form of rain, it releases latent energy. That energy release contributes to the vertical energy balance in the (receptor) cell. This energy enters “horizontally” into the cell. Similarly, in some nearby cell, some vertical energy flux went into evaporation, and that cell suffers an energy loss if the water vapor is transported out of the cell. Since our cells are large, we do not expect the horizontal energy transport to cover more than one or two cells, for local disturbances. Consequently there may be a correlation between a loss of S_{NR} in one cell and a gain in S_{NR} in a nearby cell. The annual latitude dependence of S_{NR} , which will be discussed in the last section, may well be made up of such transport contributions. A less obvious but very significant assumption is that the theory continues to work at latitudes having long periods of low solar irradiance, when cloud cover may vary significantly between polar winter and summer periods. This requires negative values of S_{NR} to maintain flux

Table 94.II: Land types and their associated albedo ranges (in percentages) deduced from a map [Fig. 5.14, by Dickinson (Ref. 18); Table 4.2 by Hartmann (Ref. 2)].

| Land type (Dickinson) | Land type (Hartmann) | Albedo range | Typical value |
|-----------------------|------------------------|--------------|---------------|
| Tundra and desert | Dry soil/desert | 20–35 | 30 |
| Grass and shrub | Short green vegetation | 10–20 | 17 |
| Crop | Dry vegetation | 20–30 | 25 |
| Wetland and irrigated | Short green vegetation | 10–20 | 17 |
| Evergreen tree | Coniferous forest | 10–15 | 12 |
| Deciduous tree | Deciduous forest | 15–25 | 17 |

Table 94.III: Corrected values for land and sea reflectivities in the high latitudes (see text). A negative latitude corresponds to the southern hemisphere. For -76° to -89° r_{land} is set at 0.6 because of the year-round Antarctic ice. The latitude -68° reflectivity is set slightly lower than Antarctica as a result of a lack of permanent ice. In latitudes 68° to the north pole, r gradually increases, taking seasonal snow and ice into account. r_{sea} at 60° and -60° is set at 0.3 to avoid a sharp jump from water set at 0.1 in the mid-latitudes to the higher polar values for ice and snow cover. These values are rough estimates for partial and seasonal snow and ice cover. Fresh snow can have an albedo up to 0.9, old, melting snow up to 0.65, and sea ice without snow cover up to 0.4 (see Ref. 2, Table 4.2, p. 88). Values not shown (—) are longitude dependent and are taken directly from satellite data in detail.

| Latitude (°) | -89 | -84 | -76 | -68 | -60 | -52 to 52 | 60 | 68 | 76 | 84 | 89 |
|--------------|-----|-----|-----|------|-----|-----------|-----|-----|-----|------|-----|
| r (land) | 0.6 | 0.6 | 0.6 | 0.55 | — | — | — | 0.4 | 0.5 | 0.55 | 0.6 |
| r (sea) | 0.6 | 0.6 | 0.6 | 0.55 | 0.3 | — | 0.3 | 0.4 | 0.5 | 0.55 | 0.6 |

balance. Negative values of S_{NR} may represent fluxes from a missing reservoir layer, which is planned for a future refinement of the model.

2. Cellular Values of Parameters

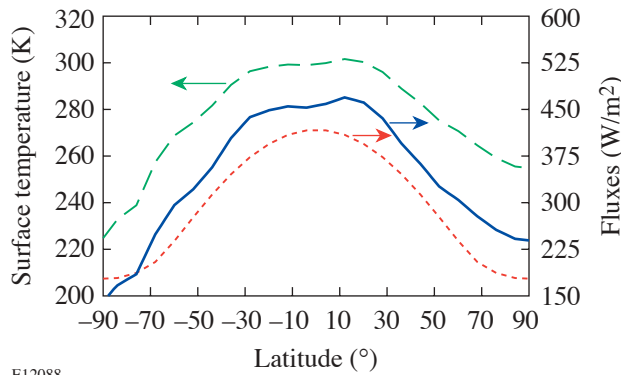
The value of a parameter g that depends on the choice of cell will be written $g(n)$, where, unless otherwise specified, n is an arbitrarily assigned cell number. To calculate the incoming solar radiative flux to a cell, we use astronomical definitions and notations to track the sun's position relative to a cell's midpoint every two weeks throughout the year. The incident radiation is the solar radiation at the distance to the earth, 1368 W/m^2 multiplied by the sine of $H(n)$, where $H(n)$ is the angle of the sun from the horizon of the surface area in cell n ,

$$S_0(n) = 1368 \sin H(n, t, t') \left(\text{Wm}^{-2} \right). \quad (3)$$

Here (see Appendix and Ref. 2, pp. 29–31 and 347–349)

$$\sin H(n, t, t') = \sin \delta(t') \sin \beta(n) + \cos \delta(t') \cos \beta(n) \cos t, \quad (4)$$

where β is the latitude, δ is the sun's declination angle, t' is the time elapsed since the vernal equinox, and t is the hour angle. During the average over 24-h periods, the angle t is limited by sunrise and sunset conditions, i.e., there is no contribution when $\sin H$ is negative. The annual average of S_0 as a function of latitude computed from Eq. (3) is plotted in Fig. 94.65,



E12088

Figure 94.65

Average annual insolation (lower curve, right-hand scale), outward infrared flux at the surface (solid curve, right-hand scale), and surface temperature (upper curve, left-hand scale) as a function of latitude. The latter two are latitude averages based on satellite data.¹⁵

along with the observed S_E and T_E . Equation (3) is adequate for the purposes of our average annual model. Monthly averages require a slight correction resulting from Earth's orbital eccentricity (see, e. g., Hartmann²). The annual average solar irradiance ranges from a minimum of 176 W/m^2 at the poles to 416 W/m^2 at the equator, with a global annual average of 342 W/m^2 .

The UV parameters A and B [Eqs. (2a) and (2b)] also become cell dependent. There are three relevant cell-varying parameters, the UV reflectivities and the absorptivity of the cloud layer. The surface reflectivity $r_s(n)$ of cell n is taken from sea and land reflectances weighted by the corresponding surface-type fractions,

$$r_s(n) = f_{\text{land}}(n)r_{\text{land}} + [1 - f_{\text{land}}(n)]r_{\text{sea}}. \quad (5)$$

This formula was used only in high-latitude regions ($|\text{lat}| \geq 60^\circ$). Remaining reflectivities came from ISCCP data.^{14,15} The atmospheric reflectivities are similarly found to be

$$r_A(n) = f_{\text{cloud}}(n)r_{\text{cloud}} + [1 - f_{\text{cloud}}(n)]r_{\text{clear}}, \quad (6)$$

where the clear air albedo (r_{clear}) can be assumed as 0.15 (Ref. 2, page 75). The planetary albedo $\alpha_p(n)$ is the fraction of original incident UV that leaves the system. On our model [see Ref. 5, Eq. (B3)] it is given by

$$\alpha_p(n) = r_A(n) + k_M(n)[1 - a(n)]^2 [1 - r_A(n)]^2 r_s(n), \quad (7)$$

which depends upon two unknowns: $a(n)$, the atmospheric UV absorptivity, and r_{cloud} [through r_A , Eq. (6)]. For absorptivity, the expression corresponding to (6) is

$$a(n) = f_{\text{cloud}}(n) a_{\text{cloud}} + [1 - f_{\text{cloud}}(n)]a_{\text{clear}}. \quad (8)$$

If we assume that clear air absorbs no UV radiation, we have

$$a(n) \equiv f_{\text{cloud}}(n)a_{\text{cloud}}. \quad (9)$$

To determine r_{cloud} and a_{cloud} , we impose a set of reasonable planetary albedo values [Ref. 2, Fig. 2.9(a), p. 33] as a constraint upon Eq. (7). Values of r_{cloud} and a_{cloud} were varied at intervals of 0.01 until we had the greatest number of matches

with the known $\alpha_p(n)$. With this bare minimum of free parameters, a match to observed values occurred in 711 of the 864 cells. Most of the unmatched (meaning more than 15% difference from the Hartmann) values were near the poles. The resulting $r_{\text{cloud}} = 0.27$ and $a_{\text{cloud}} = 0.06$ are in reasonable agreement with the parameters found in Ref. 9. These produce not only a good localized match but also give the commonly accepted global planetary albedo of 0.30 when averaged. Once adopted, these values of r_{cloud} and a_{cloud} are not changed in the course of the calculations.

The cellular IR absorptivity $\varepsilon(n)$, which is also the cellular IR emissivity, is taken to have the same form as the UV absorptivity, Eq. (8). Parameters used were $\varepsilon_{\text{cloud}} = 1$ and $\varepsilon_{\text{clear}} = 0.90$.

Application of the Model

1. Predicting $T_E(n)$

We now generalize Eqs. (1a) and (1b) to the cellular case:

$$2\varepsilon S_A(n) - \varepsilon S_E(n) = A(n)S_0(n) + S_{\text{NR}}(n) \quad (10a)$$

and

$$-\varepsilon S_A(n) + S_E(n) = B(n)S_0(n) - S_{\text{NR}}(n). \quad (10b)$$

$A(n)$ and $B(n)$ are given by equations identical to Eqs. (2a) and (2b) in which certain parameters are made cell dependent, as discussed above.

Our first attempt with the cellular model was a direct 864-cell extension of the methodology of the earlier one-cell or one-dimensional two-layer model. We refer to this application of the model as “ T_E predictive.” We allowed the annual average value of $S_{\text{NR}}(n)$ to depend on land and sea fraction and took it to be proportional to the solar input, as follows:

$$S_{\text{NR}}(n) = [0.03f_{\text{land}}(n) + 0.16f_{\text{sea}}(n)] \cdot S_0(n). \quad (11)$$

From the solution of each pair of Eqs. (10a) and (10b) for $S_E(n)$, $T_E(n)$ was calculated on the basis of the assumed $S_{\text{NR}}(n)$. The numerical coefficients in Eq. (11) were chosen by an extensive search of parameter space to produce the observed global average temperatures ($T_E = 288$ K, $T_A = 250$ K). This flux has a global average of 42.3 W/m², an improvement on the one-dimensional model⁹ in that the latter had been unable to

accommodate *any* non-zero average S_{NR} without compromising other assumed input parameters. We emphasize that the only completely arbitrary parameters in the fit were the two numerical coefficients in Eq. (11). We consider this remarkable; it endorses the general reasonableness of the elementary two-temperature model for individual cells. The form of Eq. (11) also suggests a global asymmetry in the distribution of S_{NR} . We will return to this later.

The preliminary cell results are shown in Fig. 94.66(a) and are compared with measured values [satellite data;¹⁵

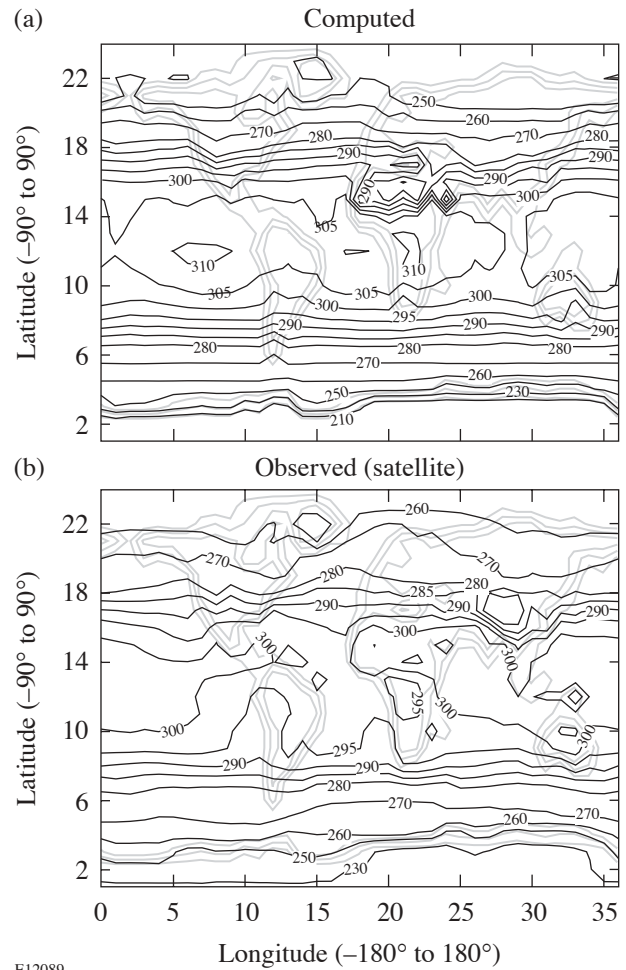


Figure 94.66

(a) Computed “ T_E -predictive mode” surface temperatures (in K) using a direct cellular extension of the elementary model of Ref. 9, as described in the text. The average nonradiative flux is 40 W/m² and the average surface temperature is 288 K. (b) Observed surface temperatures, defined as those obtained by satellite,¹⁵ with an average of 288 K. (See the caption of Fig. 94.64 for the key to the axes.)

Fig. 94.66(b)]. These diagrams show how a set of calculated locally determined temperatures [Fig. 94.66(a)] having the correct global average may disagree significantly from observed local values [Fig. 94.66(b)] having the same global average. While this is not the least bit surprising, a comparison of the two parts of Fig. 94.66 provides a qualitative evaluation of the errors that occur in the making of simple models. The agreement is closer than one might reasonably expect from simplistic models but the determined set is far from unique.

2. Predicting $S_{NR}(n)$

Because of the difficulty choosing the coefficients of Eq. (11) to produce a match with observations [Figs. 94.66(a) and 94.66(b)], we made a major change in operational procedure. The linear Eqs. (1a) and (1b) or (10a) and (10b) lend themselves equally to computing any two of the quantities S_{NR} , S_A , and S_E , given the third one and S_0 as an input. Therefore, instead of adjusting the value of S_{NR} to predict observed local surface temperatures, we did the opposite: taking $T_E(n)$ as a known input parameter from ISCCP satellite data¹¹ and $S_0(n)$ from Eq. (3), we used the balance equations to calculate $S_A(n)$ and $S_{NR}(n)$. This “ S_{NR} -predictive” mode of calculation is accomplished most easily by combining the two flux Eqs. (10a) and (10b):

$$S_{NR}(n) = [A(n) + 2B(n)] S_0(n) - (2 - \varepsilon) S_E(n). \quad (12)$$

Recall that $S_E(n) = \sigma T_E(n)^4$. Eliminating S_E from (10a) and (10b) results in the companion equation for S_A :

$$\begin{aligned} \varepsilon(2 - \varepsilon)S_A(n) \\ = [A(n) + \varepsilon B(n)]S_0(n) + (1 - \varepsilon)S_{NR}(n). \end{aligned} \quad (13)$$

The results for the annual average of $S_{NR}(n)$, calculated from the observed surface temperature $T_E(n)$, are shown in Fig. 94.67(a). $S_{NR}(n)$ and $S_A(n)$ have global averages of 64 and 236 W/m² (the latter corresponding to $T_A = 254$ K), respectively. In the earlier noncellular model,⁹ the highest value of S_{NR} that could be obtained without unreasonable parameters was 40 W/m², and in the above T_E -predictive mode it was 42.3 W/m², so the S_{NR} -predictive mode result 64 W/m² represents a further improvement. The generally quoted global average of S_{NR} is 102 to 105 W/m².^{16,17} $S_{NR}(n)$ appears to be most negative at the higher latitudes and most positive near the

equator. A negative value of $S_{NR}(n)$ corresponds to nonradiative energy transfer from the atmospheric layer to the surface layer or a lateral flow into the cell, as discussed earlier.

A distinctive feature of our results is the prominent drop of S_{NR} in the regions of the Sahara and Saudi Arabia [Fig. 94.67(a), at matrix elements (20–25, 14–16)]. Its cause is a confluence of strong effects on the two terms in Eq. (12): relatively high surface reflectivity and low cloud cover, which reduce the first term, and relatively high temperature, which increases the absolute value of the (negative) second

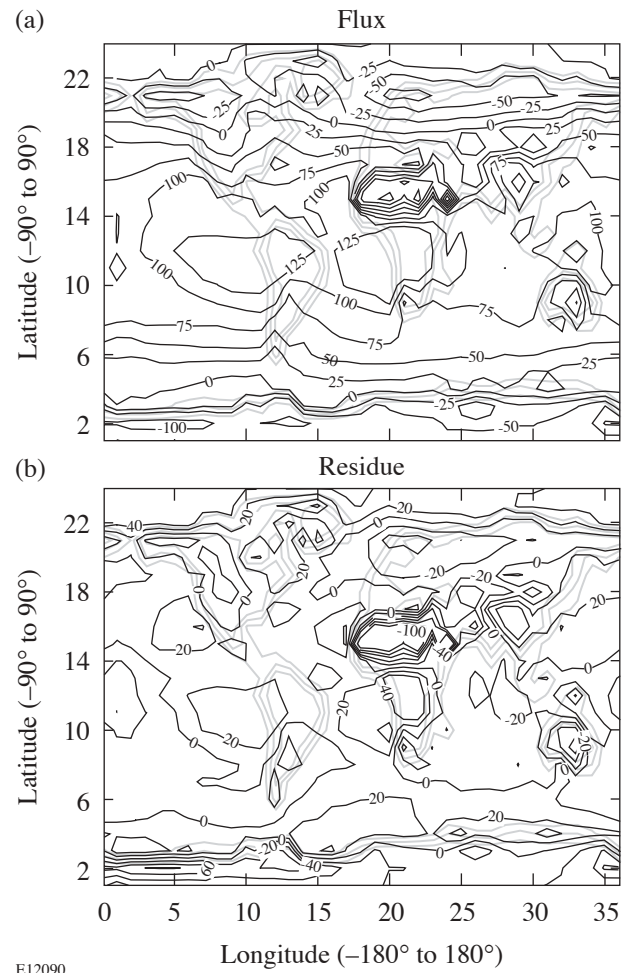


Figure 94.67
(a) Computed “ S_{NR} -predictive mode” nonradiative flux $S_{NR}(n)$ (in W/m²) using the cellular model but with surface temperatures as input. (b) $\delta S_{NR}(n)$, the residue after subtracting the annual average value of $S_{NR}(n)$ as a function of latitude [see Eq. (16)]. The one region of large residuals corresponds to the Sahara desert region. (See the caption of Fig. 94.64 for the key to the axes.)

term. A similar but milder dip appears in the eastern region of Australia.

Figures 94.67 and 94.68 reveal a possible smooth dependence of $S_{\text{NR}}(n)$ on latitude. Figure 94.67(b) shows the residues $\delta S_{\text{NR}}(n)$ after latitude averages are removed, as discussed in the next section.

3. The Zonal Average of S_{NR}

“Zonal” averages are made over cells lying within zones having the same latitude. Following convention,¹⁸ we denote zonal averages by angular brackets $\langle \dots \rangle$. If the area of cell $n = (p, q)$ is $A(p, q)$, where p is the latitude cell index and q is the longitude cell index, we have, for example,

$$\langle S_{\text{NR}}(p) \rangle = \frac{1}{A(p)} \sum_q A(p, q) S_{\text{NR}}(p, q), \quad (14)$$

where $A(p)$ is the total area of zone p ,

$$A(p) = \sum_q A(p, q). \quad (15)$$

For convenience the latitude index p will be converted into the latitude β , measured in degrees, at the center of the cell and we will write, again for example, $S_{\text{NR}}(\beta) = \langle S_{\text{NR}}(p) \rangle$.

The zonal averages $S_{\text{NR}}(\beta)$ are shown explicitly in Fig. 94.68, where a very regular latitude dependence emerges clearly. Indeed, $S_{\text{NR}}(\beta)$ can be represented to within $\pm 9 \text{ W/m}^2$ by

$$S_{\text{NR}}^{\text{fit}}(\beta) = 40 + 80 \cos 2(\beta + \Delta) - 10 \sin 6|\beta|, \quad (16)$$

with $\Delta = 5^\circ$. In Fig. 94.68 the residuals between $S_{\text{NR}}(\beta)$ and its fit are also shown. When this zonal average is removed from the cellular results of Fig. 94.67(a), the residuals [Fig. 94.67(b)] are obtained. They are noteworthy for their general smoothness and for their relatively small size, which is of the order of 5%–10% of the solar input at the surface.

It is not surprising that $S_{\text{NR}}(\beta)$ has an asymmetry between the northern and southern hemispheres. In retrospect we see that the *ad hoc* form, Eq. (11), used in the T_E -predictive calculation, was biased toward the southern hemisphere, where

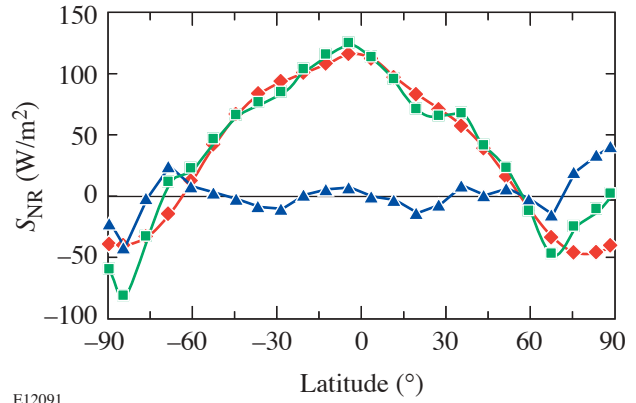


Figure 94.68

Distribution of S_{NR} by latitude. Squares represent the “experimental” values based on our model, and diamonds are the numerical fit, Eq. (16). Triangles are the residuals.

the sea fraction is dominant. Figure 94.69 shows the 18-year-average surface reflectivity in months 1 and 7 (Ref. 10), giving further insight into the peculiarities of S_{NR} . The reflectivities are slightly higher in the northern temperate zone than in the southern. In the polar regions, the times of greater solar irradiance may not occur when the surface reflectance is at its average value. Indeed, the polar regions are generally rather anomalous. We have not concerned ourselves too much with them because the model, generally limited to dealing with annual averages, lacks the ability to describe accurately the effect of Arctic and Antarctic nights in which $S_0(n) = 0$. There is some seasonal variation in the cloud cover data, which may be responsible for the fact that the interesting term $-10 \sin 6|\beta|$ does not hold in the polar regions. One is tempted to speculate on the origin of the sinusoidal term: the insolation does not have a pure $\cos \beta$ dependence because of the inclination of Earth’s axis to the plane of its orbit, and Hadley cells¹⁹ may play a role in it.

The existence of extensive databases provides the student an opportunity to explore many other effects through the medium of this theory. As an example, we have used data from ISCCP¹⁴ consisting of averages of the measured parameters at each month over an 18-year period. For each month, the average $S_{\text{NR}}(\beta, t)$ was calculated and compared to $S_{\text{NR}}(\beta)$ by looking at the difference between the two. This difference also appears to follow a trend that is most clear in the region between latitudes -60° and $+60^\circ$. For this region the difference is approximately linear and oscillates about $\beta = 0^\circ$ with a period of one year. The difference itself can be fitted well to

$$\Delta S_{NR}(\beta, t) = -285 \cdot (\beta/60^\circ) \cdot \sin(30^\circ t) \quad (17)$$

(where $t = 0$, September 15; $t = 1$, October 15; etc.).

Now, we have shown that the annual average S_{NR} follows Eq. (16), and the difference between monthly and annual values follows Eq. (17), so the monthly S_{NR} can be written as

$$S_{NR}^{fit}(\beta, t) = 40 + 80 \cos 2(\beta + \Delta) - 10 \sin 6|\beta| + \Delta S_{NR}(\beta, t) \quad (18)$$

in the specified region $-60^\circ \leq \beta \leq +60^\circ$. For the month of January, the values of S_{NR} calculated directly from the data are compared to those given by Eq. (18) in Fig. 94.70. The fitting is very close to the calculated values in the region $-30^\circ \leq \beta \leq +45^\circ$. The discrepancies of up to 50 W/m^2 outside this region are most likely due to the hemispheric asymmetry of S_{NR} . This asymmetry was ignored in Eq. (17), which is antisymmetric about $\beta = 0^\circ$ and uses a perfectly sinusoidal maximum value for $\beta = \pm 60^\circ$. The calculations from data, however, show that during the southern summer, $S_{NR}(-60^\circ, t)$ increases to close to 400 W/m^2 , but in the northern summer $S_{NR}(+60^\circ, t)$ does not even reach 300 W/m^2 . Also, at any month, the value of $S_{NR}(60^\circ, t)$ does not equal $S_{NR}(-60^\circ, t)$, as in Eq. (17), leading to an over- or underestimation of S_{NR} from Eq. (18).

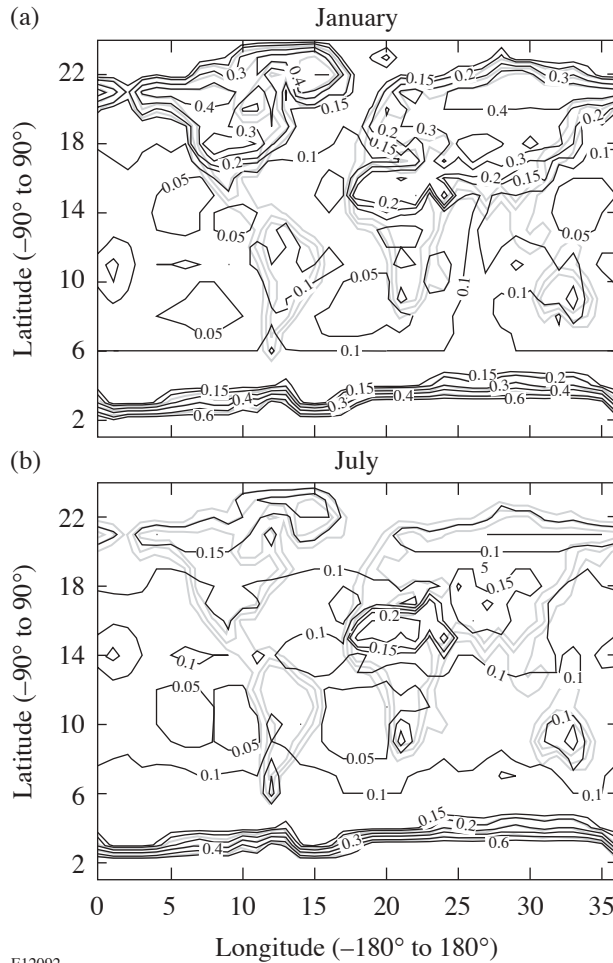


Figure 94.69 Comparison of surface reflectivities in the months of January (a) and July (b). The asymmetry between the northern and southern hemispheres seen in many climatological studies can be appreciated from the variability in the north polar region and the near-invariance in the south polar region. (See the caption of Fig. 94.64 for the key to the axes.)

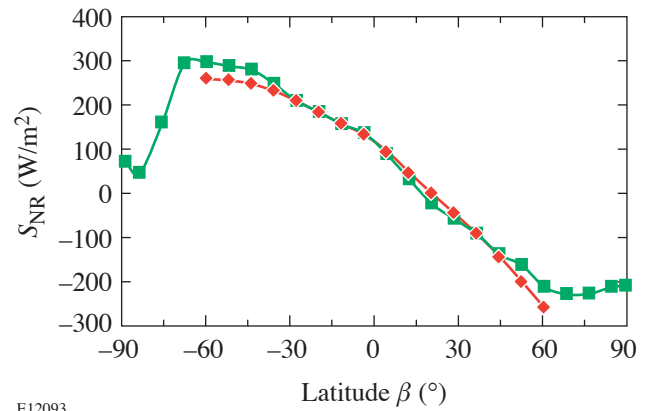


Figure 94.70 A sample determination of nonradiative flux S_{NR} for the month of January (18-year average). Diamonds: values determined from our model calculation. Squares: values determined from the fitting function, Eq. (18). The fit is meant to be valid for latitudes satisfying $-60^\circ \leq \beta \leq +60^\circ$.

Finally, in Fig. 94.71 we compare averages of S_{NR} over two months in succession (February and March 1995). The 18-year average for the respective months has been subtracted, and the polar regions have been omitted from the diagram because average monthly variations in reflectivities and cloud cover

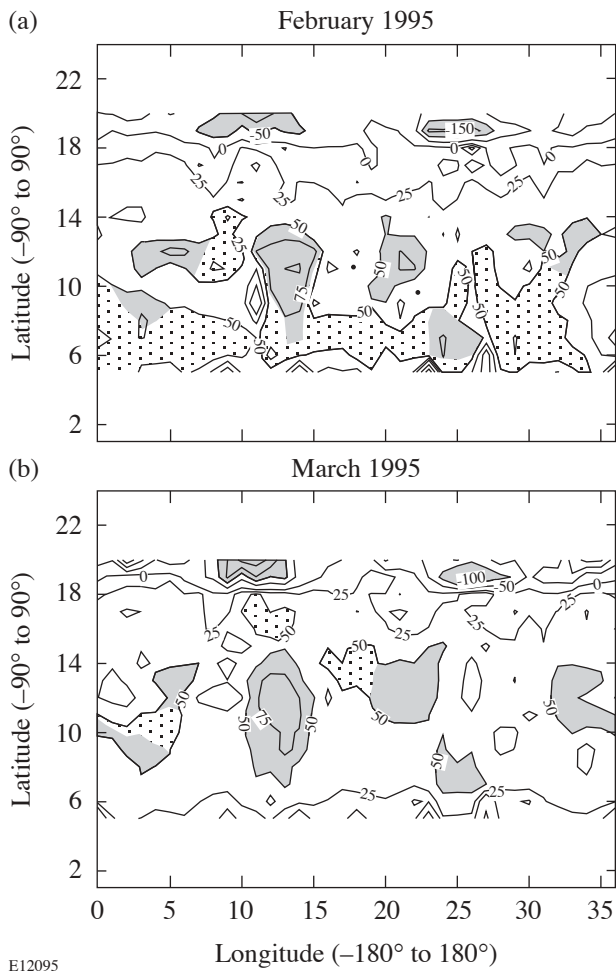


Figure 94.71

(a) The monthly values of S_{NR} for February 1995 minus the 18-year average value of S_{NR} for February, for the temperate zones. Large deviations, ~ 50 W/m^2 , in large-scale “weather” patterns are seen. (b) Similar to (a), for March 1995. Comparing with February, it can be seen that some nonradiative “weather cells” (indicated by shading) persist for at least a month and some (indicated by stippling) are more ephemeral. The largest features cover 10 to 20 cells, each computed independently.

may be large. Deviations of the order of 50 W/m^2 show the presence of large-scale, persistent nonradiative “weather systems,” each of which is composed of about 20 independent cells. These systems produce deviations in S_{NR} much larger than those shown in Fig 94.67(b). The figures serve to illustrate east–west nonradiative energy transport. Only when averages are taken over the 18-year database do the smooth results given by Eqs. (17) and (18) and Figs. 94.68 and 94.70 result.

Summary and Discussion

The two-level global model of Ref. 9 has been applied locally; that is, each cell in a grid has been assumed to have annual average temperatures and the fluxes have been determined by the cell’s own parameters and average insolation. The observed local planetary albedo is used as a control on the modeled surface and atmospheric reflectivities. In the model’s more successful (S_{NR} -predictive) implementation, the set of surface temperatures is used as input; the nonradiative flux from the surface S_{NR} and the ideal atmospheric radiative flux S_A are the principal outputs. The globally averaged S_{NR} is predicted to be about 64% of its usually quoted global value of 102 to 105 W/m^2 , an improvement over T_E -predictive models using assumed nonradiative fluxes, where values of only 0%–40% were possible.

The value of the globally averaged atmospheric radiative flux S_A is 236 W/m^2 , adequate to maintain overall radiative balance with an effective atmospheric radiative temperature of $T_A = 254$ K (recall that the emissivity is taken as 0.89, as in Ref. 9). Since our model assigns only this one temperature to the atmosphere, it is constrained to predict that the downward IR flux is identical to the upward flux. In the real atmosphere, a temperature gradient exists and the lower layers most effective in radiating downward are at a higher temperature. The downward flux should thus be greater than ϵS_A , as is observed.¹⁸ We are developing a three-temperature version of our model, to be the subject of a future article in the series, and according to preliminary estimates, an appropriately larger value of S_{NR} will be obtained that will balance the extra downward IR.

Having noted a correlation between $S_{NR}(n)$ and latitude, we examined its zonal average. A clear asymmetry resulted between the northern and southern hemispheres, illustrating the effect of asymmetry of the hemispheric land masses and the differences in reflectivity parameters resulting from the nature of the Arctic and Antarctica. Fittings of other data sets to develop formulae for individual components of S_{NR} are discussed by Budyko.⁵

We emphasize the accessibility of both the data and our model representations to students interested in applying the elementary aspects of climatology to real data. As suggestions for future workers: (1) It would be interesting to use databases averaged over different periods of time to see if long-term differences in the form of Eqs. (17) and (18) result. (2) A study of the form, structure, and persistence of these large-scale

monthly “weather patterns” during an El Niño cycle should be informative.

ACKNOWLEDGMENT

We are grateful to Profs. D. Hartmann and K. Trenberth for valuable correspondence. This work was supported in part by NSF (REU) grant PHY 99-87413.

Appendix A: Spherical Astronomy Fundamentals

The altitude H of the sun can be found by applying the law of cosines²⁰ to the observer’s spherical triangle ΔZNS , where Z is the observer’s zenith, N is the north celestial pole, and S is the sun. Then arc ZS is $90^\circ - H$; arc NZ is $90^\circ - \beta$, where β is the latitude; and arc NS is $90^\circ - \delta$, where δ is the *declination* of the sun, available from a table lookup in, e.g., Ref. 21.

List of symbols and abbreviations. [Note: symbols of the form $T_A(n)$ are not included. The meaning of such a symbol is “the value of T_A in cell n .”]

| | | | |
|-------------|---|-----------------------|--|
| A | UV atmospheric input parameter [Eq. 2(a)] | r_{sea} | Reflectivity of the sea portion of a cell |
| $A(p)$ | Area of a band of cells of latitude index p | S_0 | Solar constant averaged globally and over time, 342 Wm^{-2} |
| $A(p,q)$ | Area of a cell of latitude index p and longitude index q | S_A | Ideal radiative flux in the atmosphere or upper atmosphere layer, σT_A^4 |
| a | Atmosphere’s absorptivity in the UV | S_E | Ideal radiative flux in the surface layer, σT_E^4 |
| a_{clear} | Absorptivity of cloudless air in the UV | S_{NR} | Net nonradiative flux upward from the surface |
| a_{cloud} | Absorptivity of air with clouds in the UV | t | Solar hour angle (see Appendix) |
| B | UV surface input parameter [Eq. 2(b)] | T' | Time elapsed since the vernal equinox |
| f_{cloud} | Fraction (of a cell area) consisting of cloud | T_A | Effective radiative temperature of the upper model layer, representing that of the atmosphere |
| f_{land} | Fraction (of a cell area) consisting of land | T_E | Temperature of the lower model layer, representing that of the surface of Earth |
| H | Horizon angle of the sun | UV | Refers to that part of the spectrum of the sun that is absorbed by the atmosphere; roughly wavelengths shorter than 600 nm |
| IR | Refers to that part of the spectrum with wavelengths longer than 600 nm; largely not absorbing the sun’s spectrum but absorbing much of Earth’s | α_p | Planetary albedo |
| k_M | Multiple reflection parameter | β | Latitude associated with a set of cells |
| n | Cell label, also in matrix style p, q | δ | Solar declination angle |
| p, q | Latitude and longitude cell indexes, respectively | Δ | Fitting parameter (phase shift); see Summary and Discussion . |
| r_A | Reflectivity of the atmosphere in the UV | ε | Atmosphere’s absorptivity (and emissivity) in the IR |
| r_{clear} | Reflectivity of clear air | ε_{clear} | Clear air absorptivity (and emissivity) in the IR |
| r_{cloud} | Reflectivity of the cloud portion of a cell | ε_{cloud} | Cloud absorptivity (and emissivity) in the IR |
| r_{land} | Reflectivity of the land portion of a cell | σ | Stefan–Boltzmann constant, $5.67 \times 10^{-8} \text{ Wm}^{-2} \text{ K}^{-4}$ |
| r_S | Reflectivity of the surface in the UV | | |

The angle $\angle SNZ$ is called the sun's *hour angle* H ; instead of being measured in degrees, it is measured in time units from 12:00 noon ($1 \text{ h} = 15^\circ$). It is negative (positive) when the sun is in the eastern (western) half of the sky. These quantities are related by the spherical law of cosines:

$$\sin H = \sin \beta \sin \delta + \cos \beta \cos \delta \cos t, \quad (\text{A1})$$

At sunrise, $H = 0$; the equation determines the time at sunrise $t = -t_0$. At sunset, again $H = 0$ and $t = +t_0$. The length of daylight is then $2t_0$.

The declination of the sun can also be approximated. The sun moves along a great circle, called the *ecliptic*, which is inclined at an angle $i = 23.44^\circ$ to the celestial equator. At the vernal equinox (\sim March 21) the sun is at a point V , one of the two intersections of the celestial equator and the ecliptic, and is moving from negative to positive declination. Let the point P be on the celestial equator, with arc $NSP = 90^\circ$. Consider the spherical triangle VSP . The angle $\angle SVP = i$ and the angle $\angle SPV = 90^\circ$. The arc VS is *approximately* $\Omega t'$, where $\Omega = 360^\circ/1 \text{ yr}$ and t' is the time elapsed since the vernal equinox. From the spherical law of sines for VSP one has

$$\sin \delta = \sin i \sin \Omega t'. \quad (\text{A2})$$

Since the sun moves slightly faster (slower) on the ecliptic than average when we are at perihelion, January (aphelion, July), this is only an approximate relation.

REFERENCES

1. J. Hansen *et al.*, Proc. Natl. Acad. Sci. USA **97**, 9875 (2000).
2. D. L. Hartmann, *Global Physical Climatology*, International Geophysics, Vol. 56 (Academic Press, San Diego, 1994).
3. J. P. Peixoto and A. H. Oort, *Physics of Climate* (American Institute of Physics, New York, 1992).
4. M. I. Budyko, *Tellus* **21**, 611 (1969).
5. M. I. Budyko, *The Earth's Climate, Past and Future*, International Geophysics Series, Vol. 29 (Academic Press, New York, 1982).
6. K. E. Trenberth, J. M. Caron, and D. P. Stepaniak, *Clim. Dyn.* **17**, 259 (2001).
7. K. E. Trenberth and J. M. Caron, *J. Clim.* **14**, 3433 (2001).
8. C. Kittle and H. Kroemer, *Thermal Physics*, 2nd ed. (W. H. Freeman, San Francisco, 1980), pp. 115–116.
9. R. S. Knox, *Am. J. Phys.* **67**, 1227 (1999).
10. S. Arrhenius, *Phil. Mag.* **41**, 237 (1896).
11. J. R. Barker and M. H. Ross, *Am. J. Phys.* **67**, 1216 (1999).
12. J. Hansen *et al.*, *Mon. Weather Rev.* **111**, 609 (1983).
13. G. J. Borse, *Numerical Methods with MATLAB®: A Resource for Scientists and Engineers* (PWS Publishing, Boston, 1997).
14. C. Brest (technical contact), "ISCCP D2 Monthly Means and Climatology," data sets retrieved 21 January 2002 from the International Satellite Cloud Climatology Project, available at <http://isccp.giss.nasa.gov/products/browsed2.html>.
15. The ISCCP data for r_s was not used in regions above $\pm 52^\circ$ latitude because the data sometimes are greater than unity as a result of glaring and the angle of the satellite to the northern and southern polar regions. This being inconsistent with our definition of a reflection coefficient, the surface reflectivities in these regions were estimated from the Hartmann² Table 4.2.
16. J. T. Kiehl and K. E. Trenberth, *Bull. Am. Meteorol. Soc.* **78**, 197 (1997).
17. See M. I. Budyko, *The Earth's Climate, Past and Future*, International Geophysics Series, Vol. 29 (Academic Press, New York, 1982), p. 70.
18. R. E. Dickinson, in *Climate System Modeling*, edited by K. E. Trenberth (Cambridge University Press, Cambridge, England, 1992), Chap. 5, pp. 149–171.
19. See D. L. Hartmann, *Global Physical Climatology*, International Geophysics, Vol. 56 (Academic Press, San Diego, 1994), pp. 152–154.
20. W. M. Smart, *Text-Book on Spherical Astronomy* (Cambridge University Press, Cambridge, England, 1947).
21. R. Gupta, ed. *Observer's Handbook* (The Royal Astronomical Society of Canada, Toronto, 2002).

Reduction of the Ablative Rayleigh–Taylor Growth Rate with Gaussian Picket Pulses

Introduction

The compression of an inertial confinement fusion (ICF)¹ target must achieve high hot-spot temperatures ($T \geq 10$ keV) and shell areal densities ($\rho R \geq 300$ mg/cm²) to ignite. An ICF implosion is subject to the Rayleigh–Taylor (RT)^{2,3} instability as the shell accelerates inward and as the shell decelerates toward stagnation, causing small perturbations in the shell of the target to grow, potentially reducing the ultimate temperatures and areal densities. This instability can be mitigated two ways: reduction of the seed perturbation amplitudes and reduction of the RT growth rate. Much effort has gone into reducing the seeds of the RT instability due to the roughness of the inner and outer surfaces of the shell, as well as increasing the uniformity of the laser illumination or driving radiation. In this article, we report on the first observations of reduced RT growth rate using a prepulse or *picket* pulse^{4,5} preceding a main laser-drive pulse in planar-target experiments.

Laser ablation provides the pressure needed to implode an ICF target. For large ablation velocities and short wavelengths, ablation eliminates the RT growth because the tips of the perturbation on the outer surface of the shell ablate more quickly than the troughs of the perturbation. This is reflected in the growth rate γ of an interface bearing a spatial perturbation with wave number k , approximated by the generalized dispersion formula^{6–8}

$$\gamma = \alpha \sqrt{\frac{kg}{1+kL}} - \beta k V_a, \quad (1)$$

where g is the acceleration, V_a is the ablation velocity, and L is the density scale length, $|\partial \ln \rho / \partial z|^{-1}$, at the ablation surface. The fitting constants for polystyrene (CH) are given by $\alpha = 0.98$ and $\beta = 1.7$ (Ref. 8). The ablation velocity is given by $V_a = \dot{m} / \rho_a$, where \dot{m} is the rate of mass ablation per unit area determined by the illumination intensity and ρ_a is the density of the material just before ablation.

The RT instability is completely stabilized for all wavelengths less than some “cutoff” wavelength λ_c , which is determined by setting γ equal to 0, from Eq. (1):

$$\lambda_c = 4\pi L \left(\sqrt{1 + \frac{4\alpha^2 gL}{\beta^2 V_a^2}} - 1 \right)^{-1}. \quad (2)$$

For example, if $g \sim 10^{16}$ cm/s² (100 $\mu\text{m}/\text{ns}^2$), $V_a \sim 2$ $\mu\text{m}/\text{ns}$, and $L \sim 1$ μm , then the cutoff wavelength is given by $\lambda_c \sim 3$ μm . From Eq. (2) we see that $\lambda_c \propto V_a$ if $V_a^2 \ll gL$. By using the definition of V_a , we see that $\lambda_c \propto 1/\rho_a$. A decrease of ρ_a by a factor of 3 for the same acceleration and scale length raises the cutoff wavelength to $\lambda_c \sim 10$ μm . This may be accomplished by irradiating the target with an intense picket pulse, followed by a relaxation period before the onset of the main drive pulse.

In this scheme, the picket pulse sends a shock wave through the target, heating it. The target expands during the period of relaxation after the picket. A sufficient relaxation period allows the ablator to expand to less than solid density. As a result of the relaxation-phase expansion, the ablation velocity during the drive pulse will be greater than without the picket pulse, and the RT growth rate will be decreased.⁹

In addition to growth-rate reduction, pickets are predicted to reduce laser-induced imprint.¹⁰ The standoff distance between the critical surface and the ablation surface determines the degree to which the laser illumination perturbations are imprinted on the target.¹¹ The increased intensity of the picket results in a greater growth of the standoff distance at the start of the pulse. This benefit must be balanced—when smoothing techniques such as smoothing by spectral dispersion (SSD)¹² are used—against the loss of smoothing time when the conduction zone grows more quickly. In the experiments described here, the initial mass modulations are chosen to be large enough that laser imprint amplitudes are not significant.

We report here on direct-drive planar-target experiments with the OMEGA laser system¹³ where planar targets are used to study at the ablation surface during the acceleration phase.¹⁴ Planar geometry allows the use of through-foil x-ray radiography to determine the growth of the optical-depth modulation of an initially mass-modulated target, providing a measure of the areal-density growth. In these experiments, the planar target has a surface modulation on the side illuminated by the drive laser beams. While the target is driven, it is subject to the ablative RT instability. Analysis of the optical-depth modulation allows the determination of the RT growth rate. The fundamental Fourier-mode amplitudes of the measured optical-depth modulations will be compared with those determined from 2-D simulations, demonstrating reduction of the RT growth rate through the use of shaped pulses employing a single picket pulse.

In the following sections, (1) the design of the picket pulse using 1-D simulations will be described; (2) the experiment will be described in detail; and (3) experimental results will be compared to the results of 2-D simulations and discussed.

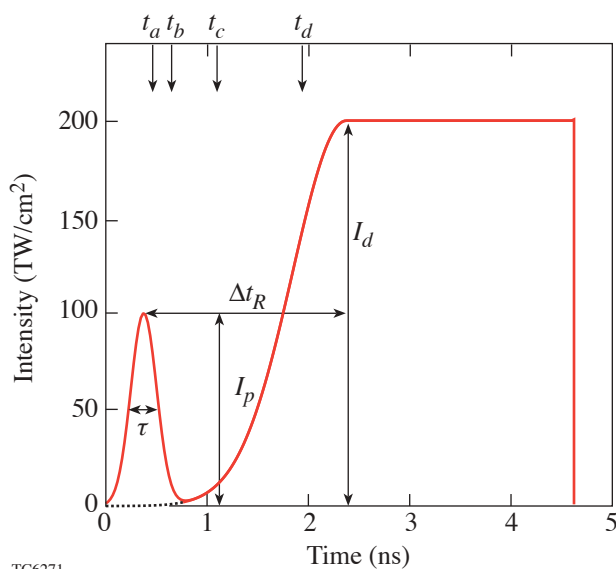
Unperturbed Planar Hydrodynamics

The laser pulses shown in Fig. 95.1 with (solid line) and without (dotted line) a picket pulse were simulated to investigate the effects of a picket pulse in planar geometry and to determine the optimal pulse shape for this experiment. The drive portion of the pulses is identical, so the only difference between the two pulses is seen in the temporal region of the picket pulse. The pulse shape with the picket pulse consists of a Gaussian picket pulse with an intensity I_p and width τ ,

followed by a period of relaxation Δt_R , and then by a drive pulse with a Gaussian rise to a period of constant intensity I_d . The evolution of a planar, 20- μm -thick CH foil driven by this laser pulse was computed with the 1-D hydrodynamic simulation code *LILAC*.¹⁵ The effects of the laser pulse can be determined by studying the spatial profile of the inverse of the pressure scale length $L_p^{-1} \equiv |\partial \ln p / \partial z|$ as a function of time [Fig. 95.2(a)]. The pressure scale length has local minima where the pressure gradient is largest. This allows shock-wave and rarefaction-wave boundaries to be identified. The mass-density profile of the foil is shown in Fig. 95.2(b) for four times: t_a , t_b , t_c , and t_d , which are also labeled in Figs. 95.1 and 95.2(a). These times represent four stages in the evolution of the foil:

Stage 1 (t_a): The picket pulse launches a shock wave (SW) into the target. At time $t_a \sim \tau$, the picket pulse ends and the pressure supporting the SW drops quickly. This drop in pressure is communicated to the target as a rarefaction wave (RW) sent into the target. The leading edge of this RW catches up to the shock wave at the sound speed of the shocked material. The RW also causes the front surface of the target to expand outward.

Stage 2 (t_b): Shortly after $t \sim t_b$, the SW reaches the rear surface of the foil. For this foil thickness, t_b is comparable to the time when the leading edge of the first RW overtakes the picket-pulse shock wave. The shock wave's breakout time is given by $t_b = d/D$, where d is the width of the foil and D is the picket shock speed.

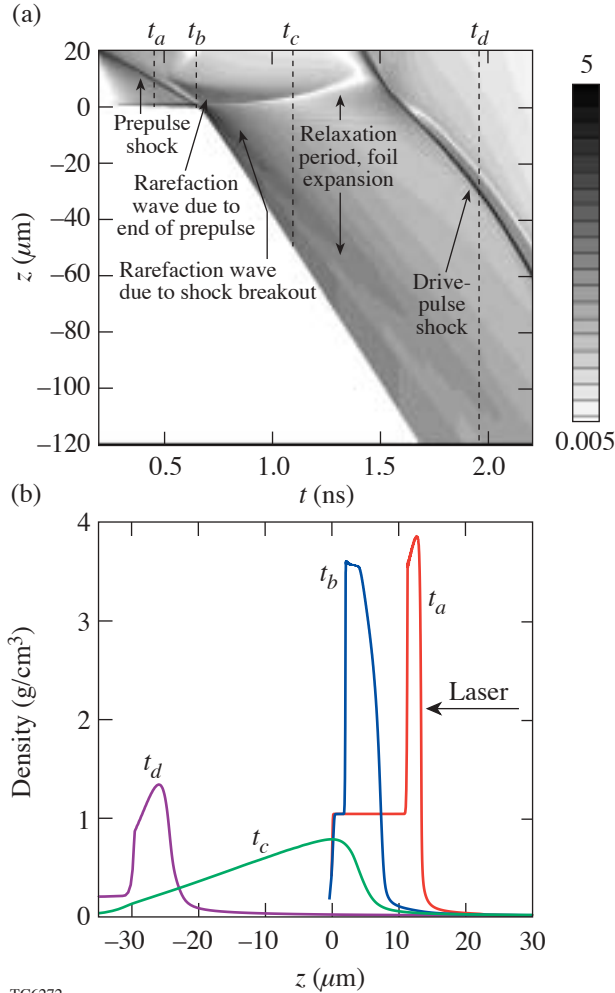


TC6271

Figure 95.1

The analytical pulse shapes used to design the planar picket-pulse experiments. The picket pulse (shown as the solid line) is a Gaussian pulse, as is the rise to the main “drive” pulse. The intensity I_p of the picket pulse is 100 TW/cm², half the intensity I_d (200 TW/cm²) of the drive pulse. The half-width $\tau/2$ at half maximum intensity of the picket pulse is 150 ps and of the Gaussian rise for the drive pulse is 750 ps. The time Δt_R from the peak of the prepulse to the maximum of the drive pulse is 2 ns. The pulse without the picket is shown as a dotted line. The drive pulse with and without the picket is identical, and the only difference is in the temporal region of the picket pulse.

Stage 3 (t_c): Once the picket-pulse shock wave reaches the rear side of the foil, a second RW is sent back from the rear toward the front of the target, potentially passing through the first (end-of-picket) RW. The picket pulse is followed by a



TC6272

Figure 95.2

(a) A space–time diagram of a 20- μm -thick plastic target driven by the picket pulse shown in Fig. 95.1. The quantity plotted is the inverse of the pressure scale length $|\partial \ln p / \partial z|$ (μm^{-1}), which has local maxima where the pressure gradient is largest, allowing shocks and rarefaction-wave boundaries to be identified. Vertical dashed lines are drawn at the times of the density plots in Fig. 95.2(b). The behavior shown is qualitatively the same as for the Gaussian picket pulse; a square picket pulse is used instead to clarify the RW boundaries. (b) The density profile at various times during the evolution of a 20- μm foil driven by the prepulse shape of Fig. 95.1 but with a square picket. The profiles shown are at 0.46 ns (t_a), during the picket pulse; 0.65 ns (t_b), after the picket pulse has ceased but before shock wave breaks out; 1.1 ns (t_c), during the relaxation period while the foil is expanding; and 1.96 ns (t_d), after the drive pulse has begun to sweep up the foil, driving a shock through it.

relaxation period Δt_R during which the foil expands approximately adiabatically for low- Z materials. If the shock wave breaks out of the foil before the drive pulse begins, the front surface of the foil expands due to the passage of two RW's. This is shown at time t_c in Fig. 95.2(b). Otherwise only the front surface will expand as the picket-pulse RW propagates into the target. If the edges of the foil expand at constant speed, the average density is approximately inversely proportional to time. The spatial peak density of the foil, using *LILAC*, is shown in Fig. 95.3(a) without the picket pulse (solid line) and with the picket pulse (dotted line).

Stage 4 (t_d): At time t_d , the drive pulse reaches its peak. The drive pulse launches one or more shock or compression waves into the target. The density profile of the foil as these shocks are launched depends on the duration of the expansion period, given approximately by $t \sim \Delta t_a - \tau/2$. The density profile, in turn, determines the density of the ablated material, the ablation velocity [see Fig. 95.3(b)], and the degree of ablative RT stabilization during the acceleration of the foil. The density scale length L , acceleration, and RT growth rate are also shown in Figs. 95.3(c)–95.3(e) for a Gaussian-rise drive pulse with (solid line) and without (dotted line) a picket pulse. The thermal relaxation time after the picket pulse and the effects of absorption of x rays from the corona plasma result in a density scale length that is increased by a factor of 2 during the drive pulse over the scale lengths without the picket. This is large enough to change the scale-length RT growth mitigation term $(1 + kL)$ from 1.3 to 1.6 for a 20- μm -wavelength perturbation. The ablation velocity is a factor of 3 to 4 larger for pulse shapes with a picket pulse than without a picket pulse, providing an even larger reduction in the growth rate [see Fig. 95.3(e)].

The intensity I_p and duration τ of the picket pulse and the length of the relaxation period Δt_R in this experiment satisfy the following constraints: (1) The picket-pulse energy is much smaller than the drive-pulse energy. (2) The duration of the pulse, including the picket pulse, is shorter than the time it takes a sound wave to cross the laser spot (which has a diameter of 600 μm at 90% intensity), allowing the shock front to remain planar, which, in turn, allows for the accurate measurement of perturbation growth with through-foil radiography. (3) The relaxation period is chosen to preclude the optical depth of the foil dropping below the sensitivity of the x-ray backlighter before being recompressed by the drive pulse.

The time-averaged ablative RT growth rate $\langle \gamma \rangle$ for a 20- μm -wavelength surface perturbation averaged over 2 ns after the start of the drive pulse is plotted in Fig. 95.4 as a

function of the three parameters: I_p [Fig. 95.4(a)], $\tau/2$ [Fig. 95.4(b)], and Δt_R [Fig. 95.4(c)]. The nominal picket parameters for this study are $I_p = 100 \text{ TW/cm}^2$, $\tau = 300 \text{ ps}$, and $\Delta t_R = 2 \text{ ns}$. Two of these values were held constant while varying the third. Figures 95.4(a) and 95.4(c) show that the average growth rate during the drive pulse is inversely dependent on the picket-pulse intensity and the relaxation time. This inverse dependence demonstrates that the main effect of the picket is to deposit sufficient energy to decompress the target. The average growth rate initially decreases with increasing picket width because the greater energy delivered by the picket

results in greater decompression of the foil. For widths greater than $\sim 150 \text{ ps}$, however, the relaxation time is insufficient to allow decompression (recall that the relation time Δt_R is given by the peak-to-peak time, which is reduced by the half-width of the picket), and the average growth rate then increases with τ . The drive pulse consisted of a 750-ps Gaussian rise to a 200-TW/cm² flattop pulse. The picket intensity was varied during the experiment, and its effect on the ablative stabilization of RT growth was observed.

Experimental Configuration

A schematic of the experimental layout (Fig. 95.5) shows the orientation of the three foils and diagnostics used in this experiment.¹⁴ The laser drive beams were incident onto the CH-foil drive target, which was mounted on a Mylar washer with a 1-mm hole in the center. A 2-mm \times 2-mm piece of 25- μm -thick uranium was mounted 9 mm from the drive foil. The backlighter beams irradiated the uranium foil in order to generate the x rays needed to radiograph the accelerated foil. A third foil (6- μm -thick aluminum) centered between the drive and backlighter foils acted as a bandpass filter for

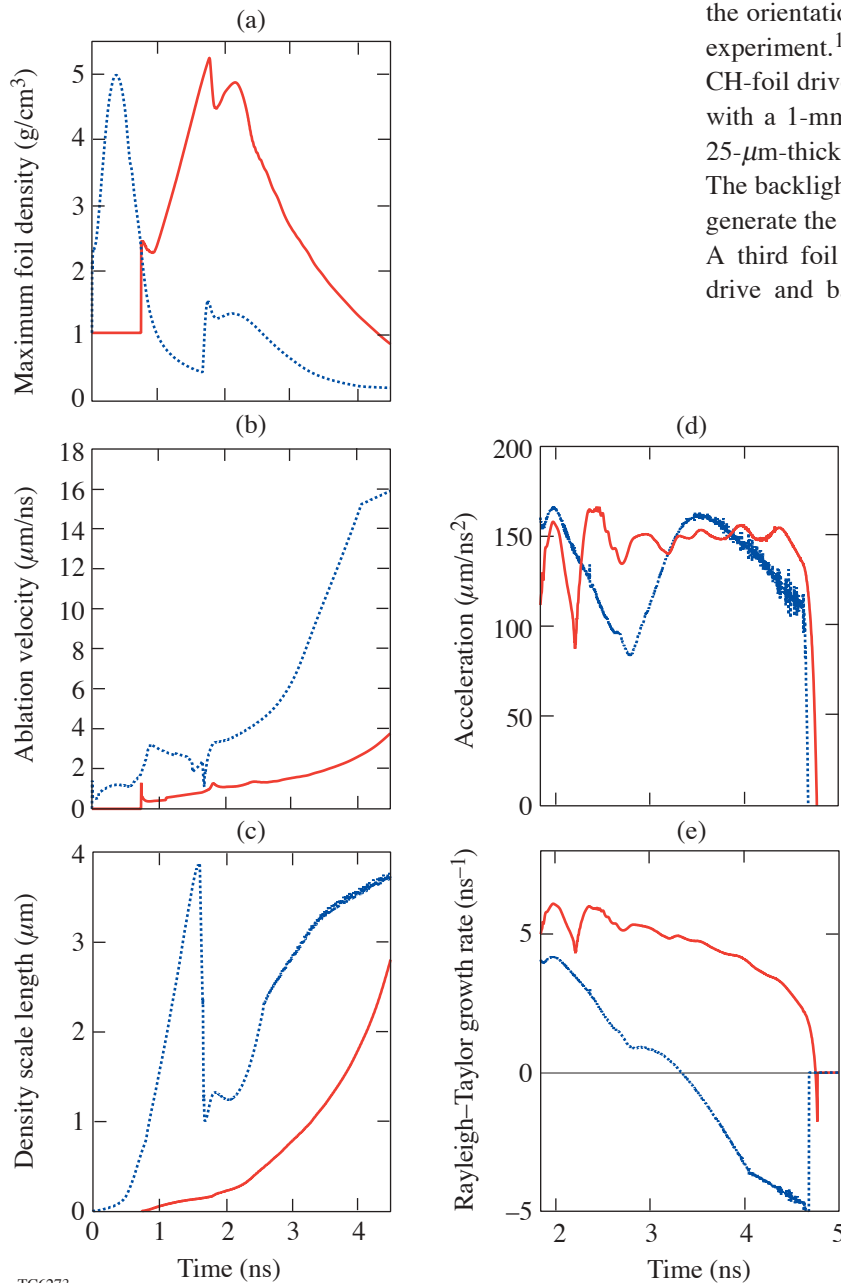


Figure 95.3

(a) The peak foil density, (b) ablation velocity, (c) density scale length at the ablation surface, (d) shell acceleration (found by differentiating twice the centroid position), and (e) the Rayleigh–Taylor growth rate [Eq. (1)] for a 20- μm perturbation are shown as functions of time as computed from 1-D *LILAC* simulations using the analytic Gaussian picket-pulse shape (dotted) and a bare drive pulse (solid). The growth rate is set to zero for imaginary values. The peak density is as much as a factor of 6 lower for the picket-pulse shape than that for the non-picket drive. The resulting ablation velocity during the drive pulse with the picket pulse is as much as a factor of 6 greater than that of the drive pulse without the picket pulse. The ablation-interface density scale length is two to three times larger for the drive pulse that includes the picket pulse. The acceleration during the target drive is comparable for both pulses. The growth rate calculated from Eq. (1) is significantly smaller when the picket pulse is added to the drive.

TC6273

x rays between 1.0 and 1.5 keV. This prevented the very-low-energy x rays from the uranium target from preheating the accelerated foil.

The mass-modulated accelerated foil was composed of a 20- μm -thick CH foil with perturbations imposed on the side irradiated by the laser. This thickness was chosen because it has about two attenuation depths for the 1.0- to 1.5-keV x rays used for radiography. The spectrally and response-weighted mean free path for x rays emitted from the backlighter target is 12 μm . The initial perturbations were (1) a wavelength of $\lambda = 60 \mu\text{m}$ and amplitude of $a = 0.025 \mu\text{m}$; (2) $\lambda = 30 \mu\text{m}$ and $a = 0.125$ and $0.25 \mu\text{m}$; and (3) $\lambda = 20 \mu\text{m}$ and $a = 0.05$ and $0.25 \mu\text{m}$. The perturbation amplitudes decreased with decreasing wavelength to ensure that the growth was measured in the “linear” ($a < \lambda/10$) regime of the RT instability. The 0.25- μm -amplitude perturbation at wavelengths of 30 μm and 20 μm was used to study the stability of this perturbation for large picket intensities where little or no growth was expected and the smaller-amplitude perturbation was below the detection threshold.

The primary diagnostic for the amplitude-growth measurements was an x-ray framing camera.¹⁶ The pinhole array was composed of eight 8- μm -diam pinholes arranged in a checker-board pattern to minimize interference from adjacent images. The framing camera had a magnification of 14.1 ± 0.1 . The noise levels on the framing camera allow the instrument to measure perturbations with amplitudes greater than 0.2 μm . As a result, the early-time amplitudes of the accelerated foils were below the detection limit. The modulation transfer function for the x-ray framing camera was measured prior to the experiment and has values of 0.87, 0.65, and 0.42 at spatial periods of 60, 30, and 20 μm . These values were used to compare the hydrodynamic simulations of the optical depth to the experimental measurements.

A second x-ray framing camera measured the spatial and temporal emissions of the backlighter at a magnification of 6 with a standard 16-pinhole array where each pinhole was 10 μm in diameter. This diagnostic was used to monitor the temporal and spatial x-ray emission from the uranium backlighter. It was filtered to be sensitive to the same x-ray

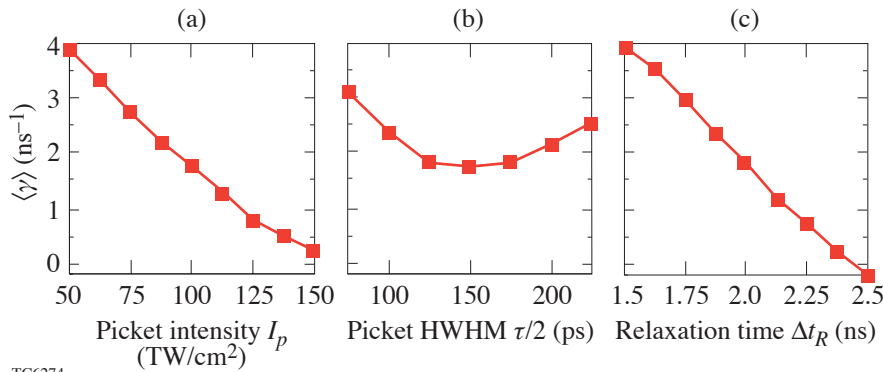


Figure 95.4 The dependence of the average ablative RT growth rate $\langle \gamma \rangle$, as determined from LILAC simulations, on picket parameters (see Fig. 95.1): (a) the picket-pulse intensity I_p , (b) duration (HWHM) $\tau/2$, and (c) the relaxation time Δt_R (given by the time from the peak of the picket pulse to the peak of the drive pulse). These variations were used to identify the optimal picket for the experiment. The growth rate is averaged over 2 ns starting from the launch of the drive-pulse shock.

TC6274

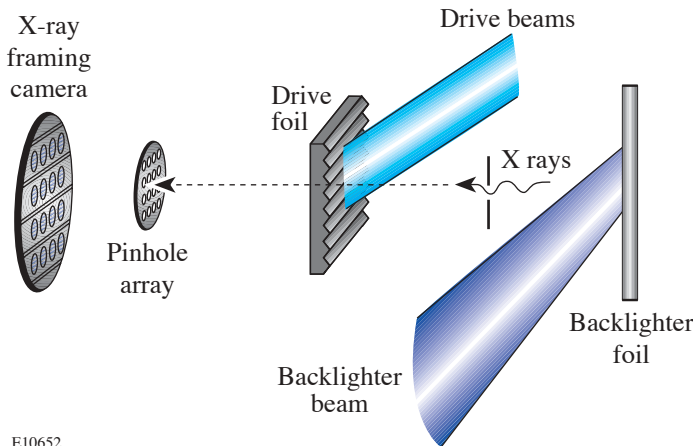


Figure 95.5 Experimental schematic of the target and primary diagnostic. The target is constructed from three foils: a uranium backlighter, an aluminum debris shield, and a CH drive foil with an imposed perturbation. The backlighter foil is 9 mm away from the drive foil with the Al shield halfway between these targets. The primary diagnostic is an x-ray framing camera with a 14.1 magnification provided by 8- μm pinholes located 24.8 mm from the accelerated target.

E10652

spectrum incident on the drive target. These data were used to determine the spatial shape of the x-ray backlighter so that it could be subtracted from the radiograph.

The time for each radiograph recorded by the framing cameras was determined by measuring when each strip on the framing camera was active and where the image was on the strip. The timing accuracy of each image relative to the drive beams was about 100 ps. The temporal resolution of both x-ray framing cameras was 80 ps.

Laser Irradiation

Planar-foil experiments on the OMEGA laser system use two independent laser sources so that separate pulse shapes can be used for the drive and backlighter beams. The beams were overlapped onto their respective targets with a radial displacement accuracy of 35 μm from the center of each foil. The backlighter pulse shape used was a 2-ns-duration square pulse. Each backlighter beam was focused to a 2.0-mm-diam spot at the 5% intensity contour with a maximum intensity where the beams overlapped on the foil of $2.0 \times 10^{14} \text{ W/cm}^2$. Planar targets with imposed mass perturbations were accelerated using ten laser beams overlapped with a total overlapped peak intensity of $1.7 \times 10^{14} \text{ W/cm}^2$. Each of the drive beams was focused to a spot size with a diameter of $\sim 930 \mu\text{m}$ (at the 5% intensity contour) and incorporated all of the beam smoothing available on OMEGA. The use of distributed phase plates,¹⁷ polarization smoothing,¹⁸ and SSD¹² resulted in a laser-irradiation nonuniformity relative to the intensity envelope of <1% over a 600- μm -diam region defined by the 90% intensity contour. Two pulse shapes were used for the drive beams: first, a pulse with a Gaussian rise to a 2-ns constant intensity (referred to as the drive pulse) and, second, this same pulse with a Gaussian picket placed ~ 2 ns ahead of the time when the drive pulse reaches constant intensity. The generic pulse shapes are shown in Fig. 95.1. The maximum drive intensity was designed to be the same for irradiation with and without a picket; however, for all data, the drive intensity with the picket was $\sim 10\%$ lower than that without the picket. To produce a clearly measurable result, the picket-pulse intensities used are greater than would be used to drive an actual ICF target.

Two-Dimensional (2-D) Simulations and Comparison with Experimental Results

Two-dimensional (2-D) hydrodynamic simulations of the experiments were performed with the Arbitrary-Lagrangian-Eulerian hydrodynamics code *DRACO*.¹⁹ These simulations

included flux-limited thermal diffusion, diffusive multigroup radiative transport (four groups were found to be sufficient), and inverse-Bremsstrahlung laser-energy deposition modeled with a straight-line ray trace. The experimentally measured pulse shape for a characteristic shot from each series (wavelength and picket intensity) was used. The Fourier transform of the optical-depth modulation of these simulations was calculated, incorporating the uranium backlighter spectrum, the filtering of the x-ray framing camera, and a correction for the camera resolution.

A comparison of the calculated and measured amplitudes of the fundamental Fourier mode of the optical-depth modulation is shown in Fig. 95.6 for a drive pulse only, a picket 50% of the drive-pulse intensity, and a picket 100% of the drive intensity. The data with and without the picket have been synchronized to the start of the measured drive pulse. Multiple shots were performed for each wavelength, with the x-ray diagnostics using a different temporal window for each shot. This allowed coverage over much of the duration of the drive pulse. There is no measured or calculated difference in the RT growth for perturbation wavelengths of 60 and 30 μm for a picket-pulse intensity of 50% of the drive pulse [Figs. 95.6(a) and 95.6(b), solid and dotted lines]. By contrast, a clear reduction in the growth rate is seen for the 50% picket data for the 20- μm -wavelength perturbation [Fig. 95.6(c), solid line]. Data for a picket with an intensity of 100% of the drive pulse [Figs. 95.6(b) and 95.6(c), dashed lines] show that the growth is clearly less for both 30- μm - and 20- μm -wavelength perturbations, and in fact, the ablation velocity during the drive pulse is large enough to stabilize the RT growth at these wavelengths. Two-dimensional hydrodynamic simulations of the experiment agree with the experimental data without and with picket pulses.

The dependence of the averaged 20- μm -wavelength RT growth rate on the picket intensity is shown in Fig. 95.7. The growth rate is calculated by fitting the experimental modulation in optical-depth data with an exponential for the pulse shapes with a picket pulse: $I_p/I_d = 50\%$ and $I_p/I_d = 100\%$. These data are plotted as solid points with error bars. The error bars are the statistical errors calculated from the exponential fit. The experimental points are compared to the *LILAC* data from Fig. 95.4(a) plotted as open circles. The picket intensity from Fig. 95.4(a) is divided by 200 TW/cm^2 to determine I_p/I_d . The average RT growth rates calculated by *LILAC* agree with the experimental data.

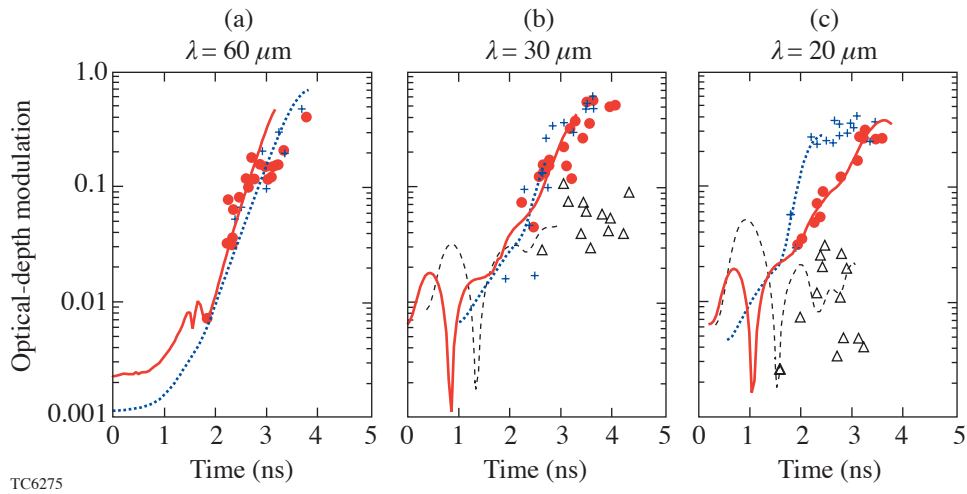


Figure 95.6

The optical-depth modulation for (a) 60- μm -, (b) 30- μm -, and (c) 20- μm -wavelength perturbations for laser pulse shapes without a picket pulse, with a picket-pulse intensity approximately 50% of the drive pulse, and with a picket-pulse intensity approximately 100% of the drive pulse. The *DRACO* 2-D hydrodynamic simulation data are shown using curves and the experimental data as symbols. *DRACO* output for a no-picket pulse is plotted as a dotted line, and experimental data for no picket are plotted as crosses. Laser pulse shapes with a picket intensity of about 50% of the drive intensity have the *DRACO* output plotted as a solid line and the experimental data as circles. A picket pulse with an intensity of about 100% of the drive intensity is shown as a dashed line for the *DRACO* output, and the experimental points are plotted as open triangles.

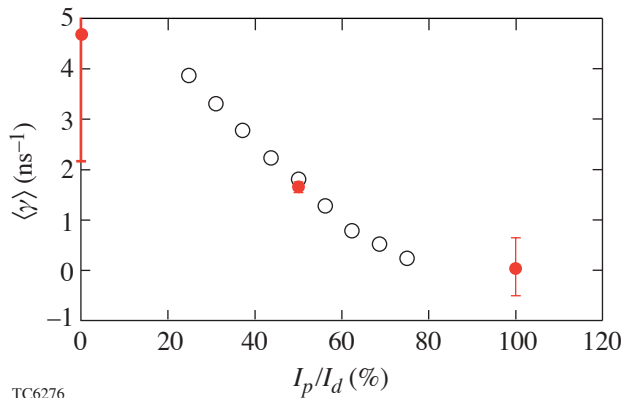


Figure 95.7

The average growth rate for a 20- μm -wavelength perturbation is plotted as a function of the picket-pulse intensity (I_p) divided by the drive-pulse intensity (I_d). The solid points are calculated by fitting the experimental data to an exponential. The error bars on the experimental points reflect the statistical error from the exponential fit. The open circles are the *LILAC* points from Fig. 95.4(a) replotted as a comparison to the measurements.

Conclusions

Experiments have been performed on the OMEGA laser system to test the reduction of the RT growth rate using a single laser picket before the main drive pulse. One-dimensional (1-D) hydrodynamic simulations used to define the experimental parameters indicate that a picket pulse with an intensity of 100 TW/cm² and a FWHM of 300 ps and separated from the drive pulse by 2 ns showed significant reduction in the RT growth rate for a 20- μm -wavelength perturbation. The picket generates a shock wave in the foil, allowing it to expand and

rarefy during the relaxation period. As a result, the foil density during the drive pulse is lowered, and the ablation velocity is correspondingly higher, lowering the RT growth rate. This has been observed experimentally in planar targets in which the RT growth rate was determined by optical-depth modulations measured with x-ray backlighting.

With a picket-pulse intensity equal to 50% of the drive-pulse intensity, the RT growth was reduced for a 20- μm -wavelength surface perturbation, but negligible growth

reduction was observed for perturbation wavelengths of 30 and 60 μm . RT growth data taken with a picket-pulse intensity equal to 100% of the drive-pulse intensity show that both the 30- and 20- μm -wavelength perturbations exhibit no significant RT growth. The modulation in optical depth as a function of time calculated from 2-D hydrodynamic simulations agrees with the experimental data.

The dependence of the time-averaged RT growth rate on the picket intensity for the 20- μm -wavelength perturbations was calculated from the experimental data. These data were then compared to the time-averaged RT growth rates calculated by *LILAC* when the experiment was designed. The ablative RT growth rate's dependence on the intensity of the picket calculated by *LILAC* agrees with the experimental data.

ACKNOWLEDGMENT

This work was supported by the U.S. Department of Energy Office of Inertial Confinement Fusion under Cooperative Agreement No. DE-FC03-92SF19460, the University of Rochester, and the New York State Energy Research and Development Authority. The support of DOE does not constitute an endorsement by DOE of the views expressed in this article.

REFERENCES

1. J. Nuckolls *et al.*, *Nature* **239**, 139 (1972).
2. Lord Rayleigh, *Proc. London Math Soc.* **XIV**, 170 (1883).
3. G. Taylor, *Proc. R. Soc. London Ser. A* **201**, 192 (1950).
4. J. D. Lindl and W. C. Mead, *Phys. Rev. Lett.* **34**, 1273 (1975).
5. V. N. Goncharov, J. P. Knauer, P. W. McKenty, P. B. Radha, T. C. Sangster, S. Skupsky, R. Betti, R. L. McCrory, and D. D. Meyerhofer, *Phys. Plasmas* **10**, 1906 (2003).
6. S. E. Bodner, *Phys. Rev. Lett.* **33**, 761 (1974).
7. H. Takabe *et al.*, *Phys. Fluids* **28**, 3676 (1985).
8. R. Betti, V. N. Goncharov, R. L. McCrory, P. Sorotokin, and C. P. Verdon, *Phys. Plasmas* **3**, 2122 (1996).
9. Laboratory for Laser Energetics LLE Review **94**, 91, NTIS document No. DOE/SF/19460-485 (2003). Copies may be obtained from the National Technical Information Service, Springfield, VA 22161.
10. T. J. B. Collins and S. Skupsky, *Phys. Plasmas* **9**, 275 (2002).
11. S. E. Bodner, *J. Fusion Energy* **1**, 221 (1981).
12. S. Skupsky, R. W. Short, T. Kessler, R. S. Craxton, S. Letzring, and J. M. Soures, *J. Appl. Phys.* **66**, 3456 (1989).
13. T. R. Boehly, D. L. Brown, R. S. Craxton, R. L. Keck, J. P. Knauer, J. H. Kelly, T. J. Kessler, S. A. Kumpan, S. J. Loucks, S. A. Letzring, F. J. Marshall, R. L. McCrory, S. F. B. Morse, W. Seka, J. M. Soures, and C. P. Verdon, *Opt. Commun.* **133**, 495 (1997).
14. J. P. Knauer, R. Betti, D. K. Bradley, T. R. Boehly, T. J. B. Collins, V. N. Goncharov, P. W. McKenty, D. D. Meyerhofer, V. A. Smalyuk, C. P. Verdon, S. G. Glendinning, D. H. Kalantar, and R. G. Watt, *Phys. Plasmas* **7**, 338 (2000).
15. M. C. Richardson, P. W. McKenty, F. J. Marshall, C. P. Verdon, J. M. Soures, R. L. McCrory, O. Barnouin, R. S. Craxton, J. Delettrez, R. L. Hutchison, P. A. Jaanimagi, R. Keck, T. Kessler, H. Kim, S. A. Letzring, D. M. Roback, W. Seka, S. Skupsky, B. Yaakobi, S. M. Lane, and S. Prussin, in *Laser Interaction and Related Plasma Phenomena*, edited by H. Hora and G. H. Miley (Plenum Publishing, New York, 1986), Vol. 7, pp. 421–448.
16. O. L. Landen *et al.*, in *Ultrahigh- and High-Speed Photography, Videography, and Photonics '93*, edited by P. W. Roehrenbeck (SPIE, Bellingham, WA, 1993), Vol. 2002, pp. 2–13.
17. Y. Lin, T. J. Kessler, and G. N. Lawrence, *Opt. Lett.* **20**, 764 (1995).
18. T. R. Boehly, V. A. Smalyuk, D. D. Meyerhofer, J. P. Knauer, D. K. Bradley, R. S. Craxton, M. J. Guardalben, S. Skupsky, and T. J. Kessler, *J. Appl. Phys.* **85**, 3444 (1999).
19. P. B. Radha, V. N. Goncharov, T. J. B. Collins, J. A. Delettrez, P. W. McKenty, and R. P. J. Town, "Two-Dimensional Simulations of Plastic-Shell Implosions on the OMEGA Laser," to be submitted to *Physics of Plasmas*.

Theory of Laser-Induced Adiabatic Shaping in Inertial Fusion Implosions: The Decaying Shock

Introduction

In inertial confinement fusion (ICF),¹ a cryogenic shell of deuterium and tritium (DT) filled with DT gas is accelerated inward by direct laser irradiation (direct drive) or by the x rays emitted by a laser-illuminated enclosure of high- Z material (indirect drive). In the shell frame of reference, the acceleration points from the heavy shell toward the hot ablated plasma, making the shell's outer surface unstable to the well-known Rayleigh–Taylor (RT) instability.² In indirect-drive ICF, the high uniformity of the blackbody x-ray radiation results in a negligible level of imprinted perturbations on the shell's outer surface. Indeed, the seeds of the Rayleigh–Taylor instability are mostly provided by the capsule's surface roughness. In direct-drive ICF, the laser-beam intensity is not spatially uniform, and the direct illumination of the shell leads to high levels of laser imprinting that seed the RT instability. The use of random phase plates³ (RPP's) has successfully shifted the spectrum of laser nonuniformities toward short wavelengths, and the implementation of either smoothing by spectral dispersion⁴ (SSD) or induced spatial incoherence⁵ (ISI) has provided significant smoothing by modulating the intensity speckle pattern in both space and time. Despite these important advances in smoothing techniques, the current level of imprinting in direct-drive ICF is still sufficiently large to substantially reduce the performance of low-adiabat implosions on the OMEGA laser and high-gain implosions on the National Ignition Facility (NIF).⁶

Since the perturbations seeded by laser imprinting grow exponentially in time during the acceleration phase, it is possible to reduce the RT-induced shell distortion by mitigating the growth rates of the RT instability. The RT growth rates for an all-DT capsule are reduced with respect to the classical value by the well-known ablative stabilization,^{7–11} leading to¹⁰

$$\Gamma \approx 0.94 \sqrt{kg} - 2.7 kV_a, \quad (1)$$

where Γ is the growth rate, g is the shell acceleration, V_a is the ablation velocity, and k is the instability wave number. The

ablation velocity represents the speed of propagation of the heat front inside the shell material and can be defined as the ratio of the ablation rate \dot{m} and the shell's outer surface (or ablation front) density ρ_{out} , leading to

$$V_a = \frac{\dot{m}}{\rho_{\text{out}}}. \quad (2)$$

The ablation rate \dot{m}_a follows a power law of the laser intensity ($\dot{m}_a \sim I_L^{1/3}$), while the ablation-front density can be written in terms of the shell entropy and ablation pressure P_a :

$$\rho_{\text{out}} = \left(\frac{P_a}{S_{\text{out}}} \right)^{3/5}, \quad (3)$$

where S_{out} is the entropy calculated inside the shell near the ablation front. Using the scaling of the ablation pressure with respect to laser intensity, $P_a \sim I_L^{2/3}$, and the definition of the normalized adiabat in DT, $\alpha \equiv P(\text{Mbar})/2.18 \rho(\text{g/cm}^3)^{5/3}$, the ablation velocity depends on the laser intensity I_L and ablation-front entropy:

$$V_a \sim \alpha_{\text{out}}^{3/5} I_L^{-1/15}. \quad (4)$$

Note that $\alpha \sim S$. Because of the weak dependence on the laser intensity, one concludes that the ablation velocity depends almost exclusively on the shell adiabat at the outer surface α_{out} . In standard target design, the shell entropy is set by the initial strong shock launched when the laser is turned on, yielding a flat-adiabat profile inside the shell. During the acceleration phase, a significant portion of the shell is ablated off, while the remainder coasts inward at a constant velocity once the laser is turned off. When the pressure builds up inside the hot spot, the shell decelerates as its kinetic energy is used to compress both the enclosed hot spot and the shell itself. It is well known that the shell kinetic energy required to compress the hot spot to ignition conditions is roughly proportional to the square of the unablated shell adiabat.^{12–14}

$$\varepsilon_K^{\text{ig}} \sim \alpha_{\text{inn}}^2, \quad (5)$$

where $\varepsilon_K^{\text{ig}}$ is the kinetic energy required for ignition and α_{inn} is the normalized adiabat of the inner (unablated) portion of the shell at the end of the acceleration phase. In addition, the energy required to achieve the maximum yield¹² is also a strong function of the in-flight adiabat:

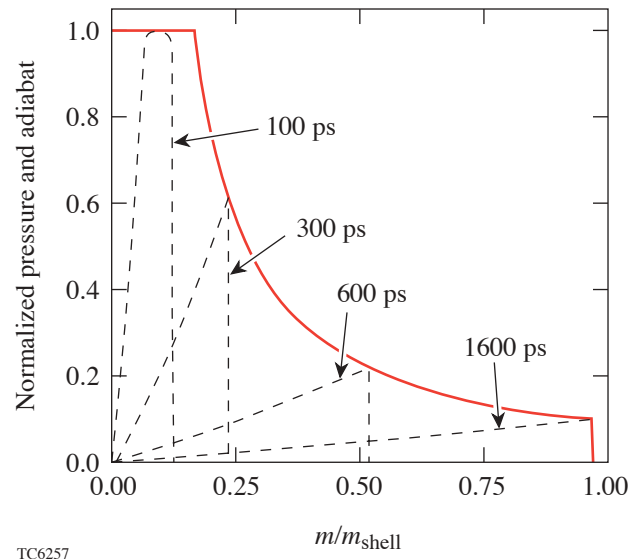
$$\varepsilon_K^{\text{max gain}} \sim \alpha_{\text{inn}}^{1.6 \pm 0.2}, \quad (6)$$

showing that high-adiabat implusions require greater kinetic energy.

In standard ICF target designs, the shell's entropy profile is flat throughout the shell such that $\alpha_{\text{inn}} = \alpha_{\text{out}}$. Since large shell adiabats improve stability while lowering the gain, it has been common practice to look for a compromise between stability on the one hand and gain on the other by choosing an intermediate optimized value of the adiabat. It is important to recognize, however, that target gain and stability depend on the local values of the adiabat at different locations in the shell. It follows that high gain and improved stability can indeed be achieved simultaneously by shaping the adiabat inside the shell to maximize the ablation-front adiabat α_{out} for better stability and to minimize the inner-surface adiabat α_{inn} for higher gain. Though the benefits of adiabat shaping have been recognized by target designers for quite some time, it has not been clear how to implement it. The first mention of adiabat tailoring is in Ref. 15, where it was speculated that adiabat shaping could be induced by the interaction of soft x rays with an ablator material having multiple absorption lines and radiation penetration depths. The first target design^{16,17} of radiation-induced adiabat shaping makes use of the x rays produced by a thin gold overcoat and by the carbon radiation in a wetted-foam ablator. Even though such a clever design can produce the desired shaping, significant complications arise from the target-manufacturing aspects, based on wetted-foam technology.

It was later recognized that adiabat shaping can also be induced by modifying the foot of the laser pulse. Two different techniques were proposed: (1) adiabat shaping via a decaying shock (DS)¹⁸ and (2) adiabat shaping via relaxation (RX).¹⁹ Adiabat shaping via a decaying shock relies on the entropy profile left behind by a strong unsupported shock that is launched by an intense laser prepulse. The prepulse is immediately followed by a lower-intensity foot, which slowly evolves into a high-power main pulse. The strong shock launched by

the intense prepulse decays after the laser power is lowered to the foot intensity. As the strong shock starts to decay, it leaves behind a shaped-adiabat profile that has its maximum at the ablation front and minimum on the shell's inner surface. Figure 95.8 shows snapshots of the normalized pressure profile behind a decaying shock (dashed curves) at different times for a 28-Mbar prepulse applied for 75 ps to a DT slab of 100- μm thickness. The solid line represents the adiabat profile left behind by the decaying shock. All the profiles are plotted versus the normalized areal-density coordinate of the foil.



TC6257

Figure 95.8

Normalized adiabat (solid) near breakout and pressure (dashed) at 100 ps, 300 ps, 600 ps, and 1600 ps for a 75-ps, 28-Mb prepulse.

Adiabat shaping by relaxation also relies on a prepulse launching a decaying shock. The prepulse intensity is much lower, however, than the DS case because the resulting decaying shock is not meant to shape the adiabat but to relax the density and pressure profiles. Indeed, the RX technique requires that the laser power is turned off after the prepulse to allow the shell to decompress and establish relaxed density and pressure profiles. RX adiabat shaping occurs later when the high-intensity foot of the main laser pulse drives a strong shock through the relaxed profiles. As the main shock propagates, it encounters the increasingly larger pressures of the relaxed profiles, causing its strength to decrease, thus leaving behind a shaped-adiabat profile with its maximum at the ablation front and its minimum on the inner surface. Because of the low-power prepulse, the RX technique can be easily implemented

on existing laser systems. Furthermore, the high-power foot of the main pulse leads to a low contrast ratio, better conversion efficiency, and therefore more energy on target.

This article is primarily concerned with a detailed theoretical treatment of laser-induced adiabat shaping by a decaying shock. Here, based on the results of Refs. 18 and 19, we assume that adiabat shaping has a stabilizing effect and focus on the decaying shock evolution. The decaying shock analysis presented here is based on analytical and numerical solutions of the gasdynamic model equations. The adiabat shape is first derived for an ideal case of a shock driven by an applied pressure in the form of a step function in time. The analytic results in the ideal case are derived using an asymptotic matching formula based on a local analysis at the rarefaction–shock interaction point and the asymptotic self-similar solution.^{23–28} The ideal adiabat shape reproduces the numerical results very accurately over the entire DS evolution as long as the shock front remains in the strong shock regime. When compared with other theoretical predictions, we find that even though the ideal adiabat shape is in qualitative agreement with Ref. 18, its magnitude is quite different and closer to the standard self-similar solution with an appropriate proportionality constant. The nonideal effects of finite mass ablation and finite residual ablation pressure are evaluated, and the resulting corrections on the adiabat shape are calculated. It is found that the most important correction comes from the residual pressure caused by the finite heat capacity of the coronal plasma, which slows down the ablation-pressure decay when the laser intensity is suddenly lowered. A convenient form of the adiabat shape is derived for carrying out detailed comparisons with the results of full one-dimensional (1-D) simulations using available ICF codes. The agreement between theory and full 1-D simulations is quite remarkable, indicating that the theoretical predictions can be used for target design purposes.

Lagrangian Hydrodynamics

As is often the case for complicated dynamical problems in gasdynamics, the analysis is greatly simplified by adopting a Lagrangian frame of reference, where the independent spatial coordinate is the mass areal density

$$m = \int_0^x \rho(x', 0) dx'. \quad (7)$$

In this coordinate, the outer shell surface is represented by $x = 0$ and $m = 0$. For simplicity, we calculate for the case of an ideal gas with adiabatic index γ and neglect convergence effects on the basis that the adiabat shaping occurs when the

inner shell surface has not yet moved and the initial aspect ratio is sufficiently large that the shell can be approximated by a uniform slab.

In the Lagrangian frame, the equations of motion for the shocked material can be written in the following conservative form:

$$\frac{\partial u}{\partial m} - \frac{\partial}{\partial t} \frac{1}{\rho} = 0, \quad (8)$$

$$\frac{\partial u}{\partial t} + \frac{\partial p}{\partial m} = 0, \quad (9)$$

$$\frac{\partial}{\partial t} \left(\frac{p/\rho}{\gamma-1} + \frac{u^2}{2} \right) + \frac{\partial}{\partial m} (pu) = 0, \quad (10)$$

governing conservation of mass, momentum, and energy, respectively. In the absence of shocks, the energy equation can be simplified, yielding the isentropic flow condition

$$p = S(m)\rho^\gamma, \quad (11)$$

where $S(m)$ is referred to as the adiabat or entropy function, which depends exclusively on the Lagrangian coordinate. Equation (11) is valid only for isentropic flow and therefore does not apply across the shock front. At the shock front, the solution of Eqs. (8)–(10) must satisfy the Hugoniot conditions obtained by rewriting Eqs. (8)–(10) in the shock frame of reference and integrating across the shock front. A straightforward calculation leads to the following jump conditions at the shock:

$$\left[\left| u + \frac{\dot{m}_s}{\rho} \right| \right] = 0, \quad (12)$$

$$\left[\left| \dot{m}_s u - p \right| \right] = 0, \quad (13)$$

$$\left[\left| \dot{m}_s \left(\frac{p/\rho}{\gamma-1} + \frac{u^2}{2} \right) - pu \right| \right] = 0. \quad (14)$$

Equations (12)–(14) can be simplified in the strong shock regime, yielding the simple relations for the areal density overtaken by the shock (\dot{m}_s), the post-shock density ρ_{ps} , and velocity u_{ps} :

$$\rho_{ps} = \frac{\gamma+1}{\gamma-1} \rho_0, \quad (15)$$

$$u_{ps} = \frac{2}{\gamma-1} \frac{\dot{m}_s}{\rho_{ps}}, \quad (16)$$

$$\dot{m}_s = \sqrt{\frac{(\gamma-1)}{2}} p_{ps} \rho_{ps}, \quad (17)$$

where p_{ps} represents the post-shock pressure. In the sections that follows, Eqs. (8), (9), and (11) and (15)–(17) are solved to determine the dynamics of the shock-induced adiabat shaping.

The General Problem of the Decaying Shock

Our analysis begins with the study of the propagation of a decaying shock driven by a constant pressure applied over a time interval Δt_{prep} . At first, we neglect all nonideal effects such as laser ablation and model the laser with a pressure applied on the outer shell surface. The general characteristics of a decaying shock are summarized below.

A uniform strong shock is launched by the ablation pressure $p_* = P_a^{\text{prep}}$ applied during the prepulse. Here we consider the case of a square prepulse and set $p_* = \text{constant}$. This strong prepulse shock compresses the shell material to a density $\rho_* = \rho_0(\gamma+1)/(\gamma-1)$ (here ρ_0 is the initial shell density) and sets the adiabat of the shocked material to a constant value $S_* = p_*/\rho_*^\gamma$. The shock velocity U_{s*} and the fluid velocity of the shocked material u_* can be approximated using the Hugoniot relations for strong shocks [Eqs. (15)–(17)], leading to

$$U_{s*} = \sqrt{\frac{(\gamma+1)^2}{2(\gamma-1)} \frac{p_*}{\rho_*}}, \quad (18)$$

$$u_* = \sqrt{\frac{2}{(\gamma-1)} \frac{p_*}{\rho_*}}, \quad (19)$$

where the relation $U_{s*} = \dot{m}_s/\rho_0$ has been used. After the interval Δt_{prep} , the laser intensity (and therefore the applied

ablation pressure) is greatly reduced causing a rarefaction wave to propagate from the ablation front toward the shock front. The leading edge of the rarefaction wave travels with the sound speed $a_* = \sqrt{\gamma p_*/\rho_*}$ inside the shocked material, which in turns travels with the post-shock velocity u_* with respect to the lab frame. The rarefaction wave's leading-edge velocity in the lab frame is therefore

$$U_r = a_* + u_* = \frac{2}{\gamma+1} \left[1 + \sqrt{\frac{\gamma(\gamma-1)}{2}} \right] U_{s*} \quad (20)$$

and is always greater than the shock velocity U_{s*} , indicating that the rarefaction wave travels faster than the shock. The shock is therefore overtaken by the rarefaction wave. The overtaking time can be determined by equating the distance traveled by the rarefaction wave with the distance traveled by the shock:

$$(u_* + a_*) \Delta t_* = d_c + U_{s*} \Delta t_*, \quad (21)$$

where $d_c = U_{s*} \Delta t_{\text{prep}} (\gamma-1)/(\gamma+1)$ is the compressed thickness of the shocked material at time $t = \Delta t_{\text{prep}}$, $a_* = \sqrt{\gamma p_*/\rho_*}$ is the shocked material sound speed, and Δt_* is the traveling time of the rarefaction wave before overtaking the shock. A simple manipulation of Eq. (21) yields the overtaking time interval

$$\Delta t_* = \frac{\Delta t_{\text{prep}}}{\sqrt{2\gamma/(\gamma-1)} - 1}. \quad (22)$$

At time $t_r = \Delta t_{\text{prep}} + \Delta t_*$, the shock and the rarefaction wave interact after having propagated through an areal density:

$$m_* = \rho_0 t_r U_{s*} = \Delta t_* \rho_* a_* = \Delta t_* \sqrt{\gamma p_* \rho_*}. \quad (23)$$

Once the shock is overtaken by the rarefaction wave ($t > t_r$), the shock strength starts to decrease, as does the entropy jump across the shock. Since the entropy of each fluid element is conserved after the shock, the adiabat is independent of time and only a function of the areal density: $S = S(m)$.

Before the shock starts to decay, the post-shock variables are uniform and their values are denoted by the subscript *: p_* , ρ_* , S_* , a_* . Using these post-shock values, one can define a set of dimensionless variables

$$\hat{\rho} \equiv \frac{\rho}{\rho_*}, \quad \hat{p} \equiv \frac{p}{p_*}, \quad \hat{u} \equiv \frac{u}{a_*}, \quad (24a)$$

$$\hat{S} = \frac{S}{S_*}, \quad z = \frac{m}{m_*}, \quad \tau = \frac{t}{\Delta t_*}, \quad (24b)$$

where m_* and Δt_* are defined in the previous section. Here, $t = 0$ represents the time when the laser power is lowered and the rarefaction wave is launched. The equations of motion [Eqs. (8), (9), and (11)] can be rewritten in a dimensionless form using the variables in Eqs. (24). A simple manipulation leads to the following form of the equations of motion:

$$\frac{\partial \hat{u}}{\partial z} = \frac{\partial \hat{\rho}^{-1}}{\partial \tau}, \quad (25a)$$

$$\gamma \frac{\partial \hat{u}}{\partial \tau} = -\frac{\partial \hat{p}}{\partial z}, \quad (25b)$$

$$\hat{p} = \hat{S}(z) \hat{\rho}^\gamma, \quad (25c)$$

with the entropy conservation equation [Eq. (25c)] valid away from the shock front. Similarly, the Hugoniot conditions in the strong shock regime can also be written in the following dimensionless form:

$$\dot{z}_s = \sqrt{\frac{\gamma-1}{2\gamma} \hat{S}(z_s)}, \quad (26a)$$

$$\hat{\rho}(z_s, \tau) = 1, \quad (26b)$$

$$\hat{u}(z_s, \tau) = \sqrt{\frac{2\hat{S}(z_s)}{\gamma(\gamma-1)}}, \quad (26c)$$

where $z_s \equiv m_s(t)/m_*$. Here the dot in \dot{z}_s indicates a derivative with respect to τ . For $0 < \tau < 1$, the rarefaction wave propagates toward the shock front and Eqs. (26) yield the standard rarefaction-wave solution

$$\hat{S} = 1, \quad \hat{p} = \hat{\rho}^\gamma, \quad \hat{\rho} = \left(\frac{z}{\tau}\right)^{\frac{2}{\gamma+1}}, \quad (27a)$$

$$\hat{u} = \frac{2}{\gamma-1} \left[\left(\frac{z}{\tau}\right)^{\frac{\gamma-1}{\gamma+1}} - 1 \right] + \sqrt{\frac{2}{\gamma(\gamma-1)}}, \quad (27b)$$

where z varies between 0 and τ . At time $\tau = 1$, the rarefaction wave overtakes the shock at the point $z = 1$. At this time, a perturbation propagating with the sound speed travels backward down the rarefaction wave while the shock strength decays as the shock front travels forward. The adiabat, which is a function of the Lagrangian coordinate z , is uniform [$\hat{S}(z) = 1$] for $z < 1$ and decays for $z > 1$. For times $\tau > 1$, Eqs. (25) need to be solved in the two domains of the rarefaction wave $0 < z < 1$ and the decaying shock $1 < z < z_s$. For $z < 1$, the function \hat{S} is known ($\hat{S} = 1$) while it is unknown for $z > 1$. At the point $z = 1$, the two solutions must satisfy the boundary conditions of continuous pressure and velocity:

$$\hat{u}(z = 1^-) = \hat{u}(z = 1^+), \quad (28a)$$

$$\hat{p}(z = 1^-) = \hat{p}(z = 1^+). \quad (28b)$$

At the trailing edge of the rarefaction wave ($z = 0$), both density and pressure are small as the applied pressure is greatly reduced after the end of the prepulse. For simplicity, we assume that the post-prepulse pressure is negligible and adopt the vacuum boundary conditions at $z = 0$:

$$\hat{\rho}(0, t) = 0, \quad \hat{p}(0, t) = 0. \quad (29)$$

It is important to observe that all the equations and initial and boundary conditions depend only on γ . It follows that the entropy $\hat{S}(z)$ is a universal function of z for any given γ and can be determined by a single numerical simulation.

Solution for $m \gg m_*$

Even though a single one-dimensional simulation is sufficient to provide the adiabat shape, it is instructive to calculate analytically the entropy distribution. It is important to realize that Eqs. (25) cannot be solved exactly with the boundary and initial conditions in Eqs. (26)–(29). It is, however, intuitive that after some time from the end of the prepulse, the shock propagation becomes independent of initial and boundary conditions and develops a self-similar character. One would expect that the solution of Eqs. (25) becomes self-similar for $z_s(t) \gg 1$ and $t \gg 1$. The self-similar solution has been

studied by several authors^{23–28} and provides the asymptotic behavior of a decaying shock. Here we review the self-similar calculation valid for $z_s \gg 1$ and then solve the decaying-shock problem in the opposite limit of $z_s(t) \approx 1$ and $\tau \approx 1$ in order to generate a matching formula approximating the solution for arbitrary z and τ .

A self-similar solution of the decaying-shock problem can be found in the limit of $m_* \rightarrow 0$. Because of the absence of characteristic quantities, it is appropriate to use dimensional variables m , t , p , ρ , and u and the following divergent form of the entropy:

$$S(m) = \frac{\sigma_*}{m^\delta} \quad (30)$$

with δ to be determined by the solvability condition. The shock trajectory can be found from the shock velocity equation [Eq. (17)] after substituting $p_{ps} = \sigma_* \rho_*^\gamma / m^\delta$ and $\rho_{ps} = \rho_*$, leading to the following differential equation:

$$\dot{m}_s(t) = \sqrt{\frac{\gamma-1}{2} \frac{\sigma_* \rho_*^{\gamma+1}}{m_s(t)^\delta}}, \quad (31)$$

which exhibits the power-law solution

$$m_s(t) = \left[\left(1 + \frac{\delta}{2} \right) t \sqrt{\frac{\gamma-1}{2} \sigma_* \rho_*^{\gamma+1}} \right]^{\frac{2}{2+\delta}}. \quad (32)$$

Since the only relevant position is the shock location $m_s(t)$, the corresponding self-similar coordinate is

$$\xi = \frac{m}{m_s(t)} \quad (33)$$

and the self-similar dependent variables are

$$\rho = \rho_* \hat{\rho}(\xi), \quad u = \frac{\dot{m}_s}{\rho_*} \hat{u}(\xi), \quad p = \sigma_* \rho_*^\gamma \hat{p}(\xi), \quad (34)$$

where $\hat{p}(\xi) = \hat{\rho}(\xi)^\gamma$. Substituting Eqs. (33) and (34) into Eqs. (8) and (9) yields the following coupled ordinary differential equations (ODE's) for \hat{u} and $\hat{\rho}$:

$$\pi(\xi) \frac{d\hat{u}}{d\xi} + r(\xi) = 0, \quad (35a)$$

$$\pi(\xi) \frac{\xi}{\hat{\rho}^2} \frac{d\hat{\rho}}{d\xi} + r(\xi) = 0, \quad (35b)$$

where

$$\pi(\xi) = \frac{\gamma-1}{2} \xi - \gamma \frac{\hat{\rho}^{\gamma+1}}{\xi^{\delta+1}}, \quad (35c)$$

$$r(\xi) = \frac{\delta}{4} (\gamma-1) \hat{u} + \delta \frac{\hat{\rho}^\gamma}{\xi^{\delta+1}}. \quad (35d)$$

The boundary conditions at the shock front are governed by the Hugoniot relations

$$\hat{\rho}(1) = 1, \quad \hat{u}(1) = \frac{2}{\gamma-1}, \quad (36)$$

while $\hat{\rho}(0)$ must vanish [$\hat{\rho}(0) = 0$] since the entropy is infinite at $m = 0$. The pressure at $m = 0$ is not assigned; it is determined instead by the self-similar solution of Eqs. (35). Integrating the momentum conservation equation [Eq. (9)] between $m = 0$ and $m = m_s(t)$ and using the Hugoniot relations leads to the following equation for the applied pressure:

$$p(m=0, t) = \frac{\partial}{\partial t} \left[\int_0^{m_s(t)} u \, dm \right], \quad (37)$$

which can be rewritten upon substitution of Eqs. (32) and (34) into the simple form

$$p(m=0, t) = \frac{1}{\rho_*} \left(\frac{\gamma-1}{2} \sigma_* \rho_*^{\gamma+1} \right)^{\frac{2}{2+\delta}} \times \frac{1-\delta/2}{(1+\delta/2)^{\frac{2\delta}{2+\delta}}} \int_0^1 \frac{\hat{u}(\xi) d\xi}{t^{\frac{2\delta}{2+\delta}}}. \quad (38)$$

Observe that Eq. (38) indicates that the applied pressure is a decaying function of time with a power-law dependence. One

can also argue that the self-similar solution represents the case of an impulsive pressure $p(m=0, t>0) = 0$ only when the zero global momentum condition is satisfied:

$$\int_0^1 \hat{u}(\xi) d\xi = 0. \quad (39)$$

In summary, the self-similar solution requires either an applied pressure of the form given in Eq. (38) or an impulsive pressure with the condition of zero global momentum [Eq. (39)]. Both the finite-pressure and zero-pressure conditions at $m=0$ impose some restrictions on the solution of Eqs. (35) near $\xi \rightarrow 0$. It is therefore useful to solve the self-similar equation near $\xi = 0$ to determine whether or not a finite- or zero-pressure solution exists. Indeed, by expanding the equations near $\xi = 0$, one finds two power-law solutions:

$$\hat{\rho}(\xi) \approx \Omega_0 \xi^{1+\frac{\delta}{2}} (1 + \Omega_1 \xi^\mu \dots), \quad (40)$$

$$\hat{\rho}(\xi) \approx \theta_0 \xi^{\frac{\delta}{\gamma}} (1 + \nu_1 \xi + \theta_1 \xi^\omega + \dots), \quad (41)$$

where $\omega = 2 - \delta/\gamma$, $\mu = (\delta + 2)(\gamma - 1)/2$,

$$\theta_1 = \frac{1}{\theta_0^{\gamma+1}} \frac{\delta(\gamma-1)}{2\gamma^2\omega(\omega-1)} \left(1 + \frac{\delta}{2} - \frac{\delta}{\gamma} \right), \quad (42)$$

$$\Omega_1 = \Omega_0^{\gamma+1} \frac{2(\alpha\gamma - \delta)(\alpha\gamma - \delta - 1)}{(\mu - \alpha)\mu} \quad (43)$$

with $\alpha = 1 + \delta/2$ and θ_0 , Ω_0 , and ν_1 representing arbitrary constants. It is important to note that Eq. (41) corresponds to the finite-pressure solution while Eq. (40) corresponds to a zero pressure at $m=0$.

1. Self-Similar Solution

Equations (35) can be numerically solved for different values of δ . For $\delta \leq 1.2748$, the solution is regular and merges with a constant-pressure solution near $\xi = 0$. Figure 95.9 shows a plot of the functions $\hat{\rho}(\xi)$ and $\hat{u}(\xi)$ for $\delta = 1.0$. Observe that $\hat{\rho}(0)$ is not zero, representing a solution with a finite applied pressure that decays in time as $t^{-2\delta/(2+\delta)}$. In agreement with Ref. 25, the ODE's [Eqs. (35)] become singular for $\delta = 1.2748$ at the point $\xi_c \approx 0.0851$, where $\pi(\xi_c)$

$= 0$. Observe that the derivatives of $\hat{\rho}$ and \hat{u} would be singular unless $r(\xi)$ also vanishes at ξ_c . Indeed, for $\delta \approx 1.2748$, both $\pi(\xi)$ and $r(\xi)$ vanish at $\xi_c \approx 0.0851$, indicating that the derivatives of $\hat{\rho}$ and \hat{u} are regular even though they may be discontinuous at ξ_c . To avoid integrating the equations through the singular point ξ_c , one can numerically solve between 1 and ξ_c and between 0 and ξ_c with the constraint that both $\hat{\rho}(\xi)$ and $\hat{u}(\xi)$ be continuous at ξ_c . The numerical integration in the $(0, \xi_c)$ interval can be performed by using the expansions in Eqs. (40) and (41) as initial conditions. Indeed, for $\Omega_0 \approx 1.8949$, the solution starting from the initial conditions in Eq. (40) matches the solution in $(\xi_c, 1)$ at the singular point ξ_c . Similarly, for $\theta_0 \approx 0.2658$, the solution starting from the initial conditions in Eq. (41) matches the other solution at ξ_c , implying that there are two valid self-similar solutions for $\delta \approx 1.2748$, corresponding to a finite and to a vanishing applied pressure. Figure 95.10 shows both solutions for $\delta \approx 1.2748$. Observe that the two solutions are identical for $\xi > \xi_c$ and differ in the interval $(0, \xi_c)$ with the dashed line representing the finite-applied-pressure solution. The existence of two valid solutions for $\delta = 1.2748$ is quite revealing. Because the finite-pressure solution requires an applied-pressure decaying as

$$p(m=0, t) \sim \frac{1}{t^{\frac{2\delta}{2+\delta}}} \sim \frac{1}{t^{0.78}} \quad (44)$$

and the zero-pressure solution requires a sudden decay, one can speculate that a pressure decay rate faster than $t^{-0.78}$ does not alter the solution for $\xi > \xi_c$, which becomes quickly self-similar with $\delta \approx 1.2748$, independent of the applied-pressure

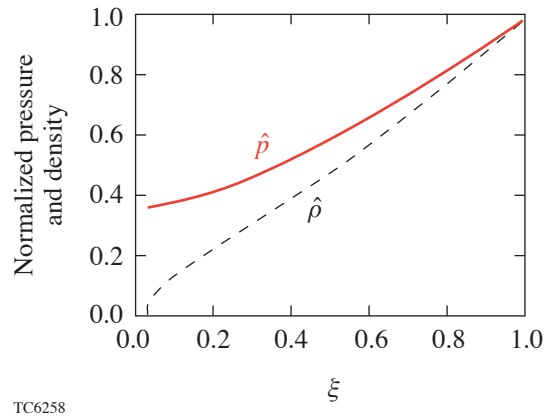
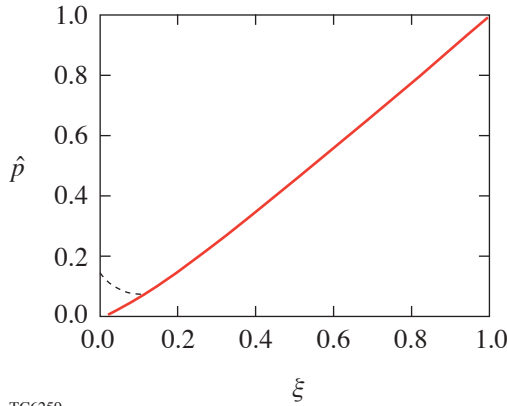


Figure 95.9
Dimensionless pressure and density as a function of self-similar coordinate for $\delta = 1.0$.

decay rate. In conclusion, the adiabat shape left behind by a decaying self-similar shock follows a power law of the areal density

$$S \sim \frac{1}{m^\delta} \quad (45)$$

with $\delta \leq 1.2748$. Values of $\delta < 1.2748$ correspond to solutions for an applied-pressure decaying as $p(m=0,t) \sim t^{-2\delta/(2+\delta)}$, while the value $\delta = 1.2748$ corresponds to solutions for a faster-decaying or impulsive pressure $[p(m=0,t) \sim t^{-\mu}$ with $\mu > 2\delta/(2+\delta)]$.



TC6259

Figure 95.10

Two self-similar solutions for the pressure given $\delta = 1.2748$. The solid line represents the vanishing-applied-pressure solution, whereas the dashed line represents the finite-applied-pressure solution.

Decaying Shock Solution near $m = m_*$

In the case of a sudden decrease of applied pressure, the self-similar solution provides an accurate asymptotic representation for $m \gg m_*$. To derive a solution valid for any m , however, we first solve near $m = m_*$ and then generate a function for S that matches both the solution near m_* and the self-similar solution for $m \gg m_*$.

Since $\hat{S}(z)$ is independent of time, one can solve near $z = 1$ (i.e., $m = m_*$) at time $\tau \approx 1$ representing the time of interaction between the shock and the rarefaction wave. The first step is to find the velocity at $z = 1$ and $\tau = 1 + d\tau$. This can be accomplished using the method of characteristics. The characteristic equations in the dimensionless coordinates are

$$\dot{z} = \pm \sqrt{\hat{p}\hat{\rho}} = \pm \sqrt{\hat{\rho}^{\gamma+1}}, \quad (46)$$

where the last term on the right-hand side applies for $z \leq 1$, where the entropy is uniform and $\hat{p} = \hat{\rho}^\gamma$.

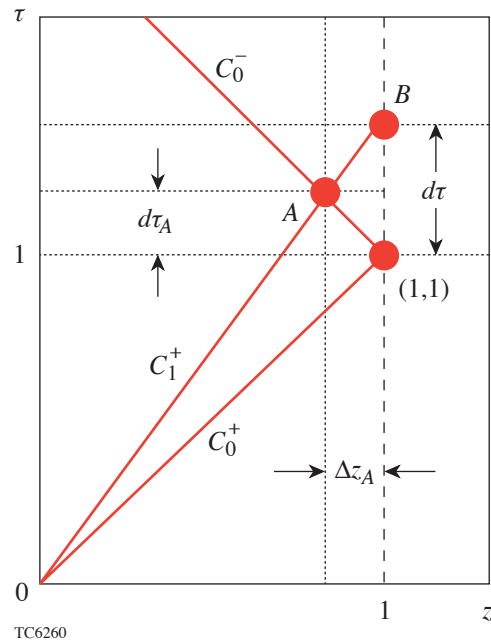
Figure 95.11 shows the characteristic C_0^+ representing the straight line $z = \tau$ and the characteristic C_0^- with a slope $\dot{z} = -1$ at $z = 1, \tau = 1$. The point A has coordinates

$$\tau_A = 1 + d\tau_A, \quad z_A = 1 - d\tau_A, \quad (47)$$

and the characteristic C_1^+ passing through A has the slope $\dot{z} = \sqrt{\hat{p}(z_A, \tau_A)^{\gamma+1}}$ at A . Notice that $d\tau_A$ has not been defined and is determined later as a function of $d\tau$. Using the rarefaction-wave solution [Eqs. (27)] and expanding \hat{p} near A , one finds the slope of C_1^+ [$\dot{z} \approx 1 - 2d\tau_A$] leading to the following form of C_1^+ near A :

$$z = (1 - 2d\tau_A)(\tau - \tau_A) + z_A. \quad (48)$$

The relation between $d\tau_A$ and $d\tau$ can be found by substituting the coordinates of B (i.e., setting $z = 1, \tau = 1 + d\tau$) into Eq. (48) yielding $d\tau = 2d\tau_A$. Using the property of the Riemann function



TC6260

Figure 95.11

The characteristics at $z = \tau = 1$ are represented by the lines C_0^+ and C_0^- . The forward characteristic at A ($z = 1 - dz_A, \tau = 1 + d\tau_A$) is shown by C_1^+ .

$J^+ = 2\hat{a}/(\gamma-1) + \hat{u}$, which is constant along C_1^+ , yields the following relation for the Riemann invariant:

$$J^+(A) = J^+(B). \quad (49)$$

This equation can be used to determine a relation between \hat{u} and \hat{a} at point B , given these quantities at point A . The values of both \hat{u} and \hat{a} at point A can be easily determined from the rarefaction-wave solution, leading to

$$\hat{u}_A = \sqrt{\frac{2}{\gamma(\gamma-1)}} - \frac{4d\tau_A}{\gamma+1}, \quad (50)$$

$$\hat{a}_A = \sqrt{\hat{\rho}_A^{\gamma-1}} = 1 - 2\frac{\gamma-1}{\gamma+1}d\tau_A. \quad (51)$$

Since point B is defined by the coordinates $z = 1$ and $\tau = 1 + d\tau$, the velocity and sound speed can be written as Taylor expansions about the point $z = 1$, $\tau = 1$, yielding

$$\hat{u}_B = \hat{u}_{1,1} + \left[\frac{\partial\hat{u}}{\partial\tau}\right]_{1,1} d\tau = \sqrt{\frac{2}{\gamma(\gamma-1)}} + \left[\frac{\partial\hat{u}}{\partial\tau}\right]_{1,1} d\tau, \quad (52a)$$

$$\hat{a}_B = \hat{\rho}_B^{\frac{\gamma-1}{2}} = 1 + \frac{\gamma-1}{2} \left[\frac{\partial\hat{\rho}}{\partial\tau}\right]_{1,1} d\tau. \quad (52b)$$

Substituting Eqs. (50)–(52) into (49) leads to the following relation between the pressure gradient and density time derivative:

$$\left[\frac{\partial\hat{p}}{\partial z}\right]_{1,1} = \frac{4\gamma}{\gamma+1} + \gamma \left[\frac{\partial\hat{\rho}}{\partial\tau}\right]_{1,1}, \quad (53)$$

where the pressure gradient enters Eq. (53) through the momentum conservation equation relating the acceleration to the pressure gradient. It is important to emphasize that all the temporal and spatial derivatives above are calculated at $z = 1^-$, which is before the shock decay region ($z > 1$). Because the pressure, entropy, density, and velocity are continuous at $z = 1$, it follows that all the time derivatives must also be continuous. Furthermore, the conservation of momentum [Eq. (9)] requires that the pressure gradient be continuous due to the continuity of the acceleration ($\partial_t u$). On the other hand,

there are no such constraints on the density and entropy gradients, which are discontinuous at $z = 1$.

The next step is to expand the Hugoniot conditions concerning the post-shock velocity at the shock front defined as $z_s = 1 + dz_s$. We start from the post-shock velocity equation

$$\hat{u}(1 + dz_s, 1 + d\tau) = \sqrt{\frac{2}{\gamma(\gamma-1)}} \hat{p}(1 + dz_s, 1 + d\tau) \quad (54)$$

and expand it near (1,1), retaining the first-order terms

$$\left(\frac{\partial\hat{p}}{\partial\tau}\right)_{1,1} \left[\sqrt{\frac{\gamma}{2(\gamma-1)}} + \sqrt{\frac{\gamma-1}{2\gamma}} \right] + \left(\frac{\partial\hat{p}}{\partial z}\right)_{1,1} \frac{3}{2\gamma} = 0. \quad (55)$$

In the derivation of (55), the equations of motions [Eqs. (25)] and the shock velocity at $\tau = 1$, $\dot{z}_s(1) = \sqrt{\gamma-1}/2\gamma$ have been used. Equations (53) and (55) can then be solved to determine the density time derivative and the pressure gradient, which depend only on the adiabatic index

$$\left(\frac{\partial\hat{p}}{\partial\tau}\right)_{1,1} = -\frac{6/(\gamma+1)}{\frac{3}{2} + \sqrt{\frac{\gamma}{2(\gamma-1)}} + \sqrt{\frac{\gamma-1}{2\gamma}}}, \quad (56)$$

$$\left(\frac{\partial\hat{p}}{\partial z}\right)_{1,1} = \frac{4\sqrt{2}\gamma(2\gamma-1)}{(\gamma+1) \left[3\sqrt{\frac{\gamma}{2(\gamma-1)}} + \sqrt{2(\gamma-1)} + \sqrt{2\gamma} \right]}. \quad (57)$$

The remaining Hugoniot condition concerning the post-shock density $\hat{\rho}(1 + dz_s, 1 + d\tau) = 1$ can also be expanded to first order and, using Eq. (56), yields the density gradient at $z = 1$, $\tau = 1$:

$$\left(\frac{\partial\hat{\rho}}{\partial z}\right)_{1,1}^+ = \frac{6/(\gamma+1)}{\frac{3}{2} \sqrt{\frac{\gamma-1}{2\gamma}} + \frac{1}{2} + \frac{\gamma-1}{2\gamma}}, \quad (58)$$

where the superscript + indicates that the derivative is calculated on the $z > 1$ side. The last step is to determine the entropy gradient at $z = 1$ using the definition of the dimensionless entropy $\hat{S} = \hat{p}/\hat{\rho}^\gamma$ and the pressure and density gradients

provided by Eqs. (57) and (58). A straightforward calculation leads to the following form of the entropy gradient at the beginning of the shock decay:

$$\left(\frac{\partial \hat{S}}{\partial z}\right)_{1,1}^+ = -\beta, \quad \beta = \frac{2\gamma}{2\gamma-1}(1+\epsilon), \quad (59a)$$

where

$$\epsilon = -1 + 2\sqrt{2} \frac{2\gamma-1}{3\sqrt{\gamma(\gamma-1)} + \sqrt{2}(2\gamma-1)}. \quad (59b)$$

For $\gamma > 1.4$, the term ϵ is typically small ($|\epsilon| < 0.06$) and asymptotically reaches the constant value -0.029 for $\gamma \rightarrow \infty$. This concludes the solution near $z = 1$. The entropy and its derivatives at $z = 1$ have been determined and can be used together with the self-similar solution to generate a matching formula approximating the entropy over the entire range of $z \geq 1$.

Matching Formula for the Adiat Shape

An approximate formula representing the entropy profile left behind by a decaying shock can be constructed by matching the solution near $m = m_*$ with the self-similar behavior for $m \gg m_*$. The matching formula must satisfy the conditions

$$\hat{S}(1) = 1, \quad \frac{d\hat{S}}{dz}(1) = -\beta, \quad \hat{S}(z \rightarrow \infty) \sim \frac{0.923}{z^\delta}, \quad (60)$$

where $\delta = 1.2748$ and $\beta = 1.459$ for $\gamma = 5/3$. It is important to notice that the self-similar solution provides only the scaling with z but not the actual coefficient. While a coefficient near unity is expected, the numerical solution of the Euler equations [Eqs. (8)–(10)] has indicated that the correct coefficient for ($\gamma = 5/3$) is 0.923. An extremely accurate representation of the adiabat profile can be obtained by choosing the following fitting formula:

$$\hat{S}(z) = \left(\frac{1+\nu}{z^{\delta/\sigma} + \nu} \right)^\sigma, \quad (61)$$

which satisfies the two conditions $\hat{S}(1) = 1$ and $\hat{S}(z \rightarrow \infty) \sim z^{-\delta}$. The parameters ν and σ can be determined by applying the other two conditions on $\hat{S}'(1)$ and on the coefficient 0.923

[Eq. (60)]. A simple calculation leads to the following values (for $\gamma = 5/3$): $\nu = -0.127$ and $\sigma = 0.591$, which upon substitution into Eq. (61) yields the adiabat shape function

$$\hat{S}(z) \approx \left(\frac{0.873}{z^{2.157} - 0.127} \right)^{0.591}. \quad (62)$$

A simpler formula for the adiabat shape can be obtained by fitting Eq. (62) with a simple power law such as

$$\hat{S}(z) \approx \frac{1}{z^{1.315}}, \quad (63)$$

which exhibits an error below 3% with respect to the numerical solution over the range $1 < z < 10$. Figure 95.12 shows the ratios between the numerical solution of the Euler equations [Eqs. (8)–(10)] and Eqs. (62) (solid) and (63) (dashed). Observe that Eq. (62) reproduces the numerical results very accurately over any range of z . Figure 95.12 also shows a comparison between the numerical solution with the adiabat shape derived in Ref. 18 (dashed–dotted) and the self-similar solution $\hat{S} = z^{-1.275}$ (dotted) of Refs. 23–28. The adiabat profile of Ref. 18, derived using a spatially frozen pressure profile, exhibits a significantly different behavior from Eq. (62), while the behavior of the self-similar solution differs mostly near $z = 1$. In view of the good agreement between the simple power law and the simulation, Eq. (63) will be used as

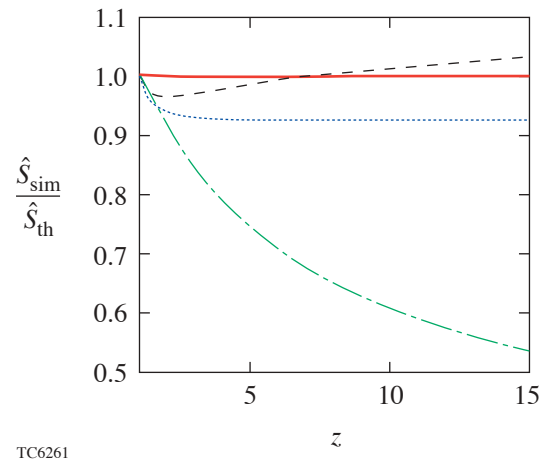


Figure 95.12

Comparison of the numerical solution of Eqs. (8)–(10) to several analytical formulas for the adiabat shape: Eq. (62) (solid); Eq. (63) (dashed); Eq. (4) of Ref. 18 (dashed–dotted); solution from Refs. 23–28 (dotted).

the adiabat shape induced by a decaying shock in an ideal gas when the applied pressure vanishes right after the end of the prepulse.

Effects of Mass Ablation and Residual Ablation Pressure

In laser-driven implsions, mass is ablated off the outer shell surface at a rate \dot{m}_a , which depends on the laser intensity $\dot{m}_a \sim I_L^{1/3}$. When the laser power is lowered after the prepulse ($t = \Delta t_{\text{prep}}$) and the rarefaction wave is launched, a fraction of the shell mass has been ablated. Since the relevant m_* is the areal density overtaken by the rarefaction wave before interacting with the shock, it is appropriate to reset the origin of the m variable so that $m = 0$ corresponds to the fluid element on the outer surface at the end of the prepulse $t = \Delta t_{\text{prep}}$. For this purpose, we denote the new mass variable as $m^{(a)} = m - m_a^{\text{prep}}$, where m_a^{prep} is the mass ablated during the prepulse and $m^{(a)} = 0$ represents the point where the rarefaction wave is launched. The time Δt_* representing the time interval between the end of the prepulse and the rarefaction–shock interaction is affected by ablation and satisfies the following equality:

$$(u_* + a_*)\Delta t_* = d_c - d_a + U_{s*}\Delta t_*, \quad (64)$$

where $d_c = U_{s*}\Delta t_{\text{prep}}(\gamma - 1)/\gamma + 1$ is the compressed thickness of the shocked material at time $t = \Delta t_{\text{prep}}$ and d_a is the thickness of the ablated portion $d_a = m_a^{\text{prep}}/\rho_* = V_a^{\text{prep}}\Delta t_{\text{prep}}$, where V_a^{prep} is the ablation velocity during the prepulse. The interval Δt_* can be derived from Eq. (64), yielding

$$\Delta t_*^a = \frac{\Delta t_{\text{prep}}}{\sqrt{2\gamma/(\gamma-1)} - 1} \left(1 - \sqrt{\frac{2\gamma}{\gamma-1}} M_a^{\text{prep}} \right), \quad (65)$$

where $M_a^{\text{prep}} \equiv V_a^{\text{prep}}/a_*$ represents the ablative Mach number during the prepulse. Observe that we have used the superscript a to discriminate between the Δt_* with [Eq. (65)] and without [Eq. (22)] ablative correction.

It is interesting to notice that M_a^{prep} is independent of the laser power. Indeed, using the well-known relations for the ablation rate and pressure,^{1,29,30} one can easily construct the following expression:

$$\dot{m}_a \text{ (g/cm}^2 \text{ s)} \approx 5.2 \times 10^5 \left[\frac{0.35}{\lambda \text{ (}\mu\text{m)}} \right] \left[\frac{P_a \text{ (Mbar)}}{20} \right]^{0.5}, \quad (66)$$

where λ (μm) is the laser wavelength in microns and P_a (Mbar) is the ablation pressure in megabars. The ablative Mach number is calculated for $\gamma = 5/3$ by setting $V_a^{\text{prep}} = \dot{m}_a^{\text{prep}}/\rho_*$, leading to

$$M_a^{\text{prep}} \approx 0.091 \left[\frac{0.25}{\rho_0 \text{ (g/cm}^3)} \right]^{0.5} \left[\frac{0.35}{\lambda \text{ (}\mu\text{m)}} \right], \quad (67)$$

where ρ_0 is the initial density in g/cm^3 before the shock. Observe that the ablative correction of Δt_* in Eq. (65) is significant and approximately equal to 20% for DT ice ($\rho_0 = 0.25 \text{ g/cm}^3$) and UV lasers ($\lambda = 0.35 \mu\text{m}$) leading to $\Delta t_*^a \approx 0.64 \Delta t_{\text{prep}}$. It follows that the areal density overtaken by the rarefaction wave's leading edge before the shock interaction has the same form as Eq. (23): ($m_*^a = a_*\Delta t_*^a\rho_*$); however, the numerical value of m_*^a is reduced with respect to Eq. (23) by approximately 20% because of the reduction in Δt_* due to the ablative correction (i.e., Δt_*^a). The analysis in the previous four sections (pp. 150–157) follows without any changes, but with the premises that m , m_* , and Δt_* used in the definitions of z and τ are replaced by $m^{(a)}$, m_*^a , and Δt_*^a , respectively, which include the ablative corrections. This leads to the following shape function from Eq. (63):

$$\hat{S} = \left[\frac{m_*^a}{m^{(a)}} \right]^\delta, \quad (68)$$

where $\delta \approx 1.315$ for a flat prepulse with an applied pressure that vanishes right after the prepulse end.

Another important effect occurring in laser-accelerated targets is that of residual heating of the ablation front. When the laser power is lowered (or turned off) at the end of the prepulse $t = \Delta t_{\text{prep}}$, the heat stored in the coronal plasma continues to flow toward the ablation front. Because of the finite heat capacity of the corona, the ablation pressure does not vanish instantaneously when the laser is turned off. Instead the ablation pressure decays in time approximately following a temporal power law:

$$P_a(t < \Delta t_{\text{prep}}) = p_*, \quad P_a(t > \Delta t_{\text{prep}}) = p_* \left(\frac{\Delta t_{\text{prep}}}{t} \right)^n. \quad (69)$$

The power index n can be determined by fitting Eq. (69) with the results of 1-D simulations using the ICF code *LILAC*.³¹ Figures 95.13(a) and 95.13(b) compare the decay of the ablation pressures from *LILAC* (solid lines) with Eq. (69) for a 100-ps prepulse inducing a 26-Mbar ablation pressure [Fig. 95.13(a)] and a 300-ps prepulse inducing a 33-Mbar pressure [Fig. 95.13(b)] on a cryogenic DT slab of 350- μm thickness. The power indices in Eq. (69) that fit the simulation results are $n \approx 2$ for the 100-ps prepulse [dashed line in 95.13(a)] and $n \approx 3$ for the 300-ps prepulse [dashed line in 95.13(b)]. It is important to notice that when the ablation pressure depends on the ratio $t/\Delta t_{\text{prep}}$, the resulting boundary conditions [discussed in **The General Problem of the Decaying Shock** (p. 151)] depend exclusively on the dimensionless time $\tau = t/\Delta t_*$ and the adiabat index γ . Indeed, one can substitute

$$\frac{t}{\Delta t_{\text{prep}}} = \frac{\tau}{\tau_0(\gamma)}, \quad \tau_0(\gamma) = \sqrt{2\gamma/(\gamma-1)} - 1 \quad (70)$$

into Eq. (69) and conclude that the appropriate boundary condition for the dimensionless applied pressure can be cast in the following form:

$$\hat{p}(z=0, \tau < \tau_0) = 1, \quad \hat{p}(z=0, \tau > \tau_0) = \left(\frac{\tau_0}{\tau}\right)^n. \quad (71)$$

It follows that for a given value of γ and power index n , a single numerical simulation provides the universal function $\hat{S}(z, n)$. As recognized in **Self-Similar Solution** (pp. 153–154), the asymptotic solution becomes self-similar when $n > 0.78$; however, the transition to a self-similar form occurs at large $z \gg 1$ (i.e., $m \gg m_*$), while the interesting range of z for ICF applications is typically below 10. In this case, it is important to determine the adiabat shape before the transition to a self-similar profile. For this purpose, we carry out the numerical solution of Eqs. (25), with boundary conditions [Eq. (71)] and different n 's, to determine the corrections caused by a finite time decay of the pressure within the interval $1 < z < 10$. For simplicity, we have maintained a power law fit for \hat{S} and calculated the power index for n varying in the range of 2–6 (Table 95.I). For $n = 2$ and 3, the numerical solution yields an adiabat shape that can be approximated with the following power laws:

$$\hat{S}[m^{(a)} > m_*^a, n=3] \approx \left[\frac{m_*^a}{m^{(a)}}\right]^{1.13}, \quad (72)$$

$$\hat{S}[m^{(a)} > m_*^a, n=2] \approx \left[\frac{m_*^a}{m^{(a)}}\right]^{1.05}.$$

Observe that the power indices are somewhat less than $\delta = 1.315$ [Eq. (63)] derived in the case of a sudden decrease in pressure (i.e., $n \rightarrow \infty$). The fact that the adiabat shape is not as steep as in the case of a sudden decrease in pressure should not be surprising since the residual applied pressure sustains the shock, preventing its rapid decay. As expected, the value of δ increases with n and reaches the asymptotic value $\delta = 1.315$ for $n \rightarrow \infty$. This concludes the theoretical analysis of the adiabat

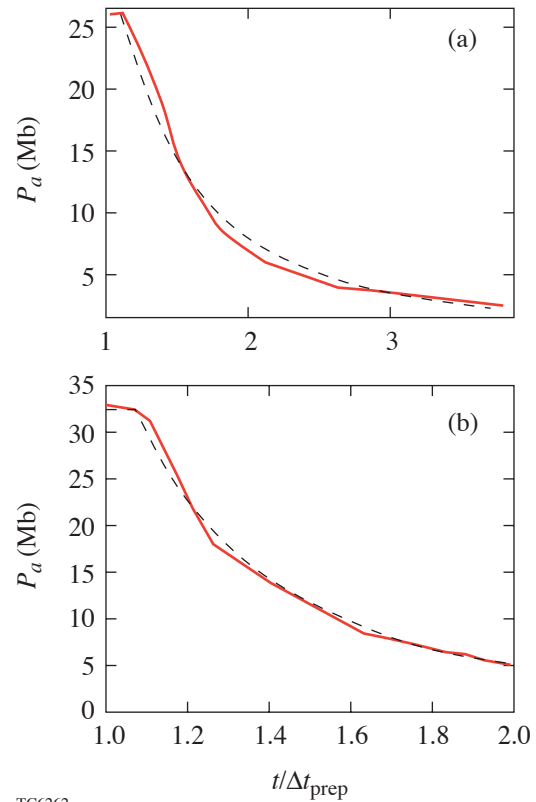


Figure 95.13

A fit of the ablation-pressure time decay from *LILAC* (solid) to a power law (dashed) for (a) a 100-ps prepulse and (b) a 300-ps prepulse.

Table 95.I: Adiabatic-shape power indices as a function of the prepulse pressure time-decay power index.

| n | δ |
|----------|----------|
| 2 | 1.05 |
| 3 | 1.13 |
| 4 | 1.2 |
| 6 | 1.25 |
| ∞ | 1.315 |

shape. The next step is to derive a set of simple formulas that can be conveniently used to design ICF-capsule or planar-foil experiments with adiabat profiles shaped by a decaying shock.

Prepulse Design Formulas for DS Shaping

Starting from the adiabat shape derived in the previous sections, it is possible to derive some simple formulas relating the laser prepulse and foot pressure/intensity, the prepulse and duration, and the desired values of the outer- and inner-surface adiabats. It is clear that the prepulse pressure initially determines the front surface adiabat; however, since the ablation front advances inside the target with the ablation velocity, the ablation-front adiabat is typically a function of time. It is therefore important to specify a reference time at which the ablation-front adiabat is determined and optimized. Since the acceleration phase starts a short time after the shock breakout, we choose to optimize the adiabat shape at shock breakout with the intent to induce the largest-possible outer-surface adiabat during the acceleration phase. It is also important to notice that for a constant pressure prepulse, the outer-surface adiabat is constant for $0 < m < m_*$ and decays for $m > m_*$.

Using the standard definition for the normalized adiabat $\alpha \equiv P(\text{Mbar})/2.18\rho(\text{g/cm}^3)^{5/3}$, one can easily determine the ablation pressure required to induce the desired outer-surface adiabat:

$$P_a(\text{Mbar}) = 19.6 \left(\frac{\alpha_{\text{out}}}{9} \right) \left[\frac{\rho_0(\text{g/cm}^3)}{0.25} \right]^{1.67}, \quad (73)$$

where ρ_0 is the initial shell density and the value $\alpha_{\text{out}} = 9$ has been chosen as a typical desired value of the ablation-front

adiabat. Here, the density of 0.25 g/cm^3 refers to the uncompressed DT ice. The laser intensity required to drive the ablation pressure in Eq. (73) can be derived by the standard relation $P_a(\text{Mbar}) = 40 [I_{15}/\lambda(\mu\text{m})]^{2/3}$, where I_{15} is the laser intensity in units of 10^{15} W/cm^2 . This relation is valid for steady-state laser absorption and needs to be used with caution, as discussed later in this section. The prepulse duration can be derived from the adiabat shape and the design values of the outer- and inner-surface adiabats. Using Eq. (72), one can write

$$\frac{\alpha_{\text{out}}}{\alpha_{\text{in}}} = \left(\frac{m_{\text{shell}}^a}{m_*^a} \right)^\delta, \quad (74)$$

where $m_{\text{shell}}^a = m_{\text{shell}}(0) - m_a^{\text{prep}}$ is the total shell areal density left after the prepulse and $\delta \approx 1$ as for typical prepulses with $\Delta t_{\text{prep}} \leq 300 \text{ ps}$. A straightforward manipulation of Eq. (74) yields the following form of the required prepulse duration:

$$\begin{aligned} \Delta t_{\text{prep}}(\text{ps}) &= 180 \left[\frac{d_{\text{shell}}(\mu\text{m})}{100} \right] \left[\frac{0.25}{\rho_0(\text{g/cm}^3)} \right]^{0.33} \\ &\times \left(\frac{9}{\alpha_{\text{out}}} \right)^{0.5 + \frac{1}{\delta}} \left(\frac{\alpha_{\text{inn}}}{3} \right)^{\frac{1}{\delta}} \frac{3^{1 - \frac{1}{\delta}}}{1 - \epsilon_a}, \end{aligned} \quad (75)$$

where d_{shell} is the initial shell thickness and $\epsilon_a = M_a^{\text{prep}} [2.23 - 1.54(\alpha_{\text{inn}}/\alpha_{\text{out}})^{1/\delta}]$ represents the ablative correction, which is typically $\epsilon_a < 0.2$ for $M_a^{\text{prep}} \approx 0.09$. Equations (73) and (75) show that an arbitrarily large adiabat ratio can be induced by simply increasing the applied prepulse pressure and decreasing the prepulse duration. There are limitations, however, with regard to the magnitude of the outer-surface adiabat and the adiabat ratio. The first constraint concerns the adiabat ratio at the shock-breakout time $\theta = \alpha_{\text{out}}/\alpha_{\text{inn}}$. The limits of θ are dictated by the mass ablated during the foot of the laser pulse following the prepulse. Since the adiabat is flat for $m < m_*^a$, the largest outer-surface adiabat (for a given inner-surface adiabat) can be achieved by tailoring the prepulse intensity and the laser foot duration in order to ablate the flat-adiabat region. This requires that

$$m_a^{\text{foot}} = m_*^a, \quad (76)$$

where $m_a^{\text{foot}} = \dot{m}_a^{\text{foot}} \Delta t_{\text{foot}}$ is the mass ablated during the time interval between the end of the prepulse and the shock-breakout time. A similar principle is used in Ref. 18.

The interval Δt_{foot} can be estimated from Eq. (26a) relating the shock velocity \dot{z}_s to the shell adiabat $\hat{S}(z) \approx 1/z^\delta$, leading to the following shock trajectory:

$$z_s(\tau) = \left[1 + \left(1 + \frac{\delta}{2} \right) \sqrt{\frac{\gamma-1}{2\gamma}} (\tau-1) \right]^{\frac{2}{2+\delta}}. \quad (77)$$

It follows that the time interval between the end of the prepulse ($\tau = 0$) and the shock-breakout time can be derived from Eq. (77) by setting $z_s = \theta^{1/\delta}$, where $\theta = \alpha_{\text{out}}/\alpha_{\text{inn}}$ is the desired adiabat ratio. This time interval represents the foot duration Δt_{foot} and depends only on the prepulse characteristics (it is independent of the foot). This is not the case in the absence of a prepulse since the foot length depends on the foot properties. In the simplest pulse shapes, the foot intensity is kept constant, such that the induced ablation pressure P_{foot} corresponds to the desired inner-surface adiabat.

It follows that the foot properties (Δt_{foot} and P_{foot}) can be summarized by the following simple formulas:

$$\Delta t_{\text{foot}} = \Delta t_*^a \left[1 + \frac{\theta_*^{\frac{2+\delta}{2\delta}} - 1}{\sqrt{\frac{\gamma-1}{2\gamma}} \left(1 + \frac{\delta}{2} \right)} \right], \quad (78a)$$

$$P_a^{\text{foot}} (\text{Mbar}) = 2.18 \alpha_{\text{inn}} \left[\frac{\rho_0 (\text{g/cm}^3)}{0.25} \right]^{1.67}, \quad (78b)$$

where $\Delta t_*^a \approx 0.64 \Delta t_{\text{prep}}$ for DT. Observe that, using (78a), Δt_*^a cancels from both sides of Eq. (76) and the maximum adiabat ratio θ_* satisfies the following equation:

$$\left[1 + \frac{\theta_*^{\frac{2+\delta}{2\delta}} - 1}{\sqrt{\frac{\gamma-1}{2\gamma}} \left(1 + \frac{\delta}{2} \right)} \right] M_a^{\text{prep}} \frac{\dot{m}_a^{\text{foot}}}{\dot{m}_a^{\text{prep}}} = 1. \quad (79)$$

Using Eqs. (66), it follows that the foot/prepulse ablation rate ratio is related to the foot/prepulse pressures and therefore adiabats through the relation $\dot{m}_a^{\text{prep}}/\dot{m}_a^{\text{foot}} = \sqrt{\theta}$. It is very important to notice that the steady-state ablation relations used in Eq. (66) and adopted in the current derivation are not very accurate during the prepulse where a steady state is not reached. Furthermore, high-performance target design requires the foot intensity to rise before the shock breaks out on the inner surface. This is commonly done to prevent secondary shock generation during the rise to full power, which would set the inner portion of the shell on a high adiabat. Since the total laser energy in a rising foot is larger than in a flat (constant-intensity) foot of the same starting power, it follows that the mass ablated during the rising foot is larger than for the flat foot. All these uncertainties in the calculation of the ablated mass can be heuristically accounted for by introducing a corrective factor χ in the ratio of mass ablation rates, thus setting

$$\frac{\dot{m}_a^{\text{prep}}}{\dot{m}_a^{\text{foot}}} = \frac{\sqrt{\theta}}{\chi}, \quad (80)$$

where $\chi > 1$ represents an enhancement with respect to the steady-state ablation rate of a flat foot. The final form of the equation governing the maximum adiabat ratio can be written in the following form:

$$\left[1 + \frac{\theta_*^{\frac{2+\delta}{2\delta}} - 1}{\sqrt{\frac{\gamma-1}{2\gamma}} \left(1 + \frac{\delta}{2} \right)} \right] M_a^{\text{prep}} \frac{\chi}{\sqrt{\theta_*}} = 1, \quad (81)$$

where θ_* is the optimized adiabat ratio. To estimate the size of the maximum adiabat ratio, we solve Eq. (81) for cryogenic DT with $M_a^{\text{prep}} \approx 0.09$ [Eq. (67)] for both the idealized case of $\chi = 1$ and for a more-realistic rising-foot case with $\chi = 1.4$. The results are given in Table 95.II. Note that the maximum adiabat ratio is lower in the rising-foot case. Because the maximum adiabat ratio is given by Eq. (81), the optimum prepulse pressure and duration are determined by Eqs. (73) and (75) upon substitutions of the maximum ratio θ_* leading to

$$P_a^{\text{prep}} (\text{Mbar}) \approx 19.6 \alpha_{\text{inn}} \left(\frac{\theta_*}{9} \right) \left[\frac{\rho_0 (\text{g/cm}^3)}{0.25} \right]^{1.67}, \quad (82)$$

Table 95.II: Maximum ratio of inner- to outer-surface adiabat as a function of the adiabat-shape power index for two values of ξ .

| δ | θ_* | |
|----------|--------------|--------------|
| | $\chi = 1.0$ | $\chi = 1.4$ |
| 1.0 | 7.6 | 5.5 |
| 1.1 | 9.6 | 6.7 |
| 1.2 | 12.0 | 8.2 |

$$\Delta t_{\text{prep}} (\text{ps}) = 42 \times 3^{2-\frac{2}{\delta}} \left[\frac{d_{\text{shell}} (\mu\text{m})}{100} \right] \times \left[\frac{0.25}{\rho_0 (\text{g/cm}^3)} \right]^{0.33} \left(\frac{9}{\theta_*} \right)^{0.5+\frac{1}{\delta}} \left(\frac{3}{\alpha_{\text{inn}}} \right)^{0.5}, \quad (83)$$

where ϵ_a has been set approximately equal to 0.18 in accordance with typical adiabat ratios of 5 to 10 and δ is provided in Table 95.I ($\delta \approx 1.05$ and $\delta \approx 1.13$ for prepulses in the 100-ps and 300-ps range, respectively).

The mass-ablated $m_a^{\text{tot}} = m_a^{\text{prep}} + m_a^{\text{foot}}$ during the prepulse and the foot of the laser pulse can be easily determined by using Eq. (80), leading to

$$m_a^{\text{tot}} = \dot{m}_a^{\text{prep}} \Delta t_{\text{prep}} \left(1 + \frac{\chi}{\sqrt{\theta}} \frac{\Delta t_{\text{foot}}}{\Delta t_{\text{prep}}} \right). \quad (84)$$

The foot/prepulse-length ratio in Eq. (84) can be derived from Eq. (78), and, after a straightforward manipulation, the total ablated mass fraction can be written in the following form:

$$\frac{m_a^{\text{tot}}}{m_{\text{shell}}} = \frac{1}{1 + \omega_a} \times \left\{ \omega_a + \left[1 + \frac{\theta^{\frac{2+\delta}{2\delta}} - 1}{\sqrt{\frac{\gamma-1}{2\gamma} \left(1 + \frac{\delta}{2} \right)}} \right] M_a^{\text{prep}} \frac{\chi}{\theta^{0.5+1/\delta}} \right\}, \quad (85a)$$

where

$$\omega_a = \frac{M_a^{\text{prep}}}{\theta^{\frac{1}{\delta}}} \frac{1.24}{1 - 2.23 M_a^{\text{prep}}}. \quad (85b)$$

Equation (85) is valid for any prepulse and can be simplified for the optimized prepulse defined by Eq. (81), leading to

$$\frac{m_a^{\text{tot}}}{m_{\text{shell}}} = \frac{1}{1 + \omega_a(\theta_*)} \left[\omega_a(\theta_*) + \frac{1}{\theta_*^{1/\delta}} \right], \quad (86)$$

where θ_* is the optimized adiabat ratio satisfying Eq. (81). Observe that Eq. (86) does not depend directly on the corrective factor χ ; however, it does depend on χ through the optimized adiabat ratio and can be conveniently used to determine the corrective factor χ when compared with numerical simulation. A single iteration is usually adequate to calculate χ . One starts by guessing a value of $\chi \sim 1$, then designs the optimized prepulse and foot by solving Eq. (81) to find θ_* ; Eqs. (82) and (83) to find Δt_{prep} and P_a^{prep} ; Eqs. (78a) and (78b) to find Δt_{foot} and P_a^{foot} ; and Eq. (86) to find the ablated mass fraction during the prepulse + foot. The pulse (prepulse + foot) is then simulated with a one-dimensional code, and the fraction of ablated mass is extracted at shock breakout from the simulation output. If this fraction is larger/smaller than the one predicted by Eq. (86), then one increases/decreases χ until Eqs. (81) and (86) yield the same value of the ablated fraction from the simulation. One then recalculates the prepulse and foot properties with the new value of χ . Typically, one adjustment of χ is sufficient to produce highly accurate results since the difference between simulated values and desired design parameters is negligible. For typical high-performance target designs,¹⁸ the ablated mass fraction [Eq. (86)] during the prepulse + foot is in the 20% range. As shown in the next section, this pulse design technique seems to be quite accurate, general, and applicable to different foot and prepulse shapes.

Simplified Adiabat Profiles and Comparison with *LILAC*

After including the “nonideal” effects of mass ablation and residual ablation pressure, it is useful to carry out a detailed comparison between the theoretical results of the previous sections and the predictions of the 1-D ICF code *LILAC*³¹ including all the relevant ICF physics. All the *LILAC* runs are carried out selecting the Thomas–Fermi equation of state. Different choices of the equation of state do not significantly alter the adiabat shape as long as the prepulse is tuned in order to induce the desired inner-surface adiabat.

To carry out a meaningful comparison of the adiabat shapes, it is convenient to rewrite the adiabat shape function [Eq. (68)] in a form that can be easily compared with the output of *LILAC*. The first obstacle is in the accurate determination of the terms $m^{(a)}$ and m_*^a in Eq. (68), which are typically hard to extract from *LILAC* output. This can be avoided by rewriting Eq. (68) using the full areal-density coordinate $m = m^{(a)} + m_a^{\text{prep}}$. Note that the ratio $\mu_a \equiv m_a^{\text{prep}}/m_*^a$ is significantly smaller than unity. For DT and a laser of $\lambda = 0.35 \mu\text{m}$,

$$\mu_a = \frac{\dot{m}_a \Delta t_{\text{prep}}}{\Delta t_*^a \rho_* a_*} \approx 1.54 M_a^{\text{prep}} \approx 0.14. \quad (87)$$

Since it is much smaller than unity, one can simplify Eq. (68) using μ_a as an expansion parameter. A straightforward manipulation leads to the following adiabat shape function including first-order corrections in μ_a :

$$\hat{S}(m > m_*^{\text{tot}}) \approx \left(\frac{m_*^{\text{tot}}}{m} \right)^{\delta_a} \left[1 + \delta \mu_a f(\eta) + \mathcal{O}(\epsilon_a^2) \right], \quad (88a)$$

where $m_*^{\text{tot}} = m_*^a + m_a^{\text{prep}}$ and $\eta = m/m_*^{\text{tot}}$ varies between $\eta_{\min} = 1$ and $\eta_{\max} = m_{\text{shell}}/m_*^{\text{tot}}$, where m_{shell} is the total shell areal density. The function $f(\eta)$ and the power index δ_a can be cast in the following form:

$$f(\eta) = \frac{\eta_{\max} - 1}{\eta_{\max} \log \eta_{\max}} \log \eta + \frac{1}{\eta} - 1, \quad (88b)$$

$$\delta_a = \delta \left(1 + \epsilon_a \frac{\eta_{\max} - 1}{\eta_{\max} \log \eta_{\max}} \right). \quad (88c)$$

It is important to observe that the function $f(\eta)$ vanishes at both $\eta = 1$ and $\eta = \eta_{\max}$ and its maximum varies between 0.16 and 0.24 for typical values of $5 < \eta_{\max} < 10$. It follows that the $\mu_a f(\eta)$ term in Eq. (88a) can be neglected and the adiabat shape for DT can be written as a simple power law:

$$\hat{S}(m > m_*^{\text{tot}}) \approx \left(\frac{m_*^{\text{tot}}}{m} \right)^{\delta_a} \approx \left(\frac{m_*^{\text{tot}}}{m} \right)^{1.062\delta}, \quad (89)$$

where the relation $\delta_a \approx 1.062\delta$ has been used in view of the fact that δ_a is approximately independent of η_{\max} as it varies between $\delta_a \approx 1.07\delta$ for $\eta_{\max} = 10$ and $\delta_a \approx 1.055\delta$

for $\eta_{\max} = 5$. Using Eq. (89), the adiabat profile can be written as a convenient function of the full areal-density coordinate m and the initial shell areal density m_{shell} :

$$\alpha \approx \alpha_{\text{inn}} \left(\frac{m_{\text{shell}}}{m} \right)^{1.062\delta}. \quad (90)$$

Obviously, Eq. (90) can be easily compared with *LILAC* output since the inner-surface adiabat and the full areal density are readily available, while the values of δ are given in Table 95.I for different prepulse durations.

We consider two prepulses with 100-ps and 300-ps duration and 300-TW/cm² intensity applied to a 200- μm and 500- μm planar DT foil, respectively. From *LILAC* output we immediately find that $\alpha_{\text{inn}} = 0.85$ and 1.18 for the 100-ps and 300-ps prepulses, respectively. According to the theory and Table 95.I, the adiabat shapes can be approximated as

$$\alpha(\sim 100 \text{ ps}) \approx \alpha_{\text{inn}} \left(\frac{m_{\text{shell}}}{m} \right)^{1.12}, \quad (91)$$

$$\alpha(\sim 300 \text{ ps}) \approx \alpha_{\text{inn}} \left(\frac{m_{\text{shell}}}{m} \right)^{1.20},$$

where the symbol \sim indicates that the two adiabat profiles can be used for prepulses in the 100-ps and 300-ps range, respectively. Figure 95.14 shows the adiabat profiles versus the normalized Lagrangian coordinate m/m_{shell} from *LILAC* (solid) and from Eqs. (91) (dashed) for the two prepulses. The good agreement between theory and simulations indicates that Eqs. (90) and (91) can indeed be used to accurately determine the adiabat profiles of typical ICF targets.

The next step is to compare the maximum obtainable adiabat ratio provided by Eq. (81) with *LILAC* simulations. We consider an 85- μm solid DT planar foil in order to simulate a typical OMEGA cryogenic shell and focus on the simple case of a flat-laser-foot intensity. The mass ablation enhancement factor χ is initially set equal to unity and then adjusted to $\chi = 0.85$ in order to recover the mass-ablated fraction of 13% as indicated by the *LILAC* simulations. We choose an inner-surface adiabat of $\alpha_{\text{inn}} = 1$ and determine the maximum adiabat ratio through Eq. (81), leading to $\theta_* \approx 10$. Equations (75) and (78) yield prepulse and foot durations of 60 ps and 1571 ps, respectively. The predicted shock-breakout time is then

$t_s = \Delta t_{\text{prep}} + \Delta t_{\text{foot}} = 1631$ ps. The required ablation pressure to induce an outer-surface adiabat of 10 is 22 Mbar. The laser prepulse intensity required to induce such an ablation pressure in 60 ps has been determined with *LILAC* to be $I_L^{\text{prep}} \approx 450$ TW/cm². The foot ablation pressure corresponding to an inner-surface adiabat $\alpha_{\text{inn}} = 1$ is 2.2 Mbar, requiring, according to *LILAC*, a foot intensity of 6.9 TW/cm². The solid curve in Fig. 95.15 represents the laser pulse profile used in *LILAC* simulations.

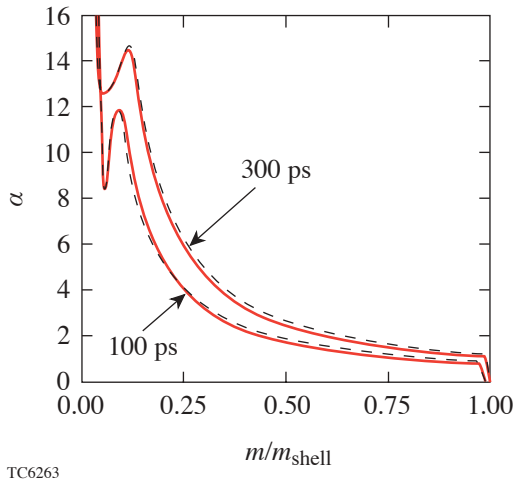


Figure 95.14
A comparison of the adiabat shapes for two *LILAC* simulations with 100-ps and 300-ps prepulses (solid lines) to the formulas generated in Eqs. (91) (dashed lines).

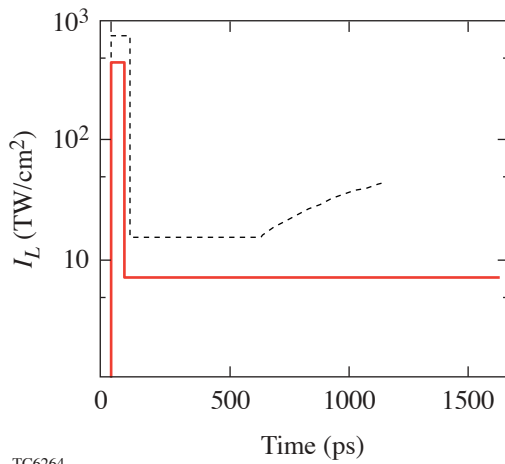


Figure 95.15
Optimal laser intensity history from *LILAC* for an 85- μm solid-DT planar foil with design specifications of $\alpha_{\text{inn}} = 1$ and flat-laser-foot intensity (solid) and $\alpha_{\text{inn}} = 2$ and rising-laser-foot intensity (dashed).

Figure 95.16(a) shows the adiabat profile at shock breakout obtained from *LILAC* using the pulse described above: a 60-ps, 450-TW/cm² prepulse followed by a 6.9-TW/cm² foot. The shock-breakout time t^{shock} according to *LILAC* is about 1632 ps, in excellent agreement with the theoretical prediction of 1631 ps. The theoretical adiabat profiles [the dashed curve provided by the first of Eq. (91)] is also in agreement with *LILAC* results, as is the prediction of the maximum adiabat ratio as indicated by the fact that the flat-adiabat region preceding the adiabat decay is completely ablated off at shock breakout. The pressure profile at shock breakout is approximately flat [Fig. 95.16(b)] with a value of about 2.2 to 2.3 Mbar in compliance with the design requirement. The ablated mass fraction is given by the abscissa of the vertical dotted line in Fig. 95.16, indicating an ablated fraction of about 13%, in agreement with the result of Eq. (86) yielding 12.6%.

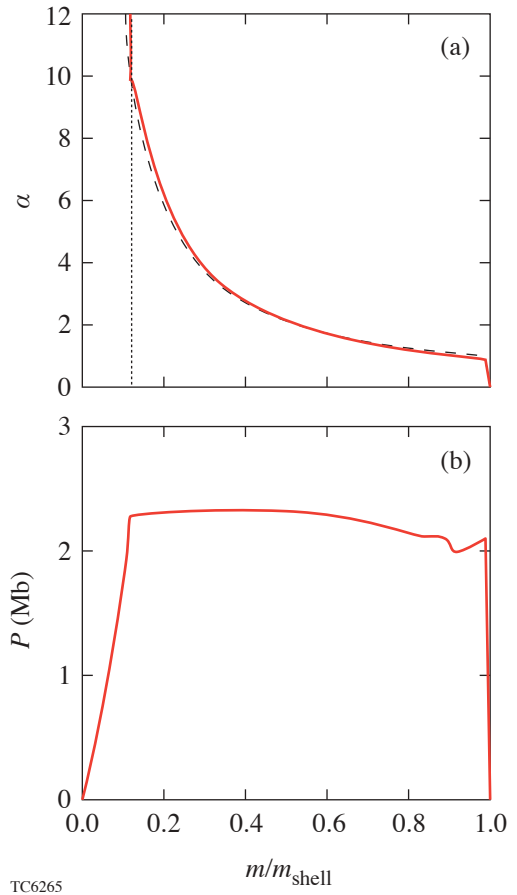


Figure 95.16
(a) Comparison of the *LILAC* adiabat profile at shock breakout for the flat-foot laser pulse given by the solid line in Fig. 95.15 with the theoretical prediction of Eq. (91) (dashed line). The ablated mass fraction from *LILAC* is shown by the vertical dotted line. (b) Pressure profile at shock breakout for the target and pulse in Fig. 95.16(a).

To apply the theory to more-realistic designs, we have also carried out the optimization for the case of a rising-foot intensity and higher inner-surface adiabat. We consider a typical OMEGA cryogenic capsule design with $\alpha_{\text{inn}} \approx 2$ and a laser foot intensity that is flat over half its length and then linearly ramped up to three times its initial intensity at shock breakout. The corrective factor χ can be determined in one iteration to be about 1.3, leading to an ablated fraction of 18% [from Eq. (86)], an adiabat ratio of 6.4 [Eq. (81)], and an outer-surface adiabat of 12.8.

The prepulse pressure and duration from Eqs. (82) and (83) are approximately 28 Mbar and 79 ps, respectively. The prepulse intensity required to induce such an ablation pressure in 79 ps is found with *LILAC* to be about 750 TW/cm². Equations (78) yield a foot duration of 1089 ps, leading to a shock-breakout time of 1169 ps, and a starting foot pressure of 4.3 Mbar. The foot is split into a 544-ps flat foot with a 15-TW/cm² laser intensity followed by a 544-ps linear ramp to 45 TW/cm². The dashed curve in Fig. 95.15 represents the laser pulse used in *LILAC* simulations.

Figure 95.17(a) shows the adiabat shape at shock breakout obtained with *LILAC* (solid line) with an inner-surface adiabat of about 2 and the theoretical prediction from Eq. (91). According to *LILAC*, the outer-surface adiabat is about 13 and the shock-breakout time is 1160 ps, in excellent agreement with the theoretical predictions of 12.8 and 1169 ps, respectively. Figure 95.17(b) shows the pressure profile at shock breakout. The characteristic pressure bump on the left is due to the intensity ramp, while the flat region on the right at about 4.3 Mb is due to the flat portion of the foot.

It is important to observe that the laser intensity required to generate the desired prepulse ablation pressure is significantly larger than the one predicted by steady ablation formulas. Indeed, according to the steady ablation theory

$$P_a(\text{Mbar}) \approx 40 \left[\frac{I_L^{15}}{\lambda(\mu\text{m})} \right]^{2/3}, \quad (92)$$

the intensity required to induce 28 Mbar of pressure is approximately 205 TW/cm². Instead, the 79-ps prepulse described above required 750 TW/cm² to generate 28 Mbar. This discrepancy comes about because the ablation process does not reach a steady state in 79 ps. Furthermore, a fast ramp of the laser intensity during the prepulse causes a hydrodynamic decoupling

between the shell and the laser with the result that most of the prepulse laser energy goes into heating the coronal plasma instead of driving the required strong shock. This explains why a very large increase in laser intensity has only a modest effect on the prepulse hydrodynamics. If one takes into account the limitations of the laser system with regard to the maximum power and power ramping rate, then the maximum prepulse pressure and outer-surface adiabat are further reduced. All of these effects need to be accounted for on a case-by-case basis through careful one-dimensional simulations.

It is important to notice that Eqs. (78) and (81)–(83) should be used with caution in determining the optimal pulse parameters when the resulting laser pulse is limited by either the laser peak power or rise time. When the prepulse is not flat, Eq. (83)

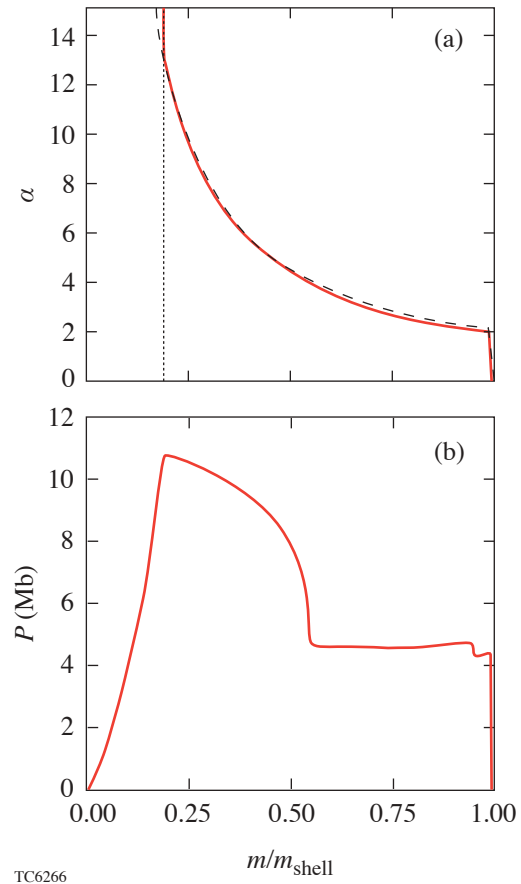


Figure 95.17

(a) Comparison of the *LILAC* adiabat profile at shock breakout for the rising-foot laser pulse given by the dashed line in Fig. 95.15 with the theoretical prediction of Eq. (91) (dashed line). The ablated mass fraction from *LILAC* is shown by the vertical dotted line. (b) Pressure profile at shock breakout for the target and pulse in Fig. 95.17(a).

for a square prepulse needs to be adjusted to reproduce the same total prepulse energy. In this case, the theoretical results are not as accurate as in the case of a square pulse and need to be refined by numerical simulations. As an example, we consider a typical OMEGA cryogenic spherical target that has an outer radius of $430 \mu\text{m}$ and a thickness of $85 \mu\text{m}$. A square prepulse is designed for an $\alpha_{\text{inn}} \approx 2$ using Eqs. (81)–(83) with an adjusted $\chi = 1.42$ in order to obtain an ablated mass fraction of 21%, as indicated by *LILAC* simulations. The maximum adiabat ratio follows from Eq. (81) leading to $\theta_* = 5.9$ with an outer-surface adiabat of about 11.8. According to Eqs. (78)–(83), the prepulse duration is about 90 ps with a foot of 1083 ps. The foot again is divided into a flat portion lasting half of the foot length followed by a linear intensity ramp to three times the initial intensity. If one takes into account the OMEGA power ramping rate limit of approximately 10 TW over 50 ps, then the prepulse can be divided into a 70-ps linear ramp to 14 TW followed by a 55-ps flattop. This is approximately equivalent to a 90-ps square pulse. The foot starts at 0.36 TW for 542 ps and a linear ramp to 1.08 TW for another 542 ps. The curve in Fig. 95.18 represents the laser pulse (prepulse + foot) used in *LILAC* simulations.

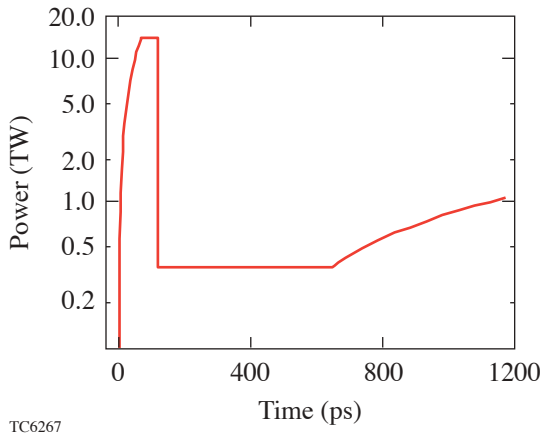


Figure 95.18
Optimal laser intensity history from *LILAC* for a typical OMEGA cryogenic DT spherical capsule with design specification of $\alpha_{\text{inn}} = 2$, rising-foot intensity, and experimental power-ramping limitations.

Figure 95.19 shows the adiabat shape for the OMEGA cryogenic capsule simulated with *LILAC* using the pulse described above. Notice that the outer-surface adiabat is about 12 and the ablated mass is about 21%, in agreement with the theoretical prediction for an equivalent square prepulse. The adiabat shape from *LILAC* (solid line) is also in good agreement with Eq. (91), indicating that the theory applies to spherical shells as well as planar foils.

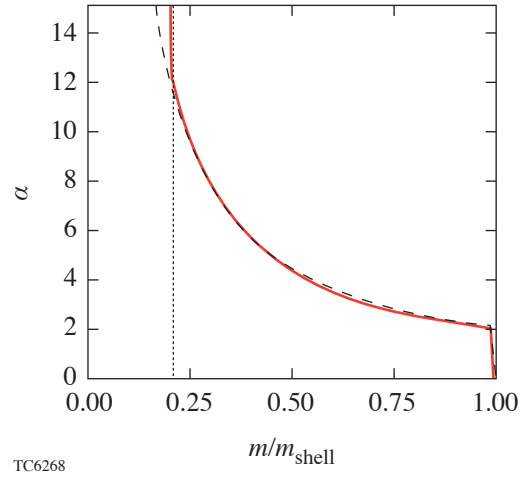


Figure 95.19
Comparison of the *LILAC* adiabat profile at shock breakout for the laser pulse shown in Fig. 95.18 with the theoretical prediction of Eq. (91). The ablated mass fraction from *LILAC* is shown by the vertical dotted line.

Conclusions

The adiabat profile induced by a decaying shock is calculated including the effects of mass ablation and residual ablation pressure. The adiabat shape follows a simple power law of the shell areal density m :

$$\alpha = \alpha_{\text{inn}} \left(\frac{m_{\text{shell}}}{m} \right)^{\delta_a}, \tag{93}$$

where α_{inn} is the inner-surface adiabat, m_{shell} is the total initial shell areal density, and m is the shell’s local areal density. The power index δ_a varies from 1.12 for a 100-ps prepulse to 1.20 for a 300-ps prepulse. The calculated profile reproduces the simulation results with only a few-percent error, and it can be used to design the optimum prepulse, which leads to the maximum adiabat ratio between the inner- and outer-shell surfaces. Our theoretical results on the ideal adiabat shape without ablation are in qualitative agreement with other published work but show improved accuracy when compared with the numerical solutions.

ACKNOWLEDGMENT

This work was supported by the U.S. Department of Energy Office of Inertial Confinement Fusion under Cooperative Agreement No. DE-FC03-92SF19460, the University of Rochester, and the New York State Energy Research and Development Authority. The support of DOE does not constitute an endorsement by DOE of the views expressed in this article.

REFERENCES

1. J. D. Lindl, *Inertial Confinement Fusion: The Quest for Ignition and Energy Gain Using Indirect Drive* (Springer-Verlag, New York, 1998).
2. Lord Rayleigh, in *Scientific Papers* (Cambridge University Press, Cambridge, England, 1900), Vol. II, pp. 200–207.
3. Y. Kato *et al.*, Phys. Rev. Lett. **53**, 1057 (1984); Laboratory for Laser Energetics LLE Review **33**, 1, NTIS document No. DOE/DP/40200-65 (1987). Copies may be obtained from the National Technical Information Service, Springfield, VA 22161.
4. S. Skupsky, R. W. Short, T. Kessler, R. S. Craxton, S. Letzring, and J. M. Soures, J. Appl. Phys. **66**, 3456 (1989).
5. R. H. Lehmburg, A. J. Schmitt, and S. E. Bodner, J. Appl. Phys. **62**, 2680 (1987).
6. P. W. McKenty, V. N. Goncharov, R. P. J. Town, S. Skupsky, R. Betti, and R. L. McCrory, Phys. Plasmas **8**, 2315 (2001).
7. S. E. Bodner, Phys. Rev. Lett. **33**, 761 (1974).
8. H. Takabe *et al.*, Phys. Fluids **28**, 3676 (1985).
9. J. Sanz, Phys. Rev. Lett. **73**, 2700 (1994).
10. R. Betti, V. N. Goncharov, R. L. McCrory, and C. P. Verdon, Phys. Plasmas **5**, 1446 (1998).
11. A. R. Piriz, J. Sanz, and L. F. Ibañez, Phys. Plasmas **4**, 1117 (1997).
12. M. C. Herrmann, M. Tabak, and J. D. Lindl, Nucl. Fusion **41**, 99 (2001).
13. A. Kemp, J. Meyer-ter-Vehn, and S. Atzeni, Phys. Rev. Lett. **86**, 3336 (2001).
14. R. Betti, K. Anderson, V. N. Goncharov, R. L. McCrory, D. D. Meyerhofer, S. Skupsky, and R. P. J. Town, Phys. Plasmas **9**, 2277 (2002).
15. J. H. Gardner, S. E. Bodner, and J. P. Dahlburg, Phys. Fluids B **3**, 1070 (1991).
16. S. E. Bodner *et al.*, Phys. Plasmas **7**, 2298 (2000).
17. L. Phillips *et al.*, Laser Part. Beams **17**, 225 (1999).
18. V. N. Goncharov, J. P. Knauer, P. W. McKenty, P. B. Radha, T. C. Sangster, S. Skupsky, R. Betti, R. L. McCrory, and D. D. Meyerhofer, Phys. Plasmas **10**, 1906 (2003).
19. Laboratory for Laser Energetics LLE Review **94**, 91, NTIS document No. DOE/SF/19460-485 (2003). Copies may be obtained from the National Technical Information Service, Springfield, VA 22161.
20. T. J. B. Collins and S. Skupsky, Phys. Plasmas **9**, 275 (2002).
21. N. Metzler, A. L. Velikovich, and J. H. Gardner, Phys. Plasmas **6**, 3283 (1999).
22. N. Metzler *et al.*, Phys. Plasmas **9**, 5050 (2002).
23. Ya. B. Zel'dovich and Yu. P. Raizer, *Physics of Shock Waves and High-Temperature Hydrodynamic Phenomena*, edited by W. D. Hayes and R. F. Probstein (Dover Publications, Mineola, NY, 2002), pp. 820–839.
24. G. I. Barenblatt, *Scaling, Self-Similarity, and Intermediate Asymptotics*, Cambridge Texts in Applied Mathematics (Cambridge University Press, Cambridge, England, 1996).
25. V. B. Adamskii, Sov. Phys.-Acoust. **2**, 1 (1956).
26. A. I. Zhukov and Ia. M. Kazhdan, Sov. Phys.-Acoust. **2**, 375 (1956).
27. W. Häfele, Z. Naturforschg. **10a**, 1006 (1955).
28. S. v. Hoerner, Z. Naturforschg. **10a**, 687 (1955).
29. C. E. Max, C. F. McKee, and W. C. Mead, Phys. Fluids **23**, 1620 (1980); Phys. Rev. Lett. **45**, 28 (1980).
30. W. M. Manheimer, D. G. Colombant, and J. H. Gardner, Phys. Fluids **25**, 1644 (1982).
31. J. Delettrez and E. B. Goldman, Laboratory for Laser Energetics Report No. 36, University of Rochester (1976).

Design of a Highly Stable, High-Conversion-Efficiency, Optical Parametric Chirped-Pulse Amplification System with Good Beam Quality

Introduction

Optical parametric chirped-pulse amplification (OPCPA) has been shown¹⁻⁷ to be well suited for front-end amplification in petawatt-class laser systems. The high-gain and large-gain bandwidth available in type-I parametric amplification using a relatively short length of material affords low spectral phase distortion and low *B*-integral accumulation.² Prepulses typical of multipass regenerative amplifiers are eliminated with simple, single-pass OPCPA arrangements, and the low thermal loading in the parametric process reduces undesirable thermal effects. The requirement for 100-mJ-level, 1054-nm chirped pulses operating at a moderate repetition rate (~5 Hz) for front-end injection into a glass-amplifier chain places significant demands on the OPCPA pump laser.^{3,5,7} The spatial and temporal characteristics of commercial pump lasers have limited their ability to achieve high pump-to-signal conversion efficiency through the OPCPA process.⁶ Recently, we reported a measurement of 29% conversion efficiency in a single-stage OPCPA at a 5-Hz repetition rate, with over 6×10^6 gain, 5-mJ output energy, and output stability better than that of the pump laser.⁷ Efficient and stable OPCPA output was achieved by carefully designing the OPCPA configuration and by optimizing the spatiotemporal profile of the pump. This significantly reduced the average power requirement of the pump laser.

The maximum OPCPA conversion efficiency is obtained when the rate of energy transfer from the pump to the signal and idler is such that all spatial and temporal points in the pulse reach peak conversion simultaneously. Maximizing the conversion efficiency thus requires the use of complementary shapes for the seed and pump spatial and temporal profiles, as described by Begishev *et al.*^{8,9} Appropriate seed temporal shapes can be approximated by spectral shaping¹⁰ or other pulse-shaping techniques.^{11,12} Ross *et al.*¹² described a multiple-stage OPCPA design that allows significant reconversion in the preamplifier stages in order to produce an approximately complementary seed shape for use with a temporally Gaussian shaped pump in the final power-amplifier stage. Since most of the pump-to-signal energy exchange will occur in the power

amplifier, a high conversion efficiency may be obtained if the seed and pump spatial shapes are also properly matched. This approach would be particularly attractive if it were desired to achieve a high pulse contrast after recompression in an all-OPCPA system without the gain shaping expected through a glass-amplifier chain.¹³ If independent control of the spatial and temporal shapes does not exist, then spatiotemporal coupling in the OPCPA process may limit the ability to simultaneously achieve high efficiency, high stability, high pulse contrast, and good beam quality. It is therefore important to understand the detailed spatiotemporal behavior of the OPCPA process in order to fully optimize a design.

Flat-top shapes for both seed and pump can also be used and can be approximated by high-order, super-Gaussian spatial and temporal shapes. Our work has shown that when the spatial and temporal shapes of the pump are high-order super-Gaussians, high conversion efficiency can be attained without the need to explicitly shape the seed pulse.⁷ The very high gain provided by the optical parametric amplification process shapes the originally Gaussian spatiotemporal profile of the seed so that the full widths at half maximum (FWHM) of the signal and pump are well matched when the amplification process begins to saturate. In the high-gain region of the amplifier, however, the finite slope of the edges of the pump beam and finite rise and fall times of the pump pulse can limit the amount of pump energy extracted due to gain narrowing.¹⁴ Gain narrowing caused by spatial and temporal variations of the pump intensity limits the overlap area of the pump and signal, reducing the energy extracted from the pump. Although the effect of gain narrowing can be reduced by heavily saturating the amplifier,¹⁴ high-order super-Gaussian shapes are preferred to both reduce the gain narrowing and maximize the conversion efficiency.

Several articles^{2,3,12,14} have discussed OPCPA performance for temporal Gaussian shapes and Gaussian or flat-top spatial shapes. This article extends this discussion by using a numerical model to systematically investigate the performance

of an OPCPA system using both Gaussian and super-Gaussian spatial and temporal shapes. This investigation includes the effects of pump–signal spatial walk-off and spatiotemporal noise to obtain good energy stability, good beam quality, and high overall conversion efficiency.

In the following sections, (1) the design goals for our OPCPA system are briefly discussed; (2) the numerical model is described; (3) a single-stage OPCPA system with no spatiotemporal noise on the input beams is considered, and it is shown that for OPA crystals with large pump–signal walk-off, such as beta-barium borate (BBO), operation of the system in the region of enhanced stability can degrade the near-field beam shape and slightly reduce efficiency; (4) a comparison is made with lithium triborate (LBO), which has a pump-beam walk-off that is a factor of ~ 8 less than that of BBO; by replacing BBO with LBO in this design, a higher efficiency and improved beam symmetry are obtained in the region of enhanced stability; (5) the output from this single-stage system with spatiotemporal noise included in the model is described; the spatiotemporal evolution of the signal near the gain peak requires that a delicate balance be maintained between gain saturation and reconversion and that a trade-off must often be made between high output energy stability and low output beam intensity modulation.

Two-Stage Considerations discusses additional design considerations when a power amplifier is introduced. The amount of reconversion required in the preamplifier to achieve efficient and stable OPCPA output is generally greater when a power-amplification stage is added. Furthermore, proper matching of the seed- and pump-beam sizes in both the preamplifier and power amplifier maximizes the energy extracted from the pump. An optimized, two-stage OPCPA design for the front end of the OMEGA EP (extended performance) laser is presented. OMEGA EP is a petawatt-class, Nd-doped phosphate glass laser system that will be constructed at LLE to provide short-pulse backlighting capabilities, to investigate fast-ignition concepts for direct-drive inertial confinement fusion, and to study high-energy-density physics. The OMEGA EP front end must provide 5-Hz pulses with a minimum energy of 250 mJ and approximately 8-nm FWHM bandwidth centered at 1054 nm for injection into the main laser chain. The two-stage OPCPA design presented here provides over 500 mJ in a 1054-nm, 2.4-ns chirped pulse with nearly 8-nm FWHM bandwidth and 40% conversion efficiency using a 527-nm pump laser wavelength.

OPCPA Design Goals

In addition to gain variations caused by nonuniform intensity at the spatial and temporal edges of the pump, spatiotemporal intensity fluctuations produce localized variations in gain, causing nonuniform energy transfer from the pump to the signal. This can further reduce conversion efficiency and produce unwanted signal-beam modulation. Spatiotemporal modulation will also produce spatial and temporal variations in the onset of reconversion in the optical parametric amplification process, affecting the signal output energy stability.^{15,16} Spatial walk-off of the pump from the signal beam can further reshape the latter. All of these issues are carefully addressed in attempting to achieve the following design goals for this OPCPA system:

1. *Maximize* pump energy extraction in each stage in order to reduce the pump average power requirement.
2. *Maintain* output signal energy stability at least as good as the pump input stability.
3. *Minimize* near-field modulation to reduce the risk of laser-induced damage to the front-end optics.
4. *Minimize* beam distortion caused by birefringent walk-off.

The current requirement for OMEGA EP is to produce compressed pulse widths of 1 to 100 ps. In the numerical model, the seed-pulse characteristics provided by a commercial mode-locked, Nd:glass laser system (GLX-200)¹⁷ with a pulse width of 200 fs⁷ were used. Since the stretched pulse width is in the nanosecond regime, the effects of the group-velocity mismatch between the pump, signal, and idler pulses are small and can be neglected in the analysis. Group-velocity dispersion is also negligible. As will be shown, spatial effects such as beam shape, pump–signal walk-off, beam-size matching, and intensity modulation significantly affect the ability to achieve the design goals.

Numerical Model

The coupled-wave equations for difference frequency generation in the slowly varying envelope approximation¹⁸ were used in the numerical integration method following the form of Craxton¹⁹ and taking into account the full spatial and temporal dependence of the three parametric waves,

$$\begin{aligned}
 \frac{\partial \tilde{E}_s(x, y, z, t)}{\partial z} &= -\frac{1}{2} \gamma_s \tilde{E}_s(x, y, z, t) + \rho_s \frac{\partial \tilde{E}_s(x, y, z, t)}{\partial y} \\
 &- i K \tilde{E}_p(x, y, z, t) \tilde{E}_i^*(x, y, z, t) \exp(-i \Delta k \cdot z), \\
 \frac{\partial \tilde{E}_i(x, y, z, t)}{\partial z} &= -\frac{1}{2} \gamma_i \tilde{E}_i(x, y, z, t) + \rho_i(t) \frac{\partial \tilde{E}_i(x, y, z, t)}{\partial y} \\
 &- i \frac{\omega_2}{\omega_1} K \tilde{E}_p(x, y, z, t) \tilde{E}_s^*(x, y, z, t) \exp(-i \Delta k \cdot z), \\
 \frac{\partial \tilde{E}_p(x, y, z, t)}{\partial z} &= -\frac{1}{2} \gamma_p \tilde{E}_p(x, y, z, t) + \rho_p \frac{\partial \tilde{E}_p(x, y, z, t)}{\partial y} \\
 &- i \frac{\omega_3}{\omega_1} K \tilde{E}_s(x, y, z, t) \tilde{E}_i(x, y, z, t) \exp(i \Delta k \cdot z),
 \end{aligned} \tag{1}$$

where subscripts s , i , and p refer to the signal, idler, and pump waves, respectively; γ is the absorption coefficient; ω is the angular frequency of the electric field; and t is the reduced time taken in the reference frame of the pulse. \tilde{E} is the complex field amplitude that has been scaled by $n^{1/2}$, where n is the refractive index of the wave derived from a Sellmeier equation.²⁰ The energy flux for each wave is thus proportional to $|\tilde{E}|^2$. The birefringence walk-off angle of the pump is given by ρ_p , whereas ρ_s and ρ_i account for the possibility of a noncollinearity among the wave vectors. By energy conservation, $\omega_i = \omega_p - \omega_s$ and the wave-vector mismatch is $\Delta k = k_p - k_i - k_s$. For a noncollinear angle ρ_s between the signal- and pump-wave-vector directions, Δk and the direction ρ_i of the idler-wave vector in the crystal are determined from the cosine rule.¹² Note that the temporal chirp of the signal pulse gives a spread in idler propagation directions. K is defined as

$$K = \frac{\omega_1}{c} (n_s n_i n_p)^{-1/2} d_{\text{eff}}, \tag{2}$$

where d_{eff} is the effective nonlinear coefficient for the type-I parametric interaction.

A split-step technique was used where Eqs. (1) were solved in the space-time domain, and spatial walk-off and noncollinear propagation were performed in the spatial-frequency domain. A linear chirp with 8-nm FWHM bandwidth was superimposed upon a 1054-nm Gaussian temporal and spatial seed for input to the optical parametric amplifier (OPA) crystals, and a 527-nm single-frequency pump was used with type-I phase matching in both collinear and noncollinear geometries. Both simulated and experimentally measured spatial and temporal shapes can be used as input to the model, and the output is available in both spatially and temporally resolved and integrated forms. Experimentally measured inputs were used in the model to achieve excellent agreement with previous experimental results⁷ and were used in the current analysis to investigate the effect of pump-beam spatiotemporal noise on the OPCPA output. In order to perform a systematic investigation of how specific design parameters affect OPCPA output, simulated beam shapes without spatiotemporal noise were also used.

Single-Stage Design Considerations

The OPCPA designs presented in this section consist of two crystals configured as a single stage with no idler separation between the crystals. The air gap between the two crystals is assumed to be zero in the model since a gap of less than ~ 4 mm introduces negligible dephasing in the conversion process.⁷ These designs provide nominally 5-mJ output energy using a pump intensity of 1 GW/cm² and a FWHM pulse width and nominal beam diameter of 1 ns and 1.5 mm, respectively (pump energy ≈ 18 mJ). The pump has a tenth-order super-Gaussian temporal and spatial shape, and the seed is Gaussian in time and space with FWHM of 1 ns and 1.5 mm, respectively. The seed input energy is 800 pJ. The considerations discussed here are also applicable for the energy-scaled designs appropriate for the OMEGA EP front end, discussed in **Two-Stage Considerations**.

Figure 95.20 shows the output signal energy versus the length of the second crystal for two different single-stage preamplifier designs, one using two BBO crystals and the other two LBO crystals. The first-crystal lengths are 10 mm and 25 mm for the BBO and LBO designs, respectively. The solid curves in Fig. 95.20 represent the nominal pump intensity of 1 GW/cm²; the dashed curves represent pump intensities that

are $\pm 5\%$ about this nominal value. These design parameters were chosen based on the measured damage threshold of the antireflective coatings on the OPA crystals. The region of highest stability for each design in Fig. 95.20 is just past the peak of the gain curve where reconversion begins.¹⁵ The detailed performance of the BBO design without spatiotemporal noise on the pump beam along with the LBO design are discussed in the next two subsections. Higher efficiency and better beam shape are achieved for LBO in the region of enhanced stability, and a trade-off must be made among efficiency, stability, and near-field beam modulation. For the LBO design, we show that this trade-off exists both with and without the inclusion of spatiotemporal noise on the pump beam.

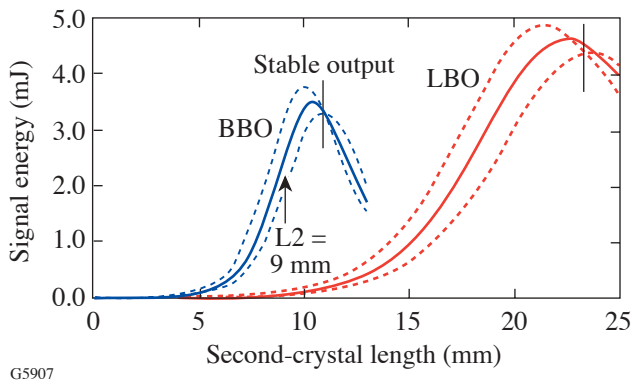


Figure 95.20

Signal output energy versus length of the second crystal for two-crystal, single-stage BBO and LBO preamplifier designs. The solid curves represent the nominal pump input intensity of 1 GW/cm^2 , and the dashed curves represent $\pm 5\%$ about this intensity. The crystal lengths that provide enhanced stability for each design are indicated by the vertical lines on the graph. The input pump and seed spatial and temporal shapes are the same for both designs, except that the pump beam is narrower in the direction orthogonal to walk-off by 9% for the LBO design and 20% for the BBO design. The arrow indicates the second-crystal length of 9 mm for the BBO design shown in Fig. 95.21(a) and discussed in the text.

1. BBO Preamplifier

The BBO preamplifier consists of two BBO crystals configured for type-I phase matching whose extraordinary axes are oriented in opposing directions for walk-off compensation.²¹ To achieve large pump-energy extraction using flattop shapes, the pump and signal widths must be well matched in the second crystal where most of the pump-energy extraction occurs. The pump-signal walk-off causes spatial gain narrowing to be greater in the walk-off direction, leading to output beam ellipticity and reduced conversion efficiency. Proper walk-off compensation requires a combination of opposing crystal orientations, lateral displacement of the seed and pump

beams on the first crystal's face, and anamorphic pump beam shaping.^{6,21} Figure 95.21(a) shows the output signal-beam shape obtained just before the peak of the BBO gain curve in Fig. 95.20 for first- and second-crystal lengths of $L_1 = 10 \text{ mm}$ and $L_2 = 9 \text{ mm}$, respectively, and a collinear phase-matching condition. The pump-beam FWHM used in Fig. 95.21 was 1.5 mm in the walk-off direction, but 20% smaller in the direction orthogonal to walk-off. The pump-beam center was offset from the seed-beam center on the first crystal's face by $280 \mu\text{m}$ opposite to the pump-beam walk-off direction (upward in Fig. 95.21). For a second-crystal length of 9 mm, the predicted efficiency of 16.9% is quite good, and the output beam shape shows little asymmetry in the walk-off direction; however, the stability is poor [see Fig. 95.20 and Fig. 95.21(a)].

Better efficiency and improved stability are obtained at the peak of the gain curve; however, spatial variations in saturation and reconversion produce intensity modulation and beam asymmetry in the walk-off direction, as shown in Fig. 95.21(b). The region of best stability is with a second-crystal length of 10.9 mm (see Fig. 95.20), but the beam shape is further degraded with a peak-to-valley modulation of $\sim 30\%$, as shown in Fig. 95.21(c). A noncollinear phase-matching angle may be considered in order to reduce the pump-signal walk-off within the crystals; however, a limitation exists because the idler beam will walk out of the interaction area even if the pump- and signal-beam propagation directions within the crystals are perfectly collinear. This effect is significant in BBO because of its large walk-off angle ($\sim 3.2^\circ$). In addition, the maximum bandwidth in a degenerate OPA is achieved in a nearly collinear geometry.² Typically, an external angle of $\sim 0.5^\circ$ in air between the pump and seed beams is used to separate the signal and idler outputs. Figure 95.21(d) shows the output signal-beam shape for an external noncollinear beam angle of 0.5° and crystal lengths that provide enhanced stability. In this case the seed beam is tilted in the direction of pump-beam walk-off in the first crystal, and only a small difference is seen between the collinear and slightly noncollinear configurations [compare Figs. 95.21(c) and 95.21(d)]. Figure 95.22 shows that gain narrowing of the chirped signal pulse is greater for the shorter crystal length, but slight pulse broadening is observed when saturation is large.

2. LBO Preamplifier

The sensitivity of beam shape to beam angle and interaction length in BBO can be alleviated to a large extent through the use of LBO. LBO has a pump walk-off angle that is a factor of ~ 8 smaller than that in BBO, a larger angular acceptance, and a sufficiently high nonlinear coefficient to make it preferable

to BBO for this application.²⁰ Although LBO has a larger refractive-index variation with temperature than BBO, the measured output stability at a 5-Hz repetition rate is better than that of the pump when the crystals are held in a temperature-controlled oven at 32°C (Ref. 7). Figure 95.20 shows the signal output energy of an LBO design that uses nearly identical input beam parameters as the BBO design. As with the BBO design, the pump-beam FWHM is matched to the seed-beam FWHM in the walk-off direction, but because the pump walk-off angle is less in LBO, the pump input beam FWHM in the direction orthogonal to walk-off is smaller by only 9% compared with 20% for BBO. This allows more pump energy to be used while maintaining the same average pump intensity of 1 GW/cm². The output signal energy at peak conversion is thus greater. The smaller walk-off angle allows greater efficiency at the

second-crystal length $L_2 = 23.5$ mm, where stability is highest ($\eta = 27.7\%$ for LBO versus $\eta = 24.2\%$ for BBO). The effect of $\pm 5\%$ seed fluctuations on the output stability is much less than 1% for the level of seed energy used (800 pJ). Additional simulations have shown that the conversion efficiency for this LBO design can approach 40% if 30th-order super-Gaussian pump shapes are used with standard Gaussian seed shapes.

Figure 95.23(a) shows the simulated output beam shape for the LBO design in the region of greatest stability. This design provides less azimuthal beam variation and higher efficiency than the BBO design [compare Figs. 95.21(d) and 95.23(a)]. The pump-beam walk-off angle in LBO is close to the 0.5° noncollinear angle between the pump and seed input beams typically used to allow separation of the idler and signal

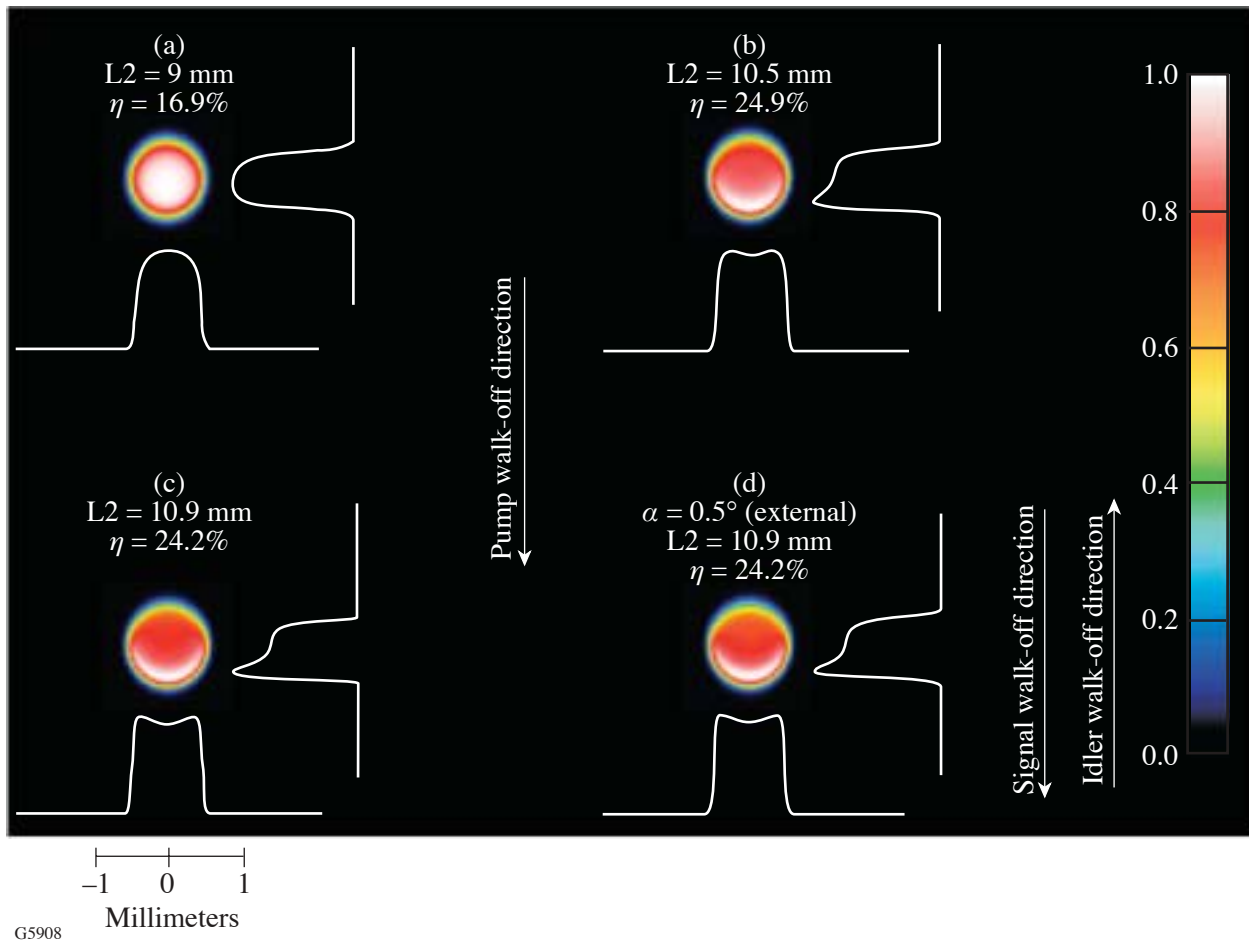


Figure 95.21

Temporally integrated, normalized signal output beam shapes for the single-stage BBO design with different second-crystal lengths L_2 for $L_1 = 10$ mm. Stability for each case is shown in Fig. 95.20. (a) $L_2 = 9$ mm (undersaturated), (b) $L_2 = 10.5$ mm (peak of the gain curve), (c) $L_2 = 10.9$ mm (region of enhanced stability), and (d) $L_2 = 10.9$ mm with an external noncollinear angle of 0.5° between the pump and seed beams. Conversion efficiencies η are indicated in the figure.

outputs; thus, for this LBO design, both crystals are oriented identically and a noncollinear angle of 0.5° is used with the pump beam offset from the seed beam by $187 \mu\text{m}$ on the first crystal's face [vertically upward in Fig. 95.23(a)]. Figure 95.23(b) shows the temporal output for the design of Fig. 95.23(a). The greater reconversion seen in the spatial and temporal center of the signal output beam in Fig. 95.23 is a result of the Gaussian spatial and temporal shape of the seed beam. Less reconversion is seen in the spatially integrated

temporal profile shown in Fig. 95.23(b). In addition to the better overall performance achieved with LBO, this design approach shows that BBO can be retrofitted with LBO, if desired, with only a change in pump-beam energy and ellipticity (by use of a prism, for example). An overall change in beam size is not required. Alternatively, using LBO instead of BBO has the advantage that a smaller aperture size is required to extract the same amount of pump energy, potentially reducing optical component cost.

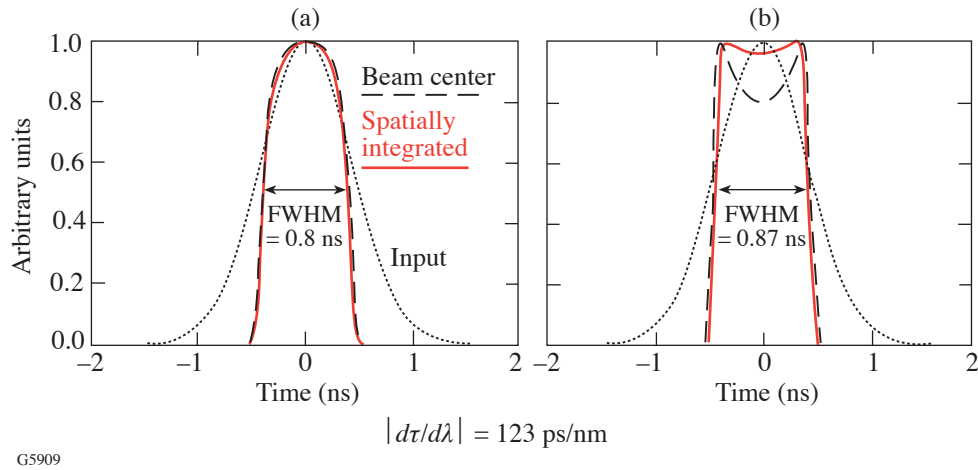


Figure 95.22

Normalized, temporal profiles for two of the BBO designs shown in Fig. 95.21. The simulation uses a 200-fs Gaussian temporal pulse that is stretched in time to provide a linearly chirped, 1.0-ns input seed pulse to the crystals. Beam center: dashed; spatially integrated: solid; input: dotted. (a) For the case of Fig. 95.21(a), the pulse shape shows little saturation and a gain-narrowing effect. (b) Saturation with reconversion is seen for the case of Fig. 95.21(d), contributing to a broadening of the pulse compared with Fig. 95.22(a). Greater reconversion is seen at beam center because of the spatial Gaussian shape of the seed.

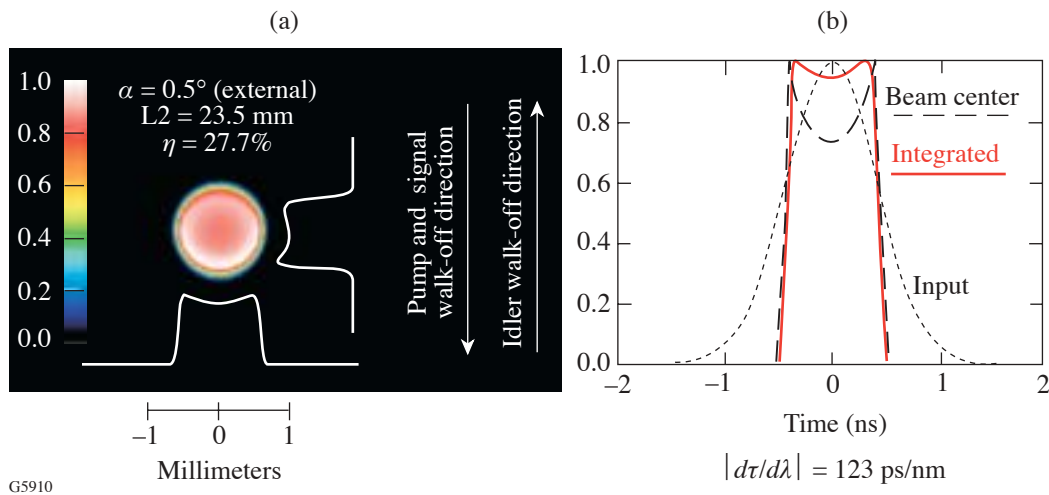


Figure 95.23

(a) Temporally integrated, normalized signal output beam shape for the single-stage LBO design in the region of enhanced stability ($L2 = 23.5 \text{ mm}$ in Fig. 95.20). The $\sim 15\%$ dip in the center is from greater reconversion in this region as a result of the Gaussian shape of the seed beam. (b) Normalized temporal profile of input seed and output signal pulses for the case shown in Fig. 95.23(a).

3. LBO Design with Spatiotemporal Noise

The experimentally measured⁷ pump spatial and temporal shapes used in the LBO design are shown in Fig. 95.24 to illustrate how pump-beam intensity modulation affects the signal output near the peak of the gain curve. In this simulation, each temporal slice of the pump beam shown in Fig. 95.24(a) is assigned a flat phase front and the same normalized spatial modulation (peak-to-mean = 25% within an area defined by 60% of the pump beam's spatial FWHM). The pump temporal pulse shape is shown in Fig. 95.24(b) and has a modulation of ~10%. Figures 95.24(c) and 95.24(d) show two temporal slices of the output signal beam, one at the peak and one at the dip of the pump pulse. The signal-beam temporal slices, separated in time by 210 ps, clearly show a spatiotemporal coupling and a delicate balance between gain saturation and reconversion. Localized regions in the signal beam corresponding to high

peak intensity in the pump beam are just beginning to reconvert at the dip of the pulse and are farther into reconversion at the peak of the pulse. In both cases, the output beam has lower peak-to-mean modulation than the pump beam. Greater smoothing is observed at the peak of the pulse due to greater overall saturation. Figure 95.25 plots the normalized output energy and temporally integrated output beam modulation for this design versus the normalized pump-beam input energy, showing that a trade-off exists in this case between intensity modulation and output energy stability. For the pump energy that provides both maximum output energy and maximum output energy stability (dotted vertical line in Fig. 95.25), the output beam modulation is less than that of the pump beam. At the peak of the output energy curve, the output energy changes by $\pm 2\%$ for pump energy fluctuations of $\pm 5\%$.

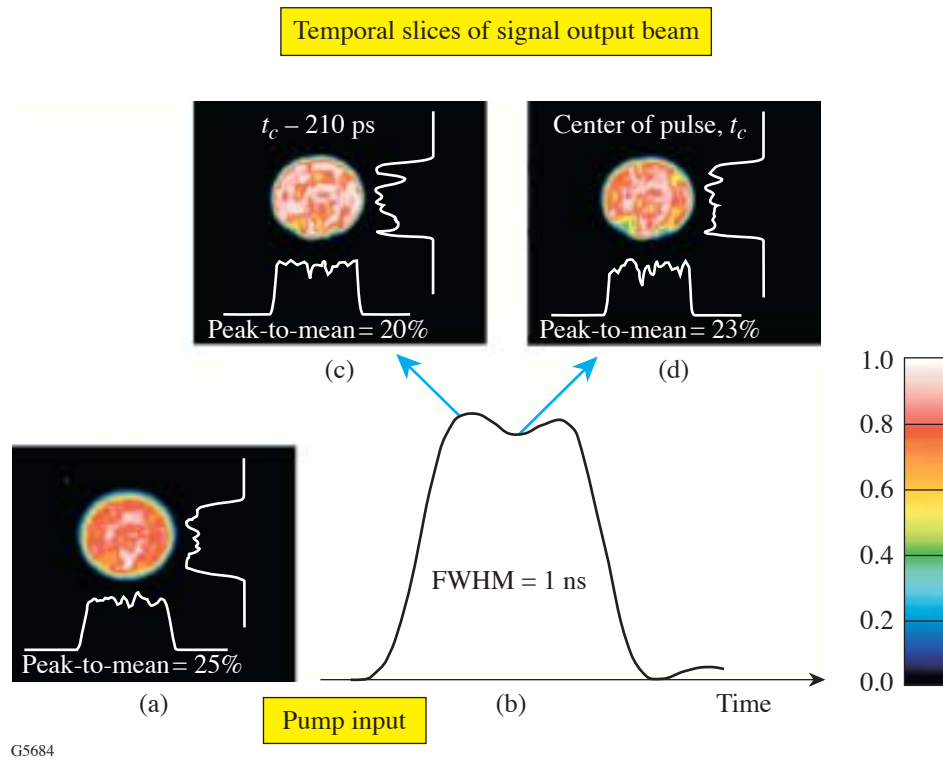


Figure 95.24

Experimentally measured pump (a) spatial and (b) temporal shapes are used to illustrate how pump-beam intensity modulation affects the signal output near the peak of the gain curve. Two temporal slices of a simulation of the output signal beam are shown in (c) and (d); one at the peak and one at the dip of the pump pulse, respectively.

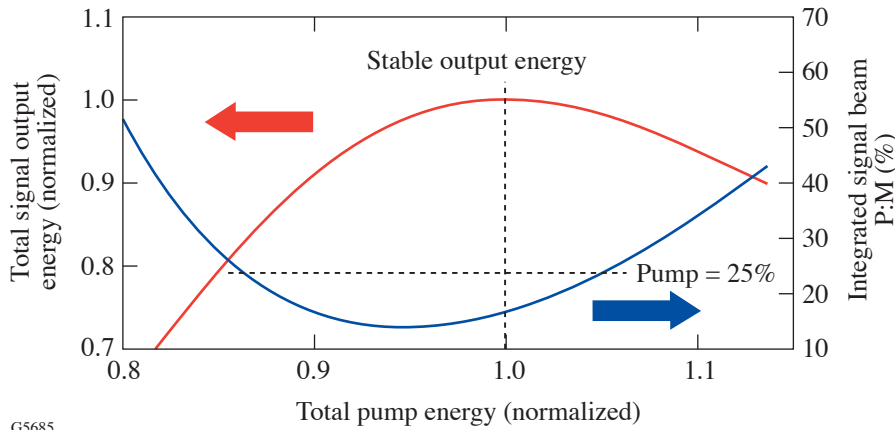


Figure 95.25 Comparison of the output energy and output beam quality for a single-stage LBO design. The axis on the left indicates the normalized signal output energy versus normalized pump input energy, while the axis on the right gives the output signal beam’s peak-to-mean intensity modulation. The graphs show that a trade-off exists between enhanced energy stability and low near-field intensity modulation.

G5685

Two-Stage Considerations

1. Pre-amplifier Modification

As noted in the previous section, the OMEGA EP front-end energy requirement of 250 mJ for injection into the Nd:glass amplifier chain requires both an energy-scaled preamplifier design and a power amplifier. Square beams will be used to provide a better fill factor than round beams in the OPA crystals and the Nd:glass multipass disk amplifiers, improving the energy extraction. A block diagram with nominal pump and signal energies for the prototype OMEGA EPOPCPA front end is shown in Fig. 95.26. The design consists of two LBO crystals configured as a single preamplifier stage followed by an LBO power amplifier. Details of this design are given in the next subsection. The design guidelines discussed for a high-efficiency, single-stage OPCPA system are similar to those required when the power amplifier is introduced.

Figures 95.27(a)–95.27(c) are simulated plots of the signal output energy from a two-stage, all-LBO design versus the length of the power amplifier for three different preamplifier lengths. The pump input beam used in these simulations was square and had a simulated, Gaussian, randomly distributed intensity modulation of 25% peak-to-mean so that the two-stage OPCPA system could be optimized simultaneously for efficiency, stability, and beam quality.

For the undersaturated preamplifier in Fig. 95.27(a), a power-amplifier length of ~14 mm provides high output stability but relatively low output energy. A preamplifier operated with a small amount of reversion is stable, as shown in Fig. 95.27(b), but does not provide sufficient stability in the power amplifier. Increasing the preamplifier length causes the power-amplifier stable region [at the foot of the three curves in

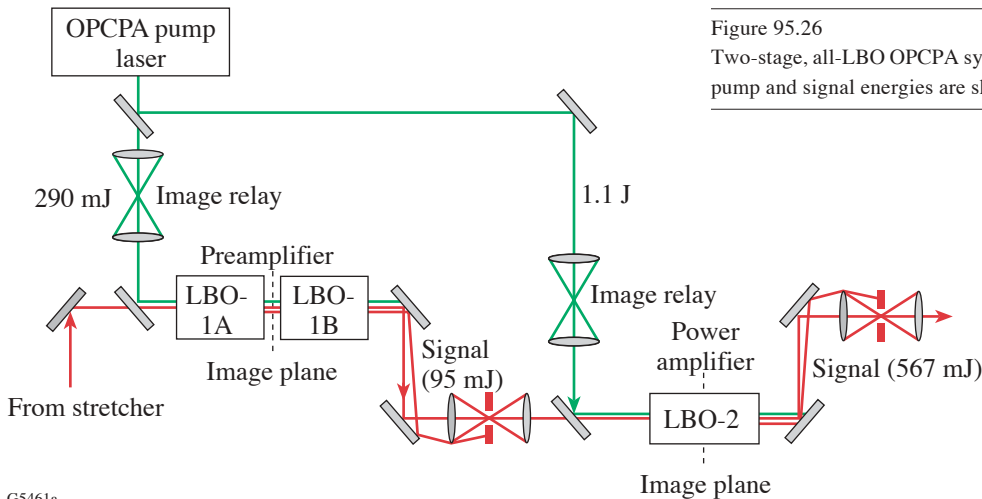


Figure 95.26 Two-stage, all-LBO OPCPA system for the OMEGA EP front end. Nominal pump and signal energies are shown.

G5461a

Fig. 95.27(b)] to move up the curve to a region of higher efficiency. Figure 95.27(c) shows that extending the preamplifier length by 2 mm provides high output energy and enhanced stability in the power amplifier. As noted for a single-stage OPCPA system, a trade-off between stability, efficiency, and beam quality also exists for a two-stage system. Care must be exercised when extending the length of the preamplifier since more reconversion may increase the preamplifier output spatiotemporal modulation beyond that of the pump beam, possibly putting downstream optics at risk. For the design of Fig. 95.27(c), the peak fluence at the output of the preamplifier is less than or equal to that of the pump.

2. “Mode-Matching” and OMEGA EP OPCPA Design

Maximizing the conversion efficiency in the power amplifier also requires that the power-amplifier seed- and pump-beam sizes be properly matched. By allowing the power-amplifier seed-beam size to closely match the pump-beam size, energy at the edges of the pump beam can be efficiently extracted. Little spatial gain narrowing is seen in the power

amplifier because of the steep edges of both the seed and pump beams and because the gain is no longer exponential.

The prototype OPCPA front end for OMEGA EP (Fig. 95.26) was designed for the amplification of a temporally stretched, 2.4-ns, 1054-nm seed pulse. The preamplifier consists of two 5 × 5 × 29.75-mm crystals configured as a single stage with no idler separation between the crystals. The power amplifier is 10 × 10 × 11 mm. The crystals are cut at 11.8° in the x-y plane of the crystal for type-I angular phase matching at 32°C. At a pump intensity of 1 GW/cm², the expected conversion efficiency is 40% with over-500-mJ signal output energy, a gain of greater than 5 × 10⁹, and an output energy stability about equal to that of the pump.

Figure 95.28 shows how overall conversion efficiency, output energy, and output stability scale with the relative size of the seed and pump beams. The pump temporal and spatial super-Gaussian orders used in this design are 10 and 20, respectively, and the seed is Gaussian in space and time.

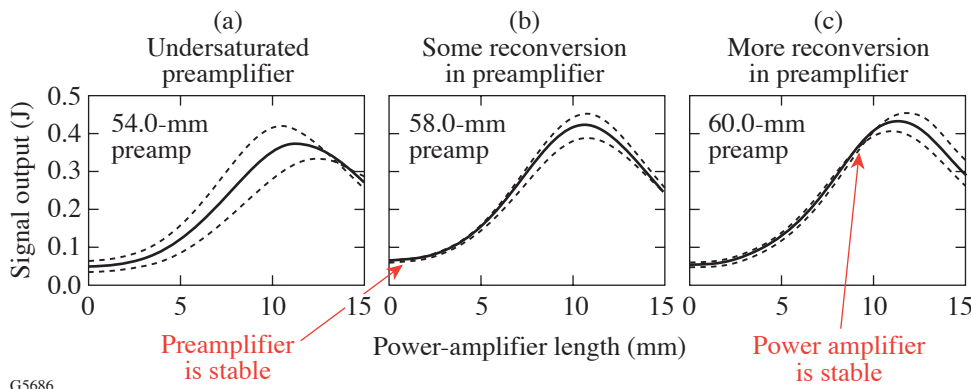


Figure 95.27 Simulated plots of the signal output energy from the two-stage, all-LBO design shown in Fig. 95.26 versus the length of the power amplifier for three different preamplifier lengths. Solid lines represent the nominal pump input intensity of 1 GW/cm², whereas the dashed lines represent ±5% about this nominal intensity.

G5686

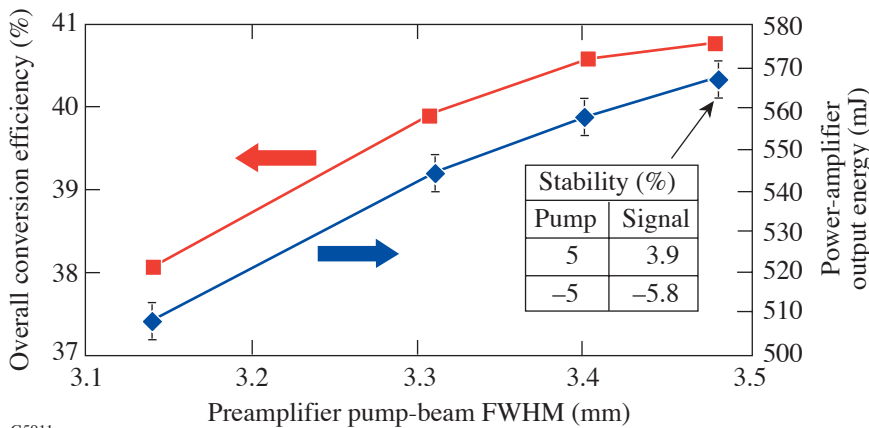


Figure 95.28 Plot of conversion efficiency (squares) and output energy (diamonds) for a two-stage OPCPA design versus the preamplifier input pump beam’s size. The pump input beam is a 20th-order super-Gaussian with nominal intensity of 1 GW/cm² for each point plotted. The seed beam of the preamplifier is Gaussian with FWHM of 3.18 mm. The error bars indicate output energy changes for ±5% pump energy fluctuations.

G5911

For the two-stage design of Fig. 95.28, the input pump beam's size and intensity at the power amplifier are kept fixed, while the input pump beam's size at the preamplifier is varied with its intensity held constant by scaling its energy. The size of the seed beam at the preamplifier and the signal-beam magnification between the two stages are kept fixed; thus the average signal intensity in both stages does not change significantly as the input pump beam's size in the preamplifier is varied. Maintaining approximately constant input intensity of the signal and pump beams in both stages allows the enhanced stability condition to be maintained and, at the same time, allows the relative size of the seed and pump beams to be varied.

Because the seed beam at the input to the preamplifier is Gaussian, the variation of the pump beam's size at the input of the preamplifier produces an effective change in the preamplifier output signal beam size, and thus, the size of the signal beam at the input to the power amplifier. Figure 95.29 shows how the signal beam's size entering the power amplifier changes with the size of the preamplifier pump beam. From Figs. 95.28 and 95.29, it is seen that output stability is essentially unchanged when the preamplifier pump beam's size is varied, while seeding the power amplifier with a beam that is smaller than the pump-beam FWHM of 6.8 mm degrades the efficiency. Closely matching the pump and signal beams' sizes at the input to the power amplifier ensures highly efficient extraction of the pump-beam energy at its edges.

The output spatial-intensity distribution for this two-stage design with simulated, Gaussian, randomly distributed spatiotemporal noise on the pump beam is shown in Fig. 95.30. The output pulse shape and phase accumulated in the OPA are shown in Fig. 95.31. The quadratic temporal phase is due to the phase mismatch across the chirped input seed pulse. Heavy saturation in the power amplifier produces an output signal beam with less spatiotemporal noise than the input pump beam.

Conclusion

We have described the detailed spatiotemporal behavior of the OPCPA process using a combination of Gaussian and super-Gaussian spatial and temporal shapes and have included the effects of pump spatiotemporal noise and pump-signal spatial walk-off. Using a three-dimensional spatial and temporal numerical model, we have shown that for single-stage OPCPA systems that operate in both the small-signal (i.e., high gain) and high-saturation regimes, the spatial and temporal gain-narrowing effect can be reduced with high-order super-Gaussian pump shapes, leading to high conversion efficiency, as demonstrated in our earlier experimental work.⁷ Additional simulations have shown that the conversion efficiency for a slightly non-degenerate, type-I parametric process can approach 40% using 30th-order super-Gaussian pump shapes in a single-stage OPCPA system with standard Gaussian seed shapes.

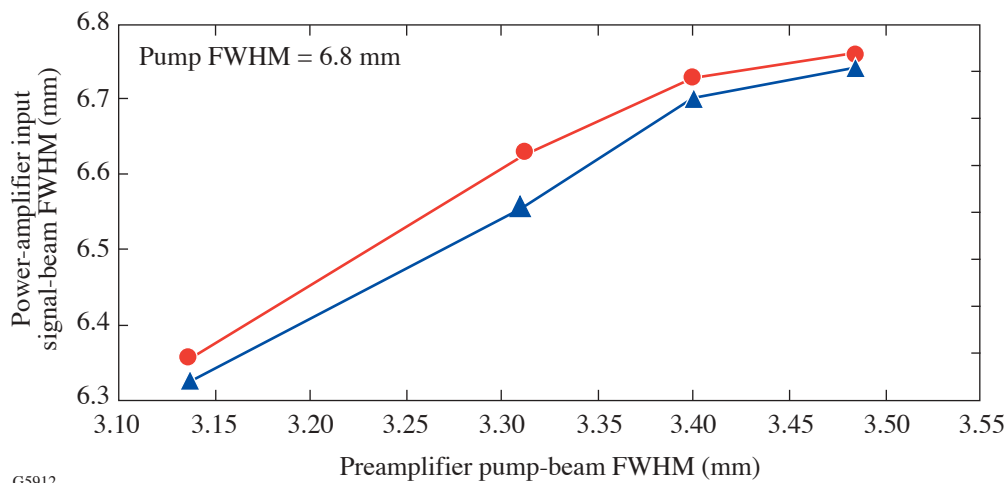


Figure 95.29

Size of the signal beam entering the power amplifier versus preamplifier pump beam's size for the two-stage design of Fig. 95.28. Triangles: in the direction of pump-beam walkoff; circles: orthogonal to walk-off. The FWHM of the pump beam entering the power amplifier is 6.8 mm.

We have also shown that the large pump–signal walk-off in BBO makes it difficult to simultaneously achieve high conversion efficiency, stable output, and good beam quality in this material. An LBO design using nearly identical input beam parameters has been shown to provide better beam quality and conversion efficiency at the crystal length where output stability is highest. A tradeoff among the efficiency, stability, and

beam quality both with and without pump spatiotemporal noise has been shown, emphasizing the importance of modeling the full spatial and temporal dependence for design optimization. For the optimized LBO design, both output energy fluctuations and spatiotemporal intensity modulations were less than those of the pump.

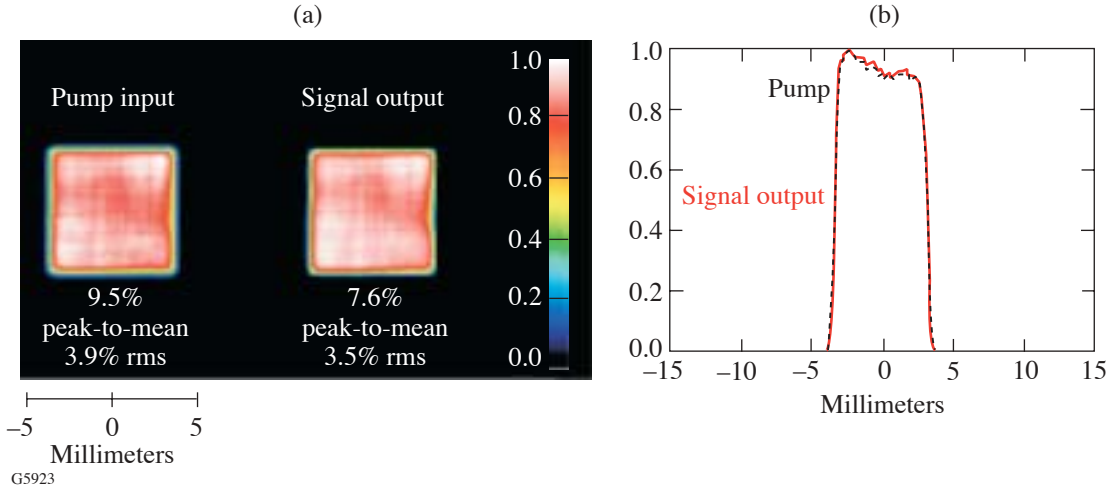


Figure 95.30 For the design shown in Figs. 95.28 and 95.29 with preamplifier pump beam’s FWHM = 3.48 mm: (a) Normalized beam cross section for the temporally integrated pump-beam input with simulated, spatiotemporal noise (left) and the power-amplifier signal output beam (right); (b) normalized horizontal lineouts through the center of each of the beams shown in (a). Signal: solid; pump: dashed.

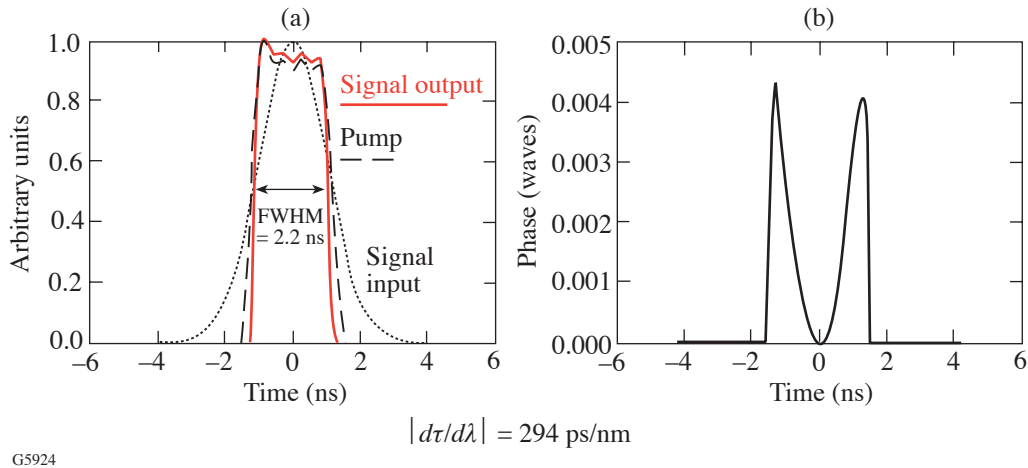


Figure 95.31 (a) Spatially integrated, normalized temporal profiles of the input pump and signal input/output pulses for the two-stage design with preamplifier pump beam’s FWHM = 3.48 mm. The seed pulse entering the first crystal of the preamplifier is shown dotted; the signal pulse out of the power-amplifier crystal is shown solid. The pump input temporal noise is 11% peak-to-valley (3% rms), whereas the amplified signal output temporal noise is only 8% peak-to-valley (2% rms). The spectral bandwidth of the output pulse is 7.5 nm. (b) Phase accumulated in the OPA for the chirped output pulse shown in (a).

The design guidelines discussed for a single-stage preamplifier were applicable when a power amplifier was added, but it was found that the preamplifier had to be operated farther into reconversion in order to obtain high efficiency and stable output from the power amplifier. Adjusting the relative size of the pump and input signal beams at the power amplifier was necessary to maximize conversion. By closely matching the pump and signal beams' sizes at the input to the power amplifier, better extraction of the pump-beam energy at its edges is achieved. These guidelines were used to design the prototype OMEGA EP OPCPA front end that met each of the design goals discussed in **OPCPA Design Goals**. This design should provide nearly 40% conversion efficiency, with stability and beam quality at least as good as that of the pump.

ACKNOWLEDGMENT

This work was supported by the U.S. Department of Energy Office of Inertial Confinement Fusion under Cooperative Agreement No. DE-FC03-92SF19460, the University of Rochester, and the New York State Energy Research and Development Authority. The support of DOE does not constitute an endorsement by DOE of the views expressed in this article.

REFERENCES

1. A. Dubietis, G. Jonusauskas, and A. Piskarskas, *Opt. Commun.* **88**, 437 (1992).
2. I. N. Ross *et al.*, *Opt. Commun.* **144**, 125 (1997).
3. I. N. Ross *et al.*, *Appl. Opt.* **39**, 2422 (2000).
4. H. Yoshida *et al.*, in *Conference on Lasers and Electro Optics*, Vol. 1, Technical Digest (Optical Society of America, Washington, DC, 2001), pp. 80–81.
5. X. Yang *et al.*, *Opt. Lett.* **27**, 1135 (2002).
6. I. Jovanovic *et al.*, *Appl. Opt.* **41**, 2923 (2002).
7. L. J. Waxer, V. Bagnoud, I. A. Begishev, M. J. Guardalben, J. Puth, and J. D. Zuegel, "High-Conversion-Efficiency, Optical Parametric Chirped-Pulse-Amplification System Using Spatiotemporally Shaped Pulses," submitted to *Optics Letters*.
8. I. A. Begishev, A. A. Gulamov, E. A. Erofeev, E. A. Ibragimov, S. R. Kamalov, T. Usmanov, and A. D. Khadzhaev, *Sov. J. Quantum Electron.* **20**, 1100 (1990).
9. I. A. Begishev, A. A. Gulamov, E. A. Erofeev, E. A. Ibragimov, S. R. Kamalov, T. Usmanov, and A. D. Khadzhaev, *Sov. J. Quantum Electron.* **20**, 1104 (1990).
10. L. J. Waxer, J. H. Kelly, J. Rothenberg, A. Babushkin, C. Bibeau, A. Bayramian, and S. Payne, *Opt. Lett.* **27**, 1427 (2002).
11. M. D. Skeldon, *Rev. Sci. Instrum.* **71**, 3559 (2000).
12. I. N. Ross *et al.*, *J. Opt. Soc. Am. B* **19**, 2945 (2002).
13. M. D. Perry, F. G. Patterson, and J. Weston, *Opt. Lett.* **15**, 381 (1990).
14. Z. Pengfei *et al.*, *Opt. Laser Technol.* **35**, 13 (2003).
15. S. K. Zhang *et al.*, *Opt. Commun.* **184**, 451 (2000).
16. M. J. Guardalben, J. Keegan, L. J. Waxer, and J. D. Zuegel, presented at the 2002 OSA Annual Meeting, Orlando, FL, 29 September–3 October 2002.
17. Time-Bandwidth Products, Inc., Zürich, Switzerland, CH-8005 (<http://www.tbwp.com>).
18. J. A. Armstrong *et al.*, *Phys. Rev.* **127**, 1918 (1962).
19. R. S. Craxton, *IEEE J. Quantum Electron.* **QE-17**, 1771 (1981).
20. V. G. Dmitriev, G. G. Gurzadyan, and D. N. Nikogosyan, *Handbook of Nonlinear Optical Crystals* (Springer-Verlag, Berlin, 1991), p. 78.
21. D. J. Armstrong *et al.*, *J. Opt. Soc. Am. B* **14**, 460 (1997).

Nonlinear Propagation of Laser Beams near the Critical-Density Surface in the Plasmas of Direct-Drive Targets

Introduction

The interaction of laser beams with plasmas near the critical-density surface is an important characteristic feature of direct-drive inertial confinement fusion (ICF) experiments.^{1,2} One of the main laser–plasma interaction processes is stimulated Brillouin scattering (SBS), which involves the decay of an incident light wave into a scattered light wave and an ion-acoustic wave. The process of forward SBS accompanies the filamentation of laser beams and can change the spatial and temporal coherence of laser light propagating into the target.^{3,4} The process of backward SBS⁵ is important because it can potentially deplete the laser-beam power delivered to the target. The spectrum of SBS-backscattered light is also useful as a diagnostic of plasma conditions.

For typical parameters of direct-drive ICF experiments,^{1,2} the thresholds for both filamentation and SBS are exceeded in the near-critical-density region. The processes of filamentation, forward SBS, and backward SBS can coexist and influence each other in this region. In this article the nonlinear propagation of light near the critical density is studied within a model that includes filamentation, forward SBS, backward SBS, the reflection of light from the critical-density surface, and the absorption of light. An important feature of our model is the nonparaxial propagation of light, which allows a description of the reflection of light from the critical-density surface and the propagation of crossing laser beams.

The instability of filaments near the critical-density surface was observed in earlier simulations.⁶ In those simulations the filament instability caused ripples on the critical-density surface. The density gradient near the critical-density surface in the simulations of Ref. 6 was sharp—of the order of several laser wavelengths—limiting the growth of backward SBS. The purpose of this article is to study the interplay between SBS, filamentation, and reflection from the critical density for incoherent laser beams and the influence of these processes on the spectra of the backscattered light.

Our model can calculate the angular distribution and the frequency spectrum of light scattered back from the near-critical-density region. This enables the influence of the spatial and temporal incoherence of the incident light on the characteristics of the backscattered light to be studied. By changing the angle of incidence of a laser beam on the critical-density surface, it is possible to demonstrate the importance of the seeding of backward SBS by laser light reflection from the critical-density surface.²

The following sections will (1) describe the theoretical model used in our simulations, (2) discuss the simulation results for the normal incidence of light on the critical-density surface, (3) cover the influence of temporal smoothing by SSD on the backscattered light, (4) demonstrate the important role of electromagnetic seeding by reflected light using simulations of the oblique incidence of light on the critical-density surface, and (5) summarize the results.

Description of the Model

The model for the nonlinear propagation of laser beams in plasmas near the critical density n_c is based on the well-known set of hydrodynamic and Maxwell equations:⁶

$$\frac{\partial n}{\partial t} + \nabla \cdot (n \vec{V}) = 0, \quad (1)$$

$$\frac{\partial \vec{V}}{\partial t} + (\vec{V} \cdot \nabla) \vec{V} = -\frac{\nabla (c_s^2 n)}{n} - \frac{\nabla |\vec{E}|^2}{16\pi n_i n_c} - 2\hat{v} \vec{V}, \quad (2)$$

$$2i \frac{\omega_0}{c^2} \frac{\partial \vec{E}}{\partial t} + \Delta \vec{E} + \frac{\omega_0^2}{c^2} \left(1 - \frac{n}{n_c} - i \frac{n v_{ei}}{n_c \omega_0} \right) \vec{E} = 0. \quad (3)$$

Here $c_s = \sqrt{(Z T_e + 3 T_i)/m_i}$ is the ion-acoustic velocity, v_{ei} is the electron–ion collision frequency, T_e and T_i are the tem-

peratures of electrons and ions, respectively, $\hat{\nu}$ denotes the damping operator that includes Landau damping and damping due to ion–ion collisions, and Δ is the Laplacian operator. In this set, the hydrodynamic equations for plasma density n and velocity \vec{V} [Eqs. (1) and (2)] are coupled to the Maxwell equation (3) for the amplitude of the transverse electric field. The transverse electric field \vec{E} can be written in the form $\vec{E} = \text{Re} [\vec{E} \exp(-i\omega_0 t)]$, where ω_0 is the laser frequency and the amplitude \vec{E} varies in time slowly compared to ω_0 .

In the model described by Eqs. (1)–(3), the laser field is coupled to the plasma by the ponderomotive force. The changes in electron temperature due to Ohmic heating of the plasma by the laser field are not taken into account. For the modeling of SBS and filamentation, the perturbations of electron temperature due to the Ohmic heating can be neglected if the wavelength of a plasma perturbation is much shorter than the electron mean free path due to collisions $\lambda_{ei} = V_{Te} / \nu_{ei}$, where $V_{Te} = \sqrt{T_e / m_e}$ is the electron thermal velocity. This condition is usually satisfied for the typical parameters of OMEGA experiments.^{1,2}

The simulations of Eqs. (1)–(3) have been performed in two spatial dimensions (longitudinal x and transverse y), assuming s -polarization for the electric field $\vec{E} = E\vec{e}_z$. The numerical code used in the simulations is based on a nonparaxial solver previously used in the modeling of self-focusing and forward and backward SBS in underdense plasmas.⁴ The size of the simulation region was $40 \lambda_0$ (in the longitudinal direction) by $200 \lambda_0$ (in the transverse direction), where λ_0 is the laser wavelength in vacuum ($\lambda_0 = 0.351 \mu\text{m}$ in our simulations). The initial plasma density in the simulation region varied from $0.65 n_c$ to $1.1 n_c$ in the longitudinal direction in order to capture the influence of the near-critical-density region on backscattering.

The initial profiles of the background plasma parameters—density, electron temperature, and plasma velocity flow—were chosen to be uniform in the transverse direction and linear in the longitudinal direction (see Fig. 95.32). The characteristic initial plasma parameters and their scale lengths were consistent with simulations using the two-dimensional hydrodynamics code *SAGE*⁷ for direct-drive ICF targets.¹ The electron temperature decreased in the direction toward the critical surface, while the electron density increased. The electron temperature at the left boundary was $T_{e,b} = 2 \text{ keV}$, the ion temperature was $T_i = 1 \text{ keV}$, and the effective ion charge number was consistent with the CH target material $Z_{\text{eff}} = \langle Z^2 \rangle / \langle Z \rangle = 5.3$. The plasma flowed from the critical

surface into the plasma corona, and the plasma flow was subsonic in the simulation region. The plasma flow decreased toward the critical surface. The position of the critical surface moved with a velocity much smaller than the plasma flow. Simulations were performed for time intervals of about 20 ps. This time interval is sufficient to develop the small-scale plasma perturbations (of the order of a few laser wavelengths) due to laser–plasma interaction. At the same time, the large-scale (hydrodynamic) profiles of plasma parameters changed insignificantly during the time interval of 20 ps.

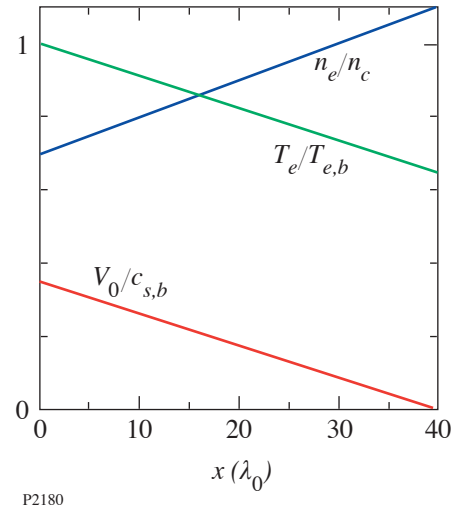


Figure 95.32

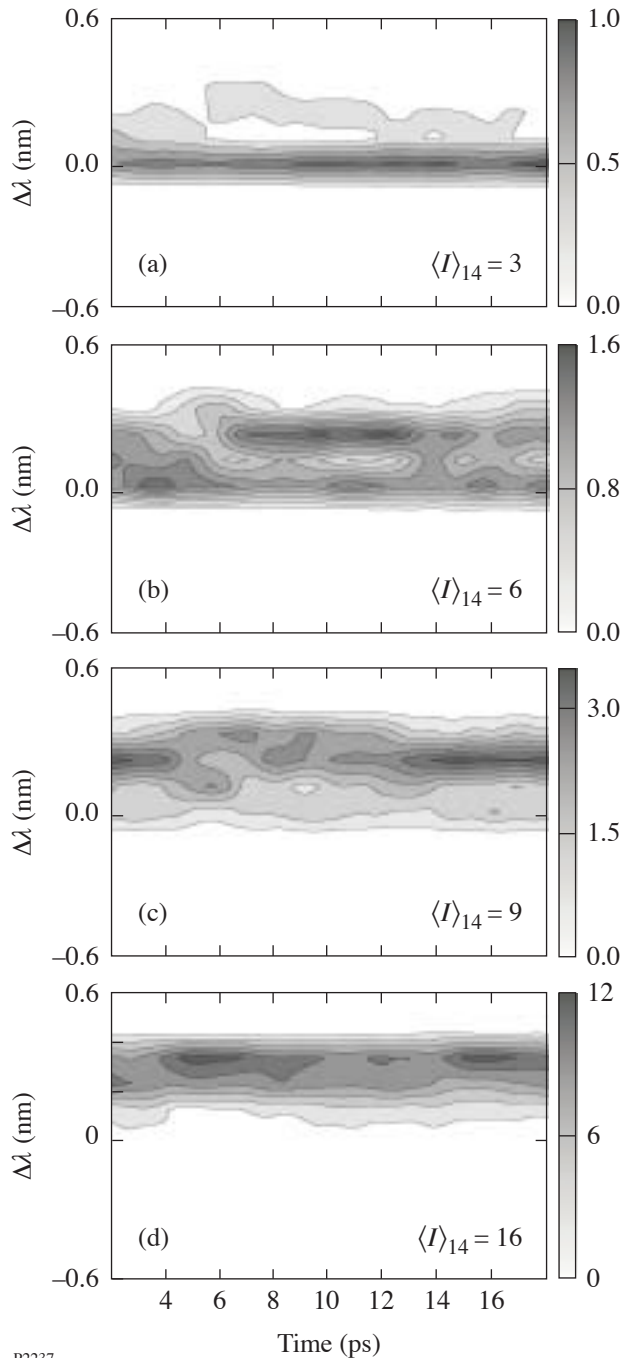
The profiles of the initial plasma parameters—electron density n_e , electron temperature T_e , and plasma flow V_0 —used in the simulations. The electron density is normalized to the critical density n_c . The electron temperature is normalized to the temperature on the left boundary $T_{e,b}$. The plasma flow is normalized to the ion-acoustic velocity on the left boundary $c_{s,b}$.

Normal Incidence of Laser Beams on the Critical-Density Surface

In the simulations, the incident light was randomized in space using phase plates,⁸ and in some simulations it was also randomized in time using smoothing by spectral dispersion (SSD).⁹ The space-averaged intensity $\langle |E|^2 \rangle_b$ of light entering the simulation region at the left boundary $x = 0$ (where $n_{\text{eb}} = 0.65 n_c$) was calculated from the space-averaged intensity of light incident on the plasma corona from vacuum $\langle |E|^2 \rangle_V$. After taking into account the absorption of light in the underdense plasma up to an electron density of $0.65 n_c$, and the field swelling, one obtains the formula $\langle |E|^2 \rangle_b = \langle |E|^2 \rangle_V (1 - A) / \sqrt{1 - n_{\text{eb}} / n_c}$, where A is the absorbed fraction of laser power in the underdense plasma below $0.65 n_c$. In the simulations it was assumed that $\langle |E|^2 \rangle_b = 0.46 \langle |E|^2 \rangle_V$, which is consistent with the absorp-

tion calculated by *SAGE* for the plasmas of OMEGA experiments.^{1,2} Most of the simulations were carried out for normal incidence of light on the critical surface.

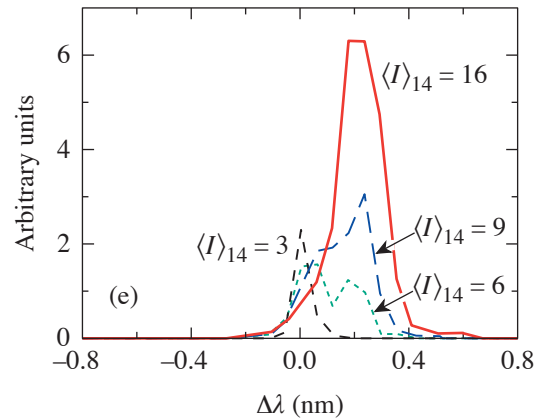
In the first series of simulations, the light incident from the left boundary was randomized by “top-hat” phase plates⁸ with *f*-number *f* = 6, but without SSD smoothing. The intensity of the incident light was varied in the range from $\langle I \rangle_{14} = 3$ to



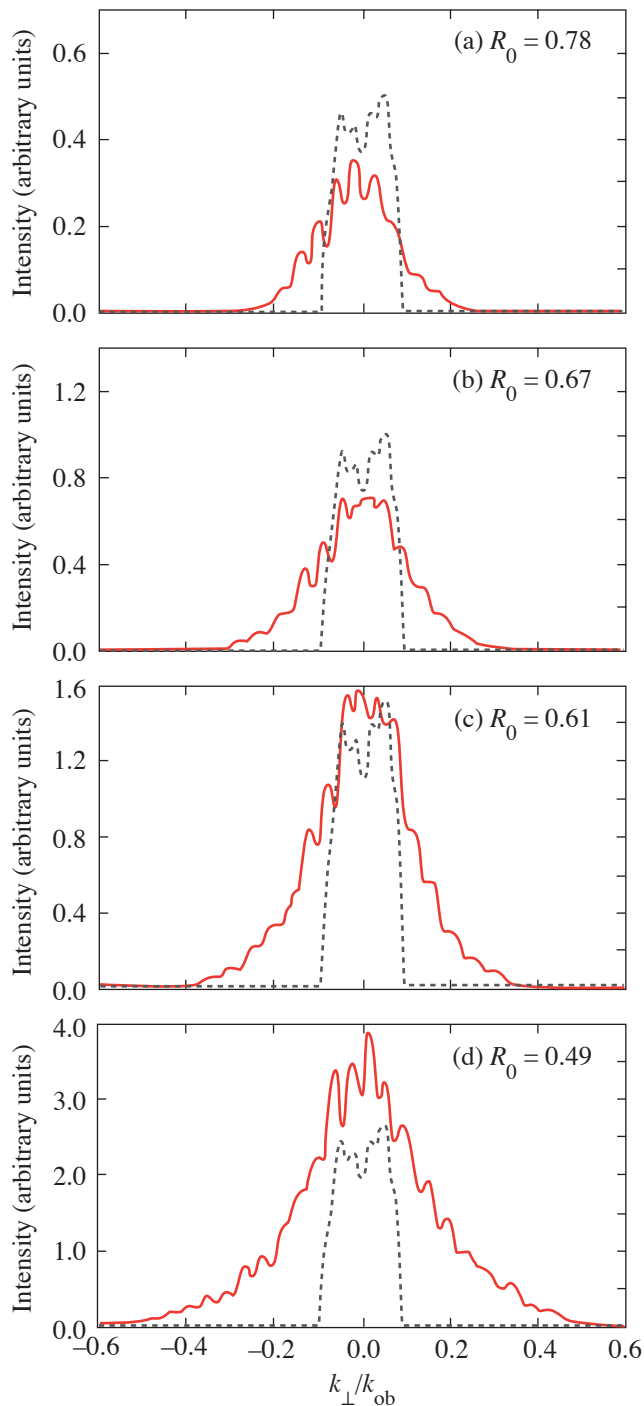
$\langle I \rangle_{14} = 16$, where $\langle I \rangle_{14} = (c \langle |E|^2 \rangle_V / 8\pi) / 10^{14} \text{ W/cm}^2$. For each value of the average intensity, three simulations with different phase-plate realizations were performed, and the backscattered-light spectra were averaged over these three simulations. Simulation results for the frequency spectra of backscattered light are shown in Fig. 95.33. At a lower intensity $\langle I \rangle_{14} = 3$, the spectrum of backscattered light [Fig. 95.33(a)] is practically unshifted relative to the wavelength of the incident light. This spectrum is consistent with the specular reflection of light from the critical-density surface. For larger intensities, Figs. 95.33(b)–95.33(d) show that the frequency spectrum of the backscattered light is red shifted and broadened. The red shift in the frequency spectrum increases moderately with the increase of laser intensity [see Fig. 95.33(e)]. Figures 95.33(a)–95.33(d) show that a simulation time of about 20 ps is sufficient to establish a stable red-shifted component in the backscattered light.

The angular distributions of backscattered light from the simulations are presented in Fig. 95.34. They are shown as a function of $k_{\perp} / k_{\text{ob}} = \sin \theta_b$, where k_{\perp} is the transverse wave vector, $k_{\text{ob}} = (\omega_0 / c) \sqrt{1 - n_{\text{eb}} / n_c}$ is the laser wave vector on the left boundary, and θ_b is the propagation angle on the left boundary. For comparison, the dashed curve in Fig. 95.34 shows the angular spectra in the linear propagation regime, which is realized at low laser intensities $\langle I \rangle_{14} \ll 1$, when the plasma nonlinearities are unimportant. The angular spread of the backscattered light in Fig. 95.34 is characterized by the

Figure 95.33
Frequency spectra of the backscattered light in the case of normal incidence for different intensities: (a) $\langle I \rangle_{14} = 3$; (b) $\langle I \rangle_{14} = 6$; (c) $\langle I \rangle_{14} = 9$; (d) $\langle I \rangle_{14} = 16$. The time-integrated frequency spectra for the same intensities are given in (e).



P2237



P2238

Figure 95.34

The angular distribution of the backscattered light (solid line) for the parameters of Fig. 95.33, as a function of $k_{\perp}/k_{\text{ob}} = \sin \theta_b$, where k_{\perp} is the transverse wave vector, k_{ob} is the laser wave vector on the left boundary, and θ_b is the propagation angle on the left boundary. For comparison, each plot also shows the angular distribution of the backscattered light in the linear propagation regime (dashed line). R_0 is the fraction of reflected laser power going into the angular domain of the linear propagation regime.

quantity R_0 , which is defined as the fraction of reflected laser power going into the angular domain of the linear propagation regime. With increasing laser intensity, the angular spread of backscattered light increases and R_0 decreases.

For the parameters of our simulations, the backscattered light spectra are influenced mostly by two processes: backward SBS and self-focusing of laser speckles. The backward SBS is expected to produce a red shift in the frequency spectrum of the backscattered light in the case of subsonic plasma flow, as in our simulations. The importance of backward SBS can be estimated by calculating the backward SBS gain in inhomogeneous plasmas, G_{SBS} .⁵ Note that in a randomized laser beam, the peak intensity in a laser speckle can be several times higher than the average light intensity,¹⁰ and the SBS gain in high-intensity speckles is also a few times larger than the average gain. Consequently, backward SBS from a randomized laser beam develops mainly in high-intensity speckles.^{4,11} For the parameters of our simulations (see Fig. 95.32), the backward SBS gain has the form $G_{\text{SBS}} = 0.24 u \langle I \rangle_{14}$, where $u = I_m / \langle I \rangle$ is the ratio of a peak intensity in a speckle to the average intensity. For a characteristic high-intensity speckle with $u = 5$, $G_{\text{SBS}} = 1.2 \langle I \rangle_{14}$. The linear theory of backward SBS predicts, for the parameters of our simulations, a red shift $\Delta\lambda$ in the backscatter frequency spectrum of 0.26 nm, which is in good agreement with the simulation results of Fig. 95.33.

The self-focusing of a laser speckle can lead to a filament instability and seed forward SBS.^{4,12} The onset of self-focusing occurs when the self-focusing parameter p_{sf} exceeds unity, where p_{sf} is defined as the ratio of the laser power in a speckle to the critical power for self-focusing.¹³ For a laser beam smoothed by a top-hat phase plate with f -number f , the self-focusing parameter has the following form:⁴ $p_{\text{sf}} = 1.23 f^2 (n_e/n_c) I_m$, where $I_m = |E|^2 / 4\pi n_c T_e$ is the normalized peak intensity in a speckle. Near the left boundary of our simulation region, the self-focusing parameter is estimated to be $p_{\text{sf}} = 0.07 u \langle I \rangle_{14} = 0.35 \langle I \rangle_{14}$ for a characteristic high-intensity speckle with $u = 5$, and $\langle I \rangle_{14}$ varies from 3 to 16. From this estimate one can see that the self-focusing parameter can exceed unity in high-intensity speckles, and self-focusing instability would start. In our simulations, the longitudinal size of a laser speckle is much larger than the SBS growth length due to a strong inhomogeneity of the background density.

The estimates for the backward SBS gain and the self-focusing parameter show that both backward SBS and self-

focusing influence the spectra of the backscattered light. For normal incidence of a laser beam on a critical-density surface, laser light reflected from the critical density can seed backward SBS. The angular and frequency spectra of the reflected light can be broadened by self-focusing. Near the critical density surface the characteristic frequency shift due to self-focusing is close to the characteristic frequency shift of backward SBS, which makes the reflected light very effective in seeding backward SBS.

Influence of Temporal Smoothing by Spectral Dispersion

A series of simulations have been performed to study the dependence of the backscattered-light spectra on temporal beam smoothing by SSD. SSD is known to be effective in suppressing the backscatter parametric instabilities in underdense plasmas.^{1,14} The effect of SSD on the backscattered light near the critical density is illustrated by Figs. 95.35 and 95.36. Figure 95.35 shows the simulated time-integrated spectra of backscattered light for the incident-light intensity $\langle I \rangle_{14} = 9$ in three cases: no SSD, SSD with a bandwidth $\Delta\nu = 0.5$ THz, and SSD with $\Delta\nu = 1$ THz. From Fig. 95.35 it is evident that the increase of SSD bandwidth does not significantly change the characteristic red shift in the frequency spectrum.

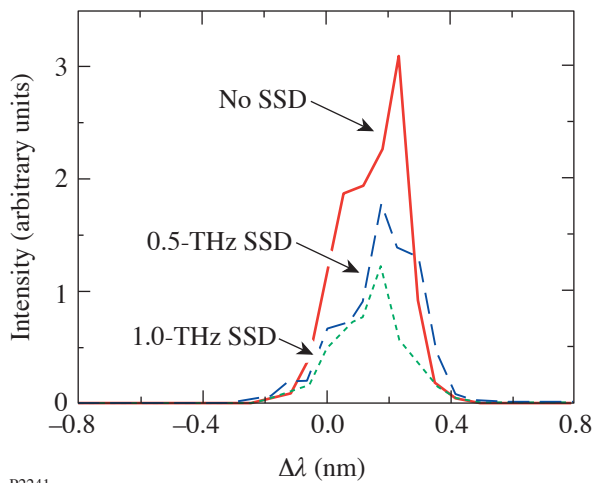


Figure 95.35 The simulated time-integrated frequency spectra of backscattered light for intensity $\langle I \rangle_{14} = 9$ in the case of no SSD, SSD with a bandwidth of 0.5 THz, and SSD with a bandwidth of 1 THz. The 1-THz SSD bandwidth of the incident light corresponds to the wavelength spread of $\Delta\lambda$ within ± 0.21 nm.

Figure 95.36 shows that the intensity of backscattered light moderately decreases with the increase of SSD bandwidth but not by more than a factor of 2. The reflectivity R in Fig. 95.36

is defined as the ratio of the backscattered-light power to the incident-light power at $n_e = 0.65 n_c$. Due to the absorption of light in the plasma corona at densities below $0.65 n_c$, the reflectivity of light leaving the plasma corona R_V is related to the reflectivity R at $0.65 n_c$ by the formula $R_V = R(1-A)^2$. In our simulations, $A = 0.74$, and the reflectivity in the near-critical-density region $R = (10 \div 35)\%$ in Fig. 95.36 corresponds to the reflectivity of light leaving the plasma corona $R_V = (0.7 \div 2.4)\%$.

The frequency spectrum of the SBS-backscattered light driven by a beam with a broadband SSD $\Delta\nu = 1$ THz (see Fig. 95.35) is more narrow than the spectrum of the incident light, which has an SSD bandwidth $\Delta\lambda = \pm 0.21$ nm.

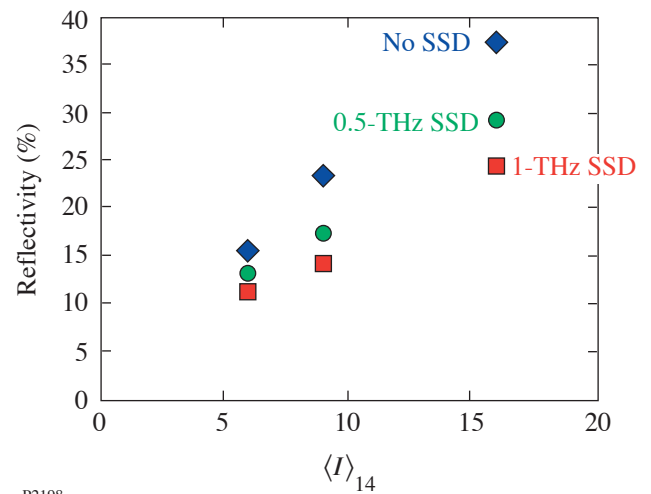


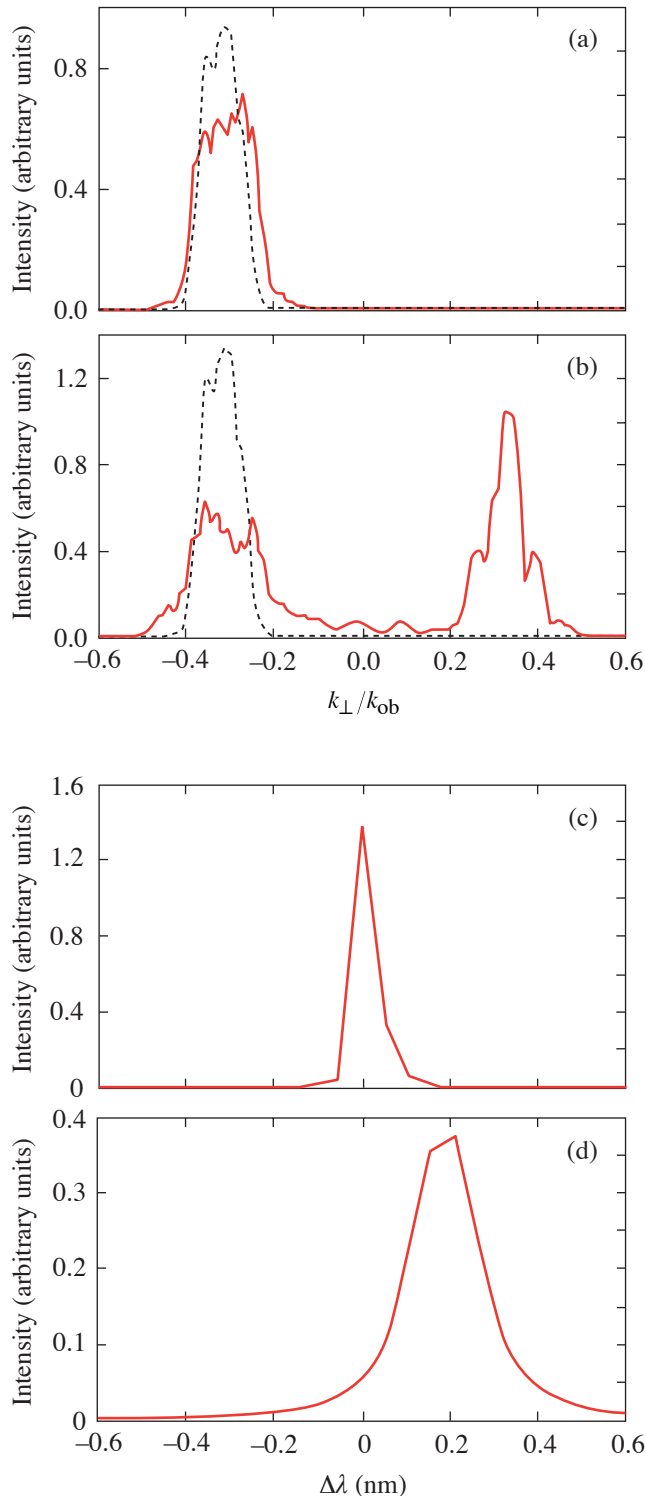
Figure 95.36 The time-integrated reflectivity R as a function of the incident-light intensity in the case of no SSD, SSD with a bandwidth of 0.5 THz, and SSD with a bandwidth of 1 THz.

Oblique Incidence of Laser Beams on the Critical-Density Surface

Laser beams, obliquely incident on the critical-density surface, have been modeled to verify the electromagnetic seeding of backward SBS by light reflected from near the critical density. In these simulations, one or two laser beams with phase plates $f/6$ and no SSD bandwidth were sent into the plasma at an angle of 20° . For this angle of incidence, the light specularly reflected from near the critical surface propagates in the angular domain, which is well separated from the incident light and the backward SBS light. Thus, the reflected light from an obliquely incident beam cannot seed backward SBS of the same beam. This result is illustrated in Fig. 95.37.

For a single incident beam with intensity of $\langle I \rangle_{14} = 6$, the angular distribution of the reflected light from the obliquely incident beam [see Fig. 95.37(a)] shows only specular reflection and no significant backward SBS. The reason is that for

$\langle I \rangle_{14} = 6$, the characteristic gain for backward SBS ($G_{\text{SBS}} = 7.2$) is not large enough, and backward SBS does not reach a noticeable level because it grows from noise in the absence of the seed from the reflected light. Under normal incidence, a beam with such intensity would produce a significant angular spreading and a red frequency shift in the reflected light (see Figs. 95.33 and 95.34).



If the intensity of an obliquely incident beam is increased to $\langle I \rangle_{14} = 9$, the characteristic gain for backward SBS becomes large enough ($G_{\text{SBS}} = 10.8$) to produce significant backward SBS from noise. The angular distribution of the reflected light for $\langle I \rangle_{14} = 9$, [Fig. 95.37(b)] has two broad maxima—one that corresponds to reflection from near-critical density and another that corresponds to backward SBS. The first maximum (near $k_{\perp}/k_{\text{ob}} = 0.3$) corresponds to the direction of the specular reflection of the incident beam. The time-integrated frequency spectrum for this part of the angular distribution [see Fig. 95.37(c)] shows no significant red shift. The other maximum of the angular distribution in Fig. 95.37(b) (near $k_{\perp}/k_{\text{ob}} = -0.3$) corresponds to the direction of backscatter from the incident beam. The time-integrated frequency spectrum for this part of the angular distribution [see Fig. 95.37(d)] is consistent with backward SBS. Light that is scattered back into the angular domain between the two maxima in Fig. 95.37(b) is not as intense as at these two maxima. Figures 95.37(c) and 95.37(d) illustrate that reflection from near-critical density and backward SBS both affect the spectra of backscattered light.

For oblique incidence, the optimal conditions for the electromagnetic seeding of backward SBS are provided by a pair of beams propagating in the same plane at the same angle of incidence. In this geometry, each beam after specular reflection provides a seed for backward SBS from the other beam. Figure 95.38 shows the angular distribution and the frequency spectrum of reflected light from a pair of beams each with

Figure 95.37

The angular distribution of reflected light (solid line) from a beam with an incidence angle of 20° and intensity (a) $\langle I \rangle_{14} = 6$ and (b) $\langle I \rangle_{14} = 9$. For comparison, each plot also shows the angular distribution of the backscattered light in the linear propagation regime (dashed line). The time-integrated frequency spectra of light reflected into the domain (c) $k_{\perp}/k_{\text{ob}} = -(0.2 \div 0.4)$ and (d) $k_{\perp}/k_{\text{ob}} = (0.2 \div 0.4)$ for intensity $\langle I \rangle_{14} = 9$.

intensity $\langle I \rangle_{14} = 4.5$ sent into the plasma at angles of $+20^\circ$ and -20° . In this case, the frequency spectrum and the angular distribution of reflected light are broader than for a single beam with an intensity equal to the total intensity of the two beams (see Figs. 95.37 and 95.38).

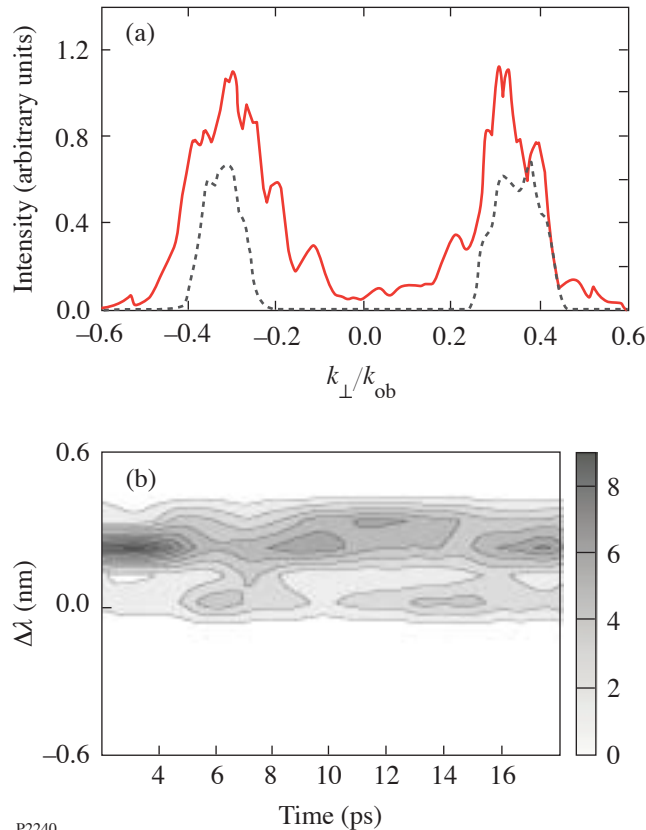


Figure 95.38 The angular distribution [solid line in (a)] and the frequency spectrum (b) of reflected light from a pair of beams with $\langle I \rangle_{14} = 4.5$ in each beam and the incidence angle of $\pm 20^\circ$. For comparison plot (a) also shows the angular distribution of the backscattered light in the linear propagation regime (dashed line).

Conclusions

Our simulations were performed for the typical parameters of direct-drive ICF plasmas.^{1,2,14} In the experiments,^{1,2,14} the red-shifted component in the frequency spectrum of the backscattered light was identified. The following features of the red-shifted component were reported: (a) The frequency shift of this component was not more than $\Delta\lambda = 0.5$ nm. (b) The addition of SSD smoothing moderately decreased the intensity of backscattered light—by not more than two times. (c) Experiments with the oblique incidence of laser beams demonstrated the dependence of the red component on the seeding by

reflection from the critical surface. All these experimentally observed features are in good agreement with the present simulation results.

In conclusion, we have studied the nonlinear propagation of randomized laser beams near the critical-density surface. Our model includes filamentation, forward and backward SBS, reflection of light from the critical-density surface, and the absorption of light. It is well suited to model the oblique incidence of laser beams on the critical-density surface and crossed-beam irradiation.

ACKNOWLEDGMENT

This work was supported by the U.S. Department of Energy Office of Inertial Confinement Fusion under Cooperative Agreement No. DE-FC03-92SF19460, the University of Rochester, and the New York State Energy Research and Development Authority. The support of DOE does not constitute an endorsement by DOE of the views expressed in this article.

REFERENCES

1. S. P. Regan, D. K. Bradley, A. V. Chirikikh, R. S. Craxton, D. D. Meyerhofer, W. Seka, R. W. Short, A. Simon, R. P. J. Town, B. Yaakobi, J. J. Carroll III, and R. P. Drake, *Phys. Plasmas* **6**, 2072 (1999).
2. W. Seka, H. A. Baldis, J. Fuchs, S. P. Regan, D. D. Meyerhofer, C. Stoeckl, B. Yaakobi, R. S. Craxton, and R. W. Short, *Phys. Rev. Lett.* **89**, 175002 (2002).
3. J. Fuchs *et al.*, *Phys. Rev. Lett.* **88**, 195003 (2002).
4. A. V. Maximov, I. G. Ourdev, D. Pesme, W. Rozmus, V. T. Tikhonchuk, and C. E. Capjack, *Phys. Plasmas* **8**, 1319 (2001).
5. M. N. Rosenbluth, *Phys. Rev. Lett.* **29**, 565 (1972).
6. E. J. Valeo and K. G. Estabrook, *Phys. Rev. Lett.* **34**, 1008 (1975).
7. R. S. Craxton and R. L. McCrory, *J. Appl. Phys.* **56**, 108 (1984).
8. Y. Kato *et al.*, *Phys. Rev. Lett.* **53**, 1057 (1984); Y. Lin, T. J. Kessler, and G. N. Lawrence, *Opt. Lett.* **20**, 764 (1995).
9. S. Skupsky, R. W. Short, T. Kessler, R. S. Craxton, S. Letzring, and J. M. Soures, *J. Appl. Phys.* **66**, 3456 (1989).
10. H. A. Rose and D. F. DuBois, *Phys. Fluids B* **5**, 590 (1993).
11. H. A. Rose and D. F. DuBois, *Phys. Rev. Lett.* **72**, 2883 (1994).
12. D. Pesme, W. Rozmus, V. T. Tikhonchuk, A. Maximov, I. Ourdev, and C. H. Still, *Phys. Rev. Lett.* **84**, 278 (2000).
13. H. A. Rose, *Phys. Plasmas* **2**, 2216 (1995).
14. W. Seka, S. P. Regan, D. D. Meyerhofer, B. Yaakobi, C. Stoeckl, R. S. Craxton, R. W. Short, H. Baldis, J. Fuchs, and C. Labaune, *Bull. Am. Phys. Soc.* **46**, 283 (2001).

Time-Resolved Photoresponse in the Resistive Flux-Flow State in Y-Ba-Cu-O Superconducting Microbridges

Introduction

High-temperature superconductors (HTS's) exhibit many properties that are very desirable for microwave-based telecommunication applications. Their main advantages are low absorption at microwave frequencies¹ and existence of HTS microwave devices based on the controlled vortex flux flow.² The most-promising material is the $\text{YBa}_2\text{Cu}_3\text{O}_{7-x}$ (YBCO) superconductor because of its well-developed technology for the fabrication and patterning of very high quality epitaxial thin films, as well as the ability to produce multilayer microstructures. YBCO is characterized by a very large critical current density $J_c > 2$ to 3 MA/cm^2 at nitrogen temperatures³ and exhibits ultrafast (~ 1 -ps) voltage photoresponse when optically excited with femtosecond laser pulses.⁴ Thus, YBCO thin films and microstructures are good candidates for generating high-power and jitter-free ultrafast electrical transients for ultrawide-frequency-band antennas⁵ for mobile communication systems. The ultrawide-band signals can be reflected by any conductor or insulator with dimensions fitting the wavelength of the signal. Therefore, the GHz-bandwidth, jitter-free pulse-driven antennas are desirable devices for high-resolution pulsed-radar systems, operating with a high (GHz) repetition rate of probing signals.

When light is incident on a superconductor, photons with an energy much larger than the superconductor energy gap 2Δ will break Cooper pairs, resulting in the appearance of highly excited quasiparticles. These excited (hot) carriers thermalize within tens of femtoseconds and, subsequently, relax their excess energy through the electron–phonon interaction process. During the relaxation, the number of excited quasiparticles becomes significantly larger than their equilibrium value, leading to a suppressed 2Δ value and a nonequilibrium condition in the entire sample. In the space domain, the 2Δ reduction resulting from the photon absorption generates a so-called “hotspot,” a localized region where superconductivity is highly suppressed or even completely destroyed.⁶

The incoming photons can also generate quantized vortex–antivortex pairs (i.e., oppositely directed fluxons),⁷ which can

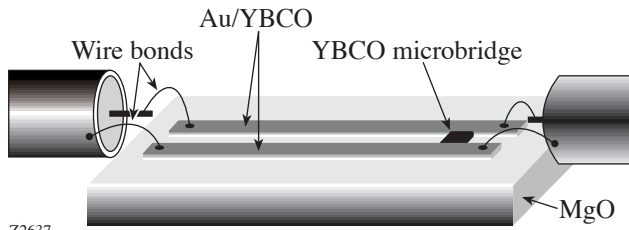
get de-pinned and start moving one toward the other transversely to the direction of the current flow, resulting in a voltage signal. When the temperature inside the optically excited hotspot exceeds the Kosterlitz–Thouless (vortex unbinding) temperature $T_{KT} \sim E_{vp}/k_B$ (where E_{vp} is a minimum energy needed to create a vortex–antivortex pair and k_B is the Boltzmann constant), the vortex–antivortex interaction can get screened, leading to the appearance of essentially unbound single vortices, whose motion brings resistance in the superconducting thin film.⁷ At lower temperatures, vortex pairs can be de-pinned by applying a bias current I that exceeds the critical current I_c . In this latter case, the superconductor is transferred into a resistive flux state when the Lorentz force exceeds the collective pinning force and bundles of vortices move, leading to a voltage signal across the superconductor.⁸

The aim of this work is to investigate ultrafast voltage transients in optically thick YBCO superconducting microbridges biased with supercritical ($I > I_c$), nanosecond-in-duration current pulses and, simultaneously, excited with femtosecond optical pulses. The above experimental arrangement allowed us to study the superconductor photoresponse in the resistive flux-flow state. The photoresponse voltage transients were recorded, and their amplitude versus bias current, laser fluence, and hotspot area were investigated. The maximal repetition rate of light-triggered YBCO bridges for applications as high-power, jitter-free, electrical pulse generators has been determined. The next section presents the test sample configuration and our experimental setup designed for time-synchronized, simultaneous electrical and optical excitations of YBCO microbridges. The last two sections present our experimental results and the summary and conclusions of our work.

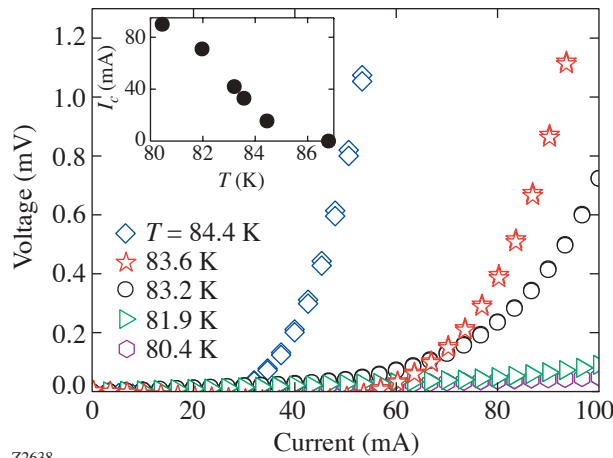
Sample Design and Experimental Setup

Our experimental samples consisted of $50\text{-}\mu\text{m}$ -long, $25\text{-}\mu\text{m}$ -wide microbridges, patterned in epitaxial 200-nm -thick YBCO films, laser ablated onto MgO substrates. The bridges were placed across $150\text{-}\mu\text{m}$ -wide, Au-covered, YBCO coplanar transmission lines (CTL), as shown in Fig. 95.39. The test structures were characterized by a zero-resistance transi-

tion temperature $T_{c0} = 86.8$ K and a transition width $\Delta T = 0.8$ K. Figure 95.40 presents the family voltage versus current $V(I)$ characteristics of our microbridge, taken at several temperatures below T_c . The resistive state with flux-creep behavior, seen as the power-law $V \sim I^n$ dependence, is clearly visible with no hysteresis upon the current ramping. The inset in Fig. 95.40 shows the $I_c(T)$ dependence near T_c . The lower-temperature measurements showed that J_c was > 3 MA/cm² at 77 K.



Z2637

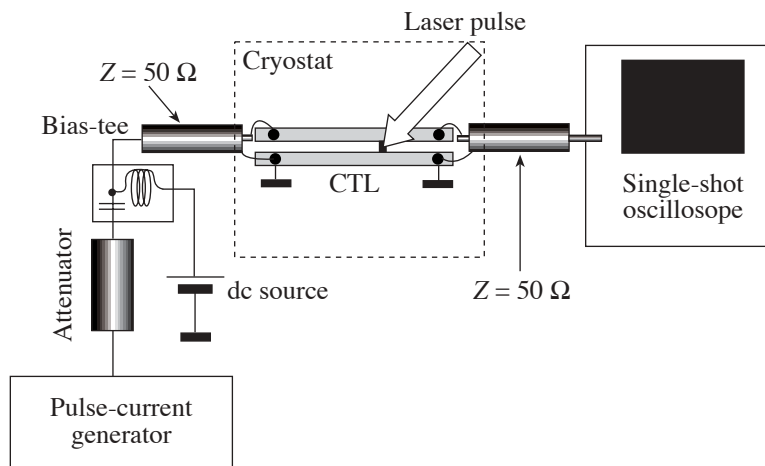


Z2638

Our experimental setup for transient photoresponse measurements of YBCO microbridges biased with supercritical current pulses is shown in Fig. 95.41. The YBCO microbridge was mounted on a cold finger, inside a temperature-controlled, continuous-flow helium cryostat. Nanosecond electrical pulses were delivered from a current generator via a semirigid coaxial cable wire-bonded to the CTL (see also Fig. 95.39). The dc bias was provided from an independent, stable current source and was combined with the pulses via a broadband bias-tee. The

Figure 95.39 Schematic of a 50- μ m-long, 25- μ m-wide YBCO microbridge incorporated into the Au-covered YBCO coplanar transmission lines used in our experiments.

Figure 95.40 Voltage versus current characteristics of our YBCO microbridge. The measurement was performed in a two-point configuration, and, subsequently, the constant, temperature-independent resistance of the contacts was numerically subtracted. The inset shows the I_c dependence on temperature in a region close to T_c .



Z2639

Figure 95.41 Experimental setup for optical excitation of a superconducting YBCO microbridge, biased with nanosecond-duration current pulses delivered from an electronic pulse generator.

A 3-GHz-bandwidth, single-shot oscilloscope (input impedance of 50Ω) was used to register transient photoresponse signals. The oscilloscope was connected with the sample via a second semirigid coaxial cable wire-bonded to the CTL. The experimental-system time resolution of our recorded transients was approximately 100 ps.

Synchronously with the electrical pulse bias, our superconducting microbridges were illuminated with 100-fs-wide, 810-nm-wavelength optical pulses, picked from an 82-MHz-repetition-rate train of pulses generated by a commercial Ti:sapphire laser. Both the current-pulse generator and the oscilloscope were synchronized with the laser system with the common repetition rate divided down to 32 kHz. The experiments were performed in the temperature range between 80 K and T_c , with the bulk of the data collected at 80.5 K, where the photoresponse was the largest and the influence of the temperature shift, due to laser heating, was minimized. The temperatures below 80 K were difficult to access since the very large values of I_c (well over 100 mA) in our samples required the generation of supercritical pulses with amplitudes exceeding the capabilities of our current-pulse generator.

Experiment Results

An ultrafast voltage transient of the optically excited, current-pulse-biased YBCO microbridge is shown in Fig. 95.42. The bridge was kept at $T = 80.5$ K and biased with a 10-ns-long current pulse with an amplitude of $I = 1.1 I_c$. The main, 10-ns-

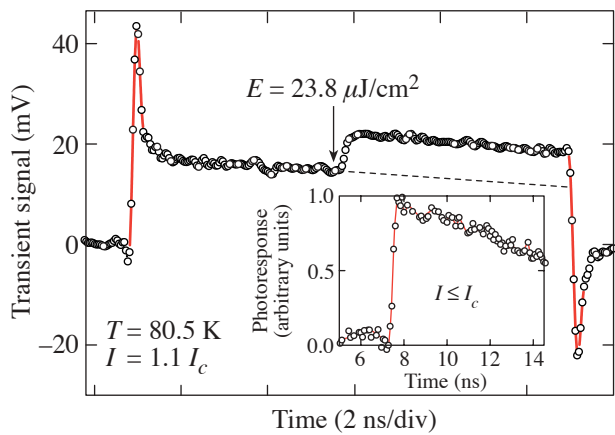


Figure 95.42 Voltage transient generated by a YBCO microbridge, maintained at $T = 80.5$ K, biased with a 10-ns-long current pulse with amplitude $I = 1.1 I_c$ and, simultaneously, excited with a 100-fs optical pulse. The arrow shows the arrival of the optical pulse. The inset presents the photoresponse relaxation when the microbridge was biased with the $I \leq I_c$ current pulse.

long signal, with sharp spikes at the beginning and the end due to the sample inductance, corresponds to the YBCO resistive response to the supercritical current-bias pulse. The arrival of an optical pulse (marked by an arrow in Fig. 95.42) with a fluence of $23.8 \mu\text{J}/\text{cm}^2$ produced an additional voltage response (photoresponse V_{photo}) with a rise time of less than 100 ps (resolution limit of our experimental setup) and an amplitude of ~ 7 mV. We note that there is apparently no relaxation in the V_{photo} transient and the sample remains in the higher-voltage state (see the dashed line indicating the continuation of the electrical transient) until the end of the electrical pulse.

If we assume, for the moment, that the main impact of the light absorption by our YBCO microbridge in the resistive state is just simple heating, we can quickly estimate the magnitude of the heat-generated V_{photo} . The incident fluence of $23.8 \mu\text{J}/\text{cm}^2$ (average power 13.8 mW) should increase the temperature of our bridge by 2.2 K, based on the estimated average temperature increase of 0.16 K/mW, for the 200-nm-thick YBCO uniformly absorbing 810-nm illumination. Analyzing the 80.4-K $V(I)$ curve shown in Fig. 95.40, the 2.2-K change in temperature should lead to an almost negligible voltage increase across the sample. Since the V_{photo} signal in Fig. 95.42 is ~ 7 mV, we can reject the simple-heating model and conclude that the photoresponse must be associated with an optically induced change in the resistive flux state of the microbridge. Photons assist the bias current in the de-pinning of additional vortices in the YBCO film and result in a transition into a higher-voltage state.

The vortex photoresponse model is also consistent with the time evolution of the V_{photo} transient. The signal rise time is very short (< 100 ps), indicating an electronic rather than heat-type interaction, and the fact that there is no relaxation after the optical excitation shows that the bridge was optically switched into a new flux state and remained there until the end of the electric pulse, which turned off the resistive state in our microbridge. The latter behavior is very different from the nanosecond-long phonon relaxation observed in the photoresponse of YBCO microbridges current driven into the purely resistive state.⁴ In addition, the inset in Fig. 95.42 shows V_{photo} for $I \leq I_c$ (below the edge of the flux-flow state). In this case, the photoresponse is due to the Cooper pair breaking, electron cooling, and the subsequent escape of phonons from the film.⁹ As expected, in the inset, the signal relaxes back to the initial level with a decay time of the order of 20 ns—the time scale characteristic for a phonon-escape-type cooling process.

The amplitude of the photoresponse as a function of the normalized current-pulse bias is shown in Fig. 95.43. We note that, initially, the V_{photo} amplitude increases very rapidly, reaches the broad maximum value of ~ 15 mV in the $1.4 < I/I_c < 2.0$ range, and starts to decrease above $2.0 I_c$. The above behavior again excludes simple heating; as in the latter case, the resistive/heating contribution would remain constant and result in a linear increase of V_{photo} as a function of I/I_c . On the other hand, in the vortex photoresponse model, the V_{photo} signal should depend on the vortex velocity v of our YBCO microbridge $v = 2\pi J \rho_n \xi_{a-b}^2 / \Phi_0$, where ρ_n is the normal-state (100-K) resistivity of the microbridge, $\xi_{a-b} = 2.5$ nm (Ref. 10) is the YBCO superconducting coherence length along the a - b direction, $\Phi_0 = 2.07 \times 10^{-15}$ Wb is the flux quantum, and J is the bridge bias current density. Simple calculation shows that for $\rho_n = 1$ m Ω cm and $I = 1.43 I_c$, $v = 2.8 \times 10^4$ cm/s, which is a very reasonable value for current-biased YBCO thin films.¹¹ For very large I/I_c values, V_{photo} decreases, which must be related to the vortex-velocity decrease associated with vortex-vortex interactions and vortex-antivortex recombination, as well as the reduction of the volume of the superconducting phase. The data presented in Fig. 95.43 allowed us to calculate the voltage responsivity R_V of our YBCO bridge, defined as the ratio of the V_{photo} amplitude to the optical power per pulse incident on the device. The maximal value of R_V , corresponding to the V_{photo} maximum in Fig. 95.43, was found to be $4.3 \mu\text{V}/\text{W}$.

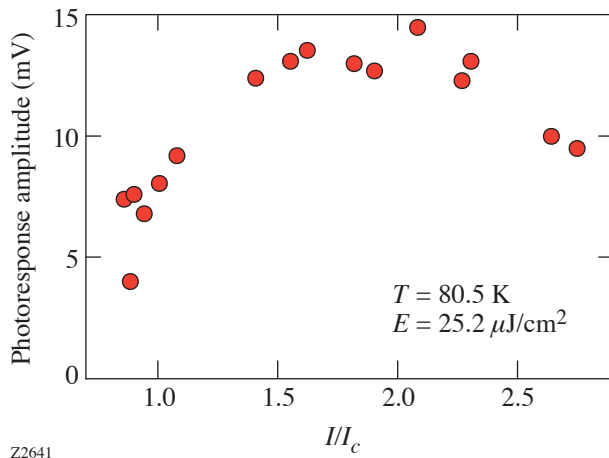


Figure 95.43
The photoresponse amplitude of a YBCO microbridge as a function of the normalized amplitude of the current bias pulse.

Figure 95.44 presents the V_{photo} amplitude dependence on the number of photons incident on the microbridge under uniform illumination, for the bias $I = 1.43 I_c$. The amplitude increases very rapidly with the laser-fluence increase, reaching a 13.6-mV saturation value at the $5.9\text{-}\mu\text{J}/\text{cm}^2$ fluence. Clearly, this dependence must reflect the process of light-induced generation of vortex-antivortex pairs in our microbridge. The minimal energy E_{vp} needed to create a vortex-antivortex pair in a YBCO superconducting film can be expressed as $E_{\text{vp}} \sim \Phi_0^2 d / (2\pi\mu_0\lambda^2)$, where $\mu_0 = 4\pi \times 10^{-7}$ H/m is a permeability of free space, λ is a magnetic penetration depth, and d is the film thickness. Thus, we have, in our case, $E_{\text{vp}} \approx 0.65$ eV for $d = 200$ nm and $\lambda = 1 \mu\text{m}$.⁷ Taking into account that an average radius of single vortex equals ξ_{a-b} , the maximal number of vortex-antivortex pairs generated in our microbridge is $\sim 6.4 \times 10^7$. This latter value corresponds to the onset of saturation of the photoresponse observed in Fig. 95.44; therefore, we can conclude that under our experimental conditions (sample geometry, current bias, etc.) higher laser fluence could not produce additional moving vortices in our YBCO microbridge and the excess light was, apparently, absorbed by the normal phase (free carriers) and converted into joule heating. The high-fluence saturation effect lets us predict that superconducting films with an artificially increased number of pinning centers⁸ should exhibit higher amplitudes of V_{photo} transients since, in this latter case, the flux-flow state before optical activation would be of lower level due to the increased pinning force.

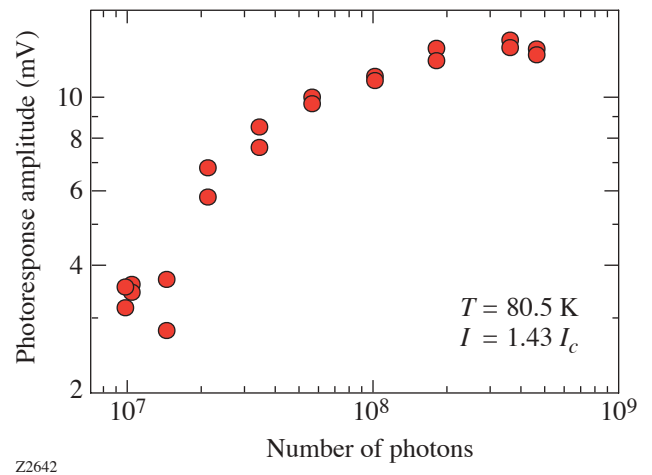


Figure 95.44
The photoresponse amplitude of a YBCO microbridge as a function of the number of photons incident on the structure.

As expected, the photoresponse of the YBCO microbridge was found to be sensitive to the diameter of the laser beam incident on the bridge. Optical imaging experiments have been done at $T = 80.5$ K with a constant average optical power of 33 mW and a beam diameter ranging from 10 μm to 100 μm . The results shown in Fig. 95.45 demonstrate that the V_{photo} amplitude increased with the increase of the spot size, exhibiting a maximum when a whole surface of the YBCO bridge is illuminated. Further opening of the optical beam resulted in a V_{photo} decrease since part of the optical energy could not excite the superconductor. The latter behavior is in very good quantitative agreement with the V_{photo} dependence on the number of photons incident on the bridge presented in Fig. 95.44.

When the laser beam was focused into a spot with a diameter smaller than the bridge width, photons could create vortices only within the excited hotspot area; the surplus of optical energy was, apparently, dissipated through electron-phonon interaction and diffused as heat toward unilluminated parts of the superconductor. It is worth noting that I_c variations over the sample length could also account for the V_{photo} growth with the hotspot-size growth. This latter line of thought was used to explain small-angle neutron-scattering measurements in Pb-In superconductors with an inhomogeneous surface.⁸ It was shown that in the case of superconducting domains possessing different I_c 's, regions with lower I_c 's were character-

ized by larger vortex velocities since v was proportional to $I - I_c$. We believe, however, that our films are uniform and, for the fixed current bias, v is constant, as was discussed in connection with Fig. 95.43.

The maximum repetition rate of the photoresponse generated by our YBCO microbridge can be estimated by progressively reducing the width of the supercritical biasing pulse, while maintaining synchronization of the optical pulse. Figure 95.46 presents the V_{photo} signal on top of the 1-ns-wide biasing transient. The minimum width of V_{photo} that we could resolve was ~ 100 ps, resulting in the maximum repetition rate in the GHz-frequency range. The main limitation on the maximum repetition rate of the vortex photoresponse signal comes actually not from optical triggering, but from the delay time t_d of the formation of the resistive state in a superconductor excited by a supercritical current pulse.^{12,13} In Ref. 12, for 20-ns-wide supercritical pulses, t_d was limited by the phonon escape time and was of the order of nanoseconds. For our 1-ns-wide current pulses with a rise time and a fall time of 47 ps and 110 ps, respectively, $t_d = 210$ ps for $I \sim I_c$ and decreased down to 140 ps when $I = 1.5 I_c$. Clearly, our much faster supercritical perturbations lead to the nonequilibrium state in YBCO; t_d in this case was limited by ~ 1 -ps electron-phonon interaction time and is predicted to be of the order of hundreds of picoseconds,¹⁴ in agreement with our measurements. Independently, following Ref. 15, one could attribute the very short value of

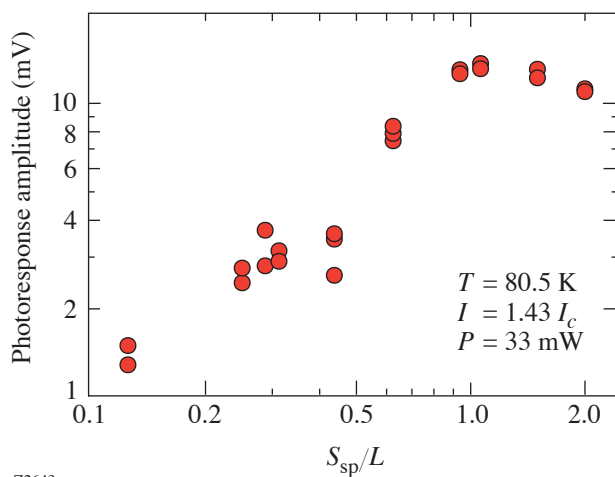


Figure 95.45
The photoresponse amplitude of a YBCO microbridge as a function of the laser beam diameter, normalized to the microbridge length.

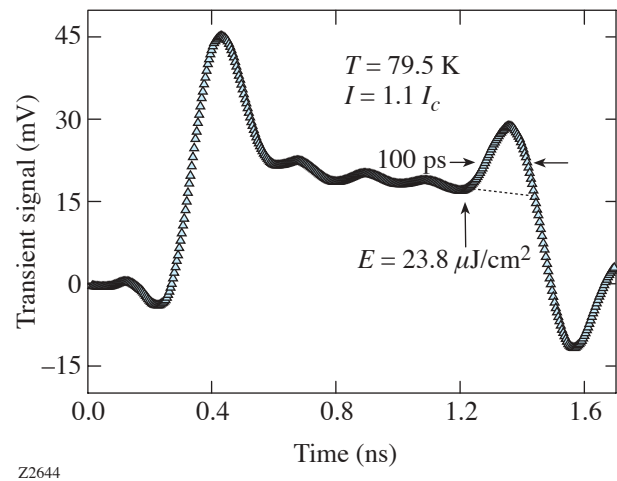


Figure 95.46
Voltage transient generated by a YBCO microbridge biased with a 1-ns-wide current pulse with amplitude $I = 1.1 I_c$ and, simultaneously, excited with a 100-fs optical pulse. The arrow shows the arrival of the optical pulse. The photoresponse signal is approximately 100 ps wide.

t_d to the ultrafast magnetic diffusion process when the superconducting bridge is transferred to the flux-flow state. More research is needed to understand the nonequilibrium switching dynamics of YBCO under the picosecond-wide, supercritical current-pulse perturbation, but this subject goes beyond the scope of this article.

Summary and Conclusions

We have demonstrated the photoresponse effect in YBCO microbridges driven into the resistive flux state by nanosecond-wide supercritical current pulses and synchronously excited with femtosecond optical pulses. It has been shown that the dynamics of the photoresponse is directly related to the motion of vortices in the superconductor. The amplitude of the photoresponse signal can be increased by a factor of 3 when the bias current increases from I_c to $1.9 I_c$, corresponding to the vortex velocity of $\sim 3 \times 10^4$ cm/s. The photoresponse amplitude also increased with the increase of the laser fluence incident on the device and reached the saturated value when light illuminated the entire microbridge, simultaneously producing the maximal number of vortex-antivortex pairs generated in our microbridge. The above conditions corresponded to the maximal value of the bridge voltage responsivity, which was calculated to be $\sim 4 \mu\text{V/W}$. The time-resolved measurements of the vortex photoresponse dynamics showed that signals as short as ~ 100 ps (our experimental resolution limit) could be generated, providing that synchronization with electrical bias pulses was preserved. From the applied point of view, we demonstrated that the YBCO superconductor in the flux-flow state can operate as a GHz-rate, high-power optically triggered switch at supercritical bias current pulses as high as $2 I_c$.

ACKNOWLEDGMENT

The authors thank Grzegorz Jung from the Ben Gurion University for valuable discussions. This work was supported by the National Science Foundation Grant DMR-0073366 and the U.S.–Israel Binational Science Foundation Grant No. 2000164. A. J. acknowledges support from the Fulbright Scholar Program.

REFERENCES

1. M. J. Lancaster, *Passive Microwave Device Applications of High Temperature Superconductors* (Cambridge University Press, New York, 1997) and references therein.
2. P. E. Goa *et al.*, Appl. Phys. Lett. **82**, 79 (2003).
3. A. Abrutis, J. P. Sénateur, F. Weiss, V. Kubilius, V. Bigelyte, Z. Saltyte, B. Vengalis, and A. Jukna, Supercond. Sci. Technol. **10**, 959 (1997).
4. M. Lindgren, M. Currie, C. Williams, T. Y. Hsiang, P. M. Fauchet, R. Sobolewski, S. H. Moffat, R. A. Hughes, J. S. Preston, and F. A. Hegmann, Appl. Phys. Lett. **74**, 853 (1999).
5. A. Jukna, J. Phys. IV, Proc. **11**, Pr11-151 (2001).
6. A. M. Kadin and M. W. Johnson, Appl. Phys. Lett. **69**, 3938 (1996).
7. A. M. Kadin *et al.*, Appl. Phys. Lett. **57**, 2847 (1990).
8. A. Pautrat *et al.*, Phys. Rev. Lett. **90**, 087002 (2003).
9. See, e.g., A. D. Semenov, G. N. Gol'tsman, and R. Sobolewski, Supercond. Sci. Technol. **15**, R1 (2002).
10. P. P. Nguyen *et al.*, Phys. Rev. B, Condens. Matter **48**, 1148 (1993).
11. S. G. Doettinger *et al.*, Phys. Rev. Lett. **73**, 1691 (1994).
12. G. Sabouret, C. Williams, and R. Sobolewski, Phys. Rev. B, Condens. Matter **66**, 132501 (2002).
13. F. S. Jelila *et al.*, Phys. Rev. Lett. **81**, 1933 (1998).
14. C. Williams, G. Sabouret, and R. Sobolewski, IEICE Trans. Electron. **E85-C**, 733 (2002).
15. Y. S. Cha and T. R. Askew, Physica C **302**, 57 (1998).

Ultrafast and Highly Sensitive Photodetectors Fabricated on High-Energy-Nitrogen-Implanted GaAs

An ion-implantation technique has been employed in the GaAs photodetector technology to obtain materials with a carrier lifetime in the picosecond and even subpicosecond regimes. Properties of proton,¹ Ar⁺,^{2,3} As⁺,^{4–6} and other ion-implanted GaAs have been investigated thoroughly. Nitrogen-ion-implanted GaAs (N⁺-GaAs) is a relatively new member in the family of ion-implanted GaAs materials. The implantation of nitrogen into GaAs was initially done to get a diluted ternary semiconductor GaAsN. Optical properties of GaAsN, such as photoluminescence⁷ and N⁺-induced band-gap reduction,⁸ have been studied. It was also noted that high-energy implantation of N⁺ ions produced a highly resistive material after high-temperature annealing.⁹ The aim of this article is to present the preparation and properties of metal–semiconductor–metal (MSM) photodetectors fabricated on high-energy-N⁺-implanted GaAs and demonstrate the performance improvement of these devices, as compared with those fabricated on low-temperature (LT)-grown GaAs.

We prepared the N⁺-GaAs material by implanting N⁺ ions with an energy E_{impl} of 700 keV and 880 keV, respectively, into 2- μm -thick, n -doped GaAs films grown by molecular beam epitaxy (MBE) on semi-insulating GaAs (001) substrates with resistivity $>10^7 \Omega \text{ cm}$ at 300 K. The implantation was performed in a linear, 900-kV accelerator,¹⁰ and the ion dose was $3 \times 10^{12} \text{ cm}^{-2}$. Figure 95.47 shows the implantation profiles of N⁺ ions in GaAs, calculated using the TRIM (transport of ions in matter) simulation program.¹¹ TRIM is the most widely used software to calculate the stopping and range of ions in matter. We note that for samples implanted with $E_{\text{impl}} = 700 \text{ keV}$ and 880 keV, the N⁺ ions reached a depth of 1250 nm and 1400 nm, respectively. Thus, in both cases, there is a thin nonimplanted layer of n -doped GaAs. This layer is expected to affect properties of our devices at very high bias voltages; it should not, however, influence our photoresponse measurements since the penetration depth of 810-nm photons is approximately 1 μm . In future devices, the contribution from the nonimplanted region, where the carrier lifetime is much longer and mobility much higher, could be minimized by implanting GaAs with higher energies and higher doses.

MSM structures, 10 μm wide and 20 μm long, with a finger width of 1 μm and finger spacing of 1.5 μm , were patterned on our two types of N⁺-GaAs materials, using conventional photolithography and a lift-off technique. The MSM devices consisted of Ti/Au contacts with a thickness of 10/160 nm. Next, the surfaces of our structures, except for the MSM area, were coated with 200 nm of SiO₂ to provide electrical insulation, and the external Ti/Au coplanar strip (CPS) lines with a thickness of 50/600 nm, needed for electrical measurements, were fabricated. To compare performance, several photodetectors with identical MSM geometries were also fabricated on LT-GaAs grown by MBE on semi-insulating GaAs substrates.

Figure 95.48 presents typical current–voltage (I – V) characteristics of both the N⁺-GaAs and LT-GaAs photodetectors measured in the dark at 300 K. The N⁺-GaAs devices exhibit

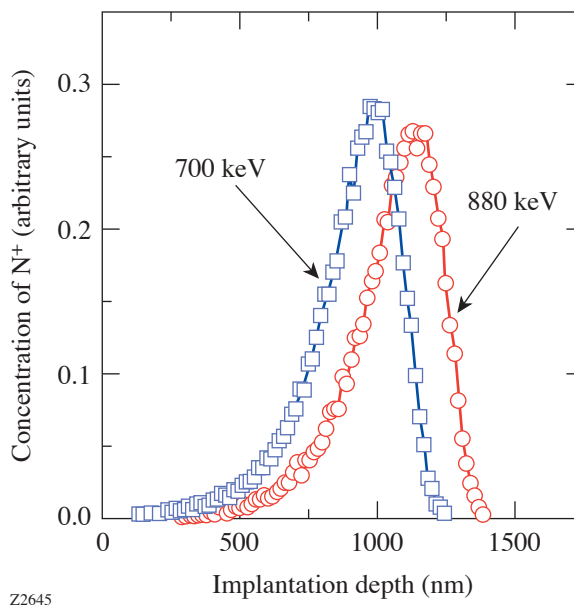


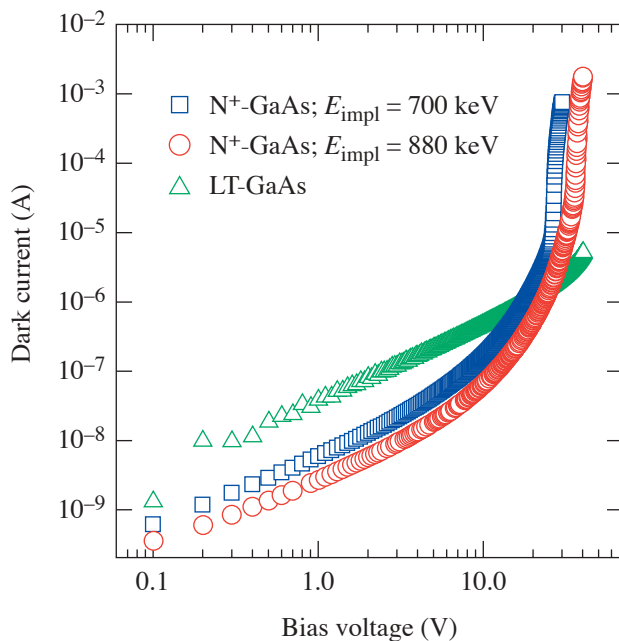
Figure 95.47 TRIM-simulated profiles of the penetration depth of implanted N⁺ ions into an n -doped GaAs film. Squares correspond to $E_{\text{impl}} = 700\text{-keV}$ GaAs and circles to $E_{\text{impl}} = 880 \text{ keV}$.

ohmic dependence up to a voltage bias $V_B \approx 6$ V and a quadratic dependence at higher biases. V_B up to 25 V and 32 V was applied to the 700-keV and 880-keV N^+ -GaAs MSM's, respectively, with no dielectric breakdown occurring. The rapid increase of the dark current at the highest V_B 's for our N^+ -GaAs photodetectors can be explained by carriers collected from the device's deep, nonimplanted region, where the conductivity is much higher. Note that the transition to the nonlinear part of the I - V occurs for the 880-keV device at somewhat higher V_B than that for the 700-keV N^+ -GaAs MSM, in accordance with the N^+ implantation profiles shown in Fig. 95.47. As expected, the LT-GaAs structures show ohmic behavior in the entire range of applied V_B (30 V max, corresponding to an average electric field of 200 kV/cm). However, their actual dark currents are significantly higher, especially at low V_B (<10 V), where the best performer, N^+ -GaAs MSM with $E_{impl} = 880$ keV, exhibits the lowest (below 10 nA) dark current.

Figure 95.49 shows the current responsivity of our N^+ -GaAs and LT-GaAs photodetectors versus the MSM bias. The devices were illuminated with continuous, 855-nm radiation from a laser diode. The beam spot was approximately

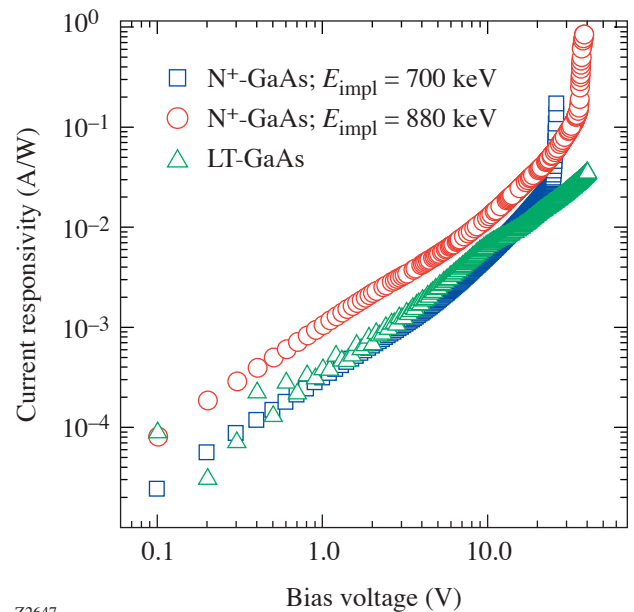
equal to the MSM active area, and the optical power incident on the photodetector was $P_{in} = 100 \mu\text{W}$. The responsivity was obtained by dividing the induced photocurrent (total current minus the dark current) by P_{in} . In comparison to the LT-GaAs device, our highly implanted N^+ -GaAs photodetector exhibited more than two times higher responsivity. At the very high bias, we observed in both of our N^+ -GaAs MSM's a drastic increase in the responsivity, which can be attributed to the partial penetration of 855-nm photons deeply into our structures and the collection of photocarriers from the nonimplanted regions of our devices.

All time-resolved photoresponse studies of our N^+ -GaAs and LT-GaAs devices were performed using 100-fs-wide, 810-nm-wavelength, 82-MHz-repetition rate optical pulses from a commercial Ti:sapphire laser. The photoresponse waveforms of our devices were recorded with the help of our electro-optic (EO) sampling system, using a total-internal-reflection LiTaO₃ microprobe, and featuring ~ 200 -fs temporal resolution.¹² The electrical transients were sampled at a spot on the CPS lines located approximately 30 μm away from the photodetectors. The time-resolved photoresponse waveforms of our devices are shown in Fig. 95.50. Under the same



Z2646

Figure 95.48
Dark I - V characteristics of the MSM photodetectors, fabricated on 700-keV N^+ -GaAs (squares), 880-keV N^+ -GaAs (circles), and LT-GaAs (triangles), respectively.



Z2647

Figure 95.49
Current responsivity of the three tested MSM photodetectors as a function of the bias voltage.

operating conditions, all of our photodetectors exhibited transients with the same 10%–90% risetime of 700 fs and the exponential falling edge with a $1/e$ decay time of ~ 2.5 ps. While the rise time is due to the $30\text{-}\mu\text{m}$ distance between the MSM and the probe beam spot, the 2.5-ps-long exponential pulse decay shows that the photoresponse dynamics is not limited by the subpicosecond carrier lifetime in either N^+ -GaAs or LT-GaAs, but corresponds to the capacitance of the MSM structure. Indeed, the calculated capacitive time constant¹³ of our photodetectors is 2.1 ps, in excellent agreement with the decay time of the transients shown in Fig. 95.50.

We note that superior responsivity of N^+ -GaAs devices translates into their high sensitivity. For $E_{\text{impl}} = 880$ keV, the N^+ -GaAs photodetector exhibits a signal peak amplitude as high as 2 V, when biased at 9 V and illuminated by an incident optical power, $P_{\text{in}} = 12$ mW. This amplitude value is more than 50% higher than that for our best LT-GaAs photodetector operated under the same conditions. Figure 95.51 presents the photoresponse amplitudes of the photoresponse transients of the three photodetectors as a function of P_{in} , with $V_B = 9$ V. We observe that all dependences are initially linear and gradually approach saturation. As we showed in Fig. 95.50, the photoresponse amplitudes of N^+ -GaAs devices are signifi-

cantly higher than the amplitude of the LT-GaAs device. They also start to saturate at significantly higher P_{in} values, looking almost linear within our tested range.

In conclusion, we have fabricated novel photodetectors based on high-energy-nitrogen-implanted GaAs. These devices show very low dark currents at low-voltage bias. These currents are almost two orders of magnitude lower than those in the best-known, commercially implemented LT-GaAs devices. Simultaneously, the current responsivity of our N^+ -GaAs photodetectors is significantly higher, as compared to LT-GaAs structures. The N^+ -GaAs devices also exhibit excellent sensitivity, with the 880-keV, N^+ -GaAs photodetector being the best performer. The latter photodetector has a peak photoresponse amplitude of up to 2 V. Under the illumination of 100-fs-wide and 810-nm-wavelength laser pulses, all tested photodetectors exhibited an ~ 2.5 -ps-wide photoresponse, limited by the MSM capacitive time constant. Our research shows that N^+ -GaAs photodetectors are very promising as highly sensitive photodetectors for high-speed applications, and they represent a cheaper alternative to LT-GaAs devices. The performance of N^+ -implanted GaAs photodetectors can be further improved by increasing the implantation depth, using higher E_{impl} and larger N^+ doses.

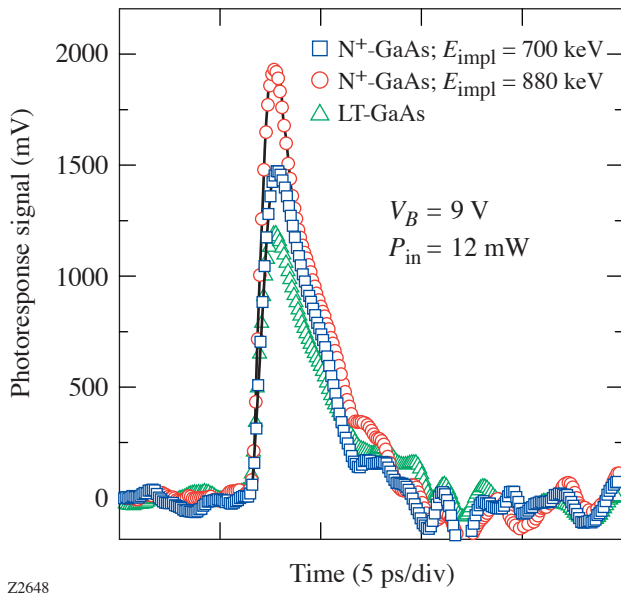


Figure 95.50

Transient photoresponse signals of the three tested MSM photodetectors, excited by 100-fs-wide, 810-nm optical pulses and recorded using the EO sampling system.

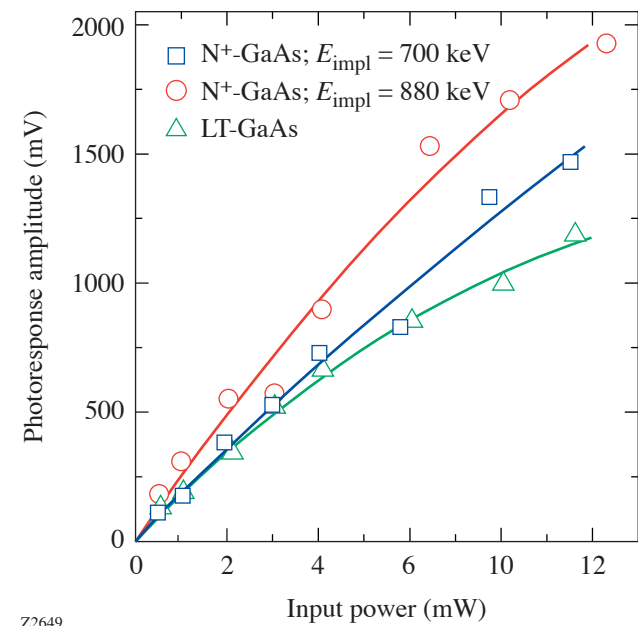


Figure 95.51

Photoresponse amplitudes of the photoresponse transients (Fig. 95.50) as a function of the bias voltage for the three tested MSM photodetectors. The solid lines are guides to the eye.

ACKNOWLEDGMENT

This work was supported by the National Science Foundation Grant INT-0078949 and by Corning Inc. Additional support was provided by NYSTAR through the Center for Electronic Imaging Systems at the University of Rochester.

REFERENCES

1. M. Lambsdorff *et al.*, Appl. Phys. Lett. **58**, 1881 (1991).
2. A. A. Kutas *et al.*, Mater. Sci. Eng. B **B34**, 32 (1995).
3. B. Breeger *et al.*, Nucl. Instrum. Methods Phys. Res. B **161**, 415 (2000).
4. A. Claverie, F. Namavar, and Z. Lilental-Weber, Appl. Phys. Lett. **62**, 1271 (1993).
5. F. Ganikhanov *et al.*, Appl. Phys. Lett. **67**, 3465 (1995).
6. H. Fujioka *et al.*, J. Appl. Phys. **78**, 1470 (1995).
7. X. Weng *et al.*, J. Appl. Phys. **92**, 4012 (2002).
8. W. Shan *et al.*, Appl. Phys. Lett. **75**, 1410 (1999).
9. J. F. Chen *et al.*, Appl. Phys. Lett. **76**, 2283 (2000).
10. P. Kováč, M. Pavlovič, and J. Dobrovodsky, Nucl. Instrum. Methods Phys. Res. B **B85**, 749 (1994).
11. J. F. Ziegler, J. P. Biersack, and U. Littmark, *The Stopping and Range of Ions in Solids*, The Stopping and Ranges of Ions of Matter, Vol. 1 (Pergamon Press, New York, 1985); see also <http://www.srim.org/>.
12. X. Zheng, Y. Xu, R. Sobolewski, R. Adam, M. Mikulics, M. Siegel, and P. Kordoš, Appl. Opt. **42**, 1726 (2003).
13. Y. C. Lim and R. A. Moore, IEEE Trans. Electron Devices **ED-15**, 173 (1968).

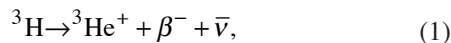
Tritiated Amorphous Silicon Betavoltaic Devices

Introduction

Hydrogenated amorphous silicon (a-Si:H) is an amorphous semiconductor whose optoelectronic properties, combined with its relatively low cost of fabrication, have made it an established material in semiconductor technology, particularly for photovoltaics and active matrix displays.^{1,2}

When prepared by conventional evaporation or sputtering, thin films of amorphous silicon contain a large concentration of defects and microvoids.^{3,4} These give rise to localized states in the energy gap of the material.^{3,4} Plasma-enhanced chemical vapor deposition (PECVD), using silicon hydrides, significantly reduces the number of defects and thereby lowers the concentration of localized states in the energy gap.³⁻⁵ It is well known that hydrogen is responsible for defect passivation.³⁻⁵ Hydrogen atoms incorporated into these films satisfy the covalent bonds at defects and microvoids and also allow the lattice to relax, thereby reducing the density of localized states by several orders of magnitude.³⁻⁵

Tritium (T) is an isotope of hydrogen and is expected to readily replace hydrogen in a-Si:H.⁶ Tritium is radioactive and undergoes beta decay according to the following reaction:



where β^- is a beta particle and $\bar{\nu}$ is an antineutrino. The antineutrino is essentially undetectable; thus tritium is considered to be a pure beta emitter. The half-life of tritium is 12.3 years, or equivalently the decay rate of tritium is $1.78 \times 10^{-9} \text{ s}^{-1}$. Accordingly, 1 cm^3 of tritium at standard temperature and pressure has an activity of 2.6 Ci. The kinetic energy spectrum of beta particles produced from the decay of tritium is shown in Fig. 95.52.⁷ The maximum energy of the beta particles is 18.6 keV while the average energy is 5.7 keV. Considering the energy distribution, the power available from the kinetic energy of the beta particles is $33.7 \mu\text{W}/\text{Ci}$.

In theory, for 1 at. % of tritium in silicon, the power released in a $1\text{-}\mu\text{m}$ film of tritiated amorphous silicon (a-Si:H:T) will be $0.08 \mu\text{W}/\text{cm}^2$. The average range of a 5.7-keV beta particle in silicon is $0.17 \mu\text{m}$; thus most of this power is trapped in the film. The incorporation of tritium into a-Si:H is expected to give rise to a family of devices in which the energy output of the radioactive process of tritium decay is integrated with the optoelectronic properties of a-Si:H.

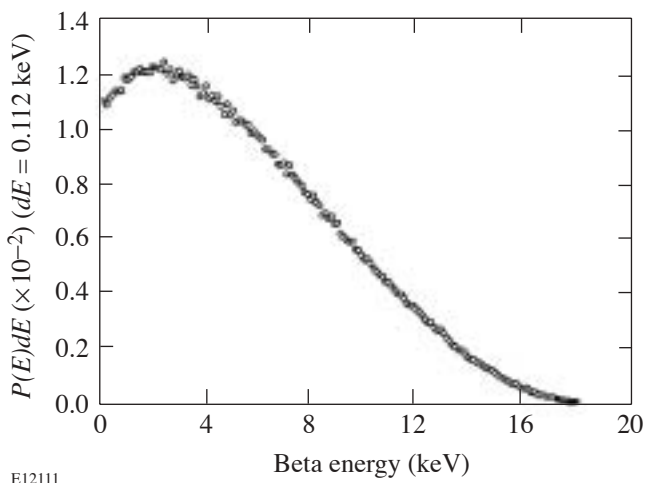


Figure 95.52
Kinetic energy spectrum of beta particles produced from the decay of tritium.⁷

Deposition of Tritiated Amorphous Silicon

A schematic of the saddle-field glow-discharge facility for the preparation of tritiated amorphous silicon is shown in Fig. 95.53. The deposition chamber is outfitted with three coarse stainless steel mesh electrodes, as shown. A glow discharge is created between the central electrode (the anode) and the outer two electrodes (the cathodes). A heated, electrically isolated substrate holder is mounted in the chamber. The substrate holder can be electrically biased.

Silane, diborane, and phosphine are available through a common port on the chamber. Tritium, which is stored as a tritide on a depleted uranium bed, is available through another port on the chamber. Each gas source is equipped with a mass-flow controller to permit independent control of flow. Evacuation of the deposition facility is provided by an oil-free system, which consists of a molecular drag pump and a diaphragm pump. A scrubber system, positioned between the two vacuum pumps, is used to strip tritium from the chamber effluent. The deposition system is housed in a nitrogen-atmosphere glovebox.

The four deposition conditions used to grow the samples that are discussed in this article are listed in Table 95.III.

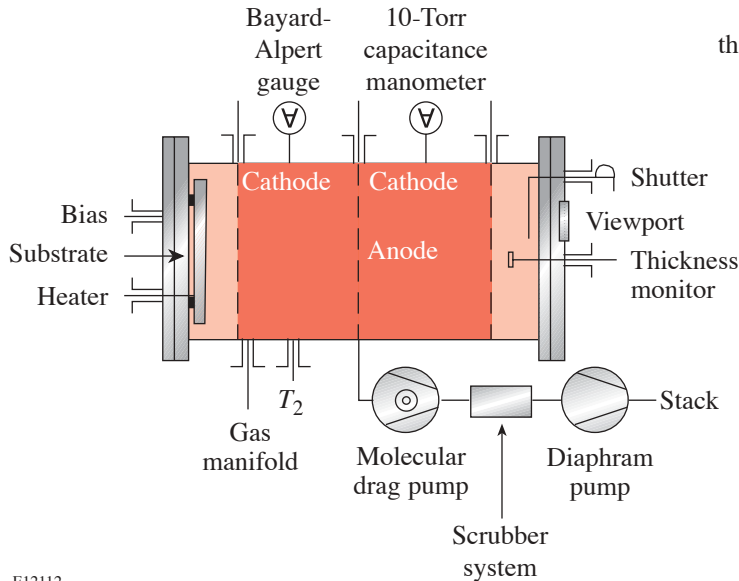


Figure 95.53

Saddle-field glow-discharge apparatus for the preparation of tritiated amorphous semiconductors.

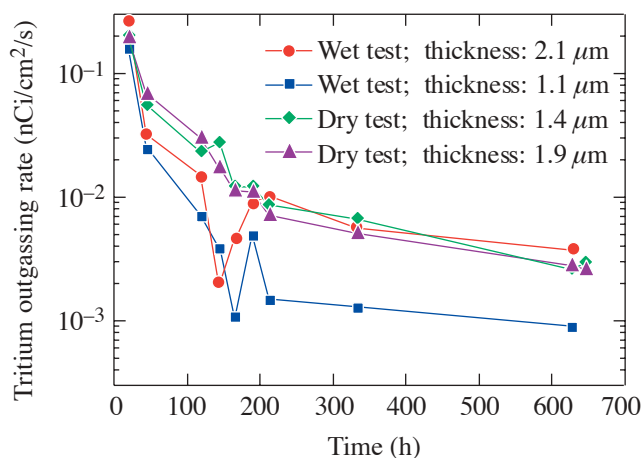
E12112

Table 95.III: Deposition conditions of the samples described in this article.

| | Deposition A | Deposition B | Deposition C | Deposition D |
|---|---------------------------|---------------------------|---------------------------|--|
| Gas flow | 2.5 sccm SiH ₄ |
| | 2.5 sccm T ₂ |
| Pressure | 50 mTorr | 50 mTorr | 50 mTorr | 50 mTorr |
| Anode potential | 700 to 710 V | 610 to 650 V | 580 to 620 V | 1010 to 1120 V ^(a) 590 to 600 V ^(b) |
| Anode current | 4 mA | 4 mA | 30 mA | 22 to 24 mA ^(a) 30 mA ^(b) |
| Substrate potential | Ground | Ground | Ground | Floating 350 V ^(a) , 280 V ^(b) |
| Substrate current | 0.4 mA | 0.4 mA | 7 to 8 mA | — |
| Substrate temperature | 300°C | 225°C | 150°C | 150°C |
| Samples described in this article | N/A | A69 | A155, A170, G181 | A206, A212, A214 |
| (a) During the first half of deposition. | | | | |
| (b) During the second half of deposition. | | | | |

Tritium Outgassing

The rate of tritium outgassing, at room temperature, from as-deposited tritiated amorphous silicon films [5 to 10 at. % of tritium, as measured by infrared spectroscopy (see Fig. 95.57)] was estimated by measuring the evolution of tritiated water from a number of a-Si:H:T samples under dry and wet or humid air ambient, as described in Ref. 8. Experimental results show that after approximately 600 h of outgassing, the total quantity of tritium desorbed from each of the samples is less than $40 \mu\text{Ci}/\text{cm}^2$. The cumulative tritium desorption under dry and wet conditions is of the same order of magnitude. This suggests that to first order, HTO is the predominant desorbing species. The rate of tritium outgassing for four samples at room temperature is shown in Fig. 95.54. The rate of outgassing is comparable for samples in dry and wet atmospheres. The a-Si:H:T samples show an initial outgassing rate of the order of $200 \text{ pCi}/\text{cm}^2/\text{s}$. After about 600 h of outgassing, the tritium outgassing rate appears to approach a value of less than $10 \text{ pCi}/\text{cm}^2/\text{s}$ or less than one part in 10^9 s^{-1} from a $1\text{-}\mu\text{m}$ film with 5 at. % of tritium. This suggests that the top few monolayers of the film are the source of the outgassing tritium.



E12113

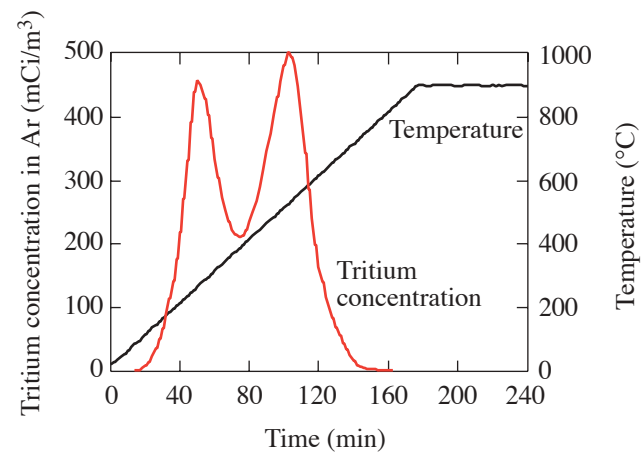
Figure 95.54
Outgassing rate from four a-Si:H:T films from deposition D (see Table 95.III).

Effusion of Tritium

Samples of a-Si:H:T were subjected to linear temperature ramping from room temperature to approximately 900°C in an argon purge. The experimental setup for tritium effusion measurements is described elsewhere.⁹ The effusion experiments were carried out at temperature ramp rates of 5, 10, 20, and $40^\circ\text{C}/\text{min}$. The tritium evolution data for two samples grown at two different substrate temperatures are shown in Figs. 95.55 and 95.56. The thickness of the samples was $\sim 0.8 \mu\text{m}$ for

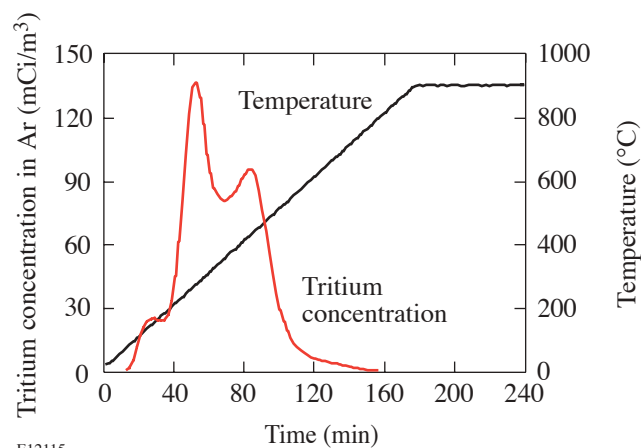
sample A155 (Fig. 95.55) and $\sim 0.2 \mu\text{m}$ for sample A69 (Fig. 95.56). The x axis indicates time while the y axis on the left shows the tritium concentration. The y axis on the right indicates the temperature of the sample.

It can be seen that significant tritium evolution occurs only when the sample temperature exceeds the growth temperature. At temperatures below the growth temperature but above room temperature there is an increase in the tritium monitor signal that is equivalent to a tritium concentration change of $100 \mu\text{Ci}/\text{m}^3$ in a volume of 1 L. This evolution is mainly due to surface tritium and represents a surface tritium concentra-



E12114

Figure 95.55
Tritium evolution from an a-Si:H:T film (A155) grown at 150°C .



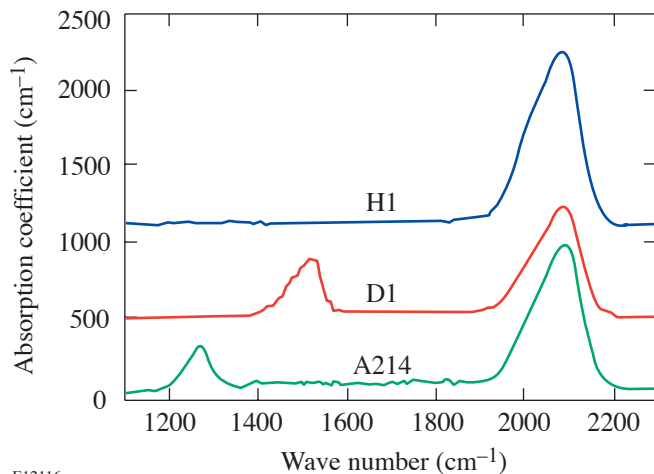
E12115

Figure 95.56
Tritium evolution from an a-Si:H:T film (A69) grown at 225°C .

tion of about $10 \mu\text{Ci}/\text{cm}^2$; this is of the same order of magnitude as that measured in the outgassing experiments presented above ($40 \mu\text{Ci}/\text{cm}^2$). Alternatively, the total number of hydrogen atoms on the surface can be estimated to be $6 \times 10^{14} \text{ cm}^{-2}$. To put this number in context, the number of silicon atoms constituting a monolayer is about 10^{15} cm^{-2} . Considering that the total atomic hydrogen content in these films is around 15 to 30 at. %, the foregoing numbers suggest that the surface hydrogen originates from the top two to three monolayers of the sample. Typical effusion profiles in Figs. 95.55 and 95.56 clearly show the presence of several peaks that are suggestive of different hydrogen-silicon binding states.

Infrared Spectroscopy

To investigate the bonding of tritium in the amorphous silicon network, we compared the infrared spectra of a hydrogenated (a-Si:H), a deuterated (a-Si:H:D), and a tritiated (a-Si:H:T) film of similar thickness (0.2 to $0.3 \mu\text{m}$). Figure 95.57 shows the high-frequency part of the spectra for the three films, with the individual curves shifted vertically with respect to each other by approximately 500 cm^{-1} , for clarity. The vibrations near 2000 cm^{-1} in the a-Si:H film indicates Si-H stretching modes.¹⁰ Very similar hydrogen peaks are observed in the a-Si:H:D and a-Si:H:T films grown with hydrogen originating from the silane gas. The deuterated and tritiated spectra show additional peaks near 1500 cm^{-1} and 1200 cm^{-1} , respectively. These peaks are attributed to Si-D



E12116

Figure 95.57

High-frequency IR vibrations of hydrogenated (H1), deuterated (D1), and tritiated (A214) amorphous silicon films. H1 and D1 have been offset with respect to A214 for clarity.

and Si-T stretching vibrations. The greater-reduced mass of the Si-D and Si-T oscillators relative to that of the Si-H oscillator is responsible for the shift to lower frequencies.

Using the harmonic potential approximation, the stretching frequencies of the Si-D(T) bonds can be calculated with respect to the Si-H bond-stretching frequency, i.e.,

$$\frac{\omega_{\text{Si-D(T)}}}{\omega_{\text{Si-H}}} = \sqrt{\frac{m_{\text{H}}[m_{\text{D(T)}} + M_{\text{Si}}]}{m_{\text{D(T)}}(m_{\text{H}} + M_{\text{Si}})}}, \quad (2)$$

where $\omega_{\text{Si-H(D,T)}}$ is the stretching frequency of the Si-H(D,T) bond, $m_{\text{H(D,T)}}$ denotes the mass of hydrogen (deuterium, tritium), and M_{Si} represents the mass of silicon. Table 95.IV tabulates the experimental and calculated ratios.

Table 95.IV: Ratio of stretching frequency of Si-D and Si-T bonds with respect to Si-H bonds.

| Ratio of Frequencies | Experimental | Calculated |
|---|--------------|------------|
| $\omega_{\text{Si-D}}/\omega_{\text{Si-H}}$ | 0.73 | 0.72 |
| $\omega_{\text{Si-T}}/\omega_{\text{Si-H}}$ | 0.61 | 0.60 |

The weak integrated intensity of the deuterium- and tritium-related vibrations, relative to that of hydrogen absorption bands, is expected since integrated intensity is inversely proportional to the reduced mass of the oscillator. An analysis of the lower-frequency modes (wagging, bending, etc.) leads to similar agreement between experimental and calculated values.¹¹ This shows that both deuterium and tritium behave as heavy hydrogen atoms in the amorphous silicon network and establish a similar bonding pattern.

Dangling Bonds in a-Si:H:T

When beta decay of tritium in a-Si:H:T occurs, a high-energy electron is released and the tritium nucleus transmutes into helium. The following processes take place in the material:

1. The beta particles created in the process of radioactive decay interact with the amorphous network and generate over 1000 electron-hole (e-h) pairs each.¹² The energy of the beta particle is insufficient, however, to cause irreversible lattice damage.^{13,14}

2. The recoil energy of the helium is about 3 eV, which is insufficient to cause irreversible lattice damage.^{14,15}
3. Helium does not stably bond with silicon; therefore, a silicon dangling bond is created at the site of each decayed tritium atom.

The rate of dangling-bond formation due to bonded tritium decay is

$$\frac{dN_{\text{db}}(t)}{dt} = \lambda N_{\text{T}} \exp(-\lambda t), \quad (3)$$

where N_{db} is the concentration of dangling bonds, N_{T} is the tritium concentration at $t = 0$, and λ is the decay rate of tritium.

Initially, the dangling bonds must be positively charged (D^+ centers); however, with time, the D^+ centers are expected to attract electrons and be converted into neutral dangling bonds (D^0 centers). This process should have a high probability due to the large number of free electrons present in the material. To stabilize the transition from a D^+ to D^0 center, however, a 15° bond-angle change is necessary.¹⁶ This reduces the probability of the conversion; consequently, we expect that reemission of electrons will compete with the D^+ to D^0 conversion process and a steady concentration of D^+ and D^0 centers will develop, determined by the tritium decay and the electron reemission process.

We investigate the formation of dangling bonds using electron spin resonance and photoluminescence. The following two sections describe the approach and summarize the results.

Electron Spin Resonance

Electron spin resonance (ESR) provides a direct measurement of the concentration of Si-dangling-bond D^0 neutral defect states.¹⁷ We have monitored concentrations of defects and studied their time evolution and annealing behavior in sample G181 ($\sim 0.6 \mu\text{m}$ thick) using a Bruker ESR spectrometer. Just after deposition, the tritium and hydrogen concentrations were 9 at. % and 22 at. %, respectively. The spin resonance was first measured after four years of storage. Due to the ongoing decay of tritium to helium, we expect the Si-dangling-bond defect concentration to be as high as $N_{\text{db}} = 5 \times 10^{21} \text{ cm}^{-3}$ at the time of the ESR measurement. An additional degradation effect by emitted beta particles, if any, would make this concentration even higher. Surprisingly, however, the measured defect spin density was only $N_d = 6.4 \times 10^{17} \text{ cm}^{-3}$. Such a large discrepancy suggests that there is an ongoing process that either eliminates the created defects or

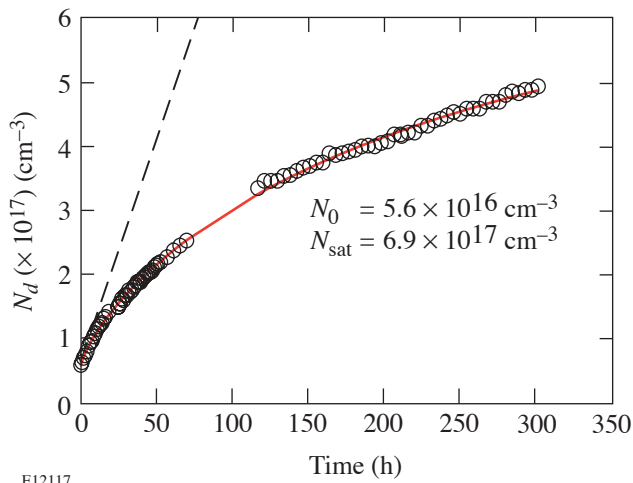
makes them invisible to ESR. The latter implies the creation of large numbers of charged defects. Dopant-like states capable of providing the necessary charge, however, are unlikely created by tritium decay. In addition, the created defects are not stable: they anneal out by heating at 150°C . This strongly suggests that their creation is likely counterweighted by an annealing process that takes place even at room temperature. As a result, defect density finally saturates at concentrations much lower than those of the decayed tritium atoms. This annealing is somewhat similar to the thermal decay of the Si-dangling-bond defects created by light (Staebler–Wronski effect¹⁸). In the latter case, typical annealing temperatures are above 150°C , while some of the defects do anneal even at room temperature due to their very broad spectrum of annealing activation energies.^{19,20} The experimental evidence for the thermal annealing of defects in tritiated a-Si is outlined below.

After the ESR measurement, the four-year-old a-Si:H:T sample was annealed at 150°C for 30 min and then rapidly cooled down to room temperature; the evolution of the ESR signal with time was subsequently monitored. The results are shown in Fig. 95.58. Annealing reduced the spin concentration to $5.6 \times 10^{16} \text{ cm}^{-3}$. After the annealing, the spin density increased rapidly, with an initial rate of creation of defect spins roughly equal to the rate of tritium decay (dashed line). After about 20 h, however, the rate of creation of spin states slowed down considerably, and the spin density again saturated at the old value of about $6.9 \times 10^{17} \text{ cm}^{-3}$ within one month. We have fitted this time evolution N_d by a stretched exponential dependence:

$$N_d(t) = N_0 + (N_{\text{sat}} - N_0) \times \left\{ 1 - \exp \left[\left(-\frac{t}{\tau} \right)^\alpha \right] \right\}, \quad (4)$$

where N_0 is the dangling-bond density at $t = 0$. The saturation value N_{sat} is approximately equal to the concentration of spin states measured after four years of storage, prior to annealing. Such dependence generally describes relaxation phenomena with time-dependent transition rates in disordered systems, including hydrogenated amorphous silicon.^{3,16,21,22} The time constant τ of Eq. (4) approximately characterizes the lifetime of newly created defects and is about 12 days at room temperature. The thermal character of the defect equilibration was further confirmed by keeping the sample at an elevated temperature of 80°C after annealing. In this case, the defect concentration saturated in less than one day and the saturation value was below 10^{17} cm^{-3} . Such an effective annealing may be a result of very high concentrations of hydrogen and tritium

in our sample, leading to clustered hydrogen regions. Experiments on samples with lower H content are being planned. It is also a challenge to explain the annealing mechanism for the defects since the concentrations of the decayed tritium atoms after four years of sample storage are very high—of the order 10^{21} cm^{-3} . One might assume that H atoms that diffuse from nearby sites annihilate these defects. In this case, H detachment from such a site should not be accompanied by the creation of a new defect. This might be possible if H comes from a large reservoir of paired H sites such as double-hydrogen complexes²³ or hydrogenated vacancies.²⁴ Further experiments are necessary to elucidate the mechanism of defect annealing.



E12117

Figure 95.58 ESR results for sample G181 after 30 min annealing at 150°C . The solid curve is a fit to the data using Eq. (4). The values of the parameters obtained from the fit are indicated in the figure. The dashed line represents the number of tritium decays calculated using Eq. (3).

Photoluminescence

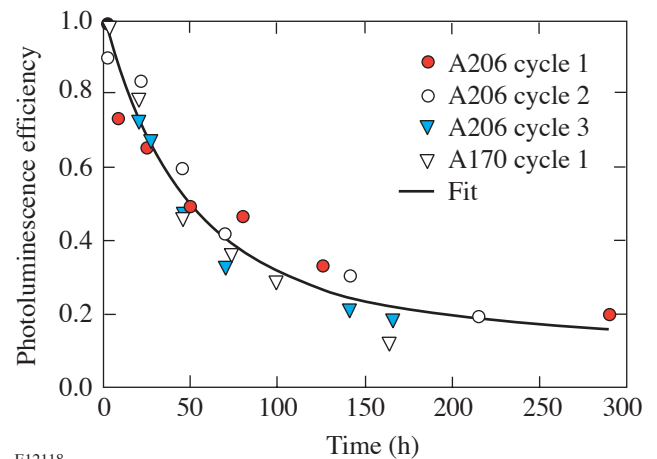
Photoluminescence (PL) of the films was measured using an Ar^+ ion laser tuned to 490 nm. Shortly after deposition, the tritiated samples exhibited strong, low-temperature PL. The PL spectrum at 5 h after deposition and its temperature dependence were similar to those observed in samples deposited under similar conditions except for hydrogen or deuterium in place of tritium in the feed gas stream. This confirms that the density-of-states (DOS) distribution in the films does not depend strongly on the hydrogen isotope used in the feed gas stream. However, the PL of the tritiated samples decreases quickly with time, due to the creation of dangling bonds that act as recombination centers for the electron-hole (e-h) pairs, thus quenching the luminescence signal.¹⁶

In Fig. 95.59 the decay of the photoluminescence is plotted as a function of time for the three successive annealing cycles of sample A206 ($\sim 0.2 \mu\text{m}$ thick). We annealed the samples at 150°C for 30 min for each cycle. The data for the initial photoluminescence decay, immediately following deposition, for sample A170 ($\sim 0.6 \mu\text{m}$ thick) are also included in the figure. It is seen to be similar to the data for sample A206. Neutral dangling bonds (D^0) are the most-effective recombination centers for e-h pairs¹⁶ and are therefore the most likely cause of the quenching of the PL signal. The solid line in Fig. 95.59 is based on the theoretical model of Sidhu *et al.*²⁵ and the values of N_d obtained from ESR measurements. According to Sidhu's model, the PL efficiency η can be written as

$$\eta = \frac{1}{1 + \tau\nu \exp\left[-\frac{2}{R}\left(\frac{4\pi}{3}N_d\right)^{-1/3}\right]}, \quad (5)$$

where ν is the attempt to hop frequency, τ is the radiative lifetime, and R is the tunneling radius. Table 95.V presents the values of the parameters obtained from the fit and the expected range for these parameters.

It should be noted that in an earlier paper²⁵ we attributed the decrease in the PL signal entirely to primary dangling bonds created through tritium decay. Over 50% of the PL decrease occurs during the first 30 h after annealing, where $D^+ \approx D^0$. Later D^+ and D^0 diverge; however, the difference in the predicted PL signal is relatively small since the concentration of dangling bonds is quite high after the first 30 h.



E12118

Figure 95.59 PL efficiency versus time for samples A206 (three cycles) and A170 (one cycle). The points represent the area of the normalized PL signals. The solid line was obtained from the model developed by Sidhu *et al.*²⁵

Table 95.V: Measured and expected values for the parameters in Eq. (5). The column labeled “fitted value” uses Eq. (4) in the Sidhu model. The “expected range” values are from the literature.

| Parameter | Fitted Value | Expected Range ^{3,4,26–28} |
|-----------|--------------|---|
| R | 2.9 nm | 1.3 to 10 nm |
| $\nu\tau$ | 1150 | $N \sim 10^{11-13} \text{ s}^{-1}, t \sim 10^{-8,-9} \text{ s}$ |

Betavoltaics

Our intrinsic betavoltaic device consists of a tritiated amorphous semiconductor $p-i-n$ junction. The beta-induced electron-hole pairs are separated by the electric field present in the depletion region of the junction. This is similar to conventional betavoltaic or photovoltaic cells except that it is powered by intrinsic tritium decay betas rather than external electrons or external photons, respectively. A schematic illustrating the intrinsic betavoltaic device is shown in Fig. 95.60.

The maximum power density P_{\max} for this configuration was measured to be $P_{\max} = 0.29 \mu\text{W}/\text{cm}^2$ (per 48 mCi/cm² per μm at 20 at. % tritium), which is approximately 16% of the theoretical maximum attainable power.²⁹ Alternatively, stacking a number of such cells in series and/or in parallel would require approximately 330 Ci to achieve a 1-mW tritium powered battery. A 1-mW battery is defined as that having this power output at the end of one tritium half-life, i.e., approxi-

mately 12 years; tacit in this definition is that the cell power output diminishes at a rate equal to the decay of tritium atoms.

As described in the previous sections, however, tritium decay creates dangling bonds. When the density of dangling bonds increases, a nonuniform electric field develops in the intrinsic region of the $p-i-n$ junction and the effective width of the space charge region is reduced.³⁰ The reduced electric field near the middle of the intrinsic region reduces the velocity of carriers and thereby increases the probability of electron-hole-pair recombination. This in turn reduces the number of electron-hole pairs available for electrical power, and the output power from the betavoltaic device decreases.

As discussed earlier, dangling bonds are inevitably created as a consequence of the radioactive decay of the bonded tritium. Fortunately, the effect of these dangling bonds on the betavoltaic device can be reduced by confining the tritium to small regions of the otherwise hydrogenated amorphous silicon intrinsic region. We used a thin slice of tritiated material and refer to this as a δ layer configuration. Now, rather than the entire intrinsic region being comprised of dangling bonds, only a fraction of it will contain a large concentration of dangling bonds. As a result, a uniform electric field will exist across most of the intrinsic region, and degradation of the betavoltaic device will be limited.

A $p-i-n$ δ layer device is illustrated in Fig. 95.61. The p and n layers of the $p-i-n$ δ layer devices were deposited

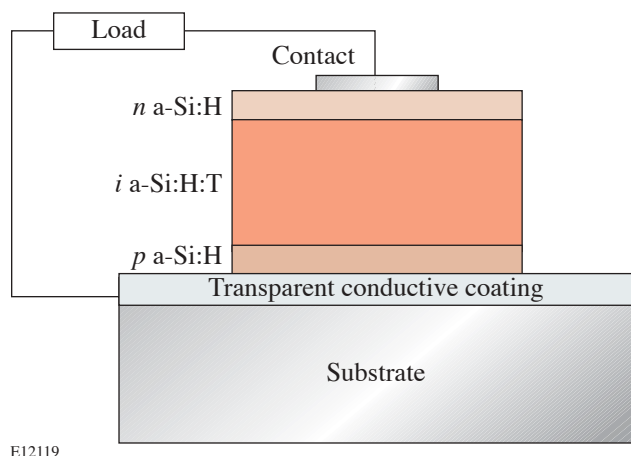


Figure 95.60
Schematic design of an intrinsic betavoltaic device.

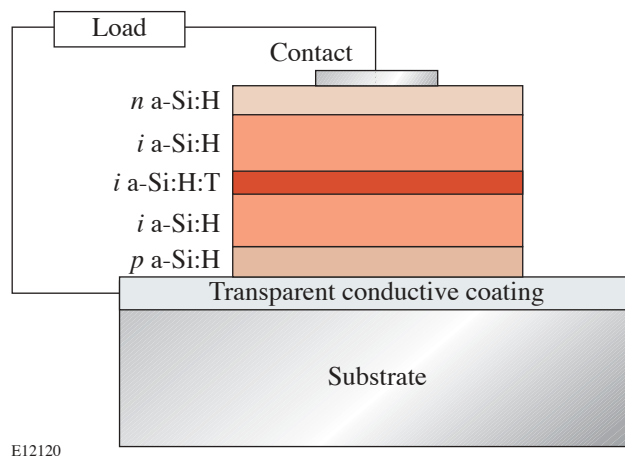


Figure 95.61
Schematic design of a $p-i-n$ δ layer device.

using a 2% gas mixture of B_2H_6 in SiH_4 and PH_3 in SiH_4 , respectively. The thickness of the p layer was approximately 120 Å, while the thickness of the n layer was approximately 200 Å. The hydrogenated portions of the intrinsic region for the devices were grown using undiluted SiH_4 , and the thickness was approximately 0.12 μm . The tritiated delta layer was deposited using tritium gas and SiH_4 . These gasses were introduced into the plasma at equal gas-flow rates of 4 standard cc/min (sccm). The deposition time was used to control the thickness of the delta region. The total chamber pressure was maintained at 140 mTorr for the time required to grow the entire intrinsic region. While growing all layers, the substrate temperature was 250°C. The anode voltage during deposition of the layers was approximately 620 V while the anode current was approximately 12 mA.

The behavior of devices with a delta layer was compared with a device whose entire intrinsic region was tritiated. We label this last device *uniform* while the three devices with a delta layer were labeled *delta 1*, 2, and 3. The thickness of the tritiated layer in *delta 1* was approximately 1/3 the thickness of the intrinsic layer in the device *uniform*. Similarly, the thickness of the a-Si:H:T layer in *delta 2* and *delta 3* were approximately 1/6 and 1/12 the thickness of the intrinsic layer in the device *uniform*, respectively. The concentration of tritium in the tritiated region of all devices was similar at about 5 at. %. Table 95.VI gives the short-circuit current and open-circuit voltage for the four devices, measured shortly after their manufacture.

Table 95.VI: Short-circuit current and open-circuit voltage for the *delta* devices and the device *uniform*.

| Device | I_{sc} (nA)±2% | V_{oc} (mV)±0.2% |
|----------------|------------------|--------------------|
| <i>uniform</i> | 0.98 | 21 |
| <i>delta 1</i> | 0.35 | 20 |
| <i>delta 2</i> | 0.14 | 9 |
| <i>delta 3</i> | 0.03 | 11 |

Of the four devices listed in Table 95.VI, the device *uniform* has the largest short-circuit current. On the whole, the differences in the short-circuit current among the devices are consistent with the difference in the thickness of the tritiated amorphous silicon layer. As the thickness of the tritiated layer is reduced, fewer beta particles are created; hence, the number of electron-hole pairs created is reduced by nearly the same ratio. Since the

structure of the delta devices is similar, the open-circuit voltages decrease monotonically with the short-circuit current. The open-circuit voltage of *delta 3* did not decrease in comparison to *delta 2*. This is most likely the result of a better junction in *delta 3*. The smaller-than-expected short-circuit current from *delta 3* is most likely due to a thinner-than-expected delta layer; the very short deposition time makes it difficult to accurately deposit the delta layer, which was expected to be 300 μm thick.

For each device, the short-circuit current under dark conditions was measured as a function of time. The remaining fraction of the initial short-circuit current as a function of time is plotted in Fig. 95.62. After approximately 200 h, the short-circuit current for *uniform* was less than 10% of its initial value. The decrease in the fractional short-circuit current for the delta-layered devices was not as rapid, and, as can be seen in Fig. 95.62, the short-circuit currents appeared to settle asymptotically to a fractional value greater than that of *uniform*. The short-circuit current for *delta 3* decreased by only approximately 50% from its initial value after 600 h of operation. This difference in behavior is because dangling bonds in the *delta* devices are isolated within a small, tritiated portion of the intrinsic region. Initially, in all the devices, there would have been a uniform electric field across the intrinsic region; however, as dangling bonds are created, the electric field weakens in a-Si:H:T sections. In the device *uniform*, the electric field is weakened throughout most of the intrinsic region. In the *delta* devices, a weak electric field exists only in the delta layer. To

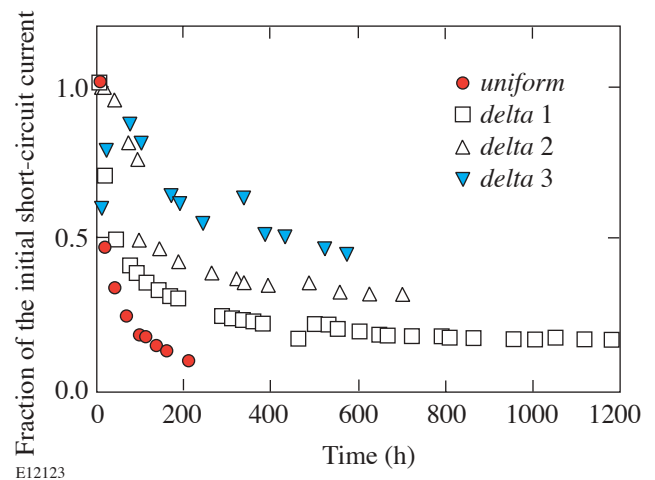


Figure 95.62 Short-circuit current as a function of time in the $p-i-n$ devices.

accommodate the reduced electric field in the a-Si:H:T delta layer, the electric field strengthens in the a-Si:H region, increasing the drift velocity of carriers and helping carriers traverse the intrinsic region without recombination. This increased drift velocity in the untritiated region will have little effect, however, on the short-circuit current once the thickness of the tritiated region exceeds the diffusion length of the carriers.

A numerical simulation was carried out to determine the spatial distribution of the beta-particle energy deposited in the intrinsic regions as a function of the delta-layer thickness and the resulting initial short-circuit current.³¹ The results of the simulations are summarized in Table 95.VII. It can be seen that as the thickness of the a-Si:H:T region is reduced, increasingly more energy is deposited in the a-Si:H regions rather than in the a-Si:H:T region. This is to be expected since as the *delta* layer becomes thinner, relatively fewer electron-hole pairs are created in the a-Si:H:T region than in the a-Si:H region since less energy is deposited in the a-Si:H:T than in the a-Si:H region.

The energy transferred from a beta particle to the amorphous silicon lattice is given by the stopping power of the material as the particle moves through the material. There is a broad distribution of kinetic energies of the beta particles from the decay of tritium (Fig. 95.52). The initial kinetic

energy of the beta particle can be averaged between the most-probable energy of about 3 keV and the average energy of 5.7 keV. The energy deposited in each section of the intrinsic region was simulated using a uniform distribution of bonded tritium atoms and taking into account the path length traveled by the beta particle as it loses energy to the lattice. The results of this calculation together with the corresponding experimental results are presented in Table 95.VIII. It can be seen that the numerical calculations agree quite well with the experimental data.

Conclusions

Tritium bonds stably in amorphous silicon. This is confirmed by outgassing, effusion, and infrared spectroscopy. The radioactive decay of tritium gives rise to the formation of dangling bonds as a consequence of tritium transmutation into helium; however, the number of dangling bonds appears to be much less than the number of decayed tritium atoms, most likely due to some form of lattice reconstruction.

Electron-hole pairs created by beta particles emitted in the process of tritium decay are separated by the built-in field of a tritiated amorphous silicon *p-i-n* junction. Dangling bonds formed in the process of tritium decay cause degradation of the current-voltage characteristic of the *p-i-n* junction with time.

Table 95.VII: Distribution of the beta-particle energy.

| Device | a-Si:H (top/bottom layer) (%) | | | | a-Si:H:T (<i>delta</i> layer) (%) | | | |
|----------------|-------------------------------|------|----|-----|------------------------------------|------|-----|-----|
| | Energy (keV) | | | | Energy (keV) | | | |
| | 1 | 2 | 3 | 5.7 | 1 | 2 | 3 | 5.7 |
| <i>delta</i> 1 | 6.9 | 20 | 35 | 34 | 87 | 60 | 30 | 31 |
| <i>delta</i> 2 | 13.7 | 36 | 43 | 40 | 36 | 27.4 | 15 | 19 |
| <i>delta</i> 3 | 27.3 | 43.5 | 46 | 45 | 22.7 | 13 | 8.3 | 11 |

Table 95.VIII: Asymptotic value of the short-circuit current as a fraction of the initial short-circuit current for the three *delta* devices.³¹

| Device | Experiment | Numerical |
|----------------|------------|-----------|
| <i>delta</i> 1 | 0.15 | 0.27 |
| <i>delta</i> 2 | 0.30 | 0.36 |
| <i>delta</i> 3 | 0.45 | 0.42 |

This degradation can be controlled, however, by confining the tritium to small volumes in the *p-i-n* junction. Consequently, tritiated amorphous silicon may find an application in self-powered *p-i-n* junction betavoltaic batteries.

ACKNOWLEDGMENT

This work was supported by Kinectrics (formerly Ontario Power Technologies), Materials and Manufacturing Ontario, and Natural Sciences and Engineering Research Council of Canada.

REFERENCES

1. R. A. Street, *Technology and Applications of Amorphous Silicon*, Springer Series in Materials Science, Vol. 37 (Springer, New York, 2000).
2. G. Bruno, P. Capezzuto, and A. Madan, eds. *Plasma Deposition of Amorphous Silicon-Based Materials*, Plasma-Materials Interactions (Academic Press, Boston, 1995).
3. R. A. Street, *Hydrogenated Amorphous Silicon* (Cambridge University Press, Cambridge, England, 1991), p. 203.
4. W. Fuhs, in *Amorphous and Microcrystalline Semiconductor Devices*, edited by J. Kanicki (Artech House, Boston, 1992), Chap. 1, Vol. II, pp. 1–53.
5. W. Luft and Y. S. Tsuo, *Hydrogenated Amorphous Silicon Alloy Deposition Processes*, Applied Physics, Vol. 1 (Marcel Dekker, New York, 1993).
6. G. Vasaru, *Tritium Isotope Separation* (CRC Press, Boca Raton, FL, 1993).
7. N. P. Kherani, "Electron Flux and Energy Distribution at the Surface of Lithium Tritide," Ph.D. thesis, University of Toronto, 1994.
8. N. P. Kherani, K. Virk, T. Kosteki, F. Gaspari, W. T. Shmayda, and S. Zukotynski, "Hydrogen Effusion from Tritiated Amorphous Silicon," to be published in *IEE Proceedings Circuits, Devices and Systems Special Issue on Amorphous and Microcrystalline Semiconductor Devices*.
9. W. T. Shmayda, A. B. Antoniazzi, and R. A. Surette, Ontario Hydro Research Division, Toronto, Canada, report no. 92-51-K (1992).
10. M. Stutzmann, in *Properties of Amorphous Silicon and Its Alloys*, edited by T. Searle (INSPEC, IEE, London, 1998), pp. 56–60.
11. L. S. Sidhu *et al.*, *J. Appl. Phys.* **85**, 2574 (1999).
12. T. Kosteski, N. P. Kherani, F. Gaspari, S. Zukotynski, and W. T. Shmayda, *J. Vac. Sci. Technol. A* **16**, 893 (1998).
13. U. Schneider, B. Schroder, and F. Finger, *J. Non-Cryst. Solids* **114**, 633 (1989).
14. M. Stutzmann, in *Amorphous and Microcrystalline Semiconductor Devices*, edited by J. Kanicki (Artech House, Boston, 1992), Chap. 4, Vol. II, pp. 129–187.
15. R. Street, D. Biegelsen, and J. Stuke, *Philos. Mag.* **B 40**, 451 (1979).
16. R. S. Crandall, *Phys. Rev. B, Condens. Matter* **43**, 4057 (1991).
17. P. C. Taylor, in *Properties of Amorphous Silicon and Its Alloys*, edited by T. Searle (INSPEC, IEE, London, 1998), Sec. 3.3, pp. 139–142.
18. D. L. Staebler and C. R. Wronski, *Appl. Phys. Lett.* **31**, 292 (1977).
19. P. Stradins and H. Fritzsche, *Philos. Mag. B* **69**, 121 (1994).
20. Q. Zhang *et al.*, in *Symposium on Amorphous Silicon Technology – 1994*, edited by E. A. Schiff *et al.* (Materials Research Society, Pittsburgh, PA, 1994), pp. 269–274.
21. A. Tagliaferro, *Mod. Phys. Lett. B* **4**, 1415 (1990).
22. J. Kakalios, R. A. Street, and W. B. Jackson, *Phys. Rev. Lett.* **59**, 1037 (1987).
23. H. M. Branz, *Phys. Rev. B, Condens. Matter* **59**, 5498 (1999).
24. S. B. Zhang and H. M. Branz, *Phys. Rev. Lett.* **87**, 105503 (2001).
25. L. S. Sidhu, T. Kosteski, S. Zukotynski, N. P. Kherani, and W. T. Shmayda, *Appl. Phys. Lett.* **74**, 3975 (1999).
26. R. A. Street and D. K. Biegelsen, in *Physics of Hydrogenated Amorphous Silicon II. Electronic and Vibrational Properties*, edited by J. D. Joannopoulos and G. Lucovsky (Springer-Verlag, Berlin, 1984), pp. 195–259.
27. W. C. Chen and L.-A. Hamel, in *Symposium on Amorphous Silicon Technology – 1996*, edited by M. Hack *et al.* (Materials Research Society, Pittsburgh, PA, 1996), pp. 759–764.
28. B. A. Wilson *et al.*, *Phys. Rev. Lett.* **50**, 1490 (1983).
29. N. P. Kherani, T. Kosteski, S. Zukotynski, and W. T. Shmayda, *Fusion Technol.* **28**, 1609 (1995).
30. K. R. Lord, II, M. R. Walters, and J. R. Woodyard, in *Proceedings of the XIII Space Photovoltaic Research and Technology Conference*, NASA Conference Publication 3278 (NASA Lewis Research Center, Washington, DC, 1994), pp. 187–196.
31. T. Kosteski, "Tritiated Amorphous Silicon Films and Devices," Ph.D. thesis, University of Toronto, 2001.

The Coherent Addition of Gratings for Pulse Compression in High-Energy Laser Systems

Introduction

Short-pulse, high-energy, and high-irradiance laser systems provide many new opportunities for studies in light-matter interaction and inertial confinement fusion, including x-ray radiography and fast ignition. Research in high-intensity, high-energy backlighting for high-energy-density physics experiments under ignition conditions and integrated fast-ignition experiments with cryogenic targets depend on the development of short-pulse, high-irradiance lasers.¹ High-power, solid-state lasers, using the chirped-pulse-amplification (CPA) scheme, incorporate pulse compressors containing holographic gratings.² The most-promising grating technology is a holographically formed grating combined with a multilayer dielectric (MLD) coating to form a highly efficient grating used in reflection.^{3–5} The four primary grating requirements, namely high diffraction efficiency, high wavefront quality, large aperture, and high damage threshold, make it a highly constrained optical system. The aperture size and damage threshold of reflection gratings determine the short-pulse energy capability of petawatt laser systems. The critical compressor component is the last grating, which experiences the shortest pulse and therefore the highest power. The highest reported damage threshold for commercially available MLD gratings is 0.6 J/cm^2 at 275-fs pulse width.⁶ Assuming a square root of time scaling, these gratings would have a damage threshold of $\sim 1.2 \text{ J/cm}^2$ for a 1-ps pulse width. For a grating with 1740 l/mm and a Littrow angle of 66.5° for $\lambda = 1054 \text{ nm}$, this surface fluence corresponds to a beam fluence, measured in a plane normal to beam propagation, of approximately 3 J/cm^2 . These gratings are currently available in approximately 50-cm lengths. Assuming a 1.8 safety factor for diffraction modulation, the above provides an energy of less than 1 kJ. Gratings with larger apertures can further extend the short-pulse energy capability of petawatt laser systems; however, since the difficult fabrication process for MLD reflection gratings may limit the ultimate size of an individual grating to less than 1 m, alternative approaches are critical to scaling toward multiple-kilojoule, short-pulse laser systems.

Concept Description

The coherent summation of multiple gratings to form a larger grating provides an alternative to meter-sized MLD gratings. We refer to this alternative as grating tiling. A tiled-grating compressor (TGC) is capable of handling greater laser energy than a grating-aperture-limited compressor. For each of the gratings within the compressor, $N \times M$ sub-aperture gratings can be mounted adjacently to form a larger tiled grating.⁷ When properly aligned, they will act as a monolithic optical element. For example, Fig. 96.1 shows a four-grating compressor with each tiled grating containing three sub-aperture gratings. The configuration is being considered for the OMEGA EP laser system. In general, the aperture, and therefore the energy, of a TGC is increased by a factor of $N \times M$ over that of grating-aperture-limited compressors. Similar to the scheme deployed by the astronomy community to construct very large telescopes⁸ using an array of mirrors, large gratings can be assembled from multiple smaller gratings. Accurate control of the position and orientation of the grooves of each grating presents a significantly greater challenge than that associated with mirror arrays. Despite the perceived difficulty, we have developed a far-field-based approach that makes grating tiling practical.^{9,10} As shown in Fig. 96.2, there are five degrees of freedom between each adjacent pair of gratings within a tiled-grating system: tip, tilt, rotation, in-plane shift, and out-of-plane shift. However, only three distinct types of optical path differences exist between closely aligned grating pairs. Relative shifts along the x and z axes result in a differential piston phase between the grating pairs. Similarly, relative rotations about the x and z axes result in a differential tilt phase between the grating pairs. Relative rotation about the y axis results in an additional tilt, while the relative shift along the y axis is inconsequential since it is parallel to the grooves of the grating. Relative tilt resulting from relative rotation about the x axis can be used to compensate relative groove rotation. In addition, the out-of-plane shift, also referred to as the piston phase error, can be used to compensate the residual error caused by the finite space between two adjacent gratings. The

effect of piston misalignment was modeled thoroughly. Theoretical simulations show the far-field irradiance resulting from relative piston-type phase error between two tiled gratings (Fig. 96.3, calculation). A half-wave piston-type error causes the focal spot to split into two symmetric spots of equal energy and irradiance. Experimental verification of the predictions for

zero and half-wave errors indicates accurate control of the relative phase between the pair of tiled gratings as described below (Fig. 96.3, measurement). We experimentally observed that the majority of the focal-spot degradation occurs closer to the half-wave error, indicating a relative insensitivity in the vicinity of piston phase error, which is a multiple of 2π .

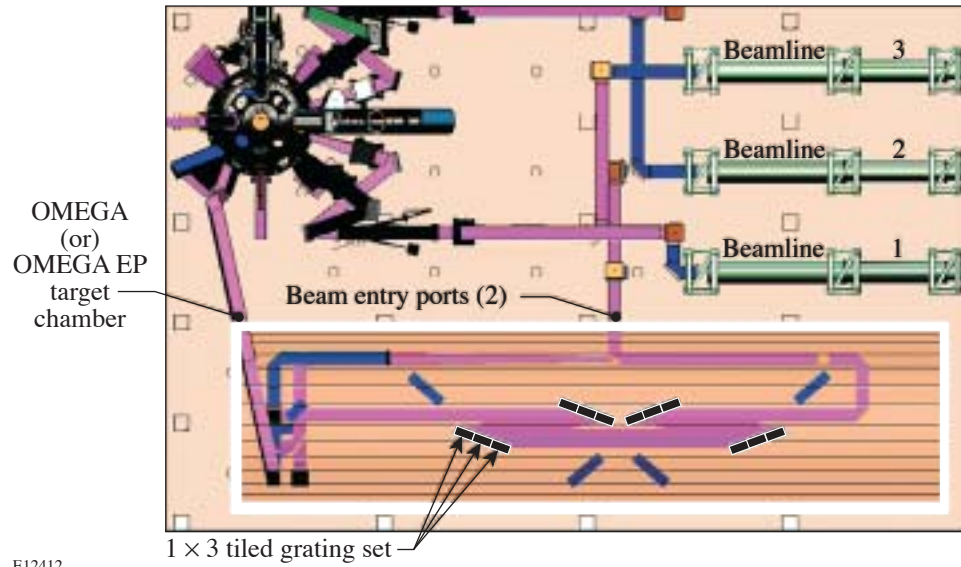


Figure 96.1

Tiled-grating compressors (TGC's) are capable of handling greater laser energy than a grating-aperture-limited compressor. For each of the gratings within a TGC, $N \times M$ sub-aperture gratings can be adjacently mounted to form a larger tiled grating. Shown here is a four-grating compressor with each tiled grating containing three sub-aperture gratings. The aperture, and therefore the energy, is increased by a factor of $N \times M$ over that of grating-aperture-limited compressors.

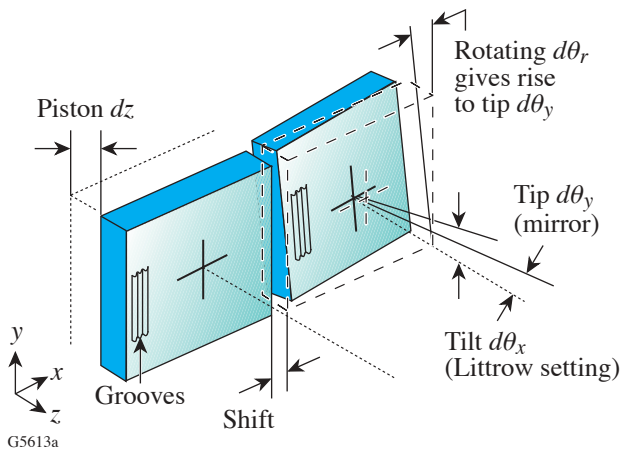


Figure 96.2

There are five degrees of freedom between each adjacent pair of gratings within a tiled-grating system. Relative shifts along the x and z axes result in a differential piston phase between the grating pairs. Similarly, relative rotations about the x and z axes result in a differential tilt between the grating pairs. Relative rotation about the y axis results in an additional tilt, while relative shift along the y axis is inconsequential since it is parallel to the grooves of the grating.

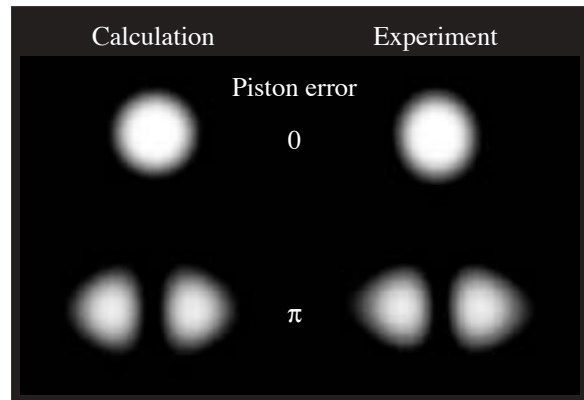
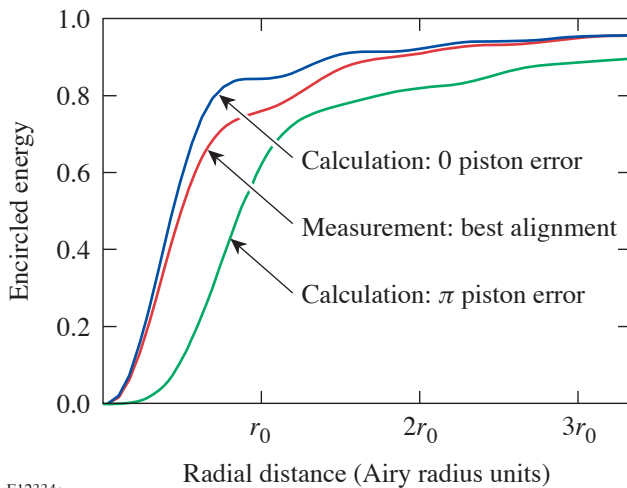


Figure 96.3

Theoretical simulations show the far-field effects from a relative piston phase error between two gratings. A π -phase shift causes the focal spot to split into two symmetric spots of equal energy and irradiance. Experimental verification of the predictions for zero and half-wave errors was achieved through accurate control of the relative piston.

Experimental Demonstrations

The feasibility of precise grating tiling was first demonstrated with continuous-wave, monochromatic laser light. The tiled-grating assembly was located within a diagnostic package consisting of a Fizeau interferometer and a focal-plane sensor. An ADE Phase Shift MiniFiz,TM Model 100 interferometer contained a laser source that illuminated a pair of Jobin Ivon 165 × 220-mm gratings, with 1740 l/mm, set up in a Littrow configuration. The gratings were independently mounted within a precision assembly to achieve submicron positioning. A Zygo transmission flat, inserted into the Fizeau cavity, served as a beam splitter to pick off a portion of the beam reflected from the tiled grating. This beam was focused by a long-focal-length lens to form an aerial image. The image was magnified and relayed by an infinity-corrected, 10× microscope objective for far-field detection with a Spectral Instruments, Model 802, CCD camera. This diagnostic package provided accurate control of the phase front, thus allowing detailed studies of the focal-plane irradiance. As shown in Fig. 96.4, near-diffraction-limited performance was obtained with a pair of tiled gratings. The measured encircled energy, truncated at e^{-2} of the azimuthally averaged irradiance, was 0.89 with a Strehl ratio of 0.94. The measured focal-spot diameter was 1.2 to 1.3 times diffraction limited (XDL) as compared to an Airy-disc diameter corresponding to 84%



E12334a

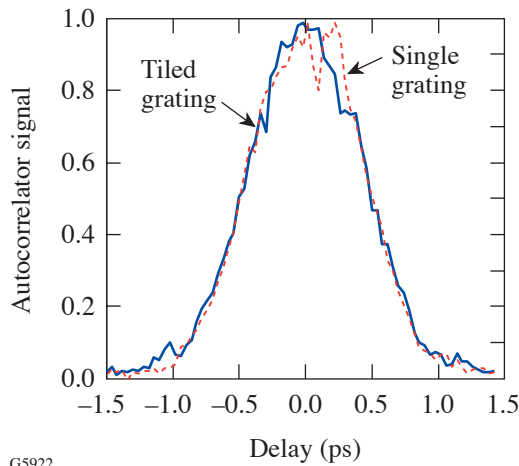
Figure 96.4

Near-diffraction-limited performance was obtained with a pair of tiled gratings. The measured encircled energy, truncated at e^{-2} of the azimuthally averaged irradiance, was 0.89 with a Strehl ratio of 0.94. The measured focal-spot diameter was 1.2 to 1.3 times diffraction limited (XDL) as compared to an Airy-disc diameter corresponding to 84% encircled energy.

encircled energy. For reference, the focal spot resulting from a π piston error is theoretically calculated to be 2.4 XDL. The small departure from theoretical predictions of ideal alignment is attributed to the cumulative wavefront error of the optics.

A demonstration of precise grating tiling was achieved by high-fidelity pulse compression within a CPA laser. The autocorrelation trace, corresponding to a Fourier-transform-limited, 650-fs, CPA laser pulse, was maintained after including a tiled-grating pair. A Positive Light laser consisted of a positively chirped, Time-Bandwidth GLX-200,TM mode-locked oscillator followed by a Spitfire,TM Ti:sapphire, regenerative amplifier. The amplifier output was a linearly chirped, nanosecond pulse with 250 ps/nm. The laser was operated at 540 Hz with 350 μ J per pulse without subsequent amplification. In normal operation the output pulse was compressed with a two-grating, two-pass compressor consisting of gold gratings with 1740 grooves per millimeter. For our demonstration of a TGC, the first grating, and necessarily the last grating in the compressor, was replaced by two tiled gratings with the same line spacing.

In a two-pass grating compressor, only the second and third gratings intercept a beam with spatial chirp of its spectrum. Both the physical gap between tiled gratings and the obscuration at the edge of each grating, where excessive wavefront gradients may need to be masked, give rise to modifications of the spectrum that can potentially cause pulse-shape distortion. Modeling of a partially dispersed beam propagated through an accurately tiled grating indicates that the primary effect from grating-to-grating gaps is pulse broadening. The percentage of broadening is approximately equal to the product of the beam-normalized gap width and beam-normalized spectral separation. For the large laser systems for which this research is aimed, this product is at most only a few percent. For the laser system used to demonstrate grating tiling, however, pulse-width broadening would have exceeded 50%; thus, accurate control of piston and tilt control would have been masked by unrelated obscuration effects. For this reason, only the first (fourth) grating was tiled. Construction of an all-tiled grating compressor is in progress and will be the subject of a future publication. A scanning, far-field autocorrelator was used to measure the compressed temporal pulse. As shown in the autocorrelation traces of Fig. 96.5, negligible pulse broadening and distortion were measured. Accurate control of the relative position of the tiled gratings, as well as accurate alignment of the TGC, resulted in compressed pulses of the same quality as those generated from a conventional grating compressor.



G5922

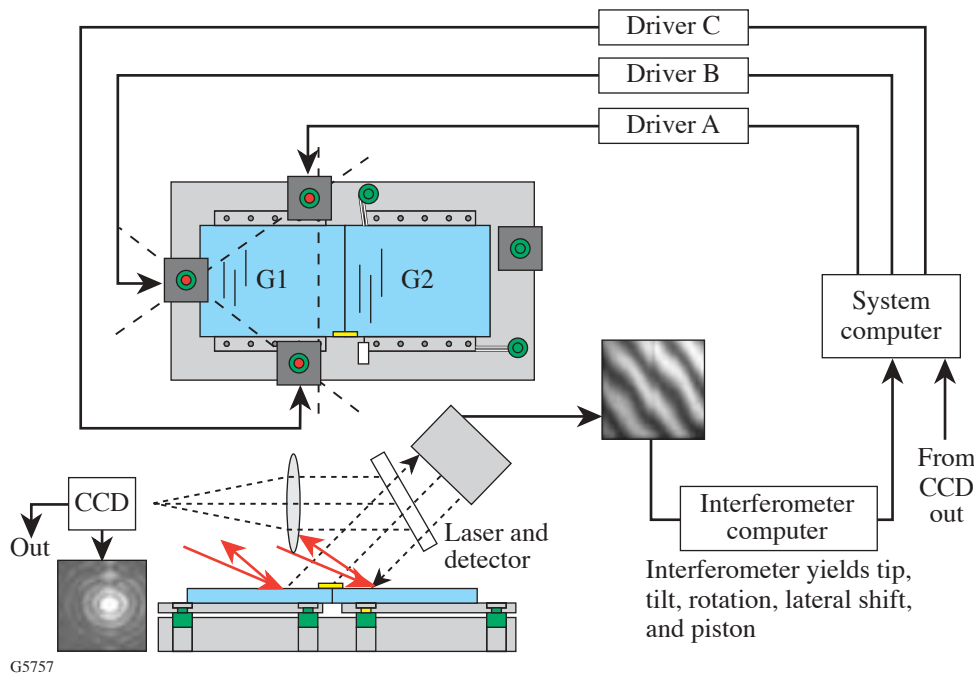
Figure 96.5

The autocorrelation trace, corresponding to a Fourier-transform-limited, 650-fs, CPA laser pulse, was maintained by replacing a single compression grating with a tiled-grating assembly. Negligible pulse broadening and distortion, as shown in the autocorrelation traces, indicate accurate control of the relative positioning of the tiled gratings as well as accurate alignment of the grating compressor.

A test bed for mounting and aligning a reduced-scale TGC for the OMEGA EP laser system is in progress. Schematically illustrated in Fig. 96.6, the tiled-grating system incorporates currently available pointing, sensor, and positioning technology. In particular, flexure mounts provide optimal characteristics for grating mounts. While flexures offer high mechanical stiffness to carry the weight of the grating substrates, they allow extremely fine motion control in the orthogonal direction. In addition, spatial synchronous phase detection can be used for accurate interferometry to monitor differential piston and tilt.

Conclusion

In conclusion, our investigations of coherently combined gratings have resulted in the demonstration of subpicosecond-pulse compression using tiled gratings. A Fourier-transform-limited, 650-fs, CPA laser pulse was maintained by replacing a single compression grating with a tiled-grating assembly. Despite the perceived difficulty, we have developed a far-field-based approach that makes grating tiling practicable. We anticipate that, in conjunction with future improvements in grating size and damage threshold, the tiled-grating compressor will significantly increase the energy and irradiance available in high-energy, short-pulse lasers.



G5757

Figure 96.6

Tiled-grating systems incorporate currently available technology for mounting and alignment. Mechanical flexures provide extremely fine motion control for relatively heavy grating substrates. The interferometer yields tip, tilt, rotation, lateral shift, and piston information.

ACKNOWLEDGMENT

This work was supported by the U.S. Department of Energy Office of Inertial Confinement Fusion under Cooperative Agreement No. DE-FC03-92SF19460, the University of Rochester, and the New York State Energy Research and Development Authority. The support of DOE does not constitute an endorsement by DOE of the views expressed in this article.

REFERENCES

1. D. M. Pennington, C. G. Brown, T. E. Cowan, S. P. Hatchett, E. Henry, S. Herman, M. Kartz, M. Key, J. Koch, A. J. MacKinnon, M. D. Perry, T. W. Phillips, M. Roth, T. C. Sangster, M. Singh, R. A. Snavely, M. Stoyer, B. C. Stuart, and S. C. Wilks, *IEEE J. Sel. Top. Quantum Electron.* **6**, 676 (2000).
2. P. Maine *et al.*, *IEEE J. Quantum Electron.* **24**, 398 (1988).
3. L. Li and J. Hirsh, *Opt. Lett.* **20**, 1349 (1995).
4. B. W. Shore *et al.*, *J. Opt. Soc. Am. A* **14**, 1124 (1997).
5. K. Hehl *et al.*, *Appl. Opt.* **38**, 6257 (1999).
6. B. Touzet and J. R. Gilchrist, *Photonics Spectra* **37**, 68 (2003).
7. T. Zhang, M. Yonemura, and Y. Kato, *Opt. Commun.* **145**, 367 (1998).
8. C. Pizarro *et al.*, *Appl. Opt.* **41**, 4562 (2002).
9. T. J. Kessler, J. Bunkenburg, and H. Huang, "Grating Array Systems for the Alignment and Control of the Spatial and Temporal Characteristics of Light," U.S. Patent Application (filed May 2003).
10. T. J. Kessler, J. Bunkenburg, H. Huang, A. Kozlov, C. Kelly, and D. D. Meyerhofer, "The Coherent Addition of Gratings for Pulse Compression in High-Energy Laser Systems," to be published in *Inertial Fusion Sciences and Applications 2003* (Elsevier, Paris, 2004).

Polar Direct Drive on the National Ignition Facility

Introduction

Recent advances in direct-drive target design have enhanced target performance beyond that achieved in the original baseline ignition design.¹ This substantially increases the probability of achieving moderate to high direct-drive target gain on the National Ignition Facility (NIF). The baseline direct-drive design for the NIF is itself very attractive. It achieves a target gain of 30 (70% of the 1-D gain) in 2-D simulations that include all expected sources of laser and target nonuniformity.¹ New developments have significantly enhanced direct-drive designs in three main areas (Fig. 96.7): (1) The fraction of laser light absorbed has been increased by almost 50% through the use of wetted-foam targets, providing increased energy coupling to the target.² This is the result of the higher-Z material in the foam (e.g., carbon), which makes the plasma more collisional. (2) The hydrodynamic stability of the target has been significantly improved by adiabat shaping, which reduces the growth of target nonuniformities induced by the Rayleigh–Taylor instability without sacrificing target gain.³ (3) Techniques using pulse shaping⁴ and radiation preheat⁵ have been developed to reduce the imprint of laser nonuniformities below that amount achieved by laser-beam smoothing alone. These enhancements allow the target to be driven to higher gain while improving hydrodynamic stability. Motivated by the enhanced performance predicted for direct-drive-ignition experiments on the NIF, this article examines the feasibility of employing direct drive, while the NIF is in the x-ray-drive configuration, as an additional approach to achieving ignition or near-ignition conditions. Polar direct drive (PDD) will couple more energy to the fuel than x-ray drive, and the compressed fuel core can be more easily accessed for high- ρR diagnostic development and fast-ignitor studies.

In the x-ray-drive configuration, the beams are clustered in the polar regions of the target chamber. To achieve the most-uniform target irradiation for direct drive, PDD repoints some of these beams toward the equator of the target (see **Beam-Pointing Strategy**, p. 213). Since these “equatorial” beams are more obliquely incident on the target than the remaining beams, they will have lower laser absorption and drive the

target less efficiently. To compensate for the difference in polar and equatorial coupling, the laser intensity near the equator is increased relative to the pole, and different pulse shapes are employed to accommodate time-dependent variations in drive and absorption. The level of drive uniformity achieved by this technique is being studied using the 2-D hydrocode *DRACO*⁶ (see **Two-Dimensional Simulation Results**, p. 215).

The target design used in these simulations employed both adiabat shaping and wetted foam (Fig. 96.7). Adiabat shaping is accomplished by means of an intensity picket imposed at the onset of laser irradiation. Because of its short duration, the shock launched by the picket is not fully supported, and it decays as it propagates through the target. This places the outer portion of the target shell, where the shock is strongest, on a high adiabat, and the inner portion of the shell, where the shock has weakened, on a low adiabat (adiabat is the ratio of the electron pressure to the Fermi-degenerate pressure). With proper choice of the picket intensity and duration, the high-adiabat region will be primarily confined to the ablation region of the target, leaving the main portion of the fuel on a low

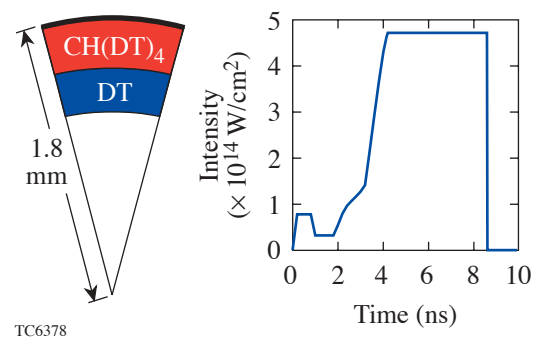


Figure 96.7

Advanced direct-drive target designs employ wetted-foam targets for increased laser absorption and a picket at the beginning of the laser pulse to provide increased hydrodynamic stability. This target and pulse shape were used for the PDD simulations.

adiabat. The higher ablator adiabat produces higher ablation velocities and enhanced ablative stabilization of the Rayleigh–Taylor instability.³ The lower adiabat of the main fuel layer allows greater compressibility of the fuel. The picket also reduces the amount of imprint on the target surface from laser nonuniformities.⁴ Picket-fence pulses have been used previously as an alternative to continuous pulse shapes.⁷ The picket used here has been specifically optimized for the purpose of shaping the adiabat in the fuel.

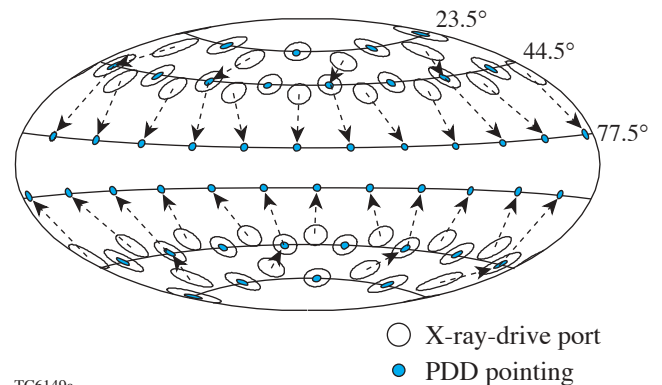
A comparison between the performance of wetted-foam designs with adiabat shaping and the performance of the baseline “all-DT” design was discussed in Ref. 2. The primary result was that wetted-foam designs achieved target gains typically two to three times higher than the gain for the all-DT target. The higher gain was the result of two factors: increased absorption and adiabat shaping. (1) Increased absorbed energy allowed more-massive targets to be driven with the same incident laser energy. (2) Adiabat shaping allowed the main portion of the fuel to be driven on a lower adiabat without compromising the shell integrity, resulting in higher areal density (ρR). The stability of the wetted-foam target during the acceleration phase of the implosion was examined with 2-D simulations that calculated linear growth factors for different modes of nonuniformity.⁸ The largest growth factor was 6.5 e foldings for a spherical-harmonic mode of 60, which is comparable to the stability obtained for the baseline x-ray-driven targets.⁹

It is not expected that polar-direct-drive targets will perform as well as “standard” direct-drive designs. In addition to the reduced laser coupling and the reduced hydrodynamic efficiency expected from the more-oblique irradiation near the equator of the target, there will be increased laser nonuniformity because the irradiation configuration has not been optimized for direct drive. For standard direct drive, the optimal irradiation distribution on target is known *a priori*; it must be uniform. For PDD, the irradiation pattern must be made intentionally nonuniform to compensate for the variations in target drive caused by variations in the laser angles of incidence around the target. As a result, PDD is a far more difficult design problem than standard direct drive. The required laser nonuniformity must be determined from computer simulations and confirmed by experiment.

Beam-Pointing Strategy

One possible irradiation strategy for PDD is to point the beams to the direct-drive positions on target, which are located along three latitudes at 23.5°, 44.5°, and 77.5° and correspond-

ing latitudes in the southern hemisphere.¹⁰ (Here, the term *NIF beams* refers to the cluster of four beams that make up a “quad”; the term *ring of beams* refers to those beams that are pointed toward a particular latitude ring on the target and not to a ring of beam ports.) This beam pointing is illustrated in Fig. 96.8: The NIF x-ray-drive beam ports are shown as open circles, and arrows show the places on the initial target surface where each of the corresponding beams is pointed. When the NIF is converted to direct drive, the 30° beams will be relocated to the 77.5° ports (together with the 50° beams). For PDD, rather than pointing the 30° beams directly to the equatorial ring, a two-step procedure was used in order to minimize the angles of incidence near the equator. The four beams at 30° were pointed to direct-drive positions at 44.5°, and four of the eight beams that were already pointed to those positions were directed toward the 77.5° ring near the equator.



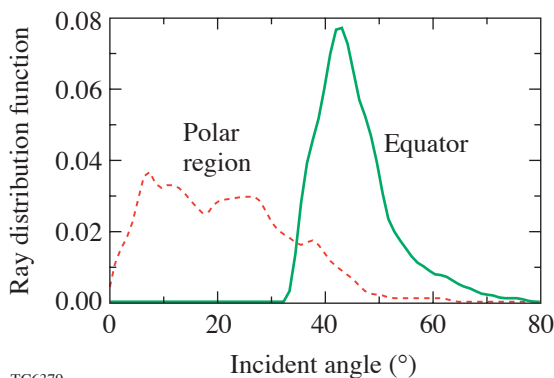
TC6149a

Figure 96.8

PDD repoints some beams from the NIF’s x-ray-drive ports toward the target equator. This figure shows the beams being directed to the direct-drive positions corresponding to three rings of beams incident upon the target in each hemisphere.

Simply pointing the beams to the direct-drive positions does not, however, necessarily produce the optimal results for target drive uniformity. There are two main reasons: (1) Since the beam axes are not radially directed, their positions on the target surface will change as the target implodes; optimal uniformity at one time during the implosion may not be optimal at a later time. (2) The distribution of incident beam angles on target is not the same for the polar and equatorial regions; as a result, there will be variations in target drive due to spatial variations in laser absorption and in the density, where absorption occurs.

An example of the different angular distributions of incident rays is shown in Fig. 96.9 for two polar angles: 20° (characteristic of the polar region) and 90° . The normalized distribution of laser energy is plotted as a function of incident ray angle. This represents the simple projection of rays from the x-ray-drive ports onto a sphere, which is the initial size of the target. Each of the distributions has been averaged over all azimuthal angles and $\pm 10^\circ$ in the polar angle. The width of the distribution is the result of contributions from overlapping beams as well as the averaging. The distribution in the polar region is heavily weighted toward angles below 40° and is typical of the distribution around the target when beams originate from the direct-drive ports. The distribution of rays in the equatorial region is dominated by angles greater than 40° .



TC6379

Figure 96.9

The distribution of incident angles for the laser rays is calculated by projecting the beams from the NIF's x-ray-drive ports onto a sphere, using the beam pointing of Fig. 96.8. The distributions have been averaged over all azimuthal angles and $\pm 10^\circ$ in polar angle.

An indication of the variation in electron densities where the energy would be deposited is given by the turning points of the rays during refraction. Using a planar approximation, the electron density n_e at the turning point of the rays is $n_e = n_c \cos^2\theta$, where n_c is the critical density and θ is the incident angle of the rays. Thus, energy in the polar region is deposited typically above $0.6 n_c$, and energy near the equator is deposited well below $0.6 n_c$.

To improve the pointing strategy, absorption physics was added to the analysis. We used a target design (described in the following section) driven by uniform irradiation to obtain the density and temperature profiles at a time near peak laser irradiation. Rays were then tracked from the NIF x-ray-drive ports through the plasma atmosphere to calculate absorp-

tion as a function of the incident angle. The relative energy among the beams, the beam pointing, and the beam-spot shapes were varied to find the configuration that gave the lowest rms variation in absorption around the target. Optimal uniformity was found by pointing the beams to latitudes that were closer to the equator than the direct-drive positions in Fig. 96.8, namely 26° , 59° , and 82° . Elliptical spot shapes were used, with the ratio of major to minor axes being 1.0, 1.25, and 1.8, respectively.

Further optimization of the irradiation strategy must take into consideration the differences in hydrodynamic efficiency that result from variations around the target in density where the laser light is absorbed; time-dependent effects resulting from the target implosion and plasma evolution; and multidimensional effects such as lateral heat flow arising from temperature variations in the laser deposition region. The 2-D simulations include all these effects and were used as guidance on how to further improve the uniformity of target drive through the use of beam pointing, laser-focal-spot shapes, and pulse shapes.

One-Dimensional Target Design Considerations

One-dimensional simulations are useful to obtain insight into the sensitivity of target drive to the distribution of incident laser rays. They were used here to obtain a first estimate of the spatial variations in laser intensity that are required to compensate for the variations in incident laser light around the target. The results also identified a realistic target design for the 2-D simulations. These estimates neglect the effect of lateral mass and heat transport, which are included in the full 2-D simulation described in the next section.

A series of 1-D simulations were performed, each corresponding to a different latitude on the target. The distributions of incident laser rays for the different latitudes were estimated as done for Fig. 96.9. In each simulation, the target was uniformly irradiated with the distribution of rays corresponding to a particular latitude. The rays were traced in the spherical plasma profiles, but because of the spherical symmetry of the problem, only the radial location of the ray entered. The goal was to find a pulse shape corresponding to each latitude such that the resulting shock positions and shell positions were similar to those for the 20° latitude, within a few microns.

We used the CH(DT)₄, 1.5-MJ design (1.35 MJ absorbed) from Ref. 1 as the starting point. The design was further optimized for a target driven with the distribution of incident laser rays characteristic of the 20° latitude. This became the

baseline for determining pulse shapes at other latitudes. The 1-D simulations showed very little variation in the required pulse shapes for latitudes between 0° and 60° . However, to obtain similar target drive with the equatorial distribution of rays, the energy in the beams had to be increased by about 30%.

These 1-D estimates indicated that a 1.1-MJ target design should be used in the 2-D simulations: this should provide enough “headroom” to increase beam energies by 30% to 50%, if necessary, to compensate for the oblique irradiation near the equator. (This assumes a 1.6-MJ capability for the NIF.) The target and pulse shape were similar to the $\text{CH}(\text{DT})_4$ design from Ref. 1, but they were scaled down for the incident energy of 1.1 MJ (see Fig. 96.7). The 1-D results were target gain = 54; absorbed energy = 1.0 MJ; peak implosion velocity = 4.1×10^7 cm/s; and peak $\rho R = 1.2$ g/cm². A stability analysis, using a postprocessor¹¹ to the 1-D code *LILAC*, showed that the mix region was only about 30% of the shell thickness during the acceleration phase of the implosion for this target.

This design was used as a baseline for the 2-D hydrodynamic simulations (see next section). In the 2-D simulations, the pulse shapes for the different rings of beams were adjusted to produce similar shock and shell conditions as achieved in the 1-D baseline simulation. Besides compensating for the reduced laser coupling at the equator, the pulse shapes had to compensate also for the lateral flow of deposited energy from the equator toward the pole. The 1-D estimates showed that coronal electron temperatures should be higher at the equator than in the nearby mid-latitude regions, due to the higher laser intensity required to drive that part of the target. This will result in lateral heat flow in the 2-D simulations.

Two-Dimensional Simulation Results

For the 2-D *DRACO* simulations, the NIF irradiation configuration was described in terms of the beams pointed to three latitude rings in each hemisphere, as shown in Fig. 96.8. The simulations discussed below used the latitudes 26° , 59° , and 82° relative to the initial radius of the target (see **Beam-Pointing Strategy**, p. 213). A ray-trace algorithm with refraction calculated the amount of laser absorption and the location of the deposited energy in the plasma atmosphere around the target. An azimuthal average of the deposition was used. Whereas a full three-dimensional ray-trace algorithm has been developed for PDD simulations in the Eulerian code *SAGE*,¹² an approximate treatment was implemented here for speed during optimization studies. The approximation used only the radial variation in the index of refraction to modify the ray trajectories and ignored lateral variations. An azimuthal aver-

age of the laser deposition determined how energy for each ring was distributed on the target. These simulations addressed only the gross nonuniformities in target drive that arise from beam placement and pointing. The effects of target-surface nonuniformities and beam nonuniformities will be examined in future work.

As the target implodes, the energy delivered to the equator changes relative to the pole because the beams are not pointed toward the target center. To compensate for the time-dependent effects, as well as 2-D effects resulting from lateral heat flow, different pulse shapes were used for the three rings of beams. A numerical algorithm was developed to automatically adjust pulse shapes during the simulation to compensate for nonuniform drive. Different tests were used to detect nonuniformities: During the time of shock propagation, variation in the mass-weighted, inward-moving velocity was used. After the time of shock breakout and during acceleration, variation in the outer position of the target shell (as defined by the location of the point at $1/e$ times peak density) was used. The pulse-shape-refinement algorithm adjusted the relative power among the pulses to increase laser deposition in regions where the target was moving too slowly and to decrease deposition in regions that were moving too rapidly. In practice the required variation in laser absorption around the target could be achieved only for long-wavelength nonuniformities because control is limited to only three degrees of freedom corresponding to the three rings of beams.

To adjust the pulse shape in each ring of beams, we calculated the energy deposition pattern for each ring separately on the target. The relative power in each ring was varied until the superposition of all the deposition patterns formed a best fit to the variation required to compensate for drive nonuniformities.

A technique known as proportional–integral–differential (PID) feedback, common in control theory,¹³ was used to adjust the pulse shape for each ring of beams on the target. The source of the feedback was the spatial perturbation formed by sampling the nonuniformity during a *DRACO* simulation and then applying the proportional, integral, and differential feedback gain terms. The integral and differential terms act to dampen and stiffen the response function. A simple prescription to find the feedback gain terms can be found in Ref. 14. The Levenberg–Marquardt nonlinear optimization algorithm¹⁵ was employed to find the optimal choice for the relative strengths among the rings of beams such that the combined absorption variation provides a best fit to the feedback perturbation. Spherical-harmonic modal space was used in lieu of physical

space in the algorithm because the Levenberg–Marquardt algorithm allows for the optimization of a predetermined set of modes. For instance, certain modes considered the most dangerous can be given a larger weight during optimization. Note that in the limit of zero feedback gain, the optimization procedure reduces to a minimization of the rms variation of absorbed energy.

The pulse-shape refinement algorithm was not able to respond adequately to nonuniformities that were highly localized around the equator. To compensate for the reduced energy deposition at the equator from the very oblique incident irradiation, it is necessary to substantially increase the relative amount of energy deposited in that region by the equatorial ring of beams. However, if the spot shape were made sufficiently elliptical to localize the energy to the equatorial region, its contribution to uniformity through beam overlap in the mid-latitudes would be reduced. The problem was addressed by using a beam profile that was parameterized as the superposition of two super-Gaussian profiles (illustrated in Fig. 96.10). The main part of the spot shape is a super-Gaussian profile that contributes to beam overlap in the mid-latitudes as well as the equator. Superimposed on this is a highly elliptical super-Gaussian profile that concentrates additional energy only in the equatorial region. The aspect ratio of the ellipse, its relative location, and its relative energy are adjustable parameters that were varied in a series of 2-D simulations to find the optimal drive uniformity. In the simulations below, the ratio of major to minor axes was 5; the center of the superimposed ellipse was offset from the main spot by 10% of the target radius in the direction of the equator; and its peak intensity was 20% of the peak intensity for the main spot. The shape of the main part of

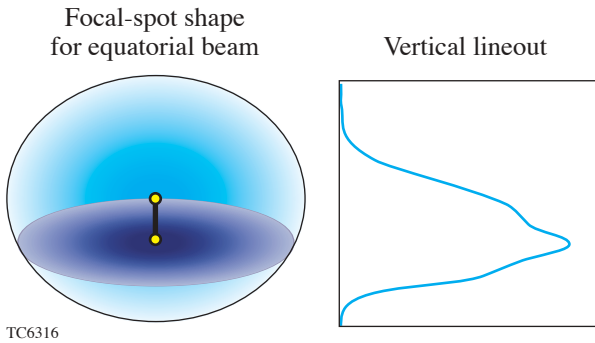


Figure 96.10

The spot shape for the equatorial ring of beams is chosen as the superposition of two super-Gaussian profiles. The larger profile contributes to irradiation uniformity at the mid-latitude regions, as well as near the equator. The highly elliptical profile concentrates additional energy very close to the equator.

the beam was also varied, and a 1.8:1 ellipse was used in the simulations below.

The three pulse shapes generated by the pulse-shape refinement algorithm resulted in the intensity variations shown in Fig. 96.11(a) for the pole and equator. The intensity variation for all polar angles is shown in Fig. 96.11(b) for the times 4.2 ns and 8 ns. At 4.2 ns, the intensity variation is relatively flat, increasing by about 30% only near the equator. This is consistent with the 1-D estimates. At 8 ns, there is a dip in the incident intensity at 45°, followed by a factor-of-2 increase at the equator. This is a 2-D effect. The temperature at the equator becomes larger than in the mid-latitudes due to the increased intensity required to drive that portion of the target. Lateral heat flow moves some of the energy deposited at the equator toward the 45° latitude. Consequently, less laser light needs to be deposited at 45° to obtain the required target drive at that location, but more energy must be deposited at the equator.

The resulting drive uniformity was adequate to achieve a high value of fuel ρR during the implosion, but further improvements in uniformity are required to actually reach ignition. The PDD simulation tracked the corresponding 1-D result up to the onset of hot-spot formation. A comparison between the PDD angularly averaged density profile and the 1-D profile at the end of the acceleration phase of the implosion is shown in Fig. 96.12. At this time, the shell radius has converged by almost a factor of 4. The positions and magnitudes of the peaks are very similar; however, there were density variations of $\pm 20\%$, pressure variations of $\pm 10\%$, and a variation in the outer surface of the shell of $\pm 5\%$. These nonuniformities continued to grow during the deceleration phase of the implosion.

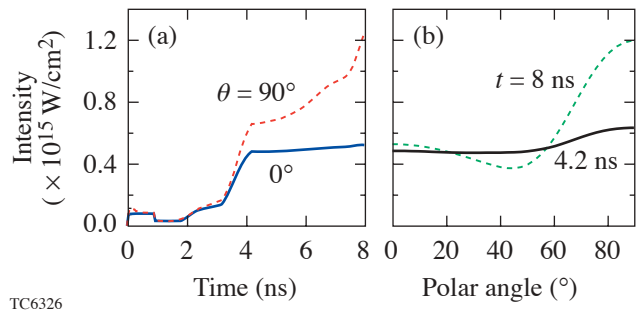
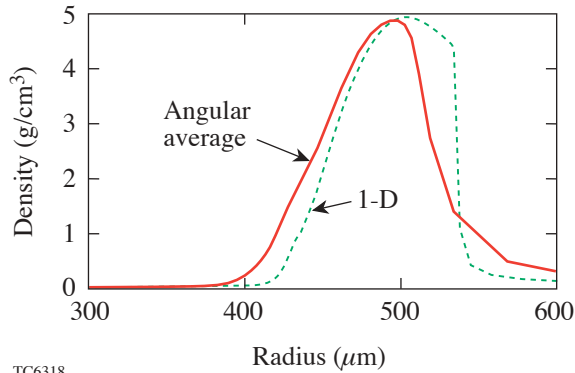


Figure 96.11

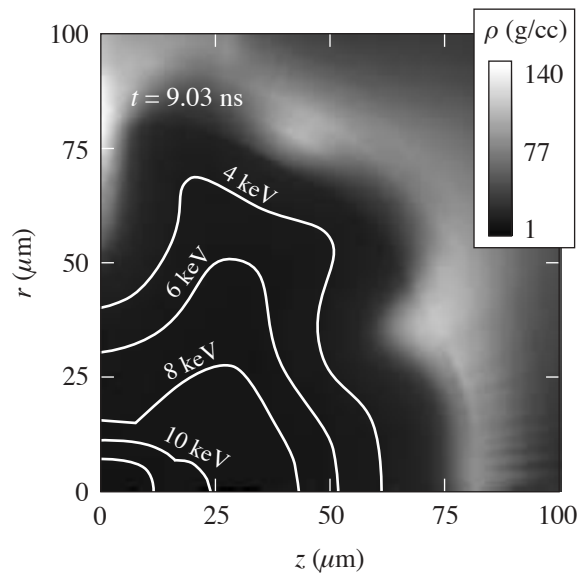
The variation in intensities at the pole and equator shows the compensation required for PDD: (a) the temporal variation in intensity at the pole and equator; (b) the angular variation in intensity at times 4.2 and 8.0 ns.

Near the time of hot-spot formation, when the shell had converged an additional factor of 6, the target nonuniformities had grown sufficiently large that the resultant shell distortion prevented further development toward ignition. A density contour plot at this time in the simulation is shown in Fig. 96.13, together with the temperature contours for 10, 8, 6, and 4 keV in the hot-spot region. High-density spikes are starting to penetrate into the hot region. In Fig. 96.14, the



TC6318

Figure 96.12
The angular average of the density profile from the PDD simulation is compared with the corresponding 1-D density profile at the end of the acceleration phase of the implosion (8.2 ns).



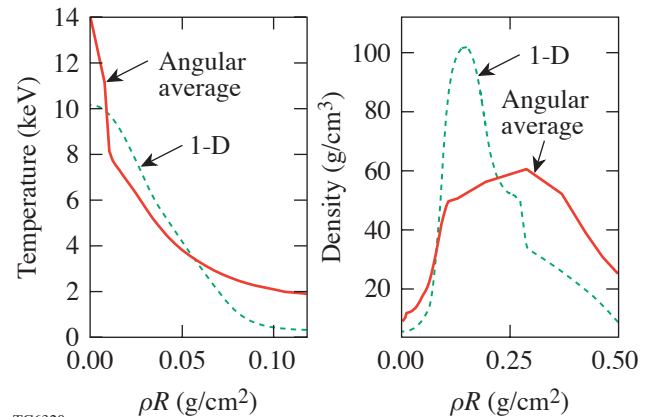
TC6319

Figure 96.13
Density contour plot at the onset of hot-spot formation (9.03 ns) shows spikes starting to penetrate the hot region. Temperature contours of 10, 8, 6, and 4 keV are shown.

angular average of both the temperature and density is compared with 1-D profiles as a function of ρR . The temperature profiles are similar, with the hot region extending to a ρR of ~ 0.1 g/cm². Over the next 100 to 200 ps, the 1-D simulation extends the hot region to a ρR of 0.2 to 0.3 g/cm² and ignition occurs. The 2-D simulation failed to continue forming the hot spot beyond this point due to extensive growth of shell distortion. In Fig. 96.14, the contribution of shell distortion is evident in the width of the angularly averaged density profile.

Even though ignition did not occur in this simulation, the conditions achieved during the time of neutron production could be very useful for the development of high- ρR diagnostics and the investigation of fast-ignitor physics.¹⁶ The neutron-averaged ρR was 1.1 g/cm², and the neutron yield was 6×10^{16} (corresponding to a target gain of 0.1).

Strategies to improve the uniformity of target drive for PDD are being developed. The automated pulse-shape refinement algorithm is being further optimized to better detect drive nonuniformity and adjust pulse shapes accordingly. For a given set of beam-pointing and spot-shape conditions, it may not be possible to achieve adequate drive uniformity by adjusting the pulse shapes. Thus, the specifications for beam pointing and spot shapes are also being refined. Target “shimming,” in which the target shell is made thinner at the equator than at the pole, is another technique that will be examined for improving drive uniformity. Conditions very close to ignition have been achieved here. An additional factor-of-2 improvement in drive uniformity will probably be adequate for the target to ignite.



TC6320

Figure 96.14
The angular averages of temperature and density profiles from the PDD simulation near the onset of hot-spot formation (9.03 ns) are compared with the 1-D results.

The computer simulations used to identify optimal irradiation strategies will be validated by experiments on the OMEGA laser.

PDD Experiments on OMEGA

Three sets of experiments planned for the OMEGA laser over the coming year are designed to validate the computer modeling of target performance driven by oblique irradiation. One set of experiments will investigate shock propagation in planar geometry using cryogenic D₂ and wetted-foam targets. The OMEGA beam geometry can irradiate a planar target with beams at 23°, 48°, and/or 60° angles of incidence. The main diagnostic will be the measurement of the time of shock breakout at the rear of the target.

The second set of experiments will irradiate spherical targets uniformly, but with all the beams repointed to make the beam axes equally oblique to the target surface. The symmetry of the OMEGA irradiation geometry can be maintained by repointing all beams by the same amount. This can be achieved as shown in Fig. 96.15: The beams of the OMEGA laser are configured as 12 pentagonal groups. The angle of incidence of each beam axis on the initial target surface can be changed from normal to 24.8° by pointing each beam to a place on the target that corresponds to the position of a neighboring beam in the pentagon. This tests the modeling of laser absorption and target drive with oblique irradiation, without introducing the complication of large variations in irradiation conditions around the target.

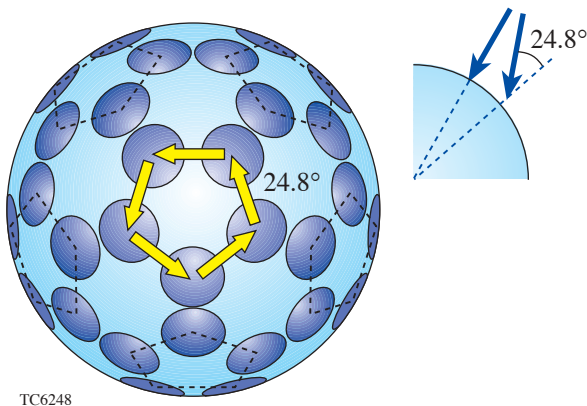


Figure 96.15

One of the PDD experiments planned for the OMEGA laser will repoint all beams by the same amount to maintain irradiation uniformity while driving an implosion with oblique irradiation.

The third set of experiments will be a more direct characterization of PDD on the NIF. In this case, 40 of the 60 OMEGA beams will be used to populate only the beam ports near the polar regions, providing a good approximation to the polar-direct-drive conditions that will occur on the NIF. The beams will then be repointed, and the pulse shapes adjusted (within the limitations of OMEGA), to drive spherical implosions. These will be compared with 2-D simulations.

Summary

The recent progress in direct-drive target design makes the direct-drive approach to inertial confinement fusion a very attractive candidate for achieving high gain on the NIF. Adiabatic shaping is a very powerful technique to enhance target stability. When combined with the increased laser absorption possible in wetted-foam targets, 1-D target gains of the order of 80 are possible.

Direct-drive target physics can be examined while the NIF is in the x-ray-drive configuration by pointing some of the beams toward the target equator. This polar-direct-drive approach presents more-difficult design problems than standard direct drive, which uses a beam configuration already optimized for the required level of irradiation uniformity. For PDD, the incident irradiation must be made intentionally nonuniform—higher in the equatorial region than in the polar region—to accurately compensate for the spatial variations in laser absorption and hydrodynamic efficiency. Simulations have not yet demonstrated ignition with PDD, and the optimization process is still in progress. Nevertheless, high values of ρR and high neutron yield have been obtained in the simulations, suggesting that, at the very least, PDD can be an attractive technique for high- ρR diagnostic development and fast-ignitor experiments. PDD might be the best approach for fast-ignitor experiments while the NIF is in the x-ray-drive configuration because of the relatively large amount of energy that can be coupled to the fuel and because the ignitor beams can access the compressed core without passing through a hohlraum.

ACKNOWLEDGMENT

This work was supported by the U.S. Department of Energy Office of Inertial Confinement Fusion under Cooperative Agreement No. DE-FC03-92SF19460 and the University of Rochester. The support of DOE does not constitute an endorsement by DOE of the views expressed in this article.

REFERENCES

1. P. W. McKenty, V. N. Goncharov, R. P. J. Town, S. Skupsky, R. Betti, and R. L. McCrory, *Phys. Plasmas* **8**, 2315 (2001).

2. S. Skupsky, R. Betti, T. J. B. Collins, V. N. Goncharov, D. R. Harding, R. L. McCrory, P. W. McKenty, D. D. Meyerhofer, and R. P. J. Town, in *Inertial Fusion Sciences and Applications 2001*, edited by K. Tanaka, D. D. Meyerhofer, and J. Meyer-ter-Vehn (Elsevier, Paris, 2002), pp. 240–245.
3. V. N. Goncharov, J. P. Knauer, P. W. McKenty, P. B. Radha, T. C. Sangster, S. Skupsky, R. Betti, R. L. McCrory, and D. D. Meyerhofer, *Phys. Plasmas* **10**, 1906 (2003).
4. T. J. B. Collins and S. Skupsky, *Phys. Plasmas* **9**, 275 (2002).
5. S. P. Obenschain *et al.*, *Phys. Plasmas* **9**, 2234 (2002).
6. A short description of the hydrocode *DRACO* is contained in P. B. Radha, V. N. Goncharov, T. J. B. Collins, J. A. Delettrez, P. W. McKenty, and R. P. J. Town, “Two-Dimensional Simulations of Plastic-Shell Implosions on the OMEGA Laser,” to be submitted to *Physics of Plasmas*.
7. J. D. Lindl and W. C. Mead, *Phys. Rev. Lett.* **34**, 1273 (1975).
8. T. J. B. Collins, S. Skupsky, V. N. Goncharov, R. Betti, P. W. McKenty, P. B. Radha, R. Epstein, A. Poludnenko, A. Frank, and S. Mitran, “High-Gain, Direct-Drive Foam Target Designs for the National Ignition Facility,” to be published in *Inertial Fusion Sciences and Applications 2003* (Elsevier, Paris, 2004).
9. M. C. Herrmann, M. Tabak, and J. D. Lindl, *Phys. Plasmas* **8**, 2296 (2001).
10. S. M. Pollaine and S. W. Haan, *ICF Quarterly Report* **8**, 15, Lawrence Livermore National Laboratory, Livermore, CA, UCRL-LR-105821-98-1 (1997).
11. V. N. Goncharov, P. McKenty, S. Skupsky, R. Betti, R. L. McCrory, and C. Cherfils-Clérouin, *Phys. Plasmas* **7**, 5118 (2000).
12. R. S. Craxton, *Bull. Am. Phys. Soc.* **48**, 56 (2003).
13. W. S. Levine, *The Control Handbook* (CRC Press, Boca Raton, FL, 1996).
14. See Ziegler–Nichols tuning rules, in K. Ogata, *Modern Control Engineering*, 3rd ed. (Prentice-Hall, New Jersey, 1997), Chap. 10, pp. 672–674.
15. W. H. Press, *Numerical Recipes in C: The Art of Scientific Computing* (Cambridge University Press, Cambridge, England, 1988), pp. 540–547.
16. M. Tabak *et al.*, *Phys. Plasmas* **1**, 1626 (1994).

Properties of Fluid Deuterium Under Double-Shock Compression to Several Megabars

The equation of state of hydrogen at pressures of a few megabars, temperatures of a few electron volts, and compressions of up to several times liquid density has been a source of ongoing experimental^{1–4} and theoretical^{5–11} controversy. Understanding the properties of hydrogen under such conditions is fundamental to the modeling of massive planets, brown dwarfs,¹² and inertial confinement fusion. At present, access to these dense, high-pressure states can be achieved only by using shock waves; Hugoniot measurements are thus the primary tool for constraining dense-hydrogen equation-of-state (EOS) models.

Determining the density of a shocked material with a compressibility as large as hydrogen requires high-precision measurements of the primary observables. This is because fractional errors in the inferred compression ratio ρ/ρ_0 are $\rho/\rho_0 - 1$ times greater than fractional errors in the observables U_s (shock speed) and U_p (particle speed). Making a measurement precise enough to discriminate between the various deuterium EOS models thus presents a significant experimental challenge.

The first experiments to study shocked deuterium above 0.2 Mbar on the principal (i.e., single-shock) Hugoniot used laser-driven shock waves and a new, absolute measurement technique—results showed five- to sixfold compression between 1 and 2 Mbar.¹ This was in general agreement with the linear-mixing model of Ross⁷ but was in significant disagreement with the original *SESAME* model developed by Kerley.⁵ Subsequent experiments using magnetically driven flyer plates and a relative measurement of U_p based on aluminum impedance matching, found slightly over fourfold compression at 0.4 Mbar, which decreased to fourfold compression at 0.7 Mbar and 1 Mbar.³ These data were consistent with a new *SESAME* model developed by Kerley⁸ (which, for clarity, we refer to as the Kerley98 model) and *ab initio* models^{10,11} but exhibit slightly higher compressibility than the original *SESAME*⁵ and significantly lower compressibility than the Ross model. Although the pressure range of these two experiments overlapped only slightly, a clear discrepancy emerged

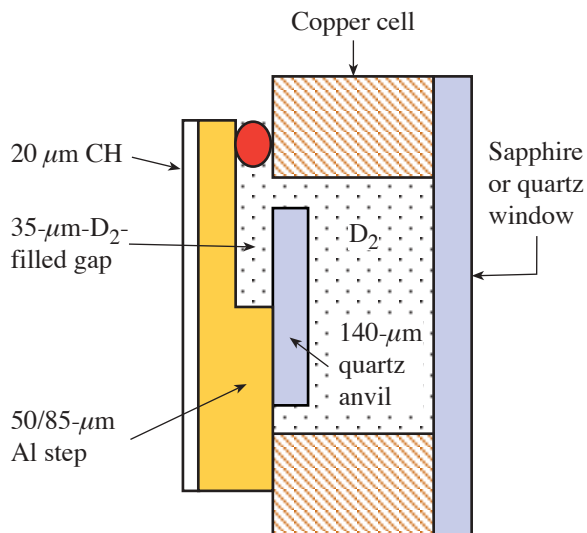
near 1 Mbar. This discrepancy may indicate a lack of understanding of the fundamental processes in hydrogen. ICF target designs can readily accommodate these differences because they occur at relatively low pressures encountered early in the implosion. Astrophysical models, however, depend greatly on the precise details of EOS models to extrapolate conditions of large planetary bodies. This small difference can have huge effects.

The first experiment to study deuterium under double-shock conditions at megabar pressures was performed by Mostovych *et al.*,² who used shocks reflected from an aluminum anvil. They recognized that the expected differences between EOS model predictions for the experimental observables are greater in a reflected-shock measurement than in a single-shock measurement. Reflected shocks thus provide a more-sensitive experimental platform for discriminating between the various models; they do, however, probe not only the principal Hugoniot but also the re-shock Hugoniots and thus are a complementary, rather than an equivalent, probe of the equation of state. The data of Mostovych *et al.*,² taken up to single-shock pressures of 1.3 Mbar, had significant uncertainties, with error bars on a single point spanning the difference between the various models; on average, however, results agreed with the more-compressible linear-mixing model of Ross.

In this study we examine the behavior of fluid deuterium shocked initially to 0.7 to 2.5 Mbar and then double shocked to 2.5 to 9 Mbar. We cover a wider range of pressures than Mostovych *et al.*² and significantly improve upon the precision of those experiments by using α -quartz—a transparent re-shock anvil material—rather than aluminum. This allows us to use a high-precision, line-imaging optical interferometer to record the shock-front velocity continuously as it transits the deuterium–quartz interface. Such an approach also minimizes any systematic errors due to shock unsteadiness and non-planarity since the measurements are localized to essentially one point in space and time. Our results are consistent with path-integral Monte Carlo (PIMC)¹⁰ models and the Kerley98

EOS at single-shock pressures less than 1 Mbar and above 2 Mbar but deviate at intermediate pressures; the Ross model does not agree with our data over the entire range under study.

This experiment was performed on LLE's OMEGA laser, a neodymium-doped phosphate glass system that operates with frequency-tripled, 0.35- μm light.¹³ To generate the shock pressures explored in these experiments, laser energies of 440 to 3100 J were delivered using a 3.7-ns-duration square pulse. The laser focal region was smoothed using distributed phase plates (DPP's), producing a uniformly irradiated 800- μm -diam spot. Targets consisted of a z -cut, α -quartz anvil mounted on the upper step of a diamond-turned aluminum pusher that was attached to a copper cell filled with cryogenic deuterium (see Fig. 96.16). A plastic ablator was used to reduce hard-x-ray generation. Three thicknesses were used for the ablator–pusher combination: 20 μm of CH on a 90- to 130- μm Al step (90- μm lower step and 130- μm upper step); 20 μm of CH on a 50- to 85- μm Al step, and 20 μm of CH plus 80 μm of CH-Br (plastic with 2% Br by atomic weight) on a 50- to 85- μm Al step. The quartz anvil was glued to the upper step with a glue thickness of ~ 1 μm and hung over the lower step as shown in Fig. 96.16. The deuterium sample explored in this experiment is trapped within the 35- to 40- μm region between the quartz anvil and the thin Al plate. By observing the solid–liquid



E12734

Figure 96.16
Characteristic cryogenic deuterium target design. Dimensions are for one of the three types of target.

transition in deuterium and using the well-known properties of deuterium on the saturation line,¹⁴ we determined that the deuterium density was 0.174 g/cm³. At this density and at the probe laser wavelength of 532 nm, the index of refraction was calculated to be 1.1381.¹⁴ The density of the quartz was measured to be 2.65 g/cm³. The index of refraction of quartz along its c axis at 532 nm was measured to be 1.547.

The shock diagnostic was a line-imaging velocity interferometer system for any reflector (VISAR),^{15,16} which measures the Doppler shift of a moving reflector. Two VISAR's with different velocity sensitivities were used to resolve 2π phase-shift ambiguities that occur at shock breakout from the aluminum and upon transit of the shock front from deuterium into quartz. The velocity sensitivities for the two VISAR instruments were 6.069 and 14.138 $\mu\text{m}/\text{ns}/\text{fringe}$ for deuterium and 4.465 and 10.400 $\mu\text{m}/\text{ns}/\text{fringe}$ for quartz. Post-processing of the VISAR images can determine the fringe position to $\sim 5\%$ of a fringe; since the measured shock velocities are 25 to 45 $\mu\text{m}/\text{ns}$ in deuterium and 14 to 24 $\mu\text{m}/\text{ns}$ in quartz, multiple fringe shifts allow the precision of the shock-velocity measurement to be $\sim 1\%$. The probe source was an injection-seeded, Q -switched, yttrium–aluminum garnet laser, operating at a wavelength of 532 nm with a pulse length of ~ 25 ns. Streak cameras with temporal windows of ~ 3 ns were used to detect the reflected probe signal. The time resolution of the VISAR and streak camera system was about 40 ps.

A sample VISAR trace is shown in Fig. 96.17(a), and the resulting velocity profile inferred from the fringe positions is given in Fig. 96.17(b). The three clear events observed in these records are marked by fringe (and, hence, velocity) shifts: The first shift represents the velocity jump that occurs when the shock crosses the aluminum–deuterium interface; the second shift, at time t_x , corresponds to the drop in shock velocity as the shock moves across the deuterium–quartz interface. Shock velocities immediately before and after the shock crosses the D₂–quartz interface are the primary observables used in this work. The third shift is the jump in velocity observed in quartz when the first shock, reverberating in the compressed deuterium gap, catches the leading shock front in quartz.

To extract the velocity profile, we average the phase information at each time over a 20- to 30- μm region. To determine shock velocities at the deuterium–quartz interface, we take linear fits a few hundred picoseconds before and after t_x and extrapolate them to t_x . This eliminates ambiguities due to slight blurring of the measured velocity in a ± 25 -ps time window centered on t_x caused by the resolution of the VISAR and

streak camera system. Figure 96.18 plots the results in terms of the primary experimental observables: the shock speed in deuterium and quartz.

To compare these observations with EOS models it is necessary to know the high-pressure U_s-U_p relation for quartz. This relation was determined by performing extensive laser-driven shock measurements on quartz,¹⁷ complementing data (reported in early Russian work) obtained using nuclear explosives,¹⁸ and found that $U_s = 3.915 + 1.297 U_p$. Taking into account the errors in the fit coefficients, this is in excellent agreement ($\sim 1\%$) with the relation found in the early Russian work ($U_s = 4.200 + 1.280 U_p$)¹⁹ over the range of pressures in our study. Our measurements were performed using impedance matching with an aluminum standard for which we utilized the experimentally derived aluminum Hugoniot rela-

tion given by $U_s(\text{Al}) = 6.541 + 1.158 U_p(\text{Al})$,¹⁹ because quartz and aluminum are closely impedance matched, the release was accurately calculated from the reflected Hugoniot.²⁰ The results change very little—and only then at the very highest pressures—if we instead use a *SESAME* EOS for aluminum.²¹

Silica is known to possess a number of polymorphic phase transitions in the solid regime below 1 Mbar.²² Above ~ 1 Mbar, where silica is a fluid, quartz Hugoniot measurements have shown no indication of a subsequent structural change.¹⁸ Our data begin at ~ 2.5 Mbar and closely follow a linear fit in U_s-U_p .

Using this fit and the impedance-matching conditions at the deuterium–quartz interface, we calculate the reflected shock curves for the different EOS models. These are shown in Fig. 96.18, where the uncertainty in the linear fit to the quartz Hugoniot is the thickness of the thick blue line (for clarity, the PIMC results, which are close to the Kerley98 predictions, are shown as squares). Plotting the data in terms of the experimental observables thus allows uncertainties in the quartz Hugoniot

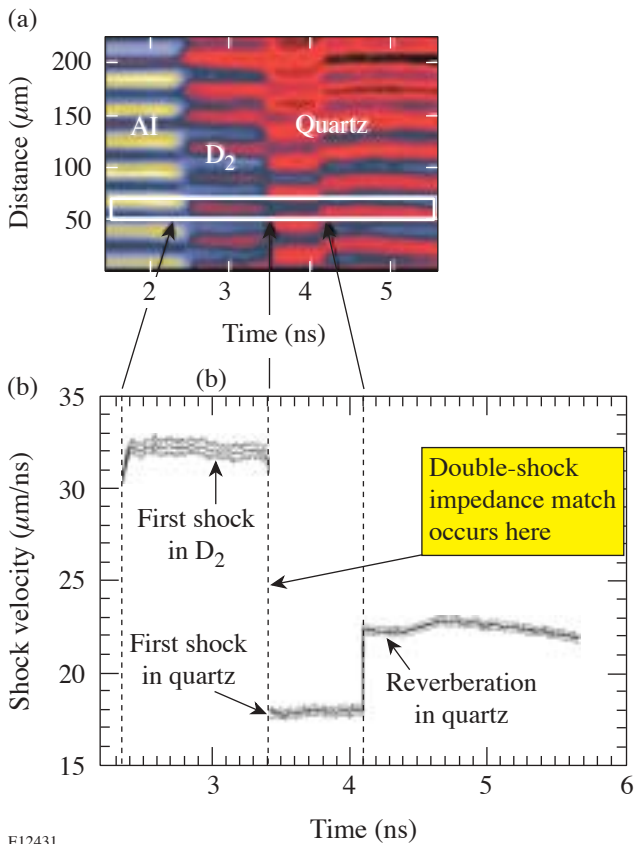


Figure 96.17

(a) Sample VISAR trace showing the signal from the reflecting shock front in deuterium and quartz. (b) Resulting velocity profile extracted from the VISAR trace in (a). Dotted lines above and below the main trace indicate the error at each time step. The shock traverses the deuterium–quartz interface at time t_x .

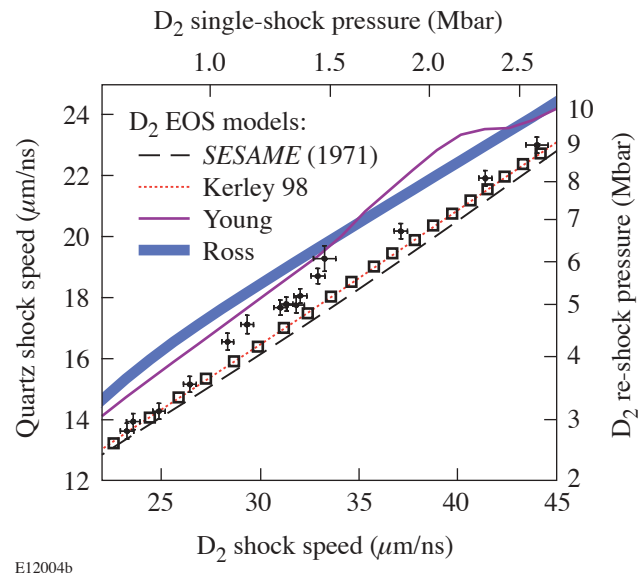


Figure 96.18

Double-shock data for fluid deuterium obtained using an α -quartz anvil (dark circles with error bars). Predictions for different equations of state are shown: *SESAME*⁵ (long dashed), Kerley98⁸ (red dotted), Young⁹ (solid), Ross' linear-mixing model⁷ (thick blue), and PIMC¹⁰ (squares). The measured uncertainty in the quartz Hugoniot is about the thickness of the lines. The estimated D_2 single-shock and re-shock pressures on the top and right axes are based on the PIMC model for D_2 and the measured quartz Hugoniot, respectively.

to be separated from measurement errors in the deuterium re-shock experiments (which are given by the error bars on the data points). We note that the difference in expected quartz shock velocities between the softer Ross model and the stiffer Kerley98 model is close to 10% over much of the range of study. Our experimental precision of $\sim\pm 1\%$ allows us to readily discriminate between these models. The results indicate that double-shock compression of deuterium from single-shock pressures between 0.7 and 2.5 Mbar cannot be adequately described over this range by any of the models shown. Between single-shock pressures of 0.7 and 1.0 Mbar, the PIMC¹⁰ and Kerley98⁸ predictions are consistent with our data; in the regime between 1.0 and 1.3 Mbar the data approach the predictions of the Young model⁹ but disagree with all models between 1.3 and 2.0 Mbar; above 2 Mbar, the results are again consistent with the stiffer PIMC and Kerley98 calculations, while at higher pressures the measurements are in agreement with the stiffer models.

A number of potential systematic effects that could compromise our data have been considered and are addressed below. The steadiness of shock-wave velocities in our experiments varied from shot to shot, depending on the laser drive, ranging from fractions of a percent to several percent over a few nanoseconds. Our new technique of determining shock velocities at essentially a single point in time using continuous measurements is not affected by such variations, unlike the transit-time measurements that were used in the earlier re-shock experiments.² To establish this, we performed extensive hydrodynamic simulations of our experimental arrangement using shock waves with a wide range of unsteadiness—rising and decaying. We saw no deviations from the steady shock case if the velocities were extrapolated to time t_x . This is confirmed experimentally where we observe no difference between the shots that were essentially steady and those that had several-percent unsteadiness.

Shock nonplanarity is also a potential problem, especially for an experiment that requires measurement of a breakout event at spatially separated positions. Since our measurement is performed at a localized point in space, we are not subject to such errors. Nonplanarity could affect our measurements if the wave is incident on the deuterium–quartz interface at an angle large enough to undergo significant refraction. Based on our measurement of the small curvature observed at the deuterium–quartz interface, we infer that the largest incident angles present in our experiments are 3° to target normal. The resulting change in the projected shock speed is less than 0.1% and can be neglected.

X-ray preheating of our target system is a process that would tend to make our data look less compressible. Using an etalon sensitive to motions as low as $0.1 \mu\text{m/ns}$, we observed no expansion of the aluminum pusher prior to shock breakout. In addition, for targets shot at similar laser energies, we saw no difference in the results whether we used a $50\text{-}\mu\text{m}$ -thick or $90\text{-}\mu\text{m}$ -thick aluminum pusher. Since the attenuation length for a 1.55-keV x ray (just below the K edge of aluminum) is $10 \mu\text{m}$, the extra $40 \mu\text{m}$ of Al would be expected to reduce the x-ray fluence by a factor of 50. The absence of any difference between results from these two targets indicates that x-ray preheat is negligible for these experiments.

In conclusion, we have performed the highest-precision re-shock experiments to date on deuterium shocked to initial pressures between 0.7 and 2.5 Mbar. Below 1 Mbar and above 2 Mbar, the results are in approximate agreement with predictions based on the PIMC and Kerley98 models—models that have near-fourfold compression on the principal Hugoniot—but disagree with these theories between 1 and 2 Mbar. In contrast to earlier re-shock results,² our higher-precision measurements are not consistent with the Ross linear-mixing model. At present, no theory adequately accounts for our observed re-shock results over the entire range under study. We emphasize that there is no model-independent way to compare re-shock measurements with principal Hugoniot measurements since second-shock pressures are affected not only by the density of the first shock but also by the sound speed (or isentropic compressibility) of the compressed states. Given that shock experiments on deuterium above 0.4 Mbar have yielded a wide range of results, the equation of state of hydrogen at megabar pressures and electron-volt temperatures remains an open question. Ultimately a variety of different experimental techniques performed over a broad region of phase space will be required before a consistent picture can emerge.

ACKNOWLEDGMENT

We thank G. I. Kerley, B. Militzer, and D. A. Young for providing model calculations and the LLE Mechanical Engineering, target fabrication, and OMEGA operations staff for their efforts during these experiments. This work was performed under the auspices of the U.S. Department of Energy by LLNL under Contract No. W-7405-ENG-48 and by the University of Rochester under Cooperative Agreement No. DE-FC03-92SF19460.

REFERENCES

1. L. B. Da Silva *et al.*, *Phys. Rev. Lett.* **78**, 483 (1997); G. W. Collins *et al.*, *Science* **281**, 1178 (1998); G. W. Collins *et al.*, *Phys. Plasmas* **5**, 1864 (1998).

2. A. N. Mostovych *et al.*, Phys. Rev. Lett. **85**, 3870 (2000); A. N. Mostovych *et al.*, Phys. Plasmas **8**, 2281 (2001).
3. M. D. Knudson *et al.*, Phys. Rev. Lett. **87**, 225501 (2001); M. D. Knudson *et al.*, Phys. Rev. Lett. **90**, 035505 (2003).
4. S. I. Belov *et al.*, JETP Lett. **76**, 433 (2002).
5. G. I. Kerley, Los Alamos National Laboratory, Report LA-4776 (1972); J. Chem. Phys. **73**, 469 (1980); J. Chem. Phys. **73**, 478 (1980); J. Chem. Phys. **73**, 487 (1980).
6. D. Saumon and G. Chabrier, Phys. Rev. A **46**, 2084 (1992); D. Saumon, G. Chabrier, and H. M. Van Horn, Astrophys. J., Suppl. Ser. **99**, 713 (1995).
7. M. Ross, Phys. Rev. B, Condens. Matter **58**, 669 (1998).
8. G. I. Kerley, Lawrence Livermore National Laboratory, private communication (2002). This model has also been referred to as the *SESAME* model (Ref. 3) but shows softer behavior than the original *SESAME* (Ref. 5) referred to in earlier publications (Ref. 1).
9. D. A. Young, in *Shock Compression of Condensed Matter—1999*, edited by M. D. Furnish, L. C. Chhabildas, and R. S. Hixson (American Institute of Physics, Melville, NY, 2000), pp. 53–56.
10. B. Militzer and D. M. Ceperley, Phys. Rev. Lett. **85**, 1890 (2000); B. Militzer *et al.*, Phys. Rev. Lett. **87**, 275502 (2001).
11. T. J. Lenosky *et al.*, Phys. Rev. B, Condens. Matter **61**, 1 (2000); L. A. Collins *et al.*, Phys. Rev. B, Condens. Matter **63**, 184110 (2001).
12. R. Smoluchowski, Nature **215**, 691 (1967); W. B. Hubbard, Science **214**, 145 (1981); W. B. Hubbard *et al.*, Phys. Plasmas **4**, 2011 (1997); G. Chabrier *et al.*, Astrophys. J. **391**, 817 (1992); G. Chabrier and I. Baraffe, Astron. Astrophys. **327**, 1039 (1997).
13. T. R. Boehly, D. L. Brown, R. S. Craxton, R. L. Keck, J. P. Knauer, J. H. Kelly, T. J. Kessler, S. A. Kumpan, S. J. Loucks, S. A. Letzring, F. J. Marshall, R. L. McCrory, S. F. B. Morse, W. Seka, J. M. Soures, and C. P. Verdon, Opt. Commun. **133**, 495 (1997).
14. P. C. Souers, *Hydrogen Properties for Fusion Energy* (University of California Press, Berkeley, 1986).
15. L. M. Barker and R. E. Hollenbach, J. Appl. Phys. **43**, 4669 (1972).
16. P. M. Celliers *et al.*, Appl. Phys. Lett. **73**, 1320 (1998).
17. D. G. Hicks *et al.*, “Measurements of the Equation of State of Quartz,” in preparation.
18. L. V. Al'tshuler, R. F. Trunin, and G. V. Simakov, Izv. Acad. Sci. USSR Phys. Solid Earth, No. 1, 657 (1965); R. F. Trunin *et al.*, Izv. Acad. Sci. USSR Phys. Solid Earth, No. 1, 8 (1971); R. F. Trunin, Phys.-Usp. **37**, 1123 (1994).
19. R. F. Trunin, ed. *Experimental Data on Shock Compression and Adiabatic Expansion of Condensed Matter* (Russian Federal Nuclear Center—VNIIEF, Sarov, 2001).
20. R. F. Trunin, *Shock Compression of Condensed Materials* (Cambridge University Press, Cambridge, England, 1998).
21. The *SESAME* table for aluminum compared in this case was #3718, given in S. P. Lyon and J. D. Johnson, Los Alamos National Laboratory, Los Alamos, CA, Report LA-UR-92-3407 (1992). For our analysis, differences between the various *SESAME* tables for aluminum are negligible.
22. See, for example, J. A. Akins and T. J. Ahrens, Geophys. Res. Lett. **29**, 31-1 (2002) and references therein.

Independent Phase and Amplitude Control of a Laser Beam Using a Single-Phase-Only Spatial Light Modulator

Laser-beam shaping is a rapidly developing field of research driven by both technological improvements of beam-shaping devices and the ever-increasing demands of applications. In high-energy laser chains, efficient beam shaping is successfully achieved in the front ends by passive methods such as beam apodization¹ or intracavity mode shaping;² however, these static techniques are unable to correct dynamic laser-beam profiles caused by alignment drifts or thermal problems.

Spatial light modulators (SLM's) are versatile devices that can modulate the polarization or the phase of laser beams at high refresh rates. It has been demonstrated that a SLM can be used to compensate for the thermal phase distortion occurring in high-energy glass amplifiers.³ Similarly, SLM's have been used in high-energy laser applications, such as intracavity beam shaping⁴ or focal-spot control.⁵ In all these applications, only the phase-modulation capability of the SLM was used; however, there are numerous applications where phase-only modulation can be achieved differently. For instance, deformable mirrors are more attractive when it comes to wavefront correction of a large, high-energy, laser beam. Their scale and damage threshold allow them to be used within the power amplifier, while SLM's are confined to the front end because of their modest size and low damage threshold. Nevertheless, a corrective device that would address both phase and amplitude simultaneously may be successfully used in high-energy lasers to significantly reduce the alignment procedure time, to improve the amplifier fill factor by injecting a more-adapted beam shape, to reduce the risk of damage in the laser chain by removing hot spots, and to improve the on-target characteristics of the beam by better control of the phase.

Several techniques have been proposed to produce complex modulation of an electromagnetic field with an SLM for encoding computer-generated holograms.^{6,7} In both cases, two neighboring pixels with a single-dimension modulation capability are coupled to provide the two degrees of freedom required for independent phase and amplitude modulation. In our work, we use a similar approach, but our requirements

differ from that of the hologram generation. First, the number of modulation points across the beam does not need to be high because spatial filtering imposes a low-pass limit on the spatial frequencies allowed in the system. Second, a high-efficiency modulation process is required to minimize passive losses. Lastly, the required amplitude-modulation accuracy should be better than measured shot-to-shot beam fluctuations for the correction to be fully beneficial.

In this article, we propose a new method to modulate both the phase and amplitude of a laser beam, with a single-phase-only SLM using a carrier spatial frequency and a spatial filter. As a result, the local intensity in the beam spatial profile is related to the amplitude of the carrier modulation, while its phase is related to the mean phase of the carrier. In the first part of this article, we show the simple relation between the transmitted intensity and the phase-modulation amplitude, and in the second part, we experimentally verify this scheme and use it to demonstrate beam shaping in a closed-loop configuration.

The principle of the modulation is depicted in Fig. 96.19 for the case of a plane wave. The SLM is used as a phase-only device that applies a one-dimensional phase grating to the electric field. As a consequence, the two-dimensional propagation integral reduces to a one-dimensional one. In such a case, the electric field transmitted—or reflected—through the modulator accumulates a phase ϕ given by

$$E' = E_0 \exp[j\phi(x)], \quad (1)$$

where E_0 can be complex and ϕ is a periodic square phase modulation, of period Λ , oscillating between the values ϕ_1 and ϕ_2 . After propagation through a lens, in an f - f configuration and under the Fraunhofer approximation, the electromagnetic field distribution at the focus of the lens is proportional to the Fourier transform of Eq. (1). To calculate the Fourier transform of E' , one can consider, for instance, the initial electromagnetic field as a sum of two square waves defined by

$$E_1 = E_0 \sum_n \delta(x - n\Lambda) \otimes \text{rect}_{\Lambda/2}(x) \exp(j\phi_1), \quad (2)$$

$$E_2 = E_0 \sum_n \delta(x - n\Lambda) \otimes \text{rect}_{\Lambda/2}(x - \Lambda/2) \exp(j\phi_2), \quad (3)$$

where δ is the Dirac function and \otimes denotes the convolution product. After some algebra, the electromagnetic field distribution at the focus, given as the sum of the Fourier transforms of E_1 and E_2 , can be written as

$$\begin{aligned} \tilde{E} \propto E_0 \sin c\left(\pi \frac{\Lambda v}{2}\right) \cos\left(\frac{\Delta\phi}{2} + \pi \frac{\Lambda v}{2}\right) \\ \times \exp\left[j\left(\frac{\phi_1 + \phi_2}{2} - \pi \frac{\Lambda v}{2}\right)\right] \sum_n \delta(v - n/\Lambda), \end{aligned} \quad (4)$$

where n is the spatial frequency, and the Dirac comb function represents the diffraction pattern created by the SLM phase grating. Removing the higher-order terms ($|n| > 0$) in this diffraction pattern with a spatial filter results in an electric field given by Eq. (5), where the amplitude is determined by the phase difference $\Delta\phi$ and the phase is equal to the average of ϕ_1 and ϕ_2 :

$$\tilde{E}(0) \propto E_0 \cos\left(\frac{\Delta\phi}{2}\right) \exp\left(j\frac{\phi_1 + \phi_2}{2}\right). \quad (5)$$

This result is still true for finite beams, provided the amplitude and phase of the initial beam slowly vary with respect to the modulation frequency. If the electromagnetic field spatially varies at higher frequencies, then the imaging system will act as a spatial filter and will modify the spatial distribution of light regardless of the application of a phase modulation on the SLM.

In the experimental setup shown in Fig. 96.20, the light source is a pulsed, 300-Hz laser, the beam of which is up-collimated so that it overfills the SLM area and is linearly polarized. It is reflected off the SLM and then imaged on an 8-bit charge-coupled-device (CCD) camera (Cohu 4910 series) or to a Hartmann–Shack wavefront sensor (Wavefront Sciences CLAS-HP). The camera was used mainly for system alignment and diagnostic or whenever high-spatial-resolution beam amplitude measurement was required. The wavefront sensor was used for simultaneous phase and amplitude measurements. We use a non-pixelated, 256-level, phase-only SLM from Hamamatsu (Model X8267) with a 20×20 -mm² active area, optically addressed by a 768×768 -pixel liquid crystal display (LCD) screen. Thanks to a slight defocus of the imaging system, a continuous phase modulation can be achieved on the SLM at the expense of a slight reduction in the resolution.

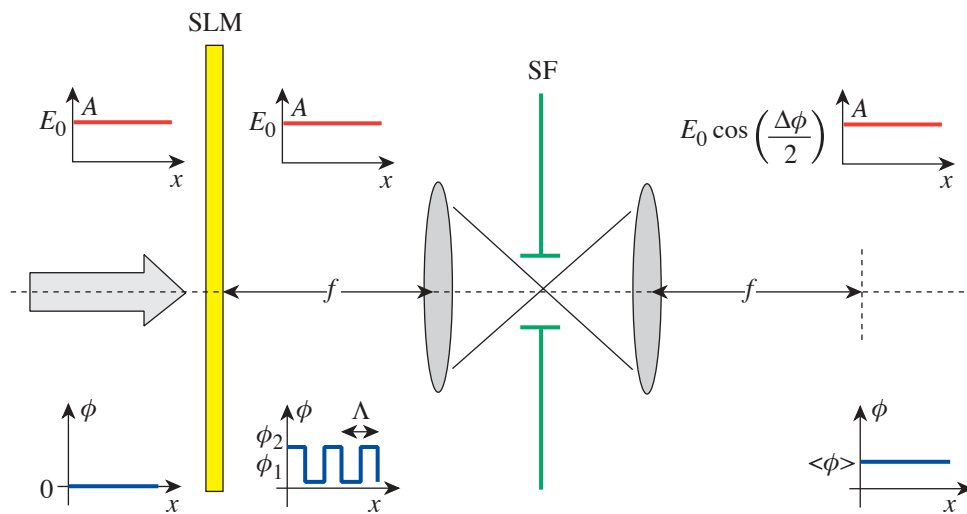


Figure 96.19

Independent phase- and amplitude-modulation scheme. The input beam is modulated in phase by the phase-only SLM and then propagates through a spatial filter (SF). The SLM is placed at a focal distance from the SF lens so the electromagnetic field distribution at the SF pinhole is proportional to the Fourier transform of the electromagnetic field distribution at the SLM location.

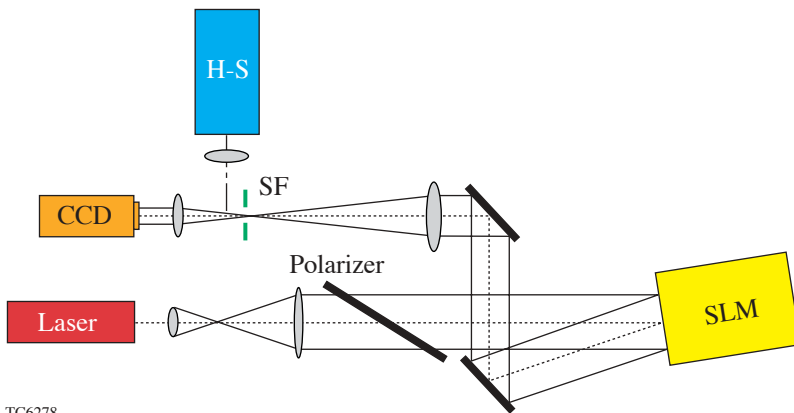
TC6277

Although the SLM was designed for normal-incidence use, we believe that a small angle of incidence does not affect the system's performance. Only a 768×768 matrix is used in the imaging. The advantages of using a non-pixelated SLM are (1) its absence of loss due to the fill factor and diffraction of pixelated SLM and (2) its high damage threshold, which we tested to be $680 (\pm 130) \text{ mJ/cm}^2$ with a 1-ns, 1053-nm Gaussian beam. This value is nearly two times better than that of the pixelated SLM that we tested.

To be relevant to beam shaping in a high-energy laser facility, such as the OMEGA laser, the pass band of the beam-shaping spatial filter must be at least as large as the spatial filters in the main laser power amplifier, which are as large as 30 times the diffraction limit. To ensure removal of the SLM carrier spatial frequency, the minimum spatial frequency must then be at least 30 times the fundamental spatial frequency of the beam. Practically, this means the minimum number of pixels required for that application is 60 across the beam (two per period). The beam f number in the spatial filter is 25, which means that the diffraction-limited focal spot is roughly $25 \mu\text{m}$ and the pinhole should be at least $750 \mu\text{m}$ in diameter.

We used a 1-mm pinhole and a modulation frequency 64 times that of the fundamental beam frequency. In the SLM plane, this corresponds to a period of 12 pixels. For lower numbers of pixels per period, the finite slope between two nearby pixels degrades the modulation profile. For larger periods, up to 24 pixels, the beam is efficiently modulated by the SLM, but the system becomes more sensitive to the pinhole alignment.

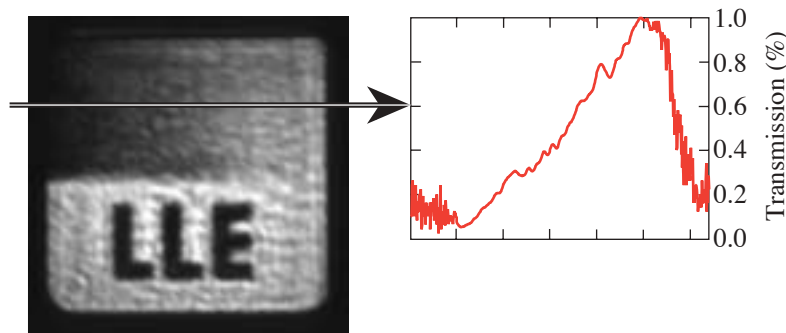
Figure 96.21 demonstrates a linear amplitude-modulation scheme, as well as high contrast and arbitrary spatial shaping. In the upper part, Eq. (5) is inverted to obtain the phase-modulation amplitude corresponding to a linear amplitude modulation, while the lower part of the image shows nearly complete extinction for a π -rad modulation and $\sim 100\%$ transmission when the phase modulation is 0 rad. The low-contrast speckle, seen in Fig. 96.21, limits the achievable extinction ratio that we measured varying from 50:1 to 10:1 across the beam. It should be noted that the extinction is achieved while only half of the dynamic range of the SLM was used (128 levels), which leaves at least half of the SLM dynamic range free for phase modulation, in the worst case.



TC6278

Figure 96.20

Experimental setup. SF: spatial-filter pinhole; H-S: Hartmann–Shack wavefront sensor. The SLM is used in reflection and a flip-in mirror is used to measure either the intensity or phase profiles.



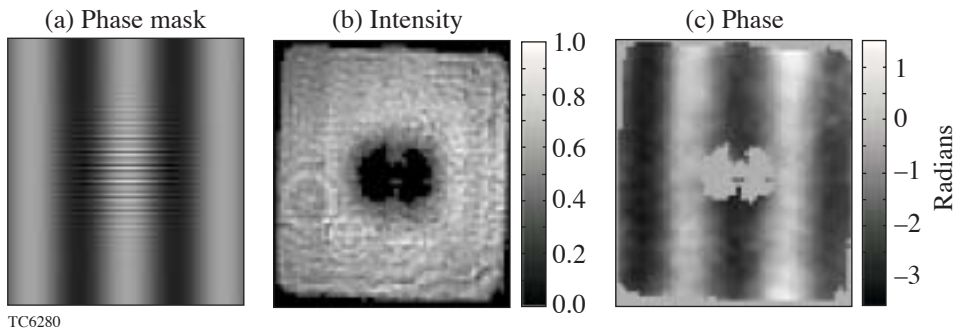
TC6279

Figure 96.21

A modulated beam demonstrates the amplitude control offered by the combined SLM/spatial-filter system. The lineout in the upper portion demonstrates the effective transmission function, while the lower part demonstrates high-contrast modulation with as much as a 50:1 extinction ratio.

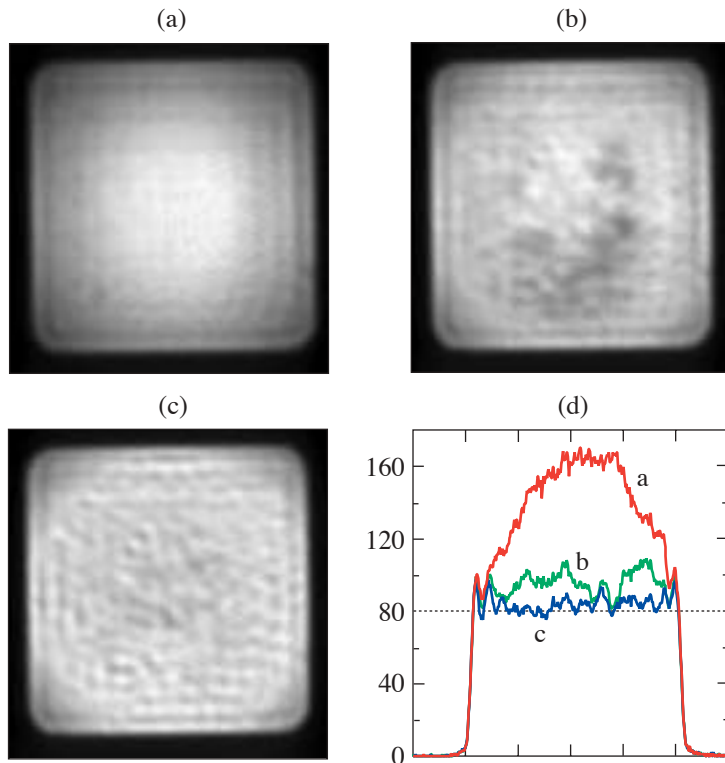
Figure 96.22 demonstrates simultaneous amplitude and wavefront-shaping performance of this system by summing two one-dimensional patterns with spatial frequencies below and above the cutoff frequency of the spatial filter, as shown by the mask in Fig. 96.22(a). Figure 96.22(b) shows the beam amplitude measured with the Hartmann–Shack sensor, while Fig. 96.22(c) illustrates the measured wavefront. Both images display data dropout near the center because the measured intensity falls below the detection threshold of the wavefront sensor. Little phase-to-amplitude coupling is observed, demonstrating that the phase information is conserved through the filter while the intensity modulation is achieved.

Figure 96.23 illustrates the performance of this beam-shaping scheme in an iterative, closed-loop configuration. A single convergence scheme is applied in which less amplitude modulation is applied where not enough transmission is achieved and more where too much is measured. For demonstration purposes, we propose to correct the pixels for which the measured intensity on a 8-bit gray scale is higher than 80 counts. After mapping the SLM to the CCD using a fiducial image, the required transmission at each location of the SLM and the corresponding phase-modulation amplitude are calculated. The first step correction result is shown by the image in Fig. 96.23(b) along with its corresponding lineout, which



TC6280

Figure 96.22 Independent phase and amplitude modulation is demonstrated. The mask (a) leads to a beam that exhibits simultaneous amplitude (b) and phase (c) modulation.



TC6281

Figure 96.23 Dynamic amplitude beam control. The initial beam (a) is shaped into top-hat beams (b) and (c). The lineouts show the typical error to the intensity goal.

shows that most of the correction factor has been underestimated since the average intensity is above 80 counts. Similarly, the correction does not lead to a uniform beam because of the spatially dependent transfer function of the SLM. Nevertheless, the error, defined as the difference between the real intensity and the goal intensity, in an rms sense, for those points initially higher than 80, is reduced from 60% to 16%. Using image (b), the error signal is reduced by changing the modulation to achieve the goal. The result of a second correction is shown in Fig. 96.23(c), where the error signal has been reduced to 8.5%, which is dominated by the speckle noise discussed earlier.

We have shown a dynamic modulation scheme that addresses simultaneously both the phase and the amplitude of a laser beam. By modulating the phase of a laser beam at high spatial frequencies, one can couple the phase-modulation amplitude to the transmission of a spatial filter in a straightforward way. Following that, we have demonstrated that this scheme can be used for beam correction.

ACKNOWLEDGMENT

This work was supported by the U.S. Department of Energy Office of Inertial Confinement Fusion under Cooperative Agreement No. DE-FC03-92SF19460, the University of Rochester, and the New York State Energy Research and Development Authority. The support of DOE does not constitute an endorsement by DOE of the views expressed in this article.

REFERENCES

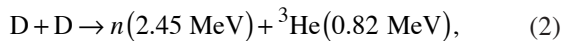
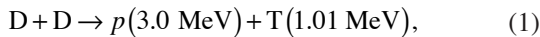
1. J. M. Auerbach and V. P. Karpenko, *Appl. Opt.* **33**, 3179 (1994).
2. V. Bagnoud, J. Luce, L. Videau, and A. Rouyer, *Opt. Lett.* **26**, 337 (2001).
3. B. Wattellier *et al.*, in *OSA Trends in Optics and Photonics (TOPS) Vol. 56, Conference on Lasers and Electro-Optics (CLEO 2001)*, Technical Digest, Postconference Edition (Optical Society of America, Washington, DC, 2001), pp. 70–71.
4. J. Bourderionnet *et al.*, *Opt. Lett.* **26**, 1958 (2001).
5. B. Wattellier *et al.*, *Opt. Lett.* **27**, 213 (2002).
6. J. A. Davis, K. O. Valadéz, and D. M. Cottrell, *Appl. Opt.* **42**, 2003 (2003).
7. P. Birch *et al.*, *Opt. Lett.* **26**, 920 (2001).

Proton Temporal Diagnostic for ICF Experiments on OMEGA

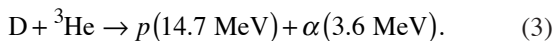
Introduction

In an inertial confinement fusion (ICF)¹ experiment, a capsule filled with deuterium (D₂) or a deuterium–tritium (DT) fuel is heated by either direct laser illumination or soft-x-ray radiation in a laser-heated hohlraum. The target is compressed to conditions under which thermonuclear fusion occurs. The fusion burn begins with spark ignition of the central hot spot² that is created by shock convergence (shock burn). A burn wave then propagates into the compressed dense fuel regions, releasing energy through fusion reactions (compressive burn).² Both a high-temperature hot spot and high areal density are necessary in cryogenic DT implosions to ignite the target and achieve high gain.^{1–3}

Experimental information about implosion dynamics is crucial for understanding capsule fuel assembly and validating numerical simulations. Areal-density evolution measurements in cryogenic D₂ or DT implosions are complicated by the lack of simple and reliable diagnostic techniques that are available with plastic-shell targets. Therefore, many experimental studies in ICF are performed with hydrodynamically equivalent “cryogenic surrogates” such as thick plastic shells filled with D³He or D₂ fuel. The primary fusion reactions that occur in imploding capsules fueled with D³He gas are



and

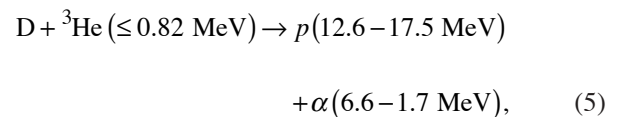
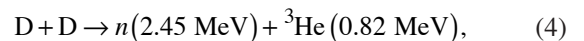


From reactions (1)–(3) one can see that with D³He both neutron diagnostics and charged-particle spectroscopy⁴ can be used on OMEGA⁵ to probe the plasma conditions during the shock and compressive burn phases of an implosion.

The capsule burn history is an important measure of target performance and implosion dynamics and is directly compa-

rable with numerical models. The neutron burn history is measured on OMEGA (and previously on the Nova laser at LLNL) using the streak camera–based neutron temporal diagnostic (NTD)^{6,7} with a time resolution of ~50 ps for DD neutrons and ~25 ps for DT neutrons. The neutron burn history contains valuable information about the capsule implosion close to the peak of compression. Since the neutron yield at shock convergence is about 100 times smaller than the yield at peak compression, it is difficult to measure the neutron shock signal using the NTD. On the other hand, the primary proton shock and compression yields are comparable in a typical D³He implosion on OMEGA.⁸ To use this unique feature of the D³He fuel, a proton temporal diagnostic (PTD), based on the NTD concept, has been developed for implosion studies at OMEGA. The PTD allows us to record the proton-production history and simultaneously measure shock bang time and compression bang time in a D³He implosion. Protons emitted from the D³He reaction lose energy when passing through the compressed capsule shell. The areal density of target material through which the protons pass determines the amount of energy loss. Therefore, by measuring the proton-production history with the PTD and simultaneously a time-integrated proton-energy spectrum by charged-particle spectroscopy, the temporal evolution of target areal density is inferred. The areal-density evolution in D³He implosions was first studied in Ref. 9 with the assumption that the D³He–proton-production history is proportional to the D₂–neutron-production history. With the development of the PTD, areal-density evolution can now be inferred using the proton-production history.¹⁰

The PTD was developed primarily for D³He implosions; however, the PTD is also sensitive to secondary protons and primary neutrons from D₂–fueled implosions. The PTD reactions of interest in a D₂ implosion are the following:



where reaction (4) is the primary reaction and (5) is the secondary. An average areal density can be inferred from the time difference of the secondary proton and primary neutron signals in the PTD.

The PTD Detector System

The PTD detector system was developed as a modification of the existing OMEGA neutron temporal diagnostic—the cryoNTD.⁷ This diagnostic was designed to operate in one of the OMEGA ten-inch manipulators (TIM’s). The PTD system, shown schematically in Fig. 96.24, is based on a fast scintillator (BC-422) that acts as a proton-to-light converter shielded by a thin (100- to 200- μm) foil against x-ray and direct laser illumination. The optical system, consisting of 11 lenses and 2 mirrors, is described in detail in Ref. 7. It transfers the scintillator light through the TIM and the vacuum window along a 3.5-m optical path to a high-speed optical streak camera¹¹ for recording. The front end of the optical system is mounted in the TIM and inserted close to the target. Since the PTD uses the existing cryoNTD optics and mechanical assembly, the current PTD scintillator is located 9 cm from the target, which is the required standoff distance for OMEGA cryogenic target operations. With additional optics, the PTD scintillator can be placed closer to noncryogenic targets. A simultaneously recorded optical fiducial provides a reference for accurate timing with respect to the incident laser pulse. Figure 96.25 shows a sample image recorded by a charge-coupled-device (CCD) camera attached to the streak camera for a D³He

implosion with a proton yield of 5.7×10^7 . The horizontal axis in the image corresponds to time. The fiducial train is seen on top of the image and the scintillator output in the center. The PTD signal is averaged across the central portion of the scintillator, and the CCD background from the bottom portion of the image is subtracted to create the final temporal trace. The streak camera flat-field and geometric distortions are included in the signal processing.

The PTD Nose Cone

The nose cone is the main difference between the PTD and the cryoNTD.⁷ The design of the PTD nose cone must satisfy several criteria: it must (1) be light tight to prevent direct laser illumination; (2) be able to sustain ablation, target debris, and the thermal impulse from the target implosion; (3) be transparent to protons with energies larger than 10 MeV; and (4) absorb as much of the soft-x-ray radiation as possible. The last requirement leads to a filter made from a high-Z material. Tantalum was chosen as the PTD filter material because of its strength and hardness and because 25-mm-diam tantalum foil disks are available commercially.¹² To avoid scintillator melting, a 0.3-mm-thick ultem plastic spacer ring was inserted between the filter foil and the scintillator. Without the spacer ring, the BC-422 scintillator is subject to a thermal impulse and may melt as a consequence. The final design of the PTD nose cone is shown in Fig. 96.26. The threaded retainer ring accommodates filter foils and scintillators of different thicknesses. The PTD nose cone itself is attached to the front end of the PTD

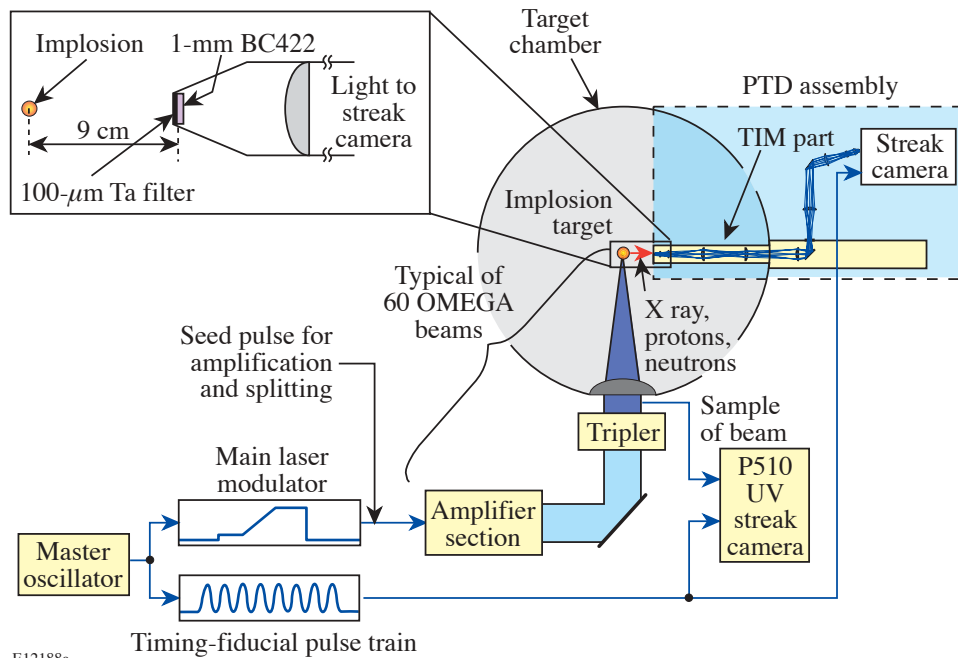


Figure 96.24 Block diagram of the PTD detector system integrated into the OMEGA facility. The fiducial system provides cross-timing between the neutron and proton signals and the incident laser pulse, which is recorded on the P510 UV streak camera.

E12188a

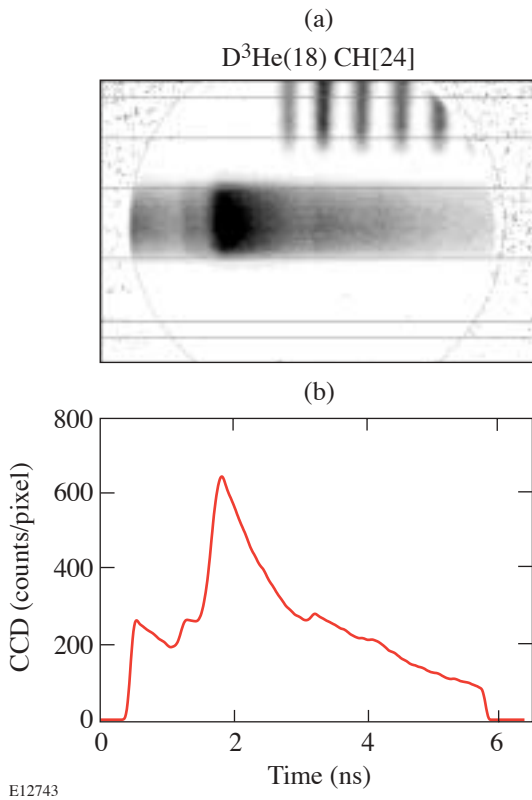


Figure 96.25
 (a) The PTD streak camera image from shot #29962 in which a 24- μm -thick plastic shell filled with 18 atm of D^3He was imploded on OMEGA with a 1-ns pulse shape and 23 kJ of energy; (b) the PTD signal averaged across the central portion of the scintillator with the CCD background subtracted and the streak camera flat-field and geometric distortions taken into account.

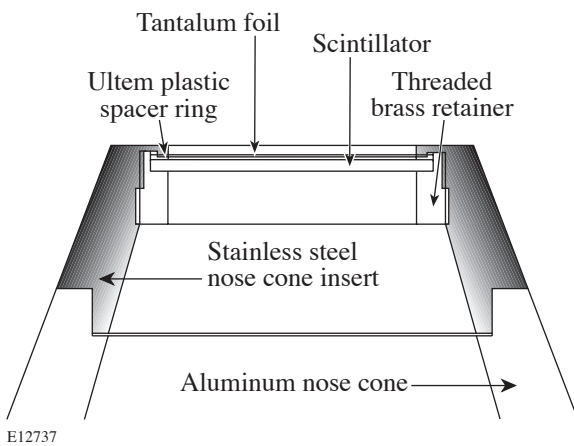


Figure 96.26
 A cross-section schematic of the PTD nose cone.

mechanical assembly by two latches. It is possible to change the PTD nose cone to the cryoNTD nose cone or to change the PTD filter foil/scintillator within the 45-min OMEGA shot cycle. Tests done with 100- μm Ta foils placed 9 cm from the target show that these foils can survive more than 50 direct-drive OMEGA shots without damage.

The PTD Background

Several sources of background affect the PTD measurements. The soft and hard x rays from a target implosion reach the PTD scintillator at 9 cm from the target about 1.4 ns before the D^3He protons. The BC-422 scintillator has a very fast rise time (<20 ps) and a decay time of ~ 1.2 ns. The scintillator decay from x rays creates a background for the proton signal. Suprathermal electrons from the two-plasmon-decay (TPD) instability are another source of background in the PTD.¹³ These electrons create hard x rays by bremsstrahlung interactions in the target and in the PTD filter foil. Since it is difficult to calculate the PTD background level, the filter thickness was optimized experimentally. The PTD background depends on many parameters such as the laser energy, pulse shape, and target design. The filter-thickness optimization required a series of identical shots where all parameters except the filter thickness were fixed. Figure 96.27 shows the PTD signal for

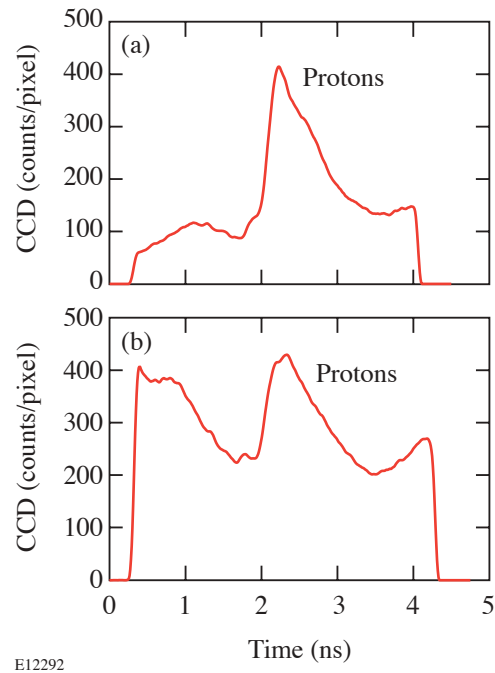


Figure 96.27
 The PTD signals from two identical D^3He implosions. Minimum x-ray background is observed with the 100- μm Ta filter in (a), while the background increases significantly with the thinner 50- μm Ta filter in (b).

two identical D^3He implosions and tantalum-filter thicknesses of 100 and 50 μm . The PTD background level with the 50- μm Ta filter is about four times higher than with the 100- μm Ta filter. This means that a Ta thickness of 50 μm is not adequate to absorb the soft x rays from target implosions. Figure 96.28 shows the PTD signal for two identical D_2 implosions and 100- and 200- μm tantalum-filter thicknesses. As expected, the area under the neutron peak remained unchanged, the area under the secondary proton peak decreased (indicating that the thicker filter was stopping some fraction of the proton spectrum), and the background level decreased only marginally. A 100- μm -thick filter appears to absorb the bulk of the soft-x-ray contribution, while the hard-x-ray contribution from TPD is only minimally affected by the thicker filter; therefore, the 100- μm tantalum filter is close to the optimal for PTD operation.

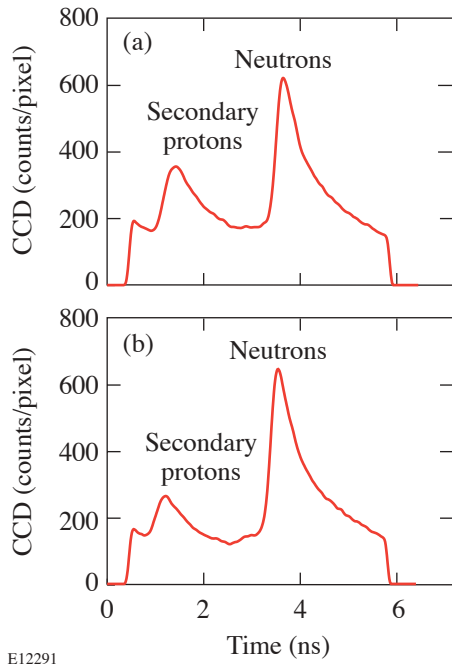


Figure 96.28
The PTD signals from two identical D_2 implosions. The background level decreases only marginally with filter-thickness increase from 100 μm Ta in (a) to 200 μm Ta in (b), while the secondary-proton signal decreases substantially.

The filter-thickness optimization discussed above was based on OMEGA operations prior to June 2003, when new distributed phase plates (DPP's) were installed and the standard spherical target diameter was reduced from 940 to 880 μm . As a result of this change, the total overlapping-beam intensity on a spherical target increased from $8.0 \times 10^{14} \text{ W/cm}^2$ to $9.4 \times 10^{14} \text{ W/cm}^2$, and, as was shown in Ref. 13, suprathermal

electrons generated from TPD increased by approximately a factor of 4. Following this change, the PTD background level increased by factor of 4, as can be seen in Fig. 96.29, where the PTD signal is shown for two OMEGA implosions using 19- μm -thick CH shells and 15-atm- D_2 fills: (a) one before the new DPP's were installed and (b) one after installation. Tests showed that suprathermal electrons hitting the Ta filter were the main contributor to the background increase. To decrease the background level, an additional 100- μm aluminum filter was added in front of the 100- μm Ta filter. The low- Z aluminum filter absorbs suprathermal electrons before they produce hard x rays in the Ta foil. The additional aluminum filter decreased the background level by about a factor of 4, as shown in Fig. 96.30 where the PTD signal is shown for two OMEGA implosions using 27- μm -thick CH shells and 15-atm- D_2 fills: one with 100 μm of Ta and one with a sandwich of 100 μm of Al and 100 μm of Ta. The additional aluminum filter also decreases the proton signal by 10% to 20% depending on the proton energy. A 100- μm beryllium filter was also tested and found to be less effective at background reduction than the aluminum. The current PTD filter used on OMEGA consists of a sandwich of 100 μm of Al and 100 μm of Ta.

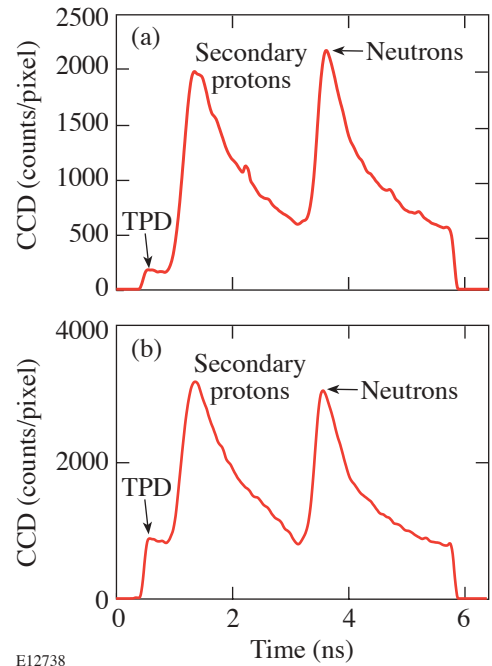
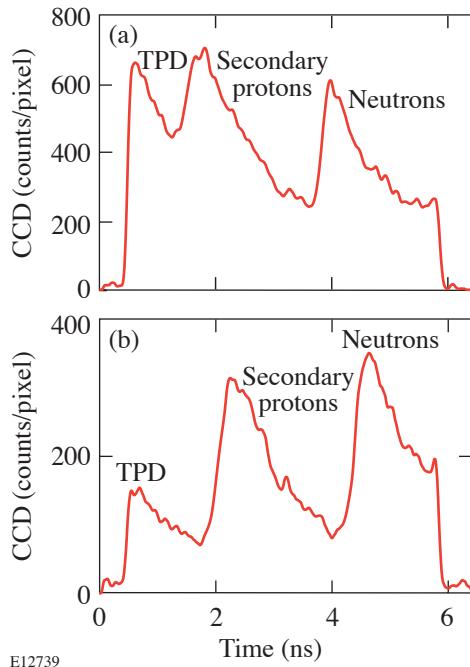


Figure 96.29
The PTD signals from two implosions of 19- μm -thick plastic shells filled with 15 atm of D_2 . The PTD background level is four times smaller in (a), where the overlapping beam intensity is $8.0 \times 10^{14} \text{ W/cm}^2$ in comparison with (b), where the overlapping beam intensity is $9.4 \times 10^{14} \text{ W/cm}^2$.



E12739

Figure 96.30

The PTD signals from two implosions of 27- μm -thick plastic shells filled with 15 atm of D_2 . Overlapping beam intensity is $9.4 \times 10^{14} \text{ W/cm}^2$. The PTD background level is four times higher with the 100- μm Ta filter in (a) than with a filter consisting of a 100- μm Al foil + 100- μm Ta foil in (b).

Data Analysis and Calibration

The time history of the scintillator signal is the convolution of the proton temporal distribution with the scintillator response. The actual proton burn history in the PTD is obtained by deconvolving the effect of the long scintillator decay from the recorded signal as described in Ref. 7.

Absolute timing is established using the OMEGA fiducial system. The OMEGA fiducial consists of a series of eight pulses spaced 548 ps apart and is synchronized to the shaped OMEGA laser pulse with a jitter of less than 20 ps. The optical fiducial is amplified separately from the main laser pulse, split, and distributed to various diagnostic instruments for precision timing. The fiducial pulse train is also recorded on the P510 ultraviolet streak cameras,¹⁴ which record the laser pulse shapes of each beam. The common optical fiducial serves as a reference for both the proton signal and the laser pulse, thus enabling very accurate timing of the PTD signals relative to the laser pulse. The recorded fiducial pulse is fitted by a pulse train of eight Gaussian pulses spaced at a well-characterized period of 548 ps. This reduces the influence of noise on the determination of the timing reference.

Since the cryoNTD⁷ was designed to measure only D_2 neutrons from cryogenic implosions at a fixed standoff distance, the fiducial requires only a single fiber delay to align the pulse train with the neutron signal. The PTD, on the other hand, is designed for multiple fusion reaction products and multiple standoff distances. Therefore, the PTD fiducial has ten delay fibers with nominal delays from 1 ns to 10 ns with a step of 1 ns. The delay fibers were characterized at LLNL with an accuracy less than 3 ps. Using the delay fibers, the PTD fiducial train position can be adjusted for x rays, D^3He protons, DD and DT neutrons, and a change of the PTD standoff distance.

The PTD streak camera has 3 \times , 5 \times , and 10 \times sweep cards that create approximately 3-ns, 5-ns, and 10-ns time windows with pixel resolutions of 7.5 ps, 13 ps, and 23 ps, respectively. The streak camera was carefully flat fielded with OMEGA fiducial pulses for each sweep card using the procedure described in Ref. 14. The streak camera flat-field and geometric distortions are included in the signal processing.

The PTD timing calibration was performed with a 100- μm aluminum filter using a 100-ps laser pulse on a spherical gold target to generate a short, intense x-ray pulse. The typical PTD calibration signal at 9 cm from the target is shown in Fig. 96.31(a), and the NTD⁶ calibration signal with a similar aluminum nose cone at 2 cm from the target is shown in Fig. 96.31(b). Comparison of the PTD and the NTD signals confirms the presence of hot electrons with energies of 100 to 300 keV in the calibration shots. The time-of-flight difference between x rays and hot electrons with 100-keV energy is 55 ps for the NTD standoff distance of 2 cm and 245 ps for the PTD standoff distance of 9 cm. This time-of-flight difference explains the falling-edge pulse shape differences between the NTD and the PTD in the calibration shots. In three shots, the PTD was calibrated relative to the OMEGA laser with an rms accuracy of ~ 5 ps.

The PTD in D^3He Implosions

The main purpose of the PTD is to measure shock-time and areal-density evolution in D^3He implosions. A series of direct-drive implosions were conducted on OMEGA with 60 beams of frequency-tripled (351-nm) UV light in a 1-ns square pulse and a total energy of 23 kJ. Full smoothing of the laser beams was used,¹⁵ and beam-to-beam energy imbalance was typically $< 5\%$ rms. Three types of capsule designs were used, all with nominal diameters of 940 μm and plastic (CH)-shell thicknesses of 20 μm , 24 μm , and 27 μm . All of the capsules were filled with 6 atm of D_2 and 12 atm of ^3He . A typical PTD image of one of the imploded capsules with a 24- μm -thick

plastic shell is shown in Fig. 96.25. The deconvolved proton burn history for this shot is compared in Fig. 96.32 with the burn histories from implosions using 20- μm - and 27- μm -thick shells. With a 5-ns time window, the PTD pixel time resolution of 13 ps is sufficient to resolve the shock coalescence and compression peaks in these D^3He implosions. It is evident

from Fig. 96.32 that the ratio of the shock yield to the compression yield in a D^3He implosion is a function of shell thickness and increases with shell thickness. A comparison of the PTD data with wedged-range-filter (WRF) spectrometer data^{4,8} shows that the shock peak is much more evident in the PTD data than in the WRF spectrometers.

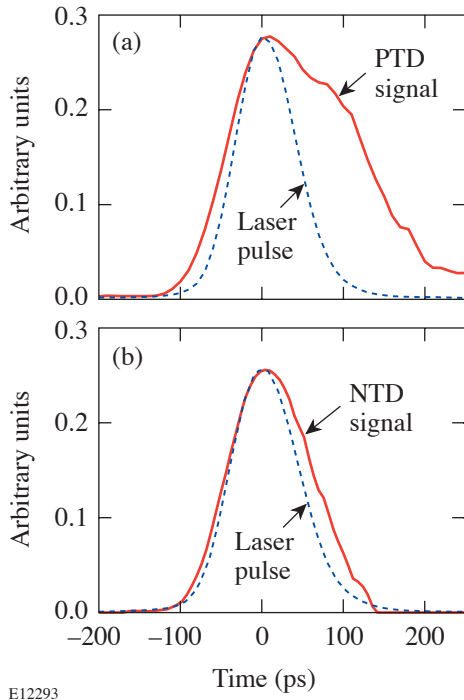


Figure 96.31
The PTD and NTD calibration signals with a 100-ps laser pulse (dashed line): (a) PTD signal (solid line) at 9 cm from a target; (b) NTD signal (solid line) at 2 cm from a target.

The primary D^3He proton yield is inferred by integrating the area under the proton shock and compression peaks. The number of CCD counts in the PTD for the 1-mm BC-422 scintillator and the filter configuration of 100 μm of Al + 100 μm of Ta is plotted against the absolute yield from the WRF spectrometers in Fig. 96.33. The PTD can measure primary D^3He proton yields and proton bang time above 1×10^7 .

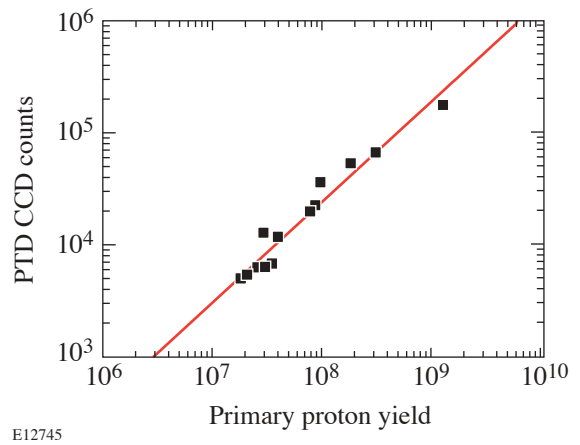


Figure 96.33
Primary D^3He proton yield measured (CCD counts) by the PTD as a function of yield measured by WRF spectrometers.

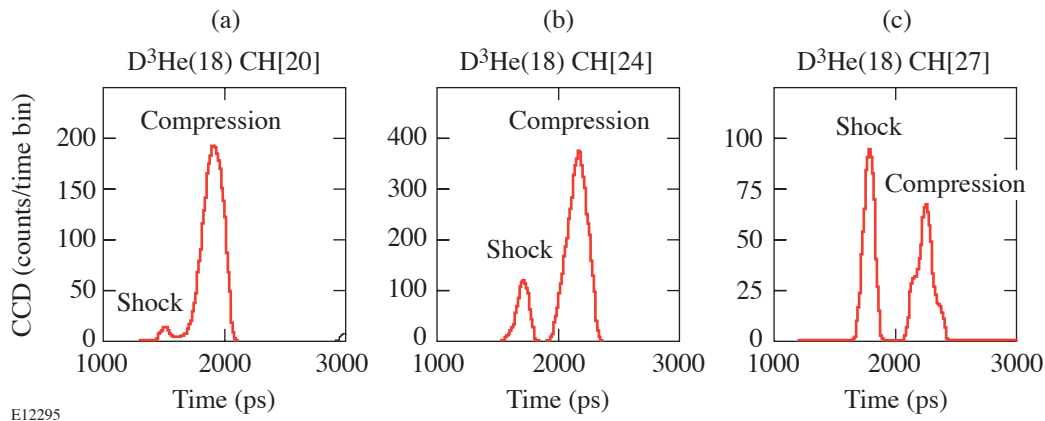


Figure 96.32
The PTD signal from implosions of plastic shells filled with 18 atm of D^3He : (a) 20- μm shell thickness; (b) 24- μm shell thickness; (c) 27- μm shell thickness.

The time accuracy of the shock and compression burn history in a D^3He implosion is mainly determined not by the detector itself, but by Doppler and geometrical broadening and ρR evolution of the fuel and shell during the implosion.^{9,10} The study of ρR evolution requires data analysis from many diagnostics and is beyond the scope of this article. A more-detailed study of shock-bang timing and ρR evolution is presented in Ref. 10.

The PTD in D_2 Implosions

A typical PTD streak camera image of a D_2 implosion with a neutron yield of 1.3×10^{11} is shown in Fig. 96.34(a) and the deconvolved PTD signal in Fig. 96.34(b). In a D_2 implosion, the first PTD peak is the signal from secondary protons with energies of 12.6 to 17.5 MeV, and the second peak is the signal from the DD neutrons with an energy of 2.45 MeV. Although the yields of secondary protons and primary neutrons differ by

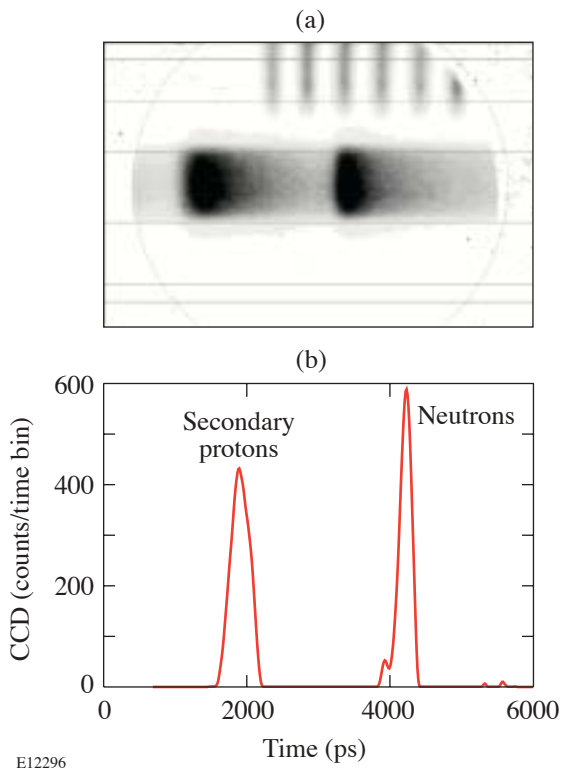


Figure 96.34

(a) The PTD streak camera image from a shot in which a 20- μm -thick plastic shell filled with 15 atm of D_2 was imploded on OMEGA with a 1-ns pulse shape and 23-kJ energy; (b) the PTD signal in this D_2 implosion. From the time-of-flight difference between the secondary-proton and the primary-neutron peaks, the average energy downshift of the secondary protons can be inferred.

a factor of 1000, the PTD signals are comparable due to the different interaction mechanisms of protons and neutrons with the scintillator.

The PTD neutron signal from a D_2 implosion can be used to determine the peak of neutron production (bang time) similar to NTD.⁶ Figure 96.35 shows a comparison of the neutron bang time measured by PTD and NTD. The error bars on this plot are 25 ps for NTD and for PTD. The bang times measured by PTD are very close to the bang times from NTD, showing only a 28-ps rms spread. Although temperature broadening of the neutron signal in the PTD is much higher than in the NTD due to different standoff distances (9 versus 2 cm), the PTD bang time is as accurate as the NTD bang time, but the neutron burn width is systematically larger in the PTD than in the NTD due to temperature (or Doppler) broadening.

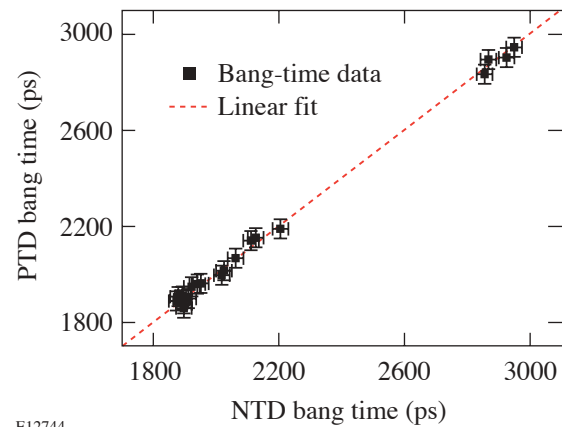


Figure 96.35

Comparison between the neutron bang times measured by the PTD and by the NTD in D_2 implosions on OMEGA.

The secondary proton peak in the PTD signal can be used to measure the secondary-proton yield in D_2 implosions. The number of CCD counts in the PTD for the 1-mm BC-422 scintillator and the filter configuration of 100 μm of Al + 100 μm of Ta is plotted against the secondary proton yield from the WRF spectrometers in Fig. 96.36. The PTD can measure the secondary proton yields in D_2 implosions above 1×10^7 .

The average energy downshift of the secondary protons from a D_2 implosion is routinely used on OMEGA to measure the total areal density of the capsule.¹⁶ The average energy downshift of the secondary protons can be inferred from the PTD based on the time-of-flight difference between the sec-

ondary proton and the primary neutron peaks [see Fig. 96.34(b)]. From the secondary proton's energy downshift, the total areal density can be calculated by using plasma-stopping formulas¹⁷ in the same way as done with the WRF data.¹⁶ Figure 96.37 compares the total-areal-density data inferred from the charged-particle spectrometers and the PTD. The comparison is not as favorable as that between the neutron bang times in the NTD and PTD due likely to known areal-density asymmetries¹⁸ on OMEGA.

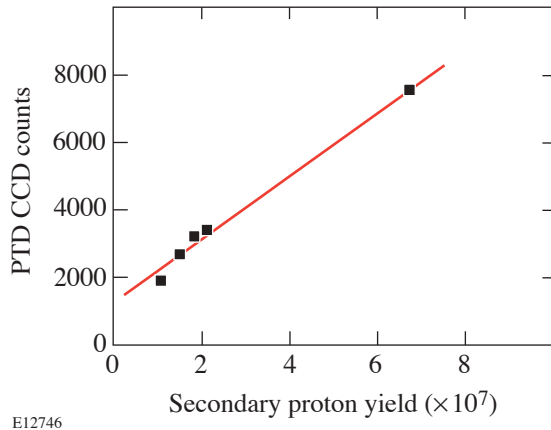


Figure 96.36
Secondary D^3He proton yield measured (CCD counts) by the PTD as a function of yield measured by WRF.

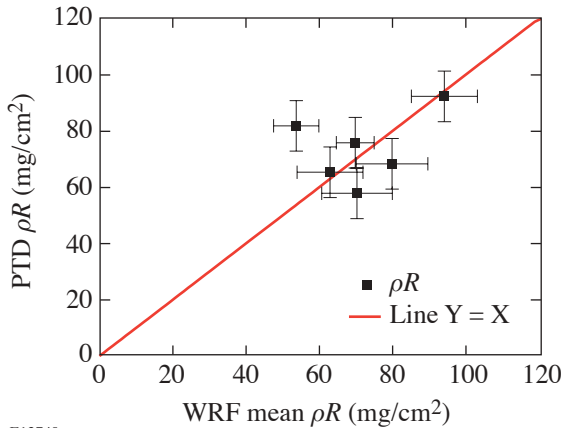


Figure 96.37
Comparison between average total ρR measured by the PTD and by the WRF in D_2 implosions.

Conclusions and Outlook

A new proton temporal diagnostic (PTD) has been developed to measure the proton burn history in ICF implosions on OMEGA. The PTD nose cone consists of a filter foil sandwich, a scintillator, and the front end of the optical relay system. This hardware is mounted in a TIM and inserted close to the target. The back end of the optical system with an optical streak camera to record the light emitted from the scintillator is mounted outside the vacuum of the target chamber. The OMEGA fiducial system is used to cross-time the x-ray, proton, and neutron signals to the incident laser pulse. An absolute timing accuracy of better than 10 ps has been achieved during the PTD calibration with 100-ps laser pulses. The PTD is able to measure the proton burn history at yields above 5×10^5 for D^3He implosions and resolve shock and compression yields. In D_2 -filled-capsule implosions including cryogenic targets, the PTD can simultaneously measure neutron bang time, neutron yield, secondary-proton yield, and average total areal density.

This article has described the first implementation of the PTD on OMEGA. The PTD standoff distance can be minimized to decrease the thermal broadening and to better fit the requirements of an experiment. Future optimization of the PTD x-ray filter is also possible. In retrospect, the choice of a Ta filter does not appear to be optimal since Al is now needed in front to absorb suprathreshold electrons. A sandwich of aluminum and gold foils will probably be superior. The PTD optimization on OMEGA will be continued in the future.

ACKNOWLEDGMENT

This work was supported by the U.S. Department of Energy Office of Inertial Confinement Fusion under Cooperative Agreement No. DE-FC03-92SF19460, the University of Rochester, and the New York State Energy Research and Development Authority. The support of DOE does not constitute an endorsement by DOE of the views expressed in this article.

REFERENCES

1. J. Nuckolls *et al.*, *Nature* **239**, 139 (1972).
2. J. D. Lindl, *Phys. Plasmas* **2**, 3933 (1995).
3. P. W. McKenty, V. N. Goncharov, R. P. J. Town, S. Skupsky, R. Betti, and R. L. McCrory, *Phys. Plasmas* **8**, 2315 (2001).
4. F. H. Séguin, J. A. Frenje, C. K. Li, D. G. Hicks, S. Kurebayashi, J. R. Rygg, B.-E. Schwartz, R. D. Petrasso, S. Roberts, J. M. Soures, D. D. Meyerhofer, T. C. Sangster, J. P. Knauer, C. Sorce, V. Yu. Glebov, C. Stoeckl, T. W. Phillips, R. J. Leeper, K. Fletcher, and S. Padalino, *Rev. Sci. Instrum.* **74**, 975 (2003).

5. T. R. Boehly, D. L. Brown, R. S. Craxton, R. L. Keck, J. P. Knauer, J. H. Kelly, T. J. Kessler, S. A. Kumpan, S. J. Loucks, S. A. Letzring, F. J. Marshall, R. L. McCrory, S. F. B. Morse, W. Seka, J. M. Soures, and C. P. Verdon, *Opt. Commun.* **133**, 495 (1997).
6. R. A. Lerche, D. W. Phillion, and G. L. Tietbohl, *Rev. Sci. Instrum.* **66**, 933 (1995).
7. C. Stoeckl, V. Yu. Glebov, S. Roberts, T. C. Sangster, R. A. Lerche, R. L. Griffith, and C. Sorce, *Rev. Sci. Instrum.* **74**, 1713 (2003).
8. R. D. Petrasso, J. A. Frenje, C. K. Li, F. H. Séguin, J. R. Rygg, B. E. Schwartz, S. Kurebayashi, P. B. Radha, C. Stoeckl, J. M. Soures, J. Delettrez, V. Yu. Glebov, D. D. Meyerhofer, and T. C. Sangster, *Phys. Rev. Lett.* **90**, 095002 (2003).
9. V. A. Smalyuk, P. B. Radha, J. A. Delettrez, V. Yu. Glebov, V. N. Goncharov, D. D. Meyerhofer, S. P. Regan, S. Roberts, T. C. Sangster, J. M. Soures, C. Stoeckl, J. A. Frenje, C. K. Li, R. D. Petrasso, and F. H. Séguin, *Phys. Rev. Lett.* **90**, 135002 (2003).
10. J. A. Frenje, "Measuring Shock-Coalescence Timing and ρR Evolution of D³He Implosions on OMEGA," to be published in *Physics of Plasmas*.
11. R. A. Lerche and R. L. Griffith, in *High Speed Photography, Videography, and Photonics V*, edited by H. C. Johnson (SPIE, Bellingham, WA, 1987), Vol. 832, pp. 266–274.
12. Goodfellow Corporation, Berwyn, PA 19312-1780.
13. C. Stoeckl, R. E. Bahr, B. Yaakobi, W. Seka, S. P. Regan, R. S. Craxton, J. A. Delettrez, R. W. Short, J. Myatt, A. V. Maximov, and H. Baldis, *Phys. Rev. Lett.* **90**, 235002 (2003).
14. W. R. Donaldson, R. Boni, R. L. Keck, and P. A. Jaanimagi, *Rev. Sci. Instrum.* **73**, 2606 (2002).
15. D. D. Meyerhofer, J. A. Delettrez, R. Epstein, V. Yu. Glebov, V. N. Goncharov, R. L. Keck, R. L. McCrory, P. W. McKenty, F. J. Marshall, P. B. Radha, S. P. Regan, S. Roberts, W. Seka, S. Skupsky, V. A. Smalyuk, C. Sorce, C. Stoeckl, J. M. Soures, R. P. J. Town, B. Yaakobi, J. D. Zuegel, J. Frenje, C. K. Li, R. D. Petrasso, D. G. Hicks, F. H. Séguin, K. Fletcher, S. Padalino, M. R. Freeman, N. Izumi, R. Lerche, T. W. Phillips, and T. C. Sangster, *Phys. Plasmas* **8**, 2251 (2001).
16. F. H. Séguin, C. K. Li, J. A. Frenje, S. Kurebayashi, R. D. Petrasso, F. J. Marshall, D. D. Meyerhofer, J. M. Soures, T. C. Sangster, C. Stoeckl, J. A. Delettrez, P. B. Radha, V. A. Smalyuk, and S. Roberts, *Phys. Plasmas* **9**, 3558 (2002).
17. C. K. Li and R. D. Petrasso, *Phys. Rev. Lett.* **70**, 3059 (1993).
18. F. H. Séguin, C. K. Li, D. G. Hicks, J. A. Frenje, K. M. Green, R. D. Petrasso, J. M. Soures, D. D. Meyerhofer, V. Yu. Glebov, C. Stoeckl, P. B. Radha, S. Roberts, C. Sorce, T. C. Sangster, M. D. Cable, S. Padalino, and K. Fletcher, *Phys. Plasmas* **9**, 2725 (2002).

Polishing PMMA and Other Optical Polymers with Magnetorheological Finishing

Introduction

Polymer optics are typically manufactured by injection molding (thermoplastics, high volume, economical), compression molding (thermosets, higher precision, and larger sizes), or diamond turning. Once formed by these techniques, polymer components are used “as manufactured,” usually without further cold working to improve surface finish or figure. This is because optical polymers are soft and possess high linear expansion coefficients and poor thermal conductivities.¹ Attempts to improve surface finish and figure using conventional grinding and polishing processes usually result in scratching, the embedding of abrasive particles, the formation of “orange peel,”² and degradation to surface figure. There are circumstances when it would be desirable to perform a classical polishing operation on a polymer surface. In some instances it is desirable to drive rms surface roughness values below 2 to 4 nm in preparation for deposition of a coating. In other applications, reduced surface form errors are required. It is advantageous to eliminate the unwanted flare from diamond-turning marks on polymer optics in order to test prototype imaging system designs.

Magnetorheological finishing (MRF) is a new polishing process that was invented and developed by an international group of collaborators at the Center for Optics Manufacturing (COM) in the mid-1990s³ and commercialized by QED Technologies, Inc. in 1997.⁴ MRF is based on a magnetorheological (MR) fluid consisting of nonmagnetic polishing abrasives (typically CeO₂ or nanodiamonds⁵) and magnetic carbonyl iron (CI) particles in water or other carriers. With the appropriate MR fluid, MRF has successfully polished a variety of materials to subnanometer rms surface-roughness levels with peak-to-valley (p-v) form accuracies to better than 20 nm. Polished materials include optical glasses (fused silica, BK7, SF6, LaK9), hard crystals and polycrystalline glass-ceramics (silicon,⁶ sapphire,⁷ Zerodur, and Nd: YLF⁸), soft UV and IR materials (CaF₂,⁹ AMTIR-1,¹⁰ polycrystalline ZnS,¹⁰ and soft phosphate laser glass), and soft, water-soluble potassium dihydrogen phosphate (KDP) frequency-conversion crystals.¹¹

A normal force of the order of 0.01 N between the abrasive particle and the part is the key to removal in most classical polishing processes. In MRF, however, there is almost no normal load.¹² Figure 96.38 shows a schematic of a part being placed into a ribbon of MR fluid. Shear stresses in the converging gap and the lateral motion of polishing abrasives across the part surface cause material removal without subsurface damage, leaving extremely clean, pit- and scratch-free surfaces. This has been shown to minimize the embedding of polishing powders,¹³ and it suggests that MRF is an excellent candidate for polishing polymer optics.

The following sections describe our work to polish optical polymers with MRF. Materials of interest include polymethylmethacrylate (PMMA), cyclic olefin polymer (COP), polycarbonate (PC), and polystyrene (PS). Goals for removal rate, surface form error reduction, and surface microroughness reduction are established; materials of interest and forms of supply are identified; metrology instrumentation and testing protocols are given; and MRF platforms are briefly reviewed. No single MR fluid was found to be entirely successful in smoothing all polymers tested; therefore, results are presented for several MR fluid and polymer combinations. Variations in the type of nonmagnetic polishing abrasive were seen to make a difference in the ability to polish. Surface degradation observed for some polymers was overcome by changing the polishing abrasive in the MR fluid. Encouraging results for PMMA are described in detail. It was possible to demonstrate both surface figure correction and smoothing in the same processing sequence. Diamond-turning marks were eliminated. Finally, the thermalization issue in cold working of optical polymers is discussed within the context of experiments that encountered long metrology cycle times and long-term figure instability.

Methodology

1. Polymer Materials and Forms of Supply

Polymers used in this work and their trade names are identified in Table 96.I, where they are rank ordered by

hardness.¹⁴ Forms of supply consisted of molded plano coupons, used as received, and/or rod stock that was subsequently diamond turned into plano pucks prior to use. Initial roughness values for the surfaces of the molded coupons (areal, $250\ \mu\text{m}$ by $350\ \mu\text{m}$; see **Metrology and Testing Protocols**, p. 241, for metrology protocols) were in the range of 300 nm to 1600 nm p-v and 2 nm to 11 nm rms. Molded-coupon surfaces were not sufficiently flat to allow for interferometric form metrology. Initial roughness values for the surfaces of the diamond-turned pucks were in the range of 50 nm to 1500 nm p-v and 4 nm to 17 nm rms. Flatness values for the diamond-turned pucks were less than $5\ \mu\text{m}$ p-v (95% aperture).

2. MRF Machine Platforms and Screening Experiments

Three MRF platforms were used to carry out experiments. The principal author and her lab partner¹⁸ conducted an initial screening experiment in late 2001 on the permanent magnet machine (PMM),¹⁹ a test bed primarily intended for undergraduate training in the basics of MRF. The goal of this work was to examine only the smoothing capability of nanodiamond abrasives contained in one of the commercial MR fluids, although the exact MR fluid formulation used was experimental and not entirely aqueous-based. A 60-s-duration circle was polished into a molded coupon at a part rotation rate of 200 rpm. Results for the four polymers listed in Table 96.I were

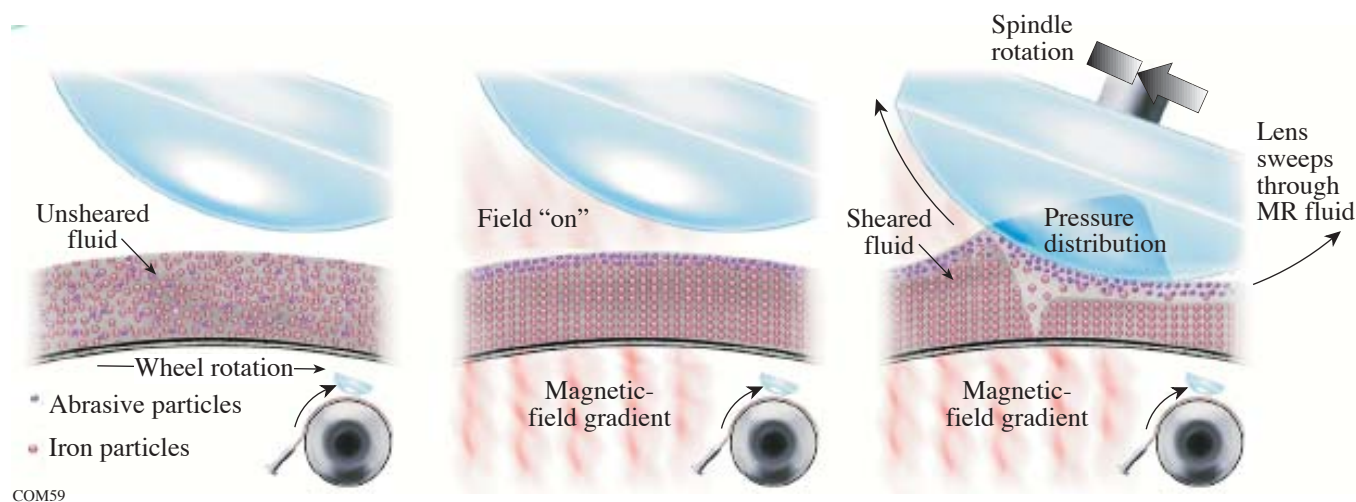


Figure 96.38

Polishing with MRF. (a) The rotating wheel carries the MR fluid ribbon under the part. (b) With the application of a magnetic field, the carbonyl iron particles form an organized structure and are pulled down toward the increasing gradient in magnetic field. Water and the polishing abrasive remain at the surface of the ribbon. (c) A converging gap is formed by placing the part into the ribbon. Solid cores of magnetic fluid form before and under the part, forcing the abrasive particles into a thin, $\sim 150\text{-}\mu\text{m}$ channel with high velocity. Shear against the part surface causes material removal with negligible normal force.

Table 96.I: Polymer materials, forms of supply, and sizes.

| Polymer | Trade Name | Rockwell (M hardness) | Form | Size (mm diameter \times thickness) | Ref. |
|---------|-------------|-----------------------|---------------------|---------------------------------------|------|
| PMMA | Acrylic | 97 | Molded coupons | 50×2.5 | (15) |
| | | | Rod stock for pucks | 48×25 | (16) |
| | | | Rod stock for pucks | $38 \times \sim 8$ | (17) |
| PS | Dow Styrene | 90 | Molded coupons | 50×2.5 | (15) |
| COP | Zeonex | 89 | Molded coupons | 50×2.5 | (15) |
| | | | Rod stock for pucks | $75 \times 25, 50 \times 8$ | (16) |
| PC | Lexan | 70 | Molded coupons | 50×2.5 | (15) |

encouraging, showing that rms roughness levels of the order of 1 to 3 nm could be achieved.

In early 2002, a series of experiments were conducted on diamond-turned PMMA and COP pucks using an MRF research platform called the spot-taking machine (STM). As previously described,¹¹ the STM is used to take spots on stationary part surfaces; it cannot be used to polish out a surface. The STM is intended for evaluating long-term MR fluid stability, material-removal rates for new MR fluids and/or new materials, spot shapes, and in-spot roughness. (In-spot roughness is higher than that achieved with polishing on a rotating part.) Results for experimental MR fluids revealed differences between the two materials under identical test conditions. Peak removal rates as large as 10 $\mu\text{m}/\text{min}$ and 20 $\mu\text{m}/\text{min}$ were obtained for COP and PMMA, respectively. These results did not correlate with material hardness. In-spot roughness values for both materials were reduced to 3 nm rms (COP) and 6 nm rms (PMMA). Diamond-turning marks were eliminated inside a spot taken on the COP part.²⁰

Most of the experiments reported in this article were conducted during 2002 and 2003 on the QED Technologies Q22Y²¹ machine used in rotational mode and programmed for uniform removal of material and/or for figure correction. Commercial CeO₂-based and nanodiamond-based MR fluids, as well as a number of experimental MR fluid formulations, were used under normal and “gentle” operating conditions. Experiments were performed with either the standard 150-mm-diam wheel installed in the machine or a smaller 50-mm-diam wheel. Wheel size affected spot size and removal rate, but it was assumed not to be an issue in evaluating smoothing of surfaces for different abrasives. Parts were mounted in the Q22Y work spindle using vacuum chucks and adapters provided with the machine. This facilitated easy removal of parts for in-process and post-process metrology, without the need for blocking and deblocking with waxes.

3. Metrology and Testing Protocols

The purpose of the work in 2002 and 2003 was to evaluate the potential of using MRF to process optical polymers. Specific objectives were to establish material-removal rates and to demonstrate reductions in surface roughness (white-light interference microscopy²²) and in surface form errors (phase-shifting laser interferometry²³). Metrology was performed in a room ($T = 68 \pm 1^\circ\text{F}$) separated from the Q22Y, which was located on the shop floor ($T = 71 \pm 1^\circ\text{F}$). Spotting was done on designated parts to determine removal rates for a given MR fluid on each polymer. For this, the Q22Y was automatically

programmed to take a series of four individual spots on the part surface. The spots were then evaluated interferometrically and reprocessed by the Q22Y software to calculate average peak removal rates.

Surface roughness was evaluated in either of two ways: Polymer coupons not previously spotted were rotated and polished with uniform removal runs. Five sites, randomly distributed over the part surface, were sampled after polishing for rms roughness. Standard instrument settings²² were employed. For some experiments with ZrO₂, the data were processed with an 80- μm high-pass filter. Diamond-turned pucks were evaluated for roughness in the same manner after 0.5- μm uniform removal runs, and/or after figure correction runs based upon interferometrically determined surface form error maps and removal spot data. Single-surface polishing experiments and one experiment to polish out both sides of a puck were performed.

Several adjustments were made in the metrology lab as a result of mounting and thermalization issues that were encountered. Metal sample-mounting clamps in the interferometer were covered with pads to broaden and reduce zones of high contact pressure on the part barrel. Thermal equilibration of a puck was performed each time it was returned to the metrology lab for testing by covering it with lens tissue and placing it between copper plates for 30 min.

4. Nonmagnetic Polishing Abrasives

Two magnetorheological (MR) fluids are currently in widespread industrial use: One composition consists of micron-sized CeO₂ powder in an aqueous suspension of magnetic carbonyl iron (CI) powder, which has been found appropriate for almost all soft and hard optical glasses and low expansion glass-ceramics. Preparation of this standard MR fluid and its performance have been described previously.²⁴ The second composition uses nanodiamond powder as the polishing abrasive, which is appropriate for calcium fluoride, IR glasses, hard single crystals like silicon and sapphire, and very hard polycrystalline ceramics^{5,11,24} like silicon carbide. Both of these MR fluids were evaluated in this work, even though the abrasives in them are not commonly used for polishing polymers. Considerations leading to a choice of alternative polishing abrasives²⁵ are complex. Not only do the hardness and chemistry of the abrasive grains need to be appropriate to soft polymers, but the type of abrasive (e.g., crystal structure, purity, median size, friability, and surface chemistry) can appreciably affect MR fluid rheology and polishing efficiency.

It has been documented that MR fluid properties in the circulation system of an MRF machine remain constant over a 12-h work day to better than $\pm 1\%$ with either of the standard mixtures, resulting in removal rates that are constant to the same level.²⁶ Alternative abrasives must be capable of forming stable suspensions at high solids concentrations without agglomeration and with good redispersibility. Due to the high concentration and high density (e.g., 7.5 g/cm^3) of CI particles, the MR fluid must be designed to also protect against sedimentation (both static and dynamic) and corrosion. MR fluid pH levels must be kept alkaline when developing new polishing abrasive formulations, again in order to prevent sedimentation and corrosion. A serious reduction in the corrosion resistance was documented for an MR fluid made with a commercial cerium oxide powder that had been milled with an acid during manufacture.²⁷ Another consideration is the potential for abrasive milling by the CI particles, which are known to be harder than most polishing abrasives.²⁸ If this occurs at all, rapid attrition of abrasive median particle size might be preferred to attrition that occurs over a long time period. That said, it has been possible to develop and examine stable aqueous-based MR fluids containing a wide variety of metal oxide polishing abrasives.

All abrasives used in this work were obtained from commercial sources as dry powders, except for the second CeO_2 sample, which was provided as a suspension. Descriptive information for each abrasive is given in Table 96.II without any specific commercial product designations. Use of SnO_2 ,²⁹ ZrO_2 ,³⁰ Al_2O_3 ,^{29,31} and SiO_2 ³¹ was motivated by the existence of these as commercial formulations intended specifically for conventional polishing of polymers. Particle size and the availability of abrasive composition data from the vendor were also important considerations. As shown in the table, many agglomerated micron-size powders were broken down with time into smaller submicron aggregates³² as a result of milling by the MR fluid. This was not the case for the TiO_2 sample, which appeared to be strongly aggregated.

Results

1. Peak Removal Rates and rms Roughness

The forms of supply limited the experiments that could be conducted. Because of their poor surface form quality, coupons of PS and PC were polished with uniform runs, removing an indeterminate amount of material, to yield roughness data. [No spots could be taken on these parts to interferometrically determine removal rates, and therefore spot data from PMMA

Table 96.II: Abrasive particles incorporated into MR fluids for polishing polymers.

| Dry abrasive | Purity ^(b) | pH in DI water | Primary particle size ^{(b),33} | Median size ^(c) | Comments |
|--|-----------------------|----------------|---|----------------------------|--|
| CeO_2 ^(a) | >95% rare earths | 7.5 | N/A | $1.6 \mu\text{m}$ | Milling in MRF machine ^(d) increased vol % of particles < $0.6 \mu\text{m}$ from 3 (3 h) to 15 (48 h); size distribution unchanged for next 10 days |
| CeO_2 (solution) | 91% | N/A | 40 nm | 96 nm | ^(b) Provided as 20.9-wt% solids in pH7.4 solution; size distribution unchanged after milling in MRF machine ^(d) for 7 days |
| Diamond ^(a) | with graphite | 2.5 | 4 nm | $1.4 \mu\text{m}$ | Milling in MRF machine ^(e) increased vol % of particles < $0.6 \mu\text{m}$ from 0.5 to 21 in 7 days |
| SnO_2 | 99% | 4.7 | N/A | 370 nm | Large agglomerates broken up with intensive sonication |
| ZrO_2 | 98% | 7.5 | 200 nm | $1.8 \mu\text{m}$ | Milling in MRF machine ^(d) increased vol % of particles <300 nm from 2 to 11 (4 days) to 72 (11 days) |
| Al_2O_3 | 99% γ phase | 4.7 | 33 nm | 93 nm | Milling in MRF machine ^(e) increased vol % of particles <225 nm from 0 to 75 in 24 h |
| TiO_2 | 99.5% rutile | 10.2 | 10 × 40 nm needles | $2.8 \mu\text{m}$ | Milling in MRF machine ^(d) increased vol % of particles < $1.0 \mu\text{m}$ from 2 to 8 in 14 days; aggregates remained |
| SiO_2 | 99.8% | 4.7 | 40 nm | N/A | ^(b) Amorphous, fumed, crystalline-free, hydrophilic |
| ^(a) Standard MR fluid constituent; ^(b) information supplied by vendor; ^(c) powder dispersed in DI water with a surfactant and intensively sonicated prior to sizing; ³³ ^(d) peristaltic pump system on Q22Y—less aggressive; ^(e) centrifugal pump system on STM—more aggressive. | | | | | |

was used as input to the machine for performing (estimated) 0.5- μm uniform removal runs.] Spots were taken on diamond-turned pucks of PMMA and COP, thus enabling (precise) 0.5- μm uniform removal runs. Roughness data were obtained from these or from figure correction runs.

Table 96.III gives results for peak removal rate and lowest achieved rms roughness for the four polymers tested. Results are displayed separately for data obtained on diamond-turned pucks and coupons. Selected observations for each polymer are given as follows:

PMMA: Peak removal rates for most abrasives were between 4 $\mu\text{m}/\text{min}$ and 6 $\mu\text{m}/\text{min}$, showing relatively little sensitivity to CI concentration. The higher rates for CeO_2 (solution), TiO_2 , and SiO_2 were obtained with the gentlest machine-

processing conditions (lower magnetic field strength and smaller wheel rpm) and were judged to be too aggressive for use. Removal rates of about 4 $\mu\text{m}/\text{min}$ are entirely adequate for polishing PMMA. For example, using the standard wheel on the Q22Y under normal operating conditions with either the standard CeO_2 -based or nanodiamond-based MR fluid, a 0.5- μm uniform removal run on a 50-mm-diam part would require ~ 20 min. Lowest achieved rms roughness values were between 1 nm and 3 nm. Results for nanodiamonds were the highest (5 nm), and those for ZrO_2 were clearly the lowest (0.5 nm). As noted in the table, the CI used with ZrO_2 had a smaller median particle size than that used with the other abrasives, and this may have contributed in part to this excellent result. As also noted, all roughness results reported in the table for ZrO_2 were obtained with an 80- μm high-pass filter. Unfiltered data for the smoothest surfaces were 0.1 nm higher.

Table 96.III: Peak removal rates and lowest achieved rms roughness values for polymers with different abrasives in MRF.

| Polishing Abrasive (vol % CI) | PMMA Acrylic | | PS Dow Styrene | COP Zeonex | | PC Lexan |
|--|---|--------------------------------|---------------------------|---------------------------------------|---------------------------|---------------------------|
| | Puck | Coupon | Coupon | Puck | Coupon | Coupon |
| | [peak removal rate, $\mu\text{m}/\text{min}$] ^(d) lowest rms roughness (nm) ^(e) | | | | | |
| CeO_2 ^(a,b) (36) | [4.0] 1.6 \pm 0.1 | | | [3.5] 1.9 \pm 0.7 ^(f) | 1.45 \pm 0.06 | |
| CeO_2 solution ^(c) (45) | [13.6] | 3.9 \pm 1.1 | 157 \pm 27 | [4.2] | 13.3 \pm 9.5 | 3.6 \pm 0.7 |
| Diamond ^(a,c) (45) | [3.7] 4.8 \pm 2.1 | | 90 \pm 60 | [2.6] 2.8 \pm 1.0 | 3.7 \pm 0.9 | 3.2 \pm 0.7 |
| SnO_2 ^(b) (36) | [6.3] 1.4 \pm 0.4 | | | [2.7] artifacts | | |
| ZrO_2 ^(b,g) (36) | [3.6] 0.50 \pm 0.06 ^(h) | 0.58 \pm 0.07 ^(h) | 61 \pm 6 ^(h) | [0.8] 62 \pm 8 ^(h,i) | 80 \pm 3 ^(h) | 71 \pm 3 ^(h) |
| Al_2O_3 ^(c) (45) | [4.0] 1.5 \pm 0.1 | | 6.1 \pm 0.2 | | 4.1 \pm 0.9 | 3.1 \pm 0.7 |
| TiO_2 ^(c) (45) | [14.6] 3.3 \pm 0.2 ⁽ⁱ⁾ | | | [7.2] 6.9 \pm 2.0 | | |
| SiO_2 ^(c) (44) | [11.6] 2.8 \pm 0.2 ⁽ⁱ⁾ | | | [4.6] 116 \pm 5 ⁽ⁱ⁾ | | |
| (a)standard MR fluid; (b)standard 150-mm-diam wheel; (c)small 50-mm-diam wheel; (d)standard dev. est. @ $\pm 2\%$, average of four spots; (e)after uniform $\sim 0.5\text{-}\mu\text{m}$ removal runs for PMMA and COP, amounts of material removed for PS and PC not determined due to lack of spot data; (f)0.2- μm removal run, measured in areas avoiding artifacts that appeared on surface; (g)smaller CI particles used in MR fluid; (h)80- μm high-pass filter; (i)inside a spot. | | | | | | |

PS: Coupons of this material were difficult to polish without increasing the surface roughness. Figure 96.39 shows the result of polishing with ZrO₂. Due to the evolution of surface artifacts rms roughness increased by nearly four times. Worse results were obtained for nanodiamonds. The best results were obtained with Al₂O₃. Initial areal p-v roughness of 1 μm was reduced to 56 nm, and the initial rms roughness of 6 nm was unchanged. No surface artifacts were generated.

COP: Under identical conditions, peak removal rates using most abrasives were two to four times lower than those measured for PMMA, except for the standard CeO₂-based and nanodiamond-based MR fluids. For these, removal rates were 13% (3.5 μm/min) and 30% (2.6 μm/min) lower, respectively. The removal rate for ZrO₂ (~0.8 μm/min) was too low to be practical, and there were other problems (see Fig. 96.39). Smoothing the surface without introducing artifacts was difficult. The values of rms roughness achieved with the standard CeO₂-based and nanodiamond-based MR fluids were lower (2 nm to 3 nm) than those measured with CeO₂ (solution), ZrO₂, TiO₂, or SiO₂, but significant numbers of surface artifacts were still generated. An artifact-free surface was obtained on a coupon using Al₂O₃, and the rms roughness was reduced from 9 nm (initial) to 4 nm (final).

PC: ZrO₂ degraded the coupon surface as seen in Fig. 96.39. Moderate numbers of artifacts developed after processing with the CeO₂ (solution) abrasive. The standard nanodiamond-based MR fluid was seen to reduce initial rms surface roughness from ~11 nm to ~3 nm. Similar results were observed for the Al₂O₃-based MR fluid (8 nm to 3 nm). The Al₂O₃-processed surface appeared to be the best.

2. Polishing COP (Zeonex) with the Standard CeO₂-Based MR Fluid

A 75-mm-diam by 25-mm-thick diamond-turned plano puck of COP (Zeonex) was processed on the Q22Y using the standard CeO₂-based MR fluid under gentle machine conditions. The spot removal rate was ~3.8 μm/min. Figure 96.40 shows areal roughness maps. The rms roughness (averaged over five sites) was reduced from ~23 nm to ~2 nm. Two figure-correction runs were also performed on the part. Over 90% of the aperture, p-v surface wavefront error was reduced from 1.53 μm to 0.39 μm. Inspection of the part after processing revealed a moderate number (~5/mm²) of artifacts on the part surface (see Fig. 96.41).

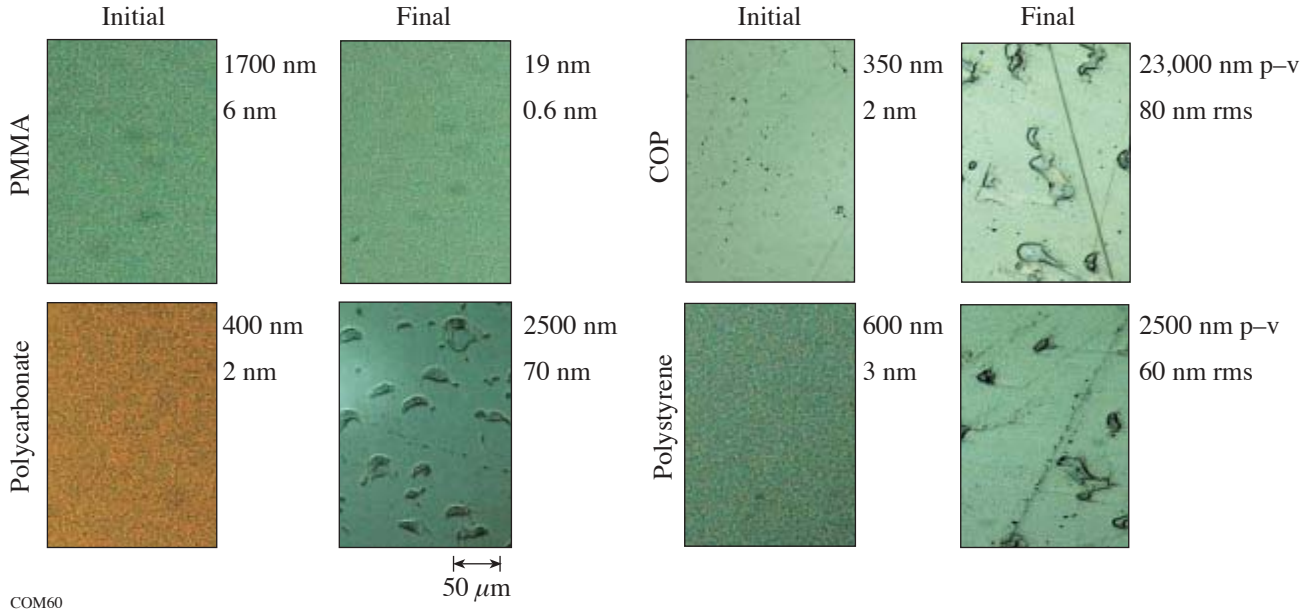


Figure 96.39 Optical microscopy of polymer surfaces after uniform 0.5-μm polishing runs with a ZrO₂-based MR fluid. Excellent results were observed for PMMA, but surface artifacts were created in PC, COP, and PS. Switching to an Al₂O₃-based MR fluid eliminated the artifact problem. (All photographs are to the scale indicated in the figure.)

3. Figure Correction and Removal of Diamond-Turning Marks on a PMMA Puck

Two 38-mm-diam by 7.8-mm-thick diamond-turned plano pucks of PMMA were processed in the Q22Y machine. One part was used to determine removal rates. White-light profilometry and laser interferometry were used to characterize one surface of the second puck for microroughness and figure (over 95% of the hard aperture) before and after each processing run. The backsides of these pucks were fine ground to simplify the metrology. Strategies were employed (described later) to minimize the time required for the pucks to come to thermal equilibrium prior to figure measurement. A ZrO₂-based MR fluid was used under standard machine conditions. This MR fluid showed excellent stability, and the experiment was conducted 9 days after the fluid had been loaded into the machine and used for other work.

The initial surface figure error of the diamond-turned PMMA puck was 4.45 μm p-v. The initial average microroughness values for this surface were 35±3 nm p-v and 3.8±0.3 nm rms. A power spectral density plot of the surface showed a strong peak at 300 lines per mm, indicating a 3-μm lateral diamond-turning groove spacing. Two figure correction runs were performed to bring down the figure error. The peak removal rate for run #1 was 3.62 μm/min and the run time was 170 min. The resulting figure error after run #1 was about 1.2 μm p-v. This value varied over time as the part recovered from the effects of handling, cleaning, and moving between the shop floor and the metrology lab. Placing the part between copper blocks in the metrology lab for 60 min and inserting padding between the part and the metal clamps in the interferometer mount helped to reduce thermal equilibration times, but ultimately the part was left in the metrology lab overnight.

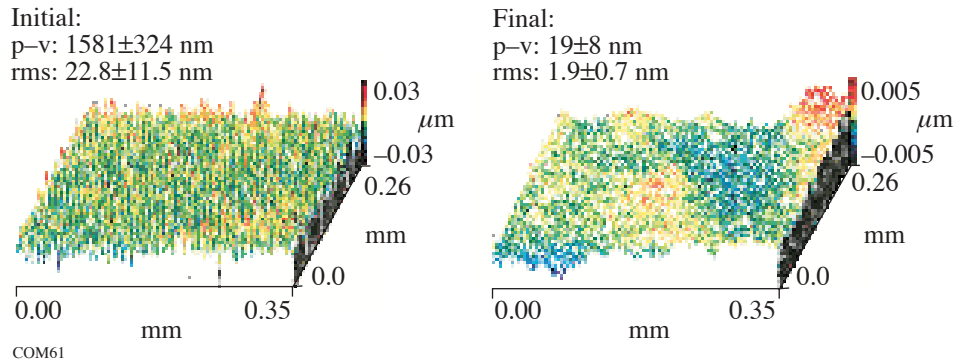


Figure 96.40

Example of areal roughness on COP surface before/after a 0.2-μm uniform removal run using a standard CeO₂-based MR fluid under “gentle” processing conditions. Numerical values given in the figure are averages of five sites.²²

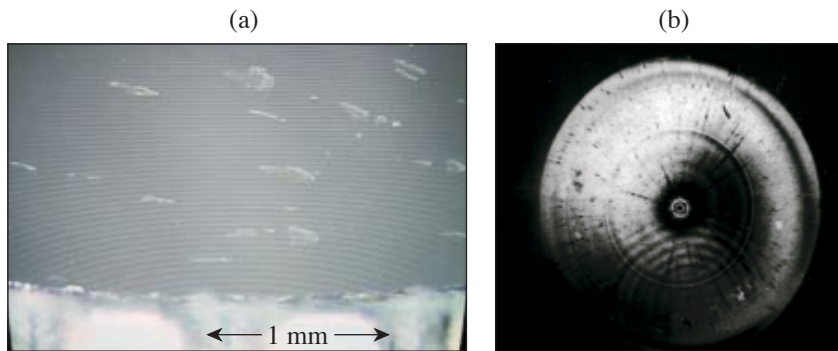
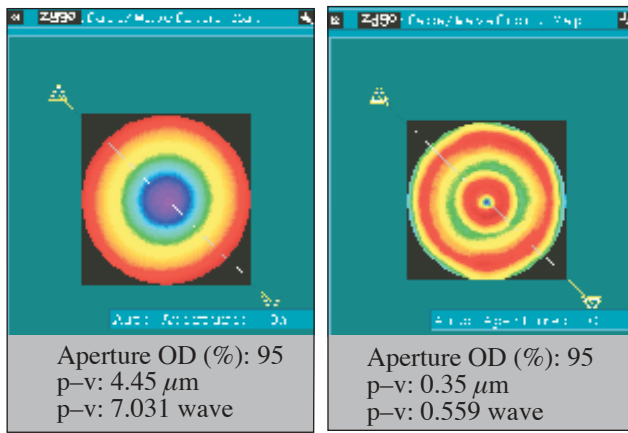


Figure 96.41

Artifacts in the surface of the COP puck at the conclusion of the polishing process: (a) view under microscope between crossed polarizers; (b) thermal printout of interferogram.

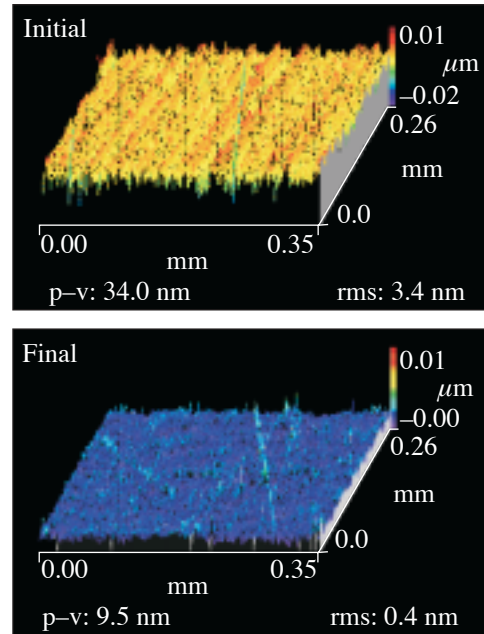
The peak removal rate for run #2 on day 2 was remeasured and found to be virtually unchanged at 3.63 $\mu\text{m}/\text{min}$. Upon completion of this second 40-min correction run, the figure error was further reduced from 1.2 μm p-v to ~ 0.35 μm p-v. Final surface microroughness values were 18.5 ± 6.8 nm p-v and 0.47 ± 0.05 nm rms. Power spectral density (PSD) plots confirmed that all diamond-turning marks had been eliminated. The PSD signature at 300 lines/mm was reduced in amplitude by over 1300 \times .



COM63

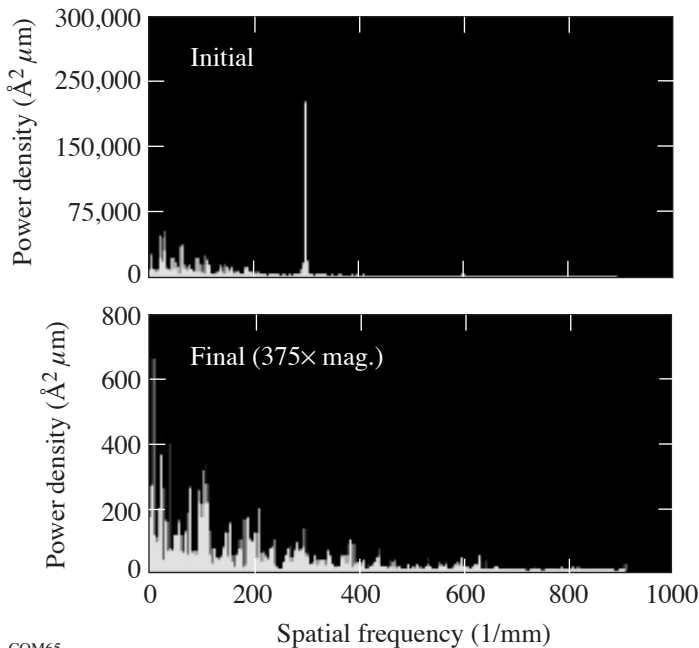
Figure 96.42 Initial and final wavefront maps for the PMMA puck (95% aperture).

Metrology results supporting the experimental findings are shown in Figs. 96.42 and 96.43. Figure 96.42 shows the initial and final wave-front maps for surface figure. Figure 96.43 shows initial and final oblique plots for surface roughness at a typical site, and Fig. 96.44 shows the initial and final power spectral density plots at the same site shown in Fig. 96.43.



COM64

Figure 96.43 Initial and final surface-roughness values for the PMMA puck at one typical site.



COM65

Figure 96.44 Initial and final PSD plots for the PMMA puck at the same site examined in Fig. 96.43. The diamond-turning mark signature at 300 lines/mm was reduced by more than 1300 \times . (The ordinate scale has been magnified by 375 \times to show the signature after MRF.)

4. Thermal Effects

Polymers require a longer time to thermalize than glasses, ceramics, or metals. This may be examined in two ways. The time ϕ (in minutes) required for a temperature gradient across the thickness t of a disk to decay to 10% of its initial value (heat being removed from only one side) is given as³⁴ $\phi = 1.67 \rho C_p t^2/k$, where ρ , C_p , and k are density, specific heat, and thermal conductivity, respectively. Table 96.IV gives a calculation of ϕ for 8-mm-thick pucks of PMMA and COP compared to the borosilicate glass BK7. The initial thermalization time for either of these polymers is four to five times longer than that for glass of equal thickness. Table 96.IV also gives a calculation of the sag S (in microns) of a part surface due to a linear temperature gradient through the thickness t as³⁴ $S = \alpha \Delta T r^2/2t$, where α , ΔT , and $2r$ are the coefficient of thermal expansion, the temperature difference across the part, and the part diameter (38 mm), respectively. A gradient of less than 0.2°C across a glass part is negligible, but for a polymer puck it is still sufficient to cause a 0.3- μm distortion.

Interferometry over 95% of its aperture was periodically performed on the 8-mm-thick PMMA puck used in the two figure correction runs previously described. The puck was “soaked” between two copper blocks for 30 min in the metrology lab and then monitored for p-v figure error after the first polishing run. Figure 96.45 shows that the initial figure error of 1.2 μm decayed to 1.0 μm after an additional 60 min. A similar measurement on the part at the conclusion of the second figure correction run showed that the same equilibration protocol was necessary to stabilize the surface figure at 0.4- μm p-v. Infrared thermometry³⁵ performed on the puck during polishing did not detect any rise in temperature above the ambient within the machine enclosure. This equilibration time is quite lengthy compared to the calculations shown above, suggesting that temperature fluctuations within the puck may

have been prolonged by the heavy traffic into and out of the metrology lab during the day. Precise interferometric testing is difficult to perform during the cold working of polymer optics.

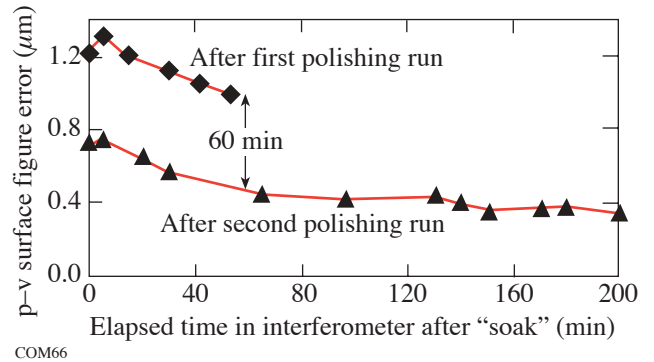


Figure 96.45 Wavefront metrology for an ~8-mm-thick PMMA puck as a function of elapsed time in the interferometer after a 30-min “soak” between copper plates. Stabilization required an additional 60 min (lines to guide the eye).

5. Long-Term Figure Instability in a PMMA Puck Polished on Both Sides

An experiment was conducted to polish out diamond-turned side 1 (S1) and side 2 (S2) of a plano PMMA puck. Puck dimensions and processing conditions were identical to those described above for the removal of diamond-turning marks. S1 was polished out on day 1 to a surface figure error of 0.33 μm p-v. S2 was polished out on day 2 to a surface figure error of 0.4 μm p-v. S1 was then monitored. Figure 96.46 shows the change in surface profile that was observed over 40 days. The center of the puck surface became concave, and by day 25 the surface figure error of S1 had degraded by almost 5 \times to 1.48 μm p-v. This had relaxed to 1.11 μm p-v by day 34, and to 1.09 μm p-v by day 40. We seek an explanation.

Table 96.IV: Thermal calculations for polymer and glass pucks 8 mm thick by 38 mm in diameter.

| | Time to reduce temperature gradient across part to 10% of initial value | | | | | Sag in part surface from temperature gradient remaining across part (μm) | | | |
|--------------------------|---|------------------|-------------|----------------|-----------------|---|--------------------------------|--------------------------------|--------------------------------|
| | ρ (g/cc) | C_p (J/g°C) | t (cm) | k (W/m°C) | ϕ (min) | α (10^{-5} cm/cm°C) | $\Delta T = 5.0^\circ\text{C}$ | $\Delta T = 1.0^\circ\text{C}$ | $\Delta T = 0.2^\circ\text{C}$ |
| Acrylic ^{14,36} | 1.19 | 1.5 | 0.8 | 0.23 | 8 | 6.7 | 7.7 | 1.54 | 0.3 |
| Zeonex ^{14,37} | 1.01 | 1.35 | 0.8 | 0.14 | 10 | 6.5 | 7.5 | 1.50 | 0.3 |
| BK-7 ³⁸ | 2.51 | 0.86 | 0.8 | 1.11 | 2 | 0.7 | 0.8 | 0.16 | 0.03 |

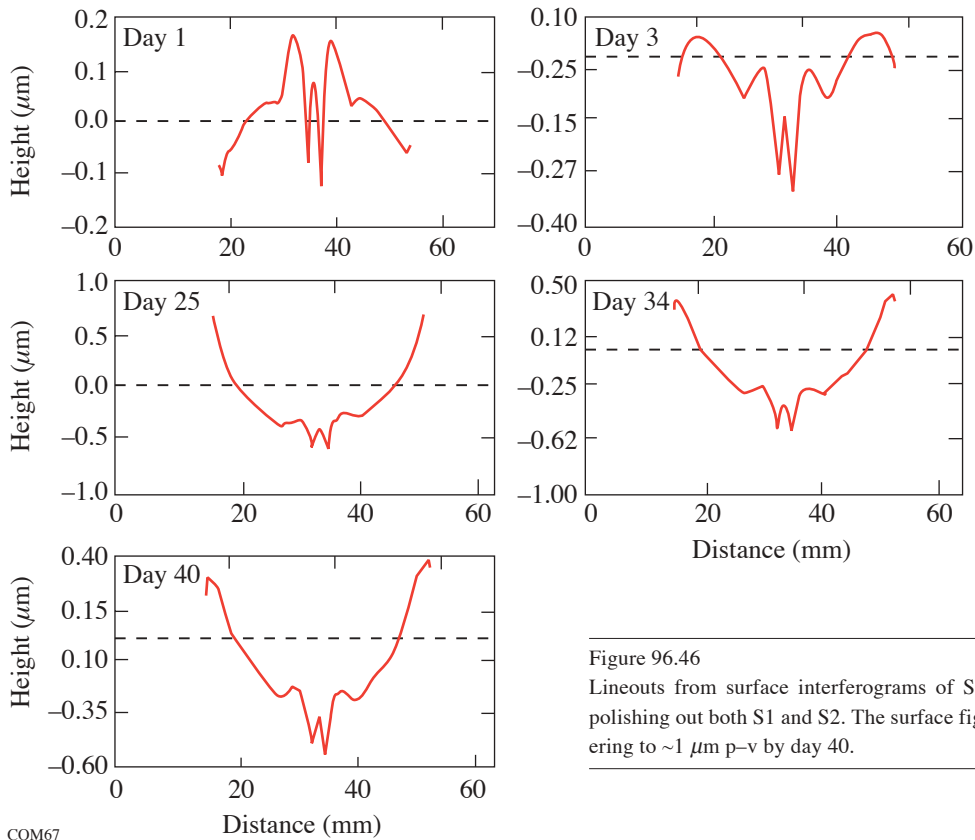


Figure 96.46

Lineouts from surface interferograms of S1 on a diamond-turned PMMA puck after polishing out both S1 and S2. The surface figure error degraded by 5× in 25 days, recovering to $\sim 1 \mu\text{m p-v}$ by day 40.

COM67

Conclusions

Experiments were conducted with conventional and experimental MR fluids to polish four optical polymers. A ZrO_2 -based MR fluid was successfully used on a Q22Y MRF machine to smooth and figure correct the plano surface of a diamond-turned PMMA part to 0.5 nm rms and 0.4 $\mu\text{m p-v}$, respectively. The diamond-turning marks were eliminated. Of the other abrasive/polymer combinations tested, Al_2O_3 showed the greatest potential for processing COP, PS, and PC without roughening or introducing surface artifacts. Issues of part thermalization for metrology were encountered. It was found that 90 min were required to stabilize the surface figure of an 8-mm-thick PMMA puck between runs and at the conclusion of a polishing experiment. Long-term surface figure instabilities were also observed for a PMMA puck after cold working both sides of the part.

ACKNOWLEDGMENT

Support for this work is provided by the Center for Optics Manufacturing. J. DeGroot is supported by the Frank J. Horton Graduate Fellowship Program.

REFERENCES

1. V. E. Sabinin and S. V. Solk, *J. Opt. Technol.* **69**, 48 (2002).
2. J. D. Lytle, "Polymetric Optics," in *Handbook of Optics*, 2nd ed., edited by M. Bass (McGraw-Hill, New York, 1995), Chap. 34, Vol. II, p. 34.13.
3. S. D. Jacobs, D. Golini, Y. Hsu, B. E. Puchebner, D. Stafford, Wm. I. Kordonski, I. V. Prokhorov, E. Fess, D. Pietrowski, and V. W. Kordonski, in *Optical Fabrication and Testing*, edited by T. Kasai (SPIE, Bellingham, WA, 1995), Vol. 2576, pp. 372–382.
4. D. Golini, S. Jacobs, W. Kordonski, and P. Dumas, in *Advanced Materials for Optics and Precision Structures*, edited by M. A. Ealey, R. A. Paquin, and T. B. Parsonage, *Critical Reviews of Optical Science and Technology* (SPIE, Bellingham, WA, 1997), Vol. CR67, pp. 251–274.
5. S. D. Jacobs, *Finer Points* **7**, 47 (1995).
6. S. R. Arrasmith, S. D. Jacobs, J. C. Lambropoulos, A. Maltsev, D. Golini, and W. I. Kordonski, in *Optical Manufacturing and Testing IV*, edited by H. P. Stahl (SPIE, Bellingham, WA, 2001), Vol. 4451, pp. 286–294.

7. I. Kozhinova, S. R. Arrasmith, J. C. Lambropoulos, S. D. Jacobs, and H. J. Romanofsky, in *Optical Manufacturing and Testing IV*, edited by H. P. Stahl (SPIE, Bellingham, WA, 2001), Vol. 4451, pp. 277–285.
8. J. D. Zuegel, V. Bagnoud, I. A. Begishev, M. J. Guardalben, J. Keegan, J. Puth, and L. J. Waxer, presented at CLEO, Baltimore, MD, 1–6 June 2003, invited paper CME3.
9. D. Golini *et al.*, *Laser Focus World* **37**, S5 (2001).
10. S. D. Jacobs, F. Yang, E. M. Fess, J. B. Feingold, B. E. Gillman, W. I. Kordonski, H. Edwards, and D. Golini, in *Optical Manufacturing and Testing II*, edited by H. P. Stahl (SPIE, Bellingham, WA, 1997), Vol. 3134, pp. 258–269.
11. S. R. Arrasmith, I. A. Kozhinova, L. L. Gregg, A. B. Shorey, H. J. Romanofsky, S. D. Jacobs, D. Golini, W. I. Kordonski, S. J. Hogan, and P. Dumas, in *Optical Manufacturing and Testing III*, edited by H. P. Stahl (SPIE, Bellingham, WA, 1999), Vol. 3782, pp. 92–100.
12. A. B. Shorey, S. D. Jacobs, W. I. Kordonski, and R. F. Gans, *Appl. Opt.* **40**, 20 (2001).
13. J. A. Menapace *et al.*, in *Laser-Induced Damage in Optical Materials: 2001*, edited by G. J. Exarhos *et al.* (SPIE, Bellingham, WA, 2002), Vol. 4679, pp. 56–68.
14. Data from *Specifications of Optical Grade Plastics*, G-S Plastic Optics, Rochester, NY 14603-1091.
15. Coupons were provided by Mr. William S. Beich, G-S Plastic Optics, Rochester, NY 14603-1091.
16. Diamond-turned pucks supplied by Mr. Paul Tolley, Syntec Technologies, Inc., Pavilion, NY 14525. Additional diamond turning of Zeonex pucks performed by Rochester Tool and Mold, Inc., Rochester NY 14611.
17. Extruded rod stock purchased from McMaster-Carr, New Brunswick, NJ 08903-0440; subsequently diamond turned by Rochester Tool and Mold, Inc., Rochester NY 14611.
18. This work was conducted by J. DeGroote and J. Watson as an independent laboratory experiment, in partial fulfillment of the requirements for the course Optics 256: Senior Lab, The Institute of Optics, University of Rochester, Rochester, NY, Fall 2001.
19. The permanent magnet machine was designed and fabricated for the Center for Optics Manufacturing in 1998 by Dr. I. Prokhorov and colleagues, Luikov Institute, Minsk, Belarus. It's capabilities and limitations are described in J. E. DeGroote, S. D. Jacobs, and J. M. Schoen, in *Optical Fabrication and Testing*, OSA Technical Digest (Optical Society of America, Washington, DC, 2000), pp. 6–9.
20. J. E. DeGroote, "Initial MRF Spotting Experiments on Optical Polymers," research project submitted in partial fulfillment of the requirements for Optics 443: Optical Fabrication and Testing, The Institute of Optics, University of Rochester, Rochester, NY, Spring 2002.
21. Q22, QED Technologies, LLC, Rochester, NY 14607.
22. Zygo NewView™ 5000 white-light optical profiler, Zygo Corporation, Middlefield, CT 06455. The instrument was set for areal mapping over 0.25 mm × 0.35 mm; 20× Mirau; FDA resolution: high; 20-μm bipolar scan; min/mod: 5.
23. Zygo GPI xPHR phase-shifting laser interferometer, Zygo Corporation, Middlefield, CT 06455.
24. S. D. Jacobs, S. R. Arrasmith, I. A. Kozhinova, L. L. Gregg, A. B. Shorey, H. J. Romanofsky, D. Golini, W. I. Kordonski, P. Dumas, and S. Hogan, in *Finishing of Advanced Ceramics and Glasses*, edited by R. Sabia, V. A. Greenhut, and C. G. Pantano, Ceramic Transactions, Vol. 102 (The American Ceramic Society, Westerville, OH, 1999), pp. 185–199.
25. A. B. Shorey, S. D. Jacobs, W. I. Kordonski, and R. F. Gans, *Appl. Opt.* **40**, 20 (2001).
26. W. I. Kordonski and D. Golini, *J. Intell. Mater. Syst. Struct.* **10**, 683 (1999).
27. I. Kozhinova, S. Jacobs, S. Arrasmith, and L. Gregg, in *Optical Fabrication and Testing*, OSA Technical Digest (Optical Society of America, Washington, DC, 2000), pp. 151–153.
28. A. B. Shorey, K. M. Kwong, K. M. Johnson, and S. D. Jacobs, *Appl. Opt.* **39**, 5194 (2000).
29. Technical product literature, Universal Photonics, Inc., Hicksville, NY 11801-1014.
30. Technical product literature, Salem Distributing Company, Winston-Salem, NC 27103.
31. Technical product literature, Buehler Ltd., Lake Bluff, IL 60044-1699.
32. *Primary particle*: homogeneously ordered, single domain, single crystal; *aggregate*: two or more primary particles, strongly bonded together and difficult to separate; *agglomerate*: ensembles of primary particles or aggregates, loosely bonded together and easily separated. Definitions taken from "Fundamentals of Particle Sizing," Technical Notes (7/94) from Nanophase Technologies Corporation, Burr Ridge, IL 60521.
33. Horiba LA-900 Particle Size Analyzer, Horiba Instruments, Inc., Irvine, CA 92714.
34. F. Cooke, N. Brown, and E. Prochnow, *Opt. Eng.* **15**, 407 (1976).
35. Minitemp® IR thermometer from Raytek, Inc., Santa Cruz, CA 95061-1820.
36. G. W. C. Kaye and T. H. Laby, *Tables of Physical and Chemical Constants and Some Mathematical Functions*, 15th ed. (Longman, London, 1986), p. 289.
37. Data from product literature, Zeon Corporation, Tokyo, Japan 100-8323.
38. Data from *Optical Glass Catalog-1994*, Schott Glass Technologies, Inc., Duryea, PA 18642.

LLE's Summer High School Research Program

During the summer of 2003, 15 students from Rochester-area high schools participated in the Laboratory for Laser Energetics' Summer High School Research Program. The goal of this program is to excite a group of high school students about careers in the areas of science and technology by exposing them to research in a state-of-the-art environment. Too often, students are exposed to "research" only through classroom laboratories, which have prescribed procedures and predictable results. In LLE's summer program, the students experience many of the trials, tribulations, and rewards of scientific research. By participating in research in a real environment, the students often become more excited about careers in science and technology. In addition, LLE gains from the contributions of the many highly talented students who are attracted to the program.

The students spent most of their time working on their individual research projects with members of LLE's technical staff. The projects were related to current research activities at LLE and covered a broad range of areas of interest including laser optics modeling, laser-beam alignment, analysis of OMEGA implosion experiments, plasma physics modeling, cryogenic target physics, liquid crystal chemistry, molecular modeling, and the development and control of laser fusion diagnostics (see Table 96.V).

The students attended weekly seminars on technical topics associated with LLE's research. Topics this year included lasers, fusion, holographic optics, atomic force microscopy, experimental error analysis, computer-controlled optics manufacturing, and microcontrollers and their applications. The students also received safety training, learned how to give scientific presentations, and were introduced to LLE's resources, especially the computational facilities.

The program culminated on 27 August with the "High School Student Summer Research Symposium," at which the students presented the results of their research to an audience including parents, teachers, and LLE staff. The students' written reports will be bound into a permanent record of their work that can be cited in scientific publications. These reports are available by contacting LLE.

One hundred and sixty high school students have now participated in the program since it began in 1989. This year's students were selected from approximately 60 applicants.

In 2003, LLE presented its seventh William D. Ryan Inspirational Teacher Award to Mr. Michael Carges, a former physics teacher at Pittsford-Mendon High School and currently at Greece Athena High School. This award, which includes a \$1000 cash prize, was presented at the High School Student Summer Research Symposium. Alumni of the Summer High School Student Research Program were asked to nominate teachers who had played a major role in sparking their interest in science, mathematics, and/or technology. Mr. Carges was nominated by Joy Yuan and Siddhartha Ghosh, participants in the 2002 Summer Program.

Mr. Ghosh wrote: "The knowledge he imparts to them [his students] set him aside from many other teachers I have had in the past. Mr. Carges strives to inspire those around him in many ways..... Mr. Carges' instruction in class was truly one of the most exemplary models I have encountered in high school."

Ms. Yuan wrote: "It takes a special kind of person to be a superior teacher. This person must have a passion for teaching and demonstrate dedication toward his job as the mold of our minds. He must have a thorough understanding of the material and knowledge..... Mr. Carges was one of the few teachers who knew what they were talking about. He was able to translate [to his students] what physicists have spent centuries doing."

Table 96.V: High School Students and Projects—Summer 2003.

| Name | High School | Supervisor | Project Title |
|--------------------|---------------------------|---------------------------|--|
| Christine Beaty | Livonia High School | C. Stoeckl | Controlling Scientific Instruments Using JAVA on LINUX |
| Ryan Blair | Canandaigua Academy | R. Boni/ M. Millechia | Characterization of the OMEGA UV Spectrometer |
| George Dahl | Allendale Columbia | M. Guardalben | Pulse-Shaping Effects in Optical Parametric Amplification |
| Margot Epstein | Sodus Central High School | W. Bittle/ J. Depatie | Automated Laser-Beam Steering |
| Wen-Fai Fong | Pittsford Sutherland | R. Epstein | Non-LTE Effects on the Speed of Sound in Plasmas |
| Christopher Forbes | Eastridge Senior High | P. Jaanimagi | Energy and Angular Distributions of Secondary Electrons Under High Electric Field |
| Nathaniel Gindele | Brighton High School | J. Knauer | Deconvolution and Calibration of Diamond PCD Detectors |
| Rohan Kekre | McQuaid Jesuit | S. Craxton | Tuning Multiple Triplers Using the UV Spectrometer |
| Kathryn Knowles | Churchville-Chili | J. Delettrez | Analysis of the Ablation Process in Rayleigh–Taylor Unstable Implosions |
| Nadine Lippa | Byron-Bergen | A. Schmid | Single-Molecule Fluorescence in Liquid Crystal Hosts |
| Anthony Noto | Greece Athena | K. Marshall | Development of Weighted Chiral Indices: Their Use in Modeling Nickel Dithiolene Systems |
| Benjamin Schmitt | Greece Arcadia | F. Marshall | X-Ray Microscope Mirror Characterization |
| Nicole Toscano | Greece Arcadia | V. Smalyuk | Compressed Core Characterization of a Cryogenic D ₂ Target at Peak Neutron Production |
| Cam Tran | Wilson Magnet | K. Marshall | Photochemically Induced Alignment of Liquid Crystals on a Polymer Surface |
| Michael Wozniak | Greece Athena | D. Harding/ S. Craxton | The Effects of Nonuniform Illumination on the Shape of Deuterium Ice Layers |

FY03 Laser Facility Report

User demand was met in FY03 by continuing to operate extended shifts during select weeks. Over 95% of planned target shots were executed for a total of 1381 shots (see Table 96.VI). Shaped-pulse cryogenic implosions highlighted the ongoing development of direct drive cryogenic capability. A total of 20 spherical and 51 planar cryogenic D₂ shots were performed. Pulse-shape performance improved dramatically with the addition of diode-pumped regenerative amplifiers. Target irradiation uniformity was improved by implementing several changes, including a new set of distributed phase plates (DPP's) and improvements to beam-pointing precision. Highlights of other achievements and active projects as of the end of FY03 include the following:

- Installation of LLE-built diode-pumped regenerative amplifiers on all three laser drivers improved pulse shape and energy stability. Production-model regens were installed on both the main and backlighter drivers, replacing flashlamp-pumped units. Additionally, the prototype diode-pumped regen on the SSD driver was replaced with a production model. A concomitant increase in pulse-shape effectiveness from 93% in FY02 to 98% in FY03 resulted.
- Adiabatic shaping using picket pulses improved the performance of direct-drive ICF targets. Picket-pulse development continued with the application of new techniques for improving picket-pulse quality and stability. Improved picket-pulse prediction routines and IR streak cameras resulted in improved picket-pulse performance.
- Laser-driver timing system modifications provided the capability to more precisely delay individual drivers with increased range. All drivers are now capable of being delayed or advanced hundreds of nanoseconds with ~100-ps precision. This new capability has been utilized extensively to improve the effectiveness of experimental campaigns.
- The implementation of a new set of DPP's provided improved irradiation uniformity for direct-drive spherical capsules. The new DPP's, designated SG4, produce a flatter intensity distribution on target than the previous set (SG3). In addition to producing a larger effective beam area on target, the SG4 DPP's have a smaller beam-to-beam shape variation than their predecessors.
- Distributed polarization rotators (DPR's) continued heavy use in FY03. All DPR's were modified for remote retraction and reinstallation, improving flexibility for reconfiguring to indirect-drive setups. Nonlinear losses in the UV were observed due to DPR reconversion. This phenomena was investigated and corrective action initiated.
- The overall OMEGA irradiation uniformity on target was improved by using active repointing. Active repointing consists of evaluating the actual beam positions on target using x-ray images of the beam spots on a 4-mm, Au-coated pointing target and then repointing individual beams. Subsequent pointing shot offsets have been reduced from ~23 μm rms to 11 μm rms.
- To allow lower beam energy while preserving pulse shape, the use of frequency-conversion-crystal doubler detuning has been implemented; it was used extensively in FY03 on limited beam sets.
- Scientists and engineers from Lawrence Livermore National Laboratory along with LLE collaborators successfully implemented a 4ω (fourth harmonic, 263 nm) target irradiation capability on one of the 60 OMEGA beams. Experiments utilizing the 4ω capability were conducted in FY03, and more extensive use is planned for FY04.
- Shot operations continued in parallel with construction of the new OMEGA EP building, which commenced in July 2003. Building construction activities were carefully monitored to ensure the stability of target positioning and beam pointing at shot time. An EP beam transport opening was also created in the east target bay wall for propagating future EP beamlines into the OMEGA target chamber.

Table 96.VI: The OMEGA target shot summary for FY03.

| Laboratory | Planned Number of Target Shots | Actual Number of Target Shots |
|--|--------------------------------|-------------------------------|
| LLE | 744 | 648 |
| LLNL* | 415 | 390 |
| LANL** | 124 | 158 |
| SNL | 25 | 30 |
| NLUF | 121 | 123 |
| CEA | 30 | 32 |
| Total | 1459 | 1381 |
| | | |
| LLE ISE | | 222 |
| LLE SSP | | 168 |
| LLE DD | | 72 |
| LLE LPI | | 61 |
| LLE RTI | | 45 |
| LLE Cryo | | 31 |
| LLE Astro | | 28 |
| LLE PB | | 21 |
| LLE Total | | 648 |
| | | |
| *Includes 39 shots in collaboration with LANL. | | |
| **Includes 8 shots in collaboration with LLNL. | | |

National Laser Users' Facility and External Users' Programs

During FY03, the number of target shots dedicated to external users of OMEGA continued to increase as 733 target shots were provided. This represents 53% of the total target shots produced by OMEGA in the last year. External users' experiments were carried out by collaborative teams under the National Laser Users' Facility (NLUF) Program as well as by teams led by scientists from Lawrence Livermore National Laboratory (LLNL), Los Alamos National Laboratory (LANL), Sandia National Laboratory (SNL), and the Commissariat à l'Énergie Atomique (CEA) of France.

FY03 NLUF EXPERIMENTS

Seven of the nine NLUF programs approved in the last NLUF Review carried out a total of 123 target shots on OMEGA in FY03. Approved experimental NLUF Programs on OMEGA include the following:

Experimental Astrophysics on the OMEGA Laser

Principal Investigator: R. P. Drake (University of Michigan)

This project involves experiments in compressible hydrodynamics and radiation hydrodynamics, relevant to supernovae and supernova remnants. The experiments produce phenomena in the laboratory that are believed to be important to astrophysics but have not yet been directly observed in either the laboratory or in an astrophysical system. During FY03, the work focused on demonstrating techniques that can be used to explore the onset of turbulence in the three-dimensional, deeply nonlinear evolution of the Rayleigh–Taylor instability at a decelerating, embedded interface and on studies of collapsing radiative shocks. These experiments required strong compression and decompression, strong shocks (Mach ~ 10 or greater), flexible geometries, and very smooth laser beams, which means that the 60-beam OMEGA laser is the only facility capable of carrying out this program. During the past year, 2.5 shot days on OMEGA were allotted to this campaign, resulting in 25 target shots.

The exciting nature of this work has motivated the development of a collaborative effort that couples a core experimental team to theoretical groups at several institutions. Simulations

guide the experimental planning to enable the acquisition of high-quality data and to provide for a comparison of several codes against the experimental data. Because they are complex and explore deep nonlinear effects, these experiments are excellent for verification and validation (V&V) of complex computer codes, including those produced by the ASCI Alliance Center at the University of Chicago. This program is also a critical steppingstone toward the use of the National Ignition Facility (NIF) both for fundamental astrophysics and as a critical component of ASCI V&V.

1. Development of Turbulence in Rayleigh–Taylor (RT) Instability at a Decelerating, Embedded Interface

As the scaling analysis in the paper by Robey *et al.*¹ indicates, it should be possible to observe the transition to a turbulent state in the evolution of the Rayleigh–Taylor instability that develops from a 3-D initial condition in the OMEGA experiments. Prior experiments on OMEGA indicated that several improvements in experimental technique were required to clearly observe the turbulent transition. During the past year, three such improvements were implemented:

- a. An iodine-doped plastic that can be used for the tracer layers in the OMEGA targets was developed. Iodine has a higher x-ray opacity than the bromine that was used previously; this enhances the contrast of the x-ray images and extends the time over which the growth of the instabilities can be observed.
- b. X-ray radiography using a backlit pinhole was implemented. Figure 96.47 shows the geometry of the initial targets using this technique. Laser beams irradiated a spot in the middle of the rear surface of a Ti foil, producing K_{α} x rays. Some of these x rays passed through a 10- μm pinhole in a Ta substrate, irradiating the target. A detector behind the target recorded the image. This technique produces much brighter images, and correspondingly improved signal-to-noise ratios, than the technique of area backlighting used previously.

c. A second x-ray-backlighting view of the target is being developed, which can look along the tracer strip (see Fig. 96.47). In this view, the strip itself is very opaque, but it will be possible to detect the lateral transport of material from the strip. The development of rapid lateral transport is a signature of the “mixing transition” that occurs with the onset of turbulence. In the initial attempt to implement the second view, the two views were not shielded well enough from one another. An improved design is currently being tested.

The first two improvements worked well and produced greatly improved data, as shown in Fig. 96.48. To demonstrate the improved techniques, targets with split perturbations were used: a single 2-D perturbation on half the interface (50- μm

wavelength, 5- μm peak-to-valley amplitude) and a second, short-wavelength mode (5- μm wavelength, 0.5- μm peak-to-valley amplitude) on the other half. This provided worthwhile data regarding the effects of a second mode to compare with simulations. In addition, it is now possible to obtain reasonable-quality data as late as 37 ns after the start of the laser pulse, which is much later than could be obtained previously. Analysis continues, but the preliminary conclusion is that the second mode has a much smaller effect than is predicted by the simulations.

2. Collapsing Radiative Shocks

Astrophysical shocks, when they become cool enough, enter a radiatively collapsing phase in which their density can increase by several orders of magnitude. All supernova remnants eventually pass through this phase; blast waves emerging from supernovae pass through this phase, and such shocks arise in a number of other contexts. Using targets filled with xenon gas is expected to produce shocks that radiatively collapse on OMEGA. The goal is to produce such shocks, diagnose their properties, and study their evolution. This may include the development of structure due to the Vishniac instability.

Figure 96.49 shows a drawing of one of the targets that were used in these experiments. The laser beams irradiate the target from above, accelerating the thin (50 μm Be or 82 μm CH) solid layer to more than 150 km/s. This drives a shock down the tube, strong enough that it is predicted to collapse. The shock has been diagnosed using radiography (from left to right) or VISAR (through the lateral tubes). Simulations predict that x-ray radiographs should observe a collapsed xenon layer that is much narrower than the xenon layer that would be seen without the effects of radiation, as illustrated in Fig. 96.50.

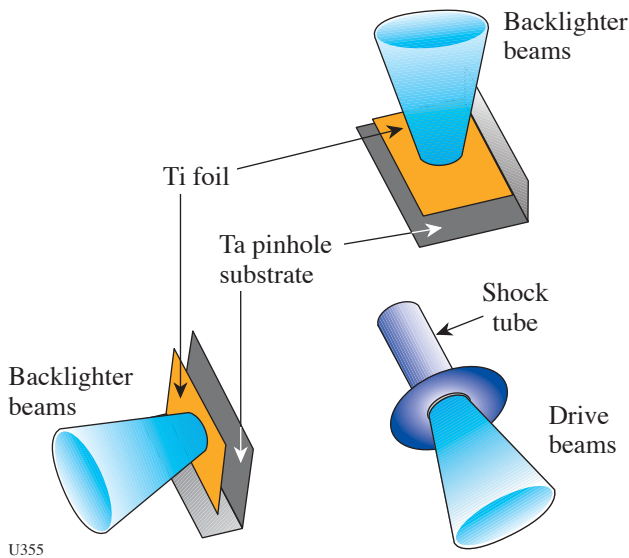
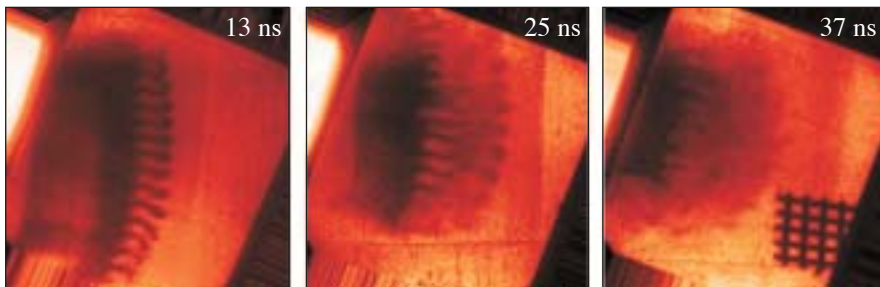
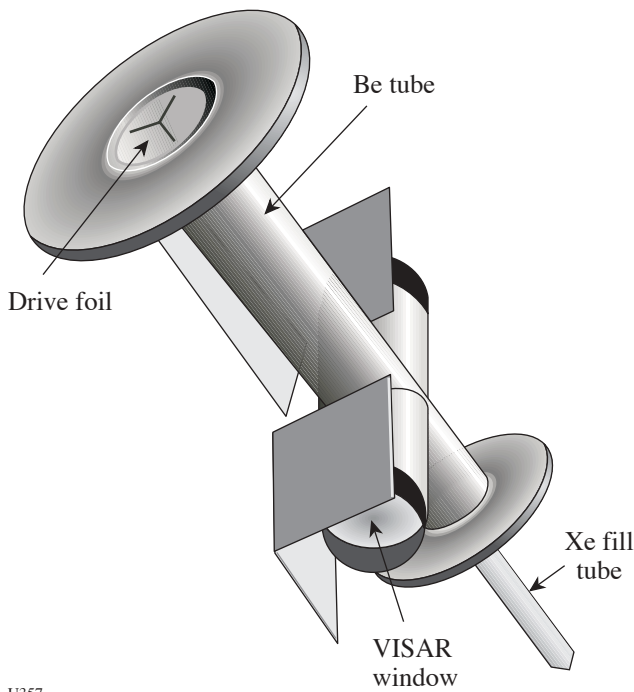


Figure 96.47
Target geometry for the Rayleigh–Taylor experiments using a backlit pinhole.



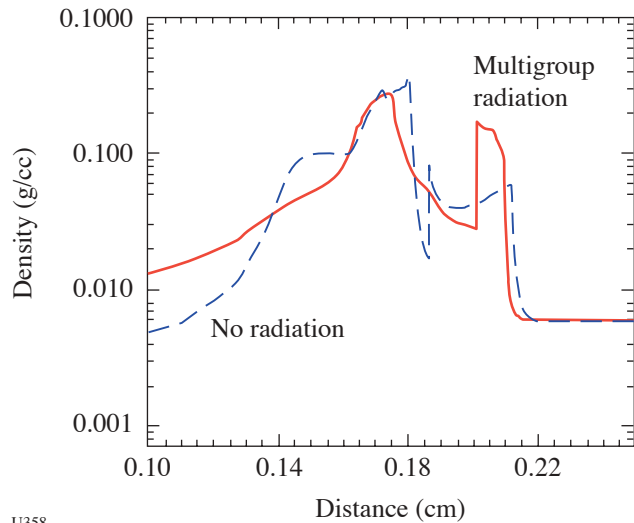
U356

Figure 96.48
Radiographs using a backlit pinhole and an iodine-doped tracer layer.



U357

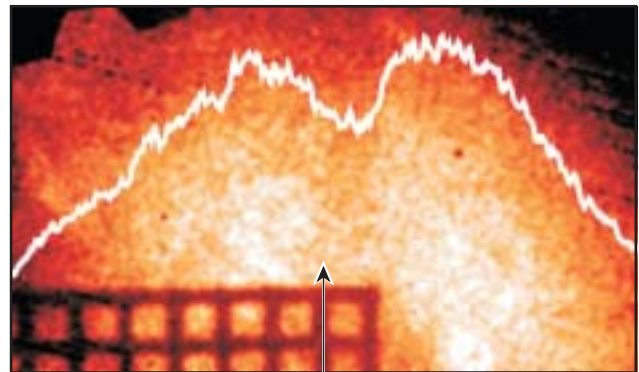
Figure 96.49
Drawing of a target used for radiative shock experiments.



U358

Figure 96.50
The effect of radiation should be to produce a thin, dense layer of xenon. The width of the layer in the simulation is just under 100 μm .

An actual radiograph, obtained using area backlighting, is shown in Fig. 96.51. A layer of xenon whose thickness is roughly consistent with the predictions of the simulation can be seen in this photograph. Since an improved signal-to-noise ratio is also required here, an attempt was made to employ a backlit pinhole for this application. Despite the similarity of the pinhole structure to those used previously with success, the specific pinhole design used for this experiment created shrapnel that damaged the imaging diagnostic. The next experiments will employ a modified backlit pinhole design; improved radiography is expected. The achievement of stronger shocks using a thinner initial layer, driven with SSD-smoothed laser beams, is also anticipated.



U359

Figure 96.51
Radiograph of a shocked layer in xenon gas. The squares in the grid are 63 μm from wire center to wire center, so the observed layer is $\sim 80 \mu\text{m}$ thick.

Several publications on experimental astrophysics were published by this group during the past year (see Refs. 1–5).

Optical-Mixing-Controlled Stimulated Scattering Instability V (OMC SSI V)

Principal Investigator: B. B. Afeyan (Polymath Research Inc.)

The principal aim of this program is to investigate the evolution of backscattering instabilities of a witness beam in the presence of optical-mixing-generated plasma waves created by beating a blue pump beam with a green probe beam. This experiment was allotted 1.5 days of OMEGA time in FY03 and a total of 21 target shots were taken. In FY03, crossed blue- and green-beam experiments were conducted in exploding foil targets for the first time on OMEGA using a wide-enough DPP-generated spot so as not to be overwhelmed with excessive green-beam filamentation. A new phenomenon was observed that not only confirms that energy was success-

fully transferred from the blue beam to the green beam, but also confirms that a significant increase in the Raman backscattering of the green beam was triggered due to its interaction with the blue. A 15-fold increase in peak energy reflected by SRS (stimulated Raman scattering) was observed at an incident green-beam energy level of 100 J, while the crossing blue beam was at 500 J as compared to the same energy in green with the blue beam off as shown in Fig. 96.52. Figure 96.52(a) shows the SRS signal from the green beam alone, while Fig. 96.52(b) shows the backscattering of the green beam when the crossing blue beam is near 500 J. Figure 96.53 shows the same phenomenon for different target illumination conditions that gave rise to a hydrodynamic expansion that reached the necessary resonant density for energy transfer between the blue and green beams later in time and at colder temperatures. The same phenomenon is observed later in time, confirming the validity

of the interpretation and the exceptional reproducibility of this instability energy transfer result, where incident blue-beam energy ends up becoming SRS-reflected energy from the green beam. This is a new wavelength conversion process where long wavelengths are produced by a controlled two-step process. It implies that the interpretation of the physics of laser-plasma interactions based on single interaction-beam experiments may be incomplete when extrapolated to predict the behavior of multiple beams crossing in a plasma. The results may not be strictly additive but highly nonlinear and multistep in nature. These new phenomena are being studied using parallel Vlasov-Maxwell simulations. Transmitted-beam diagnostics on the green probe beam confirm these findings by showing that the energy transfer from the blue to the green crossing beam was approximately a factor of 2.

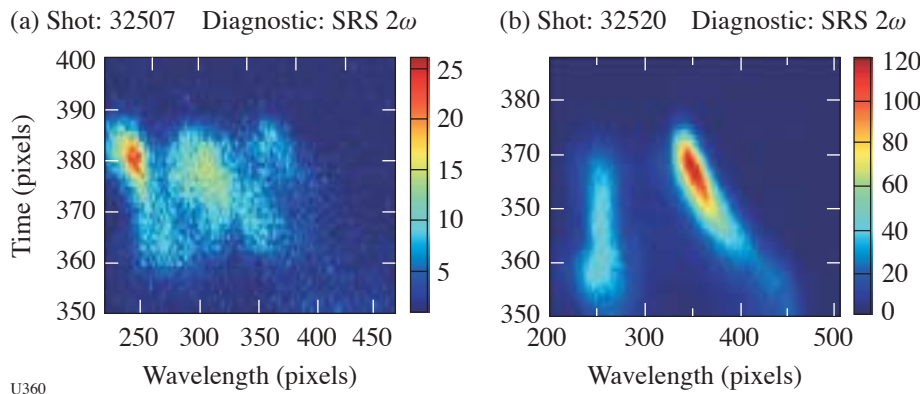


Figure 96.52
SRS reflectivity of a green beam in the absence (a) and presence (b) of a blue crossing beam. The peak reflectivity is increased by a factor of 15 or more when the signature of the peak of the exploding foil is considered (long-wavelength feature).

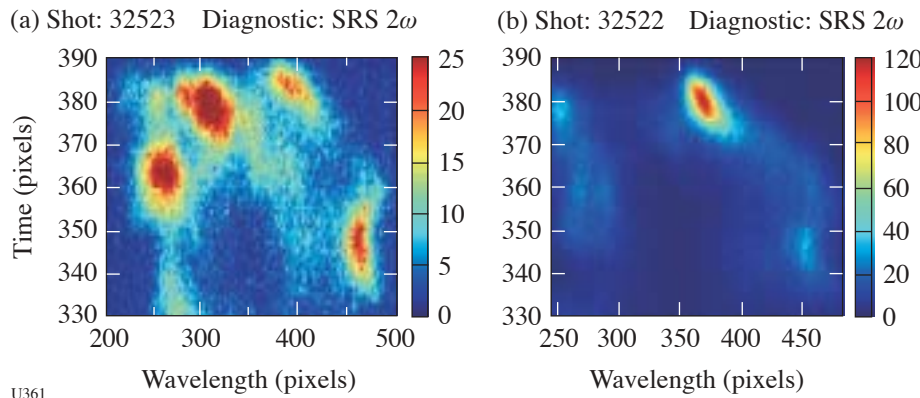


Figure 96.53
Same as Fig. 96.52 except that the plasma expansion is now delayed due to the elimination of two of the plasma heater beams. Note how Fig. 96.53(b) is very similar to Fig. 96.52(b) except for the time delay and subsequent reduction in the temporal extent of the green-beam SRS backscattering.

Time Evolution of Capsule ρR and Proton Emission Imaging of Core Structure

Principal Investigator: R. D. Petrasso (Plasma Science and Fusion Center, MIT)

This program is aimed at the use of charged-particle measurements to address important issues in inertial confinement fusion (ICF) and high-energy-density physics. During FY03, 1.5 OMEGA shot days were allotted to this program, and 18 target shots were taken. The experiments were in two main areas: proton core imaging and studies of ρR asymmetry growth.

1. Proton Core Imaging Spectroscopy (PCIS) for OMEGA Implosions

Penumbra proton imaging was used to study the spatial distributions of DD and D^3He reactions in imploded D^3He -filled capsules on OMEGA.^{6,7} The imaging was performed with a pinhole camera in which the recorder consisted of stacked sheets of CR-39 nuclear track detector separated by ranging filters, which resulted in efficient detection of 14.7-MeV D^3He protons on one sheet [see Fig. 96.54(a)] and 3-MeV DD protons on another. Measurements of the nuclear burn region are important for investigating the extent of the burn, the presence of burn asymmetries, the effects of mix and thermal conduction on the burn region, and the accuracy of code predictions. When target capsules have thin shells (e.g., 1.8 μm SiO_2), allowing both proton types to escape at burn time, the images on separate sheets of CR-39 can be used to reconstruct simultaneous radial profiles of DD and D^3He burn. These can in turn be used to determine the fuel ion temperature (T_i ; see Fig. 96.54) and the density (n_i). When capsules have thick shells (e.g., 20 μm CH), only the 14.7-MeV proton can escape through the capsule ρR at bang time and the

measured D^3He burn profile reflects the effects of compression and mix; but DD protons do escape at the earlier time of first shock coalescence, when ρR is far below its peak value, and the DD burn profile at that time can be studied. Since mix has been experimentally shown to be inconsequential at this instant, meaningful comparisons of 1-D simulations with experiments can be made.

2. Studies of ρR Asymmetry Growth Rates and the Relationship Between Laser Drive Asymmetry and ρR Asymmetry

During 2003, a series of shots were undertaken to study the implications of laser drive asymmetry for implosion dynamics and capsule performance, and several important conclusions were drawn from the resultant data. The series included six implosions of room-temperature capsules with 26- μm -thick CH shells and 18 atm of D^3He gas fill, using 60 laser beams with full beam smoothing and ~ 23 kJ of total laser energy. Illumination asymmetry was introduced in a controlled way by offsetting the capsules from target chamber center (TCC) by specific amounts, resulting in deviations of the on-target laser intensity $\delta I(\phi)$ from the mean $\langle I \rangle$ that are dominated by mode numbers 1 and 2. Diagnostics used to record crucial data included six wedged-range-filter (WRF) proton spectrometers, the proton temporal diagnostic (PTD), x-ray framing cameras, pinhole cameras, and the GMXI framing camera. Figure 96.55 illustrates sample proton spectra recorded during implosions with three different target offset amounts, showing how the spectra are dramatically different at different angles and for different offsets. Each spectrum can be decomposed into two parts representing proton emissions at the time of first shock coalescence and at bang time (these times occur roughly 1.7 and 2.1 ns after the onset of the 1-ns laser pulse, respectively).

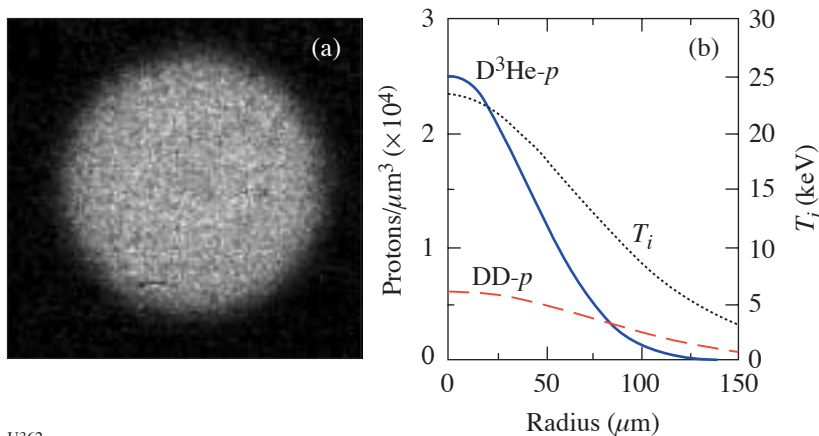
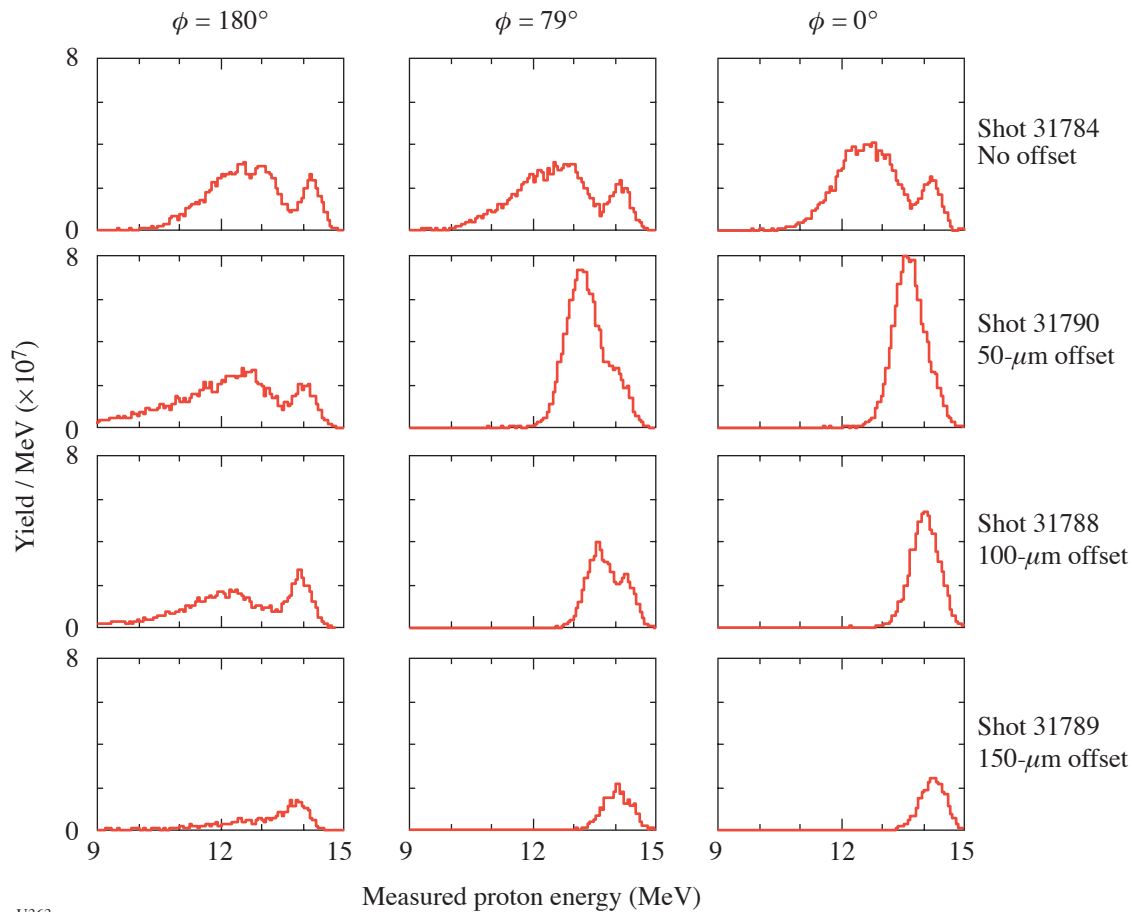


Figure 96.54
PCIS data from OMEGA shot 27456, in which the capsule consisted of 18 atm of D^3He in a 1.8- μm SiO_2 shell. (a) An image of D^3He protons made behind a 600- μm -diam pinhole. Since the pinhole is much larger than the compressed capsule, all structural information is contained in the penumbra. (b) Radial profiles of proton emissivity in the imploded capsule, inferred from five pinhole images of D^3He protons and five pinhole images of DD protons. Since the local ratio of the two reaction rates is a function of ion temperature T_i , the radial profile $T_i(r)$ can be inferred.



U363

Figure 96.55

Proton spectra recorded at three important angles with respect to the direction of offset of the capsule from target chamber center. Offsets produce an asymmetric laser drive intensity on the capsule surface, with the maximum value at 180° and the minimum at 0° (see Fig. 96.56 for an example). With no offset, the spectra are all very similar, indicating an implosion that was quite symmetric. As the offset gets larger, ρR asymmetries get progressively larger and the size of the lower-energy peak (due to emission at compression time) becomes progressively smaller while the shock-time peak maintains a relatively constant size (see Fig. 96.57).

The energy spectra of the D^3He protons were used to characterize the areal density (ρR) as a function of angle at shock time and at bang time using spectrometers at different angles. It was found that the angular shape of the drive asymmetries is imposed on the ρR variations and maintained with no phase change through shock and bang times, as shown in Fig. 96.56. The growth in amplitude was roughly consistent with that recently predicted for Bell-Plesset-like convergence effects.⁸ At each time, $\delta\rho R(\phi)/\langle\rho R\rangle \approx 0.4(C_r - 1)\delta I(\phi)/\langle I\rangle$, where C_r is the radial compression ratio at that time and $\delta I(\phi)/\langle I\rangle$ is averaged over the laser pulse. The mean ρR at each time can also be used to estimate C_r , which turns out to be essentially independent of offset at shock time but a decreasing function of offset at compression time.

Considering the fuel, the data provide information about the dynamics of shock coalescence and the state of the fuel at bang time. The character of the shock coalescence is particularly important because simulations predict that asymmetrically launched shocks will not coalesce coherently enough to heat the hot spot. It was found in the experiments that, although the shock coalescence for offset targets was smeared out in time and space, the number of D^3He protons emitted at this time was less sensitive to drive asymmetry than expected (Fig. 96.57). In fact, simulations had indicated that there would be no shock yield at all for the largest capsule offsets used. The yield at bang time, on the other hand, did diminish with increasing offset. This is qualitatively consistent with the finding from the ρR studies that the radial compression ratio decreased with increasing illumination asymmetry.

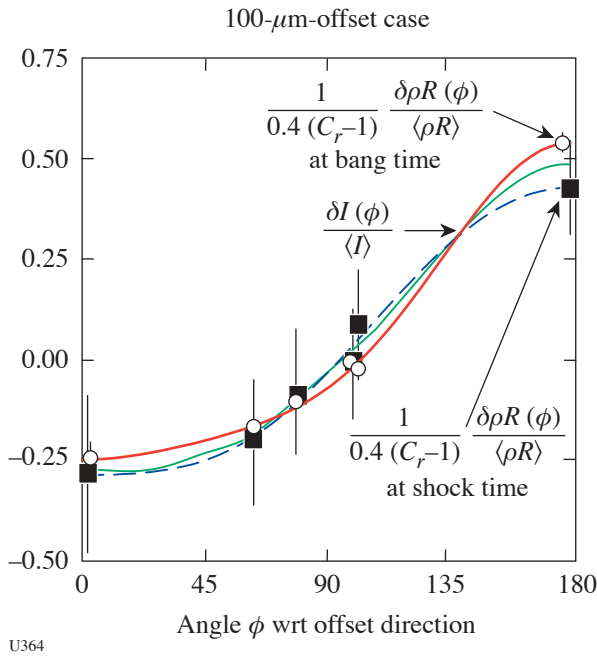


Figure 96.56
For an offset target implosion, the angular distribution of the measured ρR is similar at different times during the implosion.

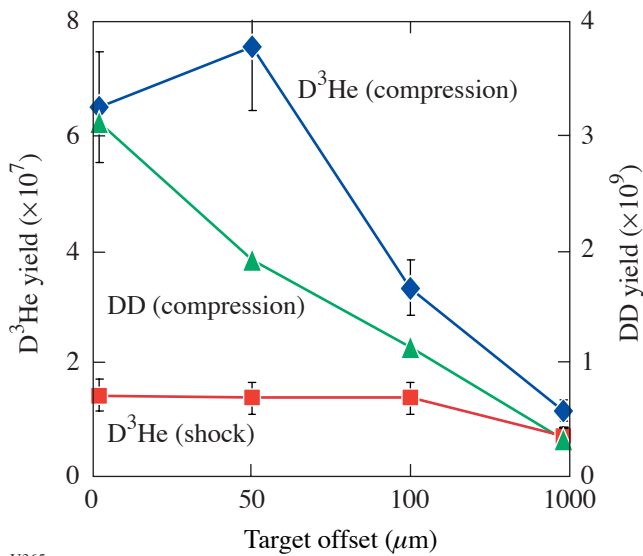


Figure 96.57
 $D^3\text{He}$ and DD proton yields as a function of the offset of targets from TCC. Despite the smearing of the shock coalescence in space and time, the $D^3\text{He}$ proton yield at shock time remains largely unaffected by the drive asymmetry caused by target offset, while the yield at compression time decreases with offset.

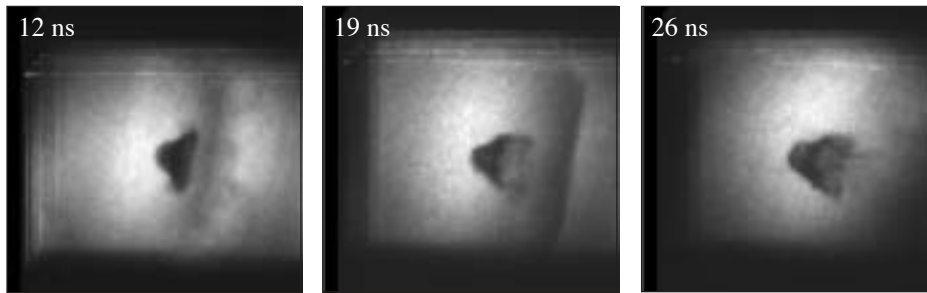
OMEGA Laser Studies of the Interaction of Supernova Blast Waves with Interstellar Clouds

Principal Investigator: C. McKee (University of California, Berkeley)

The objective of this experiment is to conduct experiments on OMEGA to (1) explore the role of turbulence in laser–target interactions and (2) study the laboratory analog of astrophysical “mass-loaded flows.” The current experiments involve the interaction of strong shocks with single and multiple dense clumps embedded in a low-density inter-clump background.

By varying the composition and size of the target, the investigators were able to systematically vary the Reynolds number (Re) of the flow and study the onset of turbulence in a compressible flow. These experiments are relevant to astrophysical flows in which powerful shock waves produced by supernovae, stellar winds, and other phenomena propagate through an inhomogeneous medium. Mass is stripped from clouds and injected into the low-density, generally hot, intercloud medium—a phenomenon known as mass loading. These experiments specifically address the question of how the mass loading is affected by the Re of the flow. It is possible to determine whether there are significant changes in the mass and momentum exchange between the cloud and the intercloud medium at Re higher than those accessible to direct numerical simulation (the limit on numerical simulations is typically $Re < 10^3$). A specific goal of the investigation is to find evidence for the transition from a vortex sheet to a turbulent wake; this appears at $Re \sim 2 \times 10^4$ in compressible flow experiments. During this first year of the study, a single dense clump (sphere) is used; future work may extend this research to the case of multiple clumps. The results of the experiments will be compared with both 2-D and 3-D direct numerical simulations using adaptive mesh refinement.

During FY03, 1.5 shot days were allocated for these studies, and 14 target shots were taken. The experiments for this first year were directed to demonstrating a clearly diagnosable transition to a turbulent flow, which the investigators believe may look like that observed in incompressible experiments. Side-on and face-on radiographic images of reasonably high quality at 5 ns (face-on only), 12 ns, 19 ns, and 26 ns were obtained. Figure 96.58 shows side-on radiographic images that display the evolution of the shocked spherical cloud at 12 ns, 19 ns, and 26 ns. At 12 ns, the shock has just passed over the cloud, and the spherical cloud displays a symmetrical extension in the axial direction with the start of a Kelvin–Helmholtz rollup of the sides of the cloud. By 19 ns, corresponding to 6.7



U366

Figure 96.58

X-ray radiographic images of the interaction of a strong shock wave with a spherical object. The sphere is initially $120\ \mu\text{m}$ in diameter and located $500\ \mu\text{m}$ from the ablative surface of a $1500\text{-}\mu\text{m}$ -diam cylindrical shock tube. (The side of each square image is approximately $1150\ \mu\text{m}$.)

crushing times, the face-on images (not shown) display the initial development of the vortex-ring instability predicted and observed in earlier work on Nova and OMEGA.^{9,10} The basic symmetry of the shocked sphere seen in the side-on radiograph indicates that the flow is most likely still laminar. At 26 ns, corresponding to 9.8 crushing times, nonaxisymmetric flow is clearly evident in the side-on radiographs with evidence of asymmetric jetting and strong Kelvin–Helmholtz instabilities. This is most likely the start of strong vortex-ring instabilities and the transition to turbulent flow. Two-dimensional simulations to model the shock–sphere interaction have been conducted. Later time evolution of the interaction will require detailed 3-D AMR simulations that will also be performed.

High-Spatial-Resolution Neutron Imaging of Inertial Fusion Target Plasmas Using Neutron Bubble Detectors

Principal Investigator: R. K. Fisher (General Atomics)

The goal of this research is to develop techniques to record the bubble spatial distribution in a high-efficiency liquid bubble chamber that may have potential use for NIF neutron imaging. This program had only limited funds and no dedicated shots in FY03. Its focus was the study of alternative bubble-recording techniques, including light scattering and x-ray transmission, with the goal of determining the most-promising method prior to initiating laboratory tests.

An initial assessment of x-ray transmission was carried out, and the following potential advantages of this approach were identified:

- a change in x-ray transmission allows measurements under expected NIF conditions since there will be many bubbles behind bubbles;
- the photoelectric effect dominates x-ray attenuation and minimizes the multiple scattering “crosstalk” issue inherent in light-scattering approaches;

- bubble-distribution measurements should be allowed over a wide range of NIF n -yields; flash x-ray timing can be chosen to optimize bubble radius and, therefore, $\Delta(\rho x)$ along x-ray paths.

1. Future Plans

- Complete preliminary assessment of x-ray and light-scattering approaches to bubble distribution measurements.
- Perform laboratory tests to address important issues, e.g., the effects of multiple scattering during light scattering/transmission measurements.
- Prepare for system tests/neutron-imaging experiments to test bubble chamber and readout techniques on OMEGA in FY05 and later.
 - The bubble chamber used will depend on the status of LLE and Russian research on bubble detector development for neutron imaging.

Dynamic X-Ray Diffraction of Shocked Single Crystals

Principal Investigator: M. Meyers (University of California, San Diego)

The NLUF x-ray-diffraction project focused on two separate goals: (1) to use the *in-situ* diffraction technique to study the response of a single-crystal lattice to shock loading, and (2) to characterize the deformation mechanisms in metals by shocked-sample recovery and electron microscopy. During FY03, two days of OMEGA shot time were allocated to this project, and 21 target shots were taken.

The *in-situ* diffraction technique provides a direct measurement of the lattice response under shock loading. It may be used to characterize a solid–solid phase transition such as the bcc–hcp transition in iron. The configuration for the diffraction

experiments was modified to use a different shock drive beam incident on the same side of the sample as the x-ray-diffraction probe in order to be able to hold the sample under compression for a longer time during the diffraction measurement. This modified geometry is shown in Fig. 96.59.

Recovery experiments provide a simple way to examine the deformation mechanisms governing high-strain-rate phenomena. By examining the residual microstructure and defect substructure with advanced analytical tools like transmission electron microscopy, the mechanisms in operation during shock loading can be inferred. The goal of these recent experiments is to probe the transition between the mechanisms of slip and twinning in single-crystal copper and copper-aluminum alloys in terms of composition, pressure, and orientation. Figure 96.60 shows micrographs of copper 2 wt% aluminum shot with laser energies of 200 J, which correlates to a peak

pressure of 40 GPa. In the first image [Fig. 96.60(a)], the orientation is [001] and four twinning variants are observed. The second image [Fig. 96.60(b)] is the orientation $[\bar{1}34]$ revealing two sets of microtwins.

Study of Driven Ion-Acoustic Waves Under Direct-Drive Conditions

Principal Investigator: H. Baldis (University of California, Davis)

The aim of this program is to study the physics of laser interactions with ion-acoustic waves (IAW's) in plasmas at conditions relevant to direct-drive inertial confinement fusion (ICF) targets on the National Ignition Facility (NIF). Though no OMEGA shots were scheduled for this program in FY03, good progress was made on the understanding of the seeding of stimulated Brillouin scattering (SBS) by a number of effects. In direct-drive ICF geometry, many laser beams overlap with different angles of incidence, at any point over the capsule. In the plasma corona surrounding the capsules, this leads to a number of wave-wave coupling configurations, which modify the initial growth of the SBS instability. Preliminary studies have been carried out, both theoretical and experimental, on the effect of reflection of laser light and forward-scattered light from the critical density, as well the effect of seeding by side-scattered SBS light from adjacent beams.

The shots allocated to this project on OMEGA in FY04 will be dedicated to experiments to characterize some of these seeding mechanisms. The recently incorporated Thomson-scattering diagnostic will be used, at 4ω , to study the amplitude and saturation of IAW's associated with SBS. An important component will be the identification of seeding of the instability, by either sidescattering from adjacent beams or reflection

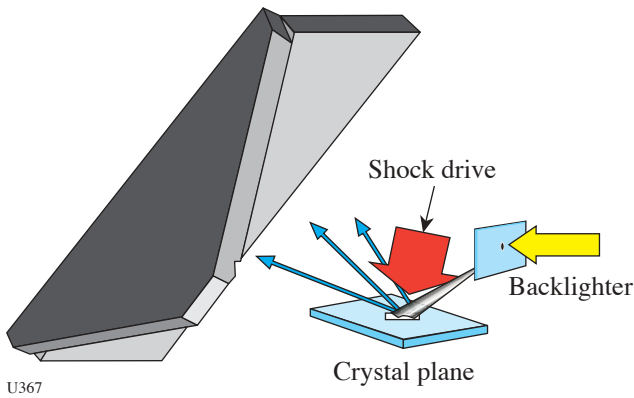


Figure 96.59 Schematic illustrating the geometry of the dynamic x-ray-diffraction experiment.

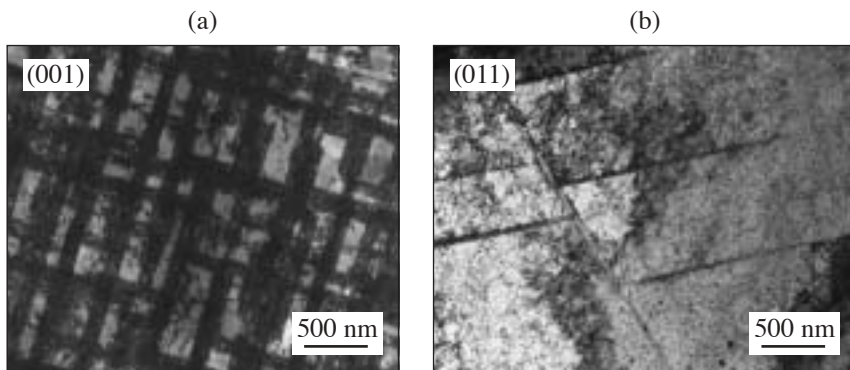


Figure 96.60 Transmission electron micrographs of a copper (2-wt%) aluminum sample irradiated with 200 J in a 2.5-ns pulse. The peak pressure in these samples was 40 GPa. (a) In copper (2-wt%) aluminum oriented to [001], four twin variants are observable at a high density; (b) in copper (2-wt%) aluminum oriented to $[\bar{1}34]$, two twinning variants are observable in considerably lower densities.

U368

of laser light from the critical density. In past experiments the nonlinear coupling from different beams has been observed using the backscattered light as a diagnostic.¹¹

Experimental and Modeling Studies of 2-D Core Gradients in OMEGA Implosions

Principal Investigator: R. C. Mancini (University of Nevada, Reno)

The objective of this program is to determine the spatially and temporally resolved two-dimensional (2-D) temperature and density core gradients of high-energy-density plasmas arising from OMEGA implosions. During the first year of the project substantial progress was made in the areas of instrument development, experiments, and data analysis.^{12,13} One full OMEGA shot day was allocated, and nine shots were taken for this program. Two multi-monochromatic-imager (MMI) instruments were built and successfully fielded in indirect-drive implosion experiments on OMEGA. The plastic shells used in the experiments were filled with deuterium and doped with a tracer amount of argon for diagnostic purposes. The first imager operates in time-integration mode, while the second one records time-resolved images. For this second instrument, new (more-efficient) multilayer mirrors were designed and fabricated as well. With the availability of these additional instruments, simultaneous (i.e., in the same shot) recording of two sets of narrowband x-ray images of the core along two quasi-orthogonal directions perpendicular to the hohlraum axis is possible. This capability is critical for extracting information about the 2-D/3-D space structure of the core. A third imager has been tested in an effort to record a third set of narrowband images along a direction parallel to the hohlraum axis. Two series of five shots each were performed during FY03. In the first series, three types of beam pointing were tested that led to the production of round, "mild-sausage," and "sausage" implosion cores with a major axis along the hohlraum axis. In this way, it has been shown that a sequence of implosion cores can be produced where 2-D spatial structure effects are gradually "turned on." Processing the image data recorded in these implosions allowed the construction of 2-D emissivity maps associated to the argon $\text{He}\beta$ and $\text{Ly}\beta$ lines. Since the $\text{Ly}\beta$ to $\text{He}\beta$ emissivity ratio is a strong function of the temperature and a weak function of the density, $\text{Ly}\beta/\text{He}\beta$ emissivity ratio maps were used to compute 2-D temperature maps of the core. Furthermore, 2-D scaled maps of the density were also obtained. Temperature and density maps show significant changes depending on the type of core, i.e., round, mild sausage, or sausage. In the second series of shots, time-resolved images were recorded.

The capsules used in both FY03 shot series were plastic shells filled with 50 atm of deuterium and doped with 0.1 atm of argon for spectroscopic diagnostic purposes. In addition to the x-ray imagers, time-resolved, space-integrated, argon K -shell x-ray line spectra were also recorded with the streaked SSCA or SSC1 crystal spectrometers in all shots. The line of sight (LOS) for these instruments was always through a laser entrance hole (LEH).

On the first series of shots, the focus was to record time-integrated images along two quasi-orthogonal directions close to the hohlraum midplane. In addition, a standard framing camera (XRFC2) was used to look at the implosion core down the hohlraum axis. A reference case of beam-pointing parameters was used to obtain round implosions (established in the team's previous NLUF project), and then the beams gradually moved (both cones, 2 and 3) in two steps of $30\ \mu\text{m}$ each with the goal of driving mild-sausage and sausage implosion cores, i.e., ovals of gradually increasing eccentricity, with the major axis along the hohlraum axis. The results of the analysis clearly show the changes in core symmetry and spatial structure of the temperature and density distribution.

In the second shot series, the goal was to record time-correlated images and spectra with time resolution. Beam pointing was set to the reference case of round cores. MMI-3a (from the team's earlier NLUF project) and MMI-3b were mounted in TIM-2 and TIM-3, respectively, and SXRFC was mounted in TIM-4 (an SSCA was mounted in TIM-6); therefore, TIM-2, TIM-3, and TIM-4 defined a system of quasi-orthogonal x - y - z axes for these shots. Time-resolved data were successfully recorded with MMI-3b.

Progress in data analysis in FY03 focused on improving the capability of performing 1-D core gradient determination in round cores, and, in the first step, on developing and testing methods for extracting 2-D temperature and density spatial gradients from image data.

Figure 96.61 shows the results of 1-D core gradient determination for a round core. The gradients were extracted using a gradient reconstruction method that searches the parameter space of gradient functions with the goals of simultaneously and self-consistently fitting the spatial emissivity profile of the argon $\text{He}\beta$ line emission (obtained from a narrowband x-ray image) and the space-integrated argon line spectra covering the spectral range of the $\text{He}\beta$, $\text{He}\gamma$, and $\text{Ly}\beta$ lines and their associated Li- and He-like satellite transitions (i.e., multi-objective data analysis). The search in parameter space is

driven by a novel application of a niched-Pareto genetic algorithm (NPGA) to plasma spectroscopy. This algorithm is actually general and can be applied to other problems of multi-objective data analysis. The error bars are determined by taking into account solutions found in the vicinity of the optimal one, and by repeating the analysis for the same case considering the angle dependence of emissivity profiles, i.e., accounting for deviations from perfect spherical symmetry. Gradient uncertainties due to these effects are then added in quadrature. The consistency of these gradients with the emissivity spatial profile extracted from the analysis of the $Ly\beta$ image was also checked. Thus, these gradients are effectively constrained by three criteria: $He\beta$ and $Ly\beta$ emissivity spatial distributions and space-integrated line spectrum. Testing this capability in 1-D cases is important before extending them for application in 2-D problems.

An alternative method for temperature determination is based on the fact that the $Ly\beta/He\beta$ emissivity ratio is a strong function of the temperature and a weak function of the density. Therefore, a space map of this emissivity ratio obtained by processing core image data can be directly transformed point by point into a space map of temperature. The temperature gradient determined by this method showed good consistency with the result obtained via the gradient reconstruction method.

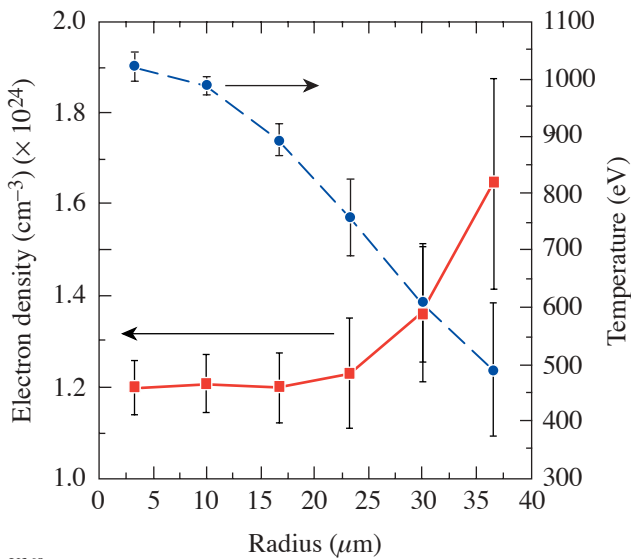


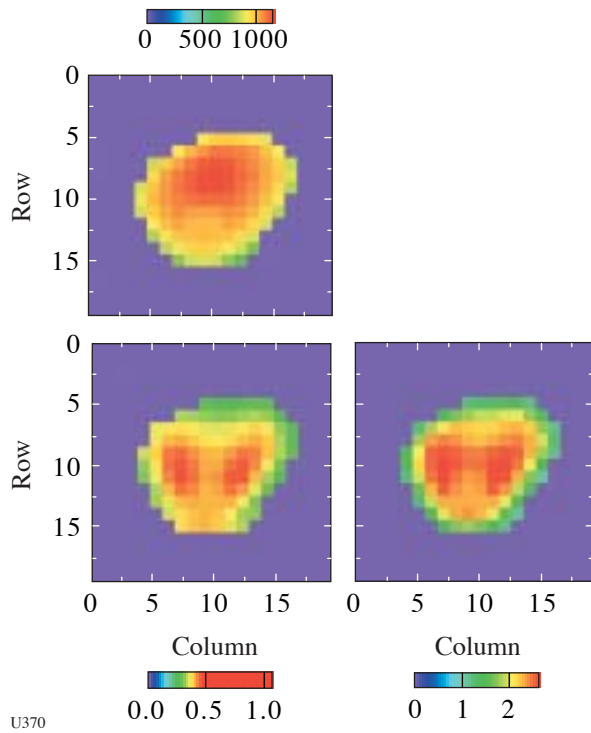
Figure 96.61
Results of 1-D core gradient reconstruction for OMEGA shot 26787.

In a first step toward determining the spatial distribution of temperature in the core beyond the 1-D approximation, the emissivity ratio method described in the previous paragraph was applied to the analysis of the image data recorded in the December 2002 shots. On shots 29885, 29889, and 29890, round, mild-sausage, and sausage cores were created intentionally (by adjusting the beam pointing) with the major axis along the hohlraum axis. Considering core slices cut perpendicular to the hohlraum axis and assuming axial symmetry (locally) in each slice, emissivity profiles in the core can be obtained from the $He\beta$ and $Ly\beta$ image data. This procedure can be interpreted as a generalized Abel inversion. Next, the $Ly\beta/He\beta$ emissivity ratio maps were interpreted and directly converted into 2-D (actually, quasi-3-D) spatial maps of core temperature. Results obtained for these three shots are displayed in Figs. 96.62–96.64. The hohlraum axis is along the vertical direction. The characteristic size of these implosion cores is 60 to 80 μm . Changes in core symmetry and temperature spatial distribution are apparent from the maps.

After the temperature map has been determined, scaled density maps can be obtained by working separately with each line emissivity map ($He\beta$ or $Ly\beta$) and solving point by point for the density given the local values of emissivity and temperature. These results are also shown in Figs. 96.62–96.64. Note that the density maps extracted from the $He\beta$ emissivity are not identical to those extracted using the $Ly\beta$ emissivity; however, they are very similar, suggesting that the process is sound. Again, changes are observed from round to sausage cores. In particular, a two-peak density (and temperature) spatial structure develops for the mild-sausage and sausage implosion cores along the major axis.

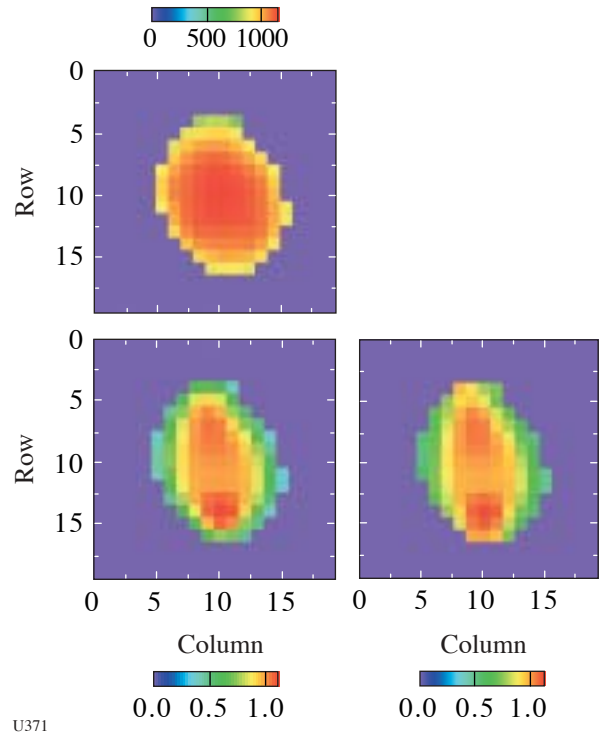
Finally, Fig. 96.65 shows the time-resolved data obtained in OMEGA shot 31594 (May 2003) with MMI-3b. Round-core beam pointing was used in this shot. Each frame is characteristic of a 50-ps time interval and displays simultaneous core images and a slit spectrum. Both images and spectra data show significant changes as a function of time that are being used to study the time evolution of the core's spatial structure. Work is in progress in the analysis of these data.

FY04 will focus on (1) obtaining time-resolved data for studying the 2-D spatial structure of round, mild-sausage, and sausage implosion cores, (2) continuing work on alternative generalized Abel-inversion procedures, (3) applying 2-D gradient reconstruction methods to determine the spatial structure of implosion cores, and (4) performing detailed comparisons between data analysis and hydrodynamic simulation results.



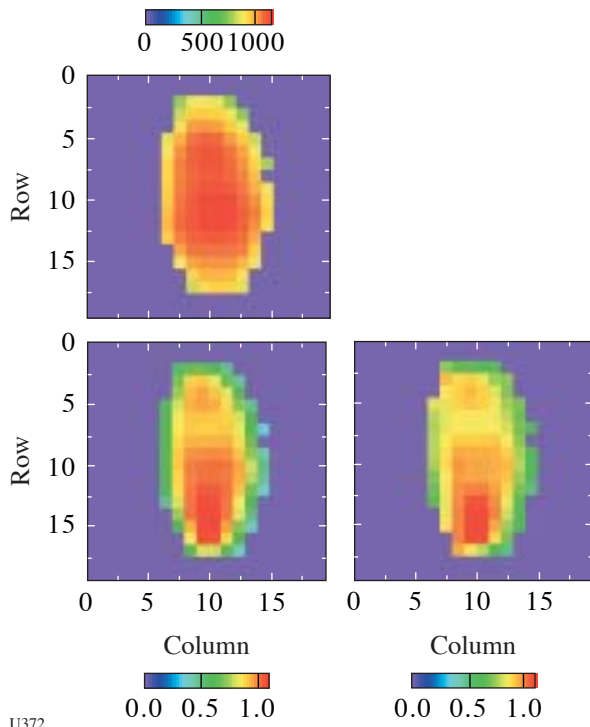
U370

Figure 96.62
Time-integrated 2-D electron temperature (top, in eV) and scaled electron-density maps (bottom, in units of $1 \times 10^{24} \text{ cm}^{-3}$) for OMEGA shot 29885, round implosion core case. Electron-density maps (left) based on $\text{He}\beta$ emissivity and (right) based on $\text{Ly}\beta$ emissivity.



U371

Figure 96.63
Time-integrated 2-D electron temperature (top, in eV) and scaled electron-density maps (bottom, in units of $1 \times 10^{24} \text{ cm}^{-3}$) for OMEGA shot 29889, mild-sausage implosion core case. Electron-density maps (left) based on $\text{He}\beta$ emissivity and (right) based on $\text{Ly}\beta$ emissivity.



U372

Figure 96.64
Time-integrated 2-D electron temperature (top, in eV) and scaled electron-density maps (bottom, in units of $1 \times 10^{24} \text{ cm}^{-3}$) for OMEGA shot 29890, sausage implosion core case. Electron-density map (left) based on $\text{He}\beta$ emissivity and (right) based on $\text{Ly}\beta$ emissivity.

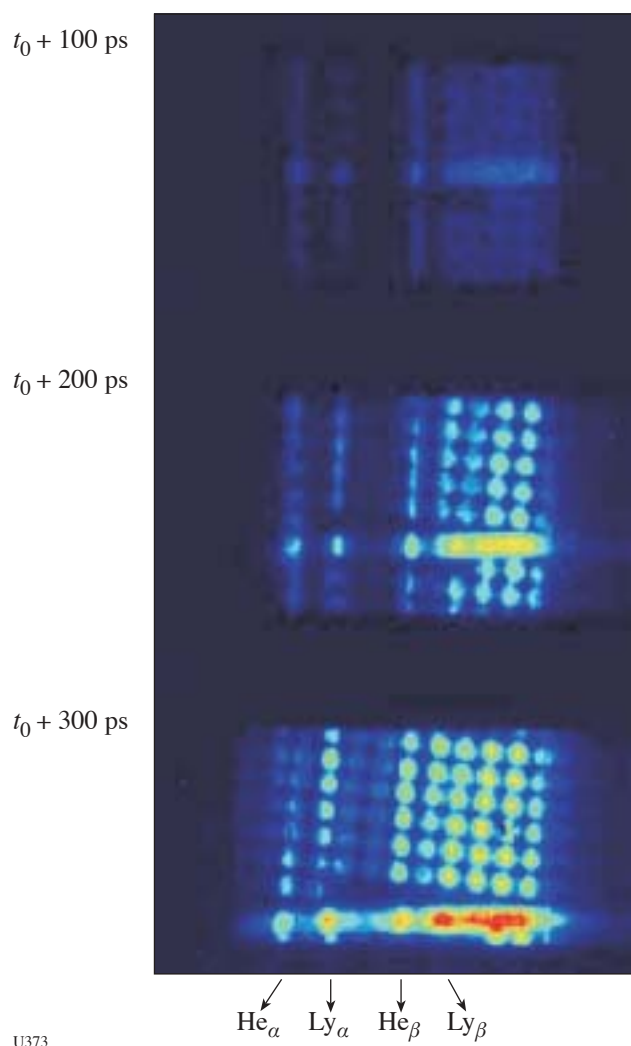


Figure 96.65
Time-resolved core images and slit spectrum recorded in OMEGA shot 31594 with MMI-3b.

Recreating Planetary Core Conditions on OMEGA: Techniques to Produce Dense States of Matter

Principal Investigator: R. Jeanloz (University of California, Berkeley)

The objective of this program is to use OMEGA to determine the nature of planetary fluids at the extreme conditions representative of the cores of the giant planets. To achieve the required conditions, this team has developed diamond anvil cell (DAC) targets for laser shock-compression experiments. With this technique the initial sample pressure is much higher than ambient (3 to 20 kbar), and the initial density may be from 1.5 to 5 times higher than ambient (depending on the sample)

compared to nonpressurized preparation methods. The higher initial density results in a significantly larger final density and lower temperature in the shock-compressed state. Single- and multiple-shock Hugoniot techniques of precompressed targets can re-create deep interior states of giant solar planets, extra-solar planets, and low-mass stars.

In FY03, 1.5 shot days were allotted to this program, and 15 target shots were performed on precompressed samples (hydrogen, helium, and nitrogen) on the OMEGA laser. As shown in Fig. 96.66, a thin ($\leq 200\text{-}\mu\text{m}$) drive diamond was laser-ablated to send a shock through the sample ($\sim 100\text{ }\mu\text{m}$ thick) loaded in a DAC. The primary diagnostic was the velocity interferometer system for any reflector (VISAR). Table 96.VII lists the first ten target shots of FY03.

Highlights of the experiments are shown in Fig. 96.67, which shows the results of shot #31455: helium precompressed to 5.5 kbar. The sample remained transparent with a particle velocity of approximately $2\text{ }\mu\text{m/ns}$. (It is likely that the laser was misaligned and the observed pressure was much lower than expected based on the incident energy.) Figure 96.68 shows the results for shot #30758: helium precompressed to 2.7 kbar. As in three other shots, one can see the shock breakout into the helium sample but the helium was nontransparent. Figure 96.69 shows the results for shot #30759: hydrogen precompressed to 3.6 kbar. The sample was nontransparent (transparent at the edges, where edge rarefaction has sufficiently lowered the pressure). At times after breakout of about 8 and 12 ns, re-shock and rattling of the shock into a more-reflective state were observed. The pressure of this shock is estimated to have been about 420 kbar with a re-shock pressure

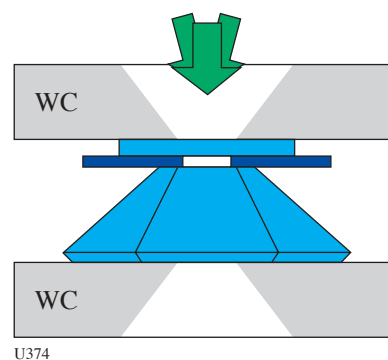


Figure 96.66
Illustration of diamond anvil cell (DAC) geometry. Tungsten carbide (WC) is used as a support for the DAC.

of about 1.1 Mbar. Figure 96.70 shows the results of shot #31457: nitrogen precompressed to 5.2 kbar. In this shot the nitrogen shock was reflecting, showing a strong decay in shock velocity from about 24 to 19 $\mu\text{m}/\text{ns}$. When the shock hit the back diamond, the VISAR fringes suddenly disappeared due to

the diamond window going opaque (consistent with a diamond shock pressure above about 1.5 Mbar). The spatial extent of the shock reflectivity implied that the radius of curvature in this shot was 300 to 400 μm , consistent with the use of 300- μm phase plates.

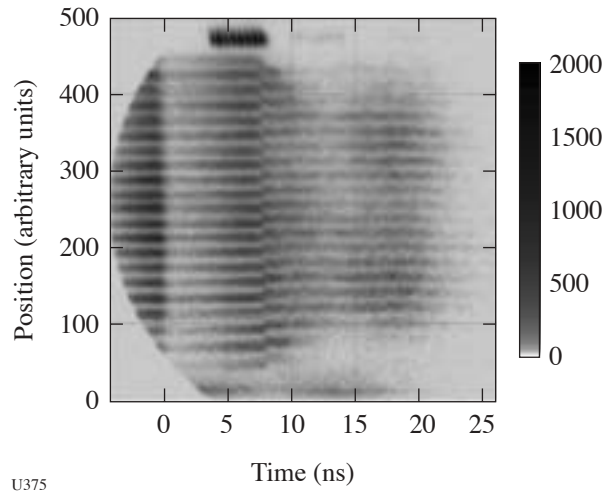


Figure 96.67
VISAR data from shot #31455: He precompressed to 5.5 kbar.

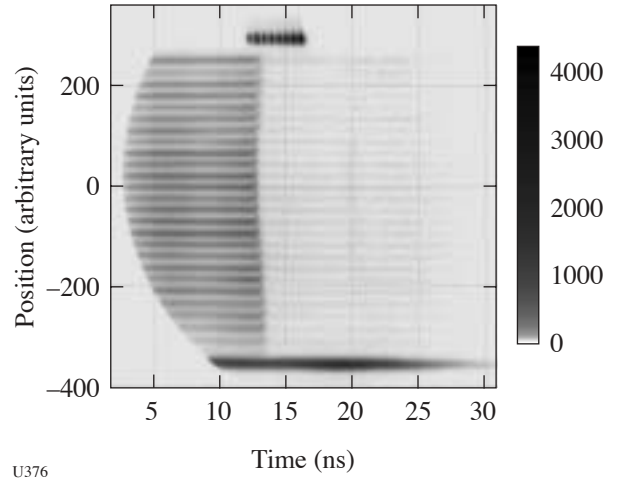
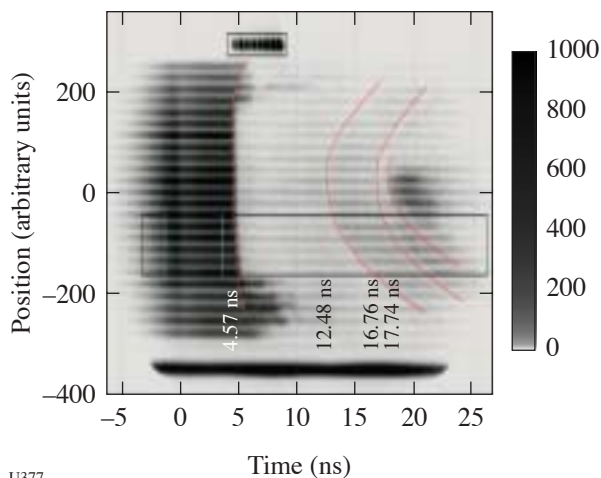


Figure 96.68
VISAR results from shot #30758: He precompressed to 2.7 kbar.

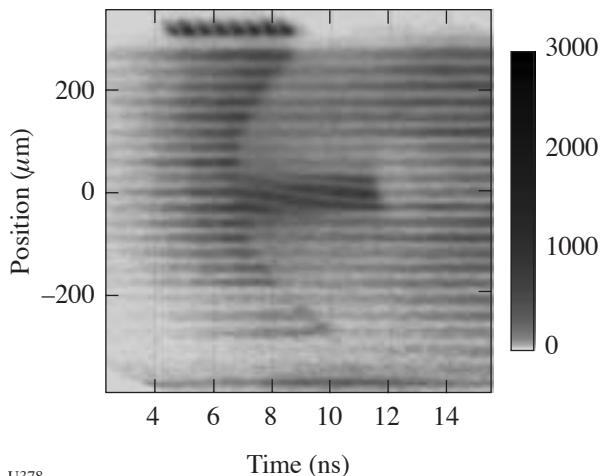
Table 96.VII: Target shots to explore planetary core conditions on OMEGA—the first ten shots of FY03.

| LLE Shot # | Sample | Initial Pressure (kbar) | Initial Density (g/cc) | Laser Intensity (W/cm^2) | Results |
|------------|--------------|-------------------------|------------------------|--|----------------|
| 30755 | He | 5.4 | 0.301 | 6.5×10^{14} | Opaque diamond |
| 30756 | He | 5.4 | 0.301 | 5.2×10^{14} | Opaque diamond |
| 30757 | Surrogate | — | — | 5.2×10^{14} | — |
| 30758 | He | 2.7 | 0.211 | 5.1×10^{13} | Nontransparent |
| 30759 | H_2 | 3.6 | 0.127 | 4.5×10^{13} | Nontransparent |
| 31454 | He | 1.6 | 0.154 | 5.3×10^{14} | Nontransparent |
| 31455 | He | 5.5 | 0.304 | 2.7×10^{14} | Transparent |
| 31456 | H_2 | 6.2 | 0.142 | 2.7×10^{14} | Nontransparent |
| 31457 | N_2 | 5.2 | 0.935 | 4.1×10^{14} | Reflecting |
| 31459 | He | 5.9 | 0.314 | 2.6×10^{14} | Nontransparent |



U377

Figure 96.69
VISAR results of shot #30759: H₂ precompressed to 3.6 kbar.

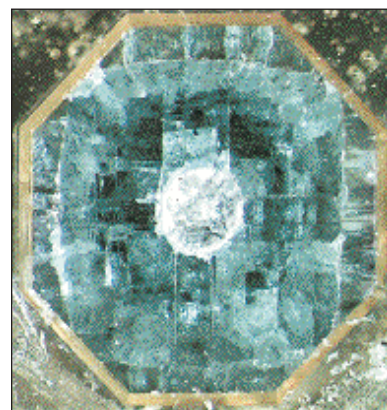


U378

Figure 96.70
VISAR results from shot #31457: N₂ precompressed to 5.2 kbar.

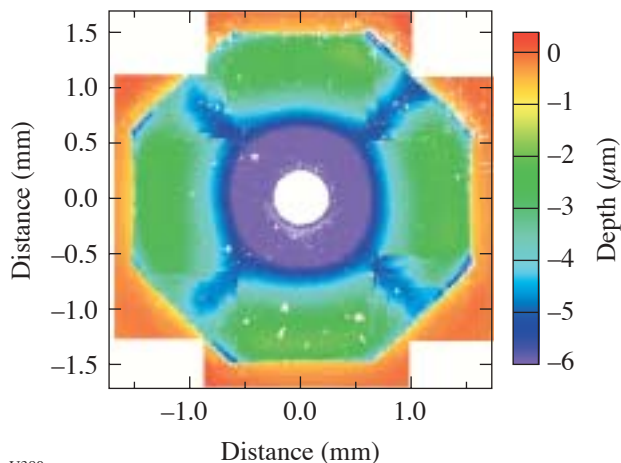
After the shock leaves the sample, it travels through a 1.2-mm-thick single-crystal diamond cut in the (100) direction. Under weak shock loading, it is found that the diamond shears along four equivalent (111) planes, leaving a distinct fourfold symmetric fracture on the diamond table (Fig. 96.71). Considering the diamond's thickness, the shock assumes a somewhat spherical front so that the shock travels in different crystallographic directions within the diamond. It is reasonable to expect that the shock velocity, and hence the shock intensity, will reflect the symmetry of the diamond lattice. In fact, evidence of this symmetry breaking was observed by

examining the recovered and deformed tungsten carbide support. When the tungsten carbide remained intact under strong shock loading, the deformation was not uniform, adopting a fourfold symmetry often characterized by a series of steps or "terraces" (Fig. 96.72). These terraced indentations occur where shear fractures along different (111) planes intersect, suggesting regions of greater stress in the diamond crystal (Fig. 96.73). It is noted that the fourfold symmetric strain cannot be caused by the tungsten carbide itself since it is amorphous and has no intrinsic fourfold symmetry.



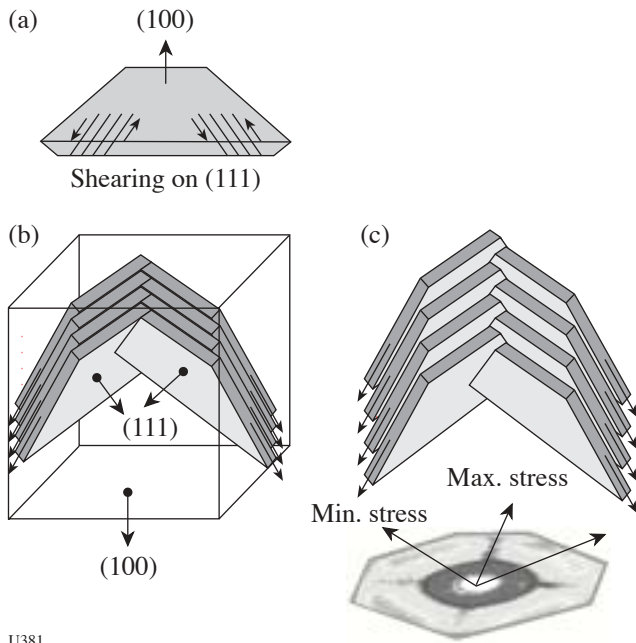
U379

Figure 96.71
Photograph of diamond table showing central spall and four-fold shearing along (111) planes.



U380

Figure 96.72
Depth profile of tungsten carbide support.



U381

Figure 96.73
Illustration of shearing mechanism and relation to the plastic deformation in the tungsten-carbide backing plate.

During the second year of this study, the experiments will focus on determining the reflectivity transition and pressure-density equation-of-state measurements in hydrogen, helium, and nitrogen at several precompression pressures. New experimental approaches will also be developed to employ higher precompression pressures above 100 kbar so that regions of phase space can be accessed where exciting new predictions for the hydrogen phase diagram have been made, including a first-order dissociation in the liquid and a negative Clapeyron slope for the melt line at high pressures. Studies of the recovered material from the samples, to investigate expected phase changes such as the formation of graphite, amorphous carbon, and crystalline tungsten carbide, as well as searches for any new unpredicted phases, will continue.

FY03 LLNL OMEGA EXPERIMENTAL PROGRAM*

In FY03 Lawrence Livermore National Laboratory (LLNL) continued to be a major user of OMEGA. LLNL's 390 experimental shots can be divided into two groups: those in support of the inertial confinement fusion (ICF) program and those in

*Acknowledgment: This work was performed under the auspices of the U.S. Department of Energy by University of California Lawrence Livermore National Laboratory under contract No. W-7405-Eng-48.

support of high-energy-density sciences (HEDS), which include materials, equation-of-state, and physics experiments.

ICF Experiments

The ICF program on OMEGA in FY03 totaled 152 shots. Highlights of these experiments include the following:

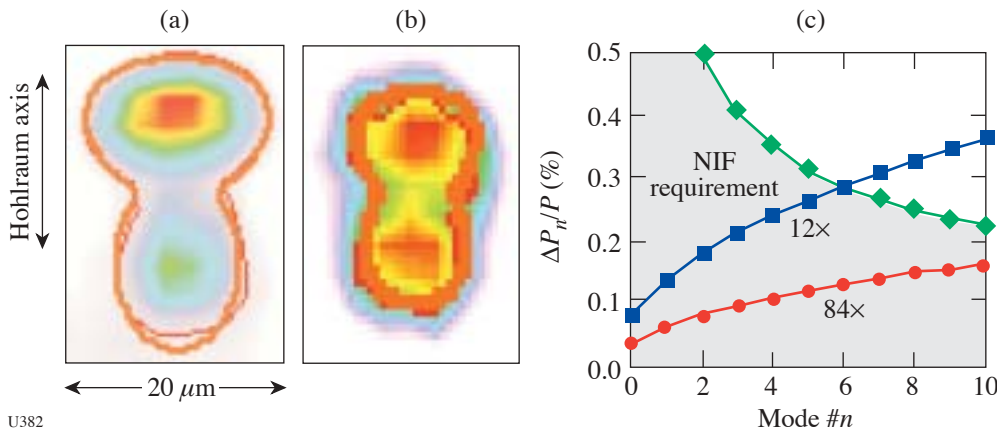
Charged-Particle Spectroscopy (CPS): These implosions, done in collaboration with MIT, measured the charged fusion reactions produced from indirectly driven ICF implosions. Initial experiments ascertained the feasibility of using multiple CPS diagnostics as a measure of implosion asymmetry.

X-Ray Thomson Scattering: These shots showed that He- and H-like Ti x rays can be spectrally measured after scattering off near-solid-density plasmas. Theoretical fits to the data are in good agreement, opening the way for using this as a diagnostic for pusher ρR on National Ignition Facility (NIF) implosions.

Cocktail (Mixtures of Materials) Hohlräume: These experiments were performed to attempt to measure a predicted improvement in x-ray conversion efficiency and soft-x-ray albedo. Preliminary results seem to verify the latter, but not the former.

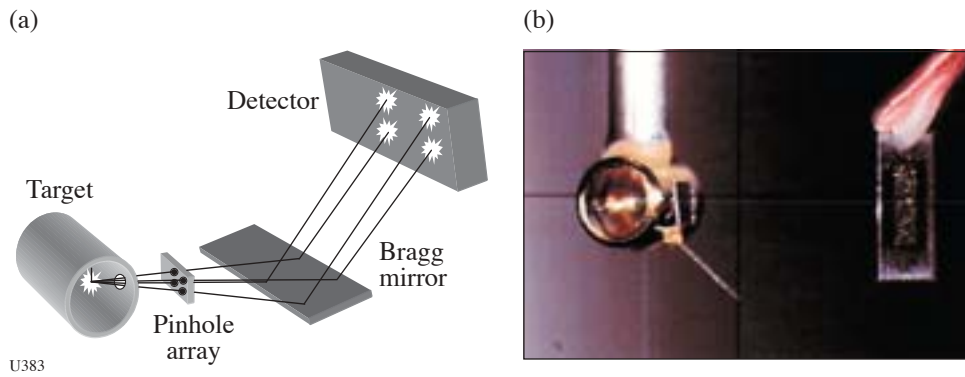
Planar Rayleigh-Taylor: A series of experiments were performed on polyimide targets to assess its usefulness as an ablator for ICF capsules. The data to date indicate a higher RT growth rate than calculated, even though acceleration measurements seem to match predictions.

Technique Development: A number of experimental techniques expected to be used on the NIF were tested with OMEGA shots. These included high-magnification x-ray imaging of imploded capsules, using target-mounted pinholes (Fig. 96.74), and development of a Kirkpatrick-Baez (KB) x-ray microscope with a spectrally narrow bandpass to look at x-ray line emission from a backlighter through a capsule. Additional experiments, done in collaboration with the University of Nevada-Reno, investigated spatially resolved spectroscopic measurements of pusher density using a Ti dopant within the inner layer of the capsule, while using Ar x-ray emission from the fuel region to deduce temperatures and densities in that region (Figs. 96.75 and 96.76).



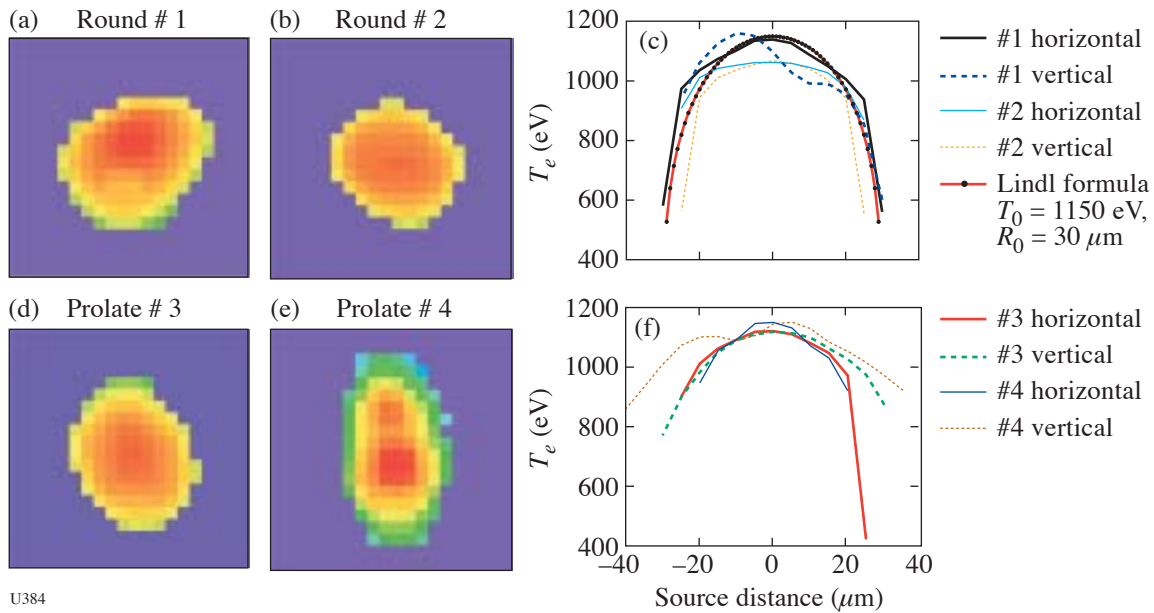
U382

Figure 96.74 Examples of x-ray images taken with target-mounted pinholes of 5- μm aperture at a magnification of (a) 87 \times and (b) 12 \times . The resolution requirements of NIF targets are shown in (c) and compared to the achievable resolution of a 12 \times and 84 \times imaging system on the NIF.



U383

Figure 96.75 Illustration of a multi-monochromatic imaging (MMI) system based on an LLE-developed technique. Several MMI systems have been fielded for both LLNL and NLUF experiments on OMEGA: (a) schematic of MMI diagnostic illustrating the concept; (b) photograph of typical configuration used on hohlraum-driven experiments on OMEGA. Each device produces hundreds of 11- μm -resolution images. Spectral dispersion is achieved by a depth-graded WB_4C multiplayer mirror with an energy resolution of ~ 75 . The devices typically cover the energy range of 3 to 5 keV.



U384

Figure 96.76 Inferred temperature maps taken on hohlraum-driven implosions of D_2 -filled, Ar-doped capsules: (a), (b) 2-D temperature profiles, and (c) radial lineout of relatively round implosions; (d), (e) 2-D temperature profiles, and (f) radial lineout of prolate implosions.

Laser-Plasma Interaction: Laser-plasma interaction (LPI) experiments were carried out to explore the interaction of the laser with the large plasmas created when gas-filled hohlraums are used. Most of these experiments used gas bags as the initial target to provide a long-scalelength plasma with good diagnostic accessibility. Experiments measured Raman (SRS) and Brillouin (SBS) scattering levels, the effect of Langmuir damping, and energy exchange through SBS in crossed-beam experiments. The 4ω probe beam was successfully used for Thomson-scattering measurements, as shown in Fig. 96.77. Additional experiments in gas-filled hohlraums investigated the effect of gas pressure on capsule hydrodynamics and possible enhanced gold-gas mixing due to preroughened

hohlraum walls. Still another experiment searched for evidence of early-time laser light directly striking the capsule in indirect-drive experiments. These results are compared to calculations in Fig. 96.78.

Several high-yield, direct-drive DT implosions were carried out in collaboration with LANL to provide high fluxes of 14-MeV neutrons for diagnostic development. The characteristics of a photoconductive diamond (PCD) device in measuring neutrons is shown in Fig. 96.79. At high neutron flux, the impedance of the transmission line (Z) causes saturation at $I_{\max} = V/Z$.

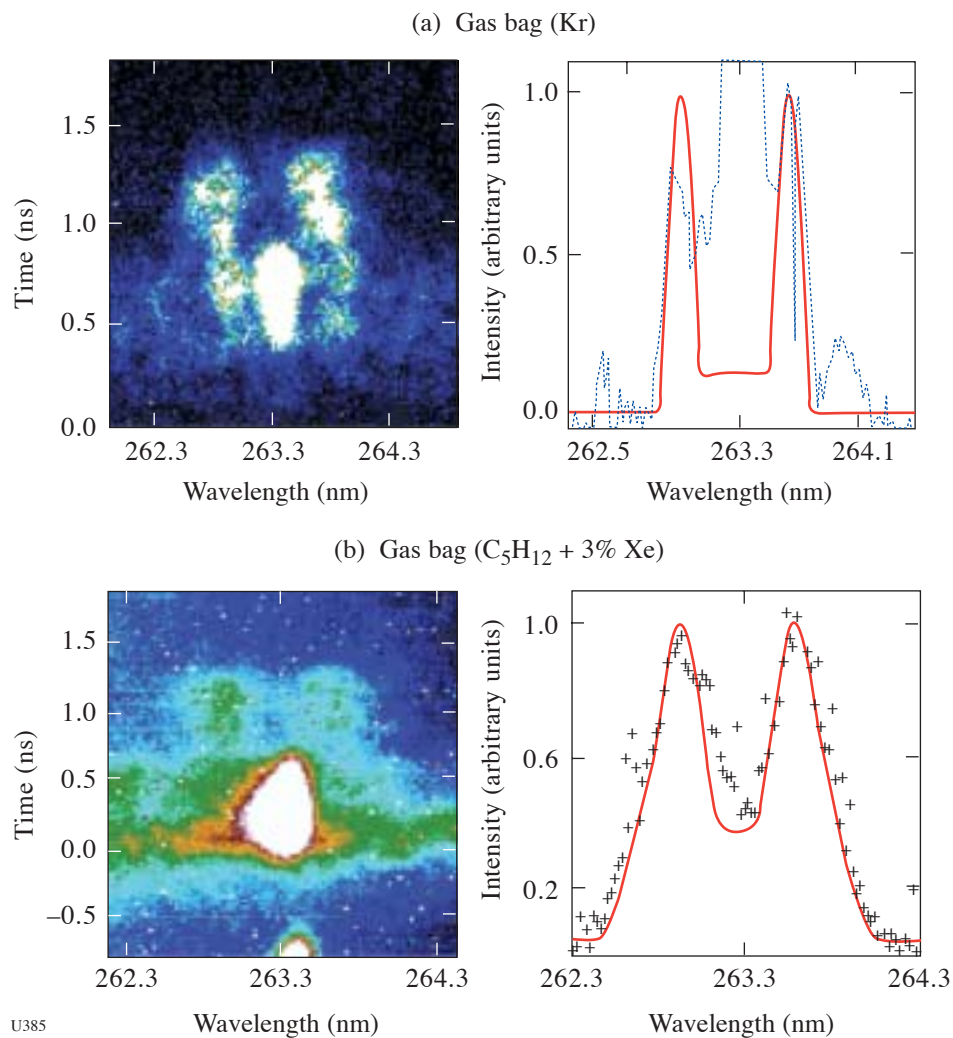


Figure 96.77

Illustrations of 4ω Thomson-scattering measurements on laser-plasma interaction experiments: (a) streaked record of Thomson-scattering signal from a Kr-filled gas-bag target; (b) streaked record of Thomson-scattering signal from C_5H_{12} -3%Xe-filled gas bag. While the heater beams are on, these measurements show an electron temperature of ~ 3.2 keV for the Kr-filled gas bag. The C_5H_{12} -3%Xe-filled gas shows an electron temperature of 1.5 keV late in time.

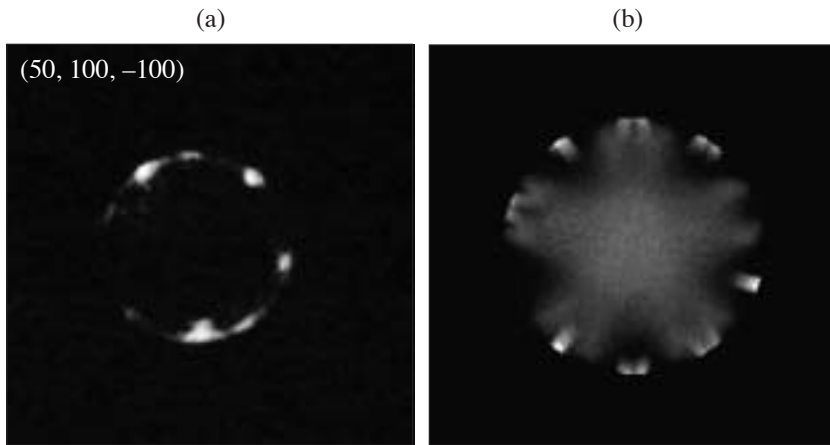
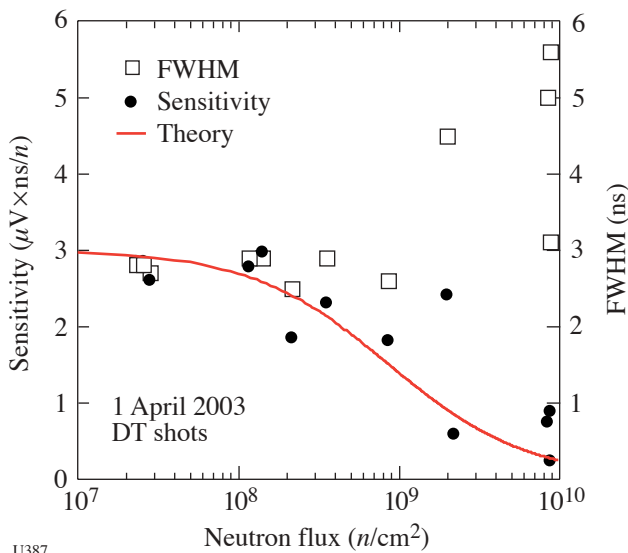


Figure 96.78
X-ray re-emission images are used to search for evidence of early-time laser light directly striking the capsules: (a) actual image; (b) experimental simulated image.

U386



U387

Figure 96.79
Experimental measurements of the sensitivity and full width at half maximum of the signal generated by a diamond detector in response to increasing neutron flux obtained from OMEGA experiments. The theoretical curve is from the x-ray work of Kania *et al.*¹⁴

HEDS/NWET Experiments

The High-Energy-Density-Science and Nuclear Weapons Effects Testing (NWET) Programs used 238 laser shots on OMEGA during FY03. Some of the experiments included the following:

IDrive: A substantial number of shots (“IDrive”) were devoted to developing techniques for measuring material properties when subjected to substantial pressures, but still in

the solid state. Low-temperature Rayleigh–Taylor experiments were performed with this experimental arrangement (Fig. 96.80).

NEL Preparation: Another large group of shots were devoted to using OMEGA to prepare for NIF early-light (NEL) experiments. These included testing concepts for point-projection backlighting using backlit pinholes as an x-ray source. An example of this work in Fig. 96.81 shows an excellent radiographic image of a propagating shock.

EOS Experiments: Equation-of-state (EOS) experiments were performed in a variety of materials by measuring the velocity of ablatively driven shocks within the material. LLNL is a major participant in an NLUF experiment that measured shock velocities through precompressed gases within diamond anvil pressure cells, as shown in Fig. 96.82. Shock experiments were also used to measure opacities at elevated pressures and temperatures.

Hot Hohlräume: Experiments were conducted with small hohlraums to develop sources at elevated radiation temperatures.

Convergent Rayleigh–Taylor: Rayleigh–Taylor instabilities were studied in a spherically convergent geometry, using pre-imposed perturbations on spherical capsules.

Double-Shell Capsules: Double-shell (one shell containing DD fuel within another, concentric, indirectly driven shell) targets were explored for a number of properties, including their sensitivity to high-energy photon preheat, and the timing of the fuel shock heating compared to the timing of the fuel compression.

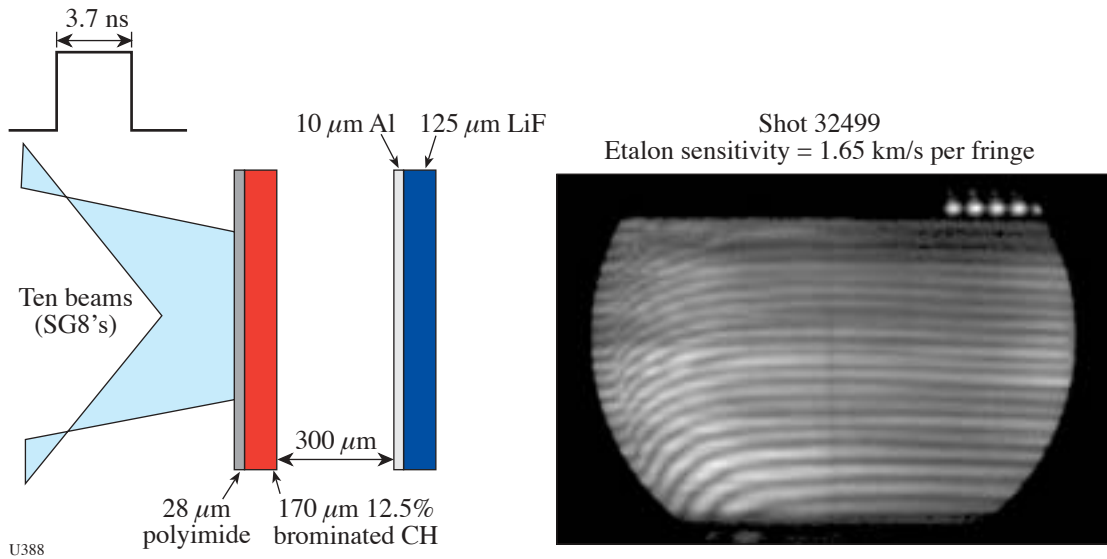


Figure 96.80
VISAR record on IDrive shot #32499 showing that smooth loading was achieved with no instabilities.

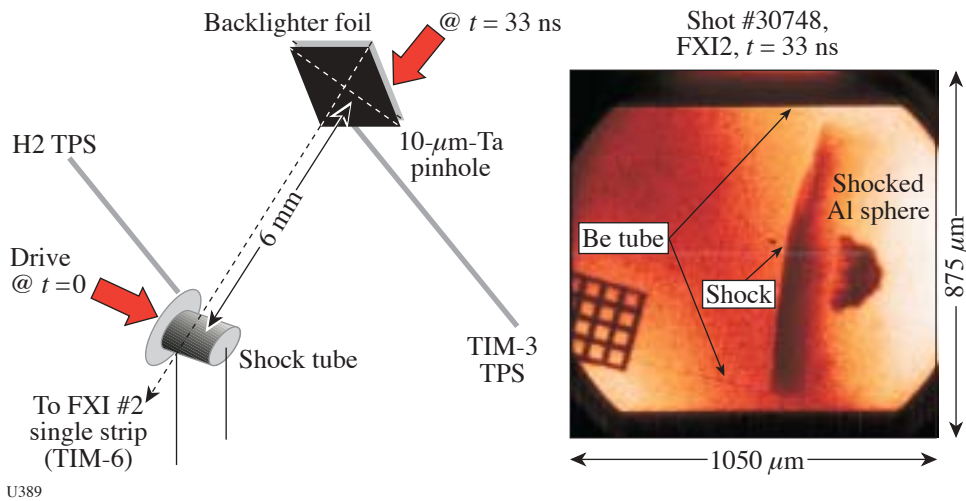


Figure 96.81
Illustration of the application of point backlighting to characterize the interaction of a shock with a spherical object.

Radiation Propagation: A number of experiments looked at the propagation of radiation in low-density materials.

Dynamic Hohraum: Another experiment looked at the possibility of using a direct-drive configuration to create a dynamic hohlraum for driving implosions.

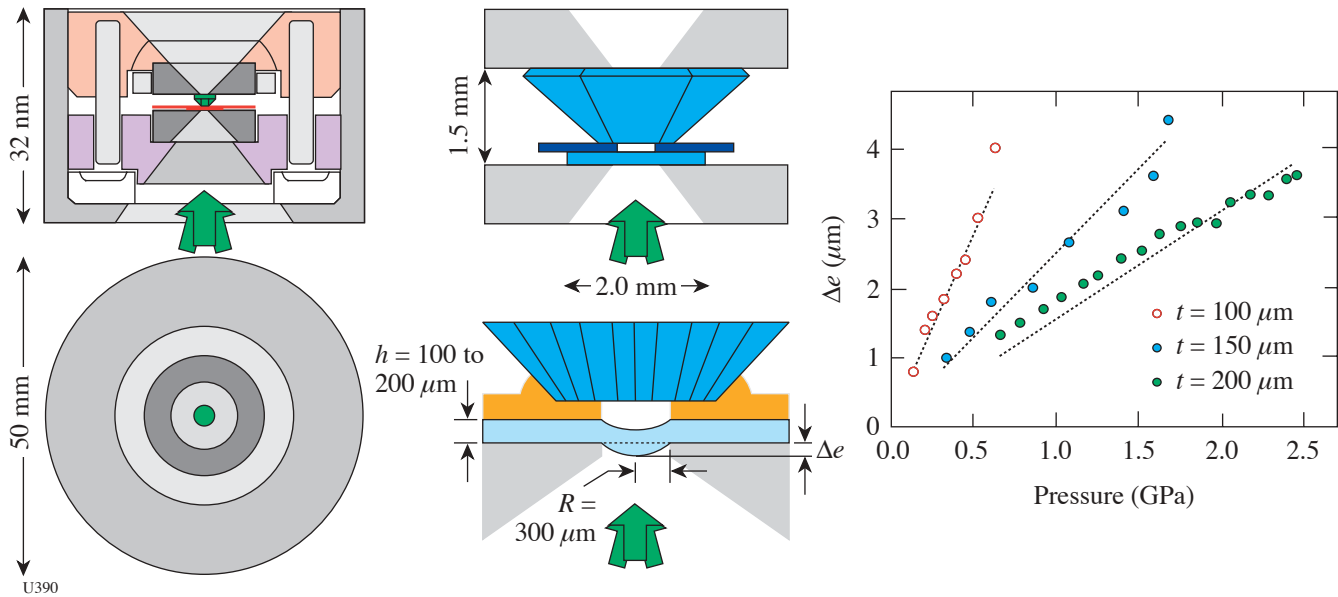


Figure 96.82
Experimental setup for an OMEGA equation-of-state experiment using a diamond anvil cell filled with a precompressed gas (such as hydrogen).

FY03 LANL OMEGA EXPERIMENTAL PROGRAMS

The Los Alamos National Laboratory (LANL) series of experiments on OMEGA in FY03 emphasized research into hydrodynamic instabilities, mix, material properties, neutron diagnostic development, and radiographic technique development for the Nation’s inertial confinement fusion and stockpile stewardship missions.

Cylinder Implosions: One phase of the hydrodynamic instability experiments investigates the Richtmyer–Meshkov instability (RMI) in a convergent, compressible, miscible plasma system in the presence of strong shocks.¹⁵ Fifty of the 60 OMEGA lasers illuminate small, hollow, epoxy cylinders with 18 kJ of energy. The center cylinder is filled with low-density foam. A very thin aluminum marker layer is placed between the foam and the epoxy. The laser energy heats the epoxy cylinder to extreme temperatures, causing approximately one-half of it to vaporize and expand outward (away from the axis), while the other half is pushed inward (implodes) by a strong shock wave. The passage of the shock wave through the target assembly heats the target materials and causes them to become plasmas. As a result, the interfaces along both sides of the marker band are accelerated, and the materials mix over time. The danger of RMI is that in an ignition capsule, if the mixing becomes severe enough, fusion reactions end and thermonuclear ignition—the ultimate goal of all ICF experiments—fails. To measure the amount of mixing, five additional OMEGA laser beams strike an iron foil at one end of the

cylinder after a small time delay. X rays are emitted, travel lengthwise through the cylinder, are imaged by a pinhole, and are recorded by a framing camera.

In a basic experiment conducted this year, a simple sinusoidal perturbation was machined into the outside of the aluminum marker layer, creating a corrugated surface with the corrugations running the length of the cylinder.¹⁶ It was hypothesized that these perturbations would grow due to the convergence of the system and the shock-driven RMI. Furthermore, it was expected that the growth rate of the perturbations would change for different numbers of perturbations. Measurements were made with targets that had 8, 16, or 28 perturbations machined into them (Fig. 96.83). As can be seen in the

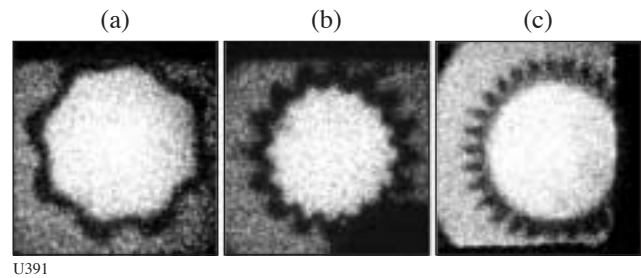
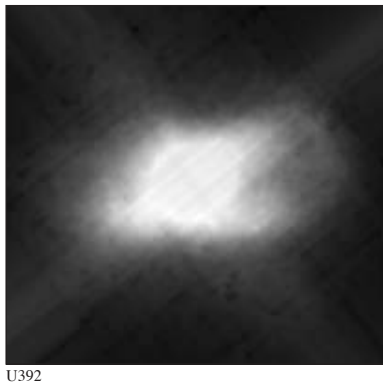


Figure 96.83
Axial radiographs of single-mode sinusoidally perturbed targets with mode numbers of (a) 8, (b) 16, and (c) 28. The dark band is the radiographically opaque aluminum marker layer.

figure, the amplitude of the corrugations at the outside of the marker layer is approximately the same in each case.

Asymmetric Direct-Drive Spheres: The asymmetric direct-drive spheres (ADDS) experiment tests the hypothesis that asymmetric implosions create more mixing of the shell material into the fusion fuel than do symmetric implosions. These directly driven 1100- μm -diam capsules were made of Si-GDP glass and filled with various pressures of DT. The convergence ratio was adjusted by varying the gas-fill pressure. The degree of asymmetry was varied from oblate to symmetric to prolate by adjusting the energy in each individual laser beam to make the correct overall pattern on the capsule.

This year, higher convergence implosions were conducted by reducing the fill pressure to 2.5 atm. These experiments had more mix than previously observed with 10 or 15 atm of gas fill. Figure 96.84 shows an x-ray image of a prolate implosion taken by the GMXI. Shell material can be seen all the way to the center. The yield was less affected by asymmetry in this experiment than it was with the 5 or 10 atm of gas fill.



U392

Figure 96.84

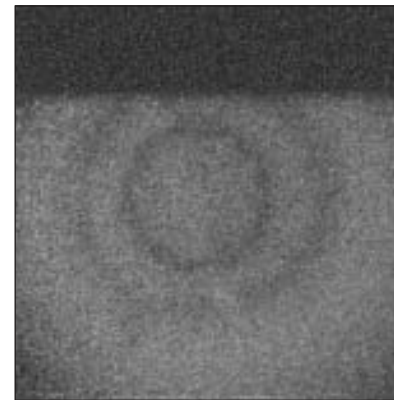
A GMXI x-ray image of a prolate implosion showing that shell material has reached the core of the imploding capsule.

Neutron Diagnostics Development: In collaboration with Lawrence Livermore National Laboratory, symmetric implosions of DT-filled capsules aided the development of the carbon-vapor-deposited (CVD) diamond detector and the palm-top LANSAs. These experiments also supported further development of the pinhole-based neutron imaging technique.

Double-Shell Targets: Direct-drive double-shell targets may provide an alternative, noncryogenic path to ignition on the National Ignition Facility (NIF).¹⁷ Experiments are being pursued on OMEGA to understand the hydrodynamics of these

implosions and the possibility of scaling them to NIF designs. The double-shell campaign examines the effect of drive, externally applied radiative preheat and foam composition on the implosion hydrodynamics, and the growth of mix due to hydrodynamic instabilities in a spherical geometry. Marker layers are implanted strategically in the capsule, and low-resolution radiography has been used to measure the zero-order hydrodynamic evolution of the capsule.

Twenty of the OMEGA laser beams were needed for backlighting, leaving only 40 beams to drive a symmetric implosion. The pointing of the remaining beams was offset from the center of the capsule to achieve a symmetric implosion. Radiographs were obtained from two different directions at multiple times with uniform area backlighting. A typical radiograph of a symmetric implosion is shown in Fig. 96.85. Neutron implosion data was also obtained simultaneously.



U393

Figure 96.85

A radiograph of a double-shell implosion target 1.7 ns after the beginning of the laser beams. The inner and outer shells and the intershell foam are clearly evident.

Supersonic Jet: In recent years we have fielded numerous supersonic-jet experiments¹⁸ on OMEGA in a collaboration between Los Alamos National Laboratory, the Atomic Weapons Establishment, Lawrence Livermore National Laboratory, the University of Michigan, and the Laboratory for Laser Energetics. These experiments help validate our next-generation radiation-hydrodynamic codes. One of the outstanding questions is whether these types of jets should become turbulent, given their high Reynolds number. We have recently modified our experiments to have more Kelvin-Helmholtz shear, to run much later in time, and to increase the chance of going turbulent. To diagnose these large (several-millimeter) jets at very late times (100 to 1000 ns), we are developing

pinhole-apertured point-projection x-ray imaging (PAPBL) using an x-ray energy of about 5 keV.

This year's experiments have concentrated on validating a new target design and overcoming technical problems arising from the PAPBL imaging technique. High spatial resolution over a large field of view was demonstrated, and recent work has given unequivocal evidence of a jet in late-time radiographs. The experiment consists of a directly driven titanium "slug" that impacts a low-density foam. The jet of titanium formed in the carbonized-resorcinal-formaldehyde (CRF) foam is diagnosed by point-projection radiography.

Significant progress was made this year in utilizing pinhole-apertured x-ray point backlighting. Adequate backlighter intensity was obtained by using two laser beams (400 J per beam, 1-ns pulse length). Figure 96.86 shows a pinhole-

aperture point-projection radiograph from the region of the resolution grid from a static-target experiment. Best fit to the experimental data is obtained by convolving a 15- μm FWHM Gaussian point-spread function with the ideal, theoretical grid transmission. This spatial resolution is comparable to that obtained in our previous pinhole-imaging experiments. The field of view of the earlier experiments was limited, however, to approximately 500 μm by the area-backlighting source, whereas that of the present point-backlit experiment covers approximately a 4-mm field of view. This represents a very significant potential increase of "information content" in comparison with the earlier work.

The new target design with PAPBL imaging successfully recorded clear evidence of the jet and the surrounding bow shock in the CRF foam (Fig. 96.87). Extensive design calculations for these experiments have been carried out at LANL

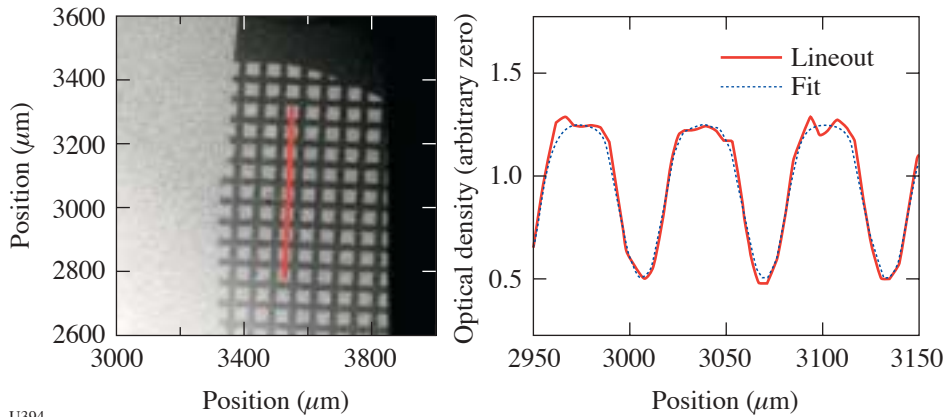


Figure 96.86
Pinhole-aperture point-backlighter image of a static (not-driven) target. Best fit to the transmission of the image of the resolution grid is obtained when the ideal grid transmission is convolved with a 15- μm FWHM Gaussian spatial-resolution function.

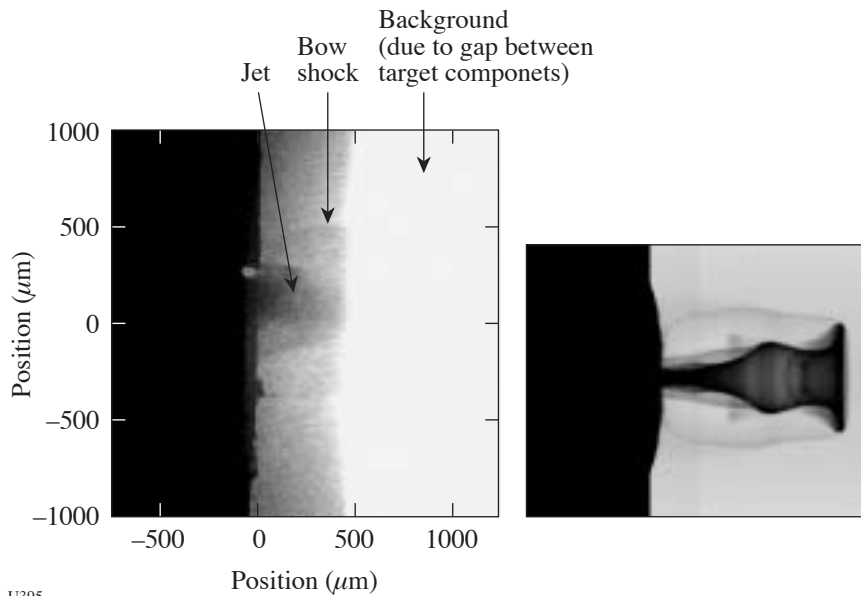


Figure 96.87
Pinhole-aperture point-projection radiographic image of the titanium jet and bow shock in CRF foam and an NYM-PETRA simulation (shown at the same spatial scale). The experimental image is partially overlaid by background emission from the target, arising from an unintentional gap between target components.

U394

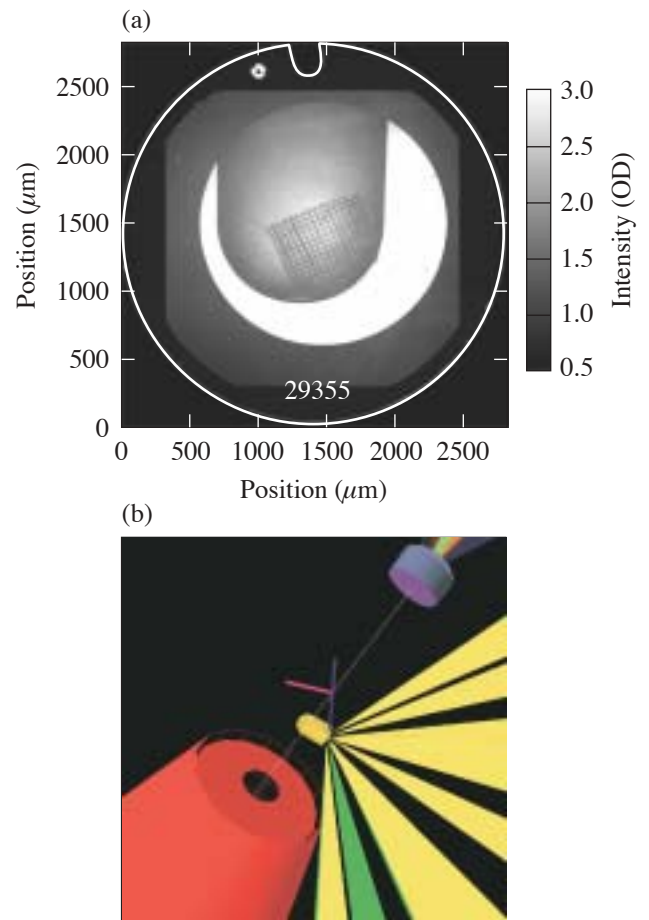
U395

using the *RAGE* code, and at AWE using the *NYM* and *PETRA* codes. Figure 96.87 also shows a simulated radiograph generated by *NYM-PETRA*. Careful analysis of the experimental images from our most-recent run indicates that the data in Fig. 96.87 are partially obscured by a region of emission resulting from an unintentional gap between the gold shield and titanium washer of the experimental package. A silver-loaded epoxy fillet, or modified shield design, would presumably reduce this problem in future experiments.

Time-Dependent Mix: The goal of the time-dependent mix experiment is the production of high-quality, time-resolved spectroscopic and imaging data that will constrain models of fuel–pusher mix in directly driven ICF implosions. The primary diagnostic marker is a thin ($0.1\text{-}\mu\text{m}$ -thick) titanium-doped CH layer introduced at the fuel–pusher interface of an ICF capsule. The timing and intensity of emission from H-like Ti have been calculated to depend on the timing and amount of Ti that reaches the center of the fuel. In the first experiments, high-quality, time-resolved Ti *K*-shell spectroscopic data were obtained from targets that had a range of shell thicknesses and fill-gas pressures. The high quality of the data indicates the viability of this approach.

X-Ray Backlighting: Los Alamos also developed an x-ray-backlighting technique at 9 keV that produces uniform, large-area, monochromatic, high-resolution images of targets used for laser-driven AGEX and high-energy-density-physics (HEDP) experiments. X-ray imaging at moderate energy in laser-driven HEDP experiments is an essential, well-established tool for observing dynamic phenomena such as shock trajectories, interface motion, and instability growth. However, the standard technique using an area backlighter, coupled with the size of the object to be radiographed, requires an inordinate amount of laser energy to produce a monochromatic x-ray source above 7 keV.

High-resolution images were obtained using a pinhole-apertured point-backlighter (PAPBL) geometry and a Zn source. Figure 96.88(a) shows the raw image, recorded on x-ray film, of a thin-walled gold hohlraum used for radiation-driven experiments. Figure 96.88(b) shows the hohlraum in the center with 12 laser beams “driving” it. The top right corner shows the backlighter substrate while the object in the lower left-hand corner is the diagnostic camera. The high resolution, large dynamic range, and penetrating ability of the 9-keV x rays are apparent.



U396

Figure 96.88

(a) Static x-ray radiograph with a 9-keV backlighter of a hohlraum with a resolution grid attached. A $62\text{-}\mu\text{m}$ ($20\text{-}\mu\text{m}$ bar width) period grid was used for spatial calibration. (b) Configuration showing diagnostic nose tip, hohlraum, and backlighter substrate.

Beryllium Ablative Microstructure Stability (BAMS): Materials experiments concentrate on measuring the shock-propagation properties of beryllium because beryllium-based alloys are prime candidates for the NIF capsule material. Since the fusion yield depends strongly on the symmetry of the capsule during implosion, the importance of the elastic anisotropy of Be in the seeding of hydrodynamic instabilities is paramount. To measure this effect directly, Los Alamos began a series of beryllium ablative microstructure stability (BAMS) experiments. To that end, a 6-ns laser pulse was designed to achieve radiation pressure in a hohlraum environment to drive over 50 Rayleigh–Taylor growth times. LLE personnel have fabricated two separate pulse shapes, carried by 13 phased beams, which closely approximate the desired drive. Preliminary analysis of radiation temperature data (Dante and VISAR) indicates close agreement with calculations.

A small Be patch was mounted on the rear wall of the hohlraum opposite the laser entrance hole. Face-on x-ray radiography in the first experiment was used to assess the influx of Au from the hohlraum walls into the diagnostic line of sight and to observe machined perturbations in a Be-Cu (0.9% by atom) alloy. Self-backlighting by Au near the laser entrance hole shows growth of the 100- μm period perturbations with evidence of a Be bubble forming near the target axis (Fig. 96.89). Future experiments will optimize radiography techniques and possibly employ gas-filled hohlraums to inhibit Au transport toward the axis.

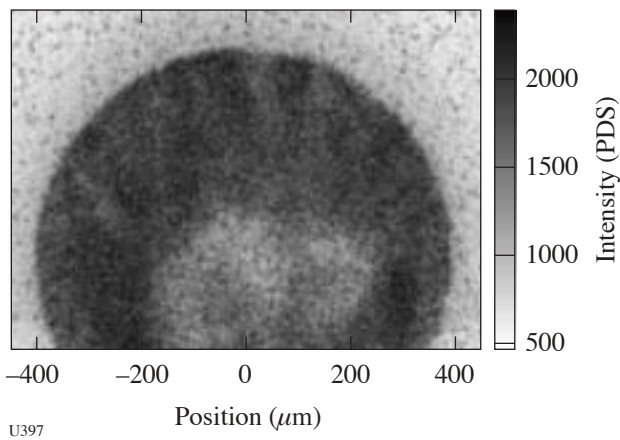


Figure 96.89
A radiograph of a sample Be backlit by Au emission within the hohlraum. The fringes correspond to the 100- μm period of machined perturbations in the Be patch. The light area on axis could be Au opacity or exclusion of Au by a Be bubble arising from the patch.

FY03 SNL OMEGA PROGRAMS

Sandia National Laboratories (SNL) carried out a total of 30 target shots on the OMEGA laser in FY03 and also participated in several of the campaigns led by other laboratories. The SNL-led campaigns included the following:

SOP/Aluminum Wedge Verification of Hohlraum Drive Temperature and Shock Temperature: In FY03, streaked optical pyrometer (SOP)¹⁹ measurements of the shock velocity in aluminum wedges were begun on OMEGA to verify hohlraum radiation temperature. The aluminum wedges in these experiments were fielded side by side with indirect-drive ICF ablator samples for the purpose of SOP intensity calibration at the $280\pm 20\text{-nm}$ bandpass. As was done years ago on Nova, this data can also be used, however, to verify the hohlraum radiation temperature.^{20,21} There were some surprises in this new data. Figure 96.90(a) shows a comparison of the pre-shot calculation with the unfolded Al-wedge SOP data from OMEGA shot 31819 (5.56 kJ, 2 ns square). The measured Al shock velocity was about 12% higher than predicted in the pre-shot *LASNEX* calculations. The result of a post-shot calculation using a drive multiplier to match the data is also indicated in the figure. Figure 96.90(b) shows the overlay of a DANTE²² measurement for a very similar previous hohlraum experiment done on a P6-P7 axis (OMEGA shot 27564; 5.53 kJ, 2 ns). It appears that both the post-shot and pre-shot versions of the drive are close to bounding the uncertainty of the DANTE measurement; however, the same conclusion is not reached in our analysis of the similar experiment employing a 1-ns drive. In this experiment (OMEGA shot 31820), the measured Al velocity was about 25% higher than the pre-shot prediction.

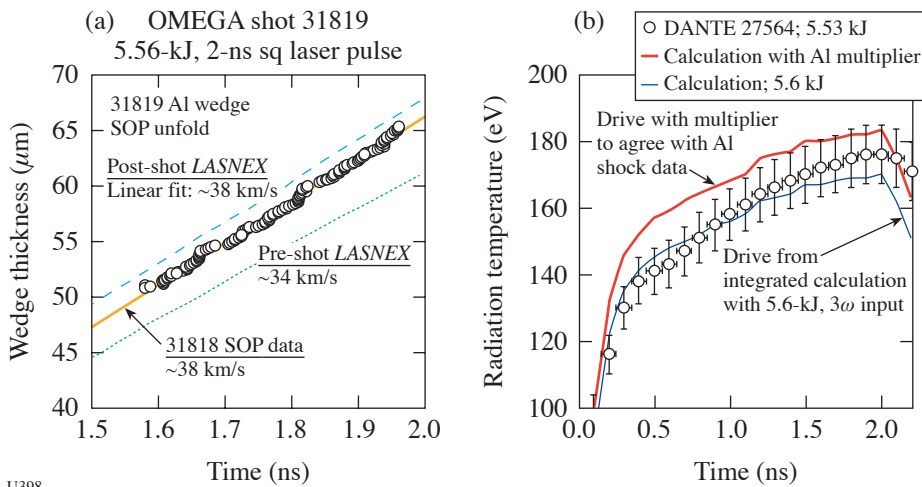


Figure 96.90
(a) Unfold of shock position versus time for Al wedge in OMEGA shot 31819 (5.56 kJ, 2 ns square) compared to pre-shot and post-shot *LASNEX* calculations. (b) Comparison of Dante unfold from OMEGA shot 27564 (5.53 kJ, 2 ns square) with drive from shot 31819 pre-shot and post-shot calculations.

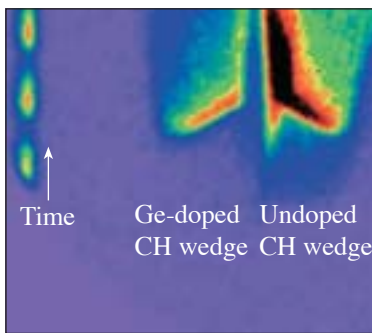
These hohlraum drive measurement comparison issues will be explored further in the FY04 SNL campaign.

Experimental Verification of Shock Temperature and Preheat Reduction in Doped Ablator Samples: In FY03, the streaked optical pyrometer (SOP)¹⁹ was used to view the preheat and shock breakout in side-by-side samples of doped and undoped indirect-drive ICF ablator samples. A key result was the experimental demonstration of preheat and shock temperature reduction via the use of mid-Z dopants in the low-Z ablator material.^{23,24} Figure 96.91(a) shows the SOP image from OMEGA shot 31821 in which side-by-side, wedge-shaped samples of $C_{38}H_{60}O_2$ and $C_{39}H_{57}O_2Ge_2$ were driven by a hohlraum radiation pulse. It is clear from the image that the intensity levels of the preheat and the shock breakout are significantly reduced in the Ge-doped sample. Figures 96.91(b) and 96.91(c) show overlays of the intensity–time lineouts of side-by-side doped and undoped samples driven at hohlraum temperatures of ~ 160 eV (OMEGA shot 31818, 2 ns square) and ~ 200 eV (OMEGA shot 31821, 1 ns square). It found that the $\sim 8\times$ reduction in preheat and the $2\times$ reduction in shock temperature are approximately consistent with *LASNEX* calculations that employ opacities based on the techniques of Refs. 25 and 26. Similar side-by-side experiments using undoped and Cu-doped beryllium samples are planned for early FY04. A new issue arising with this data is illustrated in Fig. 96.92. As indicated in the figure, the detailed analysis of the Ge-doped CH-wedge measurements indicates a shock velocity that is $\sim 12\%$ to 15% lower than the *LASNEX* calculations.

This result would appear to be in contradiction to the Al-wedge results (see previous section) in which Al shock velocity is found to be higher than the *LASNEX* prediction (a result that is found even in the experiment employing side-by-side wedges of Al and Ge-doped CH). This issue will also be explored further in FY04.

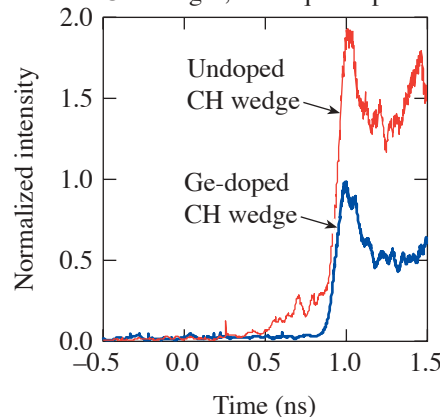
Indirect-Drive ICF Ablator X-Ray Burnthrough Measurements: To achieve indirect-drive ignition of an ICF capsule, ablator burnthrough timing must be predicted to within a few percent. In FY03, the techniques described in Ref. 27 were employed to begin using the streaked x-ray imager (SXI) diagnostic²⁸ to view time-resolved x-ray burnthrough in side-by-side samples of ablator materials having different thicknesses or dopant levels. An example of this new data is shown in Fig. 96.93. The fact that the signals from the doped and undoped CH do not overlay with 700-eV offset is consistent with the calculations only if a significant contribution of second-order, 1.4-keV flux is included. This represents a new unresolved issue: the result is contrary to our past experience with the SXI data. Another interesting new issue that has come up in the SXI data that is related to the discussions of the two previous sections is illustrated in Fig. 96.94. Here, the new information on hohlraum drive is applied to the analysis of previous polyimide x-ray burnthrough data obtained in FY02. As indicated in the figure, it appears that the application of the new Al-wedge drive data leads to a significantly improved agreement between the calculated and measured x-ray burnthrough behavior.

(a) 31821 SOP image (May 2003)



U399

(b) Shot 31818: CH/Ge and CH wedges, 2-ns sq laser pulse



(c) Shot 31821: CH/Ge and CH wedges, 1-ns sq laser pulse

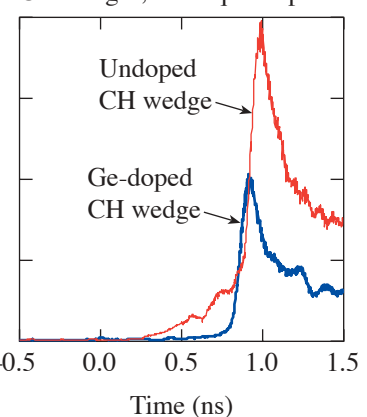
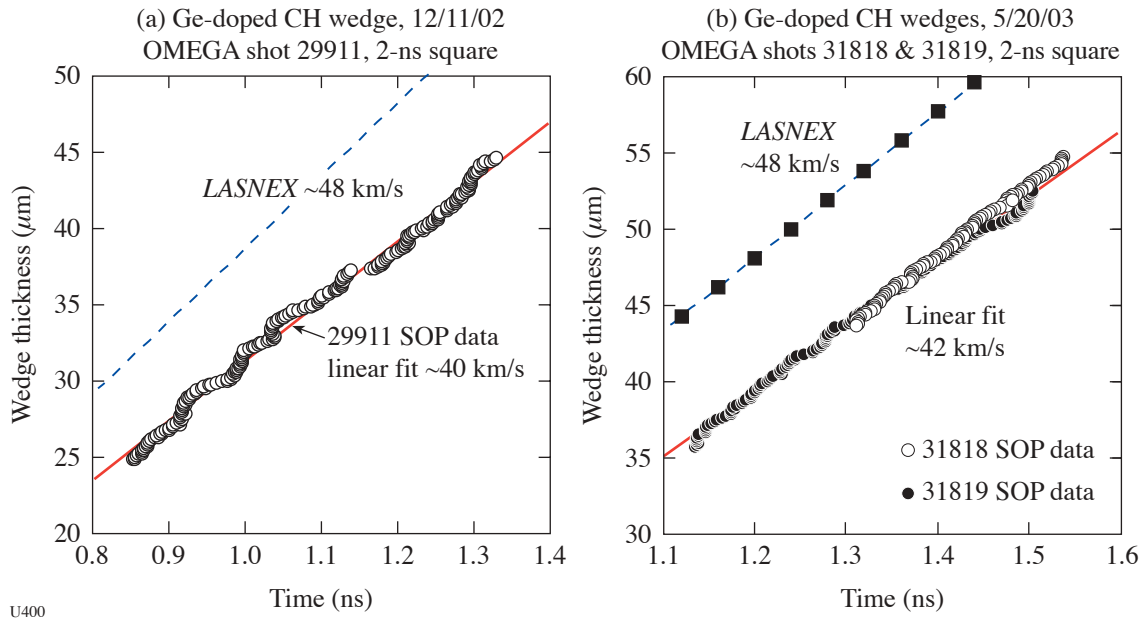


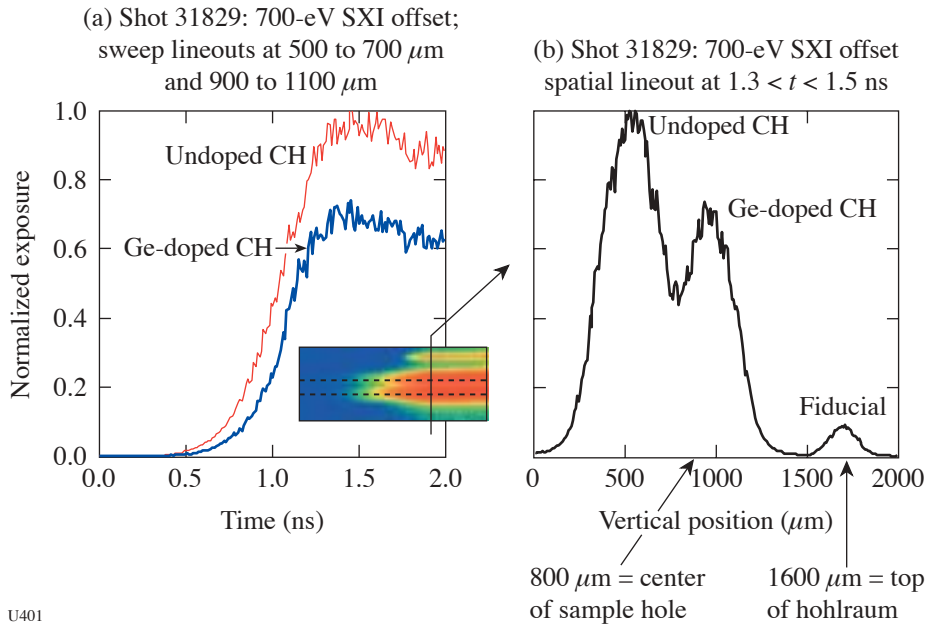
Figure 96.91

(a) SOP image from OMEGA shot 31821 in which side-by-side wedge-shaped samples of $C_{38}H_{60}O_2$ and $C_{39}H_{57}O_2Ge_2$ were driven by a hohlraum radiation pulse. (b) and (c) Overlays of the intensity–time lineouts of side-by-side doped and undoped samples driven at hohlraum temperatures of ~ 160 eV (OMEGA shot 31818, 2 ns square) and ~ 200 eV (OMEGA shot 31821, 1 ns square).



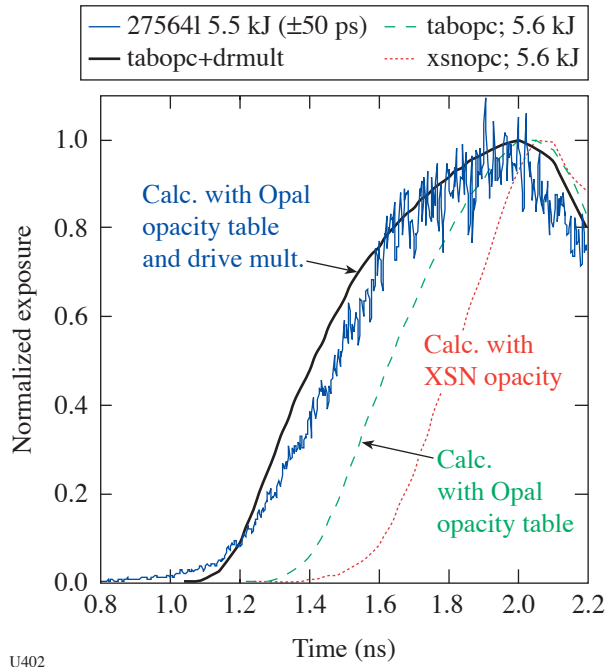
U400

Figure 96.92
Unfold of shock position versus time for Ge-doped CH wedges in (a) OMEGA shot 29911 and (b) shots 31818 and 31819.



U401

Figure 96.93
Spatial lineout through SXI streaked image including times between 1.3 and 1.5 ns for OMEGA shot 31829 employing side-by-side samples of Ge-doped and undoped CH.



U402

Figure 96.94 Comparison of *LASNEX* calculation variations to the SXI data lineout for OMEGA shot 27564.

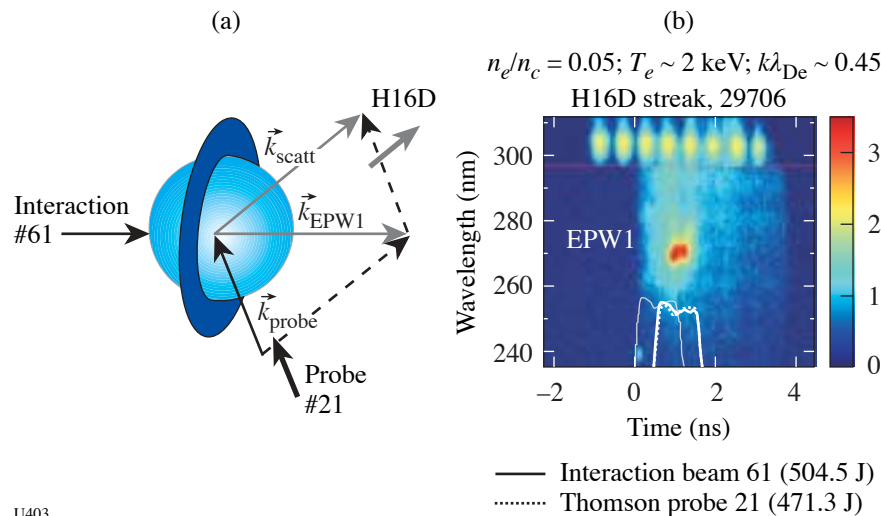
CEA PROGRAMS

The Commissariat à l'Énergie Atomique (CEA) of France was allotted three shot days on OMEGA in FY03 and carried out 32 target experiments. The experiments were focused in two primary areas: (a) laser-matter interaction and (b) diagnostics development.

First Tests of the DEMIN Spectrometer on OMEGA

a. Laser-Matter Interaction: A new Thomson-scattering configuration for probing electron-plasma waves stimulated by Raman backscattering instability (SRS) was defined and successfully tested on OMEGA in FY03. In this experiment, two OMEGA beams at 3ω were used to stimulate and probe electron-plasma waves in a plasma preformed by 40 heater beams. This configuration will be used to investigate the growth and saturation of SRS in gas-bag targets (Fig. 96.95) representative of the homogeneous plasmas that will be produced on the NIF and LMJ. For this study, Thomson scattering is a valuable complementary diagnostic of backscattering stations because it provides measurements that are spatially resolved along the interaction-beam propagation axis, thus demonstrating that SRS activity is occurring in a plasma representative of the NIF and LMJ.

b. Diagnostics Development: The DEMIN (detector micromegas for neutrons) neutron spectrometer²⁹ designed by CEA was tested for the first time during ICF experiments on OMEGA in FY03. The DEMIN concept, derived from the one used on high-energy physics,³⁰ is based on the association of a neutron-to-proton converter with a thin gas chamber (600 μm). This design has an efficiency of 10^{-3} and 10^{-6} , respectively, for 14-MeV neutrons and 1-MeV photons. This intrinsic γ -ray insensitivity allows the measurement of secondary (DD target) and tertiary (DT target) neutrons in large γ background. This γ background is induced by (n, γ) interaction on hardware present in the experimental area [noted (n, γ) on Fig. 96.96].



U403

Figure 96.95 (a) Schematic of SRS experiment showing gas-bag target geometry with an interaction beam (61) and probe beam (21). (b) Streak camera recording of Thomson signal generated by scattering from electron-plasma waves generated by the SRS instability.

Recorded DEMIN signals show this relative γ transparency by comparison with a calibrated scintillator plus photomultiplier tube (HCB12). Figures 96.96 and 96.97 present photon and neutron flux as a function of the time after the target implosion.

In both cases, the comparison of signals from DEMIN and HCB12 shows the intrinsic γ -ray insensitivity of the DEMIN spectrometer. Gamma rays induce small or non-observed signals in the time-of-flight window, where secondary and tertiary neutrons will induce signals with several tens of millivolts.

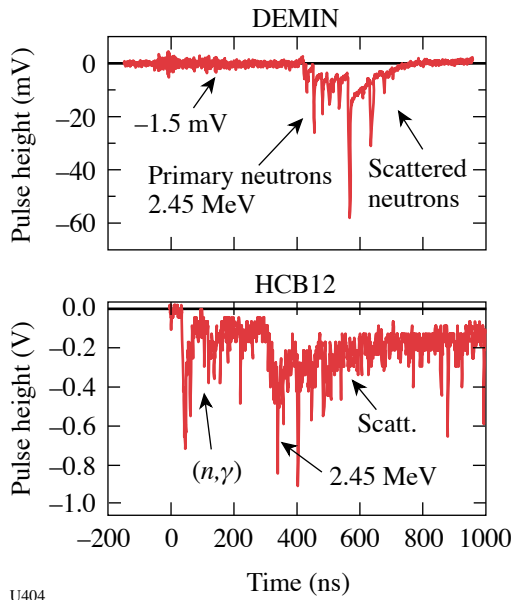


Figure 96.96
DEMIN record from DD target shot #31774. In the case of DD targets, γ rays do not induce signals before primary and scattered neutrons in DEMIN. The noise in the measurement time window of expected secondary neutrons (12 to 17 meV) is low (± 1.5 mV). In this DEMIN configuration, secondary neutrons will give several tens of millivolts. By comparison, γ rays are clearly observed by the HCB12 detector and will mask any secondary neutron signal.

U404

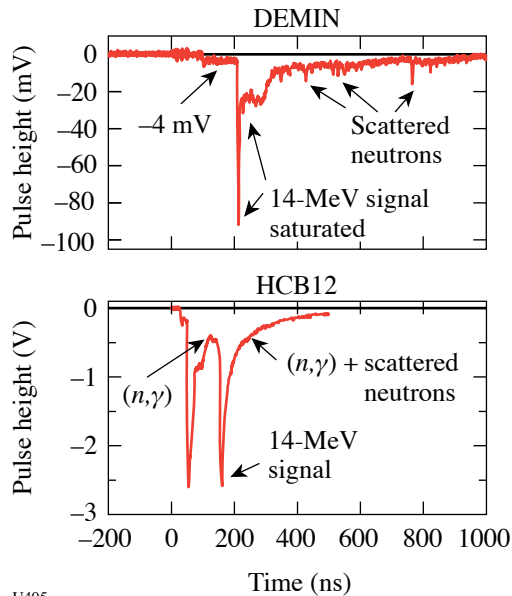


Figure 96.97
DEMIN record from DT target shot #31750. In the case of a DT target, the signal induced by the 14-MeV neutrons is saturated in DEMIN; the high yield of primary neutrons inhibits the electric field in the gas during few tens of nanoseconds. Whereas with the HCB12 detector the γ rays signal is as important as for 14-MeV neutrons, the DEMIN exhibits a low signal (≤ 4 mV).

U405

Fast Photoconductor for Neutron Spectroscopy: the SCANED Concept

The SCANED (SCattered NEutron Diagnostic) detector, designed by CEA, was tested during the DT shots campaign in May 2003. The concept is based on a photoconductor operating as a time-of-flight detector. The fast response of photoconductors is the main advantage, allowing location near the target; therefore, the neutron spectrum is recorded before the arrival of scattered neutrons and gamma rays produced on the chamber hardware. This concept is proposed for various measurements in ICF experiments: ion temperature, neutron yields, $\langle \rho R \rangle$ by secondary neutrons (DD target), and downscattered neutrons (DT target).^{31,32} Moreover, photoconductors can be an alternative for diagnostics that may be inoperative with high yields (on the NIF and LMJ).

SCANED is composed of a *n*-irradiated AsGa detector ($6 \times 4 \text{ mm}^2$) fixed in a $50\text{-}\Omega$ loaded design made of plastic and Teflon to minimize (n, n') and (n, γ) interactions. Signals are recorded by a set of three IN7100 oscilloscopes to get a large dynamic range.

The goals of the experiments performed in May were the measurement of the sensitivity to 14-MeV neutrons and the study of noise, EM effects, and the duration of the tail in the pulse shape after the prompt 14-MeV neutron interaction.

Two SCANED setups were tested at 1 m and 0.385 m from target chamber center (TCC), respectively. Figure 96.98 shows

a typical spectrum for the closest location. We easily observe 14-MeV and 2.45-MeV neutron peaks, from D+T and D+D fusion, respectively. The gamma background induced by the neutron interaction in the chamber skin is measured about 29 ns after the 14-MeV neutron signal. A DMX diode located between SCANED and the target (at 13.5 cm from the target) induces background over 10 ns after the x-ray signal is emitted by the target.

Work is in progress to improve the response of photoconductors.

Capillaries Detector for ICF Capsule Neutron Images

14-MeV imaging detector arrays have been developed by assembling glass capillaries of $85\text{-}\mu\text{m}$ mean diameter into $100 \times 100\text{-mm}^2$ coherent arrays. The capillaries are filled with a liquid scintillator whose optical index is higher than the glass index. Neutron scattering of the hydrogen nuclei of the scintillator and the recoil ions produce light in several adjacent capillaries as they lose energy. The light distribution about the scattering point determines the detector spatial resolution. A $650\text{-}\mu\text{m}$ spatial resolution has been achieved; the resolution is enhanced to $325 \mu\text{m}$ by loading deuterium in the scintillator as the recoil deuterons have shorter mean free paths than recoil protons (Fig. 96.99). This array has been tested on the OMEGA neutron imaging system (NIS). These results will permit the achievement of high resolution in neutron images with moderate magnification ratio and practical line of sight on LMJ and the NIF.

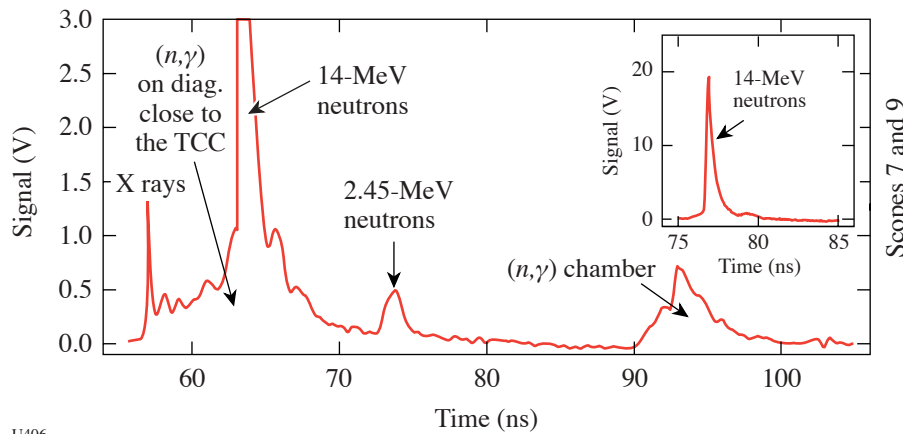
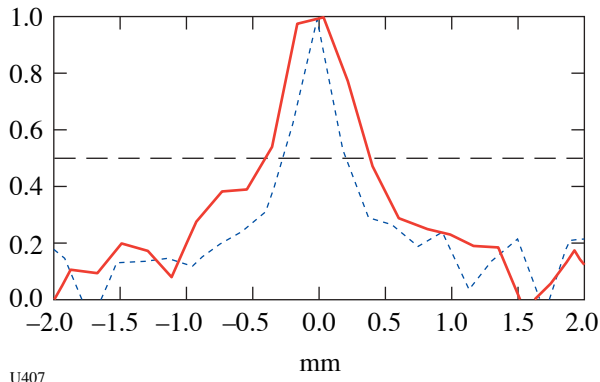


Figure 96.98
SCANED signal on shot 31756 (DT-filled target).

U406



U407

Figure 96.99

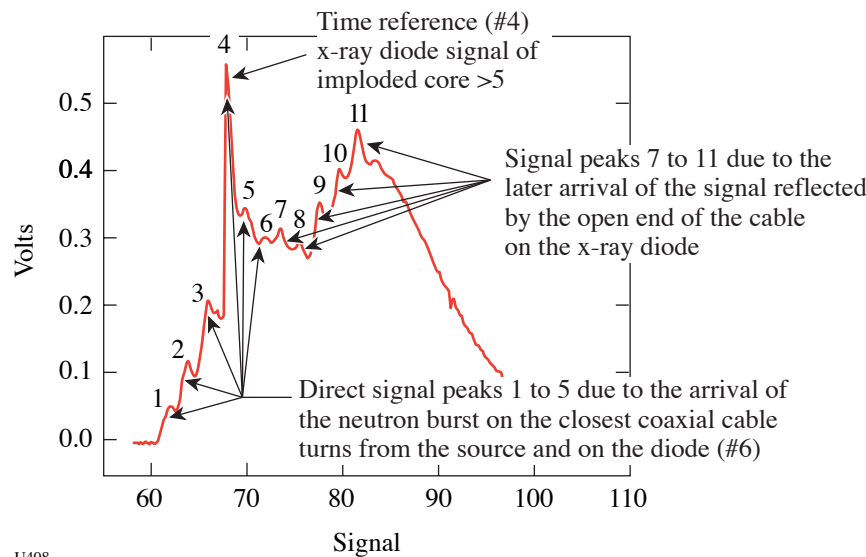
14-MeV neutron point-spread function measured in the 85- μm -diam capillaries array filled with a high-optical-index scintillator nondeuterated (solid line) and deuterated (dashed lines). Corrected from the 380- μm readout system resolution, the FWHM is 650 μm and 325 μm for the nondeuterated and deuterated scintillator, respectively.

Neutron-Induced Current Generation

High-pulsed neutron irradiation can drive a transient current generation on coaxial cables. For intense, 14-MeV neutron irradiation that will exit on future ICF facilities such as LMJ in France and the NIF in the U.S., this effect can generate a signal on a 50- Ω load as high as a few hundred volts. On such a facility, coaxial cable will be widely used to transfer the electrical signals generated by the detectors placed close to the source to their recording devices placed away from the target to be sufficiently protected against the nuclear environment induced by this neutron irradiation. All of these cables will be

affected by the parasitic signals induced by the pulsed neutron irradiation during high-yield neutron shots. No simple protective method (other than cumbersome 1-m-thick shielding) can protect the cable from this intense neutron irradiation. To investigate the potential level of this effect, OMEGA was used as an intense, pulsed, 14-MeV neutron source on direct-drive-yield neutron shots (up to 10^{14} neutrons of 14 MeV). OMEGA shots can induce a weaker but sufficient signal to be recorded if a coaxial cable can be placed sufficiently close to the target. In this case, a standard high-bandwidth coaxial cable (1/4-in.-diam, semi-rigid SMA type) was set at 25 cm on the neutron source by means of a diagnostic inserter (TIM). A weak but clear signal was recorded (Fig. 96.100).

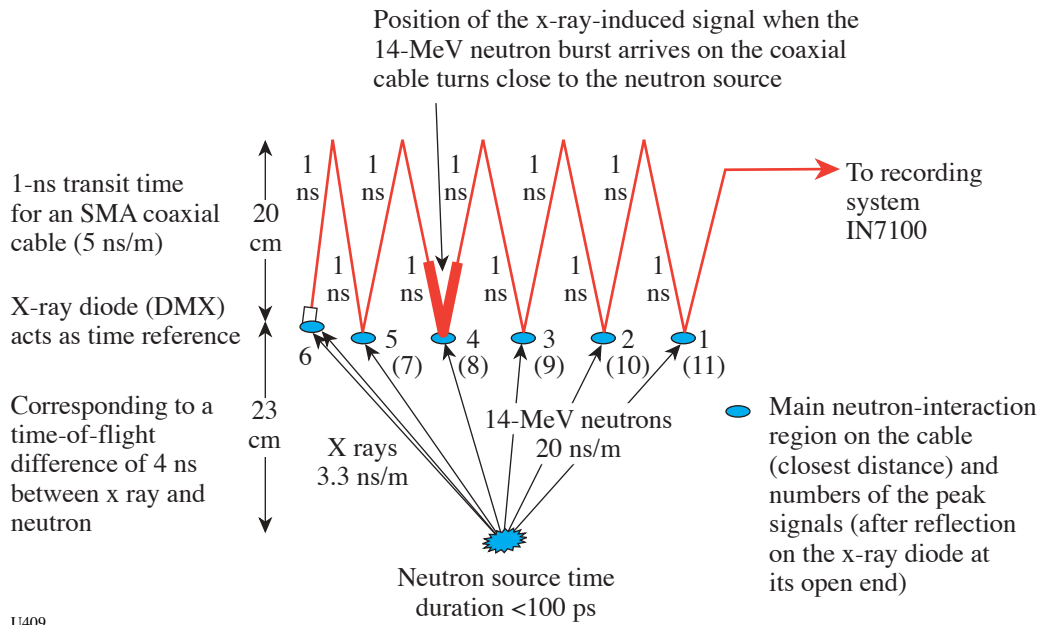
Each weak bump on this recorded signal is associated with the 14-MeV neutron burst (time duration of 100 ps, which corresponds to a space extension of 5 mm) on each U-turn of the zigzag coaxial cable placed closest to the neutron source (see Fig. 96.101). In order to accurately time-reference each induced signals with respect to the time of neutron production, a standard x-ray diode was added at the end of the coaxial cable to record the instant of the neutron production (associated with a hard-x-ray burst). This time is represented by the signal bump #4, which corresponds to the arrival of the x ray on the diode. Each of the bumps is clearly identified due to the arrival of the neutron burst at each of the U-turns (bumps 1 to 6). Moreover, each signal generated by the neutrons on each U-turn is also reflected by the coaxial end and represents later bumps (7 to 11), so a clear time reference is associated with each bump and clearly shows the effect of pulsed neutron generation on a coaxial cable.



U408

Figure 96.100

Signal recorded by a high-bandwidth (7-GHz), single-shot oscilloscope on high-yield OMEGA neutron shots.



U409

Figure 96.101

Schematic drawing of the experimental setup showing the origin of each signal bump.

REFERENCES

1. H. F. Robey *et al.*, *Phys. Plasmas* **10**, 614 (2003).
2. P. A. Keiter, R. P. Drake, T. S. Perry, H. F. Robey, B. A. Remington, C. A. Iglesias, R. J. Wallace, and J. Knauer, *Phys. Rev. Lett.* **89**, 165003 (2002).
3. A. C. Calder *et al.*, *Astrophys. J. Suppl. Ser.* **143**, 201 (2002).
4. A. Miles, D. Braun, J. Edwards, H. F. Robey, R. P. Drake, D. R. Leibbrandt, E. C. Harding, J. P. Knauer, and D. Arnett, "Numerical Simulation of Supernova-Relevant Laser-Driven Hydrodynamics Experiments on OMEGA," submitted to *Physics of Plasmas*.
5. R. P. Drake, B. A. Remington, and D. D. Ryutov, "Experimental Astrophysics with Intense Lasers," submitted to *Review of Modern Physics*.
6. R. D. Petrasso, J. A. Frenje, F. H. Séguin, C. K. Li, B. E. Schwartz, C. Stoeckl, P. B. Radha, J. A. Delettrez, D. D. Meyerhofer, S. Roberts, T. C. Sangster, and J. M. Soares, *Bull. Am. Phys. Soc.* **47**, 145 (2002).
7. B. E. Schwartz, F. H. Séguin, J. A. Frenje, R. D. Petrasso, C. K. Li, P. B. Radha, D. D. Meyerhofer, S. Roberts, T. C. Sangster, J. M. Soares, and C. Culligan, *Bull. Am. Phys. Soc.* **47**, 219 (2002).
8. C. K. Li, F. H. Séguin, J. A. Frenje, R. D. Petrasso, J. A. Delettrez, R. L. Keck, J. M. Soares, P. W. McKenty, F. J. Marshall, V. N. Goncharov, J. P. Knauer, D. D. Meyerhofer, P. B. Radha, S. P. Regan, T. C. Sangster, and W. Seka, " ρR Asymmetry in the Spherical Implosion of Inertial Confinement Fusion," submitted to *Physical Review Letters*.
9. R. I. Klein *et al.*, *Astrophys. J.* **583**, 245 (2003).
10. H. F. Robey, T. S. Perry, R. I. Klein, J. O. Kane, J. A. Greenough, and T. R. Boehly, *Phys. Rev. Lett.* **89**, 085001 (2002).
11. C. Stoeckl, R. E. Bahr, B. Yaakobi, W. Seka, S. P. Regan, R. S. Craxton, J. A. Delettrez, R. W. Short, J. Myatt, A. V. Maximov, and H. Baldis, *Phys. Rev. Lett.* **90**, 235002 (2003).
12. L. A. Welser, R. C. Mancini, J. A. Koch, S. Dalhed, R. W. Lee, I. E. Golovkin, F. Marshall, J. Delettrez, and L. Klein, *Rev. Sci. Instrum.* **74**, 1951 (2003).
13. L. A. Welser, R. C. Mancini, J. A. Koch, N. Izumi, H. Dalhed, H. Scott, T. W. Barbee, Jr., R. W. Lee, I. E. Golovkin, F. Marshall, J. Delettrez, and L. Klein, *J. Quant. Spectrosc. Radiat. Transf.* **81**, 487 (2003).
14. D. R. Kania *et al.*, *J. Appl. Phys.* **68**, 124 (1990).
15. N. E. Lanier *et al.*, *Phys. Plasmas* **10**, 1816 (2003).
16. M. M. Balkey *et al.*, "Production and Metrology of Cylindrical Inertial Confinement Fusion Targets with Sinusoidal Perturbations," Los Alamos National Laboratory report LA-UR-03-3682 (2003); to be published in *Fusion Science and Technology*.
17. W. S. Varnum, N. D. Delamater, S. C. Evans, P. L. Gobby, J. E. Moore, J. M. Wallace, R. G. Watt, J. D. Colvin, R. Turner, V. Glebov, J. Soares, and C. Stoeckl, *Phys. Rev. Lett.* **84**, 5153 (2000).
18. J. M. Foster *et al.*, *Phys. Plasmas* **9**, 2251 (2002).

19. J. A. Oertel *et al.*, *Rev. Sci. Instrum.* **70**, 803 (1999).
20. R. L. Kauffman *et al.*, *Phys. Rev. Lett.* **73**, 2320 (1994).
21. R. L. Kauffman *et al.*, *Rev. Sci. Instrum.* **66**, 678 (1995).
22. H. N. Kornblum, R. L. Kauffman, and J. A. Smith, *Rev. Sci. Instrum.* **57**, 2179 (1986).
23. R. E. Olson *et al.*, "Preheat Effects on Shock Propagation in Indirect-Drive Inertial Confinement Fusion Ablator Materials," to be published in *Physical Review Letters*.
24. R. E. Olson *et al.*, "Shock Propagation, Preheat, and X-Ray Burn-through in NIF Ignition Capsule Ablator Materials," submitted to *Physics of Plasmas*.
25. A. Bar-Shalom *et al.*, *Phys. Rev. A* **40**, 3183 (1989).
26. F. J. Rogers, B. G. Wilson, and C. A. Iglesias, *Phys. Rev. A, Gen. Phys.* **38**, 5007 (1988).
27. R. E. Olson *et al.*, *Rev. Sci. Instrum.* **74**, 2186 (2003).
28. T. J. Orzechowski *et al.*, *Phys. Rev. Lett.* **77**, 3545 (1996).
29. M. Houry *et al.*, "A New Diagnostic Design to Achieve Neutron Spectroscopy in a High Gamma Background on ICF Experiments," presented at the EuroConference on Advanced Diagnostics for Magnetic and Inertial Fusion, Varenna, Italy, 3–7 September 2001.
30. Y. Giomataris *et al.*, *Nucl. Instrum. Methods Phys. Res. A* **376**, 29 (1996).
31. D. C. Wilson *et al.*, *Nucl. Instrum. Methods Phys. Res. A* **488**, 400 (2002).
32. G. J. Schmid, LLNL, private communication (2002).

Publications and Conference Presentations

Publications

- G. P. Agrawal and D. N. Maywar, "Semiconductor Optical Amplifiers with Bragg Gratings," in *Nonlinear Photonic Crystals*, edited by R. E. Slusher and B. J. Eggleton, Springer Series in Photonics, Vol. 10 (Springer-Verlag, Berlin, 2003), Chap. 13, pp. 285–300.
- I. Begishev, V. Bagnoud, M. Guardalben, L. Waxer, J. Puth, and J. Zuegel, "Optimization of an Optical Parametric Chirped Pulse Amplification System for the OMEGA EP Laser System," in *Advanced Solid-State Photonics, OSA Technical Digest* (Optical Society of America, Washington, DC, 2003), pp. 252–254.
- G. Chen, Y. Du, S. Wang, A. E. Marino, L. L. Gregg, S. R. Arrasmith, and S. D. Jacobs, "Effect of SnO on Chemical Durability of Phosphate Glasses," *Glass Technol.* **43C**, 97 (2002).
- H. M. P. Chen, D. Katsis, and S. H. Chen, "Deterministic Synthesis and Optical Properties of Glassy Chiral-Nematic Liquid Crystals," *Chem. Mater.* **15**, 2534 (2003).
- S. H. Chen, H. M. P. Chen, Y. Geng, S. D. Jacobs, K. L. Marshall, and T. N. Blanton, "Novel Glassy Nematic Liquid Crystals for Non-Destructive Rewritable Optical Memory and Photonic Switching," *Adv. Mater.* **15**, 1061 (2003).
- S. W. Culligan, Y. Geng, S. H. Chen, K. Klubek, K. M. Vaeth, and C. W. Tang, "Strongly Polarized and Efficient Blue Organic Light-Emitting Diodes Using Monodisperse Glassy-Nematic Oligo(fluorene)s," *Adv. Mater.* **15**, 1176 (2003).
- J. E. DeGroote, S. D. Jacobs, J. M. Schoen, H. J. Romanofsky, and I. A. Kozhinova, "Magnetorheological Finishing of a Diamond Turned Poly(Methylmethacrylate) Flat," in *Optifab 2003* (SPIE, Bellingham, WA, 2003), Vol. TD02, pp. 65–68.
- C. Dorrer and D. N. Maywar, "Ultrafast RF Spectrum Analyzer for Optical Signals," *Electron. Lett.* **39**, 1004 (2003).
- Y. Geng, S. W. Culligan, A. Trajkovska, J. U. Wallace, and S. H. Chen, "Monodisperse Oligofluorenes Forming Glassy-Nematic Films for Polarized Blue Emission," *Chem. Mater.* **15**, 542 (2003).
- V. Yu. Glebov, C. Stoeckl, T. C. Sangster, D. D. Meyerhofer, P. B. Radha, S. Padalino, L. Baumgart, R. Coburn, and J. Fuschino, "Carbon Activation Diagnostic for Tertiary Neutron Measurements," *Rev. Sci. Instrum.* **74**, 1717 (2003).
- G. N. Gol'tsman, K. Smirnov, P. Kouminov, B. Voronov, N. Kaurova, V. Drakinsky, J. Zhang, A. Verevkin, and R. Sobolewski, "Fabrication of Nanostructured Superconducting Single-Photon Detectors," *IEEE Trans. Appl. Supercond.* **13**, 192 (2003).
- V. N. Goncharov, J. P. Knauer, P. W. McKenty, P. B. Radha, T. C. Sangster, S. Skupsky, R. Betti, R. L. McCrory, and D. D. Meyerhofer, "Improved Performance of Direct-Drive Inertial Confinement Fusion Target Designs with Adiabatic Shaping Using an Intensity Picket," *Phys. Plasmas* **10**, 1906 (2003) (invited).
- O. V. Gotchev, P. A. Jaanimagi, J. P. Knauer, F. J. Marshall, D. D. Meyerhofer, N. Bassett, and J. B. Oliver, "High-Throughput, High-Resolution, Kirkpatrick-Baez Microscope for Advanced Streaked Imaging of ICF Experiments on OMEGA," *Rev. Sci. Instrum.* **74**, 2178 (2003).
- Q. Guo, X. Teng, S. Rahman, and H. Yang, "Patterned Langmuir-Blodgett Films of Monodisperse Nanoparticles of Iron Oxide Using Soft Lithography," *J. Am. Chem. Soc.* **125**, 630 (2003).
- Q. Guo, X. Teng, and H. Yang, "Surface Patterns of Tetragonal Phase FePt Thin Films from Pt@Fe₂O₃ Core-Shell Nanoparticles Using Combined Langmuir-Blodgett and Soft Lithographic Techniques," in *Unconventional Approaches to Nanostructures with Applications in Electronics, Photonics,*

Information Storage and Sensing, Materials Research Society, Vol. 776, edited by O. D. Velev, T. J. Bunning, Y. Xia, and P. Yang (Materials Research Society, Warrendale, PA, 2003), pp. 187–192.

I. V. Igumenshchev, R. Narayan, and M. A. Abramowicz, “Three-Dimensional Magneto-hydrodynamic Simulations of Radiatively Inefficient Accretion Flows,” *Astrophys. J.* **592**, 1042 (2003).

S. D. Jacobs, H. M. Pollicove, E. M. Fess, and J. Schoen, “Aspheric Optics Manufacturing for Commercial and Military Systems,” in *First Symposium for Explosive Materials, Weapons, and Military Technology* (Military Academy General Mihailo Apostolski, Skopje, Macedonia, 2002), pp. 497–504.

A. Jukna and R. Sobolewski, “Time-Resolved Photoresponse in the Resistive Flux-Flow State in Y-Ba-Cu-O Superconducting Microbridges,” *Supercond. Sci. Technol.* **16**, 911 (2003).

R. K. Kirkwood, J. D. Moody, A. B. Langdon, B. I. Cohen, E. A. Williams, M. R. Dorr, J. A. Hittinger, R. Berger, P. E. Young, L. J. Suter, L. Divol, S. H. Glenzer, O. L. Landen, and W. Seka, “Observation of Saturation of Energy Transfer between Copropagating Beams in a Flowing Plasma,” *Phys. Rev. Lett.* **89**, 215003 (2002).

T. Z. Kosc, K. L. Marshall, and S. D. Jacobs, “Polymer Cholesteric Liquid Crystal Flakes for Particle Displays,” in *2003 SID International Symposium, Digest of Technical Papers*, 1st ed., edited by J. Morreale (Society for Information Display, San Jose, CA, 2003), Vol. 34, Book 1, pp. 581–583.

T. Z. Kosc, K. L. Marshall, S. D. Jacobs, and J. C. Lambropoulos, “Electric-Field-Induced Rotation of Polymer Cholesteric Liquid Crystal Flakes: Mechanisms and Applications,” in *Liquid Crystals VI*, edited by I.-C. Khoo (SPIE, Bellingham, WA, 2002), Vol. 4799, pp. 96–101.

C. K. Li, F. H. Séguin, J. A. Frenje, S. Kurebayashi, R. D. Petrasso, D. D. Meyerhofer, J. M. Soures, J. A. Delettrez, V. Yu. Glebov, P. B. Radha, F. J. Marshall, S. P. Regan, S. Roberts, T. C. Sangster, and C. Stoeckl, “Effects of Fuel–Shell Mix Upon Direct-Drive, Spherical Implosions on OMEGA,” *Phys. Rev. Lett.* **89**, 165002 (2002).

C. K. Li, F. H. Séguin, J. A. Frenje, R. D. Petrasso, J. R. Rygg, S. Kurebayashi, B. E. Schwartz, R. L. Keck, J. A. Delettrez, J. M. Soures, P. W. McKenty, V. N. Goncharov, J. P. Knauer, F. J. Marshall, D. D. Meyerhofer, P. B. Radha, S. P. Regan, T. C. Sangster, W. Seka, and C. Stoeckl, “Capsule Areal-Density Asymmetries and Time Evolution Inferred from 14.7-MeV Proton Line Structure in OMEGA D³He Implosions,” *Phys. Plasmas* **10**, 1919 (2003) (invited).

J. Li, W. R. Donaldson, and T. Y. Hsiang, “Very Fast Metal–Semiconductor–Metal Ultraviolet Photodetectors on GaN with Submicron Finger Width,” *IEEE Photonics Technol. Lett.* **15**, 1141 (2003).

S. G. Lukishova, R. W. Boyd, N. Lepeshkin, and K. L. Marshall, “Cumulative Birefringence Effects of Nanosecond Laser Pulses in Dye-Doped Planar Nematic Liquid Crystal Layers,” *J. Nonlinear Opt. Phys. Mater.* **11**, 341 (2002).

A. E. Marino, J. Hayes, L. L. Gregg, and S. D. Jacobs, “Grain Decoration in Aluminum Oxynitride (ALON) from Polishing on Bound Abrasive Laps,” in *Optifab 2003* (SPIE, Bellingham, WA, 2003), Vol. TD02, pp. 81–83.

D. N. Maywar, S. Banerjee, A. Agarwal, D. F. Grosz, M. Movassaghi, A. P. Küng, and T. H. Wood, “Impact of Relaxed Dispersion Map and Gain Ripple on Ultra-Wideband 10-Gbit/s Transmission,” *Electron. Lett.* **39**, 1266 (2003).

M. Mikulics, M. Marso, P. Kordoš, S. Stanček, P. Kováč, X. Zheng, S. Wu, and R. Sobolewski, “Ultrafast and Highly Sensitive Photodetectors Fabricated on High-Energy Nitrogen-Implanted GaAs,” *Appl. Phys. Lett.* **83**, 1719 (2003).

A. Nobile, H. Reichert, R. T. Janezic, D. R. Harding, L. D. Lund, and W. T. Shmayda, “Design of the OMEGA Laser Target Chamber Tritium Removal System,” *Fusion Sci. Technol.* **43**, 522 (2003).

S. Papernov and A. W. Schmid, “Correlations Between Embedded Single Gold Nanoparticles in SiO₂ Thin Film and Nanoscale Crater Formation Induced by Pulsed-Laser Radiation,” *J. Appl. Phys.* **92**, 5720 (2002).

- S. Papernov and A. W. Schmid, "Damage Behavior of SiO₂ Thin Films Containing Gold Nanoparticles Lodged at Predetermined Distances from the Film Surface," in *Laser-Induced Damage in Optical Materials: 2002*, edited by G. J. Exarhos, A. H. Guenther, N. Kaiser, K. L. Lewis, M. J. Soileau, C. J. Stolz, A. Giesen, and H. Weber (SPIE, Bellingham, WA, 2003), Vol. 4932, pp. 66–74.
- R. D. Petrasso, J. A. Frenje, C. K. Li, F. H. Séguin, J. R. Rygg, B.-E. Schwartz, S. Kurebayashi, P. B. Radha, C. Stoeckl, J. M. Soures, J. A. Delettrez, V. Yu. Glebov, D. D. Meyerhofer, and T. C. Sangster, "Measuring Implosion Dynamics through ρR Evolution in Inertial Confinement Fusion Experiments," *Phys. Rev. Lett.* **90**, 095002 (2003).
- J. A. Randi, J. C. Lambropoulos, S. D. Jacobs, and S. N. Shafir, "Determination of Subsurface Damage in Single Crystalline Optical Materials," in *Optifab 2003* (SPIE, Bellingham, WA, 2003), Vol. TD02, pp. 84–86.
- G. Sabouret, C. Williams, and R. Sobolewski, "Resistive Switching Dynamics in Current-Biased YBa₂Cu₃O_{7-x} Microbridges Excited by Nanosecond Electrical Pulses," *Phys. Rev. B* **66**, 132501 (2002).
- T. C. Sangster, J. A. Delettrez, R. Epstein, V. Yu. Glebov, V. N. Goncharov, D. R. Harding, J. P. Knauer, R. L. Keck, J. D. Kilkenny, S. J. Loucks, L. D. Lund, R. L. McCrory, P. W. McKenty, F. J. Marshall, D. D. Meyerhofer, S. F. B. Morse, S. P. Regan, P. B. Radha, S. Roberts, W. Seka, S. Skupsky, V. A. Smalyuk, C. Sorce, J. M. Soures, C. Stoeckl, K. A. Thorp, J. A. Frenje, C. K. Li, R. D. Petrasso, F. H. Séguin, K. A. Fletcher, S. Padalino, C. Freeman, N. Izumi, J. A. Koch, R. A. Lerche, M. J. Moran, T. W. Phillips, and G. J. Schmid, "Direct-Drive Cryogenic Target Implosion Performance on OMEGA," *Phys. Plasmas* **10**, 1937 (2003) (invited).
- A. E. Schoeffler, L. L. Gregg, J. M. Schoen, E. M. Fess, M. Hakiel, and S. D. Jacobs, "Pre-Polishing on a CNC Platform with Bound Abrasive Contour Tools," in *Optifab 2003* (SPIE, Bellingham, WA, 2003), Vol. TD02, pp. 24–27.
- F. H. Séguin, J. A. Frenje, C. K. Li, D. G. Hicks, S. Kurebayashi, J. R. Rygg, B.-E. Schwartz, R. D. Petrasso, S. Roberts, J. M. Soures, D. D. Meyerhofer, T. C. Sangster, J. P. Knauer, C. Sorce, V. Yu. Glebov, C. Stoeckl, T. W. Phillips, R. J. Leeper, K. Fletcher, and S. Padalino, "Spectrometry of Charged Particles from Inertial Confinement Fusion Plasmas," *Rev. Sci. Instrum.* **74**, 975 (2003).
- W. Seka, H. A. Baldis, J. Fuchs, S. P. Regan, D. D. Meyerhofer, C. Stoeckl, B. Yaakobi, R. S. Craxton, and R. W. Short, "Multibeam Stimulated Brillouin Scattering from Hot, Solid-Target Plasmas," *Phys. Rev. Lett.* **89**, 175002 (2002).
- M. D. Skeldon, "Optical Pulse-Shaping System Based on an Electro-Optic Modulator Driven by an Aperture-Coupled-Stripline Electrical-Waveform Generator," *J. Opt. Soc. Am. B* **19**, 2423 (2002).
- V. A. Smalyuk, J. A. Delettrez, S. B. Dumanis, V. Yu. Glebov, V. N. Goncharov, J. P. Knauer, F. J. Marshall, D. D. Meyerhofer, P. B. Radha, S. P. Regan, S. Roberts, T. C. Sangster, S. Skupsky, J. M. Soures, C. Stoeckl, R. P. J. Town, B. Yaakobi, J. A. Frenje, C. K. Li, R. D. Petrasso, F. H. Séguin, D. L. McCrory, R. C. Mancini, and J. A. Koch, "Hydrodynamic Growth of Shell Modulations in the Deceleration Phase of Spherical Direct-Drive Implosions," *Phys. Plasmas* **10**, 1861 (2003) (invited).
- V. A. Smalyuk, S. B. Dumanis, F. J. Marshall, J. A. Delettrez, D. D. Meyerhofer, S. P. Regan, T. C. Sangster, B. Yaakobi, and J. A. Koch, "Radial Structure of Shell Modulations Near Peak Compression of Spherical Implosions," *Phys. Plasmas* **10**, 830 (2003).
- V. A. Smalyuk, P. B. Radha, J. A. Delettrez, V. Yu. Glebov, V. N. Goncharov, D. D. Meyerhofer, S. P. Regan, S. Roberts, T. C. Sangster, J. M. Soures, C. Stoeckl, J. A. Frenje, C. K. Li, R. D. Petrasso, and F. H. Séguin, "Time-Resolved Areal-Density Measurements with Proton Spectroscopy in Spherical Implosions," *Phys. Rev. Lett.* **90**, 135002 (2003).
- R. Sobolewski, A. Verevkin, G. N. Gol'tsman, A. Lipatov, and K. Wilsher, "Ultrafast Superconducting Single-Photon Optical Detectors and Their Applications," *IEEE Trans. Appl. Supercond.* **13**, 1151 (2003).
- E. A. Startsev and C. J. McKinstrie, "Particle-in-Cell Simulations of Ponderomotive Particle Acceleration in a Plasma," *Phys. Plasmas* **10**, 2552 (2003).

- J. L. Sternal, S. N. Shafirir, J. A. Randi, L. L. Gregg, and S. D. Jacobs, "Refractive Index Anisotropy in Optics Using a Birefringence Mapper," in *Optifab 2003* (SPIE, Bellingham, WA, 2003), Vol. TD02, pp. 125–127.
- C. Stoeckl, R. E. Bahr, B. Yaakobi, W. Seka, S. P. Regan, R. S. Craxton, J. A. Delettrez, R. W. Short, J. Myatt, A. V. Maximov, and H. A. Baldis, "Multibeam Effects on Fast-Electron Generation from Two-Plasmon-Decay Instability," *Phys. Rev. Lett.* **90**, 235002 (2003).
- C. Stoeckl, V. Yu. Glebov, S. Roberts, T. C. Sangster, R. A. Lerche, R. L. Griffith, and C. Sorce, "Ten-Inch Manipulator-Based Neutron Temporal Diagnostic for Cryogenic Experiments on OMEGA," *Rev. Sci. Instrum.* **74**, 1713 (2003).
- C. Stoeckl, V. Yu. Glebov, J. D. Zuegel, D. D. Meyerhofer, and R. A. Lerche, "Wide-Dynamic-Range 'Neutron Bang Time' Detector on OMEGA," *Rev. Sci. Instrum.* **73**, 3796 (2002).
- A. Sunahara, J. A. Delettrez, C. Stoeckl, R. W. Short, and S. Skupsky, "Time-Dependent Electron Thermal Flux Inhibition in Direct-Drive Laser Implosion," *Phys. Rev. Lett.* **91**, 095003 (2003).
- F.-Y. Tsai, T. N. Blanton, D. R. Harding, and S. H. Chen, "Temperature Dependence of the Properties of Vapor-Deposited Polyimide," *J. Appl. Phys.* **93**, 3760 (2003).
- F.-Y. Tsai, D. R. Harding, S. H. Chen, and T. N. Blanton, "High-Permeability Fluorinated Polyimide Microcapsules by Vapor-Deposition Polymerization," *Polymer* **44**, 995 (2003).
- R. Varshneya, J. E. DeGroot, L. L. Gregg, and S. D. Jacobs, "Characterizing Optical Polishing Pitch," in *Optifab 2003* (SPIE, Bellingham, WA, 2003), Vol. TD02, pp. 87–89.
- L. J. Waxer, V. Bagnoud, I. A. Begishev, M. J. Guardalben, J. Puth, and J. D. Zuegel, "High-Conversion-Efficiency, Optical Parametric Chirped-Pulse-Amplification System Using Spatiotemporally Shaped Pump Pulses," *Opt. Lett.* **28**, 1245 (2003).
- Y. Xu, M. Khafizov, A. Plecenik, P. Kús, L. Satrapinsky, and R. Sobolewski, "Femtosecond Optical Characterization of MgB₂ Superconducting Thin Films," *IEEE Trans. Appl. Supercond.* **13**, 3316 (2003).
- B. Yaakobi, F. J. Marshall, T. R. Boehly, R. P. J. Town, and D. D. Meyerhofer, "Extended X-Ray Absorption Fine Structure Experiments Using a Laser-Imploded Target as a Radiation Source," *J. Opt. Soc. Am. B* **20**, 238 (2003).
- J. Zhang, W. Slysz, A. Pearlman, A. Verevkin, R. Sobolewski, O. Okunev, G. Chulkova, and G. N. Gol'tsman, "Time Delay of the Resistive-State Formation in Superconducting NbN Stripes Excited by Single Optical Photons," *Phys. Rev. B* **67**, 132508 (2003).
- J. Zhang, W. Slysz, A. Verevkin, O. Okunev, G. Chulkova, A. Korneev, A. Lipatov, G. N. Gol'tsman, and R. Sobolewski, "Response-Time Characterization of NbN Superconducting Single-Photon Detectors," *IEEE Trans. Appl. Supercond.* **13**, 180 (2003).
- X. Zheng, S. Wu, R. Sobolewski, R. Adam, M. Mikulics, P. Kordoš, and M. Siegel, "Electro-Optic Sampling System with a Single-Crystal 4-N, N-Dimethylamino-4'-N'-Methyl-Stilbazolium Tosylate Sensor," *Appl. Phys. Lett.* **82**, 2383 (2003).
- X. Zheng, Y. Xu, R. Sobolewski, R. Adam, M. Mikulics, M. Siegel, and P. Kordos, "Femtosecond Response of a Free-standing LT-GaAs Photoconductive Switch," *Appl. Opt.* **42**, 1726 (2003).

OMEGA External User Publications

- P. Amendt, R. E. Turner, and O. L. Landen, "Hohlraum-Driven High-Convergence Implosion Experiments with Multiple Beam Cones on the OMEGA Laser Facility," *Phys. Rev. Lett.* **89**, 165001 (2002).
- C. A. Back, J. Davis, J. Grun, L. J. Suter, O. L. Landen, W. W. Hsing, and M. C. Miller, "Multi-keV X-Ray Conversion Efficiency in Laser-Produced Plasmas," *Phys. Plasmas* **10**, 2047 (2003).
- C. W. Barnes, S. H. Batha, A. M. Dunne, G. R. Magelssen, S. Rothman, R. D. Day, N. E. Elliott, D. A. Haynes, R. L. Holmes, J. M. Scott, D. L. Tubbs, D. L. Youngs, T. R. Boehly, and P. Jaanimagi, "Observation of Mix in a Compressible Plasma in a Convergent Cylindrical Geometry," *Phys. Plasmas* **9**, 4431 (2002).
- S. H. Batha, C. W. Barnes, and C. R. Christensen, "Backlighter Predictive Capability," *Rev. Sci. Instrum.* **74**, 2174 (2003).
- C. R. Christensen, C. W. Barnes, G. L. Morgan, M. Wilke, and D. C. Wilson, "First Results of Pinhole Neutron Imaging for Inertial Confinement Fusion," *Rev. Sci. Instrum.* **74**, 2690 (2003).
- B. I. Cohen, C. J. McKinstrie, and E. A. Startsev, "Forward and Backward Stimulated Brillouin Scattering in a Nonuniform Plasma," *Phys. Plasmas* **9**, 4375 (2002).
- L. Disdier, A. Rouyer, A. Fedotoff, J.-L. Bourgade, F. J. Marshall, V. Yu. Glebov, and C. Stoeckl, "Neutron Imaging of ICF Target Plasmas," *Rev. Sci. Instrum.* **74**, 1832 (2003) (invited).
- L. Divol, R. L. Berger, B. I. Cohen, E. A. Williams, A. B. Langdon, B. F. Lasinski, D. H. Froula, and S. H. Glenzer, "Modeling the Nonlinear Saturation of Stimulated Brillouin Backscatter in Laser Heated Plasmas," *Phys. Plasmas* **10**, 1822 (2003).
- J. A. Frenje, C. K. Li, F. H. Séguin, S. Kurebayashi, R. D. Petrasso, J. M. Soures, J. Delettrez, V. Yu. Glebov, D. D. Meyerhofer, P. B. Radha, S. Roberts, T. C. Sangster, S. Skupsky, and C. Stoeckl, "Measurements of Fuel and Shell Areal Densities of OMEGA Capsule Implosions Using Elastically Scattered Protons," *Phys. Plasmas* **9**, 4719 (2002).
- S. G. Glendinning, J. Bolstad, D. G. Braun, M. J. Edwards, W. W. Hsing, B. F. Lasinski, H. Louis, A. Miles, J. Moreno, T. A. Peyser, B. A. Remington, H. F. Robey, E. J. Turano, C. P. Verdon, and Y. Zhou, "Effect of Shock Proximity on Richtmyer-Meshkov Growth," *Phys. Plasmas* **10**, 1931 (2003).
- S. H. Glenzer, G. Gregori, R. W. Lee, F. J. Rogers, S. W. Pollaine, and O. L. Landen, "Demonstration of Spectrally Resolved X-Ray Scattering in Dense Plasmas," *Phys. Rev. Lett.* **90**, 175002 (2003).
- S. H. Glenzer, G. Gregori, F. J. Rogers, D. H. Froula, S. W. Pollaine, R. S. Wallace, and O. L. Landen, "X-Ray Scattering from Solid Density Plasmas," *Phys. Plasmas* **10**, 2433 (2003).
- G. Gregori, S. H. Glenzer, R. W. Lee, D. G. Hicks, J. Pasley, G. W. Collins, P. Celliers, M. Bastea, J. Eggert, S. M. Pollaine, and O. L. Landen, "Calculations and Measurements of X-Ray Thomson Scattering Spectra in Warm Dense Matter," in *Spectral Line Shapes, AIP Conference Proceedings 645*, edited by C. A. Back (American Institute of Physics, New York, 2002), pp. 359–368.
- D. G. Hicks, P. M. Celliers, G. W. Collins, J. H. Eggert, and S. J. Moon, "Shock-Induced Transformation of Al_2O_3 and LiF into Semiconducting Liquids," *Phys. Rev. Lett.* **91**, 035502 (2003).
- J. P. Holder, K. W. Piston, D. K. Bradley, P. M. Bell, A. K. L. Dymoke-Bradshaw, and J. D. Hares, "Further Development of a Single Line of Sight X-Ray Framing Camera," *Rev. Sci. Instrum.* **74**, 2191 (2003).
- N. Izumi, R. A. Lerche, T. W. Phillips, G. J. Schmid, M. J. Moran, J. A. Koch, H. Azechi, and T. C. Sangster, "Development of a Gated Scintillation Fiber Neutron Detector for Areal Density Measurements of Inertial Confinement Fusion Capsules," *Rev. Sci. Instrum.* **74**, 1722 (2003).
- D. H. Kalantar, J. Belak, E. Bringa, K. Budil, M. Caturla, J. Colvin, M. Kumar, K. T. Lorenz, R. E. Rudd, J. Stölken, A. M. Allen, K. Rosolankova, J. S. Wark, M. A. Meyers, and M. Schneider, "High-Pressure, High-Strain-Rate Lattice Response of Shocked Materials," *Phys. Plasmas* **10**, 1569 (2003).

- D. H. Kalantar, E. Bringa, M. Caturla, J. Colvin, K. T. Lorenz, M. Kumar, J. Stölken, A. M. Allen, K. Rosolankova, J. S. Wark, M. A. Meyers, M. Schneider, and T. R. Boehly, "Multiple Film Plane Diagnostic for Shocked Lattice Measurements," *Rev. Sci. Instrum.* **74**, 1929 (2003) (invited).
- P. A. Keiter, R. P. Drake, T. S. Perry, H. F. Robey, B. A. Remington, C. A. Iglesias, R. J. Wallace, and J. Knauer, "Observation of a Hydrodynamically Driven, Radiative-Pre-cursor Shock," *Phys. Rev. Lett.* **89**, 165003 (2002).
- R. K. Kirkwood, J. D. Moody, A. B. Langdon, B. I. Cohen, E. A. Williams, M. R. Dorr, J. A. Hittinger, R. Berger, P. E. Young, L. J. Suter, L. Divol, S. H. Glenzer, O. L. Landen, and W. Seka, "Observation of Saturation of Energy Transfer Between Copropagating Beams in a Flowing Plasma," *Phys. Rev. Lett.* **89**, 215003 (2002).
- G. A. Kyrala, K. Klare, and J. Workman, "Optimizing Area-Backlighter Performance in a Difficult Geometry," *Rev. Sci. Instrum.* **74**, 2182 (2003).
- N. E. Lanier, C. W. Barnes, S. H. Batha, R. D. Day, G. R. Magelssen, J. M. Scott, A. M. Dunne, K. W. Parker, and S. D. Rothman, "Multimode Seeded Richtmyer–Meshkov Mixing in a Convergent, Compressible, Miscible Plasma System," *Phys. Plasmas* **10**, 1816 (2003).
- R. A. Lerche, N. Izumi, R. K. Fisher, L. Disdier, J.-L. Bourgade, A. Rouyer, P. A. Jaanimagi, and T. C. Sangster, "Neutron Images Recorded with High-Resolution Bubble Detectors," *Rev. Sci. Instrum.* **74**, 1709 (2003).
- C. K. Li, F. H. Séguin, J. A. Frenje, S. Kurebayashi, R. D. Petrasso, D. D. Meyerhofer, J. M. Soures, J. A. Delettrez, V. Yu. Glebov, P. B. Radha, S. P. Regan, S. Roberts, T. C. Sangster, and C. Stoeckl, "Effects of Fuel–Shell Mix upon Direct-Drive, Spherical Implosions on OMEGA," *Phys. Rev. Lett.* **89**, 165002 (2002).
- C. K. Li, F. H. Séguin, J. A. Frenje, R. D. Petrasso, R. Rygg, S. Kurebayashi, B. Schwartz, R. L. Keck, J. A. Delettrez, J. M. Soures, P. W. McKenty, V. N. Goncharov, J. P. Knauer, F. J. Marshall, D. D. Meyerhofer, P. B. Radha, S. P. Regan, T. C. Sangster, W. Seka, and C. Stoeckl, "Capsule-Areal-Density Asymmetries Inferred from 14.7-MeV Deuterium–Helium Protons in Direct-Drive OMEGA Implosions," *Phys. Plasmas* **10**, 1919 (2003).
- R. C. Mancini, L. A. Welsler, I. E. Golovkin, Y. Ochi, K. Fujita, H. Nishimura, R. Butzbach, I. Uschmann, E. Förster, F. J. Marshall, J. A. Delettrez, J. A. Koch, H. E. Dalhed, R. W. Lee, and L. Klein, "Spectroscopic Determination of Core Gradients in Inertial Confinement Fusion Implosions," in *Atomic Processes in Plasmas, AIP Conference Proceedings 635*, edited by D. R. Schultz, F. W. Meyer, and F. Ownby (American Institute of Physics, New York, 2002), pp. 61–70.
- M. J. Moran, S. W. Haan, S. P. Hatchett, N. Izumi, J. A. Koch, R. A. Lerche, and T. W. Phillips, "Energy-Resolved Neutron Imaging for Inertial Confinement Fusion," *Rev. Sci. Instrum.* **74**, 1701 (2003).
- R. E. Olson, R. J. Leeper, S. C. Dropinski, L. P. Mix, G. A. Rochau, S. H. Glenzer, O. S. Jones, L. J. Suter, J. L. Kaae, C. H. Shearer, and J. N. Smith, "Time and Spatially Resolved Measurements of X-Ray Burnthrough and Re-Emission in Au and Au:Dy:Nd Foils," *Rev. Sci. Instrum.* **74**, 2186 (2003).
- R. D. Petrasso, J. A. Frenje, C. K. Li, F. H. Séguin, J. R. Rygg, B. E. Schwartz, S. Kurebayashi, P. B. Radha, C. Stoeckl, J. M. Soures, J. Delettrez, V. Yu. Glebov, D. D. Meyerhofer, and T. C. Sangster, "Measuring Implosion Dynamics through ρR Evolution in Inertial-Confinement Fusion Experiments," *Phys. Rev. Lett.* **90**, 095002 (2003).
- H. F. Robey, Ye Zhou, A. C. Buckingham, P. Keiter, B. A. Remington, and R. P. Drake, "The Time Scale for the Transition to Turbulence in a High Reynolds Number, Accelerated Flow," *Phys. Plasmas* **10**, 614 (2003).
- G. J. Schmid, R. L. Griffith, N. Izumi, J. A. Koch, R. A. Lerche, M. J. Moran, T. W. Phillips, R. E. Turner, V. Yu. Glebov, T. C. Sangster, and C. Stoeckl, "CVD Diamond as a High Bandwidth Neutron Detector for Inertial Confinement Fusion Diagnostics," *Rev. Sci. Instrum.* **74**, 1828 (2003).
- F. H. Séguin, J. A. Frenje, C. K. Li, D. G. Hicks, S. Kurebayashi, J. R. Rygg, B.-E. Schwartz, R. D. Petrasso, S. Roberts, J. M. Soures, D. D. Meyerhofer, T. C. Sangster, J. P. Knauer, C. Sorce, V. Yu. Glebov, C. Stoeckl, T. W. Phillips, R. J. Leeper, K. Fletcher, and S. P. Padalino, "Spectrometry of Charged Particles from Inertial-Confinement-Fusion Plasmas," *Rev. Sci. Instrum.* **74**, 975 (2003).

R. E. Turner, P. A. Amendt, O. L. Landen, L. J. Suter, R. J. Wallace, and B. A. Hammel, "Role of Laser Beam Geometry in Improving Symmetry and Performance for Indirect-Drive Inertial Confinement Fusion," *Phys. Plasmas* **10**, 2429 (2003).

L. A. Welser, R. C. Mancini, I. E. Golovkin, J. A. Koch, H. E. Dalhed, R. W. Lee, F. J. Marshall, J. A. Delettrez, and L. Klein, "Spectroscopic Determination of Gradients in Indirect-Drive OMEGA Implosion Cores," in *Spectral Line Shapes, AIP Conference Proceedings 645*, edited by C. A. Back (American Institute of Physics, New York, 2002), pp. 294–301.

L. A. Welser, R. C. Mancini, J. A. Koch, S. Dalhed, R. W. Lee, I. E. Golovkin, F. Marshall, J. Delettrez, and L. Klein, "Processing of Multi-Monochromatic X-Ray Images from Indirect Drive Implosions at OMEGA," *Rev. Sci. Instrum.* **74**, 1951 (2003).

L. A. Welser, R. C. Mancini, J. A. Koch, N. Izumi, H. Dalhed, H. Scott, T. W. Barbee, Jr., R. W. Lee, I. E. Golovkin, F. Marshall, J. Delettrez, and L. Klein, "Analysis of the Spatial Structure of Inertial Confinement Fusion Implosion Cores at OMEGA," *J. Quant. Spectrosc. Radiat. Transf.* **81**, 487 (2003).

D. C. Wilson, C. R. Christensen, G. L. Morgan, M. D. Wilke, P. A. Bradley, and P. L. Gobby, "Goals for and Design of a Neutron Pinhole Imaging System for Ignition Capsules," *Rev. Sci. Instrum.* **74**, 1705 (2003).

Ye Zhou, B. A. Remington, H. F. Robey, A. W. Cook, S. G. Glendinning, A. Dimits, A. C. Buckingham, G. B. Zimmerman, E. W. Burke, T. A. Peyser, W. Cabot, and D. Eliason, "Progress in Understanding Turbulent Mixing Induced by Rayleigh–Taylor and Richtmyer–Meshkov Instabilities," *Phys. Plasmas* **10**, 1883 (2003).

Conference Presentations

R. L. McCrory, D. D. Meyerhofer, S. J. Loucks, S. Skupsky, R. E. Bahr, R. Betti, T. R. Boehly, R. S. Craxton, T. J. B. Collins, J. A. Delettrez, W. R. Donaldson, R. Epstein, J. A. Frenje, V. Yu. Glebov, V. N. Goncharov, D. R. Harding, P. A. Jaanimagi, R. L. Keck, J. H. Kelly, T. J. Kessler, J. P. Knauer, C. K. Li, L. D. Lund, J. A. Marozas, P. W. McKenty, F. J. Marshall, S. F. B. Morse, R. D. Petrasso, P. B. Radha, S. P. Regan, S. Roberts, T. C. Sangster, F. H. Séguin, W. Seka, V. A. Smalyuk, C. Sorce, J. M. Soures, C. Stoeckl, R. P. J. Town, B. Yaakobi, and J. D. Zuegel, "Progress in Direct-Drive Inertial Confinement Fusion Research at the Laboratory for Laser Energetics," 19th IAEA Fusion Energy Conference, Lyon, France, 14–19 October 2002.

The following presentations were made at the 44th Annual Meeting of the APS Division of Plasma Physics, Orlando, FL, 11–15 November 2002:

K. Anderson, R. Betti, T. J. B. Collins, M. M. Marinak, and S. W. Haan, "Adiabatic Shaping of ICF Capsules Using Ramped Pressure Profiles."

R. Betti and K. Anderson, "Theory of Laser-Induced Adiabatic Shaping in Inertial Fusion Implosions."

T. R. Boehly, T. J. B. Collins, E. Vianello, D. Jacobs-Perkins, D. D. Meyerhofer, G. W. Collins, P. M. Celliers, D. G. Hicks, and R. Cauble, "Deuterium Equation-of-State Experiments on OMEGA."

T. J. B. Collins, S. Skupsky, V. N. Goncharov, R. Betti, P. W. McKenty, and P. B. Radha, "High-Gain, Direct-Drive Foam Target Designs for the National Ignition Facility."

R. S. Craxton, S. P. Regan, J. A. Delettrez, D. D. Meyerhofer, T. C. Sangster, W. Seka, and B. Yaakobi, "Microdot Expansion Trajectories in Long-Scale-Length Plasmas on OMEGA."

J. A. Delettrez, J. P. Knauer, W. Seka, P. A. Jaanimagi, and C. Stoeckl, "Numerical Investigation of Laser Absorption and Drive Experiments of CH Spherical Shells on the OMEGA Laser."

R. Epstein, T. J. B. Collins, J. A. Delettrez, V. N. Goncharov, P. W. McKenty, P. B. Radha, and S. Skupsky, "Modeling of Fuel-Pusher Mix Effects in 1-D Simulations of Cryogenic, All-DT Ignition Capsule Implosions."

J. A. Frenje, C. K. Li, F. H. Séguin, R. D. Petrasso, J. M. Soures, J. A. Delettrez, V. Yu. Glebov, D. D. Meyerhofer, P. B. Radha, T. C. Sangster, C. Stoeckl, N. Hoffmann, and D. Wilson, "Effects of Fuel-Shell Mix on Direct-Drive Implosions of ^3He -Gas-Filled, CD-Layered Plastic Capsules on OMEGA."

T. A. Gardiner, L. Guazzotto, R. Betti, and J. Manickam, "Axisymmetric MHD Equilibria with Arbitrary Flow and Applications to NSTX."

V. Yu. Glebov, C. Stoeckl, T. C. Sangster, J. A. Delettrez, P. W. McKenty, and P. B. Radha, "Neutron Burn History Measurements of D_2 Cryogenic Targets on OMEGA."

V. N. Goncharov, "Improved Performance of Direct-Drive ICF Target Designs with Adiabatic Shaping Using an Intensity Picket" (invited).

O. V. Gotchev, V. N. Goncharov, P. A. Jaanimagi, J. P. Knauer, and D. D. Meyerhofer, "Experiments on Dynamic Overpressure Stabilization of Ablative Richtmyer-Meshkov Growth in ICF Targets on OMEGA."

L. Guazzotto and R. Betti, "Two-Dimensional MHD Simulations of Tokamak Plasmas with Poloidal Flow."

I. V. Igumenshchev, V. N. Goncharov, P. W. McKenty, and S. Skupsky, "Simulations of Cryogenic Target Implosions on OMEGA."

J. P. Knauer, V. N. Goncharov, P. W. McKenty, T. C. Sangster, R. Betti, V. Yu. Glebov, F. J. Marshall, P. B. Radha, C. Stoeckl, J. A. Frenje, C. K. Li, R. D. Petrasso, and F. H. Séguin, "Improved Performance of Direct-Drive Implosions with a Laser-Shaped Adiabatic."

M. V. Kozlov and C. J. McKinstrie, "SBS in Multiple-Species Plasmas."

S. Kurebayashi, J. R. Rygg, B. E. Schwartz, J. DeCiantis, S. Burke, J. A. Frenje, C. K. Li, F. H. Séguin, R. D. Petrasso, V. Yu. Glebov, J. M. Soures, D. D. Meyerhofer, S. Roberts, T. C. Sangster, C. Stoeckl, N. Hoffmann, and D. Wilson,

"Stopping Power and Secondary Nuclear Production in OMEGA Implosions."

C. K. Li, F. H. Séguin, J. A. Frenje, S. Kurebayashi, J. R. Rygg, B. E. Schwartz, R. D. Petrasso, R. L. Keck, J. A. Delettrez, P. W. McKenty, F. J. Marshall, D. D. Meyerhofer, P. B. Radha, T. C. Sangster, J. M. Soures, and C. Stoeckl, "Capsule Areal-Density Asymmetries and Time Evolution Inferred from 14.7-MeV Proton Line Structure in OMEGA D^3He Implosions" (invited).

J. A. Marozas and P. B. Radha, "A SSD Model for Arbitrary Pulse Shapes Used in the Multidimensional Hydrodynamic Code *DRACO*."

F. J. Marshall, P. W. McKenty, T. J. Kessler, R. Forties, J. H. Kelly, and L. J. Waxer, "Optimized Direct-Drive Uniformity."

A. V. Maximov, J. Myatt, and R. W. Short, "Modeling of Laser-Plasma Interaction Near the Critical Density."

P. W. McKenty, L. M. Elasky, D. R. Harding, F. J. Marshall, D. D. Meyerhofer, P. B. Radha, T. C. Sangster, S. Skupsky, R. L. McCrory, J. A. Frenje, C. K. Li, R. D. Petrasso, and F. H. Séguin, "Numerical Investigation into the Sensitivity of OMEGA Cryogenic Capsule Implosions to Low-Order-Mode Ice Perturbations."

D. D. Meyerhofer, J. A. Delettrez, D. R. Harding, J. D. Kilkenny, S. J. Loucks, R. L. McCrory, P. W. McKenty, S. F. B. Morse, T. C. Sangster, S. Skupsky, and C. Stoeckl, "Direct-Drive Fast-Ignition Research at LLE."

J. Myatt, A. V. Maximov, and R. W. Short, "Realistic Simulations of Stimulated Brillouin Scattering in Long-Scale-Length, Direct-Drive Experiments on OMEGA."

R. D. Petrasso, J. A. Frenje, F. H. Séguin, C. K. Li, B. E. Schwartz, C. Stoeckl, P. B. Radha, J. A. Delettrez, D. D. Meyerhofer, S. Roberts, T. C. Sangster, and J. M. Soures, "Proton and Alpha Core Imaging of OMEGA D^3He Implosions."

P. B. Radha, T. J. B. Collins, J. A. Delettrez, R. Epstein, V. Yu. Glebov, V. N. Goncharov, J. A. Marozas, P. W. McKenty, D. D. Meyerhofer, T. C. Sangster, C. Stoeckl, S. Skupsky, J. M. Soures, V. A. Smalyuk, J. A. Frenje, C. K. Li, R. D. Petrasso, F. H. Séguin, and R. P. J. Town, "The Effect of Laser Imprint on Target Performance in Direct-Drive Implosions on OMEGA."

- S. P. Regan, J. A. Delettrez, F. J. Marshall, J. M. Soures, V. A. Smalyuk, B. Yaakobi, R. Epstein, V. Yu. Glebov, P. A. Jaanimagi, D. D. Meyerhofer, P. B. Radha, T. C. Sangster, W. Seka, S. Skupsky, C. Stoeckl, D. A. Haynes, Jr., J. A. Frenje, C. K. Li, R. D. Petrasso, and F. H. Séguin, "Experimental Investigation of Fuel-Pusher Mix in Direct-Drive Implosions on OMEGA."
- J. R. Rygg, S. Kurebayashi, B. E. Schwartz, J. DeCiantis, S. Burke, J. A. Frenje, C. K. Li, F. H. Séguin, R. D. Petrasso, J. A. Delettrez, V. Yu. Glebov, V. N. Goncharov, D. D. Meyerhofer, P. B. Radha, S. Roberts, T. C. Sangster, J. M. Soures, C. Stoeckl, N. Hoffmann, and D. Wilson, "Time Evolution of OMEGA Direct-Drive D³He Capsule Implosions Inferred from Charged-Particle Spectra."
- T. C. Sangster, J. A. Delettrez, R. Epstein, V. Yu. Glebov, D. R. Harding, J. P. Knauer, R. L. Keck, S. J. Loucks, L. D. Lund, R. L. McCrory, P. W. McKenty, F. J. Marshall, D. D. Meyerhofer, S. F. B. Morse, S. P. Regan, P. B. Radha, S. Roberts, W. Seka, S. Skupsky, V. A. Smalyuk, C. Sorce, J. M. Soures, R. P. J. Town, J. A. Frenje, C. K. Li, R. D. Petrasso, F. H. Séguin, K. A. Fletcher, S. Padalino, C. Freeman, N. Izumi, J. A. Koch, R. A. Lerche, M. J. Moran, T. W. Phillips, and G. J. Schmid, "Direct-Drive Cryogenic Target Implosion Performance on OMEGA" (invited).
- B. E. Schwartz, F. H. Séguin, J. A. Frenje, R. D. Petrasso, C. K. Li, P. B. Radha, D. D. Meyerhofer, S. Roberts, T. C. Sangster, J. M. Soures, and C. Culligan, "Proton and Alpha Core Imaging Spectroscopy of Direct-Drive OMEGA Implosions."
- F. H. Séguin, R. D. Petrasso, J. A. Frenje, C. K. Li, J. R. Rygg, C. Stoeckl, P. B. Radha, J. A. Delettrez, V. Yu. Glebov, D. D. Meyerhofer, T. C. Sangster, and J. M. Soures, "Time Evolution and Asymmetries of OMEGA Direct-Drive D³He Capsule Implosions Inferred from 3.0- and 14.7-MeV Protons and 3.6-MeV Alphas."
- W. Seka, R. S. Craxton, J. Myatt, A. V. Maximov, D. D. Meyerhofer, S. P. Regan, R. W. Short, A. Simon, C. Stoeckl, R. E. Bahr, and H. Baldis, "SBS in Long-Scale Length Plasmas for Direct-Drive ICF: Comparing Experiments with Simulations."
- R. W. Short, "A Linear Model of Anomalous Stimulated Raman Scattering and Electron Acoustic Waves in Laser-Produced Plasmas."
- A. Simon and C. Stoeckl, "A Model of Hot-Electron Signals with Overlapping Pump Beams."
- V. A. Smalyuk, J. A. Delettrez, V. Yu. Glebov, V. N. Goncharov, J. P. Knauer, F. J. Marshall, D. D. Meyerhofer, P. B. Radha, S. P. Regan, S. Roberts, T. C. Sangster, S. Skupsky, J. M. Soures, C. Stoeckl, R. P. J. Town, B. Yaakobi, J. A. Frenje, C. K. Li, R. D. Petrasso, F. H. Séguin, D. L. McCrorey, and R. C. Mancini, "Hydrodynamic Growth of Shell Modulations in the Deceleration Phase of Spherical Direct-Drive Implosions" (invited).
- J. M. Soures, F. J. Marshall, J. A. Delettrez, V. Yu. Glebov, D. D. Meyerhofer, S. Roberts, T. C. Sangster, J. A. Frenje, C. K. Li, and R. D. Petrasso, "Offset, Direct-Drive, D₂-Filled CH Capsules."
- C. Stoeckl, R. E. Bahr, R. S. Craxton, S. P. Regan, W. Seka, and B. Yaakobi, "Multiple-Beam Effects on the Fast-Electron Generation due to the Two-Plasmon-Decay Instability."
- B. Yaakobi, T. R. Boehly, F. J. Marshall, D. D. Meyerhofer, R. Epstein, B. A. Remington, and S. M. Pollaine, "EXAFS Detection of Shock-Compressed Titanium."
- The following presentations were made at the 6th Workshop on Fast Ignition of Fusion Targets, St. Pete Beach, FL, 16–19 November 2002:
- J. A. Delettrez, S. Skupsky, C. Stoeckl, and P. B. Radha, "Transport of Relativistic Electrons for Modeling Fast Ignition in the 2-D Hydrocode *DRACO*."
- J. Myatt, A. V. Maximov, and R. W. Short, "Fast Electron Transport in Dense Plasmas in the Context of Fast-Ignition Studies at LLE."
- C. Stoeckl, J. A. Delettrez, A. V. Maximov, J. Myatt, P. W. McKenty, S. F. B. Morse, L. J. Waxer, T. C. Sangster, D. D. Meyerhofer, and J. D. Kilkenny, "Integrated Fast-Ignitor Experiments on the Proposed OMEGA EP Facility at LLE."
- S. D. Jacobs, "Innovations in Polishing of Precision Optics," EOS 2003 International Workshop on Extreme Optics and Sensors, Tokyo, Japan, 14–17 January 2003 (invited).

J. Li, W. R. Donaldson, and T. Y. Hsiang, "Very Fast Metal–Semiconductor–Metal Ultraviolet Photodetectors on GaN with Submicron Finger Width," *Ultrafast Electronics and Optoelectronics*, Washington, DC, 15–17 January 2003.

I. A. Begishev, V. Bagnoud, M. J. Guardalben, L. J. Waxer, J. Puth, and J. D. Zuegel, "Optimization of an Optical Parametric Chirped-Pulse Amplification System for the OMEGA EP Laser System," *2003 Advanced Solid-State Photonics*, San Antonio, TX, 2–5 February 2003.

The following presentations were made at the 5th International Workshop on Laser Plasma Interaction Physics, Banff, Alberta, Canada, 19–22 February 2003:

W. Seka, H. Baldis, S. Depierreux, R. S. Craxton, S. P. Regan, C. Stoeckl, and R. W. Short, "Experimental Observations of the Landau Cutoff for Electron Plasma Waves Driven by the TPD Instability."

R. W. Short, "On the Role of Electron-Acoustic Waves in Two-Plasmon Decay."

C. Dorrer and D. N. Maywar, "800-GHz RF Spectrum Analyzer for Optical Signals," *Optical Fiber Communication*, Atlanta, GA, 23–28 March 2003.

R. L. McCrory, D. D. Meyerhofer, S. J. Loucks, S. Skupsky, R. E. Bahr, R. Betti, T. R. Boehly, R. S. Craxton, T. J. B. Collins, J. A. Delettrez, W. R. Donaldson, R. Epstein, J. A. Frenje, V. Yu. Glebov, V. N. Goncharov, D. R. Harding, P. A. Jaanimagi, R. L. Keck, J. H. Kelly, T. J. Kessler, J. D. Kilkenny, J. P. Knauer, C. K. Li, L. D. Lund, J. A. Marozas, P. W. McKenty, F. J. Marshall, S. F. B. Morse, R. D. Petrasso, P. B. Radha, S. P. Regan, S. Roberts, T. C. Sangster, F. H. Séguin, W. Seka, V. A. Smalyuk, J. M. Soures, C. Stoeckl, K. A. Thorp, B. Yaakobi, and J. D. Zuegel, "Direct-Drive Inertial Fusion Research at the University of Rochester's Laboratory for Laser Energetics: A Review," *5th Symposium of the Current Trends in International Fusion Research: A Review*, Washington, DC, 24–28 March 2003.

The following presentations were made at the Workshop on Experience in the Management of Wastes from Fusion Facilities, Abington, United Kingdom, 25–26 March 2003:

W. T. Shmayda, "Metal Decontamination."

W. T. Shmayda, "Recovery and Enrichment of Tritium from Organic and Aqueous Liquid Waste Streams."

S. G. Lukishova, A. W. Schmid, A. J. McNamara, R. W. Boyd, and C. R. Stroud, "Dye-Doped Cholesteric-Liquid-Crystal Single Photon Source," *NIST Workshop on Single Photon Detectors, Applications, and Measurement Methods*, Gaithersburg, MD, 31 March–1 April 2003.

T. C. Sangster, "New Results in Direct-Drive Inertial Confinement Fusion," *APS April 2003 Meeting*, Philadelphia, PA, 5–8 April 2003.

Q. Guo, X. Teng, and H. Yang, "Surface Patterns of Tetragonal Phase FePt Thin Films from Pt at Fe₂O₃ Core–Shell Nanoparticles Using Combined Langmuir–Blodgett and Soft Lithographic Techniques," *2003 MRS Spring Meeting and Exhibit*, San Francisco, CA, 21–25 April 2003.

S. D. Jacobs, T. Z. Kosci, and K. L. Marshall, "Electro-Optics of Glassy Cholesteric Liquid Crystal Flakes," *NSF Workshop on Fundamental Research Needs in Photonic Materials Synthesis and Processing at the Interface*, Rochester, NY, 28–30 April 2003.

N. L. Bassett, J. B. Oliver, O. V. Gotchev, and J. P. Knauer, "Deposition of Low-Surface-Roughness Iridium for Use in an X-Ray Microscope," *The International Conference on Metallurgical Coatings and Thin Films*, San Diego, CA, 28 April–2 May 2003.

J. B. Oliver and D. Talbot, "Optimization of Deposition Uniformity for Large-Aperture NIF Substrates in a Planetary Rotation System," *46th Annual SVC Technical Conference*, San Francisco, CA, 5–6 May 2003.

The following presentations were made at the 4th Laser Operations Workshop, Aldermaston, United Kingdom, 13–15 May 2003:

D. R. Harding, “Experiences Imploding Cryogenic Targets on OMEGA.”

S. J. Loucks, “Overview of OMEGA Performance.”

S. F. B. Morse, “OMEGA EP Architecture and Linkage to OMEGA.”

L. J. Waxer, “Laser Design Considerations for Optimizing the Performance of OMEGA EP.”

T. Z. Kosc, K. L. Marshall, and S. D. Jacobs, “Polymer Cholesteric Liquid Crystal Flakes for Particle Displays,” SID International Symposium, Seminar, and Exhibition, Baltimore, MD, 18–23 May 2003.

The following presentations were made at Optifab 2003, Rochester, NY, 19–22 May 2003:

J. E. DeGroot, S. D. Jacobs, J. M. Schoen, H. J. Romanofsky, and I. A. Kozhinova, “Magnetorheological Finishing of a Diamond-Turned Poly(Methylmethacrylate) Flat.”

A. E. Marino, J. Hayes, L. L. Gregg, and S. D. Jacobs, “Grain Decoration in Aluminum Oxynitride (ALON) from Polishing on Bound-Abrasive Laps.”

J. A. Randi, J. C. Lambropoulos, S. D. Jacobs, and S. N. Shafir, “Determination of Subsurface Damage in Single Crystalline Optical Materials.”

A. E. Schoeffler, L. L. Gregg, J. M. Schoen, E. M. Fess, M. Hakiel, and S. D. Jacobs, “Pre-Polishing on a CNC Platform with Bound-Abrasive Contour Tools.”

J. L. Sternal, S. N. Shafir, J. A. Randi, L. L. Gregg, and S. D. Jacobs, “Refractive Index Anisotropy in Optics Using a Birefringence Mapper.”

R. Varshneya, J. E. DeGroot, L. L. Gregg, and S. D. Jacobs, “Characterizing Optical Polishing Pitch.”

B. Yaakobi, T. R. Boehly, F. J. Marshall, R. Epstein, D. D. Meyerhofer, B. A. Remington, S. M. Pollaine, and J. J. Rehr, “EXAFS Measurements of Shocked Materials,” 2003 National Synchrotron Light Source Users’ Meeting, Upton, NY, 20–21 May 2003.

W. T. Shmayda, “Recovery of Tritium from Tritiated Pharmaceutical Mixed Wastes for Reuse: A Commercial Reality,” 8th International Symposium on the Synthesis and Applications of Isotopes and Isotopically Labelled Compounds, Boston, MA, 1–5 June 2003.

The following presentations were made at the 15th Target Fabrication Specialists’ Meeting, Glendon Beach, OR, 1–5 June 2003:

E. L. Alfonso, R. Q. Gram, and D. R. Harding, “Modeling Temperature and Pressure Gradients During Cooling of Thin-Walled Cryogenic Targets.”

L. M. Elasky, D. J. Lonobile, W. A. Bittle, D. R. Harding, A. V. Okishev, and J. D. Zuegel, “Implementation and Effects of Closed-Loop Controls on OPO IR Sources for Cryogenic Target Layering.”

V. N. Goncharov, P. W. McKenty, D. D. Meyerhofer, S. Skupsky, T. J. B. Collins, P. B. Radha, and T. C. Sangster, “Advanced Target Designs for the Direct-Drive Inertial Confinement Fusion.”

R. Q. Gram, E. L. Alfonso, and D. R. Harding, “Heat Conduction and Absorption in Condensed Deuterium Layers.”

D. R. Harding, M. D. Wittman, L. M. Elasky, J. Sailor, and E. L. Alfonso, “Status of the Ice-Layering Development Effort on OMEGA.”

A. K. Knight, F.-Y. Tsai, M. J. Bonino, and D. R. Harding, “Status of the Polyimide Target Development Activities at LLE.”

D. D. Meyerhofer, “Progress in Direct-Drive Inertial Confinement Fusion Research at the Laboratory for Laser Energetics” (invited).

W. Seka, A. Warrick, M. D. Wittman, R. S. Craxton, L. M. Elasky, D. R. Harding, R. L. Keck, M. Pandina, and T. G. Brown, "Cryogenic Target Characterization at LLE—A Status Report."

M. D. Wittman, L. M. Elasky, D. R. Harding, W. Seka, and A. Warrick, "Effects of Cooling and Hydrogen-Ice Formation on the Out-of-Roundness of Cryogenic Fuel Capsules."

The following presentations were made at CLEO 2003, Baltimore, MD, 1–6 June 2003:

V. Bagnoud, A. Stout, and J. D. Zuegel, "Independent Spatial Phase and Amplitude Laser Beam Control with a Single Spatial Light Modulator."

J. Bunkenburg, T. J. Kessler, H. Hu, C. Kellogg, and C. Kelly, "Coherent Summation of Holographic Gratings for Pulse Compression Within Petawatt Laser Systems."

C. Dorrer, D. N. Maywar, and T. Lakoba, "Polarization-Mode Dispersion Study of a Circulating Loop."

J. Li, W. R. Donaldson, and T. Y. Hsiang, "Screening Effect in Very Fast Submicron Metal–Semiconductor–Metal Ultraviolet Photodetectors."

J.-R. Park, W. R. Donaldson, and R. Sobolewski, "Measurement for the Time-Resolved Spatial Profile of a Laser."

J. D. Zuegel, V. Bagnoud, I. A. Begishev, M. J. Guardalben, J. Keegan, J. Puth, and L. J. Waxer, "Prototype Front End for a Petawatt Laser System Using Optical Parametric Chirped-Pulse Amplification" (invited).

S. G. Lukishova, A. W. Schmid, A. J. McNamara, R. W. Boyd, and C. R. Stroud, "Demonstration of a Room-Temperature Single-Photon Source: Laser Control of Single Dye Molecule Fluorescence in Photonic-Band-Gap Liquid Crystal Host," QELS 2003, Baltimore, MD, 1–6 June 2003.

The following presentations were made at JOWOG 37, Aldermaston, United Kingdom, 9–13 June 2003:

T. R. Boehly, T. J. B. Collins, E. Vianello, D. Jacobs-Perkins, D. D. Meyerhofer, P. M. Celliers, G. W. Collins, D. G. Hicks, and R. C. Cauble, "Measurements of the D₂ EOS in the Mbar Pressure Range."

B. Yaakobi, D. D. Meyerhofer, T. R. Boehly, F. J. Marshall, D. Salzmann, R. Epstein, B. A. Remington, S. M. Pollaine, and J. J. Rehr, "EXAFS Detection of Laser Shock Heating."

The following presentations were made at the 33rd Anomalous Absorption Conference, Lake Placid, NY, 22–27 June 2003:

R. S. Craxton, "Two-Dimensional *SAGE* Simulations of Polar Direct Drive on the NIF."

J. DeCiantis, B. E. Schwartz, J. A. Frenje, F. H. Séguin, S. Kurebayashi, C. K. Li, R. D. Petrasso, J. A. Delettrez, J. M. Soures, V. Yu. Glebov, V. N. Goncharov, D. D. Meyerhofer, P. B. Radha, S. Roberts, T. C. Sangster, C. Stoeckl, and S. P. Hatchett, "Proton Core Imaging Spectroscopy on OMEGA Implosions."

J. A. Delettrez, S. Skupsky, and P. B. Radha, "Transport of Relativistic Electrons for Modeling Fast Ignition in the 2-D Hydrocode *DRACO*."

R. Epstein, "On the Bell–Plesset Effects: The Effects of Uniform Compression and Geometrical Convergence on the Classical Rayleigh–Taylor Instability."

J. A. Frenje, C. K. Li, F. H. Séguin, J. DeCiantis, J. R. Rygg, S. Kurebayashi, B. E. Schwartz, R. D. Petrasso, J. A. Delettrez, V. Yu. Glebov, D. D. Meyerhofer, T. C. Sangster, J. M. Soures, C. Stoeckl, and S. P. Hatchett, "First Measurement of Shock-Coalescence Timing and ρR Evolution of D³He Implosions at OMEGA."

J. A. Frenje, R. D. Petrasso, C. K. Li, F. H. Séguin, J. DeCiantis, S. Kurebayashi, J. R. Rygg, B. E. Schwartz, J. A. Delettrez, V. Yu. Glebov, D. D. Meyerhofer, T. C. Sangster, C. Stoeckl, J. M. Soures, S. P. Hatchett, S. W. Haan, G. J. Schmid, N. Landen, N. Izumi, and D. Stelter, “A Magnetic Recoil Spectrometer (MRS) for Precise ρR_{fuel} and T_i Measurements of Implosions at OMEGA and the NIF.”

V. Yu. Glebov, C. Stoeckl, S. Roberts, T. C. Sangster, J. A. Frenje, R. D. Petrasso, R. A. Lerche, and R. L. Griffith, “Proton Temporal Diagnostic for ICF Experiments on OMEGA.”

V. N. Goncharov, P. B. Radha, P. W. McKenty, D. D. Meyerhofer, S. Skupsky, T. J. B. Collins, and T. C. Sangster, “Advanced Target Designs for the Direct-Drive Inertial Confinement Fusion.”

S. Kurebayashi, F. H. Séguin, J. A. Frenje, C. K. Li, R. D. Petrasso, J. R. Rygg, B. E. Schwartz, J. DeCiantis, V. Yu. Glebov, J. A. Delettrez, T. C. Sangster, J. M. Soures, S. P. Hatchett, and P. A. Amendt, “Relationship of Secondary Nuclear Production to Implosion Characteristics at OMEGA.”

A. V. Maximov, J. Myatt, W. Seka, and R. W. Short, “Non-linear Propagation of Crossing Laser Beams in Direct-Drive Target Plasmas.”

J. Myatt, A. V. Maximov, and R. W. Short, “Fast-Electron Transport in Dense Plasmas in the Context of Fast-Ignition Studies at LLE.”

J. R. Rygg, F. H. Séguin, C. K. Li, J. A. Frenje, R. D. Petrasso, J. A. Delettrez, V. Yu. Glebov, V. N. Goncharov, R. L. Keck, J. P. Knauer, F. J. Marshall, P. W. McKenty, D. D. Meyerhofer, P. B. Radha, T. C. Sangster, V. A. Smalyuk, J. M. Soures, C. Stoeckl, and S. P. Hatchett, “The Effects of Implosion Asymmetry on Shock Dynamics in OMEGA Direct-Drive Experiments.”

F. H. Séguin, J. R. Rygg, J. A. Frenje, C. K. Li, R. D. Petrasso, J. A. Delettrez, J. M. Soures, V. Yu. Glebov, V. N. Goncharov, J. P. Knauer, D. D. Meyerhofer, T. C. Sangster, R. L. Keck, P. W. McKenty, F. J. Marshall, V. A. Smalyuk, and S. P. Hatchett, “Time Evolution of Areal Density Asymmetries in OMEGA Direct-Drive Implosions.”

W. Seka, H. Baldis, S. Depierreux, R. S. Craxton, S. P. Regan, C. Stoeckl, R. W. Short, A. V. Maximov, J. Myatt, and R. E. Bahr, “Investigation of the Two-Plasmon-Decay Instability Using Thomson Scattering.”

R. W. Short, “Two-Plasmon Decay, Overlapping Beams, and Electron-Acoustic Waves.”

C. Stoeckl, R. E. Bahr, V. Yu. Glebov, A. V. Maximov, J. Myatt, T. C. Sangster, W. Seka, B. Yaakobi, and J. P. Jadeau, “Experimental Scalings for the Two-Plasmon-Decay Instability.”

The following presentations were made at the XI Conference on Laser Optics, St. Petersburg, Russia, 30 June–4 July 2003.

A. V. Okishev, “Highly Stable, All-Solid-State Regenerative Amplifier for the OMEGA ICF Facility.”

A. V. Okishev, W. A. Bittle, R. Boni, W. R. Donaldson, P. A. Jaanimagi, D. Jacobs-Perkins, R. L. Keck, J. H. Kelly, T. J. Kessler, S. F. B. Morse, R. G. Roides, W. Seka, L. J. Waxer, and J. D. Zuegel, “Modern Diagnostics for Large ICF Laser Systems.”

T. R. Boehly, T. J. B. Collins, E. Vianello, D. Jacobs-Perkins, D. D. Meyerhofer, D. G. Hicks, P. M. Celliers, G. W. Collins, S. J. Moon, M. E. Foord, J. H. Eggert, and R. Cauble, “Quartz Equation-of-State (EOS) Measurements at the OMEGA Laser Facility,” 13th APS Topical Conference on Shock Compression of Condensed Materials, Portland OR, 20–25 July 2003.

The following presentations were made at the SPIE 48th Annual Meeting, San Diego, CA, 3–8 August 2003:

J. E. DeGroote, H. J. Romanofsky, I. A. Kozhina, J. M. Schoen, and S. D. Jacobs, “Polishing PMMA and Other Optical Polymers with Magnetorheological Finishing.”

L. L. Gregg, A. E. Marino, and S. D. Jacobs, “Grain Decoration in Aluminum Oxynitride (ALON) from Polishing on Bound-Abrasive Laps.”

P. A. Jaanimagi, "Breaking the 100-fs Barrier with a Streak Camera."

K. L. Marshall, B. Klehn, B. Watson, and D. W. Griffin, "Recent Advances in the Development of Phase-Shifting Liquid Crystal Interferometers for Visible and Near IR-Applications."

K. L. Marshall, B. Schudel, and I. A. Lipka, "Transition Metal Dithiolene Complexes as Near-IR Dyes for Liquid Crystal Device Applications" (invited).

T. Z. Kosc, K. L. Marshall, and S. D. Jacobs, "Polymer Cholesteric Liquid Crystal Flakes for Particle Displays: Impact of Flake Geometry and Materials Processing on Field-Induced Motion in a Fluid Host," XII International Materials Research Conference, Cancun, Mexico, 17–21 August 2003 (invited).

The following presentations were made at the Third International Conference on Inertial Fusion Sciences and Applications, Monterey, CA, 7–12 September 2003:

V. Bagnoud, I. A. Begishev, M. J. Guardalben, J. Keegan, J. Puth, L. J. Waxer, and J. D. Zuegel, "Optical Parametric Chirped-Pulse Amplifier as the Front End for the OMEGA EP Laser Chain."

T. R. Boehly, T. J. B. Collins, E. Vianello, D. Jacobs-Perkins, D. D. Meyerhofer, D. G. Hicks, P. M. Celliers, G. W. Collins, S. J. Moon, M. E. Foord, J. H. Eggert, and R. Cauble, "Deuterium Equation-of-State Measurements Using Laser-Driven Shocks."

T. J. B. Collins, S. Skupsky, V. N. Goncharov, R. Betti, P. W. McKenty, P. B. Radha, R. Epstein, A. Poludnenko, A. Frank, and S. Mitran, "High-Gain, Direct-Drive Foam Target Designs for the National Ignition Facility."

D. R. Harding, E. L. Alfonso, L. M. Elasky, L. S. Iwan, J. Sailer, W. Seka, A. Warrick, and M. D. Wittman, "Formation of Deuterium-Ice Layers in OMEGA Targets."

T. J. Kessler, J. Bunkenburg, H. Huang, A. Kozlov, C. Kelly, and D. D. Meyerhofer, "The Coherent Addition of Gratings for Pulse Compression in High-Energy Laser Systems."

C. K. Li, F. H. Séguin, J. A. Frenje, R. D. Petrasso, J. A. Delettrez, R. L. Keck, J. M. Soures, P. W. McKenty, F. J. Marshall, V. N. Goncharov, J. P. Knauer, D. D. Meyerhofer, P. B. Radha, S. P. Regan, T. C. Sangster, and W. Seka, " ρR Asymmetry in the Spherical Implosions of Inertial Confinement Fusion."

R. L. McCrory, "Progress in Inertial Confinement Fusion Research in the United States" (keynote speaker).

P. W. McKenty, T. C. Sangster, J. A. Delettrez, R. Epstein, V. Yu. Glebov, D. R. Harding, J. P. Knauer, R. L. Keck, S. J. Loucks, L. D. Lund, R. L. McCrory, F. J. Marshall, D. D. Meyerhofer, S. F. B. Morse, S. P. Regan, P. B. Radha, S. Roberts, W. Seka, S. Skupsky, V. A. Smalyuk, C. Sorce, J. M. Soures, J. A. Frenje, C. K. Li, R. D. Petrasso, F. H. Séguin, K. A. Fletcher, S. Padalino, C. Freeman, N. Izumi, J. A. Koch, R. A. Lerche, M. J. Moran, T. W. Phillips, and G. J. Schmid, "Direct-Drive Cryogenic Target Implosion Performance on OMEGA."

T. C. Sangster, "Bridging the Gap: Ignition Diagnostics for the National Ignition Facility."

S. Skupsky, R. Betti, T. J. B. Collins, V. N. Goncharov, J. A. Marozas, P. W. McKenty, P. B. Radha, T. R. Boehly, J. P. Knauer, F. J. Marshall, J. P. Harding, J. D. Kilkenny, D. D. Meyerhofer, T. C. Sangster, and R. L. McCrory, "Advanced Direct-Drive Target Designs for the NIF."

T. Z. Kosc, K. L. Marshall, and S. D. Jacobs, "Polymer Cholesteric Liquid Crystal Flake Particle Displays Utilizing Maxwell–Wagner Polarization Effects for Switching," 23rd International Display Research Conference, Phoenix, AZ, 15–18 September 2003.

UNIVERSITY OF
ROCHESTER